Gecombineerde experimenteel-numerieke studie naar de ultrasone polaire scan voor inspectie en karakterisering van (beschadigde) anisotrope materialen

Combined Experimental-Numerical Study to the Ultrasonic Polar Scan for Inspection and Characterization of (Damaged) Anisotropic Materials

Mathias Kersemans

Promotoren: prof. dr. ir. W. Van Paepegem, prof. dr. ir. J. Degrieck
Proefschrift ingediend tot het behalen van de graad van
Doctor in de Ingenieurswetenschappen: Toegepaste Natuurkunde

Vakgroep Toegepaste Materiaalwetenschappen
Voorzitter: prof. dr. ir. J. Degrieck
Faculteit Ingenieurswetenschappen en Architectuur
Academiejaar 2014 - 2015

UNIVERSITEIT GENT

ISBN 978-90-8578-739-6
NUR 924, 950
Wettelijk depot: D/2014/10.500/85

Promotors:

Prof. dr. ir. Wim Van Paepegem
Ghent University
Faculty of Engineering and Architecture

Prof. dr. ir. Joris Degrieck
Ghent University
Faculty of Engineering and Architecture

Examination Committee:

Prof. Jan Van Campenhout (Chair)	Ghent University, Belgium
Prof. Wim Van Paepegem (Promotor)	Ghent University, Belgium
Prof. Joris Degrieck (Promotor)	Ghent University, Belgium
Prof. Abigaïl Swillens (Secretary)	Ghent University, Belgium
Prof. Daniël De Zutter	Ghent University, Belgium
Prof. Koen Van Den Abeele	KU Leuven, Belgium
Prof. Lincy Pyl	Vrije Universiteit Brussel, Belgium
Prof. Guillermo Rus Carlborg	Universidad de Granada, Spain
Prof. Rymantas Jonas Kažys	Kaunas University of Technology, Lithuania

Research Institute:

Ghent University
Faculty of Engineering and Architecture
Department of Materials Science and Engineering
Technologiepark-Zwijnaarde 903
B-9052 Zwijnaarde
Belgium
Tel. +32 (0)9 331 04 25
Fax. +32 (0)9 264 58 33
Mathias.Kersemans@UGent.be
MathiasKersemans@hotmail.com

This research is funded by the Funds for Scientific Research: grant G012010N (FWO-Vlaanderen, Fonds voor Wetenschappelijk Onderzoek in Vlaanderen)

Acknowledgements

This thesis could not be produced without the help of several people, each of them contributing in their own way. Therefore, they deserve a small word of appreciation and recognition. As a full list of contributing people would substantially lengthen the PhD thesis, only a limited number of people are thanked.

First of all, I am extremely thankful to my promoters, Prof. dr. ir. Wim Van Paepegem and Prof. dr. ir. Joris Degrieck. Without their continuous help and guidance, both scientifically and personally, this work would not have been possible. I also would like to thank them for the very wide scientific freedom they gave me during my PhD research. It has been an honor to work with them.

I also wish to express my thanks to Prof. dr. Koen Van Den Abeele from KU Leuven for his thorough questioning during several review meetings, often leading to new insights. Prof. dr. ir Lincy Pyl, Prof. dr. ir. Hugo Sol and Filip Zastavnik from Vrije Universiteit Brussel are thanked for their encouragement and advice during scientific research meetings. Furthermore, I would like to express my gratitude to the jury members for reading and evaluating this dissertation.

My research was sponsored by FWO Flanders (Fonds voor Wetenschappelijk Onderzoek in Vlaanderen) through grant number G012010N. The financial support of the FWO is greatly acknowledged.

Many thanks to my master thesis students for helping me during my research: Gabriele Chiesura, Caroline Breemersch, and Maxim Solomaniuck.

The experimental work presented in this dissertation could not have been done without the help of two key persons: Lucske and Pascalleke. Whenever I needed help with the experimental setup, they (almost) always assisted me with a big smile. Based on my extensive sketches and drawings, they succeeded each time in finding an innovative solution to improve and to further fine-tune the setup.

The various numerical models have been implemented with the kind help of several persons, in particular Nicolas Lammens and Arvid Martens. They often analyzed and reviewed my numerical implementations. After a small and polite laugh, they often replaced pages of my programming by a single line of code.

I wish also to express my thanks to my (ex-)colleagues for a nice cooperation as well as their support during my PhD research. Thanks to Joachim for installing multiple times a sophisticated vapor-extractor in my

shower, to Joren for the many frisbee sessions, to Sam and Shredder for bearing the Allegria song for 4 years, to Frederic for the 'frazer' and to Bruno for making me a wealthy man. Also the support of Pieterke and Nicolleke is well appreciated. They both non-selfishly shared the newest gossips, rumors and funny stories with me. They both excelled in their commitment for keeping me up-to-date. At present, Pieterke even continues his commitment at our new workplace.
I would also like to thank my friends for their support. Without a doubt they wondered why I was so often late at an appointment or simply absent during the last few years. Well, I have briefly written the answer in the next few pages. So sit down and read it yourself.
To my family I am very thankful for their dedication and inspiration that enabled me to reach this milestone in my life.
And finally, my words will fail to express my deepest heartfelt thanks to my girlfriend Kristine, for all what she did, and still does, to help me be at this position and for her continuous support and encouragement.
Thanks!

Table of Contents

English Summary

Composite materials are manufactured by combining two (or more) materials, in view of exploiting the benefits of both, and as such to outperform classical materials. By clever choice of the basic constituents, one can tune the material properties in order to meet a certain functionality. For example, primary components in aerospace structures are nowadays often built with composites because of their excellent strength-to-weight ratio and their good structural performance. These advantages however are on the expense of a much more involved mechanical response as composites are anisotropic of nature, thus setting several challenges to material engineers and scientists. This becomes even more valid considering that, contrary to traditional materials, composites are susceptible to various microscopic damage mechanisms which potentially result in a local and directional reduction of the stiffness at the macro level. Hence, evaluation and monitoring of the local stiffness properties of a composite structure is of utmost importance to maintain structural integrity and to assure safety. Although a variety of characterization and inspection techniques (optical, modal analysis, ultrasound, eddy current, etcetera) are already available in literature, each of them has its own limited capability and applicability. Hence, full characterization/inspection of a (damaged) composite structure leaves us basically to one option: combine the results of the various inspection techniques to obtain a patchwork quilt of data. This however should not be the way of working in modern times.

The ultrasonic polar scan technique, which was originally introduced in the 1980's as a sophisticated inspection methodology, insonifies a predefined material spot with pulsed ultrasound from as many oblique incidence angles as possible, while keeping the distance between transducer and sample fixed. Simply recording the transmitted or reflected pulse amplitudes, and mapping them in a polar representation yields an ultrasonic polar scan image in which characteristics patterns, linked to bulk wave propagation, emerge. The method produced such intriguing images that it was said to provide a unique fingerprint of the mechanical stiffness of the insonified material spot. During the last thirty years, several research groups have explored the ultrasonic polar scan technique both experimentally and numerically. Unfortunately, little progress has been made concerning the experimenting, the interpretation and the analysis of an ultrasonic polar scan. As such, the true potential of the technique has not yet been identified, despite its promising capabilities for non-destructive testing and material science in general. This

immediately defines the objective of the current PhD research: perform an in-depth experimental and numerical investigation to the ultrasonic polar scan technique, and explore its capabilities as well as identify its opportunities for the inspection and characterization of (damaged) composite materials.

This dissertation consists of four major parts. Part I is dedicated to the investigation of the ultrasonic polar scan in its original implementation (transmission regime). Part II deals with a modified version in which the backscattered signal, instead of the transmitted signal, is analyzed in view of gaining additional knowledge about the insonified material. Part III extends the analysis to composite materials which have been damaged by applying different load conditions. Finally, as ultrasound is not detectable by the human senses, the global comprehension of an ultrasonic wave phenomenon is often a difficult task. Part IV discusses contributions to different full field ultrasound visualization techniques, and provides an investigation of several ultrasound phenomena which would otherwise not be understood easily.

Part I starts with an overview of the historical development of the pulsed ultrasonic polar scan, and identifies the missing pieces to become a first-class successor of the classical non-destructive testing methods. In view of bringing the technique to the next level, a mixed experimental-numerical approach should be adopted. Therefore, a fully automated 5 axes high-precision scanner has been built in order to obtain accurate, and more importantly, reproducible experiments. The implemented setup unmasked several pitfalls in the experimental recording of ultrasonic polar scans which have been overlooked or neglected till now. A high-level numerical model has been implemented in Maple and MATLAB to simulate ultrasonic polar scans for immersed multilayered materials with arbitrary viscoelastic anisotropy. Coupling high-quality experiments to true-to-nature simulation results by means of an inverse system identification procedure based on a genetic algorithm, the long standing conjecture of the ultrasonic polar scan as a fingerprinting method for materials has been successfully tackled. The inversion procedure has been applied to both metallic and composite materials. In addition, it is demonstrated how to extract 'hidden' information in an ultrasonic polar scan image by using advanced post-processing techniques. Finally, the ultrasonic polar scan methodology has been extended to the use of quasi-harmonic sound bursts, rather than ultrasonic pulses. It is demonstrated that the nature of the ultrasonic polar scan image

completely changes as the underlying physics is no longer dominated by bulk wave propagation but rather by Lamb wave propagation, although not in a one-to-one relationship. As such, the harmonic version of the ultrasonic polar scan offers an alternative fingerprint of the insonified material spot from which the elasticity tensor can be extracted. As a harmonic signal is defined by its amplitude and phase, the concept of the phase-based ultrasonic polar scan is also introduced.

Traditionally, the ultrasonic polar scan has been employed in transmission or reflection. However, it was observed during many experiments that a small amount of ultrasonic energy is backscattered to the emitter, even for large oblique incident angles. Recording of the backscattered signal for the upper hemisphere yields an ultrasonic backscatter polar scan, whose nature is described in Part II of this dissertation. Whilst the ultrasonic polar scan yields fingerprints of the mechanical material properties, the ultrasonic backscatter polar scan provides a blueprint of (hidden) geometrical features. This has been explicitly demonstrated for various geometrical damage features and inhomogeneities. It is further demonstrated that the ultrasonic backscatter polar scan is able to map an imperfect, but periodic multidirectional (sub)surface structure with high accuracy. The backscatter methodology is further extended to the absolute measurement of a local 3D strain field by exploiting the wave interaction in Bragg geometry with a deterministic surface roughness. Results have been presented for cold-rolled DC06 steel considering strain fields of 2% up to 35%, showing excellent agreement with the results of conventional strain measurement techniques.

In Part III, the developed methodologies in Part I and Part II are applied to composite materials which were subjected to a variety of loading conditions in order to induce damage features. The effect of the presence of a delamination on the ultrasonic polar scan image is investigated. In contrast with the pulsed version, the harmonic version of the ultrasonic polar scan displays a high sensitivity to the presence as well as the location of a delamination. The ultrasonic (backscatter) polar scan methodology is further applied on several composites which were damaged by quasi-static loading as well as by high-cycle fatigue loading. It is shown that the considered loadings mainly result in local and directional reduction of stiffness properties as well as in large fiber distortions. For example, a carbon fabric reinforced PPS sample showed a maximum fiber distortion of 25° when

fatigued in shear, while a reduction of 12.8% of the stiffness (along the loading direction) was found when fatigued in tension.

In the last Part IV, an in-depth investigation is performed onto the leakage and the scattering phenomena during the bounded beam insonification at a Lamb angle near the plate end. Acousto-optic schlieren imaging has been applied. Besides the traditional schlieren imaging in real space, the methodology has been extended to the imaging of ultrasonic fields in spatial frequency domain. The obtained results indicate that the Lamb wave leakage takes place near the scatterer, and that a large part of the measurement zone gets 'polluted' by the leaking fields of mode-converted Lamb waves. These observations are important to avoid misinterpretation of ultrasonic test data due to edge effects. The obtained acousto-optic schlieren results are fully supported by coupled fluid-structure interaction finite element simulations. With the same investigation tools, the ultrasonic analogue of the optical Talbot effect, which is a self-imaging or lens-less imaging effect, has been demonstrated. The obtained results reveal that the ultrasonic Talbot effect is actually a mixture of an amplitude-based and a phase-based Talbot effect, which is in sharp contrast to the classical optical Talbot effect. Finally, a new visualization technique is introduced with lots of potential: elastico-mechanoluminescent visualization of ultrasonic wave phenomena. Results are presented for the elastico-mechanoluminescent mapping of the 3D radiation field of an ultrasonic transducer.

Nederlandstalige Samenvatting

Composieten bestaan uit twee (of meer) materialen waarbij de voordelige eigenschappen van beide worden benut, om alzo het structureel gedrag van traditionele materialen te overtreffen. Door intelligente keuze van de basisbouwstenen kan men de materiaaleigenschappen afstemmen op een bepaalde functionaliteit. Bijvoorbeeld, voor kritische onderdelen in luchtvaartstructuren wordt meer en meer gebruik gemaakt van composietmaterialen omwille van hun excellente sterkte-gewichtverhouding en hun uitstekend structureel gedrag. Deze voordelen zijn ten koste van een meer complexe mechanische respons, omdat composieten anisotroop zijn van nature. Dit brengt verschillende uitdagingen met zich mee voor materiaalingenieurs en wetenschappers. Bovendien zijn composieten, in tegenstelling tot klassieke materialen, gevoelig aan verschillende microscopische schadefenomenen die, op het macroscopische niveau, accumuleren tot lokale en directionele stijfheidsdegradaties. Het is dus duidelijk dat evaluatie en opvolging van lokale materiaaleigenschappen zeer belangrijk is om zowel de structurele integriteit te handhaven als ook de veiligheid te verzekeren. Hoewel er reeds een verscheidenheid aan karakteriserings- en inspectietechnieken (optisch, modale analyse, ultrageluid, wervelstroom, enzoverder) bestaan, heeft elke techniek bepaalde limitaties in toepasbaarheid en uitvoerbaarheid. Voor de volledige karakterisering van een (beschadigde) composiet structuur blijft er dus slechts één optie open: combineren van de resultaten van de verschillende bestaande technieken, zodat een soort lappendeken van verschillende gegevens wordt verkregen. Dit zou echter niet de manier van werken mogen zijn in de huidige moderne maatschappij.

De ultrasone polaire scan, in de vroege jaren 1980 geïntroduceerd als een gesofisticeerde inspectiemethode, bestraalt een welbepaalde materiaalzone met gepulst ultrageluid vanuit zoveel mogelijke schuine invalshoeken, en dit voor een vaste afstand tussen de ultrasone emitter en het onderzochte proefstuk. Een polaire scan afbeelding wordt simpelweg bereikt door de doorgelaten of de gereflecteerde pulsamplitudes te registreren, en deze weer te geven in polaire coördinaten. Typisch komen karakteristieke patronen te voorschijn die gelinkt zijn aan de stimulatiecondities en propagatie-eigenschappen van bulkgolven. De polaire scan produceerde zulke intrigerende afbeeldingen, dat men zelfs beweerde dat de methode een unieke vingerafdruk van de mechanische stijfheid van de bestraalde materiaalzone oplevert. Gedurende de laatste 30 jaar hebben verscheidene

onderzoeksgroepen de ultrasone polaire scan techniek zowel experimenteel als numeriek geëxploreerd. Tot op heden is er helaas slechts weinig vooruitgang geboekt betreffende de interpretatie en de analyse van een ultrasone polaire scan. Zodoende is het ware potentieel van de techniek nog niet geïdentificeerd, ondanks de veelbelovende mogelijkheden voor niet-destructief testen en materiaalwetenschap in het algemeen. Dit definieert onmiddellijk de doelstelling van dit doctoraatsonderzoek: een diepgaand experimenteel en numeriek onderzoek naar de polaire scan methode, en de verschillende mogelijkheden en opportuniteiten identificeren voor de inspectie en karakterisering van (beschadigde) composietmaterialen.

De thesis bestaat uit vier grote delen. In deel I wordt de polaire scan onderzocht en geanalyseerd in zijn originele implementatie (transmissieregime). Deel II behandelt een aangepaste versie van de ultrasone polaire scan. In plaats van het transmissiesignaal, wordt het teruggekaatst signaal geanalyseerd met het oog op het verkrijgen van extra informatie over het bestraalde materiaal. In deel III wordt de analyse uitgebreid naar de inspectie en karakterisering van composieten dewelke beschadigd werden door het aanleggen van verschillende mechanische belastingen. Tenslotte, omdat ultrageluid niet waarneembaar is door de menselijke zintuigen, is het globale begrip van een ultrasoon fenomeen vaak moeilijk te bevatten. Deel IV bespreekt verschillende bijdragen tot enkele visualisatietechnieken, en past deze technieken toe bij het onderzoeken van verschillende ultrasone fenomenen.

Deel I start met een overzicht van de historische evolutie van de ultrasone polaire scan methode. De ontbrekende puzzelstukken, om een eersteklas opvolger voor de klassieke niet-destructieve methoden te worden, zijn geïdentificeerd. In principe zou de techniek moeten evolueren naar een gecombineerd experimenteel-numerieke methodologie. Wat betreft het experimentele gedeelte is een volledig geautomatiseerde scanner (5 vrijheidsgraden) met hoge nauwkeurigheid gebouwd. Hiermee kunnen accurate, en belangrijker, reproduceerbare experimenten uitgevoerd worden. De geïmplementeerde opstelling heeft verschillende mogelijke valkuilen blootgelegd die kunnen optreden tijdens de uitvoering van polaire scan experimenten. Sommige van de geïdentificeerde valkuilen werden tot op de dag van vandaag ofwel over het hoofd gezien ofwel genegeerd. Een veelzijdig numeriek model is geïmplementeerd in Maple en MATLAB om polaire scans te simuleren voor ondergedompelde gelaagde materialen met

willekeurige viscoelastische anisotropie. Dankzij de koppeling van de kwaliteitsvolle experimenten met de hoogwaardige numerieke resultaten door middel van een inverse procedure, die gebaseerd is op een genetisch algoritme, is het langdurige vermoeden dat de polaire scan vingerafdrukken van materialen oplevert succesvol bewezen. De systeemidentificatie-procedure is toegepast op zowel metallische als composietmaterialen. Daarnaast is ook gedemonstreerd hoe 'verborgen' informatie uit een ultrasone polaire scan kan worden gehaald met behulp van geavanceerde verwerkingsprocedures. Tenslotte is de polaire scan techniek uitgebreid met het gebruik van quasi-harmonisch ultrageluid, in plaats van gepulst ultrageluid. Het is aangetoond dat het uitzicht van de polaire scan afbeelding volledig verandert, en dat deze verandering moet worden toegeschreven aan het feit dat niet langer de propagatie van bulkgolven, maar de propagatie van Lamb golven het dominerend onderliggend fysisch mechanisme is. Bijgevolg biedt de harmonische versie van de ultrasone polaire scan een alternatieve vingerafdruk van de bestraalde materiaalzone, waaruit eveneens materiaaleigenschappen kunnen bepaald worden. Aangezien een harmonisch signaal beschreven wordt door een amplitude en een fase, is de analyse uitgebreid naar de fase wat resulteert in de conceptuele introductie van de fase-gebaseerde polaire scan.

Traditioneel wordt de ultrasone polaire scan gebruikt in transmissie of reflectie. Tijdens de vele uitgevoerde experimenten is het echter geobserveerd dat een klein deel van de ultrasone energie wordt teruggekaatst naar de emitter, zelfs voor zeer schuine invalshoeken. Opnemen van dit teruggekaatst signaal voor het bovenste halfrond leidt tot de ultrasone backscatter polaire scan. Deze methode in detail beschreven wordt in Deel II. Waar de ultrasone polaire scan een vingerafdruk genereert van elastische materiaaleigenschappen, genereert de ultrasone backscatter polaire scan een blauwdruk voor (inwendige) geometrische karakteristieken van het bestraalde specimen. Dit is expliciet aangetoond voor verschillende geometrie-gerelateerde materiaalbeschadigingen en inhomogeniteiten. Het is voorts aangetoond dat de ultrasone backscatter polaire scan een imperfect, maar periodiek multidirectionele oppervlaktestructuur (die mogelijks inwendig aanwezig is) in kaart kan brengen. De backscatterimplementatie is verder uitgebreid zodat een lokaal 3D rekveld kan worden opgemeten door het analyseren in Bragg-geometrie van de interactie van ultrageluid met een deterministische oppervlakteruwheid. Resultaten worden getoond voor koud-gewalst DC06 staal waarin een rekveld gaande van 2% tot 35% werd

aangebracht. Uitstekende overeenkomst is bereikt met de resultaten van conventionele rekveldmeettechnieken.

In Deel III worden de ontwikkelde methodes uit Deel I en Deel II toegepast op composiet materialen waarin verscheidene types van beschadigingen zijn geïnduceerd door het opleggen van verschillende mechanische belastingen. Het effect van de aanwezigheid van een delaminatie op de polaire scan afbeelding is onderzocht voor verscheidene dunne composieten. In tegenstelling tot de gepulste versie is de harmonische versie van de polaire scan zeer gevoelig aan de aanwezigheid, alsook de exacte locatie van een delaminatie. De ultrasone (backscatter) polaire scan is verder ook toegepast op verscheidene composieten die beschadigd werden door zowel quasi-statische als dynamische belasting. Het is aangetoond dat de beschouwde belastingen hoofdzakelijk resulteren in een lokale en directionele reductie van stijfheid enerzijds en in grote distorsie van vezeloriëntaties anderzijds. Bijvoorbeeld, een carbonweefsel versterkt PPS proefstuk vertoonde een maximale vezeldistorsie van 25° na vermoeiing in afschuiving, terwijl een stijfheidsreductie van 12.8% (langs de belastingsrichting) is gevonden wanneer vermoeiing in trekbelasting plaatsvond.

In het laatste Deel IV is een diepgaand onderzoek uitgevoerd naar de verstrooiingsfenomenen die optreden bij het bestralen van een plaatuiteinde met een begrensde ultrasoonbundel onder een Lambhoek. Voor dit onderzoek werd de acousto-optische schlieren visualisatietechniek gebruikt. Behalve de traditionele schlieren visualisatie in werkelijke ruimte, is de methode uitgebreid naar de visualisatie van ultrageluid in het ruimtelijk frequentiedomein. De verkregen resultaten tonen aan dat verstrooiing plaatsvindt in de nabijheid van de plaatuiteinde, en dat een groot deel van het meetgebied wordt 'vervuild' door lekkende velden van verschillende mode-geconverteerde Lamb golven. Deze observaties zijn van groot belang om misinterpretatie van ultrasone data, ten gevolge van randeffecten, te vermijden. De verkregen acousto-optische schlieren resultaten zijn volledig ondersteund door gekoppelde vloeistof-structuurinteractie eindige elementen simulaties. Met dezelfde onderzoekstechnieken is een ultrasone versie van het optische Talbot effect, dat een lensloos zelf-afbeeldingseffect is, gedemonstreerd. De resultaten tonen aan dat het ultrasoon Talbot effect eigenlijk een mengeling van een amplitude-gebaseerd en een fase-gebaseerd Talbot effect is, wat in duidelijk contrast staat met het klassieke optische Talbot effect. Tenslotte is een nieuwe veel belovende techniek, op basis van

elastico-mechanoluminescentie, geïntroduceerd voor visualisatie van ultrageluid. Het 3D radiatieveld van een ultrasone transducer is hiermee in kaart gebracht.

Chapter 1

Introduction

Some engineering applications where the use of composite materials is indispensable. (Figures reproduced from references [1-4]).

Overview

This chapter provides a general overview of the underlying work. A short background is provided in order to identify the objectives and to situate the research. The structure of the work is given, together with a short description of each chapter. Finally some of the innovative aspects have been shortly listed.

1. 1. Background

At present fiber reinforced plastics, so-called composites, are gaining a lot of popularity in a variety of engineering branches. Figure 1-1 shows the evolution of the carbon fiber market in the period 1970-2015.

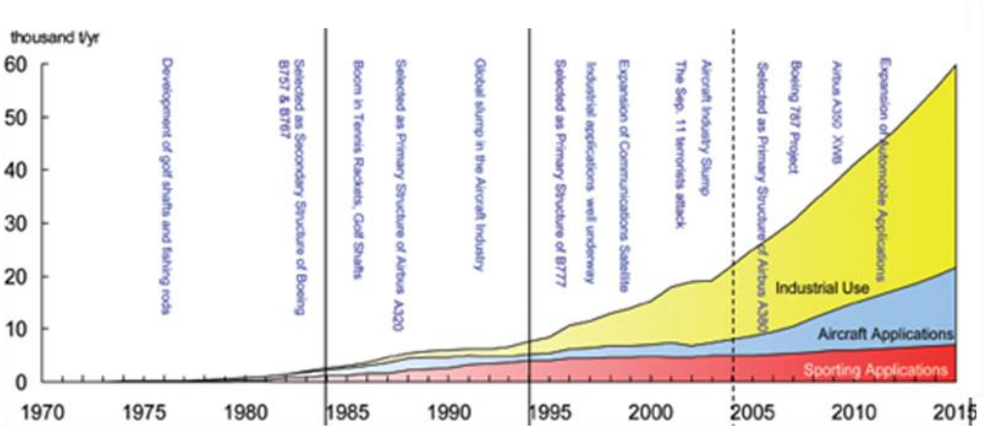

Figure 1-1: Evolution of the carbon fiber market (figure reproduced from [5]).

Basically, a composite material is manufactured by combining two materials in view of exploiting the benefits of both, and as such to outperform classical materials. In general, one usually takes a polymer matrix in which reinforcement fibers are inserted along a predefined orientation (see Figure 1-2).

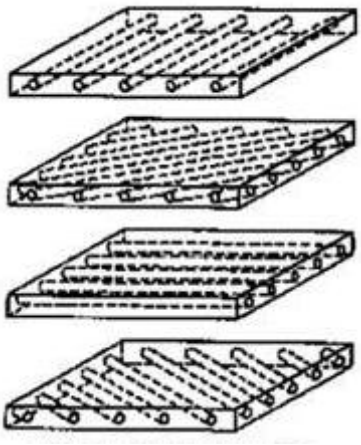

Figure 1-2: Typical structure of composite material: matrix reinforced with high strength fibers.

This is equivalent to reinforced concrete, though on a smaller scale. The type, the volume fraction and the orientation of the reinforcement fibers can be fine-tuned in order to meet a designed functionality. For example, glass fiber composites are very popular in the wind energy industry because of their excellent fatigue strength. The use of high-strength carbon fibers on the other hand typically results in a composite having a high strength-to-weight ratio, and is therefore mostly employed for aerospace applications as it leads to a more economic fuel consumption. Apart from environmental considerations, this advantage cannot be underestimated considering the price evolution of jet fuel (see Figure 1-3).

Figure 1-3: Evolution of the price for jet fuel.

Obviously, the mechanics of a composite becomes much more involved as it is mechanically anisotropic of nature, setting several challenges to material engineers and scientists. This becomes even more valid considering that, contrary to conventional materials, composites are susceptible to various microscopic damage mechanisms which potentially result in a local and directional reduction of the stiffness at the macro level. Hence, evaluation and monitoring of the local anisotropic stiffness of a composite structure is of utmost importance to assure the structural integrity and safety. As a further complication, the inspection should be done in a non-destructive and single-sided way as the backside of the structure is often inaccessible.

Although a variety of characterization and inspection techniques (optical, modal analysis, ultrasound, eddy current, etcetera) are already available in literature, each of them has its own limited capability while most techniques can only be applied under specific conditions. Hence, full characterization/inspection of a (damaged) composite structure leaves us basically to one option: combine the results of the various inspection techniques to obtain a patchwork quilt of data. This however should not be the way of working in modern times.

1. 2. Objectives

The ultrasonic polar scan technique was originally introduced by Vandreumel and Speijer in the 1980's as a sophisticated inspection methodology [6] (see schematic in Figure 1-4a). The ultrasonic polar scan method insonifies a predefined material spot with pulsed ultrasound from as many oblique incidence angles $\psi(\varphi,\theta)$ as possible, while keeping the distance between transducer and sample fixed. Simply recording the transmitted or reflected pulse amplitudes, and mapping them in a polar representation yields an ultrasonic polar scan image (see Figure 1-4b). The method produced such intriguing patterns that it was said to provide a unique fingerprint of the mechanical stiffness of the insonified material spot.

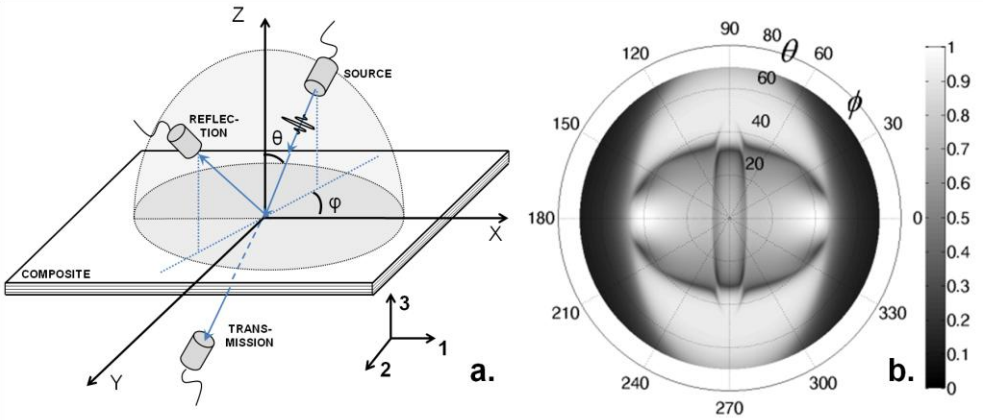

Figure 1-4: Schematic of ultrasonic polar scan (a) and a state-of-the-art ultrasonic polar scan simulation for a carbon fiber composite (b).

During the last thirty years several research groups explored the ultrasonic polar scan technique both experimentally and numerically. Unfortunately, little progress has been made concerning the experimenting, the interpretation and the analysis of an ultrasonic polar scan. As such, the true potential of the technique has not yet been identified, despite its promising capabilities for nondestructive testing and material science in general. This immediately defines the objective of the current PhD research: perform an in-depth experimental and numerical investigation to the ultrasonic polar scan technique, and explore its capabilities as well as identify its opportunities for the inspection and characterization of (composite) materials.

1. 3. Structure of the Dissertation

This dissertation consists of four major parts. Part I is dedicated to the investigation of the ultrasonic polar scan in its original implementation (transmission regime). Part II deals with a modified version in which the backscattered signal, instead of the transmitted signal, is analyzed in view of gaining additional knowledge about the insonified material. Part III extends the analysis to composite materials which have been damaged by applying different load conditions. Finally, as ultrasound is not detectable by the human eye, the global comprehension of an ultrasonic wave phenomenon is often a difficult task. Part IV discusses contributions to different full field visualization techniques, and provides an investigation of several ultrasound

phenomena which would not be understood easily without such visualization techniques. In the following, the subject of each chapter of this dissertation is shortly discussed.

Part I: Ultrasonic Polar Scan

Chapter 2 starts with a literature review on nondestructive testing and characterization techniques, with special focus to the application of ultrasound on composite materials. In addition, an overview of the historical development of the pulsed ultrasonic polar scan, as well as the main achievements at the time when this research started, is given. The missing pieces to become a first-class successor of the classical non-destructive testing methods are identified.

A fully automated 5 axes high-precision scanner has been built in order to obtain accurate and more importantly reproducible experiments. The main features of the constructed scanner are shortly discussed in Chapter 3. An overview is given to various important experimental conditions. Finally, high-quality UPS recordings are shown for different classes of materials, ranging from isotropic metals, over transversal isotropic composites, to orthotropic cross-ply hybrid composites.

In Chapter 4, a numerical modeling technique for the simulation of pulsed ultrasonic polar scans for immersed multilayered materials with arbitrary viscoelastic anisotropy is discussed. The model is based on the recently developed recursive stiffness matrix method and has been implemented in MATLAB. Regarding the computational efficiency, the here implemented recursive stiffness matrix method outperforms the global matrix simulation model which can be already found in literature. In view of getting to a mixed experimental-numerical methodology, this advantage cannot be underrated.

Chapter 5 discusses a set of pitfalls for the experimental recording of ultrasonic polar scans. These pitfalls have been gradually identified through extensive experimenting. Some of the discussed pitfalls have been overlooked for more than 15 years.

Chapter 6 presents an overview how to extract 'hidden' information in an ultrasonic polar scan experiment. As such, the (i) slowness curves, (ii) phase

velocity profiles, (iii) critical angles, (iv) walk-off angles and (v) energy velocity profiles of the bulk waves have been successfully extracted for both isotropic and orthotropic materials. In addition, a numerical and experimental investigation to the role of the immersion liquid as a lens for the ultrasonic polar scan result is performed. This lensing effect permits to zoom in/out on the results, hence broadening the class of materials which can be inspected by the technique.

In Chapter 7, the link is made between experiment and simulation in order to investigate the long standing hypothesis that the ultrasonic polar scan provides a unique fingerprint of the underlying mechanical elasticity tensor at the insonified material spot. For this, an inverse modeling technique on the basis of a genetic optimization scheme has been implemented. It is found that the ultrasonic polar scan indeed does provide a unique fingerprint of the mechanical elasticity tensor, though in a slightly different way as was originally conjectured. The system identification procedure has been successfully applied for isotropic metals and orthotropic composites.

The ultrasonic polar scan has been operated up to now with pulsed ultrasound (Pulsed Ultrasonic Polar Scan: P-UPS). In Chapter 8, a harmonic version of the technique is introduced and investigated (Harmonic Ultrasonic Polar Scan: H-UPS). It is shown that the nature of the fingerprint changes, owing to the fact that not bulk waves as in the pulsed version, but Lamb waves become dominant. As a harmonic signal is defined by its amplitude and phase, the concept of the phase polar scan is introduced.

Part II: Ultrasonic Backscatter Polar Scan

Changing the operational modus from transmission (or reflection) to backscatter yields an ultrasonic backscatter polar scan. This method employs a single transducer which is operated as both emitter and receiver. Chapter 9 describes a pulsed version of the ultrasonic backscatter polar scan and identifies several applications in the field of nondestructive testing which cannot be characterized by means of the conventional polar scan implementation in transmission or reflection.

In Chapter 10, the backscatter principle is exploited for the characterization of multidirectional hidden surface corrugations. Different backscatter

implementations have been considered, the analysis has been performed in time domain as well as in frequency domain. The obtained results show the excellent feasibility to locally map an imperfect, but periodic multidirectional surface structure with high accuracy.

At last, an ultrasonic strain gauge has been proposed in Chapter 11 on the basis of backscattered signals. The developed ultrasonic strain gauge exploits the deterministic surface roughness of a sample to extract the local 3D strain field. Results have been presented for cold-rolled DC06 steel considering strain fields of 2% up to 35%, showing good agreement with the results of several conventional strain gauge techniques.

Part III: Ultrasonic (Backscatter) Polar Scan and Damage

The developed methodologies in Part I and Part II are now applied to composite materials which were subjected to a variety of loading conditions in order to induce damage features. Chapter 12 investigates the presence of multiple delaminations in thin composites. It is shown that the original pulsed ultrasonic polar scan method shows limited sensitivity to the presence of delaminations. The harmonic version on the other hand shows good sensitivity, and even provides a means for locating the position of the delamination through depth.

Chapter 13 investigates the use of the ultrasonic (backscatter) polar scan for characterizing material damage induced by static shear loading. Results are presented for two types of popular reinforcement fibers: glass fibers and carbon fibers. The obtained results clearly reveal a local reduction in shear properties, together with severe distortion of the angular distribution of the fibers.

In Chapter 14, the analysis has been further extended to textile composites which were subjected to either shear-dominated fatigue loading or tension-tension fatigue loading. In case of the former, extraordinary fiber distortions up to 25° have been extracted. For the tension-tension fatigued composites, a directional stiffness reduction up to 12.8% has been determined.

Part IV: Ultrasound Visualization

First, a short overview of the constructed acousto-optic schlieren setup for visualizing wave phenomena is given in Chapter 15. To assist the schlieren experiments, a coupled fluid-structure interaction finite element method has been implemented. In order to acquaint with these methods, the well-known ultrasonic Schoch effect has been imaged experimentally as well as numerically.

Chapter 16 provides an in-depth discussion of the leakage and the scattering phenomena during the bounded beam insonification at a Lamb angle near the plate end. Besides the traditional acousto-optic imaging in real space, acousto-optic images have been directly captured in the spatial frequency domain, showing superior visibility.

The Talbot effect is a self-imaging or lens-less imaging technique as a direct consequence of Fresnel diffraction. The Talbot effect should apply for any wave-like feature, and has so far been demonstrated in literature for light waves, atoms, molecules, plasmons, etcetera. However, the demonstration of the Talbot effect for ultrasound waves has not yet been done. Chapter 17 provides the first experimental and numerical account on this. The obtained results reveal that the ultrasonic Talbot effect is actually a mixture of an amplitude-based and a phase-based Talbot effect.

Chapter 18 introduces a new technique with lots of potential: elastico-mechanoluminescent visualization of ultrasonic wave phenomena. Preliminary results are presented for the elastico-mechanoluminescent mapping of the radiation field of a transducer.

Finally, the conclusions of this work are summarized in the last Chapter 19 where besides the achievements of this work also some recommendations are given for future research work.

1. 4. Innovative Aspects

The novelty of this work lies in the (inverse) coupling of systematic high-quality experiments with true-to-nature numerical modeling, in view of extracting a large spectrum of material parameters in a full quantitative way. With this approach, it may be hoped that the ultrasonic (backscatter) polar

scan research enters a new era, and that the technique gets the highest respect possible, namely being investigated by numerous researchers and being practiced in real life applications. Some of the most original contributions of this dissertation to the literature can be summarized as follows:

(a) Development of a high-precision versatile scanner system which is programmed to obtain ultrasonic (backscatter) polar scan experiments in a fully automated way. However, other types of experiments can also be performed with the scanner by reprogramming.

(b) Identification of several pitfalls for the experimental recording of ultrasonic (backscatter) polar scans, and providing several suggestions to obtain high-quality experiments. Part of this research has been published in Ultrasonics [7].

(c) Numerical and experimental results of a harmonic version of the ultrasonic polar scan, and its physical interpretation, together with the conceptual introduction of a phase-based ultrasonic polar scan. Part of this research has been published in Ultrasonics [8].

(d) Extraction of bulk wave curves from a pulsed ultrasonic polar scan by means of intensive post-processing. This research has been published in Wave Motion [9].

(e) The first ever implementation of an inverse modeling scheme on the basis of a genetic algorithm for the identification of the elasticity tensor from a pulsed ultrasonic polar scan. This research has been published in Experimental Mechanics [10].

(f) Introduction of the pulsed ultrasonic backscatter polar scan, and demonstration of several applications having particular interest for nondestructive testing and material science. This research has been published in Experimental Mechanics [11].

(g) Ultrasonic characterization of a multidirectional (sub)surface corrugation in Bragg geometry. Part of this research has been published in Journal of Nondestructive Evaluation [12].

(h) Introduction of the Ultrasonic Polar Spectrogram Scan method as a fast and reliable method for characterizing the in-plane parameters of periodic, but imperfect surface structures. Journal article is in preparation.

(i) Development of an ultrasonic strain gauge for contactless and single-sided measurement of a local 3D strain field. This research has been published in Experimental Mechanics [13].

(j) The applicability of the ultrasonic (backscatter) polar scan for detecting, as well as extracting the physical characteristics of overlapping delaminations in a thin composite plate. Part of this research is published in Journal of Nondestructive Evaluation [14].

(k) Semi-characterization of quasi-static shear damage features in composites by means of the ultrasonic (backscatter) polar scan. This research has been published in Polymer Testing [15].

(l) Characterization of fatigue damage in textile composites by means of the ultrasonic (backscatter) polar scan. Both shear-dominated and tension-tension fatigue have been investigated. This research is published in Experimental Mechanics [16].

(m) Acousto-optical and FEM study, both in real space and spatial frequency domain, to the leakage and scattering effects of Lamb waves interacting with the plate ending. The obtained results indicate several inconsistencies with literature. Journal article is in preparation.

(n) Experimental and numerical demonstration of the Talbot effect for ultrasound waves. In contrast to the Talbot effect for other wave-like features, the ultrasonic Talbot effect has to be interpreted as a mixture of an amplitude-based and a phase-based Talbot effect.

(o) Demonstration of the elastico-mechanoluminescent effect for visualization purposes of a spatially distributed ultrasonic field. Journal article is in preparation.

A complete and detailed bibliographical list of the scientific output (journal articles and conference proceedings) can be found at the end of the dissertation.

1. 5. References

[1] http://www.nieuwindustrieelbeleid.be/nieuws/2013/planbureau-becijfert-overgang-naar-hernieuwbaar-energiesysteem.

[2] http://www.planet-science.com/categories/over-11s/technology/2010/12/three, -.t., -oneblast-off!.aspx.

[3] http://www.compositesworld.com/articles/formula-1-team-optimizes-car-design-to-build-process.

[4] https://sgroad.wordpress.com/category/eddy-merckx/.

[5] http://www.jeccomposites.com/news/composites-news/global-market-pan-based-carbon-fibre.

[6] Vandreumel, W.H.M. and J.L. Speijer, *Non-destructive composite laminate characterization by means of ultrasonic polar-scan.* Materials Evaluation, 1981. 39(10): p. 922-925.

[7] Kersemans, M., W. Van Paepegem, K. Van den Abeele, L. Pyl, F. Zastavnik, H. Sol, and J. Degrieck, *Pitfalls in the experimental recording of ultrasonic (backscatter) polar scans for material characterization.* Ultrasonics, 2014. 54(6): p. 1509-1521.

[8] Kersemans, M., A. Martens, K. Van Den Abeele, J. Degrieck, L. Pyl, F. Zastavnik, H. Sol, and W. Van Paepegem, *The Quasi-Harmonic Ultrasonic Polar Scan for Material Characterization: Experiment and Numerical Modeling.* Accepted for publication in Ultrasonics, 2014.

[9] Kersemans, M., N. Lammens, J. Degrieck, K. Van Den Abeele, L. Pyl, F. Zastavnik, H. Sol, and W. Van Paepegem, *Extraction of bulk wave characteristics from a pulsed ultrasonic polar scan.* Wave Motion, 2014. 51(7): p. 1071-1081.

[10] Kersemans, M., A. Martens, N. Lammens, K. Van Den Abeele, J. Degrieck, F. Zastavnik, L. Pyl, H. Sol, and W. Van Paepegem, *Identification of the Elastic Properties of Isotropic and Orthotropic Thin-Plate Materials with the Pulsed Ultrasonic Polar Scan.* Experimental Mechanics, 2014. 54(6): p. 1121-1132.

[11] Kersemans, M., W. Van Paepegem, B. Lemmens, K. Van den Abeele, L. Pyl, F. Zastavnik, H. Sol, and J. Degrieck, *The Pulsed Ultrasonic Backscatter Polar Scan and its Applications for NDT and Material Characterization.* Experimental Mechanics, 2014. 54(6): p. 1059-1071.

[12] Kersemans, M., W. Van Paepegem, K. Van den Abeele, L. Pyl, F. Zastavnik, H. Sol, and J. Degrieck, *Ultrasonic Characterizaion of Subsurface 2D Corrugation.* Journal of Nondestructive Evaluation, 2014. 33(3): p. 438-442.

[13] Kersemans, M., K. Allaer, W. Van Paepegem, K. Van Den Abeele, L. Pyl, F. Zastavnik, H. Sol, and J. Degrieck, *A Novel Ultrasonic Strain Gauge for Single-Sided Measurement of a Local 3D Strain Field.* Experimental Mechanics, 2014. 54(9): p. 1673-1685.

[14] Kersemans, M., A. Martens, K. Van Den Abeele, J. Degrieck, L. Pyl, F. Zastavnik, H. Sol, and W. Van Paepegem, *Detection and localization of delaminations in thin carbon fiber reinforced composites with the ultrasonic polar scan.* Journal of Nondestructive Evaluation, 2014. 33(4): p. 522-534.

[15] Kersemans, M., I. De Baere, J. Degrieck, K. Van Den Abeele, L. Pyl, F. Zastavnik, H. Sol, and W. Van Paepegem, *Nondestructive damage assessment in fiber reinforced composites with the pulsed ultrasonic polar scan.* Polymer Testing, 2014. 34(0): p. 85-96.

[16] Kersemans, M., I. De Baere, J. Degrieck, K. Van Den Abeele, L. Pyl, F. Zastavnik, H. Sol, and W. Van Paepegem, *Damage Signature of Fatigued Fabric Reinforced Plastic in the Pulsed Ultrasonic Polar Scan.* Experimental Mechanics, 2014. 54(8): p. 1467-1477.

PART I

This part is dedicated to the investigation, the analysis and the applications of the ultrasonic polar scan technique in its original implementation, the transmission regime.

Chapter 2

Literature Review of Non-Destructive Testing and Material Characterization with Ultrasound

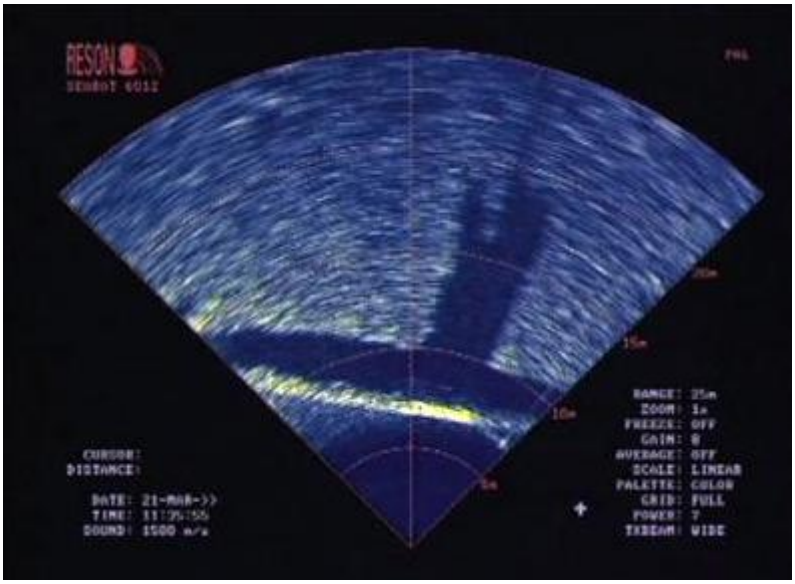

The development of SONAR (SOund NAvigation and Ranging) during World War I marked the start of ultrasonic non-destructive testing and material characterization.(Figure reproduced from reference [1]).

Overview

A historical overview of several popular techniques for non-destructive testing and material characterization is given. Focus is put to ultrasonically based techniques, for which several scientific references have been provided for the interested reader. The main scientific achievements have been given, while both the opportunities and the limitations have been identified for the different discussed techniques. Finally, the concept of the ultrasonic polar scan is discussed in-depth, while an overview of current state-of-the-art (at the beginning of the present dissertation) of the ultrasonic polar scan method is provided.

2. 1. Introduction

Thursday, March 2nd, 1854, a terrible explosion of a newly installed boiler at the 'Fales and Gray Car works' in Hartford had disastrous results, killing 20 people while dozens other were severely injured [2]. It was on this occasion that a law was passed in the state of Connecticut requiring annual visual inspection of boilers [3], which may be assumed the start of industrial non-destructive testing (NDT). Since then, the field of NDT has been revolutionized several times. Some of the most prominent NDT and characterization methods, which are still popular and widely used today, are shortly discussed.

Electromagnetic Eddy Current

The first use of electromechanical eddy current for NDT dates back to 1879, when D.E. Hughes conducted metallurgical sorting tests [4]. At present, the eddy current technique is a well established method in NDT and material inspection, and is frequently used for defect detection, classification and characterization [5-10]. However, if one is more interested in characterization of material properties, the eddy current method does not suffice. Besides, the eddy current methodology can only be applied on conductive materials which are susceptive to eddy current induction. Hence, the eddy current technique cannot be used for the inspection of glass fiber

composites, which is a big drawback for several composite engineering fields.

X-ray Radiography

In 1895, Wilhelm Conrad Rontgen discovers a new kind of rays, which he termed X-rays [11] because of the mysterious properties as it could visualize the internal structure of a living hand (see Figure 2-1). Among the many applications he proposed, he also realized that X-rays would be an excellent tool for detecting flaws in materials.

Figure 2-1: First ever X-ray photograph of a living human hand. (Figure reproduced from reference [11]).

At present, X-ray radiography is widely used in the medical world, and in a lesser extent for material inspection and NDT. The application field of X-rays for NDT is mainly focused to the detection of fiber orientation as well as evaluating crack density in fiber reinforced plastics [12-16]. One of the major problems with X-ray radiography is its noxious nature for humans, making it difficult to implement in an industrial environment. Furthermore, X-rays are useful for visualizing internal structures, while for characterization purposes of mechanical parameters it has only limited capability.

Optical Fiber Bragg Grating

Another non-destructive testing technique which is currently gaining a lot of interest concerns the use of a fiber Bragg grating. This is an optical fiber with a distributed Bragg reflector inside, reflecting that light component which matches the designed periodicity. Upon straining the optical fiber, the

periodicity of the Bragg reflector slightly changes, and in extension the frequency of the reflected light component shifts. As such, the optical fiber is often used for structural heath monitoring, i.e. the fiber is embedded in a structure in order to evaluate the performance of a structure over time. Several interesting applications have already been performed in literature [17-23]. Recently, the idea emerged to embed sensor networks made of many fiber Bragg gratings, which are then readout wireless to monitor the performance and integrity of the complete structure during operation. A high strain field measured with a fiber then might indicate material degradation or the presence of material damage. Although promising results have already been obtained with the fiber Bragg gratings, it is not yet clear whether they can detect, discern and characterize different types of damage features in (composite) materials. In addition, the method suffers from many residual effects [24-26]. Thermal effects for example can easily produce a parasitic strain field, making correct interpretation of optical fiber data difficult. If elastic characterization of a material is required, it may be clear that optical fibers contribute little to nothing as they provide a measure for the strain field. Without knowledge of the applied stress field, which most often is unknown, no information about the mechanical elasticity can be extracted.

Thermography

Non-destructive testing and inspection by means of thermography dates back to the pioneering work of Alzofon [27-28] and Green [29-31] in the 1960's. Although their approaches are still used in present research, the real breakthrough for thermography came with the invention of the infrared video camera. With this, the imaging details of thermographic NDT increased by a few factors. Now thermography is a well-known NDT technique, which has found applications in several engineering branches [32-39]. However, as thermography primarily relies on the diffusion of heat through the test object, the energy does not propagate in a straight line which obviously complicates the analysis and interpretation. This becomes even more cumbersome for the inspection of composite materials as they have anisotropic thermal properties. This is probably also the reason why characterization of material features and properties has not yet been widely demonstrated.

Ultrasound

Finally, we arrive at probably the oldest technique: ultrasound. It is nature itself who first employed ultrasound waves for the purpose of characterizing

features. Indeed, in 1794 the Italian Lazzaro Spallanzani demonstrated that blind folded bats could navigate around objects. Louis Jurine then discovered that upon covering their ears, the bats became totally disoriented and bumped on every object. From these experiments, it was hypothesized that bats produce non-audible (to the human's ear) sound, and that the bats navigate by imaging the surrounding through sound waves rather than by light. This has been later experimentally confirmed by Pierce and Griffin who visualized the supersonic notes produced by bats during navigation [40].

It was until 1880 before mankind was able to produce such non-audible sound, now called ultrasound, through the invention of the piezo-electric effect in certain crystals by the Curie brothers [41-43]. The concept of metal flaw detection by ultrasound has been first suggested in 1928 by Sergei Solokov. He introduced a through-transmission technique (pitch-catch configuration) in which a loss of transmitted energy was used to identify the presence of a flaw [44]. Similarly, he extended the method towards the reflection regime (pulse-echo configuration) by operating a single transducer as both emitter and receiver. However, the real breakthrough for ultrasonic NDT came with the work of Floyd Firestone. In 1946, he gave the first demonstration of a modern pulse-echo ultrasound technique for flaw detection [45-46]. From that date on, ultrasound became the most popular and widespread technique for material inspection. At present, ultrasonics is a vivid research area practiced all over the world, mainly because of its excellent capabilities for accurate defect detection as well as for characterization of intrinsic elastic material parameters in a fairly simple way. As a matter of fact, it is also ultrasound, together with optical fibers, which is explored at Ghent University in view of NDT and material characterization. In the next section, an account is given about several ultrasonic techniques which have found widespread application in research and industry, and which have already proven their utility for NDT and material characterization.

2. 2. Ultrasonic Non-Destructive Testing and Material Characterization

Ultrasound is defined as sound having a frequency which cannot be detected by the human ear (f >20 kHz). However, when applied for non-destructive

testing and material characterization, one usually sets the frequency range of ultrasound between 500 kHz and 20 MHz. Lower frequency makes the detection of small defects impossible, while higher frequency waves are much more attenuated upon propagation. Especially for the inspection of composite materials, the latter is detrimental. Often, one uses water as an immersion liquid to enhance the coupling of acoustic energy in the sample of interest.

This section shortly discusses some ultrasonic techniques which have become very popular in science and industry for NDT and material characterization. It is however stressed out that the given list is far from complete, and that many more implementations exist which are equally interesting. In addition, the reference list is far from complete. The references within the here given references however can further guide the interested reader.

2. 2. 1. Ultrasonic Pulse-echo and Pitch-catch Normal Incidence Techniques

The ultrasonic pulse technique has been first proposed in 1928 by Sergei Solokov, who soon thereafter experimentally demonstrated that ultrasound does reflect upon hidden flaws in metals (see Figure 2-2) [44]. Originally, the method was called reflectogram, though in 1945 Delano renamed the technique A-scan (after Amplitude-scan) [47].

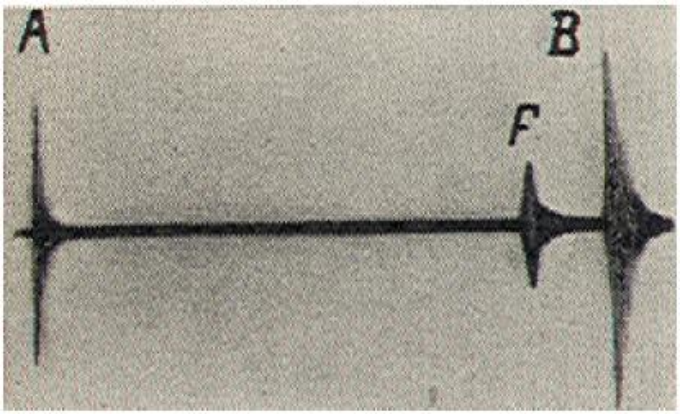

Figure 2-2: Pioneering reflectogram (A-scan) experiment by Sergei Solokov. (Figure reproduced from [44]).

A schematic of the pulse echo method is shown in Figure 2-3, the A-scan representation is displayed in the left part of the figure. The setup of the experiment could not be more simple: insonify a metal piece at normal incidence, and record the transmitted or reflected signal with a scope. Plotting the signal as a function of time or distance, several echoes can be discerned which can be classified as: Front Wall Echo (FWE), Defect Echo (DE) and Back Wall Echo (BWE).

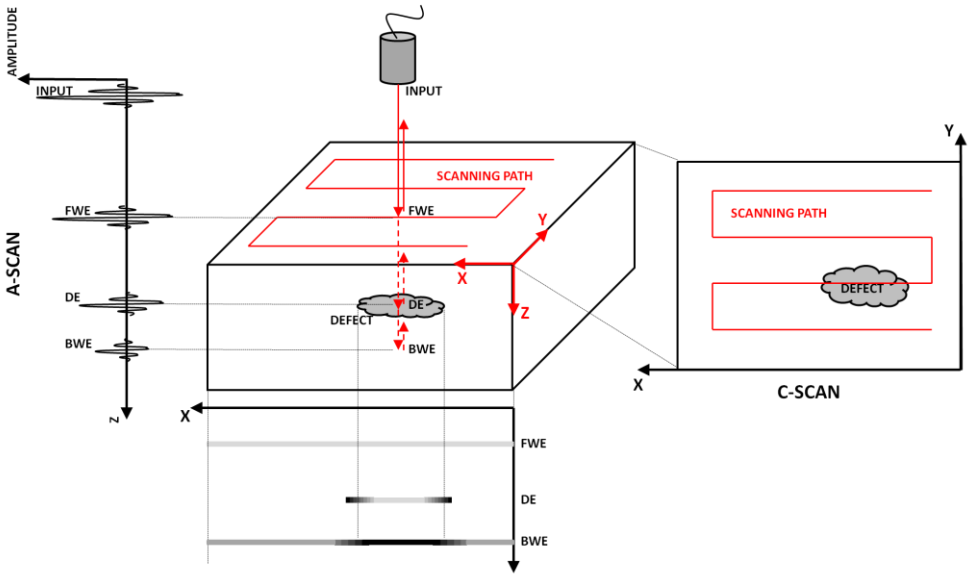

Figure 2-3: Schematic of ultrasonic pulse echo technique. A-scan representation (left), B-scan representation (below) and C-scan representation (right).

In 1954, the concept of a B-scan (after Brightness-scan) was introduced by Leksell [48]. Basically, the ultrasonic amplitude of an A-scan is color coded in view of imaging the defect along one of the sides (see bottom part of Figure 2-3). By scanning the sample in a XY-grid, the B-scan provides a representation of the defect through depth. One of the first B-scan images in NDT has been provided by Michalski in 1956 [49].

Finally, the probably best-known format for representing ultrasonic data concerns the C-scan (no abbreviation, simply the next letter in the alphabet) which was first demonstrated in 1956 by Cal Kammerer who was an ultrasound technician at the Automation Instruments Power Plant Inspection Division test lab in California [50]. The C-scan can be thought of as a

projection of the amplitude on the scanned surface (see right part of Figure 2-3). By appropriate time-gating the ultrasonic signal, C-scan images can be obtained at different depth locations.

The value of the pulse-echo and pitch-catch technique for nondestructive testing cannot be underestimated as it allows sizing and localization of different types of flaws along the direction of the ultrasonic beam. Throughout the last 50 years, it became the most popular and widespread method in both research and industry, most likely because of the simplicity of the analysis and its proven usefulness in tracing geometrical discontinuities. Focusing to fiber reinforced plastics, the method has been successfully employed for the detection of delaminations [51-53], detection of impact damage [54-56], evaluation of microscopic voids and porosities [57-59], detection of several types of geometrical defects [60-61], monitoring the growth of a crack [62], as well as other applications. Currently, a lot of effort is put in the development of phased array and phased 2D array (or phased matrix) technology [63-67], in view of increasing the accuracy, performing electronic steering and focusing of an ultrasonic beam as well as speeding up the inspection. In spite of this, a recognized disadvantage of the here discussed technique concerns its inability to provide quantitative information about the investigated material such as the mechanical elasticity. In addition, for samples with a small thickness-to-wave-length ratio, the classical C-scan reflection techniques suffer from overlapping echoes coming from (i) the top side, (ii) the bottom side and (iii) the interfaces of potential damage, even though considerable progress has been made in recent years for inspecting thin sections [68-70]. Finally, the detection of damage features which are oriented along the direction of insonification, such as vertically oriented surface breaking cracks for example, are often undetected.

2. 2. 2. Ultrasonic Polar Backscattering Method

The ultrasonic polar backscattering method, originally introduced by Y. Bar-Cohen in 1982 [71-73], settles some of the shortcomings of the classical pulse-echo method by considering an inclined angle (oblique incidence). A schematic of the ultrasonic polar backscattering method, also known under the term inclined C-scan, is shown in Figure 2-4. The method has been shown effective for the detection of (hidden) corrosion [74], the detection of (sub)surface defects [75-76], evaluation of microstructure properties and

material inhomogenities [77-78], characterizing vertical cracks [79], determination of fiber direction in composites [80-81] and the ply-by-ply characterization of matrix cracks in composite laminates [82-83].

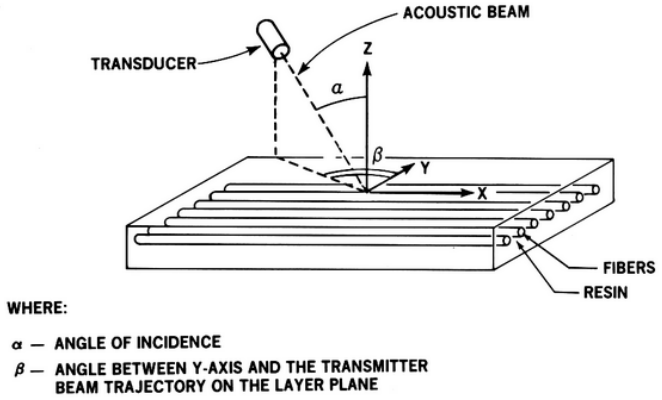

Figure 2-4: Schematic of the ultrasonic polar backscattering technique. (Figure reproduced from [71-72]).

Extending the ultrasonic polar backscattering method by varying the incident angle, the method has been employed for the evaluation of the quality of bonds [75], the characterization of (periodic) surface roughness [84-87] and the characterization of layer coatings [88]. The use of the backscatter technique has been further proposed for identification of the elastic properties of composites [80, 89]. Though, up to now only limited progress has been made in this regard.

The above cited backscattering studies were always limited to a certain incident angle or orientation angle (angle α and angle β respectively in Figure 2-4), thus implying that a certain prior knowledge is required in order to obtain the envisioned results. Moreover, the selection of particular angles most likely entails that certain signatures are left unrecorded which could be important for the prediction of the life time and failure of the structure under investigation.

2. 2. 3. (Nonlinear) Resonant Ultrasound Spectroscopy

At present, resonant ultrasound spectroscopy (RUS) is a well-established technique to infer material parameters of anisotropic (visco-)elastic materials [90-93]. The principle of the method is shown in Figure 2-5. The method

relies on the measurement of the frequencies of the sample's elastic resonances (free vibration), as they are function of the dimensions, the shape, the density and the elasticity tensor of the specimen.

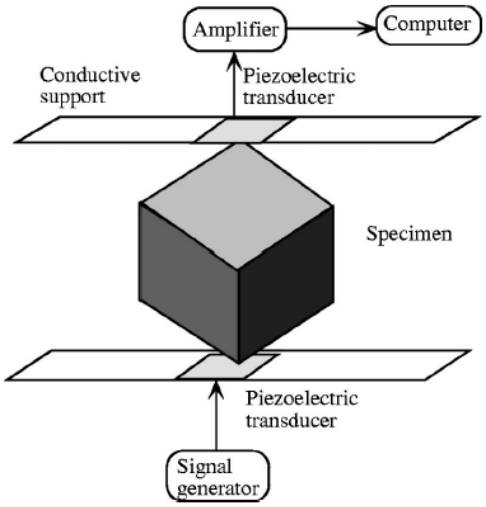

Figure 2-5: Schematic of resonant ultrasound spectroscopy. (Figure reproduced from reference [93]).

Several extensions have been proposed in literature to include the analysis of the nonlinear response in view of damage detection. As such, the method has been successfully applied to discern and monitor various damage characteristics of (anisotropic) materials [94-100]. It has been commented that the sensitivity of the nonlinear methods to material damage is much higher compared to linear approaches.

Anyway, it may be clear from the schematic of Figure 2-5 that (nonlinear) resonant ultrasound spectroscopy has limited use for application in a real environment. Indeed, it is a resonance based technique in which the specifically prepared sample needs to be mounted in a device. Although it is strictly speaking a non-destructive technique, it is useless for *in situ* determination of the material (damage) characteristics.

2. 2. 4. Bulk Wave Based Technique

A popular approach for material characterization and extraction of damage features comprises the use of bulk waves. The first to demonstrate the technique for composite material characterization was Markham as early as

1970 [101]. Determining the time delay of the bulk waves (longitudinal, shear vertical and shear horizontal polarization) which were transmitted along certain material directions, yielded the phase velocity profiles from which elasticity constants could be deduced. More recent approaches basically use the same principle as was used by Markham, though the analysis and inversion procedures evolved from which the accuracy of the determined material parameters obviously benefits. Some noteworthy numerical and experimental results can be found in [102-113]. Instead of using phase velocity profiles in view of identifying elastic constants, few authors have employed energy (or group) velocity profiles [107, 114-119]. Each set of velocity profiles is sufficient to identify elasticity constants.

In general, it can be stated that bulk wave measurements are found to be highly suited for composite material characterization. However, some problems are often encountered using this methodology. First of all, the method requires the measurements to be taken at certain material orientations. However, in reality the material symmetry orientations are *a priori* often unknown. Suppose these orientations are somehow known, then it is still a difficult task to obtain measurements in for examples plates because of the aspect ratio. Considering that most composite structures have a plate-like shape, this is a very detrimental fact. Secondly, as the bulk wave technique relies on the measurement of a time delay in order to extract velocity profiles, it is clear that the measurement has to be performed in transmission. However, in most cases the backside of a structure is not accessible. Another consequence of the time delay measurements concerns the need for relatively complex and expensive acquisition tools having sufficient sampling frequency.

2. 2. 5. Lamb Wave Based Technique

Considering an infinite region in two directions and physical boundaries in the third direction (the model of a plate), a special class of waves can exist which has been communicated as early as 1917 by Horace Lamb [120]. Depending on the symmetry of their associated displacement field, one speaks about symmetric or anti-symmetric Lamb waves (see schematic in Figure 2-6) [121].

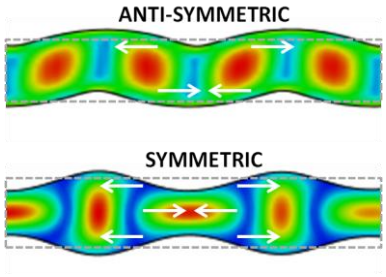

Figure 2-6: Characteristic deformation pattern for anti-symmetric (top) and symmetric (bottom) Lamb waves.

Often, Lamb waves are referred to as guided waves because they are guided by the boundaries of the elastic plate upon propagating. Another important physical consequence of the boundary conditions of the plate is the dispersive behavior of the guided waves, i.e. their physical appearance is dependent on the applied frequency and the plate thickness [121-122]. Often, a specific Lamb wave is stimulated by insonifying an immersed plate by a bounded ultrasonic beam at its corresponding Lamb angle. The dispersion curves provide a graphical representation of the Lamb wave stimulation conditions, i.e. the Lamb angles, as a function of frequency-thickness *fd*, assuming plane wave insonification [121]. Figure 2-7 displays the computed dispersion curves *θ(fd)* for aluminum. The higher the frequency-thickness *fd*, the more Lamb modes can be excited. The anti-symmetric A_0 mode and the symmetric S_0 mode on the other hand converge towards the Rayleigh wave [123-124] for increasing *fd*.

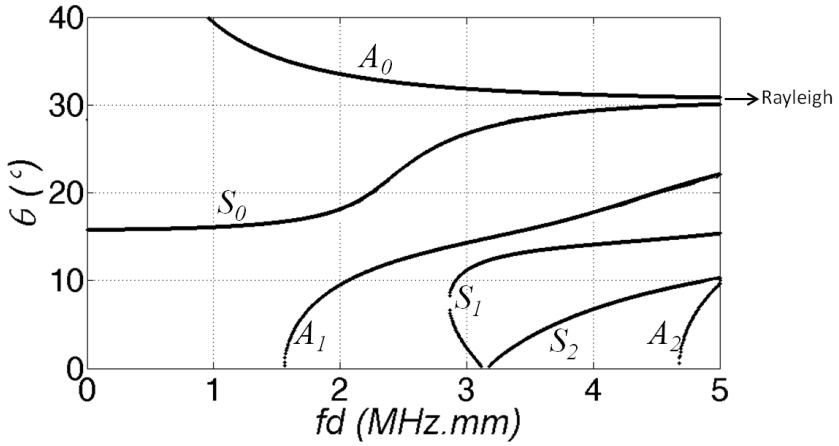

Figure 2-7: Computed dispersion curves for aluminum.

As energy is transferred from the liquid to the solid domain during bounded beam stimulation of a Lamb wave, it is clear that the reverse also takes place: the stimulated Lamb wave leaks its energy back into the surrounding liquid at the Lamb angle upon propagation along the plate. For this reason, one often terms Lamb waves in a fluid-loaded plate as 'leaky Lamb waves'. Interference of the specular reflection field and the leaking field, which are 180° out of phase, results in a total reflection field which consists of two lobes separated by a low-intensity nullzone [125-126]. This beam splitting is the famous Schoch effect [127], and is demonstrated in Figure 2-8. By varying the incident angle and experimentally searching for the Schoch effect, the various Lamb angles can be identified. The dispersion curves can then be fitted to the determined Lamb angles by optimizing the material parameters. However, it may be clear that this method is not practical for accurately characterizing composite materials.

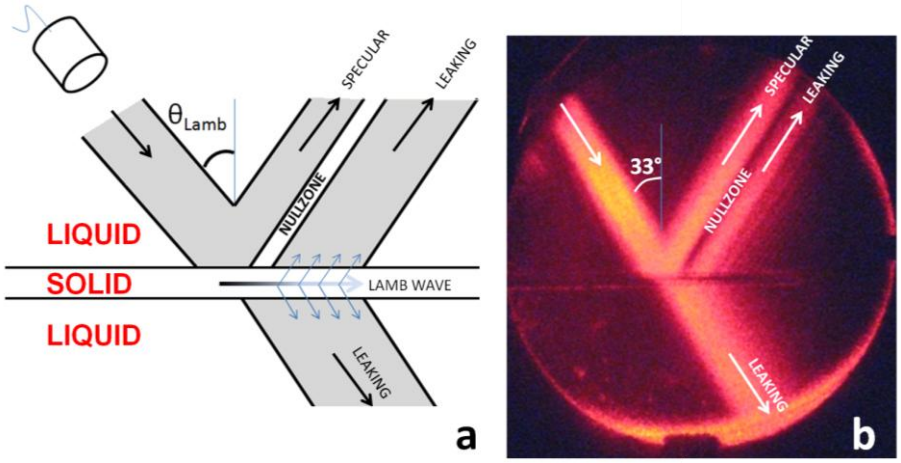

Figure 2-8: Schematic of Schoch effect (a) and acousto-optic visualization of the bounded beam insonification of aluminum (*fd* = 3 MHz.mm) at the A_0 Lamb angle (b).

An alternative is found in the recording of transmitted broadband pulse signals, along certain material symmetry orientation, as a function of the oblique incident angle θ. Normalization to the reference wave field, and subsequent analysis of the normalized signals in frequency domain then yields the transmission coefficient as a function of incident angle and frequency (the same parameters in the dispersion curves). The resulting transmission coefficient has sharp maxima which more or less relate to the condition for efficient stimulation of Lamb waves, while the global level of

the transmission coefficient is a measure for the attenuation [128-129]. An example of such a 'plane' wave transmission image is displayed in Figure 2-9 for aluminum. The similarity with the dispersion curves for aluminum (see Figure 2-7) is evident.

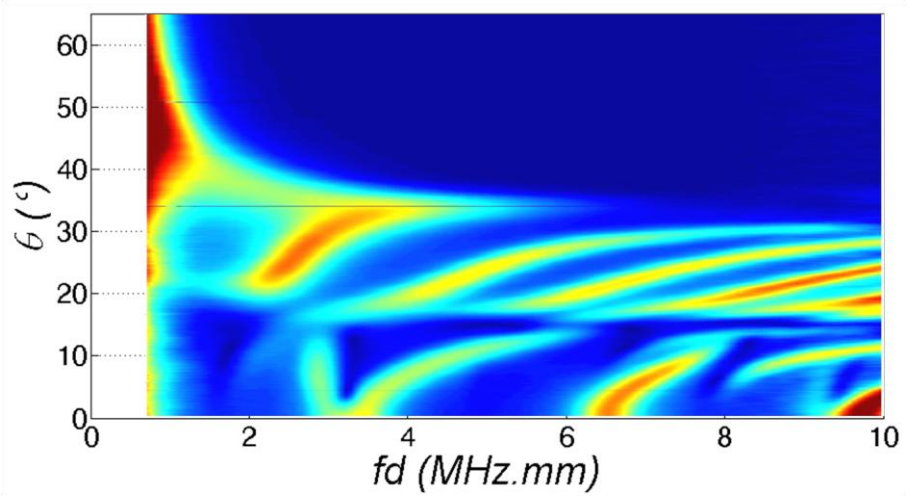

Figure 2-9: Plane wave transmission for aluminum. The color code is a measure for the amplitude of the transmitted wave.

By intelligent choice of the vertical insonification plane, the plane wave transmission technique was successfully employed by various research teams for composite material characterization [130-136]. Furthermore, the methodology has also been demonstrated in reflection modus [73, 137-141], basically yielding similar results. Finally, the plane wave transmission/reflection method has also been applied to identify as well as to characterize various damage features in composites [140, 142-143].

The main difficulty in the plane wave transmission/reflection technique concerns the choice of the vertical insonification plane. Indeed, most of the time the symmetry orientations of a composite specimen are *a priori* unknown. Considering that various load cycles on the other hand could induce local fiber distortion up to 10° [16, 144-145], the latter statement becomes even more valid. In addition, the method suffers from bounded beam effects (bounded beam effects are also the reason why the patterns in Figure 2-9 are smeared out). For this reason, several researchers have proposed scanning of the transmission/reflection field as well as the use of wide aperture transducers [113, 131, 134-136]. However, these suggestions are often difficult to implement in reality. At last, the method is fairly

complex as the total wave form needs to be captured in time domain, followed by an analysis in frequency domain. Such a spectroscopic approach introduces difficulty because of aliasing artifacts, issues with resolution in frequency space, normalization matters, spectral leakage, etcetera.

Finally, another popular way of Lamb wave based inspection and characterization concerns the stimulation, excitation and subsequent interception at a distant point of a Lamb wave. This can be done in different ways including immersion technique, contact procedure or laser technique. The latter is also known as laser ultrasonics and recently gained a lot of interest by various research teams [60, 109, 146-151]. The stimulated Lamb wave is guided along the structure and thus picks up a signature of the material characteristics upon propagation. This is clearly different to the plane wave transmission/reflection technique which puts on view the condition for efficient Lamb wave stimulation, i.e. the incident angle or the Lamb angle. The intercepted signal can then be analyzed in order to extract elasticity constants, damage features, damping characteristics, etcetera [109, 146-148, 152-156]. One of the difficulties of this inspection approach concerns the fact that the interception of the signal after some propagation distance is far from straightforward. This is easily understood realizing that anisotropy induces degeneration of the phase velocity vector and the group velocity vector [157-162]. As such, the wave energy is transported in a direction which differs from the vertical insonification plane. In addition, the technique suffers whenever curved structures have to be inspected. Though, in recent years incredible progress has been made on the understanding of Lamb wave propagation in curved composite plates [163-166].

2. 3. Ultrasonic Polar Scan (UPS)

The above sections gave a limited review of some currently popular ultrasonic NDT and material characterization techniques. Both the opportunities and limitations have been identified for the discussed ultrasonic techniques. In this section, the discussion is directed towards the ultrasonic polar scan (UPS) technique which was originally introduced by Van Dreumel and Speyer in 1981 [167]. As the UPS technique is the main subject of this dissertation, a more detailed and in-depth discussion is given about (i) the working principle, (ii) the state-of-the art research (at the beginning of this research), (iii) its promising capabilities for NDT and

material characterization and (iv) the current shortcomings to fulfill its promises.

2. 3. 1. Principle of the Ultrasonic Polar Scan

The UPS method insonifies a predefined material spot with pulsed ultrasound from as many as possible oblique incidence angles $\psi(\varphi,\theta)$, while keeping the distance between transducer and sample fixed. To enhance the coupling of ultrasonic energy into the solid, water is used as immersion liquid. A schematic of the UPS technique is shown in Figure 2-10.

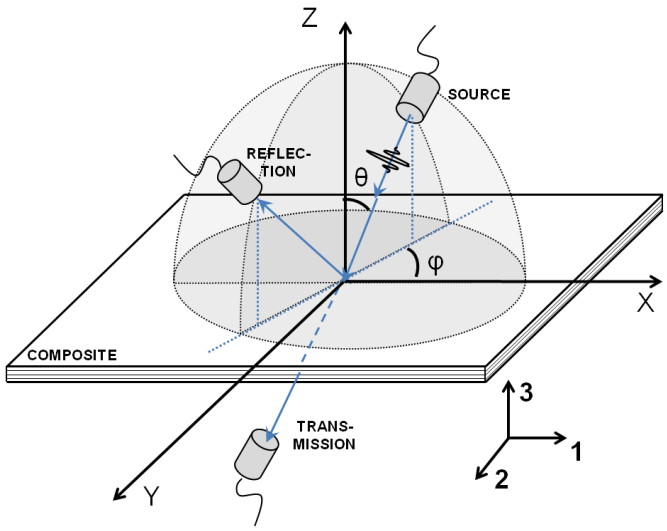

Figure 2-10: Schematic of the UPS method.

Simply recording the transmitted (or if necessary reflected) pulse amplitudes, and mapping them in a polar representation yields an UPS image. An example of a UPS recording for a unidirectional carbon epoxy laminate is shown in Figure 2-11.

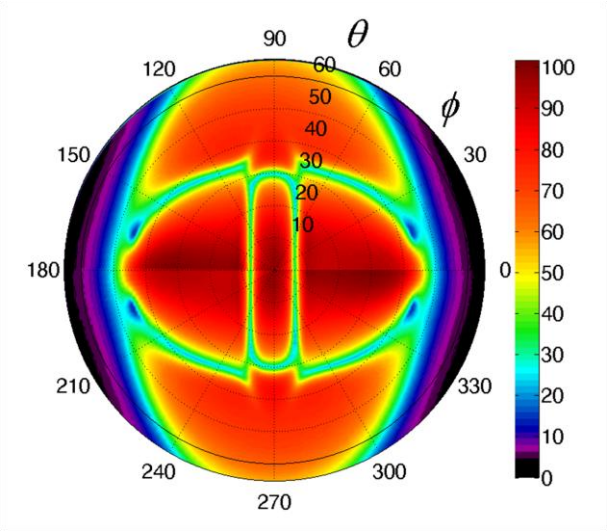

Figure 2-11: High-quality UPS image for a [0_8] carbon/epoxy laminate.

The vertical incident angle θ is put on the radial axis, the in-plane polar angle φ is represented along the angular axis, while the assigned color pigment is a measure for the transmitted (or reflected) pulse amplitude. Hence, each point in a UPS image corresponds to the transmitted (or reflected) amplitude at a unique oblique incidence angle $\psi(\varphi,\theta)$. The middle point of the UPS image should equal normal incidence $\psi(0,0)$ and thus corresponds to the arrangement of the classical C-scan.

2. 3. 2. Physical Interpretation of an Ultrasonic Polar Scan

For a virgin composite, a point-symmetric fingerprint is observed in a UPS image which consists of a set of rings (see Figure 2-11). The rings are physically connected to the stimulation of critical waves in the plate, such as leaky Rayleigh waves, leaky Lamb waves or lateral waves [128, 168-174]. The class of stimulated critical waves is merely determined by the nature of the applied ultrasonic beam. This has been explicitly demonstrated in references [171, 173-174] by means of simulation results: the use of a harmonic narrowband beam yields rings connected to the stimulation of leaky Lamb waves, while the use of a pulsed broadband beam leads towards critical bulk wave characteristics due to phase canceling of the many stimulated dispersive Lamb waves. As both classes of waves are vigorously connected to the stiffness properties, the ultrasonic polar scan method directly images the mechanical anisotropy of the scanned material spot. In the remainder of this thesis, an ultrasonic polar scan obtained with an

ultrasonic pulse is denoted by 'Pulsed Ultrasonic Polar Scan (P-UPS)', while for a harmonic wave the term 'Harmonic Ultrasonic Polar Scan (H-UPS)' is used.

As an example, the characteristic patterns in the P-UPS image displayed in Figure 2-12a are shortly discussed. The use of broadband ultrasonic pulses leads to the presence of bulk wave dominated polar contours [171-175]. In fact, the contained characteristic contours are a representative map of the critical bulk wave angles θ_{crit}^{j}, and can be classified according to the polarization state j of the stimulated bulk wave. To verify this, a numerical computation of the critical bulk wave angles of a transversal isotropic material is presented in Figure 2-12b. From this, it may be clear that the inner contour of the UPS image corresponds to the quasi-longitudinal (QL) polarization, the middle contour to the quasi-shear horizontal (QSH) polarization and the outer contour to the quasi-shear vertical (QSV) polarization. The prefix "quasi" can be omitted when propagation takes place along a symmetry direction, which then yields pure wave modes [121-122, 157, 159]. Note that the contours in the experimental recording are not a one-to-one match to the numerically computed curves, simply because the true mechanical properties of the scanned carbon/epoxy laminate are unknown. In addition, scanning of the incident angle θ (radial axis) up to 90° is experimentally not possible because of obvious mechanical considerations.

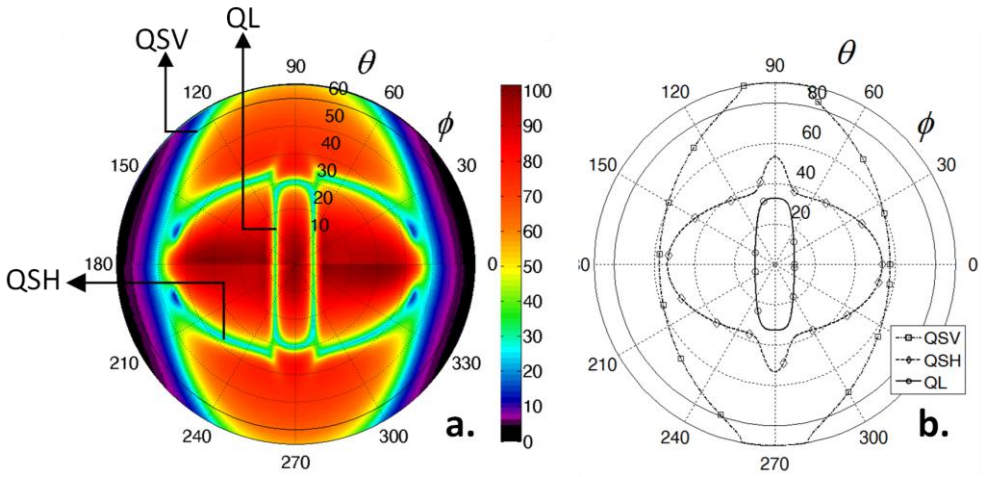

Figure 2-12: High-quality P-UPS image for a transversal isotropic [0_8] carbon/epoxy laminate (a) and critical bulk wave angles for a typical transversal isotropic material (b).

The geometrical shape of the inner P-UPS contour is mainly dictated by the bulk moduli, while the other two contours are shear moduli dominated [121-122]. For isotropic materials, the P-UPS image shows circular symmetry (see for example Figure 2-13a and Figure 2-14a), reflecting the mechanical equivalence of any two material orientations. For the transversal isotropic $[0_8]$ carbon/epoxy composite this is clearly not true as can be verified in Figure 2-12a. For example, the QL contour has a clearly stretched appearance, denoting the inequality between the in-plane stiffness along both orthogonal material orientations. The phase velocity of the QL-wave along the in-plane axes of orthotropy is given by

$$c_i^{QL} = \sqrt{C'_{ii} \big/ \rho}\,, (i = 1,2) \tag{1}$$

with C'_{ii} the elasticity constant along direction *i*, and ρ the mass density [121-122].

Hence, an increase, respectively decrease, of the elasticity constant C'_{ii} yields an increase, respectively decrease, of the phase velocity c_i^{QL} of the in-plane propagating QL wave. By taking into account Snell-Descartes' law for external born sound, which states that the components of the incident wave vector ***k***, parallel to the liquid-solid interface (12-plane), are conserved, the angle of propagation θ can be easily linked to the phase velocity *c* for a certain polar angle φ

$$\left.\frac{\sin\left(\theta_{liq}\right)}{c_{liq}}\right|_{\varphi} = \left.\frac{\sin\left(\theta_s^{QL}\right)}{c_s^{QL}}\right|_{\varphi} \tag{2}$$

where the subscript '*liq*', respectively '*s*', denotes propagation in the liquid, respectively in the solid medium.

As a polar contour indicates the stimulation of a lateral bulk wave guided along the structure, θ_s equals 90°. In combination with the known phase velocity of the immersion liquid, the incident angle θ_{crit}^{j} for a certain polar angle φ at which a critical refraction within the solid occurs, is simply given by:

$$\theta_{crit}^{j} = \sin^{-1}\left(c_{liq} \Big/ c_{s}^{j}\right) \quad with\ j = \{QL, QSH, QSV\} \tag{3}$$

Hence, the critical bulk wave angle θ_{crit}^{j} is inversely proportional to the phase velocity of bulk waves guided by the solid and, by extension to the mechanical elasticity of the solid. With this, the geometrical appearance of the QL contour in Figure 2-12 can be easily interpreted: the inward part of the contour (at $\varphi = 0°$) corresponds to high elastic stiffness, precisely because of the orientation of the inserted carbon fiber reinforcement, while the much wider part of the contour (at $\varphi = 90°$) corresponds to lower stiffness, mainly reflecting the low elasticity of the epoxy matrix of the composite in the direction transverse to the fibers. Any change in the elasticity tensor alters the directional wave speed, and thus yields a positional shift of the P-UPS contours.

It can be further observed in Figure 2-12a that part of the QSH contour is not captured in the P-UPS recording. This is easily understood considering that along the symmetry directions no coupling structure is present for the incident longitudinal wave to convert its polarization towards shear horizontal. In addition, the numerical computation (Figure 2-12) reveals that part of the QSV contour is missing. This is due to the fact that the QSV wave has a phase velocity in that particular direction which is lower than the phase velocity of the immersion liquid. According to Snell-Descartes' law, this would imply a complex-valued critical angle, which for the present application has no physical meaning.

2. 3. 3. Historical Development and State-of-the-Art

In this section, an overview of the historical development of the ultrasonic polar scan is given. An account is given on the current (at the beginning of this dissertation) state-of-the-art.

Van Dreumel and Speyer

We start with the pioneering work of Van Dreumel and Speyer in the early 1980's [167, 176]. Some of the first ever recorded P-UPS images by Van Dreumel and Speyer are displayed in Figure 2-13. It may be clear that the obtained images have a different view, depending on the mechanical nature of the scanned material.

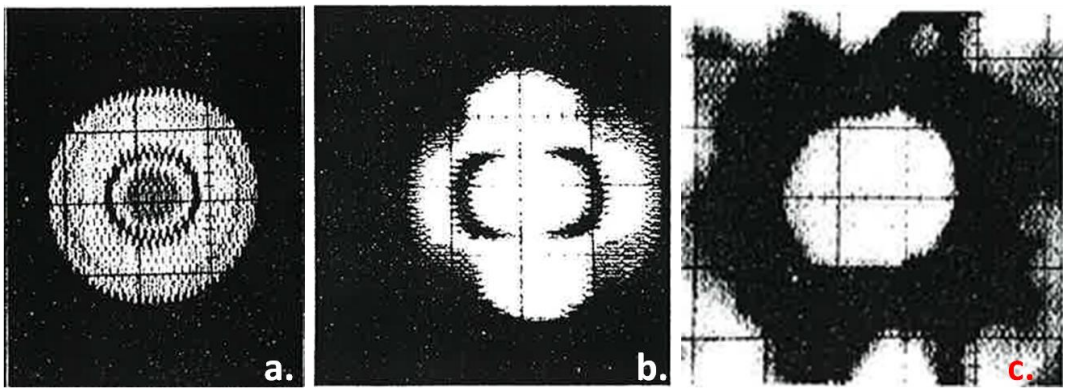

Figure 2-13: Pioneering P-UPS images obtained by Van Dreumel and Speyer in 1981: aluminum (a), unidirectional glass fiber composite (b) and square weave carbon fabric laminate (c). (Figure has been reproduced from reference [167]).

The P-UPS images display characteristic rings which have been attributed to the nature of critical bulk wave angles. The beauty of the intriguing patterns made the pioneering authors state that: "*A library of Polar-patterns, stored as "fingerprints", raises the possibility of laminate identification by pattern recognition.*" It is unfortunate that in the years after, only one sequel study has been performed by Van Dreumel and Speyer to further explore the capabilities of the ultrasonic polar scan. In that study, they used the P-UPS technique for the determination of the fiber direction and stacking order of composite materials [176].

Degrieck

It took fifteen years before the technique has been investigated again for the purpose of NDT and material characterization through the work of Joris Degrieck [171-172]. He used a modernized scanning system to obtain more accurate and detailed P-UPS experiments. For practical reasons, the recording mode was changed from through-transmission to double through-transmission, as was originally introduced by Rokhlin [103]. An example of his superior P-UPS recordings can be found in Figure 2-14 for various materials.

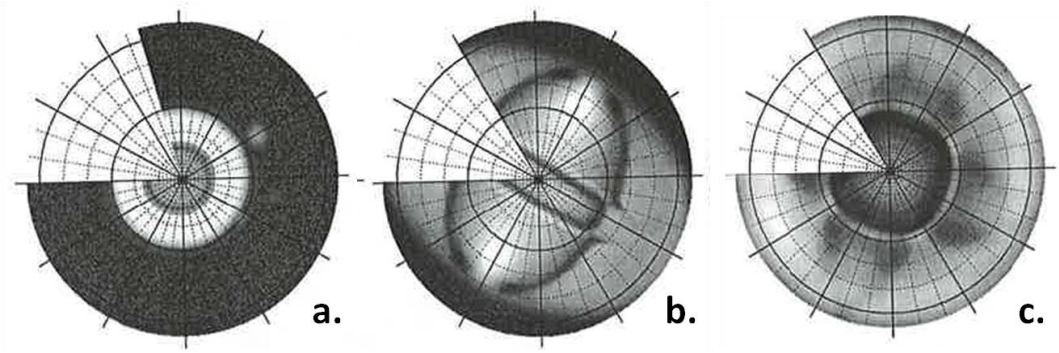

Figure 2-14: Superior P-UPS recordings obtained by Degrieck between 1996 and 2003: aluminum (a), unidirectional carbon fiber composite (b) and glass fabric laminate (c). (Figure reproduced from references [171-172]).

The work of Degrieck has identified several practical applications of the P-UPS technique for composite materials: estimation of the fiber direction [171-172], determination of fiber volume fraction [171-172], determination of the porosity [172] and detection of fatigue damage [172]. In addition, he and co-worker Van Leeuwen implemented as first a numerical procedure for simulating UPS images of homogeneous composites [177-178], in view of bringing the technique to the next level: full quantitative characterization of the elastic properties of composite materials using a mixed experimental-numerical approach. For this, they extended the initial theoretical work of Nayfeh and Chimenti [128] to account for damping as well as for the spectral content of a broadband ultrasonic pulse. Although the gap between experiment and simulation has never been bridged, their numerical results did contribute to the physical understanding of the formation of a UPS image.

Declercq

The ultrasonic polar scan research has been further extended by Nico Declercq when he worked under the guidance of Joris Degrieck. He applied the technique for monitoring tension-tension induced fatigue damage in glass fiber composites by detecting changes in the characteristic fingerprint (see Figure 2-14) [179].

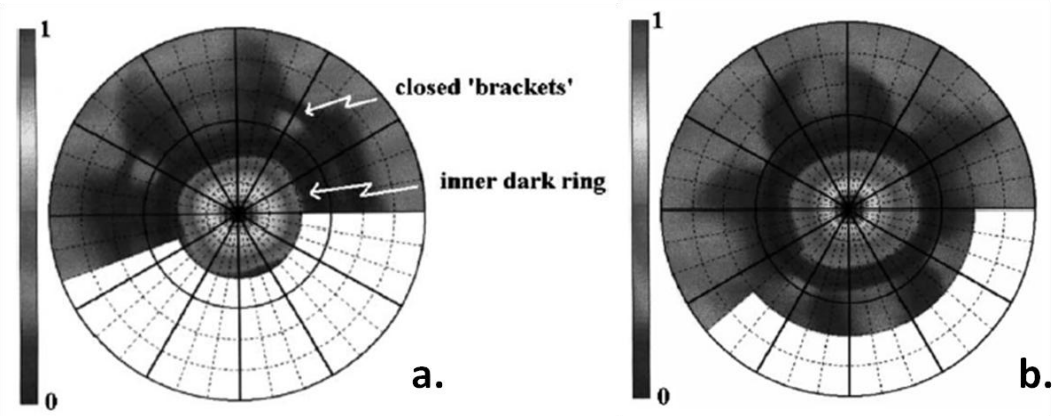

Figure 2-15: P-UPS experiments of glass fiber composite: before fatigue (a) after fatigue (b). (Figure reproduced from reference [179]).

In addition, Declercq extended the simulation technique towards layered viscoelastic materials having arbitrary anisotropy using the global matrix method [173-174]. As such, the simulation model can be applied to a wide range of layered composites.

Upon leaving to Georgia Institute of Technology campus Lorraine in Metz (France), an ultrasonic Polar C-scanner has been built by Inspection Technology Europe BV which is now located at Declercq's lab. With their modern polar-C scanner, they have made polar scan images of composites which were damaged by inducing tension and bending until failure occurred (see Figure 2-16) [180]. From those results, they concluded that the P-UPS is capable of detecting damage in composites due to tension and bending. It was further stated in that publication that the recording of the time-of-flight (TOF) value, instead of the maximum amplitude, shows superior sensitivity to the damage features, though on the expense of more complex data acquisition. Anyhow, it may be clear that the quality of Degrieck's experiments (Figure 2-14) has never been attained again.

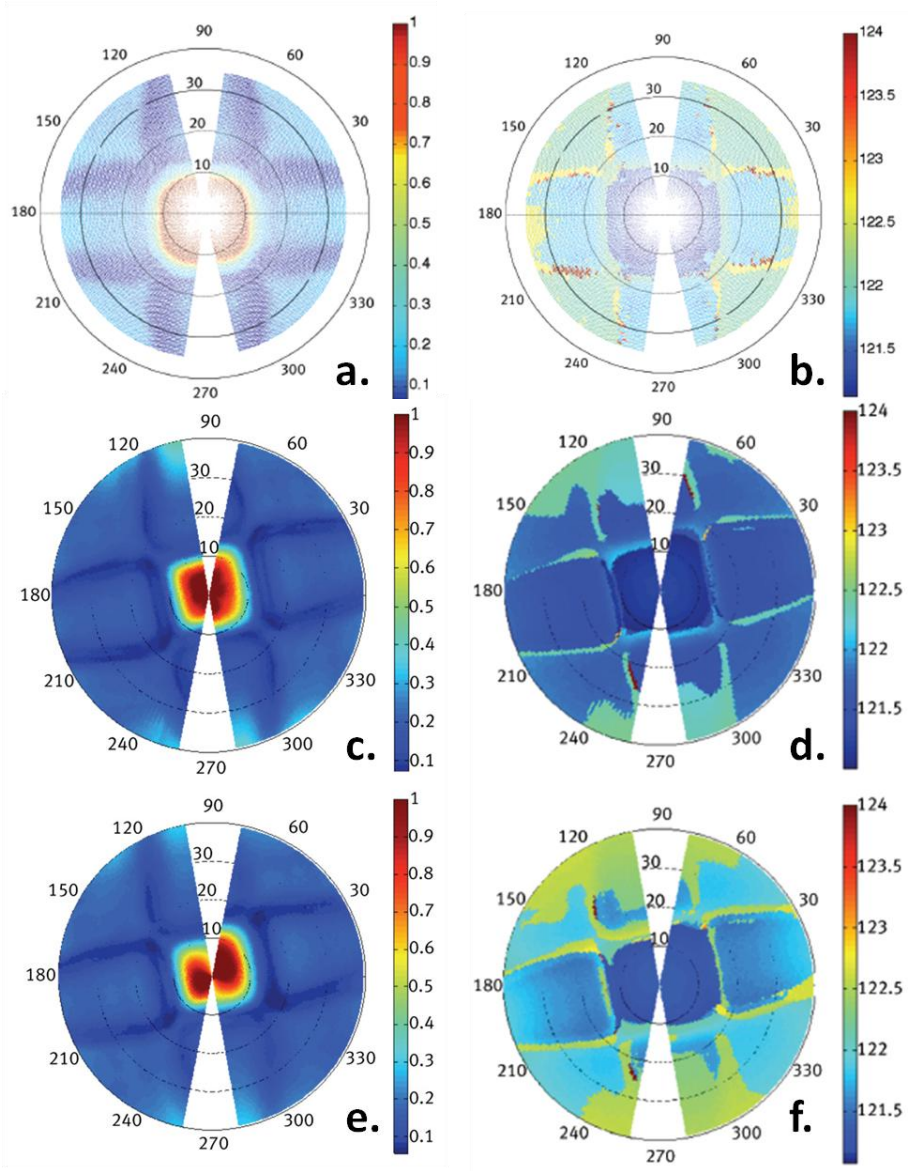

Figure 2-16: P-UPS experiments of glass fiber composites: virgin sample (a-b), tensile fractured sample scanned near fracture location (c-d) and tensile fractured sample scanned farther away from fracture location (e-f). Left row corresponds to amplitude recording, right column to TOF recording. (Figure reproduced from reference [180]).

Besides the three mentioned research laboratories (Delft University, Ghent University and Georgia Institute of Technology), no other research institutes (to the author's best knowledge) have further explored the capabilities of the

ultrasonic polar scan. Bearing in mind the many promising applications of the UPS methodology, this is difficult to understand.

2. 3. 4. Interests and Opportunities

Contrary to the classical ultrasonic C-scan, the UPS method insonifies a single material spot at many oblique incidence angles $\psi(\varphi,\theta)$. For this reason, the ultrasonic polar scan is well suited for the inspection of anisotropic fiber reinforced composite materials, having different mechanical properties in different material directions.

The UPS method does not require the selection of particular insonification planes, consequently no *a priori* knowledge about the specimen of interest is required. This however is on the expense of a more involved experimental methodology as two angles, instead of one angle, need to be varied.

The UPS simply records amplitude values for which the most elementary electronics suffice. This is in strong contrast with the various spectroscopic approaches discussed above, requiring complex and expensive acquisition modules. In addition, it is well known that spectroscopic approaches produce additional difficulty because of aliasing artifacts, normalization matters, resolution in frequency domain, spectral leakage, etcetera. For possible industrial implementation, these difficulties should not be underrated.

The UPS method is fully applicable to samples where only single-sided access is available. This is easily understood considering that the method does not require time measurements, but simply puts on view stimulations conditions. Sample preparation on the other hand is also ubiquitous: the method is applicable to thick as well as plate-like specimens. As such, the methodology is fully applicable for *in situ* measurements, at least on the condition that a miniaturized apparatus is constructed. With the current progress in phased array and phased matrix technology, it may be expected that the complex mechanical movement within an ultrasonic polar scan experiment can be fully replaced by an electronic analogue. This could provide the basis for the construction of a hand-held scanner which meets in-field requirements.

As a single spot is being insonified, the UPS should be capable of measuring local composite material characteristics.

Finally, the UPS method has the promising capability to characterize elastic material parameters as well as to extract damage features which reflect the composite's health. As such, the UPS provides a versatile methodology which could revolutionize the field of NDT and material characterization.

2. 3. 5. Current Shortcomings

The above paragraphs identified many promising features of the ultrasonic polar scan for NDT and material characterization. However, many of these promising capabilities were identified already more than 30 years ago. Till now, few of these capabilities have been only demonstrated in a pure qualitative way, despite the opportunities this would create for science and industry.

To the author's belief, the barrier for transforming the current UPS technique to a full quantitative methodology is found in the limitations of conducted studies so far, which may be summarized in three main points:

- Lack of high quality experimental data (see the various low-quality experiments shown in Section 2.3.3).
- Lack of a true-to-nature and computationally efficient simulation model.
- Lack of adequate inverse modeling techniques to couple experiment to simulation.

It is the author's intent to tackle these three shortcomings as good as possible, in order to bring the UPS technique in a new era, and to become a first-class successor of conventional quantitative NDT and characterization methods.

2. 4. Conclusions

A limited review has been given concerning several NDT and characterization techniques which are currently popular in science and industry. Both the opportunities and limitations have been identified.

A historical overview of the ultrasonic polar scan is given, starting from the pioneering work of Van Dreumel and Speyer, over the work of Degrieck, up to the recently obtained results by Declercq. A short physical background is given for the main features observed in a UPS image. Finally, the interest of

the UPS method for NDT and material characterization has been shortly outlined. In addition, it is discussed what further steps are required to bring the technique to the level, and to become a full quantitative NDT technique for composite materials.

2. 5. References

[1] http://pacific.scoop.co.nz/2011/10/probable-wwii-submarine-wreck-found-in-papua-new-guinea/.

[2] http://www.midcontinent.org/rollingstock/builders/TracyFales.htm.

[3] http://globalnde.wordpress.com/2012/09/24/history-of-ndt/.

[4] Yolken, T.H., *Selecting a Nondestructive Testing Method, Part III: Eddy Current Testing*, in *The AMMTIAC Quarterly*.

[5] Auld, B.A. and J.C. Moulder, *Review of advances in quantitative eddy current nondestructive evaluation.* Journal of Nondestructive Evaluation, 1999. 18(1): p. 3-36.

[6] Sophian, A., G.Y. Tian, D. Taylor, and J. Rudlin, *A feature extraction technique based on principal component analysis for pulsed Eddy current NDT.* Ndt & E International, 2003. 36(1): p. 37-41.

[7] Lebrun, B., Y. Jayet, and J.C. Baboux, *Pulsed eddy current signal analysis: Application to the experimental detection and characterization of deep flaws in highly conductive materials.* Ndt & E International, 1997. 30(3): p. 163-170.

[8] Chen, T.L., G.Y. Tian, A. Sophian, and P.W. Que, *Feature extraction and selection for defect classification of pulsed eddy current NDT.* Ndt & E International, 2008. 41(6): p. 467-476.

[9] Blodgett, M.P. and P.B. Nagy, *Eddy current assessment of near-surface residual stress in shot-peened nickel-base superalloys.* Journal of Nondestructive Evaluation, 2004. 23(3): p. 107-123.

[10] Sophian, A., G.Y. Tian, D. Taylor, and J. Rudlin, *Electromagnetic and eddy current NDT: a review.* Insight, 2001. 43(5): p. 302-306.

[11] Rontgen, W.C., *On a New Kind of Rays.* Nature, 1896. 53.

[12] Buffiere, J.Y., E. Maire, J. Adrien, J.P. Masse, and E. Boller, *In Situ Experiments with X ray Tomography: an Attractive Tool for Experimental Mechanics.* Experimental Mechanics, 2010. 50(3): p. 289-305.

[13] Liao, T.W. and Y.M. Li, *An automated radiographic NDT system for weld inspection: Part II - Flaw detection.* Ndt & E International, 1998. 31(3): p. 183-192.

[14] Liao, T.W. and J.W. Ni, *An automated radiographic NDT system for weld inspection .1. Weld extraction.* Ndt & E International, 1996. 29(3): p. 157-162.

[15] Wang, G. and T.W. Liao, *Automatic identification of different types of welding defects in radiographic images.* Ndt & E International, 2002. 35(8): p. 519-528.

[16] Sket, F., A. Enfedaque, C. Alton, C. González, J.M. Molina-Aldareguia, and J. Llorca, *Automatic quantification of matrix cracking and fiber rotation by*

X-ray computed tomography in shear-deformed carbon fiber-reinforced laminates. Composites Science and Technology, 2014. 90(0): p. 129-138.

[17] Peters, K., M. Studer, J. Botsis, A. Iocco, H. Limberger, and R. Salathe, *Embedded optical fiber Bragg grating sensor in a nonuniform strain field: Measurements and simulations.* Experimental Mechanics, 2001. 41(1): p. 19-28.

[18] De Waele, W., J. Degrieck, W. Moerman, L. Taerwe, and P. De Baets, *Feasibility of integrated optical fibre sensors for condition monitoring of composite structures - Part I: Comparison of Bragg-sensors and strain gauges.* Insight, 2003. 45(4): p. 266-271.

[19] Degrieck, J., W. De Waele, and P. Verleysen, *Monitoring of fibre reinforced composites with embedded optical fibre Bragg sensors, with application to filament wound pressure vessels.* Ndt & E International, 2001. 34(4): p. 289-296.

[20] Chapeleau, X., M. Drissi-Habti, and T. Tomonori, *Embedded Optical Fiber Sensors in Civil Engineering Composite Structures.* Materials Evaluation, 2010. 68(4): p. 408-415.

[21] Greene, J., C. Kozikowski, R. O'Neal, S. Poland, M. Camden, and L. Simmons, *Optical fiber strain gages for high-cycle fatigue monitoring of ceramic matrix composite materials*. Process Control and Sensors for Manufacturing, ed. R.H. Bossi and D.M. Pepper. Vol. 3399. 1998. 6-11.

[22] Yang, Y.C. and K.S. Han, *Damage and failure monitoring of fiber-metal laminates using optical fiber sensors*, in *Advances in Nondestructive Evaluation, Pt 1-3*, S.S. Lee, et al., Editors. 2004. p. 690-695.

[23] Luyckx, G., E. Voet, N. Lammens, and J. Degrieck, *Strain Measurements of Composite Laminates with Embedded Fibre Bragg Gratings: Criticism and Opportunities for Research.* Sensors, 2011. 11(1): p. 384-408.

[24] Lammens, N., D. Kinet, K. Chah, G. Luyckx, C. Caucheteur, J. Degrieck, and P. Megret, *Residual strain monitoring of out-of-autoclave cured parts by use of polarization dependent loss measurements in embedded optical fiber Bragg gratings.* Composites Part a-Applied Science and Manufacturing, 2013. 52: p. 38-44.

[25] Pagnotta, L. and A. Poggialini, *Measurement of residual internal stresses in optical fiber preforms.* Experimental Mechanics, 2003. 43(1): p. 69-76.

[26] Luyckx, G., E. Voet, N. Lammens, W. De Waele, and J. Degrieck, *Residual strain-induced birefringent FBGs for multi-axial strain monitoring of CFRP composite laminates.* Ndt & E International, 2013. 54: p. 142-150.

[27] Alzofon, F.E., *AN INFRARED NONDESTRUCTIVE TESTING SYSTEM FOR ROCKET MOTORS.* Materials Evaluation, 1965. 23(11): p. 537-&.

[28] Alzofon, F.E. and A.D. McDonald, *INFRARED EVALUATION OF MICROWELD QUALITY.* Materials Evaluation, 1967. 25(8): p. 183-&.

[29] Green, D.R., *EMISSIVITY INDEPENDENT INFRARED THERMAL TESTING METHOD.* Materials Evaluation, 1965. 23(2): p. 79-&.

[30] Green, D.R., *PRINCIPLES AND APPLICATIONS OF EMITTANCE-INDEPENDENT INFRARED NONDESTRUCTIVE TESTING.* Applied Optics, 1968. 7(9): p. 1779-&.

[31] Green, D.R., *THERMAL AND INFRARED NONDESTRUCTIVE TESTING OF COMPOSITES AND CERAMICS.* Materials Evaluation, 1970. 28(9): p. A26-&.

[32] Avdelidis, N.P., B.C. Hawtin, and D.P. Almond, *Transient thermography in the assessment of defects of aircraft composites.* Ndt & E International, 2003. 36(6): p. 433-439.

[33] Ball, R.J. and D.P. Almond, *The detection and measurement of impact damage in thick carbon fibre reinforced laminates by transient thermography.* Ndt & E International, 1998. 31(3): p. 165-173.

[34] Busse, G., D. Wu, and W. Karpen, *Thermal wave imaging with phase sensitive modulated thermography.* Journal of Applied Physics, 1992. 71(8): p. 3962-3965.

[35] Choi, M., K. Kang, J. Park, W. Kim, and K. Kim, *Quantitative determination of a subsurface defect of reference specimen by lock-in infrared thermography.* Ndt & E International, 2008. 41(2): p. 119-124.

[36] Harizi, W., S. Chaki, G. Bourse, and M. Ourak, *Mechanical damage assessment of Glass Fiber-Reinforced Polymer composites using passive infrared thermography.* Composites Part B: Engineering, 2014. 59(0): p. 74-79.

[37] Li, T., D.P. Almond, and D.A.S. Rees, *Crack imaging by scanning pulsed laser spot thermography.* Ndt & E International, 2011. 44(2): p. 216-225.

[38] Manohar, A. and F.L. di Scalea, *Determination of Defect Depth and Size Using Virtual Heat Sources in Pulsed Infrared Thermography.* Experimental Mechanics, 2013. 53(4): p. 661-671.

[39] Schmutzler, H., M. Alder, N. Kosmann, H. Wittich, and K. Schulte, *Degradation monitoring of impact damaged carbon fibre reinforced polymers under fatigue loading with pulse phase thermography.* Composites Part B: Engineering, 2014. 59(0): p. 221-229.

[40] Pierce, G.W. and D.R. Griffin, *Experimental Determination of Supersonic Notes Emitted by Bats.* Journal of Mammalogy, 1938. 19.

[41] Curie, J. and P. Curie, *Developpement, par pression, de l'electricite polaire dans les cristaux hemiedres a faces inclinees.* Comptes Rendus de l'Academie de Sciences, 1880. 91.

[42] Curie, J. and P. Curie, *Sur l'electricite polaire dans les cristaux bemiedres a faces inclinees.* Comptes Rendus de l'Academie de Sciences, 1880. 91.

[43] Curie, J. and P. Curie, *Cantractions and dilatations produites par des tensions dans les cristaux hemiedres a faces inclinees.* Comptes Rendus de l'Academie de Sciences, 1880. 93.

[44] Solokov, S.Y., *On the Problem of the Propagation of Ultrasonic Oscillations in Various Bodies.* Elek. Nachr. Tech., 1929. 6.

[45] Firestone, F.A., *The Supersonic Reflectoscope, an Instrument for Inspecting the Interior of Solid Parts by Means of Sound Waves.* The Journal of the Acoustical Society of America, 1946. 17(3): p. 288 - 299.

[46] Firestone, F.A. and J.R. Frederick, *Refinements in supersonic reflectoscopy. Polarized sound.* Journal of the Acoustical Society of America, 1946. 18.

[47] Bergmann, L., *Der Ultraschall*. 1954, Leipzig: S.Hirzel Verlag.

[48] Leksell, L., *Echo-encephalography: detection of intracranial complications following head injury.* Acta Chirurgica Scandinavia, 1954. 110.

[49] Zimmer, A., J. Vrana, J. Meiser, W. Maximini, and N. Blaes, *EVOLUTION OF THE ULTRASONIC INSPECTION OF HEAVY ROTOR FORGINGS OVER THE LAST DECADES.* AIP Conference Proceedings, 2010. 1211(1): p. 1631-1638.

[50] *NDT Industry News: Ultrasonic C-scan Inspection - an Americal Innovation in 1956.* Pacific Northwest Section of American Society of Nondestructive Testing, 2004. 47(8).

[51] Tsao, C.C. and H. Hocheng, *Computerized tomography and C-Scan for measuring delamination in the drilling of composite materials using various drills.* International Journal of Machine Tools and Manufacture, 2005. 45(11): p. 1282-1287.

[52] Wu, H.Y.T. and G.S. Springer, *MEASUREMENTS OF MATRIX CRACKING AND DELAMINATION CAUSED BY IMPACT ON COMPOSITE PLATES.* Journal of Composite Materials, 1988. 22(6): p. 518-532.

[53] Wooh, S.C. and C. Wei, *A high-fidelity ultrasonic pulse-echo scheme for detecting delaminations in composite laminates.* Composites Part B-Engineering, 1999. 30(5): p. 433-441.

[54] Růžek, R., R. Lohonka, and J. Jironč, *Ultrasonic C-Scan and shearography NDI techniques evaluation of impact defects identification.* Ndt & E International, 2006. 39(2): p. 132-142.

[55] Imielińska, K., M. Castaings, R. Wojtyra, J. Haras, E.L. Clezio, and B. Hosten, *Air-coupled ultrasonic C-scan technique in impact response testing of carbon fibre and hybrid: glass, carbon and Kevlar/epoxy composites.* Journal of Materials Processing Technology, 2004. 157–158(0): p. 513-522.

[56] Berketis, K., D. Tzetzis, and P.J. Hogg, *Impact damage detection and degradation monitoring of wet GFRP composites using noncontact ultrasonics.* Polymer Composites, 2009. 30(8): p. 1043-1049.

[57] Kas, Y.O. and C. Kaynak, *Ultrasonic (C-scan) and microscopic evaluation of resin transfer molded epoxy composite plates.* Polymer Testing, 2005. 24(1): p. 114-120.

[58] Daniel, I.M., S.C. Wooh, and I. Komsky, *Quantitative porosity characterization of composite materials by means of ultrasonic attenuation measurements.* Journal of Nondestructive Evaluation, 1992. 11(1): p. 1-8.

[59] Guo, N. and P. Cawley, *The non-destructive assessment of porosity in composite repairs.* Composites, 1994. 25(9): p. 842-850.

[60] di Scalea, F.L. and R.E. Green, *High-sensitivity laser-based ultrasonic C-scan system for materials inspection.* Experimental Mechanics, 1999. 39(4): p. 329-334.

[61] D'Orazio, T., M. Leo, A. Distante, C. Guaragnella, V. Pianese, and G. Cavaccini, *Automatic ultrasonic inspection for internal defect detection in composite materials.* Ndt & E International, 2008. 41(2): p. 145-154.

[62] De Baere, I., S. Jacques, M. Kersemans, W. Van Paepegem, and J. Degrieck, *Experimental Study of the Crack Growth of a Carbon Fabric Reinforced PPS under Mode I and Mode II Loading Conditions*. Icem15: 15th International Conference on Experimental Mechanics, ed. J.F. SilvaGomes and M.A.P. Vaz. 2012.

[63] Holmes, C., B.W. Drinkwater, and P.D. Wilcox, *Post-processing of the full matrix of ultrasonic transmit-receive array data for non-destructive evaluation.* Ndt & E International, 2005. 38(8): p. 701-711.

[64] Hand, J.W., A. Shaw, N. Sadhoo, S. Rajagopal, R.J. Dickinson, and L.R. Gavrilov, *A random phased array device for delivery of high intensity focused ultrasound.* Physics in Medicine and Biology, 2009. 54(19): p. 5675-5693.

[65] Drinkwater, B.W. and P.D. Wilcox, *Ultrasonic arrays for non-destructive evaluation: A review.* Ndt & E International, 2006. 39(7): p. 525-541.

[66] Angelsen, B.A.J., H. Torp, S. Holm, K. Kristoffersen, and T.A. Whittingham, *Which transducer array is best?* European Journal of Ultrasound, 1995. 2(2): p. 151-164.

[67] Long, R., J. Russell, and P. Cawley, *Ultrasonic phased array inspection using full matrix capture.* Insight - Non-Destructive Testing and Condition Monitoring, 2012. 54(7): p. 380-385.

[68] Kazys, R. and L. Svilainis, *Ultrasonic detection and characterization of delaminations in thin composite plates using signal processing techniques.* Ultrasonics, 1997. 35(5): p. 367-383.

[69] Baskaran, G., K. Balasubramaniam, C.V. Krishnamurthy, and C.L. Rao, *Ray based model for the ultrasonic time-of-flight diffraction simulation of thin walled structure inspection.* Journal of Pressure Vessel Technology-Transactions of the Asme, 2005. 127(3): p. 262-268.

[70] Satyanarayan, L., K.B. Kumaran, C. Krishnamurthy, and K. Balasubramaniam, *Inverse method for detection and sizing of cracks in thin sections using a hybrid genetic algorithm based signal parametrisation.* Theoretical and Applied Fracture Mechanics, 2008. 49(2): p. 185-198.

[71] Bar-cohen, Y. and R.L. Crane, *Acoustic-backscattering imaging of subcritical flaws in composites.* Materials Evaluation, 1982. 40(9): p. 970-975.

[72] Bar-Cohen, Y. and R.L. Crane, *The Acoustic Backscattering Method as a Means of Characterizing Composites and Imaging Flaws. Patent no 4,457,174*. July 3 1984.

[73] Bar-Cohen, Y. and A. Mal, *Characterization of Composite Laminates using Combined LLW and PBS Methods*, in *Review of Progress in Quantitative Nondestructive Evaluation*, D. Thompson and D. Chimenti, Editors. 1991, Springer US. p. 1555-1560.

[74] Bar-Cohen, Y., A.K. Mal, and M.E. Lasser. *NDE of hidden flaws in aging aircraft structures using obliquely backscattered ultrasonic signals (OBUS)*. 1999.

[75] Kwon, S.D., M.S. Choi, and S.H. Lee, *The applications of ultrasonic backward radiation from a layered substrate submerged in liquid.* Ndt & E International, 2000. 33(5): p. 275-281.

[76] Nagy, P.B. and J.H. Rose, *SURFACE-ROUGHNESS AND THE ULTRASONIC-DETECTION OF SUBSURFACE SCATTERERS.* Journal of Applied Physics, 1993. 73(2): p. 566-580.

[77] Kim, H.C., J.K. Lee, S.Y. Kim, and S.D. Kwon, *Influence of the microstructure on the ultrasonic backscattered energy from a liquid/solid interface at the Rayleigh angle.* Japanese Journal of Applied Physics Part 1-Regular Papers Short Notes & Review Papers, 1999. 38(1A): p. 260-267.

[78] Nagy, P.B. and L. Adler, *Increased incoherent backscattering from a liquid-solid interface at the Rayleigh angle.* Journal of the Acoustical Society of America, 1994. 96(4): p. 2537-2545.

[79] Jacques, F., F. Moreau, and E. Ginzel, *Ultrasonic backscatter sizing using phased array – developments in tip diffraction flaw sizing.* Insight - Non-Destructive Testing and Condition Monitoring, 2003. 45(11): p. 724-728.

[80] Nagy, P.B., A. Jungman, and L. Adler, *Measurements of backscattered leaky lamb waves in composite plates.* Materials Evaluation, 1988. 46(1): p. 97-100.

[81] Bechtold, G., K.M. Gaffney, J. Botsis, and K. Friedrich, *Fibre orientation in an injection moulded specimen by ultrasonic backscattering.* Composites Part a-Applied Science and Manufacturing, 1998. 29(7): p. 743-748.

[82] Kinra, V.K., A.S. Ganpatye, and K. Maslov, *Ultrasonic ply-by-ply detection of matrix cracks in laminated composites.* Journal of Nondestructive Evaluation, 2006. 25(1): p. 39-51.

[83] Aymerich, F. and S. Meili, *Ultrasonic evaluation of matrix damage in impacted composite laminates.* Composites Part B-Engineering, 2000. 31(1): p. 1-6.

[84] Sukmana, D.D. and I. Ihara, *Surface roughness characterization through the use of diffuse component of scattered air-coupled ultrasound.* Japanese Journal of Applied Physics Part 1-Regular Papers Brief Communications & Review Papers, 2006. 45(5B): p. 4534-4540.

[85] De Billy, M., F. Cohentenoudji, A. Jungman, and G.J. Quentin, *POSSIBILITY OF ASSIGNING A SIGNATURE TO ROUGH SURFACES USING ULTRASONIC BACKSCATTERING DIAGRAMS.* Ieee Transactions on Sonics and Ultrasonics, 1976. 23(5): p. 356-363.

[86] De Billy, M. and G. Quentin, *MEASUREMENT OF THE PERIODICITY OF INTERNAL SURFACES BY ULTRASONIC TESTING.* Journal of Physics D-Applied Physics, 1982. 15(10): p. 1835-1841.

[87] Shin, Y.C., S.J. Oh, and S.A. Coker, *SURFACE-ROUGHNESS MEASUREMENT BY ULTRASONIC SENSING FOR IN-PROCESS MONITORING.* Journal of Engineering for Industry-Transactions of the Asme, 1995. 117(3): p. 439-447.

[88] Song, S.-J., D.-J. Yang, H.-J. Kim, S.D. Kwon, Y.-Z. Lee, J.-Y. Kim, and S.-C. Choi, *Characterization of TiN coating layers using ultrasonic backward radiation.* Ultrasonics, 2006. 44, Supplement(0): p. e1083-e1087.

[89] Kim, Y.H., S.J. Song, and S.D. Kwon, *Determination of Phase Velocity Dispersion Curves and Group Velocity in a Plate Using Backward Radiated Leaky Lamb Waves.* AIP Conference Proceedings, 2004. 700(1): p. 150-157.

[90] Maynard, J., *Resonant ultrasound spectroscopy.* Physics Today, 1996. 49(1): p. 26-31.

[91] Longo, R., T. Delaunay, D. Laux, M. El Mouridi, O. Arnould, and E. Le Clezio, *Wood elastic characterization from a single sample by resonant ultrasound spectroscopy.* Ultrasonics, 2012. 52(8): p. 971-974.

[92] Isaak, D.G. and I. Ohno, *Elastic constants of chrome-diopside: application of resonant ultrasound spectroscopy to monoclinic single-crystals.* Physics and Chemistry of Minerals, 2003. 30(7): p. 430-439.

[93] Lee, T., R.S. Lakes, and A. Lal, *Resonant ultrasound spectroscopy for measurement of mechanical damping: Comparison with broadband viscoelastic spectroscopy.* Review of Scientific Instruments, 2000. 71(7): p. 2855-2861.

[94] Muller, M., A. Sutin, R. Guyer, M. Talmant, P. Laugier, and P.A. Johnson, *Nonlinear resonant ultrasound spectroscopy (NRUS) applied to damage assessment in bone.* Journal of the Acoustical Society of America, 2005. 118(6): p. 3946-3952.

[95] Solodov, I., J.X. Bai, and G. Busse, *Resonant ultrasound spectroscopy of defects: Case study of flat-bottomed holes.* Journal of Applied Physics, 2013. 113(22).

[96] Ohtani, T. and Y. Ishii, *Nonlinear Resonant Ultrasound Spectroscopy (NRUS) Applied to Fatigue Damage Evaluation in a Pure Copper*, in *Nonlinear Acoustics: State-of-the-Art and Perspectives*, T. Kamakura and N. Sugimoto, Editors. 2012. p. 204-207.

[97] Payan, C., V. Garnier, J. Moysan, and P.A. Johnson, *Applying nonlinear resonant ultrasound spectroscopy to improving thermal damage assessment in concrete.* The Journal of the Acoustical Society of America, 2007. 121(4): p. EL125-EL130.

[98] Van den Abeele, K.E.A., P.A. Johnson, and A. Sutin, *Nonlinear elastic wave spectroscopy (NEWS) techniques to discern material damage, part I: Nonlinear wave modulation spectroscopy (NWMS).* Research in Nondestructive Evaluation, 2000. 12(1): p. 17-30.

[99] Van den Abeele, K.E.A., J. Carmeliet, J.A. Ten Cate, and P.A. Johnson, *Nonlinear elastic wave spectroscopy (NEWS) techniques to discern material damage, Part II: Single-mode nonlinear resonance acoustic spectroscopy.* Research in Nondestructive Evaluation, 2000. 12(1): p. 31-42.

[100] Meo, M., U. Polimeno, and G. Zumpano, *Detecting Damage in Composite Material Using Nonlinear Elastic Wave Spectroscopy Methods.* Applied Composite Materials, 2008. 15(3): p. 115-126.

[101] Markham, M.F., *Measurement of the elastic constants of fibre composites by ultrasonics.* Composites, 1970. 1(3): p. 145-149.

[102] Castagnede, B., J.T. Jenkins, W. Sachse, and S. Baste, *Optimal determination of the elastic-constants of composite-materials from ultrasonic wave-speed measurements.* Journal of Applied Physics, 1990. 67(6): p. 2753-2761.

[103] Rokhlin, S.I. and W. Wang, *DOUBLE THROUGH-TRANSMISSION BULK WAVE METHOD FOR ULTRASONIC PHASE-VELOCITY MEASUREMENT AND DETERMINATION OF ELASTIC-CONSTANTS OF COMPOSITE-MATERIALS.* Journal of the Acoustical Society of America, 1992. 91(6): p. 3303-3312.

[104] Baudouin, S. and B. Hosten, *Immersion ultrasonic method to measure elastic constants and anisotropic attenuation in polymer-matrix and fiber-reinforced composite materials.* Ultrasonics, 1996. 34(2-5): p. 379-382.

[105] Hosten, B., D. Hutchins, and D. Schindel, *Air-Coupled Ultrasonic Bulk Waves to Measure Elastic Constants in Composite Materials*, in *Review of Progress in Quantitative Nondestructive Evaluation*, D. Thompson and D. Chimenti, Editors. 1996, Springer US. p. 1075-1082.

[106] Balasubramaniam, K. and S.C. Whitney, *Ultrasonic through-transmission characterization of thick fibre-reinforced composites.* Ndt & E International, 1996. 29(4): p. 225-236.

[107] Degtyar, A.D. and S.I. Rokhlin, *Comparison of elastic constant determination in anisotropic materials from ultrasonic group and phase velocity data.* Journal of the Acoustical Society of America, 1997. 102(6): p. 3458-3466.

[108] Balasubramaniam, K. and N.S. Rao, *Inversion of composite material elastic constants from ultrasonic bulk wave phase velocity data using genetic algorithms.* Composites Part B-Engineering, 1998. 29(2): p. 171-180.

[109] Wu, T.T. and Y.H. Liu, *On the measurement of anisotropic elastic constants of fiber-reinforced composite plate using ultrasonic bulk wave and laser generated Lamb wave.* Ultrasonics, 1999. 37(6): p. 405-412.

[110] Reddy, S.S.S., K. Balasubramaniam, C.V. Krishnamurthy, and M. Shankar, *Ultrasonic goniometry immersion techniques for the measurement of elastic moduli.* Composite Structures, 2005. 67(1): p. 3-17.

[111] Vishnuvardhan, J., C.V. Krishnamurthy, and K. Balasubramaniam, *Genetic algorithm reconstruction of orthotropic composite plate elastic constants from a single non-symmetric plane ultrasonic velocity data*. Composites Part B-Engineering, 2007. 38(2): p. 216-227.

[112] Vishnuvardhan, J., C.V. Krishnamurthy, and K. Balasubramaniam, *Genetic algorithm based reconstruction of the elastic moduli of orthotropic plates using an ultrasonic guided wave single-transmitter-multiple-receiver SHM array.* Smart Materials & Structures, 2007. 16(5): p. 1639-1650.

[113] Adamowski, J.C., F. Buiochi, and R.T. Higuti, *Ultrasonic material characterization using large-aperture PVDF receivers.* Ultrasonics, 2010. 50(2): p. 110-115.

[114] Every, A.G. and W. Sachse, *Determination of the elastic constants of anisotropic solids from acoustic-wave group-velocity measurements.* Physical Review B, 1990. 42(13): p. 8196-8205.

[115] Deschamps, M. and C. Bescond, *Numerical-method to recover the elastic-constants from ultrasound group velocities.* Ultrasonics, 1995. 33(3): p. 205-211.

[116] Kim, K.Y., R. Sribar, and W. Sachse, *Analytical and optimization procedures for determination of all elastic constants of anisotropic solids from group velocity data measured in symmetry planes.* Journal of Applied Physics, 1995. 77(11): p. 5589-5600.

[117] Wang, L.T., *Determination of the ray surface and recovery of elastic-constants of anisotropic elastic media - a direct and inverse approach.* Journal of Physics-Condensed Matter, 1995. 7(20): p. 3863-3880.

[118] Pluta, M., M. Schubert, J. Jahny, and W. Grill, *Angular spectrum approach for the computation of group and phase velocity surfaces of acoustic waves in anisotropic materials.* Ultrasonics, 2000. 38(1-8): p. 232-236.

[119] Castellano, A., P. Foti, A. Fraddosio, S. Marzano, and M.D. Piccioni, *Mechanical characterization of CFRP composites by ultrasonic immersion tests: experimental and numerical approaches.* Composites Part B: Engineering, 2014. accepted manuscript.

[120] Lamb, H., *On Waves in an Elastic Plate.* Proceedings of the Royal Society A-Mathematical Physical and Engineering Sciences, 1917(93): p. 114-128.

[121] Rose, J.L., *Ultrasonic Waves in Solid Media*. 1999: Cambridge University Press. 454.

[122] Auld, B.A., *Acoustic Fields and Waves in Solids, second edition*. 1990, Florida: Krieger publishing company. 856.

[123] Lord Rayleigh, F.R.S., *On Waves Propagated along the Plane Surface of an Elastic Solid.* Proceedings of the London Mathematical society, 1885. s1-17(1): p. 4-11.

[124] I.A.Viktorov, *Rayleigh and Lamb waves*. 1967, New York: Plenum. 154.
[125] Bertoni, H.L. and T. Tamir, *Unified theory of Rayleigh-angle phenomena for acoustic beams at liquid-solid interfaces.* Applied physics, 1973. 2(4): p. 157-172.
[126] Tamir, T. and H.L. Bertoni, *Lateral displacement of optical beams at multilayered and periodic structures.* Journal of the Optical Society of America, 1971. 61(10): p. 1397-1413.
[127] Schoch, A., *Der Schalldurchgang durch plate.* acustica, 1952. 2.
[128] Nayfeh, A.H. and D.E. Chimenti, *Ultrasonic wave reflection from liquid-coupled orthotropic plates with application to fibrous composites.* Journal of Applied Mechanics-Transactions of the Asme, 1988. 55(4): p. 863-870.
[129] Nayfeh, A.H., *Wave Propagation in Layered Anisotropic Media: with applications to composites*. 1995, New York: North-Holland.
[130] Hosten, B. and M. Castaings, *Transfer-matrix of multilayered absorbing and anisotropic media - measurements and simulations of ultrasonic wave-propagation through composite-materials.* Journal of the Acoustical Society of America, 1993. 94(3): p. 1488-1495.
[131] Cawley, P. and B. Hosten, *The use of large ultrasonic transducers to improve transmission coefficient measurements on viscoelastic anisotropic plates.* Journal of the Acoustical Society of America, 1997. 101(3): p. 1373-1379.
[132] Castaings, M., B. Hosten, and T. Kundu, *Inversion of ultrasonic, plane-wave transmission data in composite plates to infer viscoelastic material properties.* Ndt & E International, 2000. 33(6): p. 377-392.
[133] Kumar, P.P., K. Balasubramaniam, and C.V. Krishnamurthy, *Determination of transmission spectra using ultrasonic NDE.* Transactions of the Indian Institute of Metals, 2006. 59(2): p. 181-184.
[134] Kumar, P.P., C.V. Krishnamurthy, and K. Balasubramaniam, *Elastic constants inversion from ultrasonic transmission spectra obtained using a wide aperture PVDF sensor*, in *Review of Progress in Quantitative Nondestructive Evaluation, Vols 25A and 25B*, D.O. Thompson and D.E. Chimenti, Editors. 2006. p. 1127-1132.
[135] Bouzidi, Y. and D.R. Schmitt, *A large ultrasonic bounded acoustic pulse transducer for acoustic transmission goniometry: Modeling and calibration.* Journal of the Acoustical Society of America, 2006. 119(1): p. 54-64.
[136] Puthillath, P., C.V. Krishnamurthy, and K. Balasubramaniam, *Hybrid inversion of elastic moduli of composite plates from ultrasonic transmission spectra using PVDF plane wave sensor.* Composites Part B-Engineering, 2010. 41(1): p. 8-16.
[137] Karim, M.R., A.K. Mal, and Y. Barcohen, *INVERSION OF LEAKY LAMB WAVE DATA BY SIMPLEX ALGORITHM.* Journal of the Acoustical Society of America, 1990. 88(1): p. 482-491.
[138] Bar-Cohen, Y. and S.S. Lih, *Ultrasonic system for automatic determination of material stiffness constants*. 2000, Google Patents.
[139] Bar-Cohen, Y. and S.S. Lih, *Experimental enhancements of LLW dispersion data acquisition and implementation challenges to NDE of composites.* Materials Evaluation, 1999.

[140] Bar-Cohen, Y., A.K. Mal, S.-S. Lih, and Z. Chang. *Composite materials stiffness determination and defects characterization using enhanced leaky Lamb wave dispersion data acquisition method*. 1999.

[141] Bar-Cohen, Y., A.K. Mal, and S.-S. Lih, *NDE of composite materials using ultrasonic oblique insonification.* Journal Name: Materials Evaluation; (United States); Journal Volume: 51:11, 1993: p. Medium: X; Size: Pages: 1285-1296.

[142] Bar-Cohen, Y., A.K. Mal, and Z. Chang. *Composite material defect characterization using leaky Lamb wave dispersion data*. 1998.

[143] Fortineau, J., E. Le Clezio, F.V. Meulen, and G. Feuillard, *Moisture content characterization in composite materials based on ultrasonic transmission measurements.* Journal of Applied Physics, 2007. 101(11).

[144] Kersemans, M., I. De Baere, J. Degrieck, K. Van Den Abeele, L. Pyl, F. Zastavnik, H. Sol, and W. Van Paepegem, *Nondestructive damage assessment in fiber reinforced composites with the pulsed ultrasonic polar scan.* Polymer Testing, 2014. 34(0): p. 85-96.

[145] Kersemans, M., I. De Baere, J. Degrieck, K. Van Den Abeele, L. Pyl, F. Zastavnik, H. Sol, and W. Van Paepegem, *Damage Signature of Fatigued Fabric Reinforced Plastic in the Pulsed Ultrasonic Polar Scan.* Under review in Experimental Mechanics, 2014.

[146] Audoin, B. and C. Bescond, *Measurement by LASER-generated ultrasound of four stiffness coefficients of an anisotropic material at elevated temperatures.* Journal of Nondestructive Evaluation, 1997. 16(2): p. 91-100.

[147] Clorennec, D., C. Prada, and D. Royer, *Laser Ultrasonic Inspection of Plates Using Zero-Group Velocity Lamb Modes.* Ieee Transactions on Ultrasonics Ferroelectrics and Frequency Control, 2010. 57(5): p. 1125-1132.

[148] Chai, J.F. and T.T. Wu, *Determinations of anisotropic elastic constants using laser-generated surface waves.* The Journal of the Acoustical Society of America, 1994. 95(6): p. 3232-3241.

[149] Prada, C., O. Balogun, and T.W. Murray, *Laser-based ultrasonic generation and detection of zero-group velocity Lamb waves in thin plates.* Applied Physics Letters, 2005. 87(19).

[150] Balogun, O., T.W. Murray, and C. Prada, *Simulation and measurement of the optical excitation of the S-1 zero group velocity Lamb wave resonance in plates.* Journal of Applied Physics, 2007. 102(6).

[151] Murray, T.W., O. Balogun, C. Prada, D. Clorennec, and D. Royer, *Theory and applications of laser generated zero-group velocity lamb mode resonance*, in *Review of Progress in Quantitative Nondestructive Evaluation, Vol 27a and 27b*, D.O. Thompson and D.E. Chimenti, Editors. 2008. p. 255-262.

[152] Alleyne, D.N. and P. Cawley, *The interaction of Lamb waves with defects.* Ultrasonics, Ferroelectrics and Frequency Control, IEEE Transactions on, 1992. 39(3): p. 381-397.

[153] Seale, M.D., B.T. Smith, and W.H. Prosser, *Lamb wave assessment of fatigue and thermal damage in composites.* The Journal of the Acoustical Society of America, 1998. 103(5): p. 2416-2424.

[154] Seth, S.K., S.M. Spearing, and S. Constantinos, *Damage detection in composite materials using Lamb wave methods.* Smart Materials and Structures, 2002. 11(2): p. 269.

[155] Su, Z., L. Ye, and Y. Lu, *Guided Lamb waves for identification of damage in composite structures: A review*. Journal of Sound and Vibration, 2006. 295(3–5): p. 753-780.

[156] Marzani, A. and L. De Marchi, *Characterization of the elastic moduli in composite plates via dispersive guided waves data and genetic algorithms.* Journal of Intelligent Material Systems and Structures, 2013. 24(17): p. 2135-2147.

[157] Merkulov, L.G. and L.A. Yakovlev, *Propagation and reflection of ultrasonic beams in crystals.* Soviet Physics - Acoustics, 1962. 8(1): p. 6.

[158] Potel, C., S. Baly, J.F. de Belleval, M. Lowe, and P. Gatignol, *Deviation of a monochromatic Lamb wave beam in anisotropic multilayered media: Asymptotic analysis, numerical and experimental results.* Ieee Transactions on Ultrasonics Ferroelectrics and Frequency Control, 2005. 52(6): p. 987-1001.

[159] Balasubramaniam, K. and C.V. Krishnamurthy, *Ultrasonic guided wave energy behavior in laminated anisotropic plates.* Journal of Sound and Vibration, 2006. 296(4-5): p. 968-978.

[160] Wang, L. and F.G. Yuan, *Group velocity and characteristic wave curves of Lamb waves in composites: Modeling and experiments.* Composites Science and Technology, 2007. 67(7-8): p. 1370-1384.

[161] Voloshinov, V.B., V.I. Balakshy, L.A. Kulakova, and N. Gupta, *Acousto-optic properties of tellurium that are useful in anisotropic diffraction.* Journal of Optics A: Pure and Applied Optics, 2008. 10(9): p. 095002.

[162] Kersemans, M., N. Lammens, J. Degrieck, K. Van Den Abeele, L. Pyl, F. Zastavnik, H. Sol, and W. Van Paepegem, *Extraction of bulk wave characteristics from a pulsed ultrasonic polar scan.* Wave Motion, 2014. In Press DOI: 10.1016/j.wavemoti.2014.05.001.

[163] Towfighi, S. and T. Kundu, *Elastic wave propagation in anisotropic spherical curved plates.* International Journal of Solids and Structures, 2003. 40(20): p. 5495-5510.

[164] Fong, K.L.J., *A study of curvature effects on guided elastic waves*. 2005, University of London.

[165] Jiangong, Y., W. Bin, and H. Cunfu, *Characteristics of guided waves in graded spherical curved plates.* International Journal of Solids and Structures, 2007. 44(11–12): p. 3627-3637.

[166] Treyssède, F., *Mode propagation in curved waveguides and scattering by inhomogeneities: Application to the elastodynamics of helical structures.* The Journal of the Acoustical Society of America, 2011. 129(4): p. 1857-1868.

[167] Van Dreumel, W.H.M. and J.L. Speijer, *Non-destructive composite laminate characterization by means of ultrasonic polar-scan.* Materials Evaluation, 1981. 39(10): p. 922-925.

[168] Buchwald, V.T. and A. Davis, *SURFACE WAVES IN ANISOTROPIC ELASTIC MEDIA.* Nature, 1961. 191(479): p. 899-&.

[169] Nayfeh, A.H. and D.E. Chimenti, *Propagation of guided-waves in fluid-coupled plates of fiber-reinforced composite.* Journal of the Acoustical Society of America, 1988. 83(5): p. 1736-1747.

[170] Ting, T.C.T. and D.M. Barnett, *Classifications of surface waves in anisotropic elastic materials.* Wave Motion, 1997. 26(3): p. 207-218.

[171] Degrieck, J. *Some possibilities of nondestructive characterisation of composite plates by means of ultrasonic polar scans*. in *Emerging technologies in nondestructive testing (ETNDT)*. 1996. Patras, Greece: A.A. Balkema.

[172] Degrieck, J., N.F. Declercq, and O. Leroy, *Ultrasonic polar scans as a possible means of non-destructive testing and characterisation of composite plates.* Insight, 2003. 45(3): p. 196-201.

[173] Declercq, N.F., J. Degrieck, and O. Leroy, *Ultrasonic polar scans: Numerical simulation on generally anisotropic media.* Ultrasonics, 2006. 45(1-4): p. 32-39.

[174] Declercq, N.F., J. Degrieck, and O. Leroy, *Simulations of harmonic and pulsed ultrasonic polar scans.* Ndt & E International, 2006. 39(3): p. 205-216.

[175] Vandreumel, W.H.M. and J.L. Speijer, *Non-destructive composite laminate characterization by means of ultrasonic polar-scan.* Materials Evaluation, 1981. 39(10): p. 922-925.

[176] Van Dreumel, W.H.M. and J.L. Speijer, *Polar-Scan, a Non-Destructive Test Method for the Inspection of Layer Orientation and Stacking Order in Advanced Fiber Composites.* Materials Evaluation, 1983. 41(9): p. 1060-1062.

[177] Degrieck, J. and D. Van Leeuwen, *Calculation of Reflection and Transmission Coefficients of Complex Harmonic Ultrasonic Waves at Homogeneous Anisotropic Liquid-coupled Plates.* WTCM report, 1993.

[178] Degrieck, J. and D. Van Leeuwen, *Simulatie van een Ultrasone Polaire Scan van een Orthotrope Plaat (in Dutch)*, in *the 3rd Belgian National Congress on Theoretical and Aplied Mechanics*. 1994: Liege, Belgium.

[179] Declercq, N.F., J. Degrieck, and O. Leroy, *On the influence of fatigue on ultrasonic polar scans of fiber reinforced composites.* Ultrasonics, 2004. 42(1-9): p. 173-177.

[180] Satyanarayan, L., J.M. Vander Weide, and N.F. Declercq, *Ultrasonic Polar Scan Imaging of Damaged Fiber Reinforced Composites.* Materials Evaluation, 2010. 68(6): p. 733-739.

Chapter 3

Experimental Implementation of the Ultrasonic Polar Scan

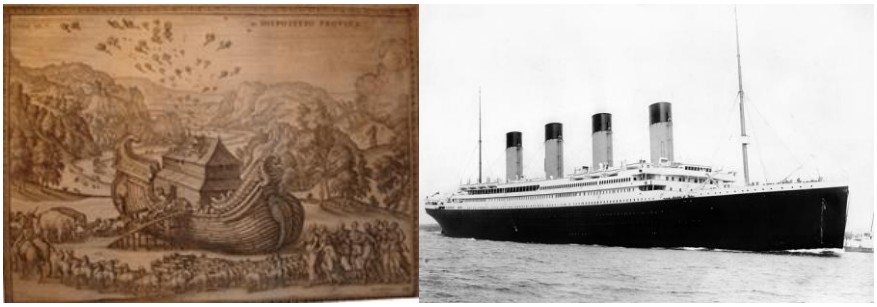

Amateurs built Noah's Ark, experts the Titanic. Drawing by Petrus Van Der Bocht of the shipping of Noah's Ark (left), and photograph of the Titanic departing for its first and unfortunately also its last journey (right).

Summary

This chapter presents a general overview of the in-house developed experimental facility to record high-quality ultrasonic polar scans. A description of the fully automated mechanical scanner is provided, various features are discussed in detail. In addition, a dedicated investigation is performed to several important experimental conditions. For example, the nature of the radiation field of a typical transducer is investigated in-depth by means of experimental recording and ultrasonic holography. The performance of the implemented setup is demonstrated qualitatively, and high-quality UPS experiments are presented for various (an)isotropic materials.

Currently, effort is put in the construction of a hand-held UPS scanner which meets in-field requirements. The current status of the miniaturization process is given.

3. 1. Introduction

It may be clear from the previous chapter that one of the barriers for transferring the UPS technique to the next level concerns the low quality of current experiments. Although commercial scan systems are available [1], it has been opted in this research to build and construct a versatile scanner in-house. This is mainly prompted because of a number of reasons. First of all, the poor experimental results obtained by other labs indicate that a more elaborate system is required. Secondly, the limited accessibility of the user to the steering and software of a commercial scanner makes it is practically impossible to adjust the system whenever needed. Indeed, a commercial scanner has limited flexibility to extend the operational regime to different types of experiments. And finally, the cost price of such a commercial system lies well above the research funding which was kindly provided by the FWO (Fonds voor Wetenschappelijk Onderzoek, Vlaanderen) through grant number G012010N. The main body of the here discussed scanner was already built during the research of Joris Degrieck [2]. Though, many modifications have been implemented to increase the flexibility, to lower the experimental time and to enhance the quality of the experiments.

3. 2. Global Overview Mechanical Implementation

A high-performance multi-axes scanner has been developed, having three translational and two rotational axes (see Figure 3-1). The scanner has been installed on a rigid frame to reduce the influence of external vibration. Each axis of motion is driven by a brushless DC-motor which is programmed using LABVIEW in order to fully automate the movement involved in an ultrasonic polar scan experiment. Obviously, other types of experiments have also been programmed in LABVIEW (for example C-scanning). The controlling commands are communicated to the motors by a high-speed USB-to-CAN module. In order to increase the flexibility of the setup, the operator can manually change (within certain bounds) different settings, such as angular range, angular resolution, motor speeds, etcetera.

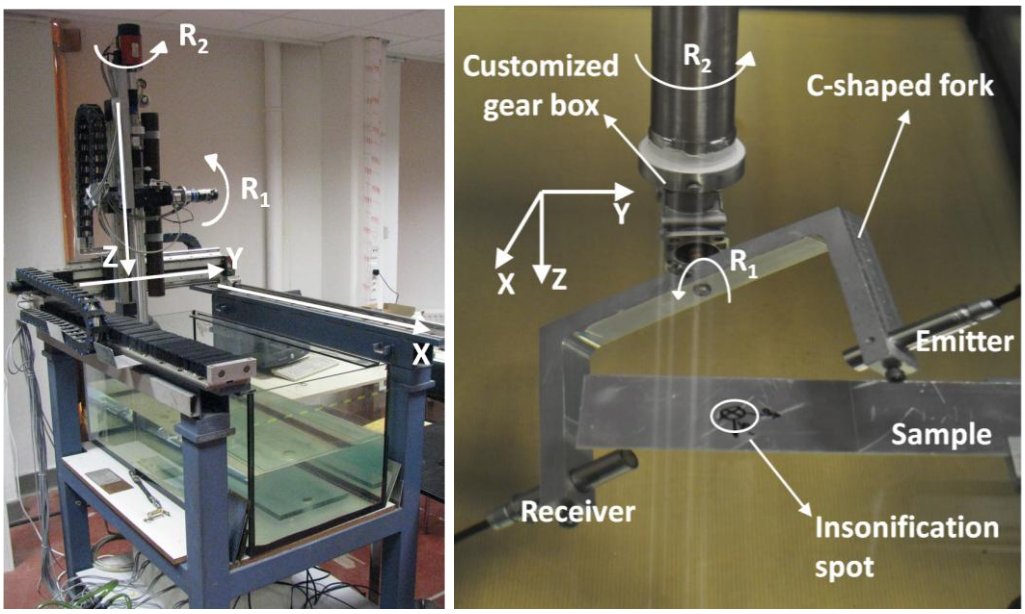

Figure 3-1: Multi-axes scanner (left) and detail of the scanner head (right). The mounted C-shaped fork is used for transmission recordings.

To transfer the motor movement to the rotational movement of the transducers, a customized gear box was produced in our lab (see Figure 3-1). Basically, we transformed two commercial gear boxes (type bonfiglioli) into a single gear box with upgraded properties. In order to decrease its clearance as well as to extend its applicability in submersion experiments, several additional high-precision parts have been milled and installed. In this way, the gear box can be immersed in water without further additional problems,

while the clearance could be reduced to around 0.1°. This is significantly lower compared to the 0.65° clearance of a typical commercial gear box. The manufactured gear box has two exit shafts which rotate in opposite directions, thus allowing to perform UPS measurements in reflection, back-reflection (also called backscatter), through-transmission and double through-transmission mode. A schematic of the different recording modes is given in Figure 3-2.

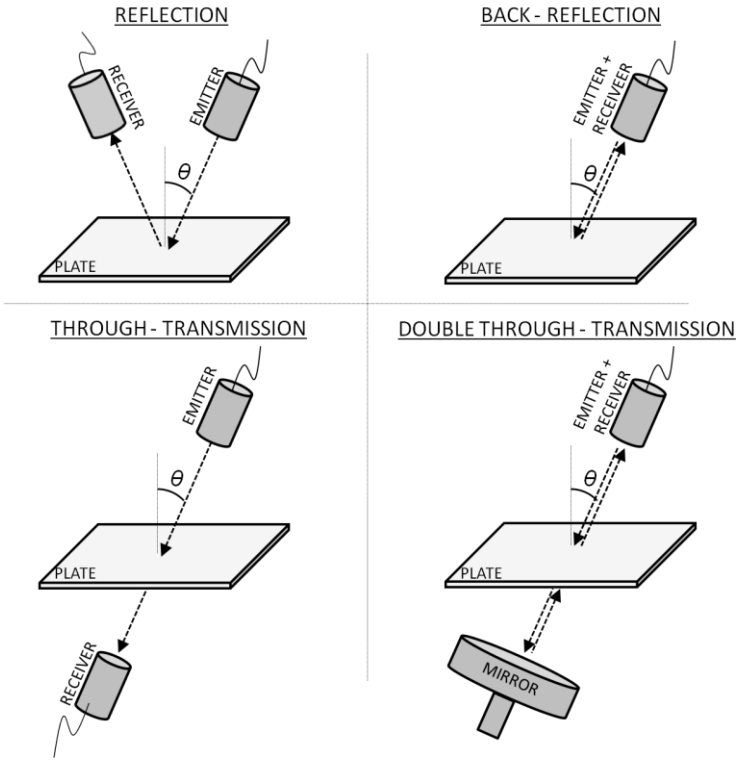

Figure 3-2: Different recording modes in which the implemented scanner can be operated.

To ease the mechanical implementation, the transmission recordings are performed with a C-shaped fork (see Figure 3-1). When operating the scanner in the double-through transmission mode, the receiver is replaced by an acoustic mirror which is made of stainless steel. The mirror has a cylindrical shape with a diameter of 51 mm and a thickness of 22 mm, and has a high surface finishing degree to prevent any diffractional effects upon reflection.

A schematic of the full experimental facility is displayed in Figure 3-3. The water tank has the dimensions Length x Width x Height = 1200x600x550 mm^3.

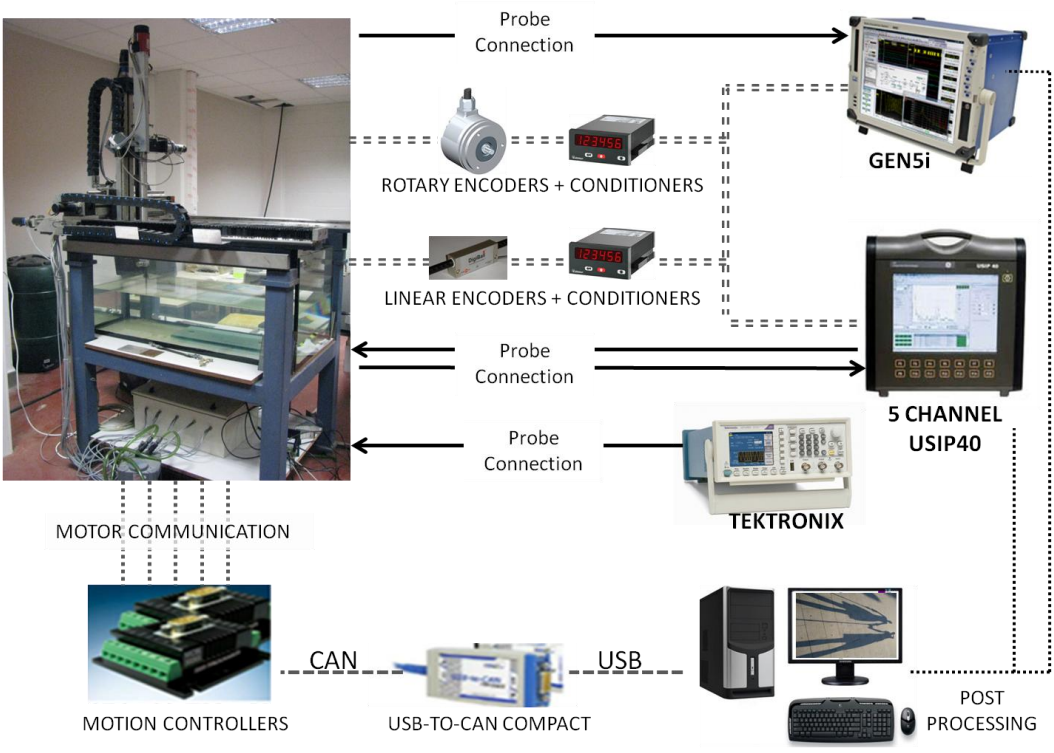

Figure 3-3: Schematic of experimental setup.

3. 3. Motion and Control

A schematic of the path of movement, involved during a UPS experiment, is displayed in polar coordinates in Figure 3-4. The incident angle θ is put on the radial axis, the polar angle φ on the angular axis. Hence, each point in the polar plot defines a unique incidence angle $\psi(\varphi,\theta)$. The solid arrows represent the polar angle sections where measurements are performed. In this schematic only 7 sectors (fixed φ) are illustrated for clarity, in reality this number is typically 360. The dotted arrows represent the compensation in both X- and Y-direction upon changing the polar angle φ. This compensation is essential in order to ensure the insonification of a single predefined material spot when using the C-shaped fork. In this configuration, the scanning is done in a continuous way in the vertical incidence plane, which corresponds to the θ-direction (the scan axis), while the scanning in the

horizontal plane, which corresponds to the φ-direction (the index axis), proceeds in discrete steps. Upon changing the polar angle φ, the direction of movement for the scan axis is reversed. Besides reasons of convenience for the mechanical implementation, this particular movement of the UPS has been chosen as it increases the performance as well as the control. Indeed, the first run for $-80° \leq \theta \leq 80°$ at $\varphi = 0°$ should yield symmetric results, since at a fixed polar angle φ, the incident angle $\theta = \alpha°$ is acoustically equivalent to the complementary incident angle $\theta = -\alpha°$ (at least in the case of undamaged material). Furthermore, note that the first run at $\varphi = 0°$ insonifies the material spot at exactly the same incidence angles as the last run at $\varphi = 180°$, and consequently should yield the same recording. Any deviation in these two control sectors then indicate that the UPS experiment has not been obtained in a proper way. The gray circles in Figure 3-4 represent a standstill (in the order of 2 seconds) in order to process and store the data of the last sector scan that was performed.

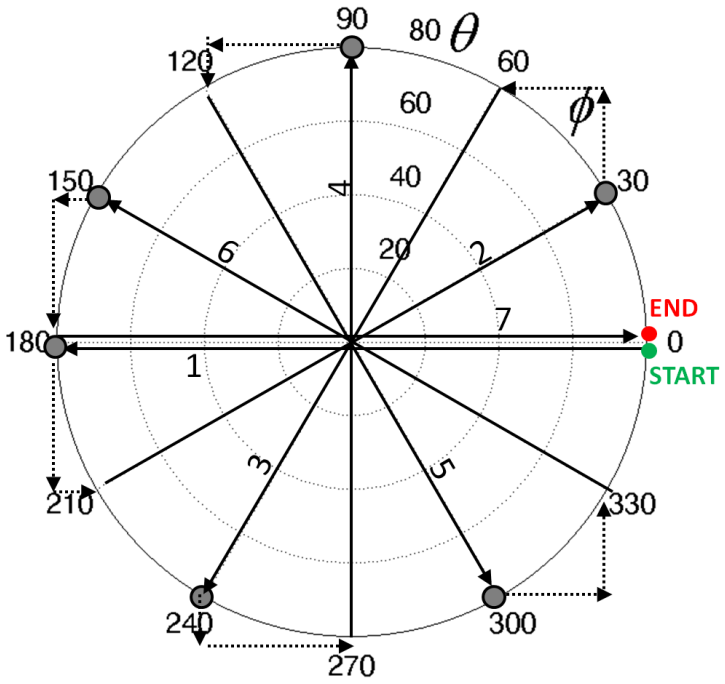

Figure 3-4: Schematic of the motion path, represented in polar coordinates.

Besides the recording of wave signals, it is clear that also the actual direction of insonification has to be accurately known and stored. In our set-up, high-precision position feedback is assured by the use of both linear and rotational relative position encoders, having an accuracy of $\Delta r = 0.007$ mm and

$\Delta\alpha = 0.01°$ respectively (see Figure 3-3). Besides accurate position feedback, the encoders further provide a means for time-triggering the acoustic circuit. Redundant vibrations, inherent to any mechanical construction with moving parts, may be a source of degradation for the experimental recording. As the ultrasonic circuit is triggered by the installed position encoders, peripheral vibrations could be interpreted as legitimate encoder pulses, causing a walk-off between the stored and the actual position of the ultrasonic transducer. To cope with this, an electronic axis jitter suppression has been applied in order to separate the legitimate encoder pulses from the axis vibrations.

In most applications, it is sufficient to set the resolution of the UPS experiment at $\Delta\varphi = 0.5°$ for the index axis and at $\Delta\theta = 0.05°$ for the scan axis. For obvious mechanical considerations, it is impossible to scan the complete hemisphere. In this dissertation, the scanning is most of the time limited to $\theta \in [-70°,+70°]$ and $\varphi \in [0°,180°]$. At each incidence angle $\psi(\varphi,\theta)$, a timed sequence is carried out in which an acoustic pulse is launched by the emitting transducer to the investigated material spot and subsequently recorded in one or multiple modes, i.e. reflection, back-reflection, through transmission or double through-transmission. With these parameters, a single UPS experiment involves ultrasonic wave measurements at more than 1,000,000 unique incidence angles $\psi(\varphi,\theta)$. Exploiting the symmetry of the investigated material, it is in principle sufficient to scan only part of a spherical surface, e.g. $\theta \in [0°,+70°]$ and $\varphi \in [0°,45°]$ for orthotropic symmetry [3], thereby significantly reducing the experimental scanning time. However, this is not considered here since in reality composite materials rarely exhibit perfect symmetry. In addition, the anisotropic nature of a sample is often *a priori* unknown.

To limit the amount of recorded data during the experiment, only the maximum amplitude and/or its associated time-of-arrival within the received signal is recorded on-the-fly, employing a maximal sampling rate of 400 MHz with 12-bit resolution. For this, the USIP40 module (General Electric) is available, as well as the Gen5i Oscilloscope (see Figure 3-3). The motors have been programmed in order to cover as many incidence angles $\psi(\varphi,\theta)$ as possible per second, while taking care that both stability is retained and overshoot is prevented. The implemented motor settings (acceleration, speed and deceleration) for the rotational R_1 axis generate the motion profile shown in Figure 3-5. Note that the angular velocity profile and the angular acceleration profile are only qualitatively represented as they have been put

in arbitrary units. It can be readily observed that the considered settings produce gentle and smooth endings without overshoot for the incident angle θ, from which the stability obviously benefits. In the limit, the setup can insonify and process ~2,000 incidence angles $\psi(\varphi,\theta)$ per second. However, most of the time a lower scanning speed (~1,200 incidence angles $\psi(\varphi,\theta)$ per second) has been selected.

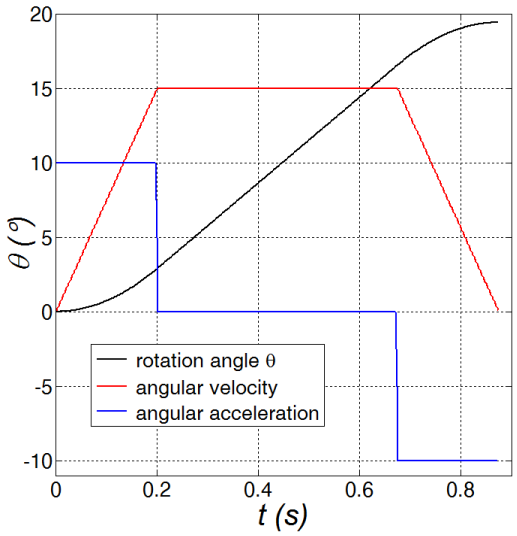

Figure 3-5: Motion profiles of the R1 axis (incident angle θ).

The combination of the automated mechanical scanner with the dedicated data-acquisition allows to keep the experimental time for recording a UPS experiment to less than 15 minutes, which is quite acceptable considering the large amount of information obtained.

3. 4. Piezo-electric Transducers

Piezo-electric transducers have been employed to record UPS experiments in this dissertation. Different sets of transducers have been purchased within the frequency range 1 - 15 MHz (H1K, H2K, H5K, H5M, focused H5M, H10M and H15M) [4].

3. 4. 1. Time Domain Analysis

Basically, the piezo-electric crystal is shocked by an electric discharge which is produced by the USIP40 apparatus (see Figure 3-3). Because the

associated voltage level of the discharge (up to 400 V according to the technical specification [5]) was too high for the oscilloscope (Gen5i) to record, saturation is observed at a voltage of more or less 10V.

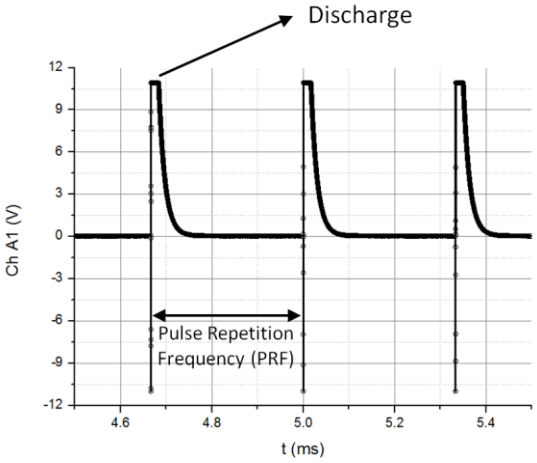

Figure 3-6: Electrical discharge used as input for piezo-electric transducer.

The shocked piezo-electric crystal in turn gets mechanically deformed and produces a short vibration. The characteristics of the generated vibration, such as spectral frequency content, are basically function of the physical dimensions of the piezo-electric crystal. Figure 3-7 shows the typical generated pulse (measured with the ONDA HGL-0400 needle hydrophone, which was kindly provided by the research lab of Prof. Koen Van Den Abeele (KU Leuven - Campus Kortrijk)) in both time domain and temporal frequency domain for the H5K transducer. It can be observed that the frequency range is quite broad, and peaks around 4 MHz. The latter is quite peculiar as it concerns a measurement for the H5K transducer, which should produce a broadband signal with a central frequency of $f_c = 5$ MHz (according to the manufacturer's documentation [4]). As three such H5K transducers have been purchased, the output of the other two transducers was also checked. It was found that the central frequency for the two other H5K transducers peaks around 4.6 MHz and 5.1 MHz. As these transducers have been newly purchased, it is probable that the deviation is due to small manufacturing faults.

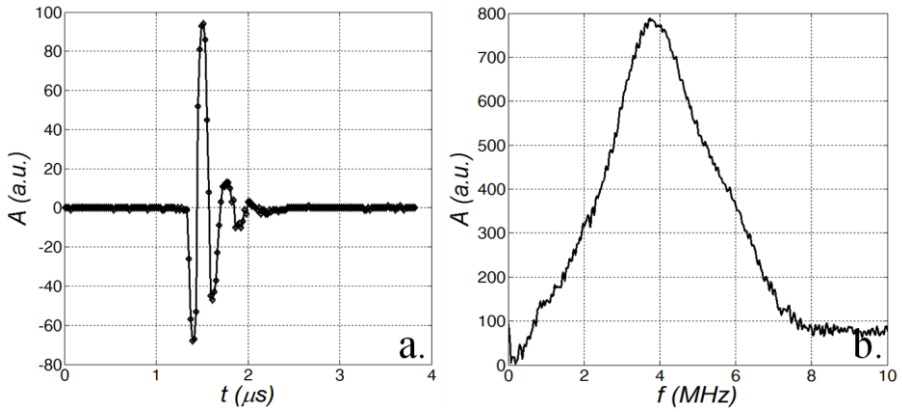

Figure 3-7: Output signal of H5K transducer: time domain (a) and temporal frequency domain (b).

In case inspection with harmonic signals is aimed, the programmable wave function generator (Tektronix) is used to excite the piezo-electric crystals (see Figure 3-3). Hence, harmonic ultrasonic polar scan (H-UPS) images can also be obtained with the present setup. As such H-UPS experiments are unprecedented in literature, they deserve to be described in a distinct chapter. The experimental and numerical H-UPS results will be presented and discussed in detail in Chapter 8.

3. 4. 2. Spatial Domain Analysis

It may be clear that good understanding of the spatial shape of the employed ultrasonic beam in a UPS experiment is of utmost importance for the correct recording and subsequent analysis and interpretation. Therefore, the output pressure of the H5K transducer has been spatially investigated with a needle hydrophone. A schematic of the measurement procedure is displayed in Figure 3-8. The first procedure scans the XY-plane in order to obtain a cross-section of the sound beam at a certain z-position. The second procedure scans the XZ-plane (or equivalently the YZ-plane) to obtain a longitudinal section of the radiated sound beam. The transducer has been operated in the quasi-harmonic regime using the Tektronix wave function generator (more details about the quasi-harmonic regime is given in Chapter 8). The distribution of both the amplitude and the phase of the radiated field has been measured.

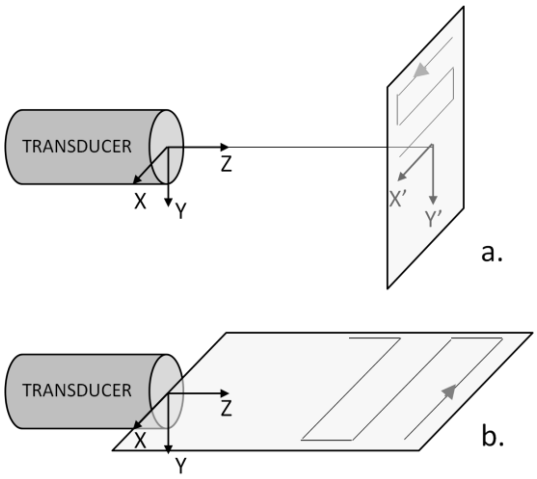

Figure 3-8: Schematic of the procedure to measure the spatial distribution of a sound field: XY cross-section (a) and XZ longitudinal section (b).

Cross-sectional recordings for the H5K transducer, excited at $f = 5$ MHz, are shown in Figure 3-9 for different z-positions. The XY-grid has been scanned at a spacing of 0.1 mm. The amplitude recordings clearly show radial intensity oscillations for $z < 65$ mm which should be attributed to near-field features. For $z > 65$ mm, the amplitude distribution of the H5K radiation field evolves towards a main lobe, which obviously corresponds to the far-field region. It is further interesting to note that the radiation field shows small amplitude variations in angular direction (best seen for the recording at $z = 5$ mm). For a perfect circular radiator, one should expect rotational symmetry of the radiated field.

The phase recordings on the other hand indicate that the transducer's face was (most probably) slightly tilted around the X-axis. In addition, circular patterns can be observed which become more clear and outspoken for larger *z*-values. Each of these circles corresponds to a 2π phase jumps (phase wrapping), revealing that the wave front evolves towards a spherical shape. This comes as no surprise considering the spatially bounded nature of the circular radiator.

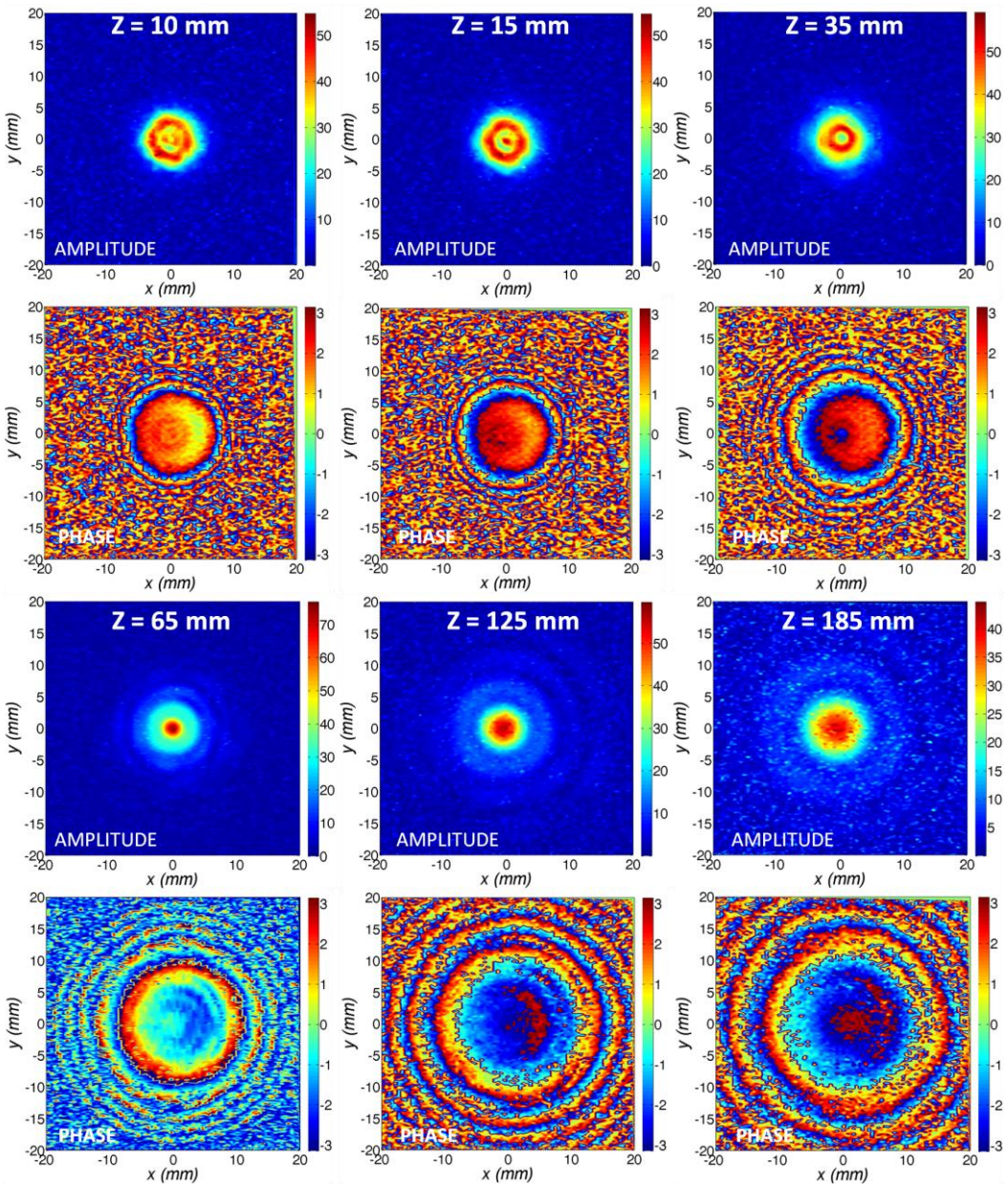

Figure 3-9: Cross-sectional recordings (amplitude and phase) for the H5K transducer (*f* = 5 MHz) at several *z*-values.

A longitudinal section of the H5K transducer has also been obtained in the YZ-plane, and is displayed in Figure 3-10. Here, the near-field and far-field region can be readily identified (indicated on the figure). The longitudinal section thus indicates that measurements should be ideally obtained at a distance of at least ~65 mm. Below this value, near-field features will

severely complicate the analysis and interpretation. The C-shaped fork employed for the UPS experiments (see Figure 3-1) allows measurements to be taken at a distance between ~80 mm and ~150 mm. For a perfect circular transducer, the XZ-section should equal the YZ-section. Though, the observed asymmetry in the cross-sectional recordings (see Figure 3-9) indicate that this will most probably not be the case. Unfortunately, the longitudinal section in the XZ-plane has not been recorded and therefore cannot be compared to the longitudinal section in the YZ-plane.

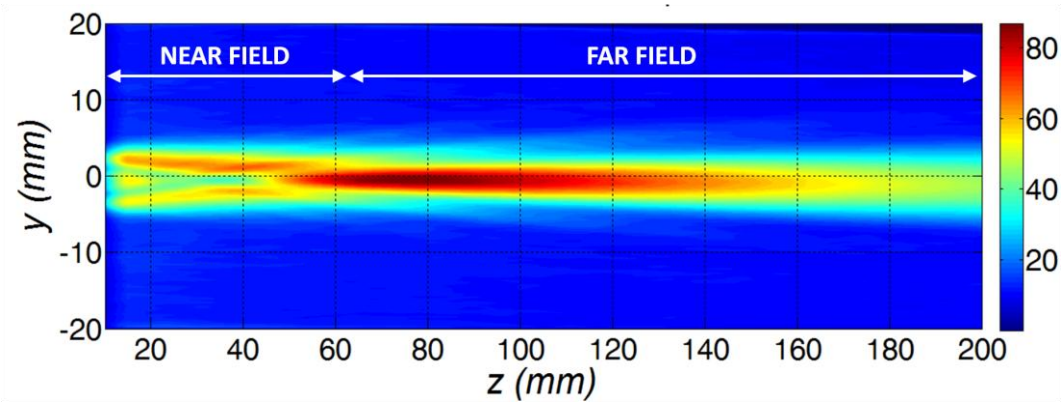

Figure 3-10: Longitudinal section (amplitude) in the YZ-plane for the H5K transducer (*f* = 5 MHz).

The above presented experiments are a powerful tool to characterize and spatially map beam properties. However, as the experiments are time-consuming and difficult to perform, this soon becomes cumbersome and annoying when different transducers should be characterized. In addition, whenever a cross-sectional recording at for example *z* = 90 mm is required, a new recording has to be made.

For this reason, a holographic procedure has been implemented, for which only a single cross-sectional recording is required to reconstruct the full 3D beam field. In the next section, the implemented ultrasonic holography procedure is shortly described and demonstrated for the H5K transducer.

3. 4. 3. Holographic Reconstruction Procedure for 3D Spatial Characterization of an Ultrasonic Beam

The holographic reconstruction procedure is actually equivalent to a linear system whose output *o(t)* equals the convolution in real space of the input

i(t) with the system response function *r(t)* [6]. In frequency domain, this simply corresponds to the multiplication of the Fourier transforms of *i(t)* and *r(t)*. As such the output in frequency domain *O(f)* is obtained. Application of the inverse Fourier transform then yields the output in time domain *o(t)*. Applied to our case, this beam propagation model, which is implemented in MATLAB, becomes:

1. Record the cross-sectional amplitude and phase distribution at a certain *z*-value, and evaluate the complex-valued cross-sectional distribution. This distribution will be used as the input *i(x,y)* for the beam propagation method.

2. Take the fast Fourier transform of the input *i(x,y)* to obtain $I(k_x,k_y)$. Here k_x and k_y are the wave numbers in *x*- and *y*-direction.

3. We are interested in free space propagation, the free space transfer function can be written in spatial frequency domain as [6]

$$R(k_x,k_y) = \exp\left(-i\sqrt{\left(k^2-\left(k_x^2+k_y^2\right)\right)}\,d\right) \qquad (1)$$

   with *k* the wave number of the considered beam, and *d* the distance over which the wave needs to be propagated.

4. Multiply $I(k_x,k_y)$ with the free space transfer function $R(k_x,k_y)$ to obtain the output $O(k_x,k_y)$ in spatial frequency domain.

5. Take the inverse fast Fourier transform of $O(k_x,k_y)$ to obtain the output signal *o(x,y)* in real space. This is a representation of the ultrasonic distribution propagated over a distance *d*.

6. As the fast Fourier transform should comply to periodicity, effects at the borders of the computational domain could play an important role during propagation over a large distance *d*. To anticipate, one can choose a sufficiently large computational domain. Though, the computational time will likewise increase drastically. Instead, we applied an absorbing function in real space *t(x,y)* to intercept any edge effects:

$$t(x,y) = \exp\left(-\left(\frac{\sqrt{(x^2+y^2)}}{0.97\,L/2}\right)^{50}\right) \tag{2}$$

with L the characteristic length of the computational domain.

The absorbing function, for L = 40 mm, is displayed in Figure 3-11, and corresponds to a plateau with its outer region exponentially decaying towards zero.

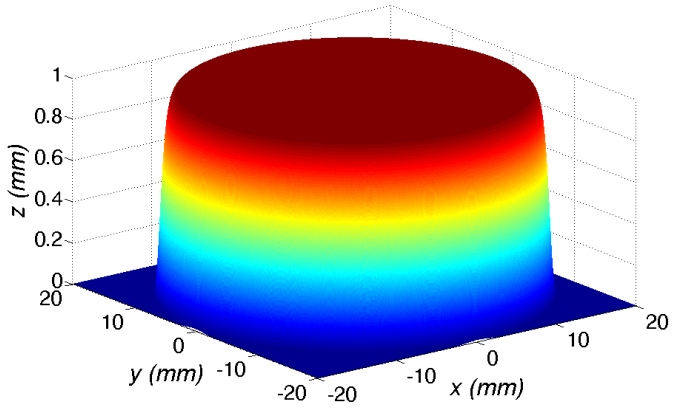

Figure 3-11: Function to absorb energy leakage at the boundaries of the numerical domain.

It may be clear that the absorbing function is only efficient when applied to small propagation distances as edge effects should be suppressed at the very onset. Or in other words, edge effects should be located within the active zone (zero-valued region) of the absorbing function to be eliminated. Hence, to propagate a beam over a large distance d, the computation algorithm needs to be split in a set of consecutive reconstructions with each involving a smaller distance d_i. As such the implemented holographic reconstruction is an iterative process, in which the output of step *j-1* is used as input for step *j*. It was found, for our particular application, that discretizing the propagation distance in steps of 1 mm is more than sufficient to avoid the presence of any edge effects.

7. A further extension is needed in case backward beam propagation (towards the transducer) is envisioned. Indeed, within the range of k_x and k_y also evanescent waves are included whenever the condition

$k_x^2 + k_y^2 > k^2$ is fulfilled. Since these evanescent waves decay quickly in the direction of propagation, they can be ignored without further consequence for forward beam propagation. However, in case of backward beam propagation, these waves should be excluded as they display an exponential growth in negative direction.

To concretize and to demonstrate the procedure, the experimental cross-sectional recording at z = 65 mm (see middle column of Figure 3-12) has been used as input for the holographic reconstruction procedure. First, the recording has been propagated backwards over a distance d = 55 mm in order to reconstruct the ultrasonic field at z = 10 mm (see left column of Figure 3-12). Afterwards, the recording has been forward propagated over a distance d = 60 mm to reconstruct the ultrasonic field at z = 125 mm (see right column of Figure 3-12). The effect of the absorbing function can be readily identified in the outer region of the reconstructed cross-sections.

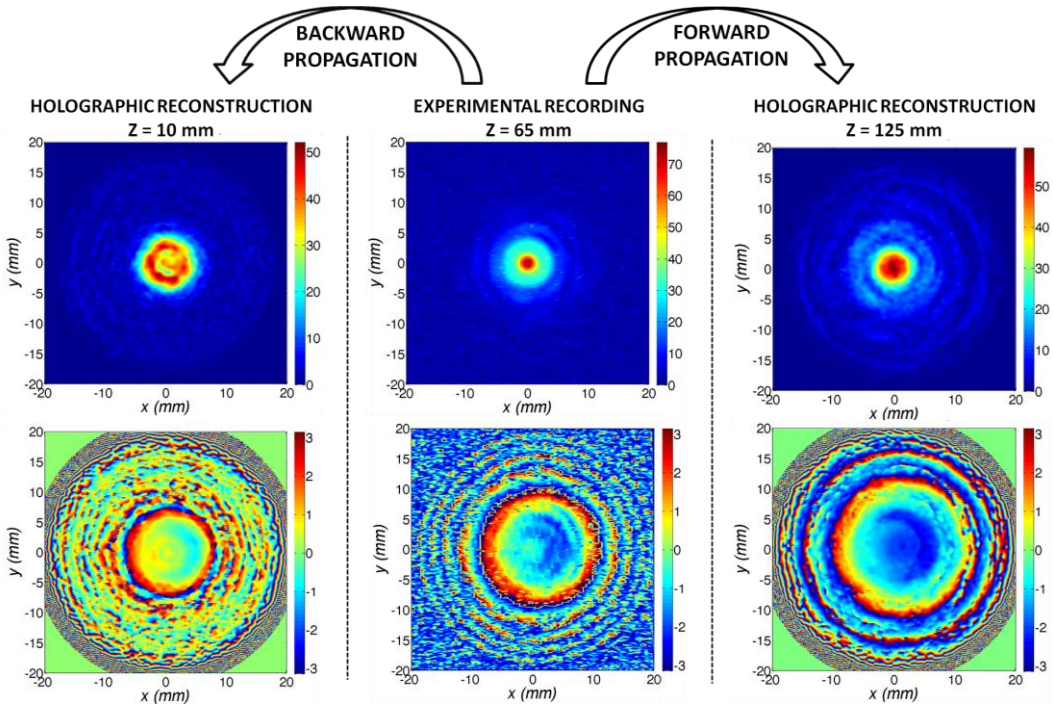

Figure 3-12: Demonstration of holographic reconstruction of ultrasonic beam. Left column: reconstructed cross section at z = 10 mm; middle column: experimentally recorded cross-section at z = 65 mm (used as input); right column: reconstructed cross section at z = 125 mm. The top row corresponds to amplitude values, the bottom row to phase values.

The reconstructed cross-sections can be compared in a straightforward way to the experimental recordings (see Figure 3-9 at the corresponding *z*-values). It can be observed that excellent agreement is obtained regarding the amplitude distribution, for both the backward and forward propagated beam. The reconstructed phase results on the other hand do have the same shape as the recorded ones, though a clear offset between both can be observed. This comes as no surprise as the wave length, and in extension the phase, is highly sensitive to the wave speed in the water. For the present results, a fixed wave speed of c_{liq} = 1483 m/s has been assumed. However, it is clear that water temperature and impurities can slightly alter this value, thus causing an offset between the recorded and reconstructed phase distribution.

The excellent agreement between reconstruction and experimental recording can be further verified by considering the subtraction of the recorded and the reconstructed cross-sections (see Figure 3-13).

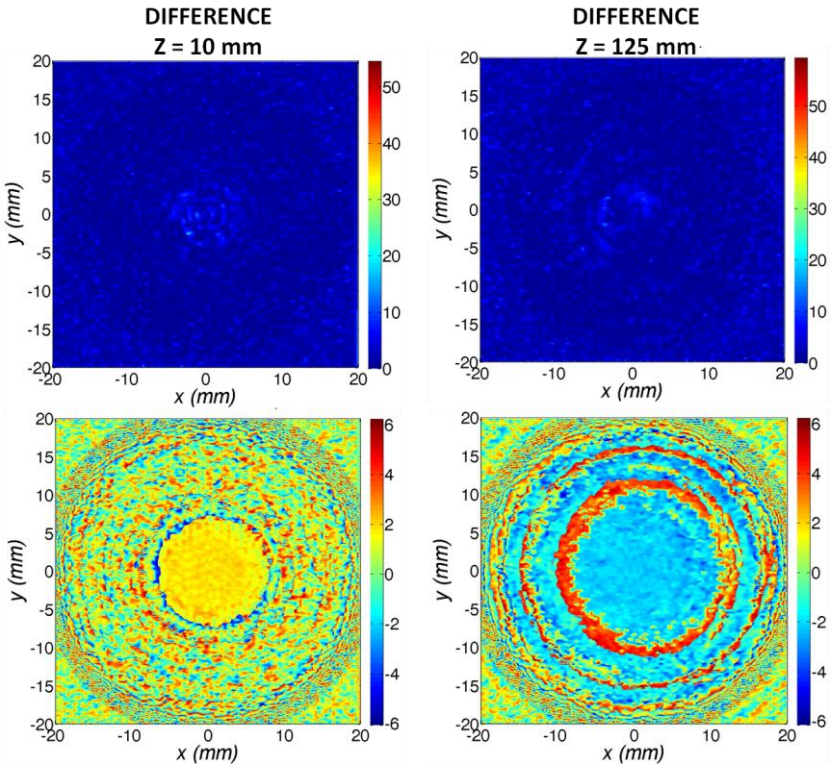

Figure 3-13: Subtraction (absolute value) of the recorded and the reconstructed cross-sections at *z* = 10 mm (left) and *z* = 125 mm (right).

The recorded cross-section at $z = 65$ mm is further used for the reconstruction of the longitudinal section in both the XZ- and the YZ-plane. The reconstructed sections are displayed in Figure 3-14. First of all, the global view of both reconstructions corresponds well to the experimental recording in the YZ-plane (see Figure 3-10). In addition, the reconstructed YZ-section affirms the slightly tilted angle of the sound beam around the X-axis. Comparison of the reconstructed XZ- and YZ-section reveals some small differences in the amplitude distribution, especially notable in the near-field region. These variations were already hinted by the cross-sectional recordings (see Figure 3-9) and cross-sectional reconstructions (see Figure 3-12) in which angular amplitude variations were observed.

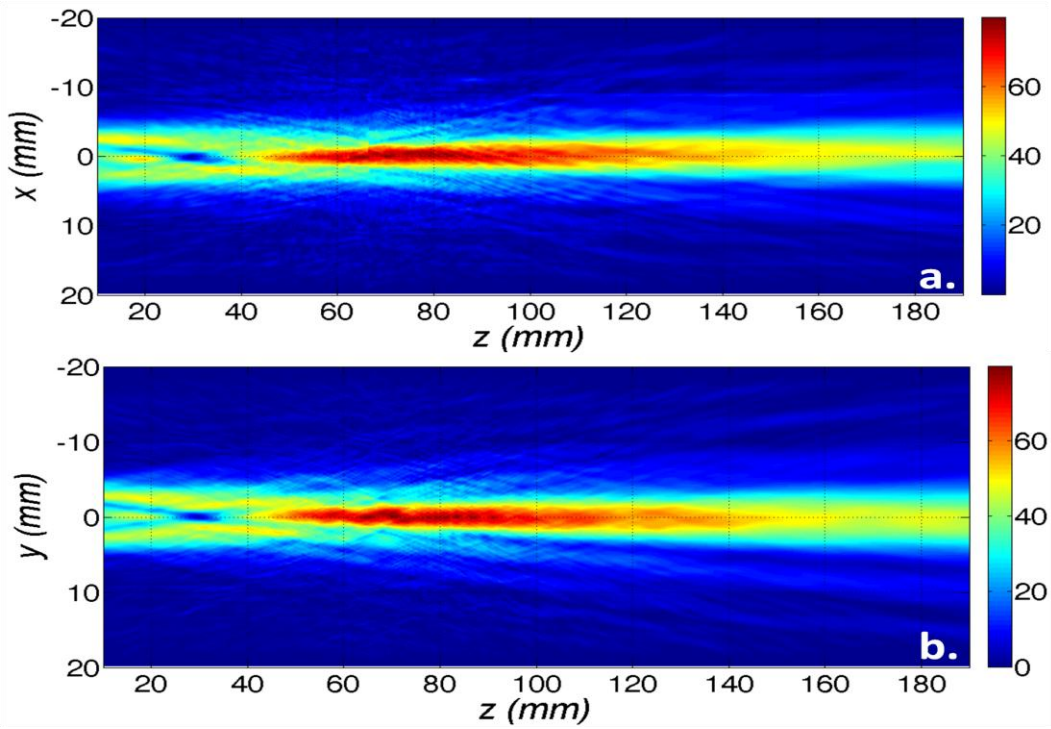

Figure 3-14: Reconstructed longitudinal section in the XZ-plane (a) and in the YZ-plane (b).

For the correct recording and subsequent analysis and interpretation of UPS experiments, accurate knowledge of the spatial distribution of the sound beam is of utmost importance. Therefore, the holographic reconstruction procedure has been applied for the different transducers employed in this dissertation. It may be clear that the other transducers show similar features

as for the H5K transducer. For reasons of brevity however, these results are not shown.

3. 5. Immersion Liquid

Previous section already indicated the importance to have accurate knowledge about the immersion liquid when the phase is involved. In this dissertation, the experiments have always been performed in water (unless it is specified differently), having a density of 1000 kg/m^3. The wave speed c_{liq} has been explicitly measured as a function of water temperature T.

Many authors determine the wave speed by measuring the time of an ultrasonic pulse to propagate a certain distance d (see Figure 3-15a). However, as the active piezo-electric crystal is shielded from the immersion liquid by a membrane, the measurement does not take into account the sound path δ within the piezo-electric transducer. In addition, the sound speed for that short path δ is unknown (although this should ideally match with the wave speed in water to reduce internal reverberations).

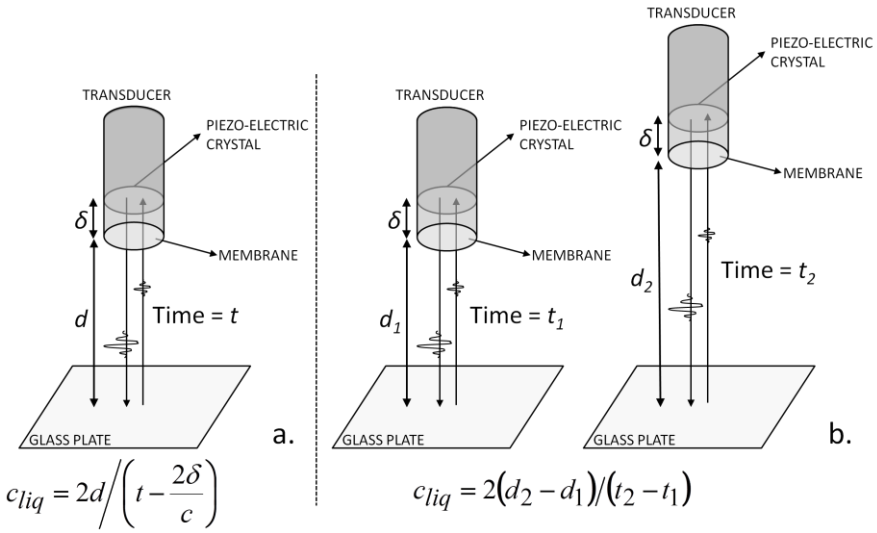

Figure 3-15: Measurement of the wave speed in water: inaccurate method (a) and accurate method (b).

Instead, the sound speed in water has been measured in this dissertation by evaluating the change in travel time Δt when increasing the propagation path with a known distance Δd (see Figure 3-15b). This method cancels the

contribution of the sound propagation in the shielding membrane of the transducer, and thus yields an expression which can be used to evaluate the wave speed in water. To have accurate knowledge about the change in propagation distance Δd, the developed scanner has been employed (0.007 mm accuracy for linear movement). The temperature T of the water bath has been measured by an analogue thermometer with its indicator scale divided in steps of 0.5°C. The water temperature is increased by simply adding boiling water. The water is continuously stirred and blended by a water pump to avoid local hot or cold zones. Wave speed measurements have been obtained at several water temperatures T. The obtained results are graphically displayed in Figure 3-16. It can be observed that the wave speed c_{liq} is almost linearly proportional to the water temperature T. In general, the experiments in this dissertation have been obtained at a water temperature between 14°C and 20°C.

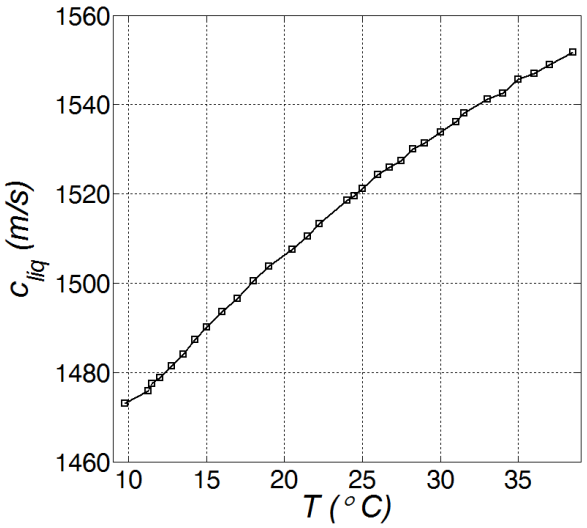

Figure 3-16: Wave speed c_{liq} as a function of water temperature T.

Unfortunately, it was noted that also the type (tapped or demineralized) and the purity (algae) of the water has a large impact on the exact wave speed c_{liq}. Hence, for experiments which are quite sensitive to the exact value of the wave speed, the wave speed has been measured at the very moment. For general applications, a wave speed of c_{liq} = 1483 m/s has been assumed.

3. 6. Performance of the Implemented Scanner

The previous sections provided an account on the implemented scanner, and gave an overview of some important experimental conditions. Though, the most important feature of the experimental facility has not yet been talked about: what about the quality of the obtained experimental recordings?

3. 6. 1. Sector Scan at Fixed Polar Angle φ

In order to demonstrate the robustness, stability and accuracy of the developed experimental setup, an aluminum sample has been scanned 10 times according to the UPS principle. The scanning is performed in transmission, two 'identical' H5K transducers have been used which were located ~130 mm apart from each other. As such, the experiments have been obtained in the far-field (see Figure 3-10 and Figure 3-14). The emitter is excited at the harmonic frequency $f = 5$ MHz (the associated sound beam was shown in Figure 3-9 and Figure 3-10). Because of the mechanical isotropic nature of aluminum it suffices to scan a single sector, i.e. to vary the incident angle θ and to keep the polar angle φ fixed. The recorded transmission amplitudes as a function of incident angle θ are shown in Figure 3-17 for the 10 sector scans.

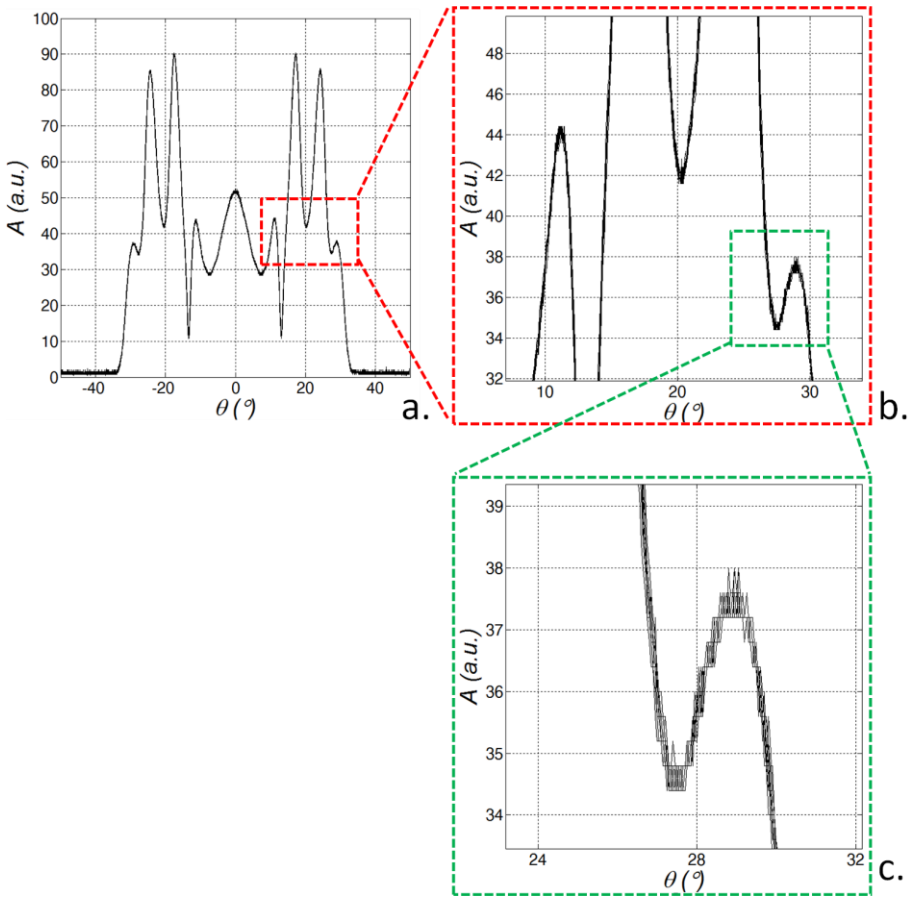

Figure 3-17: Transmission amplitudes of 10 different sector scans as a function of incident angle θ (a), magnification (b) and 2x magnification (c).

It can be readily observed that the 10 experimental recordings basically give the same result (see the magnifications in Figure 3-17). This is further affirmed by evaluating the median and the standard deviation σ for the 10 sector scans (see Figure 3-18). Note that in Figure 3-18a the standard deviation is represented by error bars, and is plotted every 5 data points to keep the figure clear. Figure 3-18b explicitly displays the standard deviation σ as a function of incident angle θ. Horizontal patterns can be observed, which are merely a consequence of the finite resolution of the acquisition software. The incident angles θ which correspond to an extremum in the transmission amplitude have an increased standard deviation. Still, it may be clear that the maximum standard deviation is very small and is limited to ~0.75% of the associated transmission amplitude.

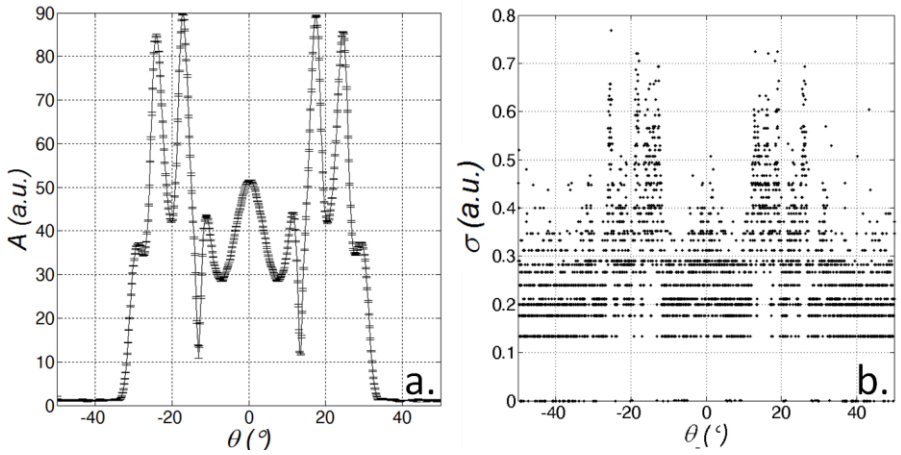

Figure 3-18: Median and standard deviation σ superimposed as error bars (a) and evaluation of the standard deviation σ (b) for the 10 sector scans.

Figure 3-19 displays the extracted transmission amplitude minima (blue) and maxima (red) for the 10 sector scans. The maximum variation in incident angle θ between a single extremum was only 0.05°, the angular resolution at which the scans were recorded. Hence, the here presented results indicate the excellent performance of both the scanner and the data-acquisition to record transmission amplitudes in an accurate and robust way. As it is known that the positions of the extrema in the transmission amplitude put on view several material characteristics [7-10], it may be hoped for that the current high-quality experimental facility opens the way for quantitative application of the UPS for material identification.

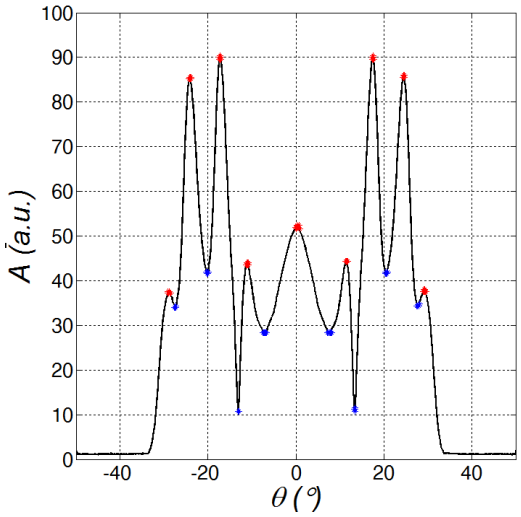

Figure 3-19: Identified minima (blue) and maxima (red) of the 10 sector scans.

3. 6. 2. Ultrasonic Polar Scan Recordings

At last, several high-quality UPS experiments, which have been obtained with the developed scanner, are shown for several (an)isotropic materials. The presented set of experiments has been randomly chosen by the author. Many more UPS experiments have been recorded for different materials. Figure 3-20 displays several UPS experiments for materials with mechanical isotropy. The mechanical isotropy is clearly identified by the circular patterns. Though, it is noted that the experiment for the plexiglass with the periodic surface structure (Figure 3-20c) slightly deviates from the circular symmetry.

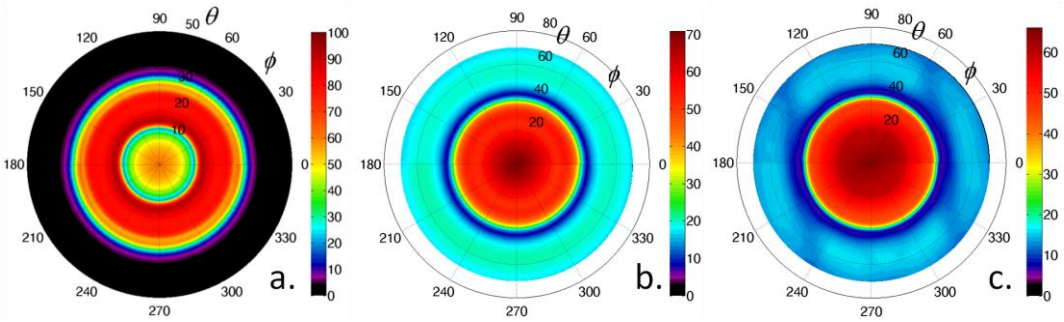

Figure 3-20: UPS recordings for aluminum (a), plexiglass (b) and plexiglass with periodic surface roughness (c).

Figure 3-21 displays the UPS recording for a transversal isotropic carbon/epoxy laminate. The lower mechanical symmetry class (compared to isotropy) is clearly reflected in the drastic change of characteristic contours in the UPS experiment.

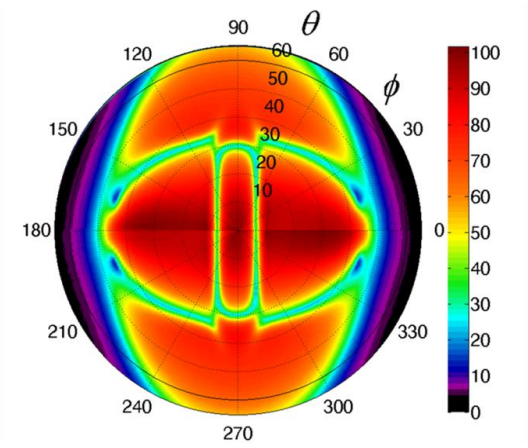

Figure 3-21: UPS recording for a unidirectional [0_8] carbon fiber composite.

Some UPS recordings for cross-ply (fibers along 0° and 90° orientation) carbon fiber reinforced plastics are presented in Figure 3-22. Together with the mechanical nature, the general patterns in the UPS recordings become more complicated.

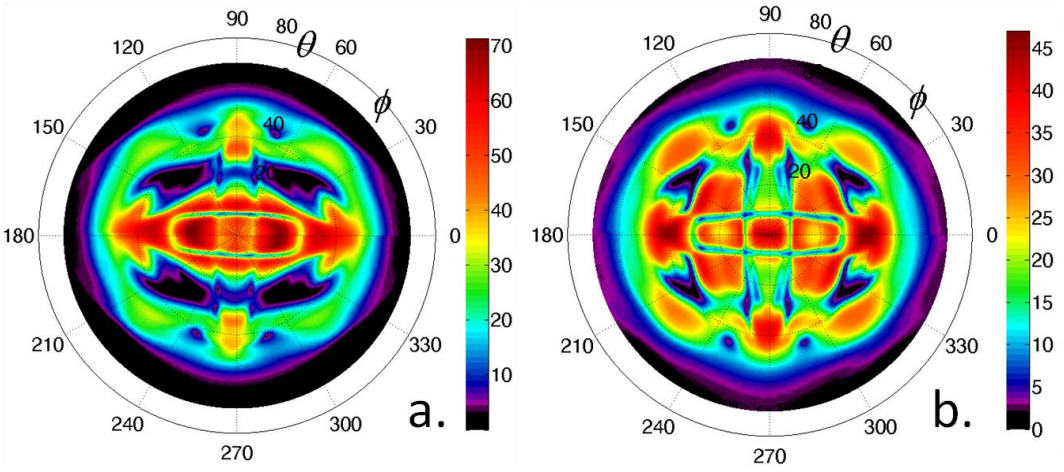

Figure 3-22: UPS recordings for cross-ply laminates: $[0,90]_S$ (a) and [0,water,90,water,90,0] (b) carbon/epoxy.

Figure 3-23 displays UPS recordings for angle-ply (fibers along ±α° orientation) composites, considering both carbon and glass reinforcement fibers.

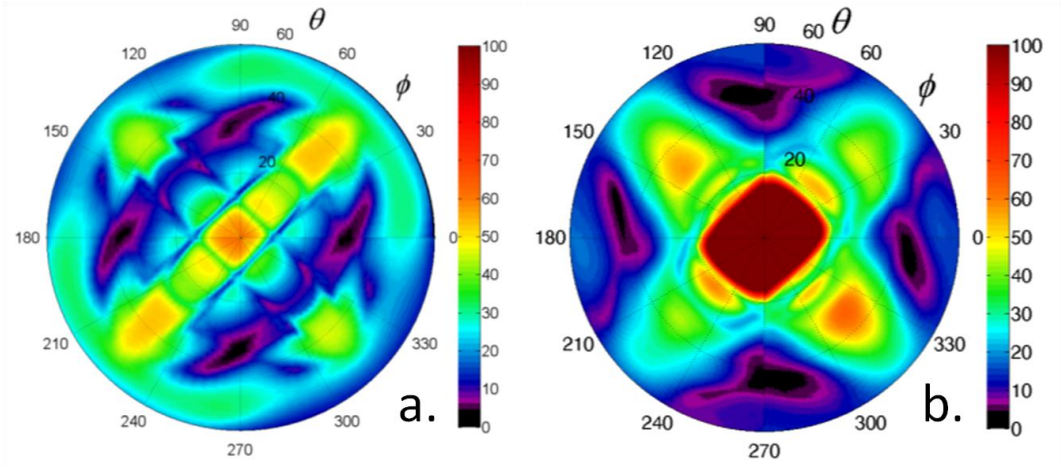

Figure 3-23: UPS recordings for angle-ply laminates: $[-45,+45]_S$ carbon/epoxy (a) and $[-45,+45]_S$ glass/epoxy (b).

The UPS recording for a cross-ply $[0_3,90_4]_S$ hybrid carbon/epoxy-glass/epoxy is shown in Figure 3-24. The laminate is hybrid in the sense that both carbon fibers (0° orientation) and glass fibers (90° orientation) were used to reinforce the epoxy matrix.

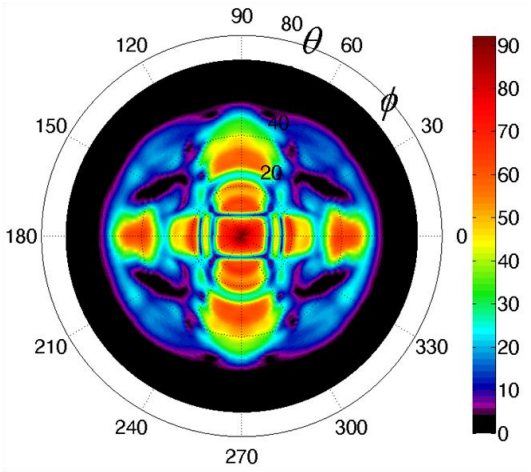

Figure 3-24: UPS recording for a cross-ply $[0_3,90_4]_S$ hybrid carbon/epoxy-glass/epoxy laminate.

Finally, some examples are shown of UPS recordings for carbon fabric reinforced plastics (see Figure 3-25).

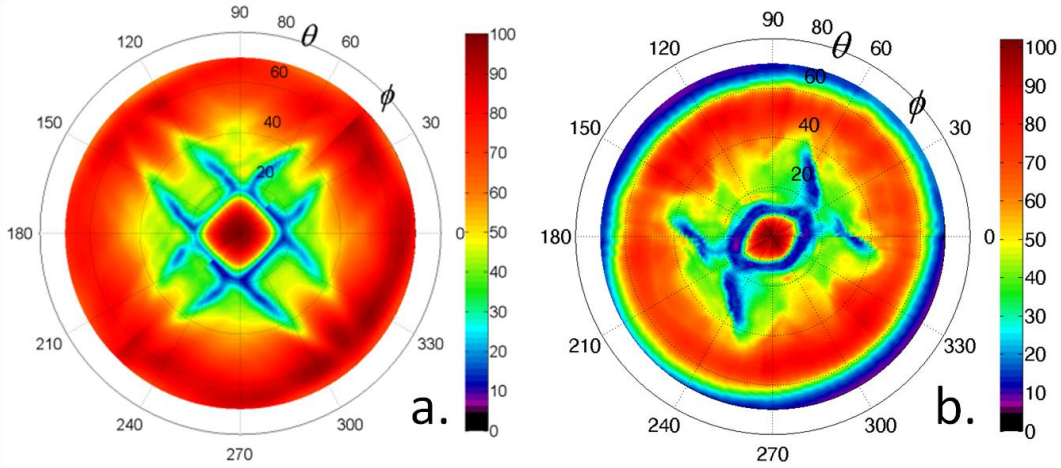

Figure 3-25: UPS recordings for a 5-harness satin weave carbon/PPS laminate (a) and for a 2/2 twill weave carbon/epoxy laminate (b).

It may be clear that the quality of the current UPS recordings outperforms the state-of-the-art UPS recordings found in literature (see the various figures shown in Chapter 2). Again, this is a strong indicator of the superior performance of the developed and implemented experimental setup. For the interpretation, analysis and application of the UPS technique, this is obviously a huge step forward.

3. 7. Next Generation UPS Scanner

The current experimental facility suffices for performing experiments on a laboratory scale and for exploring the capabilities of the UPS method in a scientific manner. Though, for future industrial implementation of the UPS technique, the developed scanner is too bulky and obsolete. For this reason, a prototype of a miniaturized UPS facility has been built. The miniaturized scanner is basically a hand-held scanner which meets in-field requirements. The device is operated in reflection or backscatter mode. Figure 3-26 displays the current status of the miniaturized UPS apparatus. The main parts have already been installed, though at the time of writing the thesis it was not yet possible to perform UPS recordings with the device.

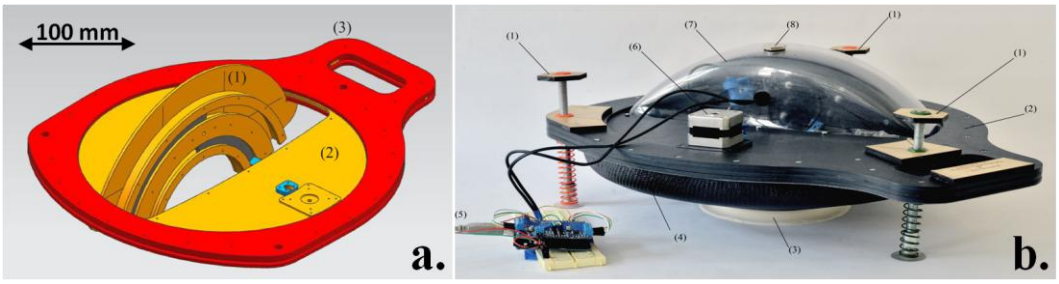

Figure 3-26: Miniaturized UPS facility: CAD drawing (a) and prototype (b). The global dimension of the prototype is ~400 mm.

3. 8. Conclusions

An account is given on the developed and implemented experimental facility. The developed scanner has been programmed in LABVIEW in order to obtain high-quality UPS experiments in a fully automated manner.

Details are given about important experimental conditions such as the spatial characteristics of the generated ultrasonic beam and the properties of the

immersion liquid. Knowledge of these features is important for the correct recording and subsequent analysis and interpretation of experiments.

The robustness and accuracy of the developed setup is demonstrated. Several experimental recordings are presented for various (an)isotropic solids, showing superior quality with respect to state-of-the-art UPS experiments in literature. As such, it may be hoped for that the current high-quality recordings contribute to the further development and exploration of the UPS technique for material characterization and NDT.

Finally, the current status of the construction of a hand-held UPS scanner is given. Such a miniaturized device is necessary for implementation of the UPS technique in industry, and to meet in-field requirements.

3. 9. References

[1] http://www.inspectietechniek.com/nl/producten/c-scan-systemen.

[2] Degrieck, J., *Analyse van impact op een vezelversterkte kunststof (In Dutch).* Ghent University, Faculty of Applied Sciences, (Ghent), PhD Thesis, 1990.

[3] Auld, B.A., *Acoustic Fields and Waves in Solids, second edition*. 1990, Florida: Krieger publishing company. 856.

[4] *Ultrasonic Transducers For Flaw Detection and Sizing*, in *Technical data sheet, General Electric Sensing & Inspection Technologies*. 2008.

[5] http://www.ge-mcs.com/en/ultrasound/system-instrumentations/usip-40.html.

[6] Goodman, J.W., *Introduction to Fourier Optics*. 2nd ed. 1996, New York: McGraw-Hill.

[7] Degrieck, J. *Some possibilities of nondestructive characterisation of composite plates by means of ultrasonic polar scans*. in *Emerging technologies in nondestructive testing (ETNDT)*. 1996. Patras, Greece: A.A. Balkema.

[8] Degrieck, J., N.F. Declercq, and O. Leroy, *Ultrasonic polar scans as a possible means of non-destructive testing and characterisation of composite plates.* Insight, 2003. 45(3): p. 196-201.

[9] Declercq, N.F., J. Degrieck, and O. Leroy, *Ultrasonic polar scans: Numerical simulation on generally anisotropic media.* Ultrasonics, 2006. 45(1-4): p. 32-39.

[10] Declercq, N.F., J. Degrieck, and O. Leroy, *Simulations of harmonic and pulsed ultrasonic polar scans.* Ndt & E International, 2006. 39(3): p. 205-216.

Chapter 4

Numerical Implementation of the Ultrasonic Polar Scan

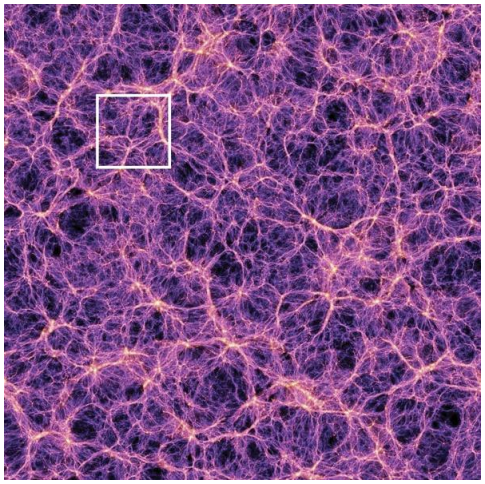

Last decades, the increase in computing power has revolutionized our understanding of nature. Recently, mankind was even able to simulate the big bang and to mimic the fabric of our known universe. (Figure reproduced from reference [1]).

Summary

Several numerical schemes have been implemented in Maple and MATLAB in order to simulate the interaction of an obliquely incident ultrasonic wave, bounded in time and space, with an immersed multilayered anisotropic viscoelastic medium. As such, high-level ultrasonic polar scan simulations can be performed in order to assist experimental recordings, and to pave the road for a mixed experimental-numerical methodology.

4. 1. Introduction

For the ultrasonic polar scan to become a non-destructive inspection technique capable of quantifying different material features, it should evolve to a fully coupled hybrid experimental-numerical methodology. In the previous Chapter 3, the experimental implementation has been described. The second thing needed is a numerical model which allows accurate simulation of ultrasonic polar scans for immersed multilayered anisotropic viscoelastic media. Such a simulation model for ultrasonic polar scans has already been provided in literature [2-3]. However, that simulation model is founded on the global matrix approach [4-6], meaning that the equations of the different material layers are gathered in a single matrix. If properly implemented, this method is unconditionally stable [7]. Though, for an increasing number of layers the dimensions of the global matrix are increasing likewise. As matrix inversion is required to obtain a solution, the global matrix method becomes soon cumbersome. Considering that the UPS involves the computation of many unique incidence angles $\psi(\varphi,\theta)$, it is clear that a computationally more efficient modeling approach is required in order to successfully couple simulation to experiment. In literature, a variety of different numerical approaches with improved computational performance are present for simulating wave propagation in multilayered anisotropic media, such as the transfer matrix method and its modified versions [8-12], Floquet wave formulation [13-14], recursive stiffness matrix method [15-19], the impedance matrix method [20], the hybrid compliance-stiffness matrix method [21-22] as well as asymptotic methods [21, 23].

In this chapter, different numerical models for simulating ultrasonic polar scans, which have been implemented in Maple and MATLAB, are discussed. The transfer matrix technique and the stiffness matrix technique, each having improved computational efficiency and stability when compared to the global matrix model [2-3], are highlighted.

4. 2. Plane Wave in an Unbounded Medium

In tensorial notation, Newton's law, linking the components of the displacement vector **u** to the stress tensor **σ**, is described as

$$\frac{\partial \sigma_{ij}}{\partial x_j} = \rho \ddot{u}_i \tag{1}$$

To obtain a closed system, the above equations need to be complemented with constitutive equations relating the stresses to the strains. When the material is linear and only small deformations are considered, the generalized Hooke's law may be used

$$\sigma_{ij} = C_{ij\ln} \varepsilon_{\ln} \tag{2}$$

with C_{ijln} the symmetrical stiffness tensor of rank 4, and

$$\varepsilon_{\ln} = \frac{1}{2}\left(\frac{\partial u_l}{\partial x_n} + \frac{\partial u_n}{\partial x_l}\right) \tag{3}$$

Combination of the above three equations yields the wave equation for an infinite medium in terms of the displacement components u_i with $i=x,y,z$:

$$\rho \ddot{u}_i = \frac{1}{2} C_{ij\ln}\left(\frac{\partial^2 u_l}{\partial x_j \partial x_n} + \frac{\partial^2 u_n}{\partial x_j \partial x_l}\right) \tag{4}$$

Searching for a plane wave solution of Equation (4) in the form of

$$u_i = p_i \exp\left(i\left(k_j x_j - \omega t\right)\right) \tag{5}$$

with $\boldsymbol{k}$ denoting the wave vector, we obtain Christoffel's equation for anisotropic bulk media

$$\left(\rho\omega^2\delta_{il} - C_{ijln}k_j k_n\right)p_l = 0 \tag{6}$$

which links the wave vector $\boldsymbol{k}$ to the polarization direction $\boldsymbol{p}$.

Equation (6) leads to an orthogonal classical eigenvalue problem, which is solved by demanding non-trivial solutions by setting the determinant of the coefficient matrix to zero:

$$\left|\rho\omega^2\delta_{il} - C_{ijln}k_j k_n\right| = 0 \tag{7}$$

and is followed by the determination of the corresponding eigenvectors. In the case of general anisotropy, six independent solutions can be found. For symmetry higher than or equal to monoclinic symmetry, the number of independent solutions reduces to three because of the equivalence between waves propagating in positive and negative direction.

The Voigt procedure is considered in order to be uniform with generally accepted notation. Basically, the fourth order tensor C_{ijln} with $i,j,l,n = 1...3$ is converted into a second order tensor C_{pq} with $p,q = 1...6$. If $i = j$ then $p = i$, and if $l = n$ then $q = l$; if $i \neq j$ then $p = 9-(i+j)$, and if $l \neq n$ then $q = 9-(l+n)$ [6].

4. 3. Plane Wave in a Layer

For bounded media, such as a plate or a layered composite, the wave equation analysis has to be complemented with appropriate boundary conditions at the layer interfaces. For generality, we consider a layered plate, consisting of N arbitrary viscoelastic anisotropic layers (see Figure 4-1). We assume that the xz-plane of the global coordinate system corresponds to the incident plane and that this plane is rotated over an orientation or polar angle φ with respect to the material coordinate system. At the top and bottom of each layer, a local coordinate system is introduced for the representation of

the partial waves travelling in negative, respectively positive *z* direction in order to improve the computational efficiency and avoid numerical overflow when partial waves become evanescent [5, 7].

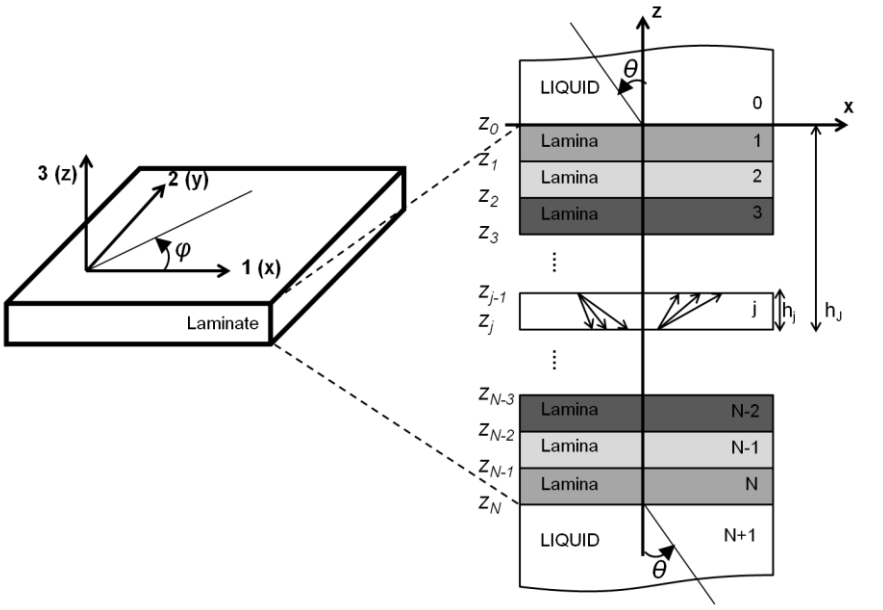

Figure 4-1: Scheme of an immersed multi-layered structure consisting of N visco-elastic anisotropic laminae and definition of the global coordinate system. The angles (φ,θ) represent the direction of incidence of the ultrasonic wave.

In accordance with the partial wave technique, and assuming orthotropic symmetry, the displacement vector $\mathbf{u}^j$ in the j^{th} layer may be written as the summation of the three partial wave solutions as [24]

$$\boldsymbol{u}^j = \sum_{n=1}^{3} \left(a_n^{+j} \boldsymbol{p}_n^{+j} \exp\left(ik_{n,z}^{+j} \left(z - z_j \right) \right) + a_n^{-j} \boldsymbol{p}_n^{-j} \exp\left(ik_{n,z}^{-j} \left(z - z_{j-1} \right) \right) \right) \exp\left(i\left(k_x x + k_y y - \omega t \right) \right) \quad (8)$$

with $\mathbf{u}^j = \left(u_x^j, u_y^j, u_z^j \right)^{\mathrm{T}}$, where T represents the transpose operator, $\mathbf{p}_n^{\pm j} = \left(p_x^{\pm j}, p_y^{\pm j}, p_z^{\pm j} \right)_n^{\mathrm{T}}$ the unit displacement polarization vectors corresponding to waves with the $\mathbf{k}_n^{\pm j}$ wave vectors for layer *j*, in which the superscript ± stands for propagation in +*z* or -*z* direction.

For externally born sound, both the polarization vectors $\mathrm{p}_n^{\pm j}$ and the wave numbers $k_{n,z}^{\pm j}$ for each layer can be found by solving the Christoffel equation in combination with Snell's law, stating that the horizontal component of the wave vector of the incident wave $k_x^j = k_x^{liq} (= k_x^0)$ is conserved. Note that $k_{n,z}^{+j} = -k_{n,z}^{-j}$, and in the remainder of the text we will therefore apply the notation $k_{n,z}^{+} = -k_{n,z}^{-} = k_{n,z}^{j}$.

Using the generalized Hooke's law, the stress vector $\boldsymbol{\sigma}^j = \left(\sigma_{31}^j, \sigma_{32}^j, \sigma_{33}^j\right)^{\mathrm{T}}$ of the j^{th} layer can be related to the plane wave displacement fields as follows

$$\boldsymbol{\sigma}^j = \sum_{n=1}^{3} \left(a_n^{+j} \boldsymbol{d}_n^{+j} \exp\left(ik_{n,z}^j \left(z - z_j \right) \right) + a_n^{-j} \boldsymbol{d}_n^{-j} \exp\left(ik_{n,z}^j \left(z - z_{j-1} \right) \right) \right) \exp\left(i\left(k_x x + k_y y - \omega t \right) \right) \tag{9}$$

where the components $\left(d_i^{\pm j}\right)_m$ of vector $\mathbf{d}_i^{\pm j}$ are related to the polarization vector $\mathbf{p}_i^{\pm j}$ by $\left(d_i^{\pm j}\right)_m = \left(C_{i3\ln}^j k_n^j p_l^{\pm j}\right)_m$ and $k_n^j = \sqrt{k_x^2 + k_y^2 + (k_{n,z}^j)^2}$.

4. 4. Plane Wave in a Multilayer

4. 4. 1. Transfer Matrix Method

At the top of layer *j* the displacement and stresses (Equation (8) and Equation (9)) can be written as

$$\begin{bmatrix} \boldsymbol{u}^{j-1} \\ \boldsymbol{\sigma}^{j-1} \end{bmatrix} = \begin{bmatrix} \boldsymbol{P}^- & \boldsymbol{P}^+ \boldsymbol{H}^+ \\ \boldsymbol{D}^- & \boldsymbol{D}^+ \boldsymbol{P}^+ \end{bmatrix}^j \begin{bmatrix} \boldsymbol{A}^- \\ \boldsymbol{A}^+ \end{bmatrix}^j \tag{10}$$

where $\boldsymbol{A}^{\pm j} = \left[a_1^{\pm j}, a_2^{\pm j}, a_3^{\pm j} \right]^T$ is the vector of partial wave amplitudes, $\boldsymbol{P}^{\pm} = \left[\boldsymbol{p}_1^{\pm}, \boldsymbol{p}_2^{\pm}, \boldsymbol{p}_3^{\pm} \right]$ contains the polarization unit vectors for each partial wave, $\boldsymbol{D}^{\pm} = \left[\boldsymbol{d}_1^{\pm}, \boldsymbol{d}_2^{\pm}, \boldsymbol{d}_3^{\pm} \right]$ the matrix with the stress vectors for each partial

wave, $\boldsymbol{H}^{\pm} = \begin{bmatrix} \exp\left(ik_{1,z}^{\pm} h_j\right) & 0 & 0 \\ 0 & \exp\left(ik_{2,z}^{\pm} h_j\right) & 0 \\ 0 & 0 & \exp\left(ik_{3,z}^{\pm} h_j\right) \end{bmatrix}$ contains the propagators $\exp\left(ik_{n,z}^{\pm} h_j\right)$ with h_j the thickness of the j^{th} layer.

In a similar way, the displacements and stresses at the bottom of the j^{th} layer can be written as

$$\begin{bmatrix} \boldsymbol{u}^j \\ \boldsymbol{\sigma}^j \end{bmatrix} = \begin{bmatrix} \boldsymbol{P}^- \boldsymbol{H}^- & \boldsymbol{P}^+ \\ \boldsymbol{D}^- \boldsymbol{H}^- & \boldsymbol{D}^+ \end{bmatrix}^j \begin{bmatrix} \boldsymbol{A}^- \\ \boldsymbol{A}^+ \end{bmatrix}^j \tag{11}$$

By eliminating the partial wave amplitudes $\boldsymbol{A}^{\pm j}$ from Equation(10) and Equation (11), the displacements and stresses at the top of the j^{th} layer are linked to the ones at the bottom of the j^{th} layer:

$$\begin{bmatrix} \boldsymbol{u}^j \\ \boldsymbol{\sigma}^j \end{bmatrix} = \begin{bmatrix} \boldsymbol{P}^- \boldsymbol{H}^- & \boldsymbol{P}^+ \\ \boldsymbol{D}^- \boldsymbol{H}^- & \boldsymbol{D}^+ \end{bmatrix}^j \left(\begin{bmatrix} \boldsymbol{P}^- & \boldsymbol{P}^+ \boldsymbol{H}^+ \\ \boldsymbol{D}^- & \boldsymbol{D}^+ \boldsymbol{H}^+ \end{bmatrix}^j \right)^{-1} \begin{bmatrix} \boldsymbol{u}^{j-1} \\ \boldsymbol{\sigma}^{j-1} \end{bmatrix} = \boldsymbol{B}^j \begin{bmatrix} \boldsymbol{u}^{j-1} \\ \boldsymbol{\sigma}^{j-1} \end{bmatrix} \tag{12}$$

with $\boldsymbol{B}^j$ the transfer matrix of the j^{th} layer.

This process can be repeated in order to account for multiple layers in a structure. As such, a structure with J layers has a total transfer matrix $\underline{\boldsymbol{B}}^J$ which can be computed by multiplying the transfer matrix of the j^{th} layer $\boldsymbol{B}^j$ with the total transfer matrix of the J-1 layers $\underline{\boldsymbol{B}}^{J-1}$:

$$\underline{\boldsymbol{B}}^J = \boldsymbol{B}^j \underline{\boldsymbol{B}}^{J-1} \tag{13}$$

Hence, the total transfer matrix for a N-layered structure is computed in a recursive way, and can be written as the direct product of the transfer matrix of the N different layers

$$\underline{\boldsymbol{B}} = \underline{\boldsymbol{B}}^N = \prod_{j=1}^{N} \boldsymbol{B}^j = \left(\boldsymbol{B}^N \left(\boldsymbol{B}^{N-1} \ldots \left(\boldsymbol{B}^3 \left(\boldsymbol{B}^2 \boldsymbol{B}^1\right)\right)\ldots\right)\right) \tag{14}$$

The relation between the displacements and the stresses at the top and the bottom of the *N* layered structure is then

$$\begin{bmatrix} \boldsymbol{u}^N \\ \boldsymbol{\sigma}^N \end{bmatrix} = \underline{\boldsymbol{B}}^N \begin{bmatrix} \boldsymbol{u}^0 \\ \boldsymbol{\sigma}^0 \end{bmatrix} \tag{15}$$

Because of the cascading nature of the transfer matrix approach, no matrix more than $(6x6)$ has to be computed, making the method computationally efficient. Though, the transfer matrix method suffers whenever the incident angle is larger than the critical angle in some layer [12]. This yields an evanescent partial wave, which is characterized by an imaginary wave number, implying that the propagators $\exp\left(ik_{n,z}^{\pm} h_j\right)$ in $\boldsymbol{H}^{\pm}$ become real-valued and very small. This becomes even worse whenever the layer thickness, or equivalently the frequency, increases. The matrix $\begin{bmatrix} \boldsymbol{P}^- & \boldsymbol{P}^+\boldsymbol{H}^+ \\ \boldsymbol{D}^- & \boldsymbol{D}^+\boldsymbol{H}^+ \end{bmatrix}^j$ will thus become singular, and as the evaluation of Equation (12) requires inversion of this matrix this leads to numerical instability.

4. 4. 2. Stiffness Matrix Method

To solve the instability of the transfer matrix method, the propagator matrix $\boldsymbol{H}^{\pm}$ should be isolated such that the appearance of singular matrices is avoided. The stiffness matrix technique rearranges the terms in Equation (10) and Equation (11) to obtain

$$\begin{bmatrix} \boldsymbol{u}^{j-1} \\ \boldsymbol{u}^j \end{bmatrix} = \begin{bmatrix} \boldsymbol{P}^- & \boldsymbol{P}^+\boldsymbol{H}^+ \\ \boldsymbol{P}^-\boldsymbol{H}^- & \boldsymbol{P}^+ \end{bmatrix}^j \begin{bmatrix} \boldsymbol{A}^- \\ \boldsymbol{A}^+ \end{bmatrix}^j \tag{16}$$

and

$$\begin{bmatrix} \boldsymbol{\sigma}^{j-1} \\ \boldsymbol{\sigma}^j \end{bmatrix} = \begin{bmatrix} \boldsymbol{D}^- & \boldsymbol{D}^+\boldsymbol{H}^+ \\ \boldsymbol{D}^-\boldsymbol{H}^- & \boldsymbol{D}^+ \end{bmatrix}^j \begin{bmatrix} \boldsymbol{A}^- \\ \boldsymbol{A}^+ \end{bmatrix}^j \tag{17}$$

By eliminating the partial wave amplitudes $\boldsymbol{A}^{\pm j}$ from Equation (16) and Equation (17), the stresses are related to the displacements at top and bottom of the j^{th} layer by

$$\begin{bmatrix} \boldsymbol{\sigma}^{j-1} \\ \boldsymbol{\sigma}^{j} \end{bmatrix} = \begin{bmatrix} \boldsymbol{D}^{-} & \boldsymbol{D}^{+}\boldsymbol{H}^{+} \\ \boldsymbol{D}^{-}\boldsymbol{H}^{-} & \boldsymbol{D}^{+} \end{bmatrix}^{j} \left(\begin{bmatrix} \boldsymbol{P}^{-} & \boldsymbol{P}^{+}\boldsymbol{H}^{+} \\ \boldsymbol{P}^{-}\boldsymbol{H}^{-} & \boldsymbol{P}^{+} \end{bmatrix}^{j} \right)^{-1} \begin{bmatrix} \boldsymbol{u}^{j-1} \\ \boldsymbol{u}^{j} \end{bmatrix} = \boldsymbol{K}^{j} \begin{bmatrix} \boldsymbol{u}^{j-1} \\ \boldsymbol{u}^{j} \end{bmatrix} \tag{18}$$

with $\boldsymbol{K}^{j} = \begin{bmatrix} \boldsymbol{K}_{11}^{j} & \boldsymbol{K}_{12}^{j} \\ \boldsymbol{K}_{21}^{j} & \boldsymbol{K}_{22}^{j} \end{bmatrix}$ the $(6x6)$ stiffness matrix of the j^{th} layer. The $\boldsymbol{K}_{11}^{j}$, $\boldsymbol{K}_{12}^{j}$, $\boldsymbol{K}_{21}^{j}$ and $\boldsymbol{K}_{22}^{j}$ are $(3x3)$ submatrices of the stiffness matrix $\boldsymbol{K}^{j}$. Contrary to the transfer matrix technique, the $\boldsymbol{H}^{\pm}$ matrix cannot produce any singularity as it is not located anymore in a single column nor along the diagonal.

Similar as for the total transfer matrix, the total stiffness matrix $\underline{\boldsymbol{K}}^{N}$ of a N-layered structure can be expressed in a recursive way according to

$$\underline{\boldsymbol{K}} = \underline{\boldsymbol{K}}^{N} = \begin{bmatrix} \underline{\boldsymbol{K}}_{11}^{N} & \underline{\boldsymbol{K}}_{12}^{N} \\ \underline{\boldsymbol{K}}_{21}^{N} & \underline{\boldsymbol{K}}_{22}^{N} \end{bmatrix} = \begin{bmatrix} \underline{\boldsymbol{K}}_{11}^{N-1} + \underline{\boldsymbol{K}}_{12}^{N-1}\left(\boldsymbol{K}_{11}^{N} - \underline{\boldsymbol{K}}_{22}^{N-1}\right)^{-1} \underline{\boldsymbol{K}}_{21}^{N-1} & -\underline{\boldsymbol{K}}_{12}^{N-1}\left(\boldsymbol{K}_{11}^{N} - \underline{\boldsymbol{K}}_{22}^{N-1}\right)^{-1} \boldsymbol{K}_{12}^{N} \\ \boldsymbol{K}_{21}^{N}\left(\boldsymbol{K}_{11}^{N} - \underline{\boldsymbol{K}}_{22}^{N-1}\right)^{-1} \underline{\boldsymbol{K}}_{21}^{N-1} & \boldsymbol{K}_{22}^{N} + \boldsymbol{K}_{21}^{N}\left(\boldsymbol{K}_{11}^{N} - \underline{\boldsymbol{K}}_{22}^{N-1}\right)^{-1} \boldsymbol{K}_{12}^{N} \end{bmatrix} \tag{19}$$

with $\boldsymbol{K}^{N}$ the stiffness matrix of the N^{th} layer and $\underline{\boldsymbol{K}}^{N}$, $\underline{\boldsymbol{K}}^{N-1}$ the total stiffness matrix of the first N respectively N-1 layers.

The relation between the displacements and the stresses at the top and the bottom of the N layered structure becomes

$$\begin{bmatrix} \boldsymbol{\sigma}^{0} \\ \boldsymbol{\sigma}^{N} \end{bmatrix} = \begin{bmatrix} \underline{\boldsymbol{K}}_{11}^{N} & \underline{\boldsymbol{K}}_{12}^{N} \\ \underline{\boldsymbol{K}}_{21}^{N} & \underline{\boldsymbol{K}}_{22}^{N} \end{bmatrix} \begin{bmatrix} \boldsymbol{u}^{0} \\ \boldsymbol{u}^{N} \end{bmatrix} = \underline{\boldsymbol{K}}^{N} \begin{bmatrix} \boldsymbol{u}^{0} \\ \boldsymbol{u}^{N} \end{bmatrix} \tag{20}$$

The stiffness matrix method patches the numerical instability of the transfer matrix method by rearranging the propagator matrix $\boldsymbol{H}^{\pm}$, while equivalent computational effort is required. However, the rearrangement of the propagator matrix $\boldsymbol{H}^{\pm}$ introduces another instability, this time for a layer

thickness tending to zero. Indeed, by setting the thickness $h = 0$ the matrix $\begin{bmatrix} \boldsymbol{P}^{-} & \boldsymbol{P}^{+}\boldsymbol{H}^{+} \\ \boldsymbol{P}^{-}\boldsymbol{H}^{-} & \boldsymbol{P}^{+} \end{bmatrix}^{j}$ in Equation (18) becomes singular as the propagator matrix $\boldsymbol{H}^{\pm}$ reduces to the identity matrix $\boldsymbol{I}$. Inversion of the singular matrix then yields an undefined solution, producing a numerical instability. Obviously, this numerical instability is only important for thin layer modeling, and thus could be ignored in common composite materials.

As both the transfer and stiffness matrix method connect stresses and displacements at the surfaces of a layer, they are obviously closely related to each other. The relation between the transfer matrix $\underline{\boldsymbol{B}}$ and the stiffness matrix $\underline{\boldsymbol{K}}$ can be written as [17]

$$\underline{\boldsymbol{B}} = \begin{bmatrix} -\left(\underline{\boldsymbol{K}}_{12}\right)^{-1}\underline{\boldsymbol{K}}_{11} & \left(\underline{\boldsymbol{K}}_{12}\right)^{-1} \\ \underline{\boldsymbol{K}}_{21} - \underline{\boldsymbol{K}}_{22}\left(\underline{\boldsymbol{K}}_{12}\right)^{-1}\underline{\boldsymbol{K}}_{11} & \left(\underline{\boldsymbol{K}}_{12}\right)^{-1}\underline{\boldsymbol{K}}_{22} \end{bmatrix} \tag{21}$$

Analogously, the stiffness matrix $\underline{\boldsymbol{K}}$ can be formulated in terms of the transfer matrix $\underline{\boldsymbol{B}}$ as

$$\underline{\boldsymbol{K}} = \begin{bmatrix} -\left(\underline{\boldsymbol{B}}_{12}\right)^{-1}\underline{\boldsymbol{B}}_{11} & \left(\underline{\boldsymbol{B}}_{12}\right)^{-1} \\ \underline{\boldsymbol{B}}_{21} - \underline{\boldsymbol{B}}_{22}\left(\underline{\boldsymbol{B}}_{12}\right)^{-1}\underline{\boldsymbol{B}}_{11} & \left(\underline{\boldsymbol{B}}_{12}\right)^{-1}\underline{\boldsymbol{B}}_{22} \end{bmatrix} \tag{22}$$

When considering a fluid-loaded solid structure, as is the case for an ultrasonic polar scan, it is assumed that the fluid carries no shear waves. Hence, continuity of normal displacement and normal stress, or equivalently the condition of zero shear stresses is imposed at the liquid-solid interface. In this case, we are only interested in finding the coefficient $a_1^{+(N+1)}/a_1^{+0}$ for transmission and a_1^{-0}/a_1^{+0} for reflection.

4. 5. Ultrasonic Polar Scan Expansion

The above procedure is valid for a single oblique incidence angle, and thus should be extended to incorporate all possible oblique incidence angles in order to simulate a UPS. The intrinsic elasticity tensor $\boldsymbol{C}_{ij\ln}^{I}$ in the principal

material coordinate system can be transformed into an elasticity tensor $\boldsymbol{C}_{ij\ln}^{R}$ in a rotated coordinate system, with *z* the rotation axis, according to

$$\boldsymbol{C}_{ij\ln}^{R} = \boldsymbol{R}\, \boldsymbol{C}_{ij\ln}^{R}\, \boldsymbol{R}^{T} \tag{23}$$

in which $\mathbf{R}^{(T)}$ is the (transposed) rotation matrix defined as

$$\boldsymbol{R}^{(T)} = \begin{bmatrix} c^2 & s^2 & 0 & 0 & 0 & -2cs \\ s^2 & c^2 & 0 & 0 & 0 & 2cs \\ 0 & 0 & 1 & 0 & 0 & 0 \\ 0 & 0 & 0 & c & s & 0 \\ 0 & 0 & 0 & -s & c & 0 \\ cs & -cs & 0 & 0 & 0 & c^2 - s^2 \end{bmatrix}^{(T)} \tag{24}$$

with $s = \sin(\varphi)$ and $c = \cos(\varphi)$.

Applying the above considerations for every possible angle of oblique incidence $\psi(\varphi,\theta)$ result in a plane wave simulation of the ultrasonic polar scan of lossless media.

4. 6. Plane Wave in an Immersed Viscoelastic Multilayer

Since real materials in general exhibit internal energy losses, it is necessary to account for damping in the elastic constitutive relation [2-3, 25-26]. This is especially indispensable for epoxy-based materials which typically combine energy-storing features of elastic media and the dissipating features of viscous liquids, and as such are viscoelastic of nature. In general, damping is a complex phenomenon, which depends on the wave-type, acoustic frequency, temperature, etc. As only limited knowledge is available about the damping characteristics of common materials, the easiest and most generic approach to model acoustic losses is by considering a viscous damping term.

A Kelvin-Voigt solid consists of both a viscous damper and an elastic spring which are connected in parallel (see schematic in Figure 4-2).

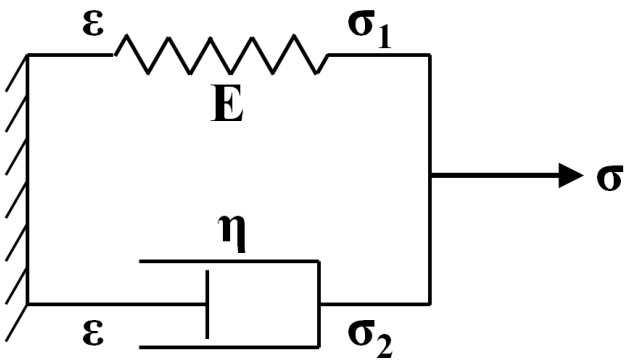

Figure 4-2: Kelvin-Voigt model (1D) for viscoelastic solids.

As the 1D Kelvin-Voigt solid is loaded by a stress σ, the stress is distributed over the spring and the damper in such a way that the strain ε is the same for the spring and the damper

$$\sigma = \sigma_1 + \sigma_2 \tag{25}$$

A linear elastic material is described by Hooke's law

$$\sigma = E\varepsilon \tag{26}$$

Newton's law for a viscous liquid is

$$\sigma = \eta \, d\varepsilon / dt \tag{27}$$

with η the viscosity.

Substituting Equation (26) and Equation (27) into Equation (25) yields

$$\sigma = E\varepsilon + \eta \, d\varepsilon / dt \tag{28}$$

For wave problems, the field variables have a time dependency

$$\begin{aligned} \sigma &= \tilde{\sigma} e^{i\omega t} \\ \varepsilon &= \tilde{\varepsilon} e^{i\omega t} \\ u &= \tilde{u} e^{i\omega t} \end{aligned} \tag{29}$$

Combining Equation (29) with Equation (28) then gives a similar equation as in standard elasticity theory (see Equation (26))

$$\tilde{\sigma} = E\tilde{\varepsilon} + i\omega\eta\tilde{\varepsilon} = C(\omega)\tilde{\varepsilon} \tag{30}$$

with $C(\omega) = C' + i\omega C''$ the frequency dependent complex valued elastic modulus.

The real part of $C(\omega)$ represents the capacity to store energy, the imaginary part the dissipation of energy which is function of the frequency. For general anisotropic media we obtain

$$\sigma_{ij} = C_{ij\ln}\varepsilon_{\ln} \tag{31}$$

with $C_{ij\ln}$ the complex-valued symmetrical stiffness tensor.

Hence, the viscoelastic character of solids can be easily accounted for by considering a complex valued elasticity tensor. The effect of a complex elasticity tensor on the UPS simulation is demonstrated in Figure 4-3 for an aluminum sample. The real-valued elasticity tensor corresponds to $C = C'$, while the complex elasticity tensor corresponds to $C = C' - i0.008C'$. The imaginary elasticity constants have been selected in order to have a clear visualization of the effect of attenuation. Typically, the imaginary elastic constants have lower values for standard aluminum. To highlight the frequency dependent attenuation, UPS simulations have been performed at different frequencies. The UPS simulations show decreased transmission amplitudes (note the amplitude scale) when complex material parameters are entered, thus reflecting the viscoelastic material properties. Increase of *fd* leads to an increased reduction of the transmission amplitudes.

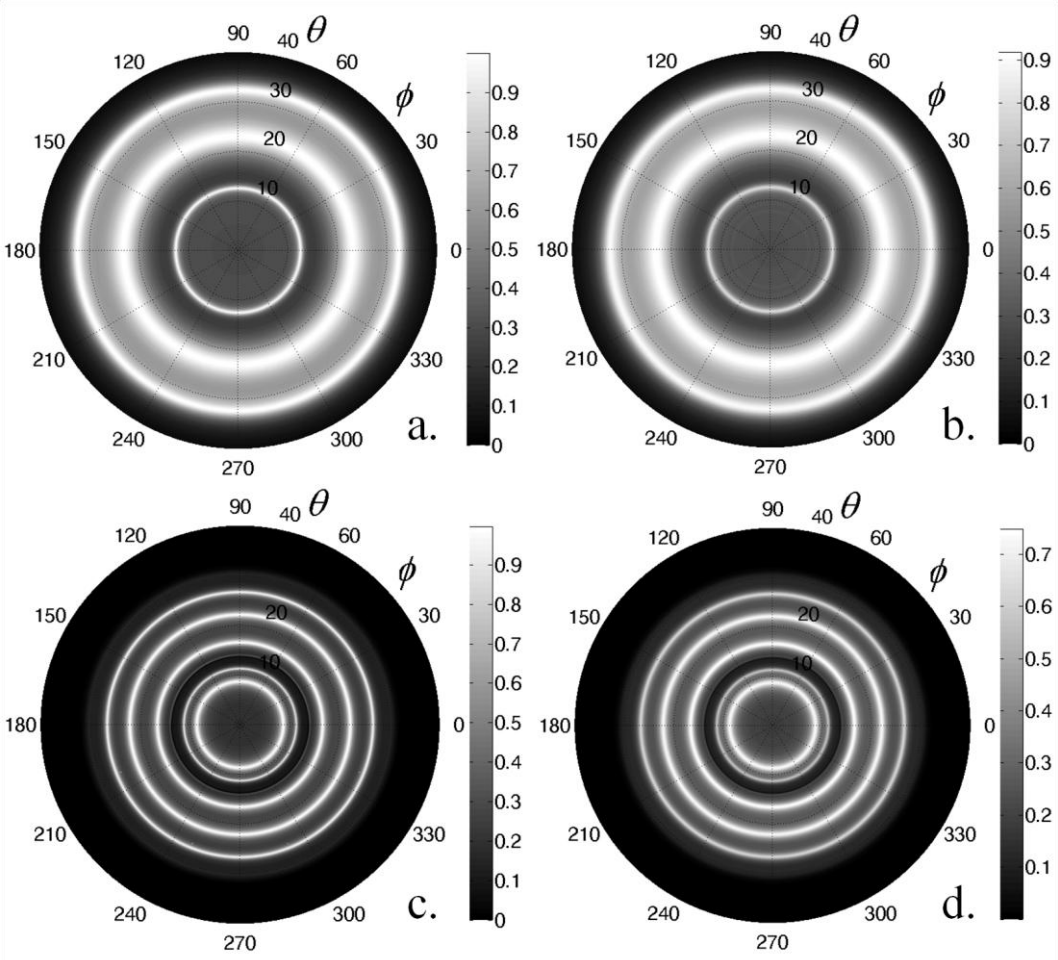

Figure 4-3: The effect of complex elasticity constants for the UPS simulation of aluminum: *fd* = 2.5 MHz.mm (a-b) and *fd* = 7.5 MHz.mm (c-d). Left column: real *C*-tensor $C = C'$, right column: complex *C*-tensor $C = C' - i\,0.008C'$.

4. 7. Bounded Wave in an Immersed Viscoelastic Multilayer

The previous discussion is only valid when considering plane wave interaction. In practice however, the plane wave assumption is unrealistic because an ultrasonic wave is often bounded in space as well as in time (see Section 3.4 of previous Chapter).

4. 7. 1. Spatially Bounded Wave

The results shown in Figure 3.9 illustrate that a flat immersion transducer does not produce a plane wave sound beam at all, not even in a good approximation (as often assumed in literature [2-3]). A more appropriate angular response of such type of transducer may be represented by a circular radiator using the first order Bessel distribution. Though, because of the housing of the piezoelectric element, the displacement field at the surface of the transducer is rather inhomogeneous and decays exponentially towards the edge, with different decay constants in different directions. Therefore, instead of assuming a uniform Bessel distribution, the measured sound beam profile, that ought to be used as input for our model, has been fitted to an anisotropic 2D Gaussian distribution by means of the Levenberg-Marquardt algorithm [27-28]. As such, the profile considered in the model satisfies

$$G_{2D} = A_0 + A\exp\left[-\frac{1}{2}\left(\left(\frac{x-x_0}{\sigma_x}\right)^2 + \left(\frac{y-y_0}{\sigma_y}\right)^2\right)\right] \qquad (32)$$

with A_0 the level of acoustic noise, A the maximum amplitude, x_0 and y_0 the center of the surface fit along the x-, respectively the y-coordinate while σ_x and σ_y represent the width of the surface fit along the x-, respectively the y-coordinate.

The choice for the computationally more attractive Gaussian profile is further motivated by the fact that the angular frequency content for both distributions can be considered to be very alike [29]. Of course, change of the emission frequency induces a modification in the sound radiation pattern, and thus alters the function parameters of Equation (32). The function parameters have been determined for the different employed ultrasonic frequencies. For reasons of brevity, we only list the optimized distribution parameters, together with their standard error δ, for a 5 MHz bounded beam (see Table 1).

Table 1: Function parameters and standard error δ of the nonlinear fit of the 2D amplitude profile of a 5 MHz sound beam at the measurement plane z = 130 mm, according to Equation (32). Where applicable, the units are in mm.

A_0	A	x_0	σ_x	y_0	σ_y
4.060	41.700	0.777	3.024	0.178	2.875

δ_{A_0}	δ_A	δ_{x_0}	δ_{σ_x}	δ_{y_0}	δ_{σ_y}
0.0279	0.3012	0.0219	0.0224	0.0207	0.0211

Once the fitted anisotropic 2D Gaussian surface is fully parameterized, it can be decomposed by application of the Fourier theorem in a continuum of harmonic plane waves and evanescent waves propagating in specific angular directions

$$A(x,y,z) = \int_{-\infty}^{+\infty}\int_{-\infty}^{+\infty} \tilde{A}(k_x,k_y)\exp\left(j\left(k_x x + k_y y + k_z z\right)\right)dk_x dk_y \qquad (33)$$

with k_x, k_y, k_z the wave number in x-,y-, respectively z-direction, and $\tilde{A}(k_x,k_y)\exp(jk_z z)$ the local plane wave spectrum.

Note that the integration limits are -∞ and +∞, hence the range of k_x and k_y includes evanescent waves whenever the condition $k_x^2 + k_y^2 > k^2$ is fulfilled. Since these waves decay quickly in the direction of propagation, they can be ignored without any further consequences. Another worry is that, for large incident angles θ, the Fourier decomposition may lead to an unrealistic representation since the possibility exists that plane waves with an upward pointing wave vector $\boldsymbol{k}$ are incorporated. However, the experimental restriction of the incident angle θ, being limited to 70°, together with the typical small angular spectrum of the transducers involved, makes the above concern of no importance for the modeling.

In practice and for reasons of computational efficiency, the two-dimensional fast Fourier transform 2DFFT has been implemented instead of the continuous decomposition. Each (discrete) plane wave component is then multiplied by its corresponding reflection or transmission coefficient, and the resulting signal is reconstructed using an inverse 2DFFT.

The bounded beam effect is demonstrated in Figure 4-4 for an aluminum sample at fd = 7.5 MHz.mm. Note that the bounded beam has an integrating effect, causing the merging of the characteristic contours at $\theta \approx 9°$ and $\theta \approx 11°$ as well as the disappearance of the sharp characteristic contour at $\theta \approx 14°$. This result reveals that the common assumption [2-3] that the H-UPS patterns are a one-to-one relationship with Lamb wave stimulation

conditions does not hold for bounded beam insonification. More details, both numerically and experimentally, will be given in Chapter 8.

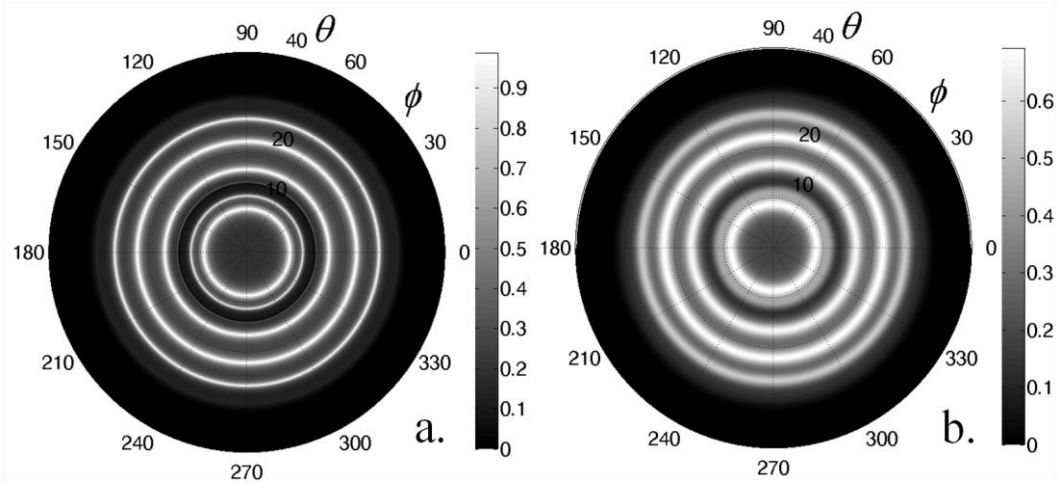

Figure 4-4: The bounded beam effect for the UPS simulation of aluminum at *fd* = 7.5 MHz.mm: harmonic plane wave (a) and harmonic bounded wave (b).

4. 7. 2. Temporally Bounded Beam

The employment of an ultrasonic pulse on the other hand involves a wide spectrum of harmonic plane waves, each having a specific frequency and associated amplitude (see Figure 3.7 for an ultrasonic pulse with center frequency $f_c \approx 4$ MHz). The ultrasonic pulse in time domain $g(t)$ has been decomposed into its plane wave spectrum by means of a Fourier integral

$$g(t) = \int_{-\infty}^{+\infty} \hat{g}(f)\, e^{-i2\pi ft} df \tag{34}$$

The complex-valued reflection and transmission characteristics are calculated as a function of frequency *f*, and are used in an inverse Fourier integral to attain the received and transmitted pulse signal in time domain

$$R(t) = \int_{-\infty}^{+\infty} R(f)\hat{g}(f)\, e^{i2\pi ft} df \tag{35}$$

and

$$T(t) = \int_{-\infty}^{+\infty} T(f)\hat{g}(f)\, e^{i2\pi ft} df \tag{36}$$

For computational efficiency again, we employ the fast Fourier transform and select discrete frequency values in the spectrum of the ultrasonic pulse. The inverse fast Fourier transform is then used to pass to the time domain.

As an example, consider an ultrasonic pulse with center frequency f_c = 7.5 MHz (see Figure 4-5).

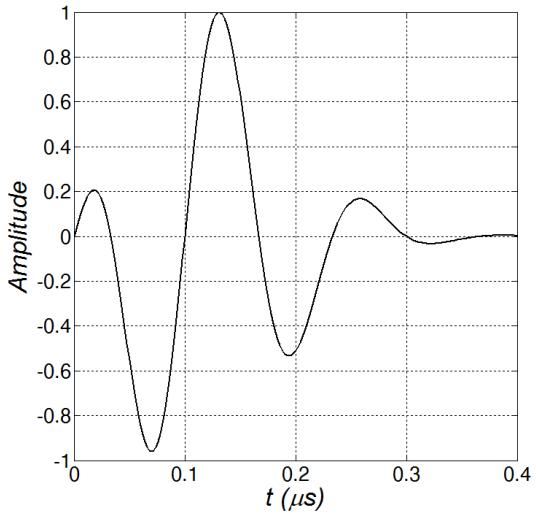

Figure 4-5: Ultrasonic pulse with center frequency f_c = 7.5 MHz.

In Figure 4-6, the decomposition and reconstruction of the signal is shown for different frequency densities, ranging from poor (Figure 4-6a) over average (Figure 4-6b) to good (Figure 4-6c) resolution in temporal frequency domain. According to Nyquist, it is sufficient to reconstruct the signal whenever the sampling frequency is higher than two times the involved frequencies. It is clear that this is satisfied for the three considered cases, hence the reconstructed signal yields the original pulse.

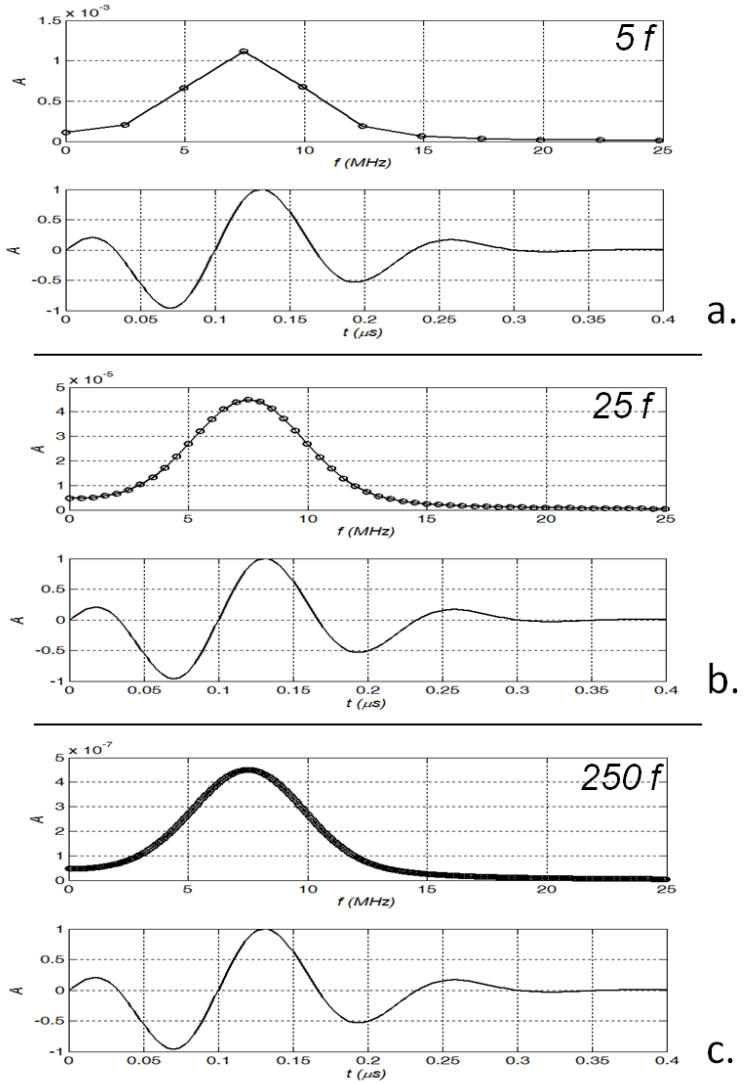

Figure 4-6: Decomposition and reconstruction of the ultrasonic pulse shown in Figure 4-5: poor density - 5 bins (a), average density - 25 bins (b) and good density - 250 bins (c) in frequency domain.

However, it can be expected that poor resolution in frequency domain is not sufficient for computing pulsed transmission and reflection characteristics in a correct way because of the highly dispersive character of Lamb waves involved (see for example the dispersion curves shown in Figure 2.7). The influence of the number of selected frequencies in the FFT decomposition for the transmission amplitude as a function of incident angle θ is explicitly demonstrated in Figure 4-7 for aluminum. The blue curve is computed by

selecting only the central frequency (7.5 MHz), and as such correspond to the harmonic solution putting on view Lamb wave stimulation conditions (θ_{A3} = 8.7°, θ_{S3} = 11.3°, θ_{S2} = 14.0°, θ_{A2} = 16.6°, θ_{S1} = 22.1°, θ_{A1} = 26.6° and $\theta_{S0} \approx \theta_{A0} \approx$ 29.8°). Increase of the number of frequencies in the decomposition changes the computed transmission characteristic drastically. At a large frequency density, the transmitted pulse amplitudes converge to a steady state solution due to phase cancelling of multiple interfering Lamb modes [2-3]. Hence, instead of putting on view Lamb mode stimulation conditions, the converged transmission curve exposes the conditions for in-plane bulk wave stimulation (θ_L = 13.7° for longitudinally polarization and θ_S = 28.7° for the shear polarization). Hence, it is clear that insufficient sampling of the ultrasonic pulse in frequency domain yields a transmission profile which is a mixture of lamb wave and bulk wave characteristics, making a correct interpretation and subsequent analysis impossible. Therefore, in the remainder of this thesis, P-UPS simulations have been performed considering at least 200 dominating frequencies in the temporal spectrum of the ultrasonic pulse.

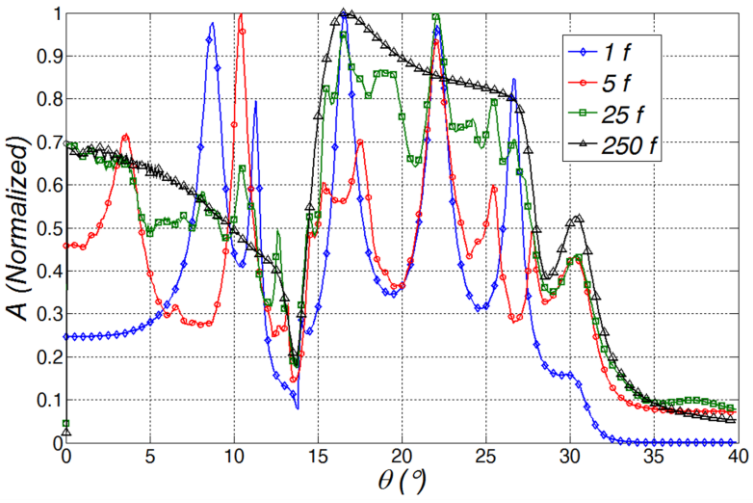

Figure 4-7: Normalized transmission pulse amplitude as a function of incident angle θ for aluminum. Different number of discrete frequencies have been considered in the Fourier decomposition of the pulse with central frequency f_c = 7.5 MHz.

Figure 4-8 displays the UPS simulation for aluminum, considering both a harmonic (f = 7.5 MHz) and a pulsed (f_c = 7.5 MHz) ultrasonic wave. As already stated before, the H-UPS image has characteristics contours which

put on view Lamb wave angles, while the characteristics contours in a P-UPS image relate to critical bulk wave angles.

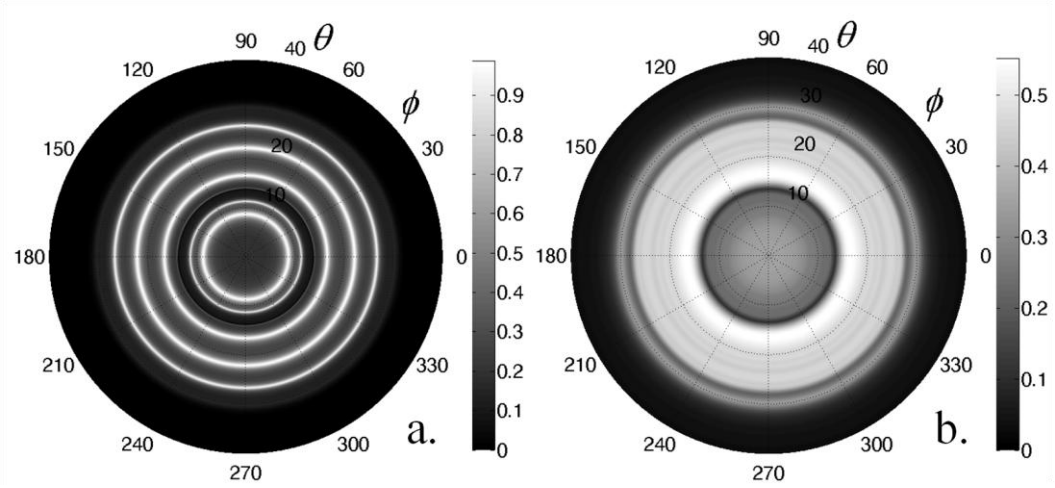

Figure 4-8: UPS simulation of aluminum at *fd* = 7.5 MHz.mm: harmonic wave (H-UPS) (a) and pulsed wave (P-UPS) (b).

4. 8. Illustrative Simulations

This section provides a few examples of H-UPS and P-UPS simulations for a variety of common anisotropic symmetry classes, considering representative elastic material parameters. Unfortunately, the imaginary material parameters are most of the time unknown, therefore they have been chosen to best knowledge.

4. 8. 1. Isotropic Layer

Figure 4-9 displays H-UPS and P-UPS simulations for both aluminum and lead. The circular symmetry in the UPS images clearly exposes the isotropic nature of both materials.

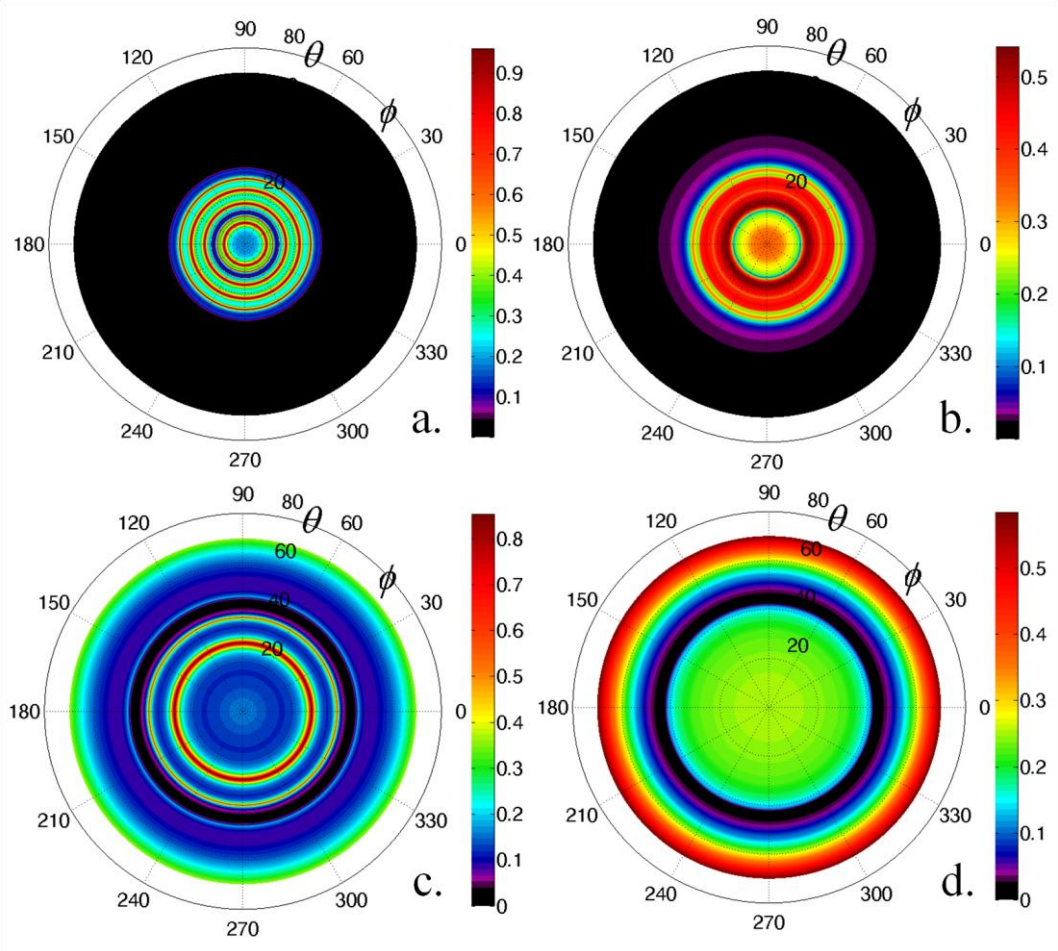

Figure 4-9: H-UPS (left) and P-UPS (right) simulations: aluminum at *fd* = 7.5 MHz.mm (a-b) and steel at *fd* = 3 MHz.mm (c-d).

4. 8. 2. Cubic Layer

Figure 4-10 displays H-UPS and P-UPS simulations for both body-centered cubic (bcc) iron alpha and face-centered cubic (fcc) austenitic stainless steel. It is clear that the patterns in the UPS images become more complex due to the lower symmetry class of the cubic materials.

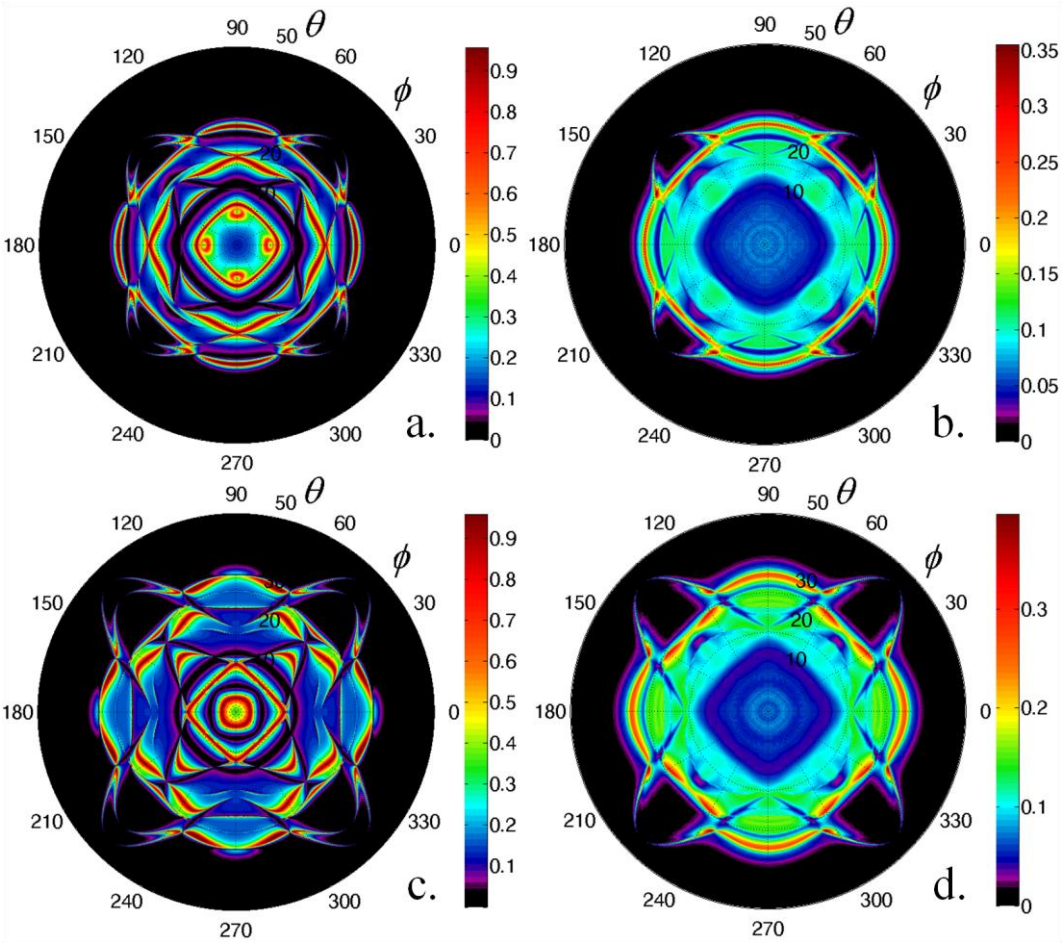

Figure 4-10: H-UPS (left) and P-UPS (right) simulations: iron-alpha bcc crystal (a-b) and austenitic fcc crystal (c-d) at *fd* = 5 MHz.mm.

4. 8. 3. Transversal Isotropic Layer

Figure 4-11 displays H-UPS and P-UPS simulations for a carbon/epoxy layer which possesses transversal isotropic symmetry.

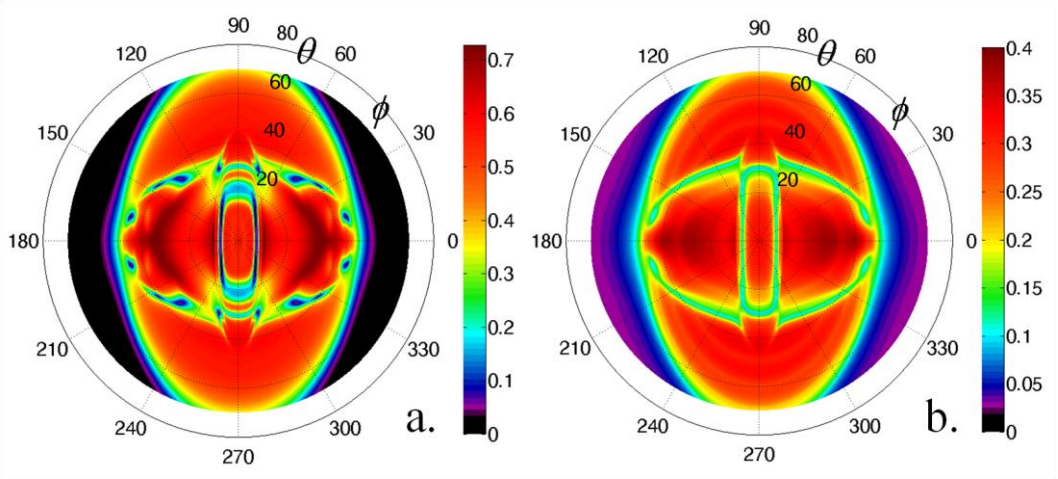

Figure 4-11: H-UPS (left) and P-UPS (right) simulations for transversal isotropic carbon/epoxy layer at *fd* = 4 MHz.mm.

4. 8. 4. Angle-ply Multilayer

Figure 4-12 displays H-UPS and P-UPS simulations of angle-ply laminates which are composed by placing several transversal isotropic C/E layers (see Figure 4-11) in a specific stacking sequence. Figure 4-12a displays a cross-ply $[0_2,90_2]_S$ laminate, which is a commonly used stacking sequence in industry. Figure 4-12b displays a rather exotic angle-ply laminate, composed of 19 layers stacked from 0° to 180° in steps of 10°.

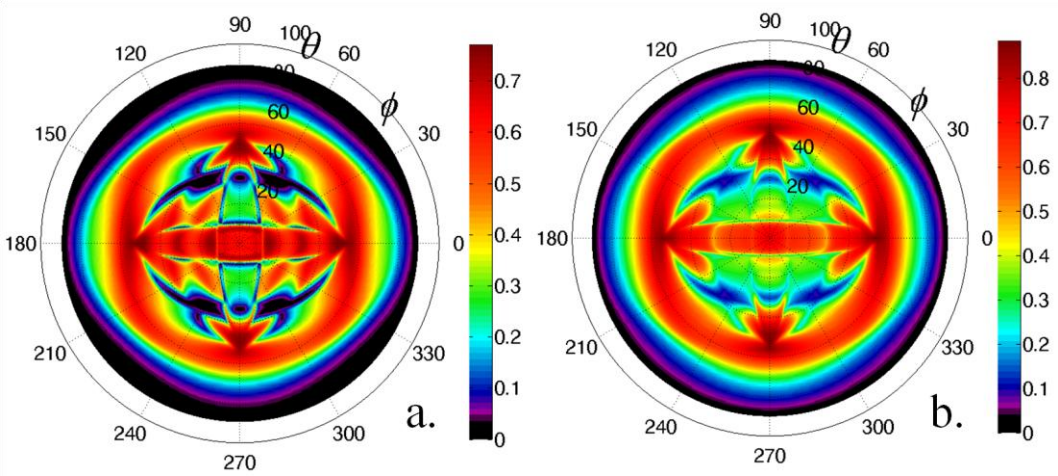

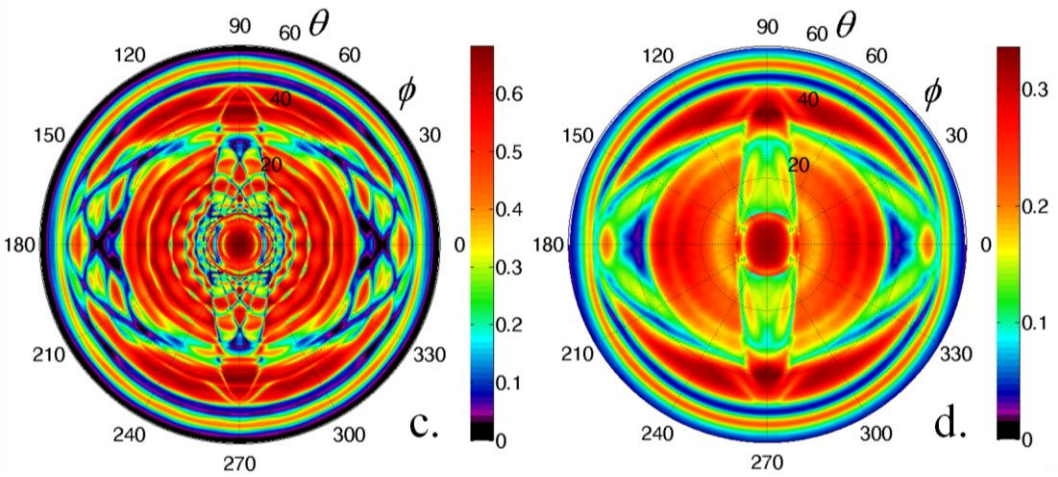

Figure 4-12: H-UPS (left) and P-UPS (right) simulations for a cross-ply $[0_2,90_2]_S$ carbon/epoxy laminate at *fd* = 5.5 MHz.mm (a-b) and for an exotic angle-ply laminate at *fd* = 12.4 MHz.mm (c-d).

4. 8. 5. Hybrid Angle-ply Multilayer

Figure 4-13 displays H-UPS and P-UPS simulations of a cross-ply hybrid multilayer composite, i.e. the solid is composed by stacking layers of different materials.

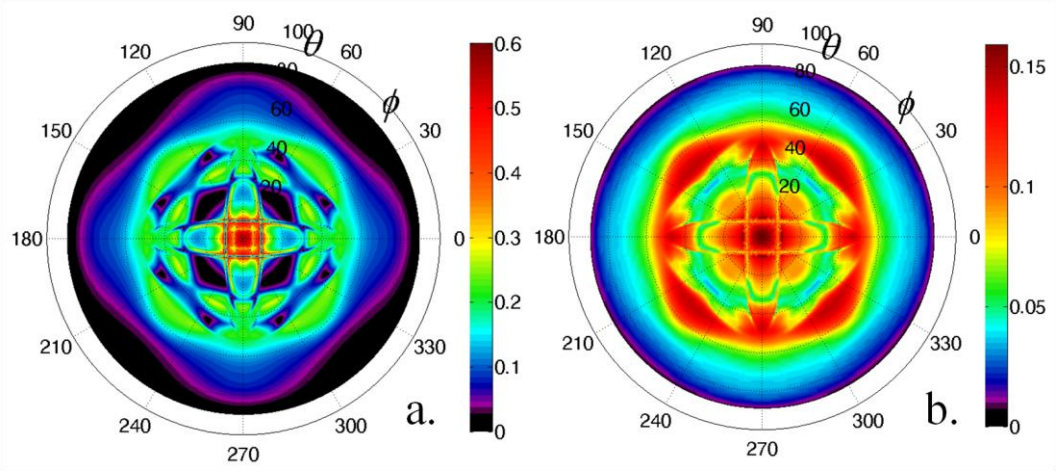

Figure 4-13: H-UPS (left) and P-UPS (right) simulations for a cross-ply hybrid carbon/epoxy-lead laminate at *fd* = 4.8 MHz.mm.

4. 9. Conclusions

The different matrix methods, coupled to a FFT decomposition of the transducer field in space and time, can simulate wave propagation in immersed multilayered media having arbitrary viscoelastic anisotropy. Several features in the modeling approach have been highlighted, in order to show how accurate simulation results can be obtained. Once the received signal is reconstructed in the simulations, the signal analysis can be performed in an analogous manner as done for the experimental signals. As such, it provides a complete simulation tool for the ultrasonic polar scan. Compared to existing models for the simulation of UPS, the here implemented approach has a greatly improved computational efficiency. Roughly speaking, a H-UPS simulation for a single layer with high angular resolution takes a few seconds. Obviously, the more layers involved, the higher the computational time. Anyway, the improved computational efficiency paves the road for a mixed experimental-numerical methodology, thus enabling different quantification purposes with the UPS technique. This will be discussed more into detail in later chapters.

4. 10. References

[1] Gnedin, N.Y., *Cosmology: Digitizing the Universe.* Nature, 2005. 435: p. 572-573.

[2] Declercq, N.F., J. Degrieck, and O. Leroy, *Ultrasonic polar scans: Numerical simulation on generally anisotropic media.* Ultrasonics, 2006. 45(1-4): p. 32-39.

[3] Declercq, N.F., J. Degrieck, and O. Leroy, *Simulations of harmonic and pulsed ultrasonic polar scans.* Ndt & E International, 2006. 39(3): p. 205-216.

[4] Mal, A.K., *WAVE-PROPAGATION IN LAYERED COMPOSITE LAMINATES UNDER PERIODIC SURFACE LOADS.* Wave Motion, 1988. 10(3): p. 257-266.

[5] Schmidt, H. and G. Tango, *EFFICIENT GLOBAL MATRIX APPROACH TO THE COMPUTATION OF SYNTHETIC SEISMOGRAMS.* Geophysical Journal of the Royal Astronomical Society, 1986. 84(2): p. 331-359.

[6] Rose, J.L., *Ultrasonic Waves in Solid Media*. 1999: Cambridge University Press. 454.

[7] Schmidt, H. and F.B. Jensen, *A FULL-WAVE SOLUTION FOR PROPAGATION IN MULTILAYERED VISCOELASTIC MEDIA WITH APPLICATION TO GAUSSIAN-BEAM REFLECTION AT FLUID-SOLID INTERFACES.* Journal of the Acoustical Society of America, 1985. 77(3): p. 813-825.

[8] Haskell, N.A., *The Dispersion of Surface Waves on Multilayered Media.* The Seismological Society of America, 1953. 43(1): p. 17-34.

[9] Thomson, W.T., *Transmission of Elastic Waves through a Stratified Solid Medium.* Journal of applied physics, 1950. 21(2): p. 5.

[10] Nayfeh, A.H., *Wave Propagation in Layered Anisotropic Media: with applications to composites*. 1995, New York: North-Holland.

[11] Castaings, M. and B. Hosten, *DELTA-OPERATOR TECHNIQUE TO IMPROVE THE THOMSON-HASKELL-METHOD STABILITY FOR PROPAGATION IN MULTILAYERED ANISOTROPIC ABSORBING PLATES.* Journal of the Acoustical Society of America, 1994. 95(4): p. 1931-1941.

[12] Hosten, B. and M. Castaings, *Transfer-matrix of multilayered absorbing and anisotropic media - measurements and simulations of ultrasonic wave-propagation through composite-materials.* Journal of the Acoustical Society of America, 1993. 94(3): p. 1488-1495.

[13] Potel, C., P. Gatignol, and J.F. de Belleval, *Energetic criterion for the radiation of floquet waves in infinite anisotropic periodically multilayered media.* Acustica, 2001. 87(3): p. 340-351.

[14] Safaeinili, A. and D.E. Chimenti, *Floquet analysis of guided-waves in periodically layered composites.* Journal of the Acoustical Society of America, 1995. 98(4): p. 2336-2342.

[15] Wang, L. and S.I. Rokhlin, *Stable reformulation of transfer matrix method for wave propagation in layered anisotropic media.* Ultrasonics, 2001. 39(6): p. 413-424.

[16] Rokhlin, S.I. and L. Wang, *Ultrasonic waves in layered anisotropic media: characterization of multidirectional composites.* International Journal of Solids and Structures, 2002. 39(21-22): p. 5529-5545.

[17] Rokhlin, S.I. and L. Wang, *Stable recursive algorithm for elastic wave propagation in layered anisotropic media: Stiffness matrix method.* Journal of the Acoustical Society of America, 2002. 112(3): p. 822-834.

[18] Wang, L. and S.I. Rokhlin, *Recursive stiffness matrix method for wave propagation in stratified media.* Bulletin of the Seismological Society of America, 2002. 92(3): p. 1129-1135.

[19] Rokhlin, S.I., D.E. Chimenti, and P.B. Nagy, *Physical Ultrasonics of Composites*. 2011: Oxford University Press. 378.

[20] Hosten, B. and M. Castaings, *Surface impedance matrices to model the propagation in multilayered media.* Ultrasonics, 2003. 41(7): p. 501-507.

[21] Tan, E.L., *Hybrid compliance-stiffness matrix method for stable analysis of elastic wave propagation in multilayered anisotropic media.* Journal of the Acoustical Society of America, 2006. 119(1): p. 45-53.

[22] Tan, E.L., *Stiffness matrix method with improved efficiency for elastic wave propagation in layered anisotropic media.* Journal of the Acoustical Society of America, 2005. 118(6): p. 3400-3403.

[23] Wang, L.G. and S.I. Rokhlin, *Modeling of wave propagation in layered piezoelectric media by a recursive asymptotic method.* Ieee Transactions on Ultrasonics Ferroelectrics and Frequency Control, 2004. 51(9): p. 1060-1071.

[24] Auld, B.A., *Acoustic Fields and Waves in Solids, second edition*. 1990, Florida: Krieger publishing company. 856.

[25] Deschamps, M. and B. Hosten, *The effects of viscoelasticity on the reflection and transmission of ultrasonic-waves by an orthotropic plate.* Journal of the Acoustical Society of America, 1992. 91(4): p. 2007-2015.

[26] Baudouin, S. and B. Hosten, *Immersion ultrasonic method to measure elastic constants and anisotropic attenuation in polymer-matrix and fiber-reinforced composite materials.* Ultrasonics, 1996. 34(2-5): p. 379-382.

[27] Levenberg, K., *A method for the solution of certain non-linear problems in least squares.* Quarterly of Applied Mathematics, 1944. 2.

[28] Marquardt, D.W., *AN ALGORITHM FOR LEAST-SQUARES ESTIMATION OF NONLINEAR PARAMETERS.* Journal of the Society for Industrial and Applied Mathematics, 1963. 11(2): p. 431-441.

[29] Lobkis, O.I., A. Safaeinili, and D.E. Chimenti, *Precision ultrasonic reflection studies in fluid-coupled plates.* Journal of the Acoustical Society of America, 1996. 99(5): p. 2727-2736.

Chapter 5

Pitfalls in the Experimental Recording of Ultrasonic (Backscatter) Polar Scans

Artwork of M.C. Esher depicting inconsistency at different scales.

Summary

This chapter investigates experimental difficulties encountered during the ultrasonic inspection of a component. The discussion is focused to errors and inconsistencies during oblique incidence measurements, and more specifically during ultrasonic (backscatter) polar scan measurements. Close inspection of the experimental data reveals several pitfalls which, until now, have been unknown or neglected. Each pitfall is explicitly demonstrated by means of a pulsed ultrasonic (backscatter) polar scan experiment. A solution, whether it is mechanical, numerical or a combination of both, is proposed and discussed.

5. 1. Introduction

The limited quantitative exploration and use of the ultrasonic polar scan technique can be primarily ascribed to limitations of current theoretical models as well as to the difficulty to perform accurate, and more importantly, reproducible experiments. Many controlling parameters within the set-up, both of physical and mechanical nature, affect the quality of the results of the pulsed ultrasonic (backscatter) polar scan (P-U(B)PS) experiment. Recently, it has been commented that "*too many sloppy mistakes are creeping into scientific papers"* [1-2]. Hence, the identification of factors which could possibly introduce any bias in the scientific data is of great importance [3]. During intensive experimental research over the last few years, several factors have been gradually identified as responsible for a serious decrease of the accuracy and reproducibility of a P-U(B)PS experiment. In order to obtain accurate experiments, which is crucial to become a fully quantitative method, a proper setting of these parameters should be taken into consideration. In this chapter, we make an inventory of the most important difficulties, illustrate each of them by a real experiment and present a feasible mediation, either mechanical, numerical or a combination of both. Once the experimental set-up is fine-tuned to overcome these pitfalls, it is expected that the recording of high-level P-U(B)PS experiments, in combination with true-to-nature numerical computations, will facilitate the technique to become a fully quantitative non-destructive characterization method.

5. 2. Experimental Pitfalls

The current section classifies several pitfalls for the recording of a P-U(B)PS, and each of them is illustrated by a real experiment. Wherever applicable, a feasible mechanical mediation, numerical solution or a combination of both is presented and discussed to anticipate or correct these issues. Table 5-1 shows an overview of the importance of the identified pitfalls for the different operation modes, i.e. transmission, backscatter and double through-transmission mode. The reflection mode has been excluded as no experiments were obtained in that particular operation mode.

Table 5-1: Overview of the relevance of the different pitfalls for the various operation modes.

	Transmission	*Backscatter*	*Double through-transmission*
PITFALL 1: Twin rings	No	No	Yes
PITFALL 2: Coordinate system	Yes	Yes	Yes
PITFALL 3: Translational shift	Yes	No	No
PITFALL 4: Sloshing	Yes	Yes	Yes
PITFALL 5: Clearance	Yes	Yes	Yes
PITFALL 6: Air	No	Yes	No
PITFALL 7: Edge effect	No	Yes	No

5. 2. 1. Pitfall 1: Difficulties in the Double Through-Transmission Recording

During the last decades, researchers have consistently applied the double through-transmission method (also referred to as 2T) for the recording of a P-UPS [4-7] as well as for other oblique incidence applications [8-9]. In this implementation, the transducer in the transmission field is replaced by an acoustic mirror. Doing so, the transmitted ultrasound gets back-reflected from the mirror and can be recorded by the same emitting transducer. One of the major advantages of this configuration is that only one transducer is required, limiting the cost of the implementation. Furthermore, as the transmitted sound beam is totally reflected by the mirror back to the emitting transducer, the ultrasonic wave is forced to interact a second time with the solid, resulting in more defined and detailed polar contours. It is even possible to extend this idea and to work in multi through-transmission recording (4T, 6T, etcetera) [10] by exploiting the flat surface of typical

immersion transducers. Of course, at some point the amplitude of the $(2n)^{th}$ transmission becomes too low to make a proper measurement. Another advantage of the 2T method is that the acoustic mirror neutralizes the lateral beam shift of the transmitted ultrasonic beam. The advantage of the latter cannot be overestimated whenever thick samples are investigated with transducers having a limited diameter.

Figure 5-1a displays the P-UPS results for a $[0]_8$ carbon/epoxy laminate, recorded in double through-transmission. At first sight, no peculiarities or anomalies are observed when compared to the numerically computed P-UPS displayed in Figure 5-1b. As input for this simulation, we used a complex C-tensor which was obtained through inversion of P-UPS data of a similar carbon/epoxy laminate [11-13]. More details about the identification procedure of material parameters is given in Chapter 7. In-depth inspection of individual scanning lines extracted from the experimental data however reveals the presence of closely spaced amplitude dips which are persistently observed at all polar angles φ. To substantiate this, the scan sections at $\varphi = 45°$ and at $\varphi = 60°$ for the $[0]_8$ carbon/epoxy laminate are shown in Figure 5-2 for both the experimental and numerical results. There is not a single indication of double amplitude dips to be observed in the numerically computed curves.

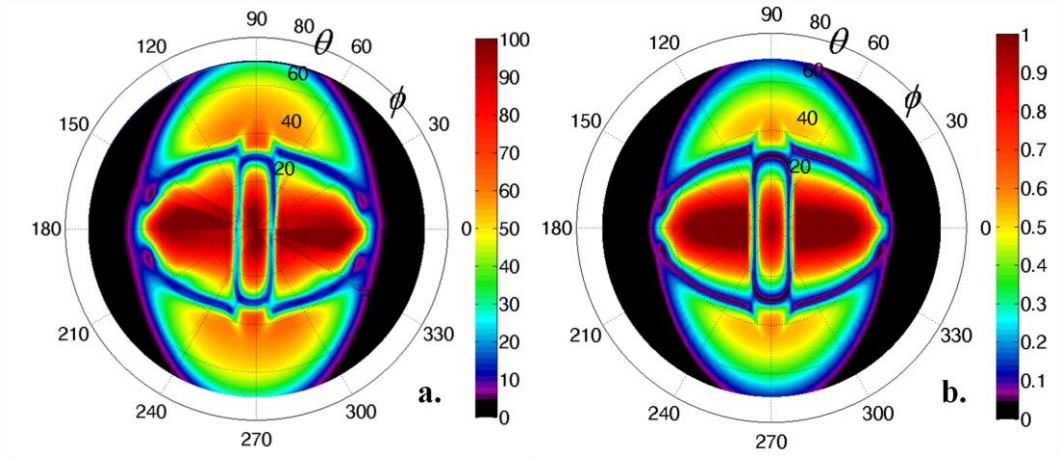

Figure 5-1: Experimentally obtained P-UPS results in 2T regime (a) and numerically computed P-UPS (b) for a $[0]_8$ carbon/epoxy laminate.

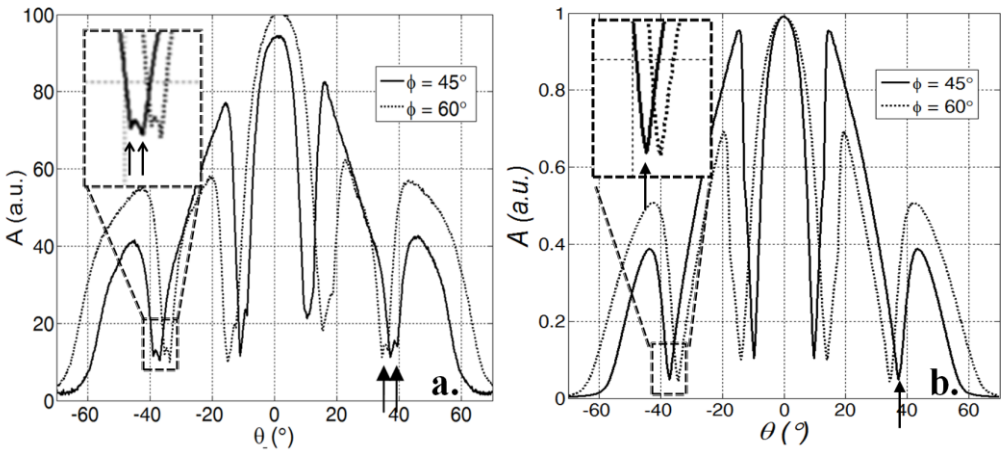

Figure 5-2: Measured P-UPS sections in 2T regime (a) and numerically computed P-UPS sections (b) at polar angles φ = 45° and φ = 60° for a $[0]_8$ carbon/epoxy laminate. The insets accentuate the topological difference between the experiment and the numerical computation.

The presence of local amplitude dips corresponds to a high local curvature value in the amplitude versus angle recording. Hence, in order to accentuate these amplitude dips, we adapted the data acquisition and recorded the difference between subsequent amplitude recordings in the scan axis direction. In doing so, a representation is obtained of the gradient of the transmission coefficient, and by extension to the second order difference, of the curvature of the transmission coefficient [14]. The 'curvature P-UPS', obtained in double through-transmission recording, is shown in Figure 5-3a for the same $[0]_8$ carbon/epoxy laminate as considered in Figure 5-1a. The observed double amplitude dips are clearly visible in the curvature P-UPS in the form of two closely spaced polar rings, as if each ring has its own twin brother/sister.

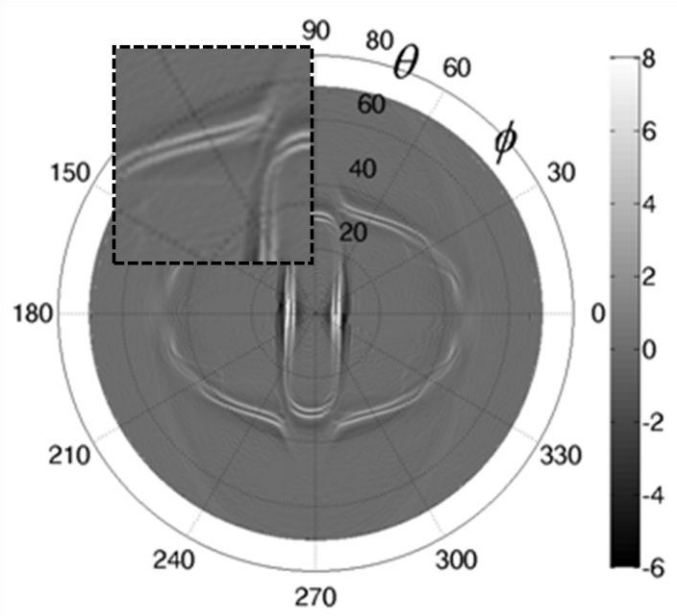

Figure 5-3: Curvature P-UPS for a $[0]_8$ carbon/epoxy laminate recorded in double through-transmission regime. Note the appearance of twin rings.

As polar scan measurements were merely used for qualitative purposes in the past, this feature has been overlooked (or neglected) for several years. Nevertheless, the importance of unambiguous transmission minima for the characterization of materials cannot be understated since the mechanical stiffness of the insonified spot is encrypted in the exact location of the polar contours as they correspond to the location of the critical bulk wave angles [4-5, 15-17]. Any dubious feature in the recording imposes a significant enlargement of the error on the stiffness values. The exact physical origin of the twin-effect can be identified by considering the ray path involved in the double through-transmission regime (see Figure 5-4). Indeed, even the smallest angular misalignment $\Delta\theta$ between the ultrasonic transducer and the acoustic mirror will cause an erroneous recording since the back-and-forth ray paths differ from each other. In order to overcome this, a high precision mounting mechanism was devised in order to self-align the transducer with respect to the fixed acoustic mirror. In principle, this solution should be sufficient, however, in reality we observed that the twin effect still remains present now and then.

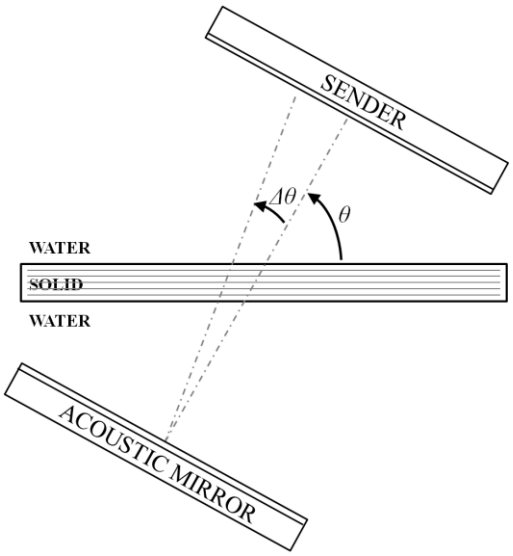

Figure 5-4: Ray path involved in 2T recording. A small angular misalignment $\Delta\theta$ between sender and acoustic mirror causes a different back-and-forth ray path.

Further investigation of the persisting problem led to a dedicated investigation of the beam pattern of the employed acoustic transducers. Figure 5-5 displays the measured radiation field of a typical immersion transducer along a plane containing its axis, together with a cross section of the amplitude distribution parallel to the transducer surface (see also Section 3.4).

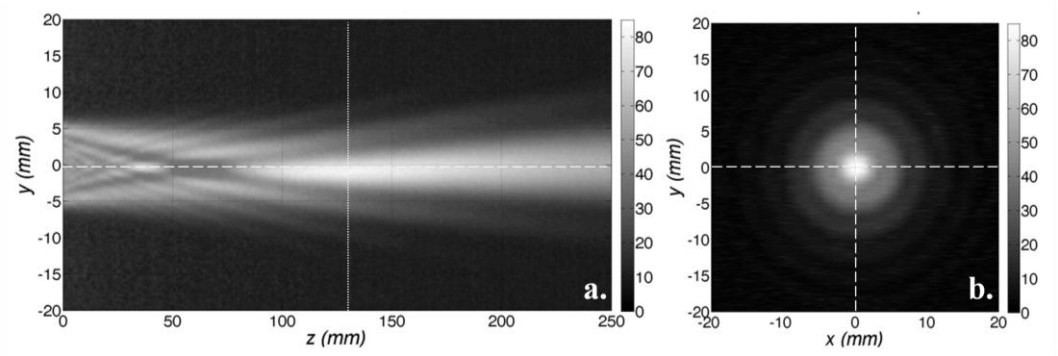

Figure 5-5: Amplitude of the radiation field of a typical transducer operating at a frequency f = 5 MHz: (a) YZ-section and (b) XY-section at z = 130mm (dotted line in (a)). The dashed lines guide the eye, note the small skewing of the beam.

The recording reveals that the radiation pattern is not completely symmetric with respect to the physical center line of the transducer. Similar skewing behavior has been obtained for various other transducers. The skewing can be understood considering that the electrical wiring has to be fixed somehow to the active piezoelectric element. Disassembling of a (broken) transducer revealed that the wiring is simply soldered at some arbitrary place to the active element, which thus distorts its operation. Although the beam skewing is quite limited, it is bothersome for the P-UPS application. The inherent beam skewing of transducers implies that the twin-effect simply cannot be neutralized by means of a high-precision mounting mechanism only, which brings us to the conclusion that the double through-transmission regime irrefutably leads to the formation of twin rings, and as a consequence this modus operandus should be avoided for any P-UPS application directed towards a proper characterization of the laminate. As a comparison, the curvature P-UPS, recorded in single through-transmission, for the $[0]_8$ carbon/epoxy laminate is shown in Figure 5-6. It can be readily verified that the twin effect is not present anymore, confirming the connection between the 2T recording scheme and the presence of twin rings. Further experimental results shown in this dissertation are therefore recorded in single through-transmission.

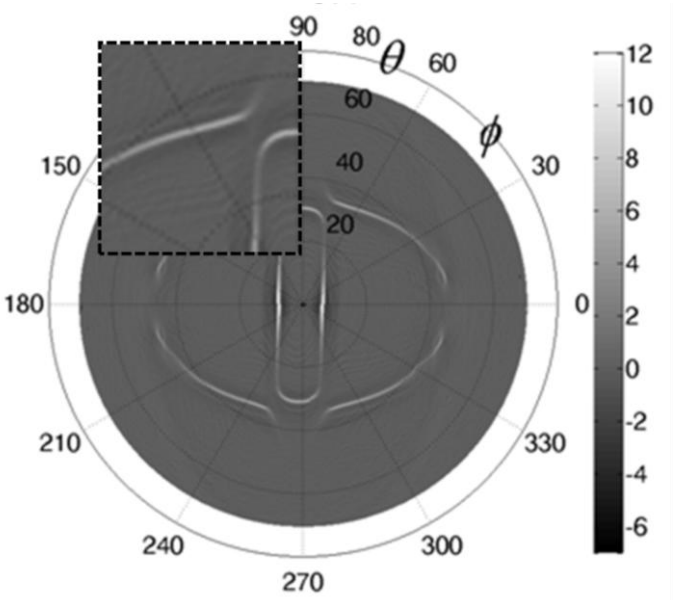

Figure 5-6: Curvature P-UPS for a $[0]_8$ carbon/epoxy laminate recorded in single through-transmission regime.

5. 2. 2. Pitfall 2: Misalignments in the Material Coordinate System and the Scanner Coordinate System

The P-UPS insonifies a material spot for all possible angles of oblique incidence $\psi(\varphi,\theta)$, where the angle of normal incidence $\psi(\varphi,0)$ is defined as the reference. It is very tempting to incrementally adjust the angle of incidence $\psi(\varphi,\theta)$ in order to maximize the intensity of the surface echo, and consequently consider this as the correct zero position. However, the experiment is then obtained in the material reference system $X'Y'Z'$. The mechanical movement of the scanner on the other hand always takes place in its own reference system XYZ, and thus a systematic error in the measurement of the position $\psi(\varphi,\theta)$ can be induced. For the scanning path of the robot considered in our set-up (see Figure 3.4), the consequences of this error should become evident when comparing the recorded scan results at $\psi(0°,\theta)$ (first scan sector) with the recordings at $\psi(180°,\theta)$ (last scan sector). As illustrated in Figure 5-7, a clear horizontal shift between the first and the last run of a P-UPS experiment can be observed. The first scan section $\psi(0°,\theta)$ is nicely symmetric to the θ-coordinate. Inspection of the last scan section $\psi(180°,\theta)$ however, reveals that the symmetry to the θ-coordinate is not satisfied anymore. Hence the experiment did start, but certainly did not end in the material coordinate system $X'Y'Z'$.

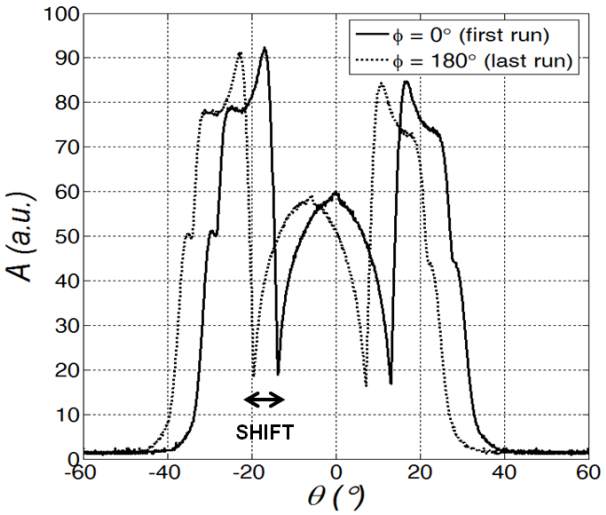

Figure 5-7: The first and last run in a P-UPS experiment for an aluminum sample. The incorrect reference coordinate system introduces a horizontal shift.

The complete P-UPS experiment obtained by starting in the incorrect *X'Y'Z'* coordinate system is shown in Figure 5-8a (for viewing purposes an exaggerated misalignment was set). Obviously the presence of the discrete jump in the polar contours will impede the accurate determination of the C-tensor through inverse modeling. To overcome this problem, one could opt to numerically compensate for this error. However, the more correct approach is of course to record the experiment *ab initio* in the correct scanner coordinate system *XYZ*. This can be simply achieved by exploiting the horizontality of the free surface of the immersion liquid in combination with the bottom transducer which is used in pulse echo. Maximizing the echo at the water-air interface leads to the identification of the upward vertical direction $\psi(\varphi,180°)$ in the scanner coordinate system *XYZ*. Hence, rotation over $\theta = 180°$ defines the direction of normal incidence $\psi(\varphi,0)$ which should be used as a reference. Taking into account this procedure, each P-UPS experiment is automatically obtained in the same scanner coordinate system *XYZ*. One can clearly observe in Figure 5-8b that the discrete jump between the contour lines in the upper and lower half spaces has been neutralized almost completely by the use of a correct reference.

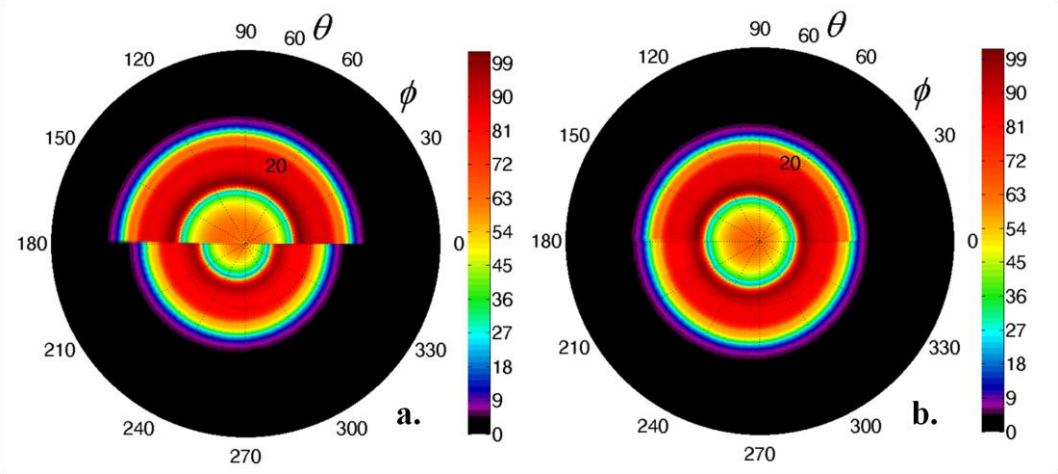

Figure 5-8: P-UPS for an aluminum sample. Measurements taken in the incorrect material coordinate system *X'Y'Z'* (a) and in the correct scanner coordinate system *XYZ* (b).

Another peculiarity that can be attributed to the mismatch between the scanner coordinate system *XYZ* and the material coordinate system *X'Y'Z'* is that the contour lines in the fingerprint are not always exactly centered (see Figure 5-9a). Indeed, the direction of normal incidence in the *XYZ* system

does not necessarily correspond to the direction of normal incidence in the *X'Y'Z'* material system.

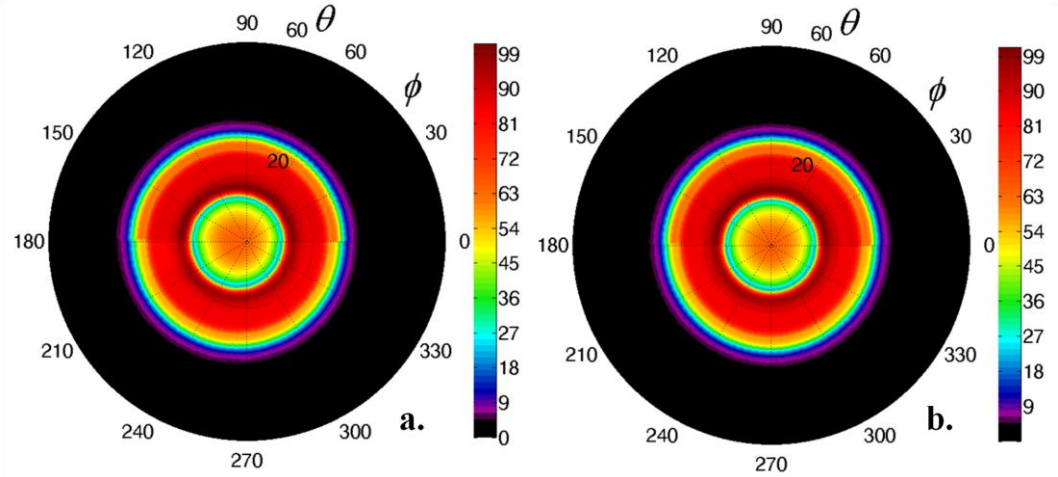

Figure 5-9: P-UPS for an aluminum sample: slight misalignment (a) and proper alignment (b) between scanner and material coordinate system.

To mediate this problem, the above discussed alignment of the ultrasonic transducer along the zero axis of the scanner reference system *XYZ* should be followed by a positioning of the sample under investigation in such a way that its surface echo gets maximized. This can be done by placing the sample in a holder which can be rotated by means of micro screws. When the surface echo is maximized, both the ultrasonic transducer and the sample under investigation are positioned in the correct scanner coordinate system *XYZ*. Proper positioning of the transducer and the sample within the scanner coordinate system results in the P-UPS recording shown in Figure 5-9b. Alternatively, in cases where it is impossible to position the investigated sample in line with the scanner *XYZ* system, one can numerically search for the center of the recorded P-UPS, and use a translation in polar coordinates $\Delta\psi(\Delta\theta,\Delta\varphi)$ to neutralize the coordinate system misalignment.

5. 2. 3. Pitfall 3: Translational Shift of the Centerline of the Ultrasonic Transducers

Any translational misalignment Δ of the sender and receiver pair may cause unwanted intensity variations in the polar scan. The reason for this can be easily understood by considering the schematic representation shown in Figure 5-10. Indeed, as a result of oblique insonification, a characteristic

beam shift is present after traversing the solid layer. Hence, for a given transducer misalignment and depending on the polarity of the incident angle θ, the transmitted signal will be recorded at a different position at the surface of the receiving transducer. Since the sensitivity of the membrane of the transducer decays gradually towards the edges of the circular surface because of the housing, the recorded amplitude value will be affected.

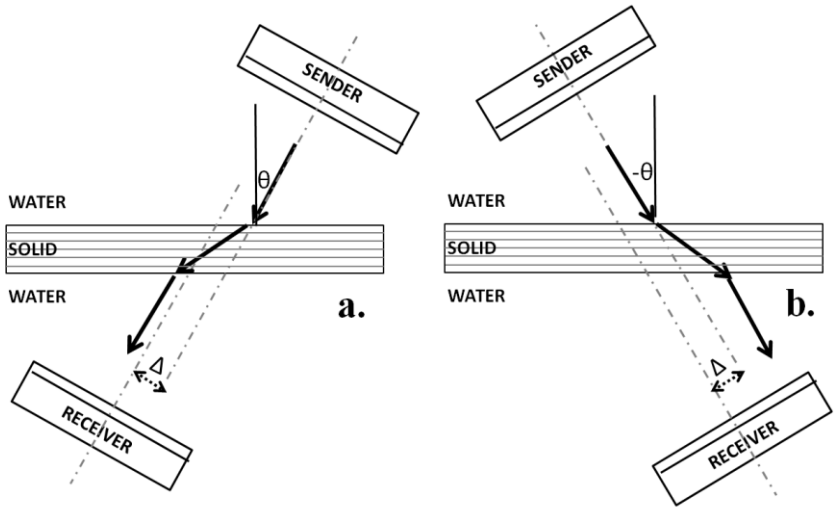

Figure 5-10: Influence of translational misalignment Δ of the transducers for two equivalent incidence angles: (a) $\psi(\varphi,+\theta)$ and (b) $\psi(\varphi,-\theta)$. The transmitted signal is captured at different locations of the receiver's surface.

The effect of a translational misalignment Δ can be observed in Figure 5-11, in which a drop in amplitude can be observed for the equivalent incidence angles $\psi(\varphi,\theta)$ and $\psi(\varphi+180°,\theta)$ (Note that these angles corresponds to the angles $\psi(\varphi,+\theta)$ and $\psi(\varphi,-\theta)$). Although this alignment error does not affect the exact position of the characteristic contours within the P-UPS plot (and consequently has no or negligible influence on the characterization of the mechanical elasticity), it does critically affect the exact amplitude levels which are linked to the damping properties of the material at the insonified material spot. Hence in view of characterizing the damping tensor, it is crucial to record the transmission amplitude with as high precision as possible.

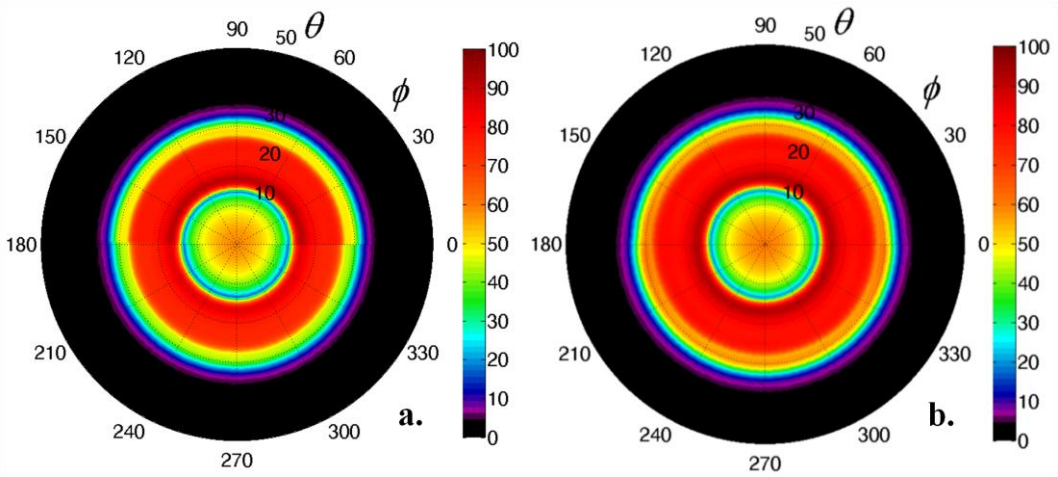

Figure 5-11: P-UPS for an aluminum sample: with a translational misalignment $\Delta \neq 0$ (a) and without a translational misalignment $\Delta = 0$.

As a consequence of the physically induced lateral beam shift in transmission, these results furthermore indicate that the P-UPS in transmission should be interpreted with caution whenever the thickness of the solid layer, and thus the lateral beam shift, becomes comparable to the physical dimensions of the receiving transducer. The samples under investigation in this work had a maximum thickness of 2 mm, which is sufficiently thin to avoid the above concern. In case thicker samples are investigated, a receiver with larger lateral dimensions has to be employed, or the measurement has to be performed in reflection.

5. 2. 4. Pitfall 4: Sloshing of water and redundant vibrations caused by rotational movement

To obtain an accurate P-UPS recording, the sample has to be insonified at a sufficiently large number of incidence angles $\psi(\varphi,\theta)$. However, in order to keep the experimental time as low as possible, the measurements should be performed relatively fast. Our current laboratory set-up allows to cover around 2000 incidence angles $\psi(\varphi,\theta)$ each second. Since several parts are moving through the water, appropriate experimental settings for the control of the mechanical axes have to be taken into account to avoid sloshing of the water (see Section 3.3). Although sloshing is of no importance for the acoustic wave itself (Doppler effects do not play any role), the water movement can affect the mounted sample because it is never completely rigid. When the sample starts waving with the water, it will obviously

influence the P-UPS recording. An example of this effect on the P-UPS is shown in Figure 5-12. The white arrows indicate an inaccurate recording as a consequence of slight water sloshing.

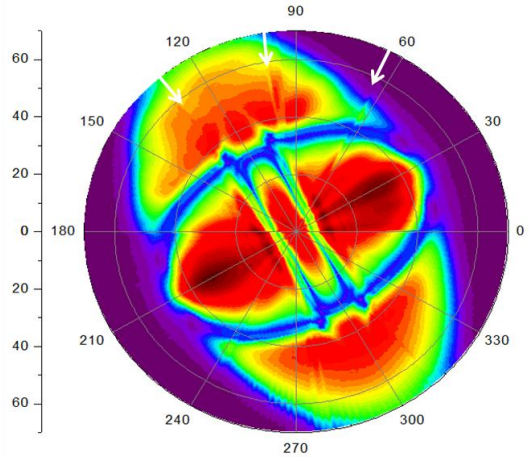

Figure 5-12: P-UPS for a $[0]_8$ carbon/epoxy laminate, showing the effect of sloshing of the water as indicated by the white arrows.

Among the control parameters for the mechanical axes that cause water sloshing, the far most important ones concern (i) the acceleration profile, (ii) the deceleration profile and (iii) the maximum rotation speed. The settings should be fine-tuned such that the sloshing is kept within reasonable limits. The controlling parameters for the various axes have been programmed such to reduce water sloshing as much as possible (see Section 3.3). It is clear that the various controlling parameters might be different, depending on the components used to create the scanner. Apart from sloshing, the use of excessively high scanning speeds could cause overlap of two subsequent ultrasonic signals within one time gate. It has been taken care of that this never occurs in our experimental implementation.

5. 2. 5. Pitfall 5: Gear Clearance

The use of gears cannot be avoided in order to allow for the complicated movement involved in the UPS scanning process. Even more, gears are indispensible to increase the scanning resolution. Unfortunately, common gears always exhibit a non-negligible backlash, which has obvious consequences for the position $\psi(\varphi,\theta)$ during the reversal of the movement for the scan axis. As shown in Figure 5-13a, a high clearance manifests itself in

the form of crenulated results in θ-direction, making the experimental results less accurate for quantifying purposes.

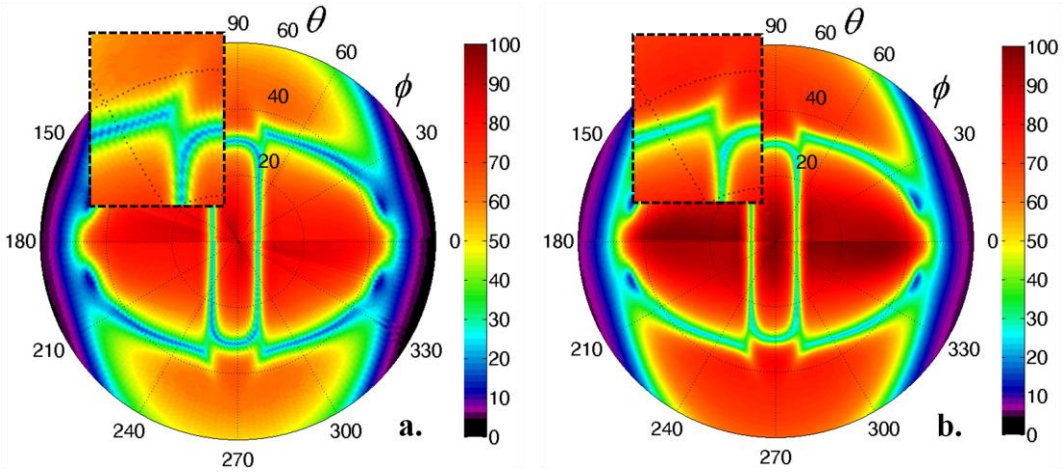

Figure 5-13: P-UPS for a $[0]_8$ carbon/epoxy laminate: Results using a commercial gear with a large clearance (a) and in-house developed gear with a smaller clearance. The inset shows a magnified portion of the P-UPS experiment.

To overcome this, one could opt for the installation of high-precision gears. However, such gears are very costly, and furthermore, only a few types can be immersed in water. To save costs, a customized gear was produced in our lab (see Section 3.3). The insets of Figure 5-13 clearly illustrate the improvement of the quality of the UPS when recorded with the currently installed in-house developed high-precision gear box as opposed to a standard commercial gear box.

5. 2. 6. Pitfall 6: Distortion by Air Bubbles

Both the surface of the sample and the acoustic transducer are susceptible to the accumulation of air bubbles due to degassing of the immersion liquid. Because of the large difference in acoustic impedance at the liquid-air interface, the air bubbles work as scatterers for the incident acoustic wave. The recordings in both transmission (P-UPS) and backscatter (P-UBPS) mode are shown in Figure 5-14 for an aluminum sample immersed in degassed immersion fluid, i.e. no air bubbles are present. The P-UPS image has the familiar view, while the P-UBPS image shows only measurable backscatter at near-normal incidence angles. For a flat and smooth

homogeneous sample, it could have been expected that no backscatter is present for large oblique incidence angles.

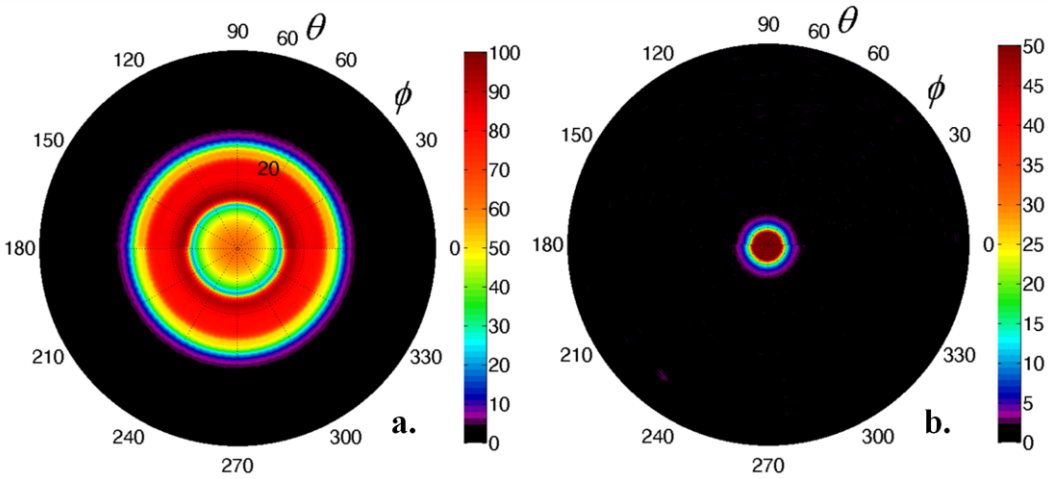

Figure 5-14: P-UPS (transmission) (a) and P-UBPS (backscatter) (b) recording for an aluminum sample, both recorded in degassed water.

The effect of air bubbles is illustrated in Figure 5-15, in which P-U(B)PS recordings for an aluminum sample are presented for various levels of air bubble density (few bubbles, many bubbles). The typical dimension of the air bubbles is less than 1 mm in diameter.

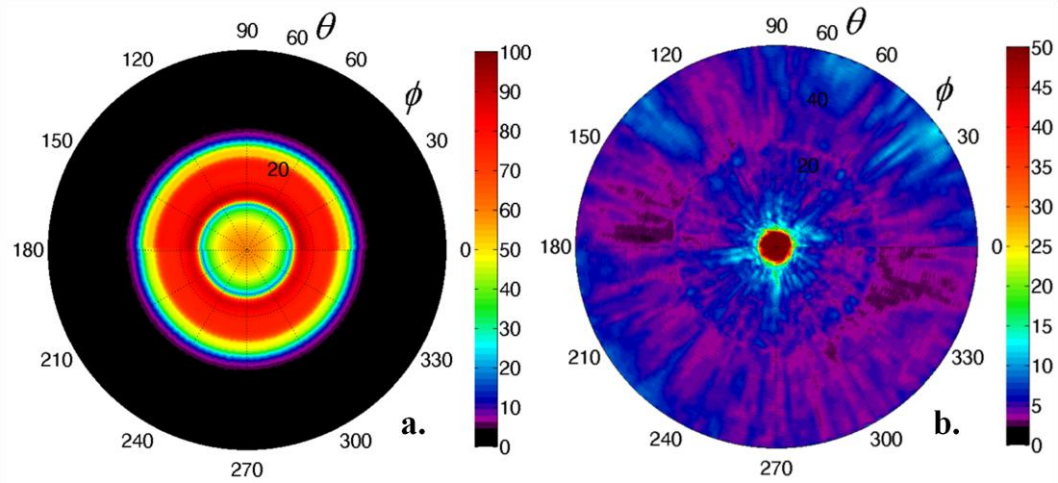

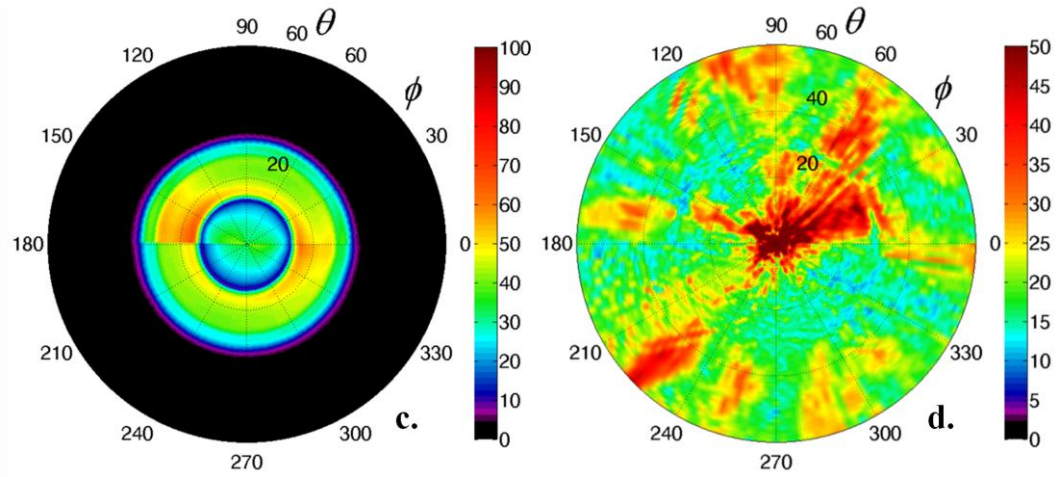

Figure 5-15: P-UPS (left) and P-UBPS (right) for an aluminum sample: few air bubbles (a-b) and many air bubbles (c-d).

No changes are observed in the geometrical shape of the P-UPS image with respect to the P-UPS results shown in Figure 5-14. The amplitude level on the other hand clearly decreases proportionally with the density of air bubbles. The maximum amplitude of the P-UPS results in the presence of few, respectively many air bubbles is lowered by 4.53%, respectively 34.98% with respect to the P-UPS result of Figure 5-14. A comparison of the mean amplitude value of the P-UPS results can be done in a similar way, giving a lowering of 4.71% and 45.44% with respect to the bubble-free P-UPS recording. The multitude of air bubbles at top and bottom surfaces of the sample prevents the acoustical energy to be efficiently transmitted through the aluminum sample, hence distorting the P-UPS measurement.

More drastic changes can be observed in the P-UBPS results. Even a small amount of air bubbles introduces significant backscatter at oblique incidence angles, which as such could be interpreted as a flawed material zone. This becomes even worse for the sample with many air bubbles. Hence, compared to the transmission measurements, the backscatter measurements are much more sensitive to the accumulation of air bubbles. This is important to be aware of as even the smallest amount of air bubbles pollute the backscatter data significantly.

Nevertheless, the accumulation of air bubbles is a well-known problem for ultrasonic NDT, and basically two solutions exist to overcome this problem. One could either take into account a sufficient time (typically in the order of

24 hours) for the water to degas in a natural way and wipe off the air bubbles with a paint brush. A more suitable solution involves the application of a spray nozzle system to fill the water tank. Although counter-intuitive, it has been reported that the spraying technique works very well for avoiding the formation of air bubbles [18]. We consider a third alternative which works as well, at least in a laboratory environment. By adding a small amount of surfactant to the immersion liquid, the surface tension of the liquid lowers leading to an accelerated degassing. After a few minutes, numerous air bubbles form on the surface of both the transducers and the sample, after which it suffices to simply wipe them off with a paint brush.

5. 2. 7. Pitfall 7: Distortion by Edge Effects of the Sample

It is found that the finite size of a sample has a major influence for the reliability of P-UBPS experiments, while this is of minor importance for P-UPS results. To illustrate the distortion due to edge effects, we consider the recorded P-UBPS of an aluminum sample having limited dimensions (see Figure 5-16). The particular material spot under investigation is marked by the 'X' on the photograph of the sample, and is located approximately 30 mm from the edges. Despite the isotropic and homogeneous nature of the scanned aluminum sample, increased backscatter can be observed for certain directions.

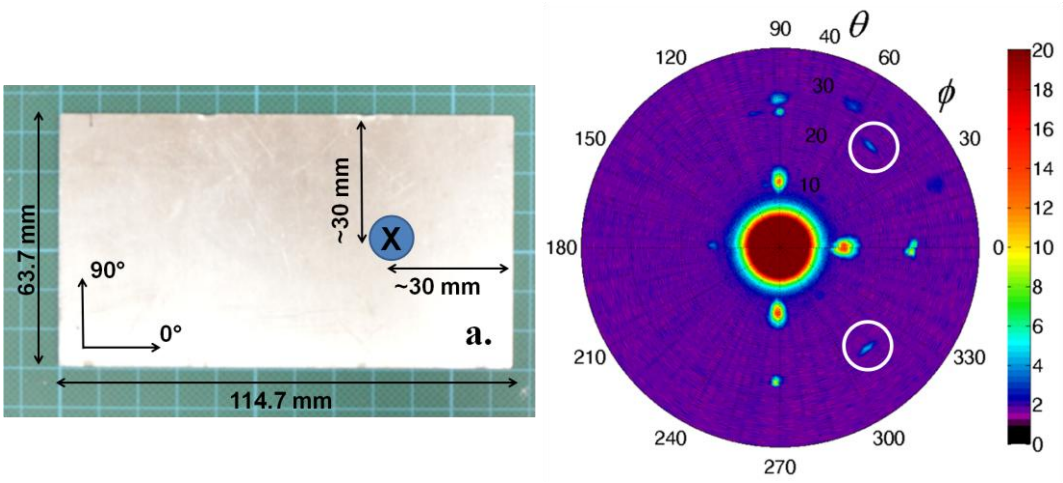

Figure 5-16: Photograph of the insonified aluminum sample (a) and recorded P-UBPS (b) showing distinct backscatter spots at oblique incidence angles.

The formation of parasitic backscatter images can be readily understood by considering that the polar scan principle basically relies on the stimulation of guided waves in the solid [4-5, 16-17]. Hence the physical edges of the sample cause the stimulated guided waves to be reflected, and in some cases to be mode-converted. If the guided wave impinges perpendicularly on the edge, the back-reflected guided wave leaks its energy into the immersion fluid towards the acoustic transducer, making the edge a source of increased backscatter [19-21]. In Figure 5-17, the P-UBPS results for the amplitude and the corresponding time-of-flight-diffraction (TOFD) (in microseconds) analysis are shown as obtained on the small size aluminum plate. To reduce the scatter in the TOFD based backscatter map, only those results are shown which correspond to a certain threshold level of backscatter amplitude.

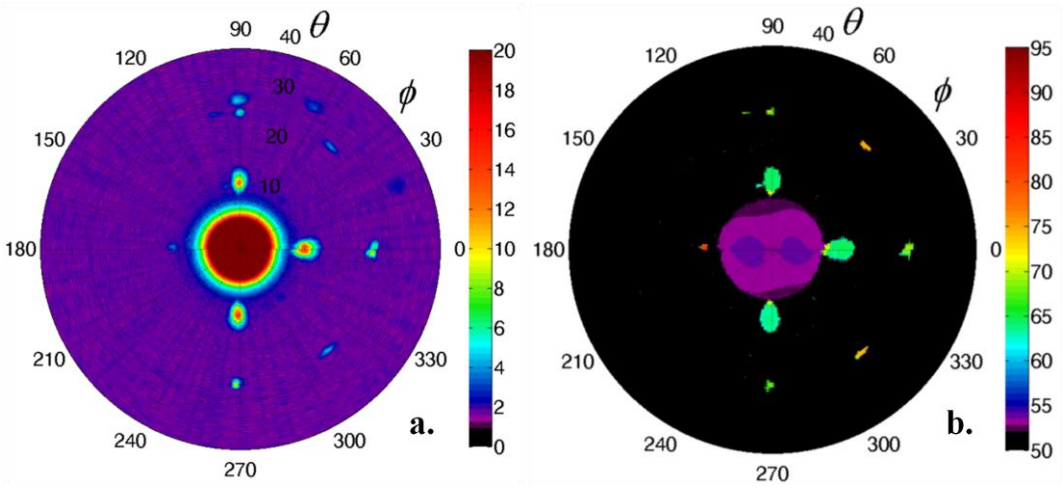

Figure 5-17: Recorded P-UBPS for an isotropic and homogeneous aluminum sample: amplitude (a) and TOFD (b) recording.

The free edges of the rectangular aluminum sample near the insonified spot, can be identified in the backscatter map at φ = [0°, 90°, 270°]. Basically, a free edge produces two parasitic backscatter spots. The inner parasitic backscatter spots at $\theta \approx 13.7°$ correspond to the in-plate reflection of a longitudinally polarized bulk wave, leaking energy back to the transducer. The outer backscatter spots at $\theta \approx 28.7°$ to the leaking of the reflected shear polarized bulk wave. The higher propagation speed of the longitudinal component, compared to the shear polarized wave, is clearly reflected in the TOFD based backscatter map. Moreover, the TOFD measurements can be used to estimate the physical distance to the edges by taking into account the mechanical properties of the insonified sample. For this case, the TOFD

values of the backscatter spots at φ = [0°, 90°, 270°] predict edges distances of d ~ [28.0 mm, 29.7 mm, 26.4 mm], which is fairly close to the insonification spot displayed in Figure 5-16a. In addition, a closer inspection of the backscatter map reveals another backscatter spike around the direction ψ(180°,13.5°). In accordance with the TOFD map, this spike originates from a feature at a distance d ~ 94.5 mm, which corresponds to the most remote edge. The reduced intensity of the backscatter spot at φ = 180° can be explained by the fact that the acoustic wave is damped upon propagation (material damping as well as damping as a consequence of energy leakage to the surrounding fluid). Apart from the parasitic backscatter spikes associated to the perpendicular free ends of the sample, backscatter spikes can also be observed as a result of a corner interaction (indicated by white circles in Figure 5-16b).

Elimination of the edge and corner effects can be obtained by respecting a sufficient distance between the targeted spot and the edges of the insonified structure, i.e. by using large enough samples. However, as this might not always be possible in practice, the most practical and probably the only workable solution involves the complementary analysis of the TOFD value in addition to the amplitude recording. In this way, the backscatter signals which correspond to an edge or corner reflection can be identified and eliminated. Again, the importance of this observation cannot be overrated since in reality every structure has limited dimensions and thus could potentially produce a 'ghost' backscatter image. For industrial applications, such as the quantification of corrosion, misinterpretation of the backscatter data could incorrectly lead to needless, and often very expensive, replacement of a structural component.

5. 3. Conclusions

Several pitfalls in the experimental recording of a P-U(B)PS have been identified, some of which have been persistently overlooked or neglected for several years. Each of these pitfalls has been illustrated with a P-U(B)PS experiment. A solution, whether it is mechanical, numerical or a combination of both, has been proposed and discussed. One of the most notable conclusions that can be deduced from the here reported pitfalls concerns the inappropriateness of the double through-transmission recording for high-quality polar scan applications. The downside of using double through-transmission can be best seen in the 'curvature P-UPS', in which

twin rings became apparent, causing ambiguity in the identification of critical bulk wave angles. In addition, the presented P-UPS pitfall study clearly reveals that several weaknesses of the current version of the polar scan technique are related to mechanical movements and alignments. This strongly suggests that the next generation of polar scans should be preferably based on a system without mechanical components, providing a fixed alignment, and involving mature phased matrix technology to allow flexibility in excitation and recording. In view of this, we are currently considering the construction of a hand-held hemisphere containing a large number of transducers which can be activated both individually and in cooperation. With this, the full immersion of the structure can be replaced by a custom-made fluid-filled bag providing local coupling to the sample under consideration. In addition, and most relevant for industrial applications, the phased matrix technology easily permits measurements in reflection. The prototype of the miniaturized UPS scanner shown in Section 3.7 can be considered as an intermediate stage of our final goal.

In attendance of such technology to be developed, the tips and tricks gathered in this chapter can help to largely reduce the experimental difficulties inherent to the current polar scan implementation for obtaining accurate and reproducible experiments. This may lead to a revival of the ultrasonic polar scan as a quantitative, contactless NDT technique on laboratory scale. Furthermore, it is expected that the combination of high-quality experiments with numerical simulations will eventually facilitate the inverse characterization of the local mechanical stiffness (both elasticity and attenuation) of (an)isotropic plates.

5. 4. References

[1] *Error prone.* Nature, 2012. 487(7408): p. 406-406.
[2] *Must try harder.* Nature, 2012. 483(7391): p. 509-509.
[3] Ramadas, C., A. Hood, I. Khan, and K. Balasubramaniam, *Effect of misalignment of air-coupled probes on Ao Lamb mode propagating in a metal plate.* Ultrasonics, 2014. 54(5): p. 1401-1408.
[4] Degrieck, J. *Some possibilities of nondestructive characterisation of composite plates by means of ultrasonic polar scans*. in *Emerging technologies in nondestructive testing (ETNDT)*. 1996. Patras, Greece: A.A. Balkema.
[5] Degrieck, J., N.F. Declercq, and O. Leroy, *Ultrasonic polar scans as a possible means of non-destructive testing and characterisation of composite plates.* Insight, 2003. 45(3): p. 196-201.

[6] Declercq, N.F., J. Degrieck, and O. Leroy, *On the influence of fatigue on ultrasonic polar scans of fiber reinforced composites.* Ultrasonics, 2004. 42(1-9): p. 173-177.

[7] Satyanarayan, L., J.M. Vander Weide, and N.F. Declercq, *Ultrasonic Polar Scan Imaging of Damaged Fiber Reinforced Composites.* Materials Evaluation, 2010. 68(6): p. 733-739.

[8] Rokhlin, S.I. and L. Wang, *Ultrasonic waves in layered anisotropic media: characterization of multidirectional composites.* International Journal of Solids and Structures, 2002. 39(21-22): p. 5529-5545.

[9] Wang, L. and S.I. Rokhlin, *Ultrasonic wave interaction with multidirectional composites: Modeling and experiment.* Journal of the Acoustical Society of America, 2003. 114(5): p. 2582-2595.

[10] Kersemans, M., W. Van Paepegem, D. Van Nuffel, G. Luyckx, I. De Baere, F. Zastavnik, J. Gu, H. Sol, K. Van Den Abeele, and J. Degrieck, *Polar scan technique for material characterization and identification of new operating regimes*, in *15th International Conference on Experimental Mechanics (ICEM15)*, J.F. Silva Gomes and M.A.P. Vaz, Editors. 2012, INEGI: Porto, Portugal.

[11] Kersemans, M., K. Van Den Abeele, N. Lammens, J. Degrieck, F. Zastavnik, J. Gu, L. Pyl, H. Sol, and W. Van Paepegem. *Determination of the Fiber Direction and the C-Tensor of a UD Carbon/Epoxy Composite by means of the Ultrasonic Polar Scan*. in *Proceedings of the 2013 International Congress on Ultrasonics (ICU 2013)*. 2013. Singapore.

[12] Kersemans, M., N. Lammens, G. Luyckx, J. Degrieck, and W. Van Paepegem, *Quantitative Measurement of the Elastic Properties of Orthotropic Composites by means of the Ultrasonic Polar Scan Method.* JEC Composites, 2012. 75(75): p. 48 - 52.

[13] Kersemans, M., A. Martens, N. Lammens, K. Van Den Abeele, J. Degrieck, F. Zastavnik, L. Pyl, H. Sol, and W. Van Paepegem, *Identification of the elastic properties of isotropic and orthotropic thin-plate materials with the pulsed ultrasonic polar scan.* Experimental Mechanics, 2014. In Press DOI: 10.1007/s11340-014-9861-7.

[14] Kersemans, M., W. Van Paepegem, N. Lammens, K. Van Den Abeele, F. Zastavnik, J. Gu, H. Sol, and J. Degrieck, *'Gradient' Polar Scan Technique for Material Characterization*, in *IEEE International Ultrasonics Symposium (IUS2012)*. 2012: Dresden, Germany.

[15] Van Dreumel, W.H.M. and J.L. Speijer, *Non-destructive composite laminate characterization by means of ultrasonic polar-scan.* Materials Evaluation, 1981. 39(10): p. 922-925.

[16] Declercq, N.F., J. Degrieck, and O. Leroy, *Ultrasonic polar scans: Numerical simulation on generally anisotropic media.* Ultrasonics, 2006. 45(1-4): p. 32-39.

[17] Declercq, N.F., J. Degrieck, and O. Leroy, *Simulations of harmonic and pulsed ultrasonic polar scans.* Ndt & E International, 2006. 39(3): p. 205-216.

[18] Petricola, D.L., *Adding and maintaining bubble-free water in ultrasonic scanning systems.* Materials Evaluation, 2007. 65(9): p. 875-880.

[19] Elkettani, M.E., P. Pareige, F. Luppe, and J. Ripoche, *Experimental study of the conversion of lamb waves at the end of an immersed plate.* Acustica, 1996. 82(2): p. 251-259.

[20] Morvan, B., N. Wilkie-Chancellier, H. Duflo, A. Tinel, and J. Duclos, *Lamb wave reflection at the free edge of a plate.* Journal of the Acoustical Society of America, 2003. 113(3): p. 1417-1425.

[21] Galan, J.M. and R. Abascal, *Lamb mode conversion at edges. A hybrid boundary element-finite-element solution.* Journal of the Acoustical Society of America, 2005. 117(4): p. 1777-1784.

Chapter 6

Wave Curves Extraction from P-UPS Data

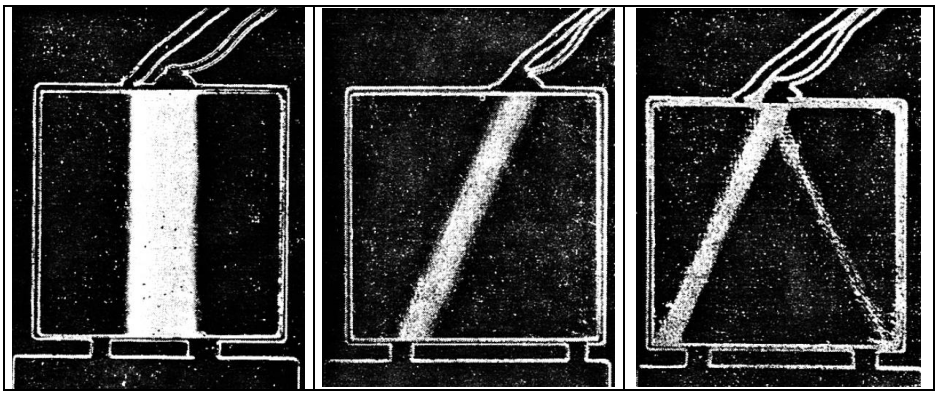

Pioneering shadowgraph experiments of Merkulov and Yakovlev (Figure reproduced from reference [1]) revealing the deflection of the wave energy transportation from the wave normal in anisotropic crystals.

Summary

The ultrasonic inspection as well as the interpretation of recorded ultrasonic signals is well established for isotropic materials. The opposite is true for materials such as crystals and fiber reinforced composites which are mechanically anisotropic in nature. The anisotropy causes a degeneration of the energy transportation direction and the wave propagation direction, for all possible polarization types. As such, it is extremely difficult to deliver ultrasonic energy to the region of interest. Hence, to correctly inspect or characterize an anisotropic sample, the material properties and wave characteristics are actually required in advance. Of course, this nullifies the original intent of material inspection and characterization.

By analyzing and post-processing a single P-UPS experiment, all the relevant directional wave characteristics have been extracted for the different polarized waves without prior knowledge. The P-UPS analysis for a unidirectional carbon/epoxy laminate revealed an extraordinary angular deflection of the wave energy up to ~70° for the quasi-horizontally polarized bulk wave. In addition, we also demonstrate a lensing effect which permits to zoom in/out in the P-UPS fingerprint, effectively broadening the class of materials which can be investigated by the P-UPS technique.

6. 1. Introduction

Inspection and characterization of materials by means of ultrasonic techniques is, at first sight, an easy and straightforward task. This is true to some extent for the investigation of isotropic materials because the different types of defects are most of the time limited to a few, while the nature of the ultrasonic wave propagation in isotropic solids is not dependent on the propagation direction.

In case of investigating anisotropic materials with ultrasonic methods, this statement is not valid anymore since the complexity of ultrasonic wave interaction in anisotropic solids increases significantly. Besides the directional nature of wave propagation, the energy transportation direction

could show a walk-off during propagation [1-3]. Hence, to fully acknowledge bulk wave propagation in anisotropic materials as a consequence of externally borne sound, a lot of information is required. To demonstrate this, Figure 6-1 presents the famous shadowgraph experiments of Merkulov and Yakovlev (taken from reference [1]). Figure 6-1a shows the ultrasonic intensity in case of exciting the top surface of an isotropic crystal. In accordance to our intuition, the direction of wave energy is normal to the surface excitation. Figure 6-1b on the other hand, shows the ultrasonic intensity in case of exciting the top surface of an anisotropic crystal. In the latter case, it can be readily verified that the ultrasonic intensity distribution deviates from the vertical.

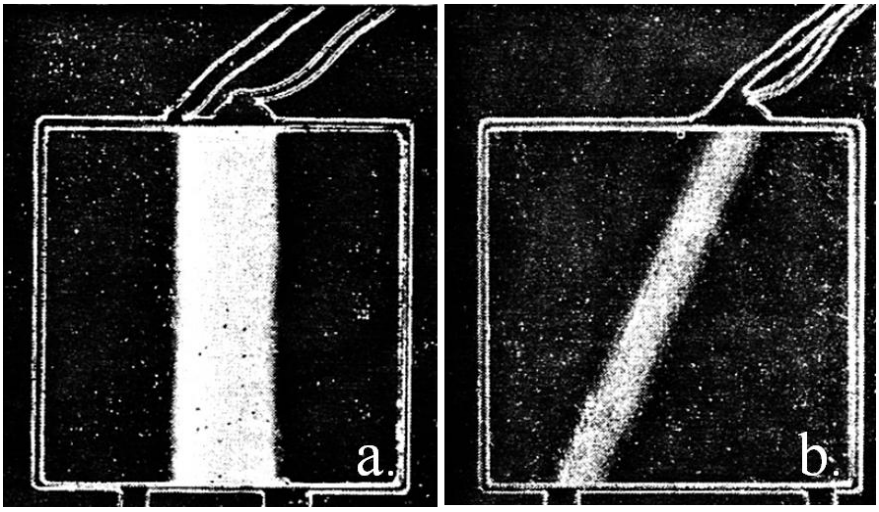

Figure 6-1: Pioneering shadowgraph experiment of Merkulov and Yakovlev (Figure reproduced from reference [1]), visualizing the walk-off phenomenon in crystals: isotropic crystal (a) and anisotropic crystal (b).

Figure 6-2 shows a schematic to interpret the shadowgraph experiment of Merkulov and Yakovlev, as well as to identify several important quantities. An ultrasonic wave is stimulated at the top surface of the anisotropic medium, hence it has its wave vector $\boldsymbol{k}$, or analogously its phase velocity $\boldsymbol{c_{ph}}$, directed along the vertical. However, due to the anisotropic nature of the solid, the energy transportation, or equivalently the energy velocity $\boldsymbol{c_E}$, of the stimulated ultrasonic wave deviates from this vertical direction by the walk-off angle ξ. It is clear that profound knowledge of the directional walk-off angles ξ is of utmost importance in the field of NDT as it could introduce

unusual beam focusing, inaccurate defect sizing, confusion in feature selection, etc. [4-7].

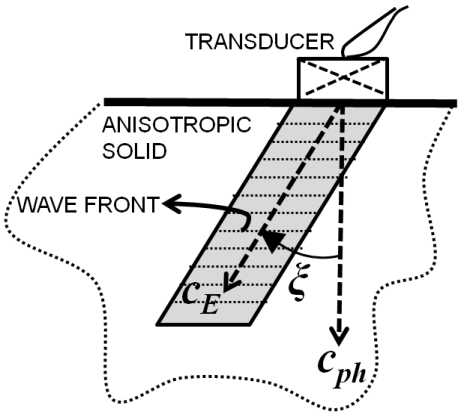

Figure 6-2: Schematic representation of the walk-off phenomenon.

As structural composite materials are most of the time plate-like, one is merely interested in in-plane material characteristics and in extension to wave propagation guided by the plate. Figure 6-3a displays the 2D analogue of the walk-off phenomenon for a composite plate, in which the ultrasonic beam skews towards the fiber direction (1-axis) upon propagation. For composites, which often have an in-plane fiber reinforcement, skewing of guided waves only takes place in the 12-plane. As such, the analysis can be simplified to a large extent [2-3]. A schematic of the geometrical relation between the slowness vector ***s***, which corresponds to the inverse of the phase velocity vector $\boldsymbol{c_{ph}}$, and the walk-off angle ξ is shown in Figure 6-3b for an anisotropic composite plate. Note that along the symmetry direction of the composite plate, being the 1-direction (or φ = 0°) and the 2-direction (or φ = 90°), only pure waves are allowed which do not display any walk-off.

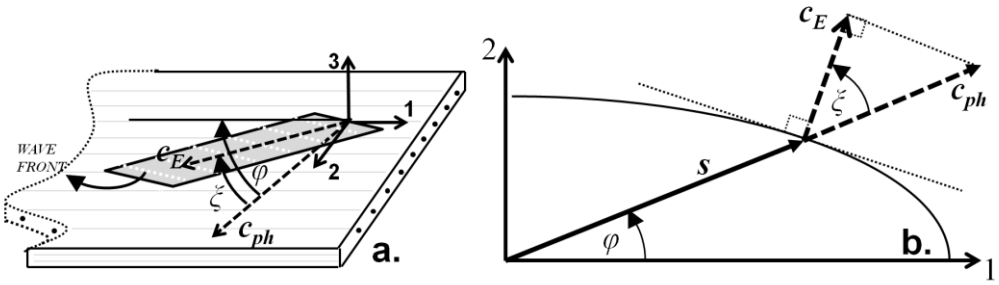

Figure 6-3: Walk-off phenomenon in a composite plate (a) and schematic of the relation between the slowness vector *s* and the walk-off angle ξ (b).

Basically, complete understanding of bulk wave propagation in immersed anisotropic solids can only be obtained through the knowledge of (i) the critical bulk wave angle profiles $\boldsymbol{\theta_{crit}}$, (ii) the phase velocity profile $\boldsymbol{c_{ph}}$, (iii) the slowness vector $\boldsymbol{s}$, (iv) the walk-off angle profile $\boldsymbol{\xi}$ and (v) the energy velocity profile $\boldsymbol{c_E}$, and this for the three different polarization states of bulk waves, i.e. the (quasi-)longitudinal (QL), the (quasi-) shear horizontal (QSH) and the (quasi-) shear vertical (QSV) polarized wave [2-3].

Several techniques have been reported in literature on the determination of the characteristic wave curves [8-12]. Unfortunately, all these techniques only provide part of the relevant wave propagation characteristics, and comprise a complex experimental setup as well as advanced post-processing analysis. The P-UPS technique on the other hand covers all relevant wave curves in a single experiment without the need of specific sample preparation. Moreover, the P-UPS provides the local directional wave curves since a single material spot with diameter of ~5 mm (which corresponds to the physical dimensions of the here employed ultrasonic beam) is insonified. Hence, it is possible to scan a plate with the P-UPS at different physical spots in order to retrieve its mechanical (in)homogeneity. Another advantage is that the P-UPS technique does not involve the use of complex time-signal measurements, but simply relies on the recording of the transmitted (or if necessary the reflected) amplitude, which has obvious advantageous for industrial implementation. Note that also the local attenuation characteristics play a major role for wave propagation in anisotropic media. As a matter of fact, the tensorial attenuation is also encoded in the global color scale of a P-UPS experiment [13-15]. Though, we do not deal with this quantity in the present chapter and solely focus on the contour-related quantities, being the five aforementioned profiles.

6. 2. Theoretical Background

Plane wave propagation in an infinite elastic anisotropic solid is effectively described by the well-known Christoffel equation (Einstein summation convention) [2-3].

$$\left(\rho\omega^2\delta_{il} - C_{ij\mathrm{l}\mathrm{n}}k_j k_n\right)p_l = 0 \tag{1}$$

with ρ the density, ω the circular frequency, δ the Kronecker delta, $\boldsymbol{C}$ the elasticity tensor, $\boldsymbol{k}$ the unit wave vector and $\boldsymbol{p}$ the polarization vector of the

mechanical wave. This leads to an orthogonal classical eigenvalue problem for which three independent solutions exist in case of a symmetry higher than or equal to monoclinic symmetry [3]. The eigenvalue problem is solved by demanding nontrivial solutions, which is equivalent to setting the determinant of the coefficient matrix equal to zero:

$$\left|\rho\omega^2\delta_{il} - C_{ij\ln}k_j k_n\right| = 0 \tag{2}$$

The $\boldsymbol{k}$ vector solutions of Equation (2) subsequently yield the slowness vectors $\boldsymbol{s} = \boldsymbol{k}/\omega$, and equivalently the phase velocities $\boldsymbol{c_{ph}} = \boldsymbol{1_s}/s$ with $\boldsymbol{1_s}$ the unit vector of $\boldsymbol{s}$. The obtained solutions can then be entered back into the system of original homogeneous equations to calculate the eigenvectors in order to confirm the wave type and character, i.e. (i) quasi-longitudinal (QL), (ii) quasi-shear horizontal (QSH) or (iii) quasi-shear vertical (QSV) polarized wave. Along symmetry directions, the prefix quasi can be omitted, resulting in pure wave modes (see Figure 6-3b). For externally born sound, Snell's law has to be taken into account which states that the components of the incident wave vector $\boldsymbol{k}$, parallel to the liquid-solid interface (12-plane), are conserved

$$\begin{cases} k_1^{inc} = k_1^s \\ k_2^{inc} = k_2^s \end{cases} \tag{3}$$

With this, it is straightforward to compute the incident angle θ_{crit} at which the incident wave is critically refracted, producing a lateral wave being guided by the structure.

Application of Poynting's theorem leads to the velocity at which energy is transported. However, as most of the considered materials are approximately lossless, for which the energy velocity c_E equals the group velocity c_g, it is sufficient to determine the group velocity c_g, the computation of which is much more straightforward. Hence the energy velocity c_E can be computed as

$$c_E \approx c_g = -\frac{\nabla_k\left(\left|\rho\omega^2\delta_{im} - C_{iklm}k_k k_l\right|\right)}{\partial\left(\left|\rho\omega^2\delta_{im} - C_{iklm}k_k k_l\right|\right) \Big/ \partial\omega} \tag{4}$$

Finally, the walk-off angle ξ corresponds to the deviation between the direction of the phase velocity $\boldsymbol{c_{ph}}$ and energy velocity $\boldsymbol{c_E}$ (see Figure 6-3b). Alternatively, the walk-off angle ξ can also be computed on the basis of the slowness curves by considering the deviation between the slowness vector and the outward normal on the curve (see Figure 6-3b). The relation between the phase velocity c_{ph}, c_E and ξ can be written as

$$c_E^j(\zeta,\theta) = {c_{ph}^j(\varphi,\theta)} \Big/ {\cos\left(\xi^j(\varphi,\theta)\right)} \tag{5}$$

with ζ the energy propagation angle, defined as $\zeta = \varphi + \xi$, and the superscript *j* represents the polarization of the bulk wave.

As an example, the computed wave curves for a water-immersed $[0]_8$ carbon/epoxy material, using the mechanical properties listed in Table 6-1, are presented in Figure 6-4.

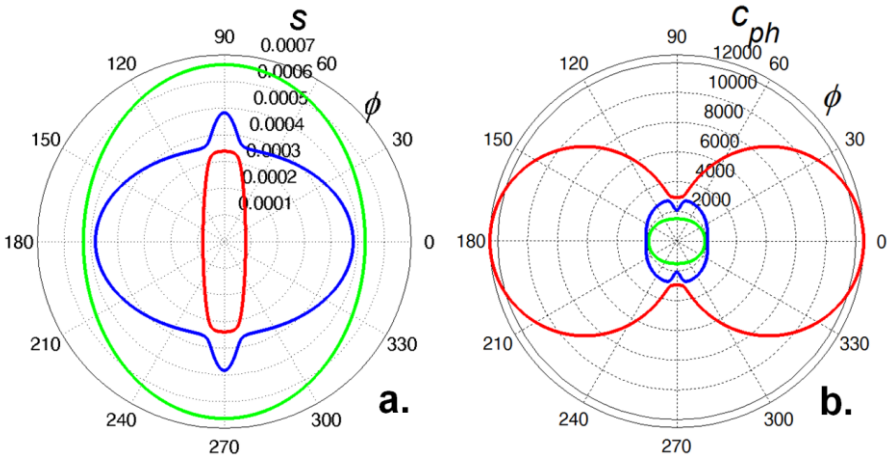

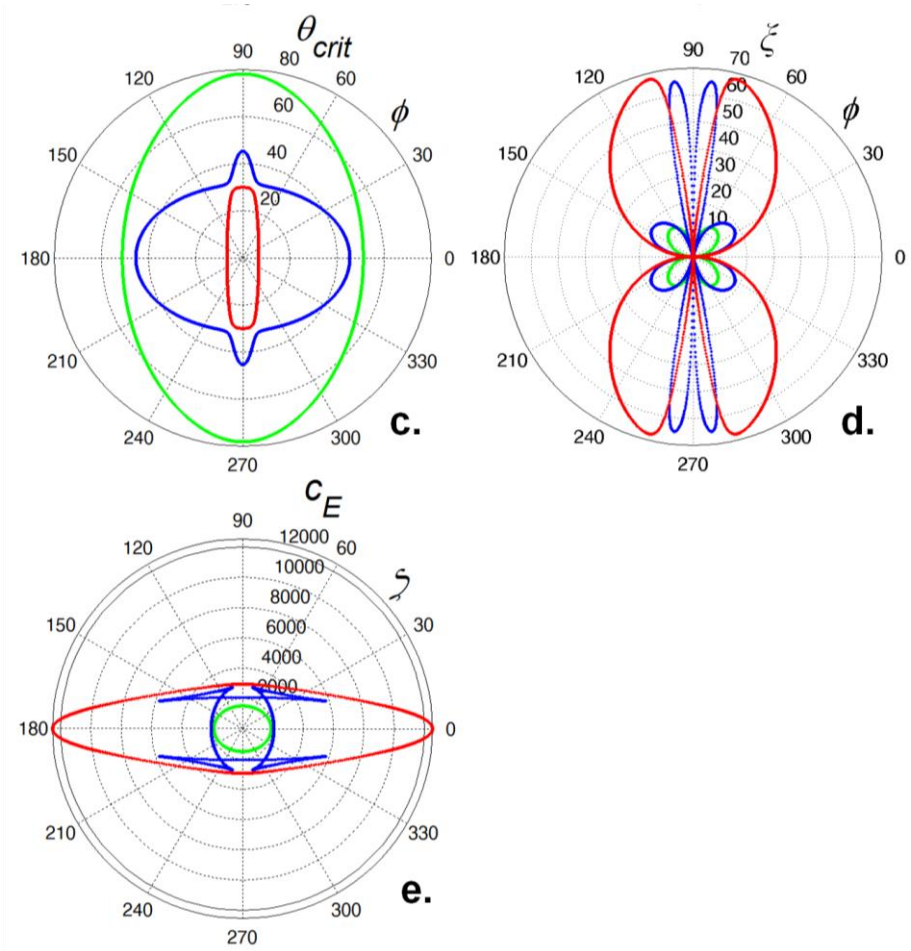

Figure 6-4: Computation of slowness s^j (a), phase velocity c_{ph}^j (b), critical bulk wave angle θ_{crit}^j (c), walk-off angle ξ^j (d) and energy velocity c_E^j (e) for a liquid immersed orthotropic material, with *j* = QL (red), QSH (blue) and QSV (green).

Table 6-1: Mechanical properties used for the computation of the wave profiles shown in Figure 6-4.

LIQUID		**SOLID**	
K [GPa]	2.18	E_1 [GPa]	$230\cdot(1-0.0025i)$
		$E_2 = E_3$ [GPa]	$10.1\cdot(1-0.03i)$
		$v_{12} = v_{13}$ [-]	$0.324\cdot(1-0.01i)$
		v_{23} [-]	$0.461\cdot(1-0.015i)$
		G_{12} [GPa]	$6.39\cdot(1-0.03i)$

		G_{13} [GPa]	$5.35\cdot(1-0.02i)$
		G_{23} [GPa]	$3.38\cdot(1-0.05i)$
ρ [kg/m^3]	1000	ρ [kg/m^3]	1528.6

In this chapter, the color red, blue and green is systematically preserved for the QL, QSH and QSV polarization respectively. The computed slowness curves s^j, with j = QL, QSH and QSV, in the 12-plane are shown in Figure 6-4a. Because of the anisotropic nature of the simulated material, the slowness curves have a non-circular shape. From these curves, the phase velocity profiles c_{ph}^j are easily computed by considering the inverse of the slowness (Figure 6-4b). Application of Snell's law for externally born sound leads to the critical bulk wave angles θ_{crit}^j (Figure 6-4c). The walk-off angle ξ^j, which prescribes the deviation of the energy flow from the phase velocity direction, is determined by considering the local gradient of the slowness (Figure 6-4d). Note that the simulated carbon/epoxy laminate shows an extraordinary walk-off angle $\xi \approx 68°$, caused by the large degree of mechanical anisotropy. Along the symmetry directions of the material, no walk-off is present between the phase velocity and energy velocity direction, hence resulting in pure modes. When considering an arbitrary orientation φ, the walk-off angle becomes non-zero, i.e. the energy flows in a different direction than the phase velocity direction, thus resulting in quasi modes (see Figure 6-4d). It is clear that profound knowledge of this concept is of utmost importance in the field of composite material inspection in order to avoid misinterpretation of test data. The energy velocity c_E^j, which is plotted as a function of the energy propagation angle ζ, is presented in Figure 6-4e. Note that all the quantities are put in SI-units and that the units are not explicitly added to each figure, simply because of visualization matters.

6. 3. P-UPS Extracted Wave Curves

It is clear that the theoretical computation of the directional bulk wave curves is straightforward. However, experimental determination of the relevant profiles for the different polarization states, for which in general multiple experiments have to be performed, is much more challenging. Especially when a local representation of the bulk wave characteristics of a plate-like material is required. In this section, it is illustrated how to efficiently extract the five aforementioned profiles from a single P-UPS experiment. We demonstrate the procedure for two materials: an isotropic

aluminum plate and an autoclave manufactured unidirectional $[0]_8$ carbon-epoxy laminate.

6. 3. 1. Isotropic Aluminum

The P-UPS, recorded with a pulsed signal having a center frequency f_c = 5 MHz, for an isotropic aluminum sample with a plate thickness of d = 0.6 mm, is shown in Figure 6-5a. The circular patterns within the P-UPS image clearly reflect the underlying mechanical isotropy of the scanned material spot.

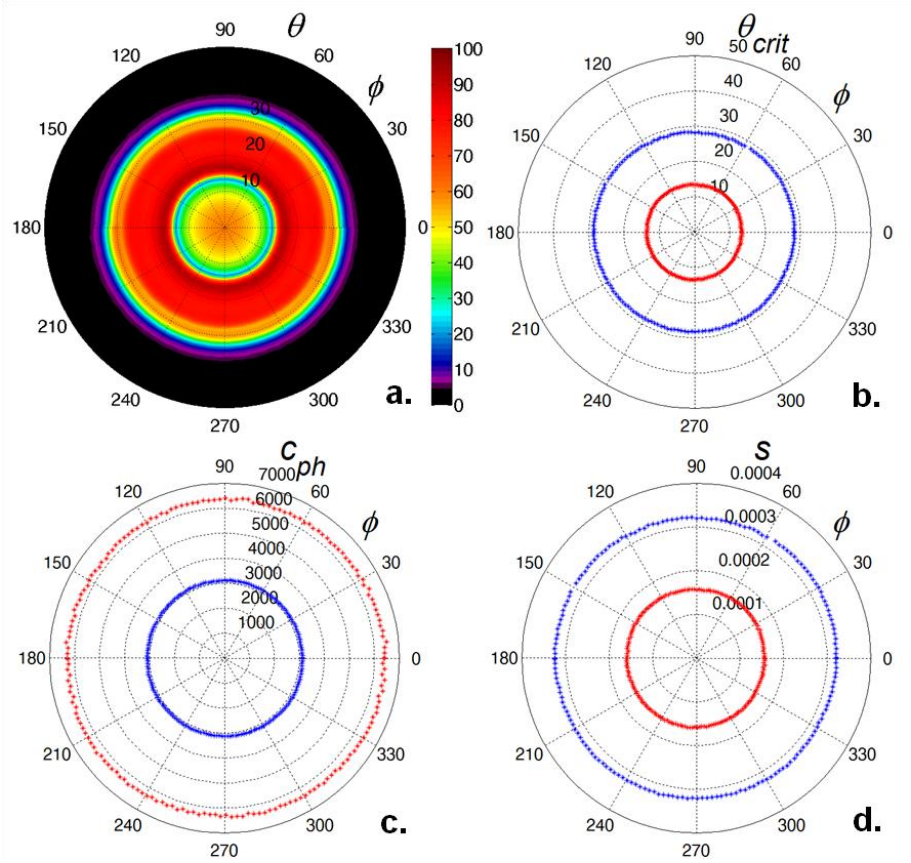

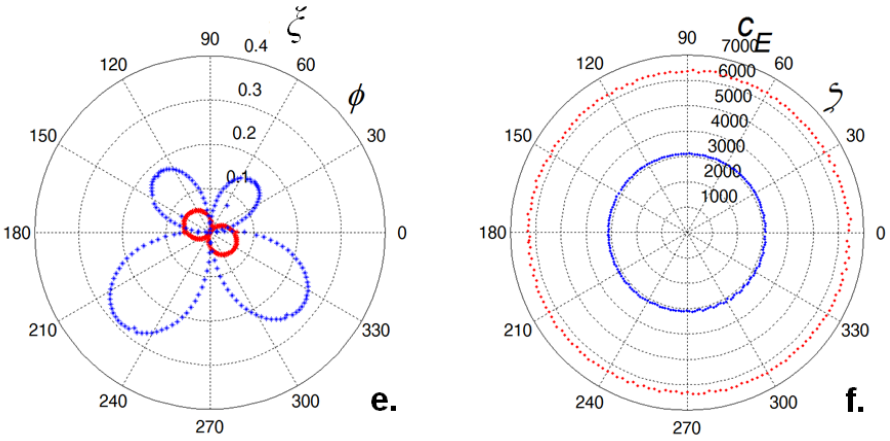

Figure 6-5: P-UPS for an aluminum sample recorded at $f_c d$ = 5 MHz x 0.6 mm = 3 MHz.mm (a). Extracted bulk wave curves: critical angle θ_{crit}^{j} (b), phase velocity c_{ph}^{j} (c), slowness s^{j} (d), walk-off angle ξ^{j} (e) and energy velocity c_{E}^{j} (f).

In principle, the critical bulk wave angles θ_{crit}^{j} can be extracted by searching for local transmission amplitude minima in the recorded P-UPS. Instead, for reasons of robustness, we implemented an algorithm which searches for zones characterized by a high local surface curvature (second derivative in the θ-direction). Furthermore, it is crucial for the extraction procedure that the origin $\psi(\varphi,\theta) = \psi(0,0)$ of the P-UPS experiment effectively corresponds to normal incidence (see Section 5.2.2). Most of the time, this is not satisfied because of positioning errors of the sample in the experimental setup [16]. In order to neutralize this deviation, the correct normal incidence $\psi(\varphi_0,\theta_0)$ is searched for by numerically determining the geometrical midpoint of the extracted critical angles θ_{crit} of the bulk waves

$$(\varphi_0,\theta_0) = \frac{1}{P}\sum_{j=1}^{P}\left(\tan^{-1}\left(\frac{\sum_{i=1}^{N}\theta_{i,crit}^{j}\sin\varphi_i}{\sum_{i=1}^{N}\theta_{i,crit}^{j}\cos\varphi_i}\right),\frac{\sqrt{\sum_{i=1}^{N}\theta_{i,crit}^{j\,2}}}{N}\right) \qquad (6)$$

with P the number of different polarization states (QL, QSH and QSV) and N the number of experimental data points along φ-direction.

Translation of the experimental data $(\varphi,\theta)\rightarrow(\varphi+\varphi_0,\theta+\theta_0)$ yields the angles (φ',θ') in the correct reference system

$$\begin{aligned}\theta' &= \sqrt{\theta^2+\theta_0^2-2\theta\theta_0\cos(\varphi-\varphi_0)}\\ \varphi' &= \tan^{-1}\left(\frac{\theta\sin\varphi-\theta_0\sin\varphi_0}{\theta\cos\varphi-\theta_0\cos\varphi_0}\right)\end{aligned} \tag{7}$$

Applying this scheme is essential to obtain the correct critical angles θ_{crit}^{j} for the different polarized bulk waves (see Figure 6-5b). Note that only two polarizations are present because of the degeneracy of the SH and SV waves, which is characteristic for materials possessing mechanical isotropy. Applying Snell-Descartes' law for externally born sound with water as the immersion liquid, the phase velocity c_{ph}^{j} can be easily computed (Figure 6-5c). A comparison between the obtained average values for the phase velocity c_{ph}^{j}, together with their standard deviation σ, and the literature values is presented in Table 6-2, showing excellent agreement.

Table 6-2: Comparison between literature [2] and obtained phase velocity c_{ph}^{j} and energy velocity c_{E}^{j} for aluminum. Although the walk-off angles ξ^{j} (see Figure 6-5e) indicate that the insonified aluminum has a very small level of mechanical anisotropy, it is here assumed to be perfectly isotropic.

	LITERATURE [2]	***EXPERIMENT***	***RELATIVE ERROR***
c_{ph}^{QL}	6350 [m/s]	6348.9 ± 41.34 [m/s]	0.02%
c_{ph}^{QSV}	3130 [m/s]	3117.9 ± 12.40 [m/s]	0.39%
c_{E}^{QL}	6350 [m/s]	6348.8 ± 41.54 [m/s]	0.02%
c_{E}^{QSV}	3130 [m/s]	3118.0 ± 12.46 [m/s]	0.38%

Inversion of the phase velocity profiles c_{ph}^{j} leads to the slowness curves s^{j}, which are shown in Figure 6-5d. The next step involves the computation of the walk-off angle ξ^{j} by considering the local gradient of the slowness profile [2-3]

$$\xi^{j}(\varphi,\theta)=\tan^{-1}\left[\frac{1}{\theta}\frac{\partial\overrightarrow{s^{j}}(\varphi,\theta)/\partial\varphi}{\partial\overrightarrow{s^{j}}(\varphi,\theta)/\partial\theta}\right] \tag{8}$$

As the presence of noise significantly amplifies upon differentiation, it is most common to first fit the slowness curves by means of a representative function. We consider spline functions, which were first introduced by Schoenberg [17], to fit the experimental data points. Contrary to approximation methods using higher order polynomials, the spline approach is highly suited to fit different kinds of scattered data points (with possibly a large number of constraints) in a numerically stable way. A p^{th} degree non-uniform rational B-spline curve $C(u)$ is defined by [18]:

$$C(u)=\frac{\sum_{i=0}^{n}N_{i,p}(u)w_iP_i}{\sum_{i=0}^{n}N_{i,p}(u)w_i} \tag{9}$$

with w_i the weigths, P_i the control points and $N_{i,p}(u)$ the p^{th} degree basis functions defined on the non-uniform knot vector $U(u)$. The i^{th} B-spline basis function of p-degree, denoted by $N_{i,p}(u)$, is defined in a recursive manner according to De Boor [19]:

$$\begin{aligned}N_{i,0}(u)&=\begin{cases}1 & \text{if } u_i\le u<u_{i+1}\\ 0 & \text{otherwise}\end{cases}\\ N_{i,p}(u)&=\frac{u-u_i}{u_{i+p}-u_i}N_{i,p-1}(u)+\frac{u_{i+p+1}-u}{u_{i+p+1}-u_{i+1}}N_{i+1,p-1}(u)\end{aligned} \tag{10}$$

Here, we consider rational cubic B-splines and assume for simplicity uniformly spaced knots. Because of the nature of the P-UPS contours, periodic boundary conditions have been applied to the B-spline. To mitigate the influence of outlying data points, robust fitting is applied by considering the method of iteratively reweighted least squares (IRLS) [20], applying following weight function W_l

$$W_l = \exp\left(-\frac{\alpha}{2(1-\alpha)\,\tilde{r}_l}\, r_l^2\right) \tag{11}$$

with α a weighting parameter, r_l the residuals of the l^{th} iteration and $\tilde{r}_l$ the absolute mean value of the residuals of the l^{th} iteration.

A plot of W_l for different values of the weighting parameter α, given arbitrary residuals r_l, is shown in Figure 6-6. For $\alpha = 0$, W_l reduces to a constant, resulting to the ordinary unweigthed least-squares procedure. For $\alpha = 1$, W_l reduces to the Dirac function which yields highly unstable results. In general, α is chosen within these two extremes.

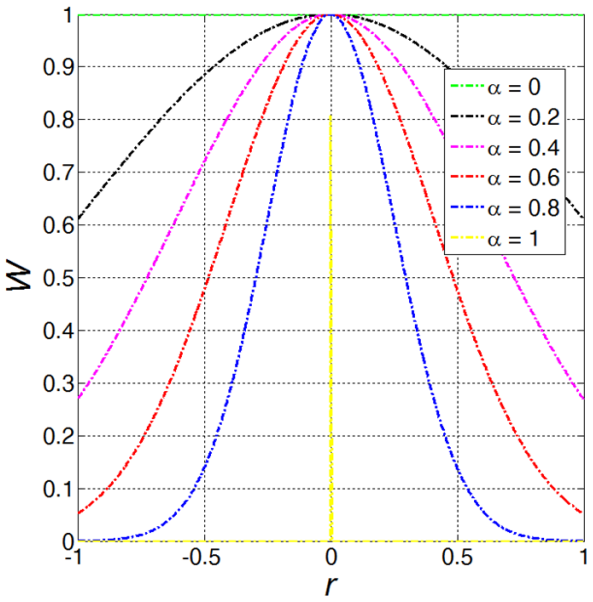

Figure 6-6: Weight function W_l for different values of the parameter α.

Hence,we start by setting $w_l = 1$. Then a regression model is fitted to the given weights w_l. A variance function is then estimated by regressing the squared residuals. The fitted values from the estimated variance function are considered to obtain the new weigths w_l, which are then used to refit the model. It was found that three iterations are sufficient to stabilize the estimated regression coefficients.

Figure 6-7 displays the IRLS fitted rational B-spline, considering 4 knots and different weight parameters α, to the extracted QL and QSV slowness data points for the aluminum sample. The influence of the weight parameter

α on the spline fit can be observed, although it can be considered to be rather small for the aluminum results. In the remainder of this chapter, we set the weigth parameter α at 0.8 to fit the experimental data. The nonlinear fit with $\alpha = 0.8$ yields a phase velocity of $c_{ph}^{QL} = 6350.7 \pm 4.99$ m/s and $c_{ph}^{QSV} = 3117.6 \pm 5.30$ m/s, which is in good agreement with both literature and the 'raw' data. The nonlinear fit is then used to determine the walk-off angle profiles by evaluating Equation (8), the results are shown in Figure 6-5e. It can be observed that a small walk-off angle ξ^j is present for certain polar angles φ, indicating a small degree of mechanical anisotropy. Nevertheless, the values are well below 1° which suggests that, for most applications, the aluminum can be considered as being effectively isotropic of nature.

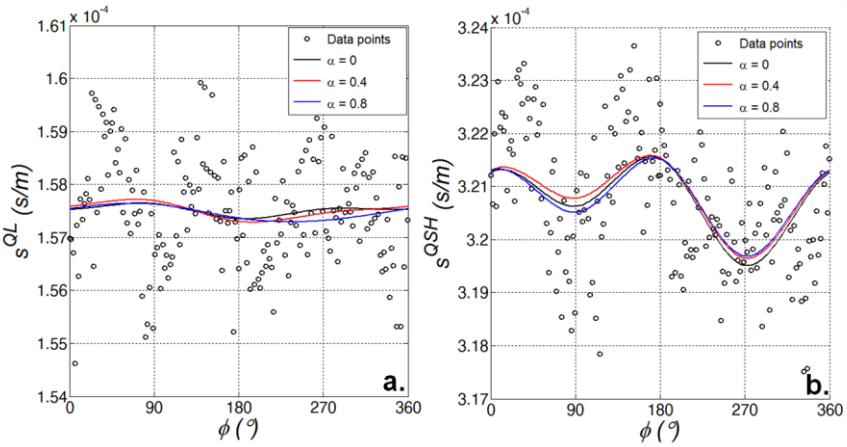

Figure 6-7: P-UPS extracted slowness (circles) and IRLS fitted rational B-spline (solid curves) considering different weight parameters α: quasi-longitudinal (QL) polarization (a) and quasi-shear vertical (QSV) polarization (b).

Finally, the energy velocity c_E^j, which is expressed as a function of the energy propagation angle ζ, with $\zeta = \varphi + \xi$, can be determined as the projection of the phase velocity c_E^j on the direction normal to the slowness curves s^j. The extracted energy velocity profiles are presented in Figure 6-5f. The obtained average values for the energy velocity c_E^j, together with their standard deviation σ, are listed in Table 6-2. We note that nearly identical values are obtained for the phase velocity c_{ph}^j as for the energy velocity c_E^j, as is expected for isotropic materials. Again, good agreement is

obtained with values listed in literature, indicating the robustness of the implemented processing technique.

6. 3. 2. Orthotropic $[0]_8$ Carbon/Epoxy Laminate

In the previous section, results were presented for an aluminum sample. Far more interesting is the case of a fiber reinforced plastic with a high degree of mechanical anisotropy. Typically, such materials have large walk-off angles ξ along several material orientations. The material under investigation is an autoclave manufactured orthotropic $[0]_8$ carbon/epoxy laminate with plate thickness $d \approx 1.1$mm. The P-UPS recorded with center frequency $f_c = 5$ MHz is shown in Figure 6-8a.

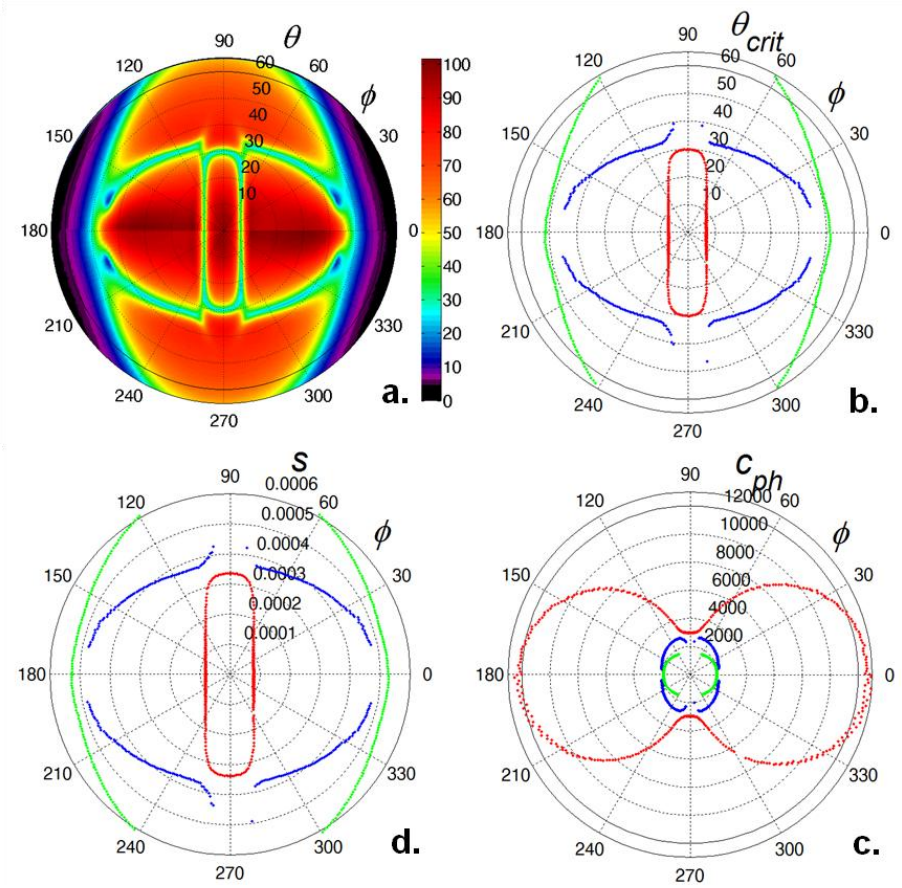

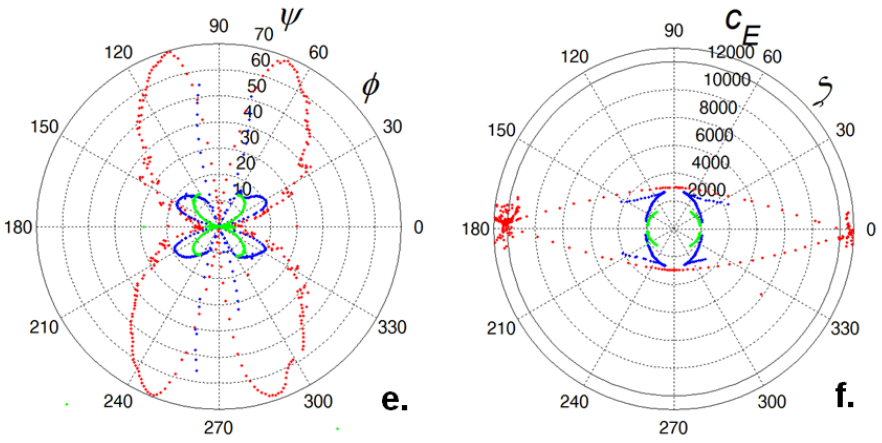

Figure 6-8: P-UPS for a $[0]_8$ carbon/epoxy laminate recorded at $f_c d$ = 5 MHz x 1.1 mm = 5.5 MHz.mm (a). Extracted bulk wave curves: critical angle θ_{crit}^{j} (b), phase velocity c_{ph}^{j} (c), slowness s^{j} (d), walk-off angle ξ^{j} (e) and energy velocity c_E^{j} (f).

It is clear that the characteristic features of the P-UPS fingerprint have completely changed in comparison with the results presented in Figure 6-5a. The asymmetry in the P-UPS experiment directly reflects the anisotropic nature of the scanned material spot. Note that, along the symmetry directions $(\phi = k \cdot \pi/2)$, part of the contour associated to the QSH wave is missing, due to the fact that at those directions no coupling structure is present to efficiently convert the incident QL wave to a QSH wave. Furthermore we note that also the contour associated with the QSV wave is not completely captured. Contrary to the QSH wave, the origin of the latter can be attributed to the low phase velocity c_{ph} associated to the QSV wave, at least when compared to the wave speed c_{liq} of the immersion liquid. According to Snell-Descartes' law, this results in a very large critical bulk wave angle, and eventually a complex valued critical bulk wave angle which has no physical meaning for the present application. Because of these features, the translational correction (Equation (6)) of the experimental data for the $[0]_8$ laminate has been determined on the basis of the quasi-longitudinal related contour. Subsequently, we adapted the extraction procedure to handle those regions where no data is available by dividing the P-UPS image in 4 quadrants, and by applying the extraction procedure consecutively to each quadrant separately. In contrast to the results for the aluminum sample, the setting of the parameters for the IRLS spline fitting procedure is far more

important. This is explicitly demonstrated in Figure 6-9 for part of the QSH polarization.

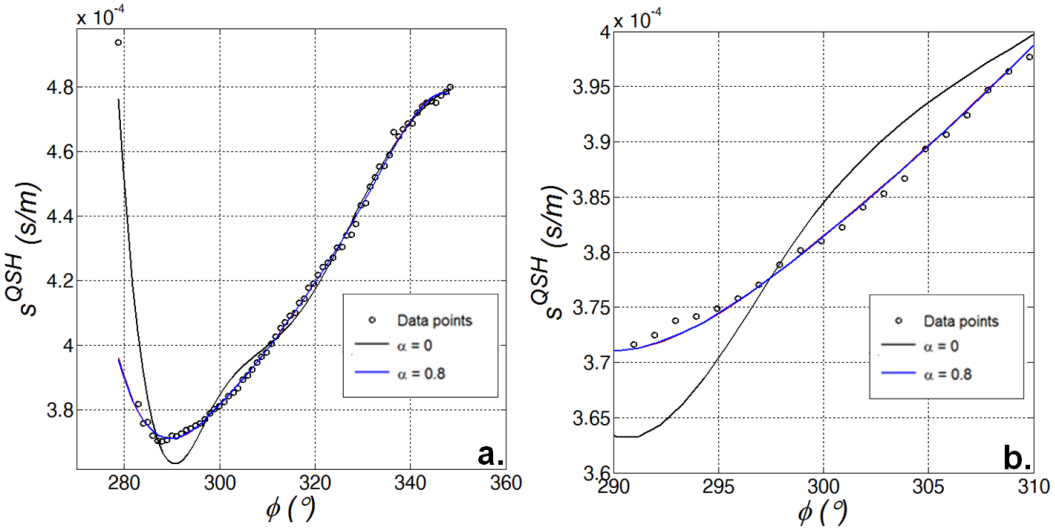

Figure 6-9: P-UPS extracted slowness (circles) and IRLS fitted rational B-spline (solid curves) considering different weight parameter α: quasi- shear horizontal (QSV) polarization for $\varphi \in$ [270°-360°] (a) and for $\varphi \in$ [290°-310°] (b).

The extracted profiles for the $[0]_8$ carbon/epoxy sample are shown in Figure 6-8b-f. Note the good similarity of these curves to the numerically computed curves (Figure 6-4a-e), indicating the appropriateness of the implemented procedure for extracting the relevant bulk wave curves. Similar as for the simulation example, it can be observed that the laminate exhibits an extremely large walk-off angle ξ^{QL} = 69.51° for the QL polarized bulk wave propagating in the 12-plane at the polar angles φ = (73.4°, 106.6°, 253.4°, 286.6°). This implies that the insonification of the carbon/epoxy laminate at for example $(\varphi, \theta_{crit}^{QL})$ = (106.6°,23.3°) stimulates a QL wave into the solid which transports its energy in the 12-plane along (φ^*, θ^*) = (176.1°,90°).

Interestingly, the walk-off phenomenon deforms the spatial profile of the propagating sound beam itself. Moreover, as a realistic divergent bounded sound beam can be decomposed in a collection of plane waves by application of the spatial Fourier transform, each having a specific energy propagation direction, the walk-off phenomenon implies that certain incidence directions could introduce a beam-(de)focusing effect within the

solid [2, 21-23]. This is schematically illustrated in Figure 6-10 for the case where focusing of the energy occurs.

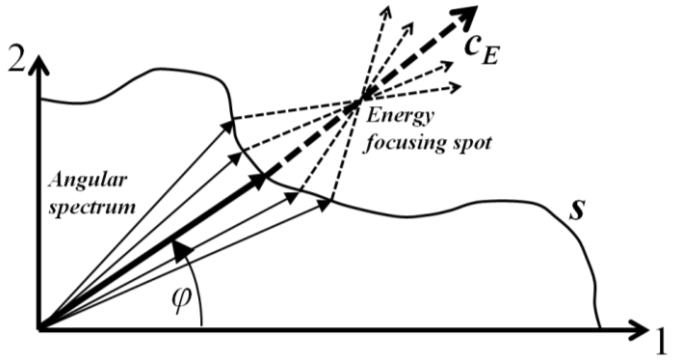

Figure 6-10: Focusing effect of a divergent bounded beam in an anisotropic plate.

Granted that most part of the slowness curves s^j of the $[0]_8$ carbon/epoxy laminate naturally introduces a defocusing effect, one can spot several zones at the slowness curve s^{QSH} associated to the QSH wave, in which beam focusing effectively appears as if it were a lens. This has been explicitly indicated in Figure 6-11 with black arrows. An exact computation of the energy redistribution and focusing can be found in literature [4, 6, 21-22].

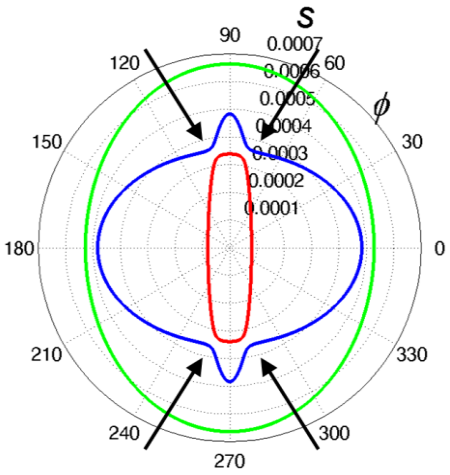

Figure 6-11: Identification of focusing conditions of the QSH wave occurs during propagation in the 12-plane of a $[0]_8$ carbon/epoxy laminate.

6. 4. Lensing effect of the Immersion Liquid for the P-UPS

As mentioned above, the possibility exists that (part of) a contour cannot be captured by the P-UPS technique when a low phase velocity c_{ph}^{j} is involved, implying that the technique has limitations for investigating low bulk wave velocity materials (like for example the $[0]_8$ carbon/epoxy laminate). This limitation can be alleviated by considering the application of a different immersion liquid which reduces the c_{liq}/c_{ph}^{j} ratio. Indeed, by changing the immersion liquid, a physical zooming can easily be obtained as illustrated in Figure 6-12 where P-UPS simulations are shown for the $[0]_8$ carbon/epoxy laminate (with the complex material parameters listed in Table 6-1) when immersed in water, in isopropyl alcohol (zoom out) as well as in a water/glycerol mixture (zoom in). The properties of the different liquids used for these simulation are listed in Table 6-3.

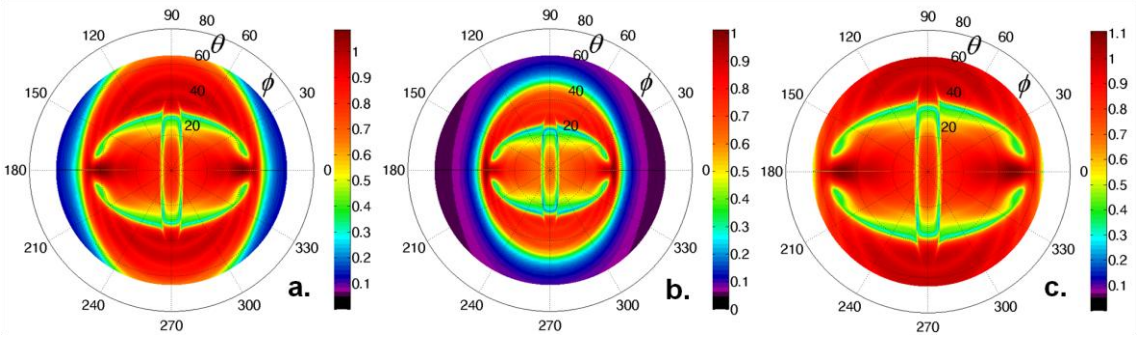

Figure 6-12: P-UPS simulations for a carbon/epoxy composite: immersed in water (a), in isopropyl alcohol (b) and in water/glycerol mixture (35%-65% ratio) (c).

Table 6-3: Acoustic properties of different immersion liquids.

	c_{liq} [m/s]	ρ_{liq} [kg/m^3]
Water	1475.4	1000
Isopropyl Alcohol	1170	786
Glycerol	1904	1260

Besides some minor amplitude variations in the transmission coefficient, which is merely due to the coupling efficiency at the specific liquid-solid

interface, the results clearly reveal the zooming effect on the characteristic patterns in the P-UPS result. While the water immersed P-UPS misses part of the QSV contour, this information is fully retrieved by applying isopropyl alcohol as the immersion liquid. The opposite is true when immersion takes place in a water/glycerol mixture, resulting in a close-up view of the QL and QSH contours, and in the complete absence of the QSV contour.

Note that the immersion fluid only influences the wave curve map of the critical bulk wave angles θ_{crit}^{j} obtained through the P-UPS technique, since the wave characteristics within the solid obviously remain unchanged upon different fluid loading. Hence, the concept of artificial zooming is a handy feature in order to expand the applicability of the P-UPS technique to a broader range of materials.

However, changing the coupling liquid from water to isopropyl alcohol in order to put on view the complete in-plane bulk wave characteristics is easier said than done. Because of safety regulations in our laboratory (open tank, with immersed translation and rotation accessories) we are not allowed to work with chemical products that are inflammable. We therefore only demonstrate the 'close-up' zooming effect experimentally for a $[0]_8$ carbon/epoxy laminate immersed in various water/glycerol liquids, each having its specific mixture ratio (see Figure 6-13). As the mixture ratio increases, the P-UPS image is gradually zoomed in (best seen in the insets of Figure 6-13), which fully supports the numerical computations. During the experiments, it was noted that the 35%-65% mixture basically consisted of two liquid phases: a saturated water/glycerol phase and a pure glycerol phase. Around $\varphi = 60°$, we stirred the immersion liquid as we observed that a small layer of pure glycerol was surrounding the investigated sample. This explains the sudden increase in transmitted amplitude as pure glycerol attenuates an ultrasonic wave better than the 35%-65% phase. Towards the end of the experiment, it can be observed that the transmission amplitude steadily decreases. Again this has to be attributed to the steady accumulation of a pure glycerol layer at the free surfaces of the sample.

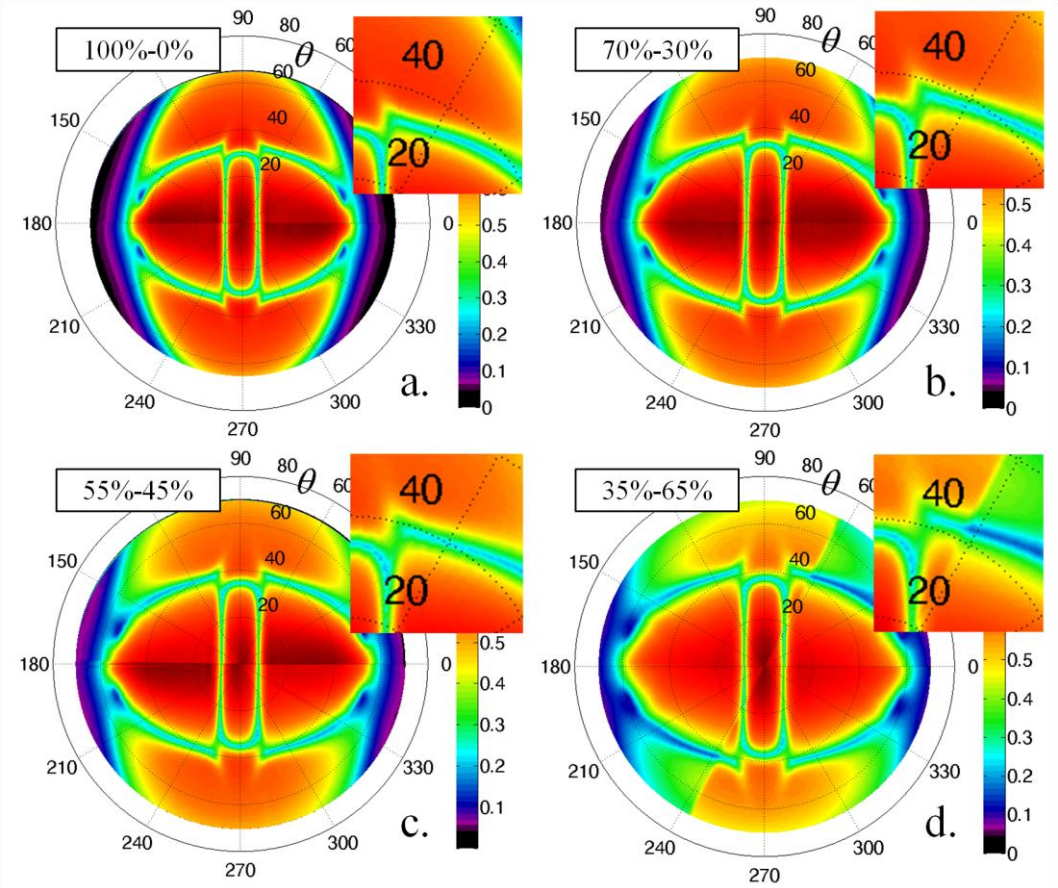

Figure 6-13: P-UPS for a $[0]_8$ carbon/epoxy laminate recorded at $f_c d$ = 5.5 MHz.mm in a water-glycerol mixture: (a) 100%-0% (pure water), (b) 70%-30%, (c) 55%-45% and (d) 35%-65%. The lensing effect is best seen in the insets.

6. 5. Conclusions

This chapter outlined a procedure to efficiently extract relevant bulk wave characteristics: (i) critical bulk wave angle profile, (ii) phase velocity profile, (iii) slowness curve, (iv) walk-off angle profile and (v) energy velocity profile, for the different polarization states by analyzing a single experimental P-UPS recording. The obtained wave curves represent the local material characteristics. The extraction procedure has been demonstrated for an aluminum and an autoclave manufactured $[0]_8$ carbon/epoxy laminate, both having plate-like features. Comparison of the experimental results with numerical modeling yields satisfying agreement. The obtained results show

that the $[0]_8$ carbon/epoxy laminate exhibits an extraordinary large walk-off angle $\xi^{QSH} \approx 70°$. As such, we emphasize that it is extremely important to properly understand the walk-off concept in order to correctly interpret the obtained signals in NDT and material inspection in general.

In addition, it is shown that the applicability of the P-UPS technique can be extended in order to investigate a broader range of materials, simply by considering a different immersion liquid. Apart from enhancing the coupling of the ultrasonic waves to the solid, the immersion liquid can also produce a lensing effect which provides a means to zoom in or out on the P-UPS fingerprint in order to capture all relevant P-UPS contours.

6. 6. References

[1] Merkulov, L.G. and L.A. Yakovlev, *Propagation and reflection of ultrasonic beams in crystals.* Soviet Physics - Acoustics, 1962. 8(1): p. 6.

[2] Rose, J.L., *Ultrasonic Waves in Solid Media*. 1999: Cambridge University Press. 454.

[3] Auld, B.A., *Acoustic Fields and Waves in Solids, second edition*. 1990, Florida: Krieger publishing company. 856.

[4] Balasubramaniam, K. and C.V. Krishnamurthy, *Ultrasonic guided wave energy behavior in laminated anisotropic plates.* Journal of Sound and Vibration, 2006. 296(4-5): p. 968-978.

[5] Potel, C., S. Baly, J.F. de Belleval, M. Lowe, and P. Gatignol, *Deviation of a monochromatic Lamb wave beam in anisotropic multilayered media: Asymptotic analysis, numerical and experimental results.* Ieee Transactions on Ultrasonics Ferroelectrics and Frequency Control, 2005. 52(6): p. 987-1001.

[6] Amirkhizi, A.V., A. Tehranian, and S. Nemat-Nasser, *Stress-wave energy management through material anisotropy.* Wave Motion, 2010. 47(8): p. 519-536.

[7] Nolan, C.J. and W.W. Symes, *Anomalous reflections near a caustic.* Wave Motion, 1997. 25(1): p. 1-14.

[8] Balasubramaniam, K. and N.S. Rao, *Inversion of composite material elastic constants from ultrasonic bulk wave phase velocity data using genetic algorithms.* Composites Part B-Engineering, 1998. 29(2): p. 171-180.

[9] Chu, Y.C. and S.I. Rokhlin, *A method for determination of elastic-constants of a unidirectional lamina from ultrasonic bulk velocity-measurements on [0/90] cross-ply composites.* Journal of the Acoustical Society of America, 1994. 96(1): p. 342-352.

[10] Balasubramaniam, K. and S.C. Whitney, *Ultrasonic through-transmission characterization of thick fibre-reinforced composites.* Ndt & E International, 1996. 29(4): p. 225-236.

[11] Vishnuvardhan, J., C.V. Krishnamurthy, and K. Balasubramaniam, *Genetic algorithm reconstruction of orthotropic composite plate elastic constants*

from a single non-symmetric plane ultrasonic velocity data. Composites Part B-Engineering, 2007. 38(2): p. 216-227.

[12] Wang, L. and F.G. Yuan, *Group velocity and characteristic wave curves of Lamb waves in composites: Modeling and experiments.* Composites Science and Technology, 2007. 67(7-8): p. 1370-1384.

[13] Kersemans, M., K. Van Den Abeele, N. Lammens, J. Degrieck, F. Zastavnik, J. Gu, L. Pyl, H. Sol, and W. Van Paepegem. *Determination of the Fiber Direction and the C-Tensor of a UD Carbon/Epoxy Composite by means of the Ultrasonic Polar Scan*. in *Proceedings of the 2013 International Congress on Ultrasonics (ICU 2013)*. 2013. Singapore.

[14] Declercq, N.F., J. Degrieck, and O. Leroy, *Simulations of harmonic and pulsed ultrasonic polar scans.* Ndt & E International, 2006. 39(3): p. 205-216.

[15] Kersemans, M., W. Van Paepegem, A. Martens, K. Van Den Abeele, L. Pyl, F. Zastavnik, H. Sol, and J. Degrieck, *The Quasi-Harmonic Ultrasonic Polar Scan for Material Characterization: Experiment and Numerical Modeling.* Submitted to Ultrasonics, 2013.

[16] Kersemans, M., W. Van Paepegem, K. Van Den Abeele, L. Pyl, F. Zastavnik, H. Sol, and J. Degrieck, *Pitfalls in the Experimental Recording of Ultrasonic (Backscatter) Polar Scans for Material Characterization.* Ultrasonics, 2014. In Press DOI: 10.1016/j.ultras.2014.04.013.

[17] Schoenberg, I.J., *Contributions to the problem of approximation of equidistant data by analytic functions.* Quarterly of Applied Mathematics, 1946. 4: p. 45-99; 112-141.

[18] Piegl, L.A. and W. Tiller, *The NURBS book*. 2nd ed. 1997, New York: Springer-Verlag. 647.

[19] De Boor, C., *On calculating with B-splines.* journal of approximation theory, 1972. 6: p. 50-62.

[20] Holland, P.W. and R.E. Welsch, *Robust Regression using Iteratively reweighted least-squares.* Communications in Statistics - Theory and Methods, 1977. 6(9).

[21] Imamura, K. and S. Tamura, *Negative refraction of phonons and acoustic lensing effect of a crystalline slab*. Physical Review B, 2004. 70(17).

[22] Espinosa, V., V.J. Sanchez-Morcillo, K. Staliunas, I. Perez-Arjona, and J. Redondo, *Subdiffractive propagation of ultrasound in sonic crystals.* Physical Review B, 2007. 76(14).

[23] Every, A.G., A.A. Maznev, W. Grill, M. Pluta, J.D. Comins, O.B. Wright, O. Matsuda, W. Sachse, and J.P. Wolfe, *Bulk and surface acoustic wave phenomena in crystals: Observation and interpretation.* Wave Motion, 2013. 50(8): p. 1197-1217.

Chapter 7

Identification of Complex Elasticity Tensor of (An)isotropic Materials from P-UPS Data

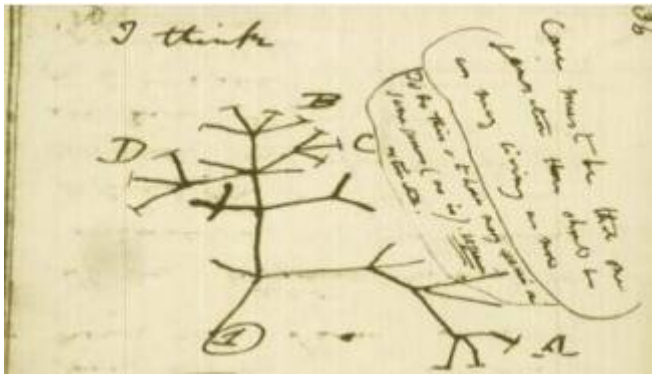

Darwin's groundbreaking diagram on the evolution of species which is founded upon three principles: variation, selection and heredity. At present, Darwin's principle has been mimicked in a multiplicity of optimization procedures.

Summary

Already in the early 1980's, it has been conjectured that the pulsed ultrasonic polar scan (P-UPS) provides a unique fingerprint of the underlying mechanical elasticity tensor at the insonified material spot. Until now, that premise has not been thoroughly investigated, nor validated, despite the opportunities this would create for NDT and materials science in general. In this chapter, the first-ever implementation of an inverse modeling technique on the basis of a genetic optimization scheme is reported in order to extract local material characteristics from an amplitude recorded P-UPS. The system identification procedure has been applied to both metals and fiber reinforced plastics.

7. 1. Introduction

Besides the classical ultrasonic C-scan, which has already proven its usefulness in detecting defects, delaminations as well as material heterogeneities, several more advanced techniques can quantitatively monitor the mechanical performance in order to ensure the designed functionality of a composite structure. At present, (nonlinear) resonant ultrasonic spectroscopy ((N)RUS) is a well-established technique to infer elasticity constants [1], and even monitor damage progression [2-4], of anisotropic materials. However, (N)RUS is a resonance based technique, in which the specifically prepared sample needs to be mounted in a device, making it useless for *in situ* determination of the material characteristics. The latter restriction also holds for techniques which are based on time measurements of bulk waves because measurements have to be taken at specific material orientations [5-11]. Besides, for anisotropic media the propagation- and energy velocity are decoupled (see Chapter 6), making the correct recording and subsequent interpretation of experimental data a rather difficult task. Plane wave transmission characteristics have been used by various research teams to extract the (visco)elastic material properties [12-13]. Basically, the sample is insonified at a few well-chosen oblique incidence angles with a broadband ultrasonic pulse which resembles a plane wave [14]. The transmitted wave field is recorded in time, normalized to the reference wave field, and further analyzed in the frequency domain. In this way the transmission coefficient is obtained as a function of the frequency.

The resulting transmission coefficient has maxima which relate to the condition for efficient stimulation of Lamb waves (similar as in the H-UPS), while the global level of the transmission coefficient is a measure for the attenuation. Another closely related technique which gained a lot of popularity over the last years concerns the application of guided waves, such as Lamb waves, Rayleigh waves, etcetera, which probe the structure under investigation. The stimulated guided wave interrogates the structure upon propagation, hence the recorded signal contains a watermark of the material characteristics [15-16]. The main disadvantage of such a guided wave based approach concerns the complexity of the data acquisition and the extensive post-processing in order to obtain the envisioned results, especially when the investigated structure is for example not-flat/curved [17-19]. Besides, the guided wave technique provides a global representation of the material characteristics, while it is often needed to obtain the material characteristics at a local material spot.

The characteristic contours in a UPS image are linked to the generation of critically refracted (quasi-)bulk waves in the case of sound pulses [20], and thus are from a physics point of view directly connected to the mechanical properties of the sample material at the targeted spot. Already in the early 1980's, it has been conjectured that the pulsed ultrasonic polar scan provides a unique fingerprint of the underlying mechanical elasticity tensor at the insonified material spot [20-26]. Until now, that premise has not been thoroughly investigated, nor validated, despite the opportunities this would create for NDT and materials science in general. Considering that the P-UPS methodology relies on a simple amplitude measurement, and is fully applicable to thin plate-like materials for which neither specific sample preparation, nor prior knowledge about the mechanical nature of the sample is required, makes it very appealing for industrial implementation to identify material characteristics. In addition, the P-UPS offers an enormous amount of redundant data from which an inversion procedure would obviously benefit to efficiently extract material properties with a high degree of accuracy, even in the presence of scatter.

In this chapter, we report on the first-ever implementation of an inverse modeling technique on the basis of a genetic optimization scheme in order to extract local material characteristics from an amplitude recorded P-UPS. The next section gives a short description of the implemented system identification procedure, which is based on an optimization procedure by

means of a genetic algorithm (GA). Inversion results are first presented and discussed for synthetic data, in order to explore the opportunities as well as the limitations of the method for material characterization. Thereafter, the system identification procedure is applied to experimentally obtained P-UPS experiments for several annealed aluminum samples in different mechanical health, cold-rolled DC06 steel samples and an autoclave manufactured $[0]_8$ carbon fiber reinforced plastic plate.

7. 2. Genetic Algorithm: Optimization Procedure

Since the characteristic contours in a P-UPS image are a representation of the in-plane critical bulk wave angles for all polarization states [20], it is clear that the inversion procedure should be based on the well-known Christoffel equation (see analysis in Section 6.2). Application of Snell-Descartes' law for externally born sound leads to the determination of the critical bulk wave angles which can then be compared to the characteristic contours in a P-UPS image.

By selecting an appropriate set of elastic constants, the computed in-plane bulk wave angle profiles can then be matched with the P-UPS contours. In general, composite materials are anisotropic of nature, in which orthotropy can be considered the most common symmetry class. A full description of the orthotropic nature can be given by knowledge of nine elastic constants. Hence it is clear that an appropriate set of these nine constants, to obtain a good fit with the contours in the P-UPS image, cannot be simply obtained by trial and error. This is especially true considering that the elastic constants describe a highly nonlinear space. Instead, an optimization scheme is employed which relies on the principle of Darwin, i.e. an abstraction is made in terms of a population in which the hierarchy is determined by the survival of the fittest (see Figure 7-1). A set of different C_{ij}'s corresponds to a complete population in the GA, while a single elasticity tensor C_{ij} corresponds to an individual in the population. The choice for a genetic optimization procedure is mainly triggered by its great flexibility for optimizing nonlinear multi-dimensional problems, its capability to converge to the near optimum of the problem regardless the initial guess and the fact that a GA can be easily parallelized, reducing the computational effort. An even more important advantage of GA's concerns its capability to not remain trapped in a suboptimal solution since a population covers different parts of the parameter space. GA's have already been successfully employed in

various studies for inverting wave velocity data in order to obtain a measure of the mechanical properties [7, 9, 16].

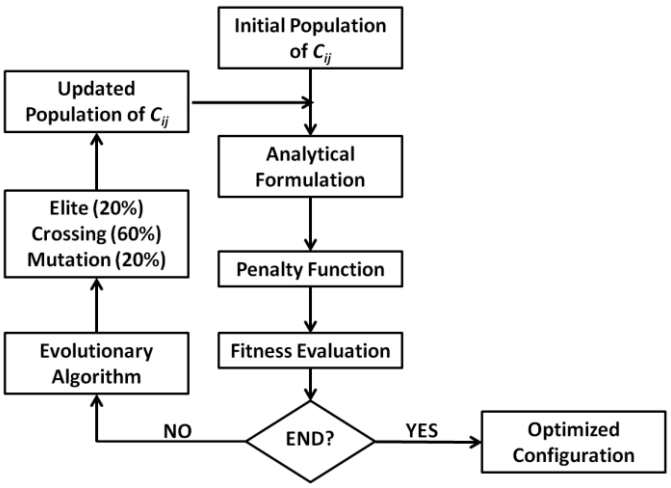

Figure 7-1: Schematic of the optimization algorithm.

Basically we start with a random initial population, consisting of 100 individuals, i.e. 100 unique elasticity tensors C_{ij}, from which the corresponding critical bulk wave profiles are computed through application of Christoffel's equation in combination with the Snell-Descartes' law. The parameter space needs bounds in which the GA has a complete freedom of selectivity in order to obtain the optimized set of elasticity constants C_{ij}. Of course, these bounds should be chosen as narrow as possible to speed up the inversion process, while assuring that the space contains the optimal solution. Typically, we set the bounds at ±90% of the estimated elasticity constants C_{ij} to make sure that the parameter space contains the optimal solution. The increment at which the elasticity parameters can be updated, is chosen fairly small in order to improve the accuracy. The computed critical bulk wave angle profiles are then simply superposed on the P-UPS from which a measure of their fitness is obtained by summing the interpolated P-UPS amplitudes at the exact coordinates of the computed curves, and this for the different polarization states

$$\sum_k \sum_l A_I\left(\varphi_k, \theta^l_{k,Christ}\right) \tag{1}$$

with $A_I\left(\varphi_k, \theta^l_k\right)$ the interpolated transmitted pulse amplitude at coordinates $\left(\varphi_k, \theta^l_{k,Christ}\right)$ in which φ_k, respectively $\theta^l_{k,Christ}$, represents the polar

direction, respectively the computed critical bulk wave angle for a given elasticity tensor C_{ij} and $l = QL, QSH, QSV$ denotes the quasi-longitudinal, the quasi-shear horizontal and the quasi-shear vertical polarization state.

This is illustrated in Figure 7-2 for an arbitrary elasticity tensor C_{ij}.

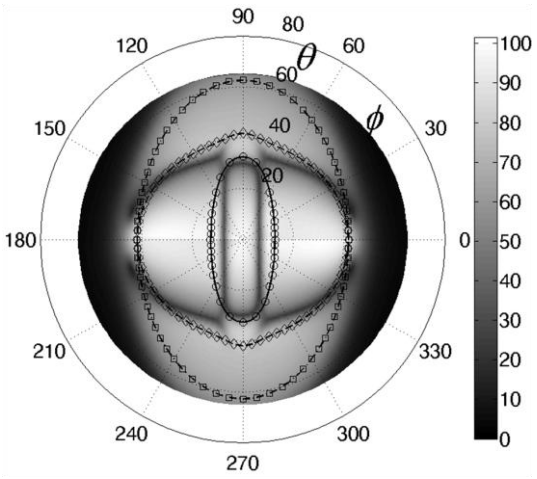

Figure 7-2: P-UPS experiment for a $[0]_8$ carbon/epoxy laminate. The critical bulk wave angle profiles, computed for an arbitrary elasticity tensor C_{ij}, are superposed.

Since the computed profiles should merge to the low-amplitude contours in the P-UPS image in order to obtain a qualified elasticity tensor C_{ij}, it is clear that the above criterion has to be minimized:

$$\min\left(\sum_{k}\sum_{l=QL,QSH,QSV} A_I\left(\varphi_k, \theta^{l}_{k,Christ}\right)\right) \tag{2}$$

The fact that the superimposed lines do not fully match the P-UPS contours in Figure 7-2 clearly reveals that the current elasticity tensor C_{ij} cannot be regarded as the optimal elasticity tensor C_{ij}.

It is noted that the P-UPS contours are also characterized by a high local curvature value (see Section 5.2.1), hence the fitness criterion can also be adapted in order to maximize the summed curvature values. In fact, this criterion is applied to the P-UPS data of the metallic samples because of the accelerated convergence.

The above procedure is executed for each elasticity tensor C_{ij} in the current population, the obtained fitness values for that population are then sorted in descending order. After this, the current population generates the next population by producing descendants. This step is basically dictated by three descendant-generation rules. First, those individuals having superior fitness values are directly recruited in the next generation according to the principle of elitism, thus forming the elite children (20%). Second, crossover children are formed by randomly mixing the characteristics of any two individuals (60%). Lastly, the next population is further complemented with random mutations of an individual by randomly flipping bit values from 0 to 1 and vice versa, thus resulting in a set of mutated individuals (20%). Once the next generation is created, the fitting procedure is repeated in order to obtain a fitness value of the updated generation. This loop is repeated for many updated populations, until convergence is obtained. The stopping procedure is activated when two criterions are satisfied at the same time. The variation of the fitness value of both the best individual and the mean of the current population should be sufficiently small over 10 subsequent generations. Once these conditions are fulfilled, the procedure is stopped and the optimized elasticity tensor C_{ij} is obtained. Figure 7-3 shows a graphic representation of the evolution of the fitness for the mean (blue) and for the best individual (black) of a population during the inversion procedure. Hence it can be readily seen that the fitness value is high at the start of the inversion procedure (Generation 0), and converges to a steady state at the end of the inversion procedure (Generation 174). While the fitness value of the best individual steadily decreases, the mean fitness shows an unsteady course with several sharp peaks. This behavior is typical for a genetically based procedure, as it does not work in a deterministic way.

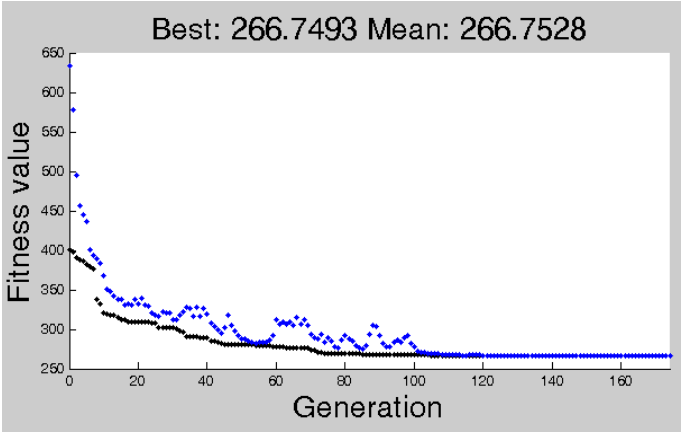

Figure 7-3: Evolution of mean fitness value of the current generation (blue) and fitness of the best individual within the current generation (black) during optimization.

Nevertheless, our first inversion results revealed that our basic assumption, being the fact that the P-UPS contours provide a one-to-one relationship with the in-plane critical bulk wave angles [20, 22], is not exactly valid. This is numerically demonstrated in Figure 7-4 for a hypothetical transversal isotropic material.

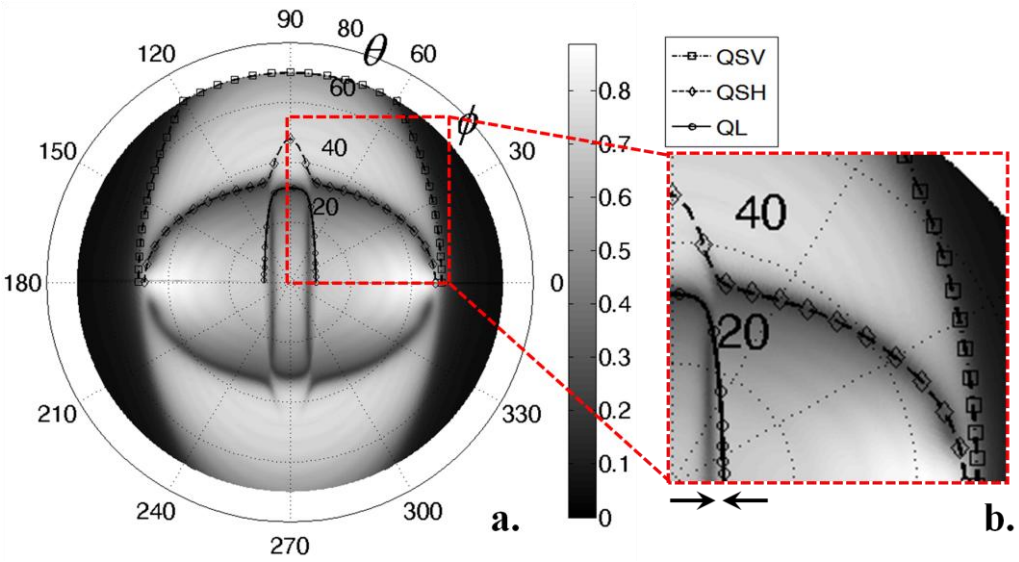

Figure 7-4: P-UPS simulation at *fd* = 5 MHz.mm for a hypothetical orthotropic material with the computed critical bulk wave angle profiles superposed for the range $\varphi \in [0°,180°]$ (a) and magnification to accentuate the discrepancy between P-UPS contours and critical bulk wave angle profiles (b).

It can be seen that the superposed critical bulk wave angle profiles slightly deviate from the characteristic contours in the numerically computed P-UPS, although both have been computed with the same set of material parameters. Especially for the inner contour, which relates to the stimulation of the in-plane propagating quasi-longitudinally (QL) polarized bulk wave, and in extension to the stiffness modulus C_{ii}, this discrepancy can be clearly observed along $\varphi = 0°$ (see Figure 7-4b). The position of this P-UPS minimum is rather dictated by that incident angle θ where the shear wave component in the solid becomes dominant over the longitudinally polarized component [27]. Although the angular deviation can be considered to be small, it is critical to account for in order to obtain a correct and accurate inversion of the elasticity tensor C_{ij} from a P-UPS image. Especially when considering that the here considered composite material has a very high mechanical stiffness along $\varphi = 0°$, which implies that the inner contour has a small incident angle θ. According to Snell-Descartes' law, any small change in incident angle θ then results in a substantial change in wave speed and in extension to the underlying mechanical stiffness. Therefore, the system identification procedure on the basis of the Christoffel solutions should be extended to account for this discrepancy.

The extension of the inversion procedure basically relies on the same scheme as described in Figure 7-1. Though, the initial population is now defined by the elasticity tensor C_{ij} obtained in the first inversion procedure. From this set of elasticity tensors C_{ij}, P-UPS sectors at a few fixed polar angles φ are computed. The P-UPS simulations are performed according to the recursive stiffness matrix method (see Chapter 4) [28-31]. By allowing small perturbations in the elasticity tensor C_{ij}, the local minima in the computed P-UPS sections are matched with the observed minima in the P-UPS experiment. The main reason why only a few sectors are considered, instead of the full P-UPS image, is mainly triggered by computation constraints. Indeed, the simulation of a P-UPS, having the same angular resolution as a P-UPS experiment, involves the computation of more than 1 million incidence angles [32]. Moreover, since an ultrasonic pulse is employed, it is critical to account for its temporal frequency content to obtain a realistic simulation. The latter is taken care of by means of a Fourier integral. To speed up this process, the integral is replaced by its discrete counterpart being the fast Fourier transform (FFT), in which typically around 400 dominating frequencies are selected in the spectrum of the ultrasonic pulse. Finally, the simulated P-UPS has to be fitted to the recorded P-UPS.

Although the first optimization step on the basis of Christoffel's equation provides a good estimation of the elasticity tensor C_{ij}, still numerous P-UPS simulations with updated material properties are needed in order to fine-tune the material properties. With current high performance numerical facilities, such a full P-UPS inversion would take several days. On the contrary, by starting from the elasticity tensor C_{ij} obtained in the first optimization step and considering only a few sectors of the P-UPS in the second optimization step, the processing time of the complete inversion procedure could be limited to less than 5 minutes on a standard computer.

7. 3. Inversion of Synthetic P-UPS Data

In order to demonstrate the described procedure to extract the local in-plane mechanical parameters from P-UPS data, results are first presented for synthetic data. A numerically computed P-UPS, at fd = 3.5MHz.mm, is generated for a transversal isotropic material with stiffness parameters listed in the first column of Table 7-1. The imaginary elasticity parameters (which describe attenuation characteristics) have been fixed at 2.5% of the real part of the elasticity tensor. The inversion procedure is then applied to the P-UPS simulation in order to retrieve the employed mechanical properties. The parameter bounds for the optimization procedure are fixed at ±90% of the actual material properties. Because the initial population of the GA is composed of a set of randomly chosen individuals and the optimization procedure does not flow in a deterministic way, it is clear that the inversion procedure is a stochastic process in which the determined optimum cannot be considered to be fixed. To assure the appropriateness of the implemented inversion procedure for the problem considered here, the inversion has been applied ten times to the numerically computed P-UPS image from which the standard error σ is determined. In addition, the inversion procedure has been applied to synthetic data with added scatter. The scatter has been modeled by adding a random number, within the interval $[-X,+X]/100$ in case of a scatter level of X%, to the transmission amplitudes. Afterwards the absolute value of the scattered amplitudes is considered in order to avoid the presence of non-physical negative amplitude values. A scatter level of 5%, 15% and 30% has been considered. Figure 7-5a-b displays the numerically computed P-UPS, used as an input for the inversion procedure, with no scatter and scatter level 30%.

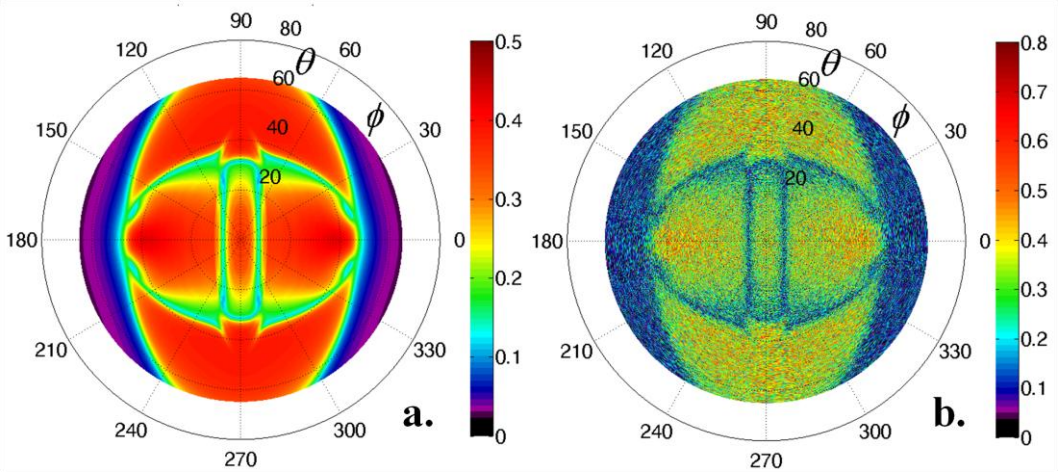

Figure 7-5: P-UPS simulation: no scatter (a) and 30% scatter (b).

The optimization results for the synthetic data are grouped and listed in Table 7-1. Note that the last row (C_{23}) has been indirectly obtained by applying the well-known symmetry relation of transversal isotropic media [33]. As such, it provides an additional measure for the appropriateness of the here considered inversion procedure.

Table 7-1: Inversion results for synthetic data: mean value ± standard deviation (relative error in %). The last row is put in gray as it has been obtained in an indirect way.

	Input [GPa]	*Output [GPa]*			
		Scatter 0%	*Scatter 5%*	*Scatter 15%*	*Scatter 30%*
C_{11}	117.43	117.46 ± 0.50 (+0.03%)	118.05 ± 3.05 (+0.53%)	114.99 ± 5.91 (-2.12%)	130.55 ± 23.93 (+10.05%)
$C_{12} = C_{13}$	4.99	5.03 ± 0.07 (+0.96%)	5.05 ± 0.38 (+1.20%)	4.96 ± 0.70 (-0.54%)	5.76 ± 2.39 (+13.39%)
$C_{22} = C_{33}$	13.94	13.96 ± 0.08 (+0.15%)	14.01 ± 0.10 (+0.50%)	13.97 ± 0.30 (+0.19%)	14.76 ± 1.32 (+5.57%)
C_{44}	3.90	3.91 ± 0.07 (+0.27%)	3.89 ± 0.06 (-0.28%)	3.92 ± 0.11 (+0.48%)	3.98 ± 0.29 (+1.95%)
$C_{55} = C_{66}$	7.19	7.16 ± 0.00 (-0.44%)	7.13 ± 0.04 (-0.87%)	7.06 ± 0.13 (-1.82%)	6.62 ± 0.93 (-8.56%)
$C_{23} = C_{22} - 2C_{44}$	6.14	6.14 ± 0.21 (0.00%)	6.23 ± 0.08 (-1.47%)	6.13 ± 0.47 (-0.16%)	6.8 ± 0.89 (-10.75%)

It is clear that the optimized constants for the non-scattered data are very close to the input constants, while the standard error σ is fairly small. Although the error and standard deviation of the inversion results for the data with scatter increase, it can be readily verified that good inversion results are obtained up to 15% scatter, indicating the robustness of the method. Considering the large amount of useful data in a P-UPS, this could have been foreseen. Further increase of the scatter level up to 30% deteriorates the accuracy of the inversion results significantly. However, 30% scatter can be considered to be extremely high in most realistic environments.

In conclusion, we extracted the elastic parameters C_{11}, C_{12}, C_{22}, C_{44} and C_{55} in a stable and robust way by inverting (scattered) P-UPS data of a hypothetical material. For a material with a lower symmetry class than transversal isotropy, one can further decouple C_{66} from C_{55}. However, to obtain the remaining orthotropic parameters (C_{13}, C_{23} and C_{33}) a second P-UPS has to be performed in another material symmetry plane. Nevertheless, since most structural components are plate-like, these characteristics are of minor importance.

7. 4. Inversion of Experimental P-UPS Data

In this section, the inversion procedure is applied to amplitude recorded P-UPS experiments: (i) different extruded and annealed aluminum samples, (ii) cold-rolled DC06 steel samples and (iii) a carbon fiber reinforced laminate possessing a large degree of anisotropy. For the inversion of experimentally obtained P-UPS images, the bounds are fixed at ±90% of the estimated material properties.

7. 4. 1. Annealed Aluminum

Two annealed extruded aluminum samples with different chemical composition, having a respective thickness d_1 = 1.5 mm (Al_1) and a thickness d_2 = 1.4 mm (Al_2), are scanned. The density of the samples was measured according to ASTM D792 (2008): "Standard Test Methods for Density and Specific Gravity (Relative Density) of Plastics by Displacement", a value of ρ = 2676.6 kg/m^3 for Al_1 and ρ = 2693.2 kg/m^3 for Al_2 is determined. The recorded P-UPS for Al_2 is shown in Figure 7-6. Obviously, the recorded P-UPS of Al_1 is very similar and is therefore omitted. The mechanical isotropy

of the aluminum sample Al_2 is clearly reflected in the circular shape of the characteristic patterns. Furthermore, only 2 characteristic contours are discerned because of the degeneration of the QSH and QSV wave in case of isotropy.

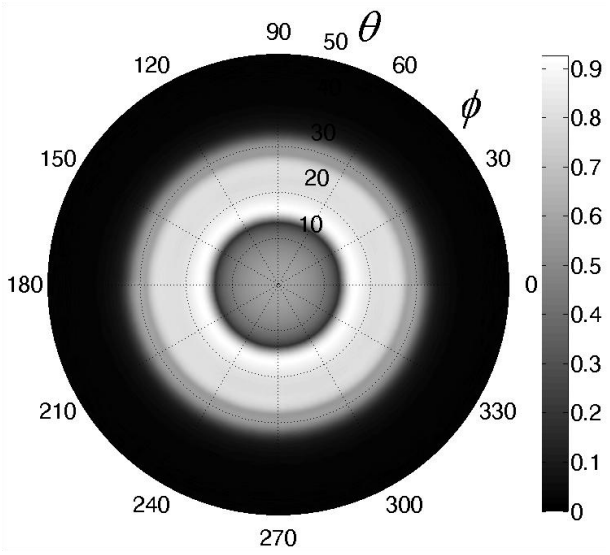

Figure 7-6: Recorded P-UPS at *fd* = 5 MHz x 1.4 mm for the Al_2 sample.

Because of human error when mounting the sample in the experimental setup, the recorded experiment has to be centered first to the polar axes [34]. This procedure is similar as described in Section 6.3.1. The inversion procedure is then applied ten times to the centered P-UPS experiment in order to extract the local material parameters. Because of the isotropy of the aluminum sample, it is clear that the inversion procedure can be limited to the optimization of two material parameters, being C_{11} and C_{44}. In addition, to narrow down the bounds for the 2D parameter space, one could perform a rough sweep over an arbitrary parameter space and evaluate the objective function. A graphical representation of such a sweep is shown in Figure 7-7. Hence, by selecting the red-colored regions (good fitness), the bounds for the parameter space can be significantly narrowed which will speed up the inversion procedure.

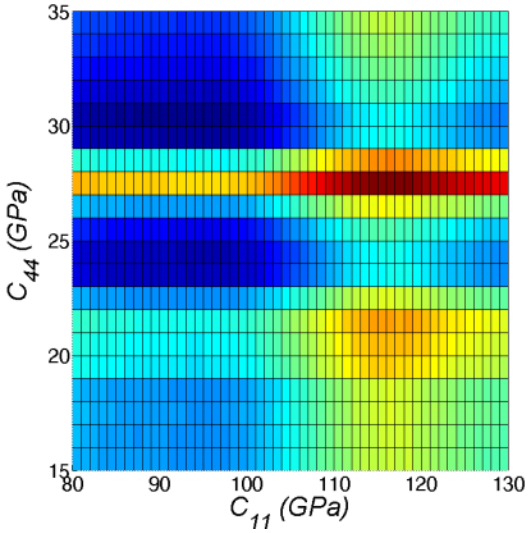

Figure 7-7: Rough sweep over 2D parameter space for the investigated aluminum sample. The red color corresponds to good fitness value, the blue color to bad fitness value.

Anyhow, the parameter space for the inversion procedure has been expanded to C_{11}, C_{12}, C_{22}, C_{44}, C_{55} and C_{66}, in order to confirm the mechanical symmetry of the investigated aluminum samples. Also wide bounds (±90% of the estimated material properties) for the parameters have been applied to assure that the optimal solution is enclosed. The results are listed in Table 7-2. The number between parentheses represents the standard deviation of the inversion procedure.

Since we obtained slightly deviating material parameters for both aluminum samples, each sample has been scanned a second time at a different location. It is clear that the second P-UPS scans yield very consistent inversion results in comparison with the results obtained from the first P-UPS scans. Since both aluminum samples are from a different class of alloy, it can be stated that the observed deviation in material parameters between both samples Al_1 and Al_2 is a reflection of their slightly different chemical composition, rather than experimental or numerical error.

Table 7-2: Inversion results for the different aluminum samples. The inversion procedure has been applied ten times, from which the mean value and standard deviation (between brackets) is obtained.

		C_{11} [GPa]	C_{12} [GPa]	C_{22} [GPa]	C_{44} [GPa]	C_{55} [GPa]	C_{66} [GPa]
Al_1	P-UPS 1	105.1093 (0.275)	54.1320 (0.255)	105.2437 (0.5037)	25.5220 (0.000)	25.5220 (0.000)	25.5220 (0.000)
	P-UPS 2	104.9295 (0.000)	53.8854 (0.000)	104.9292 (0.001)	25.5220 (0.000)	25.5220 (0.000)	25.5220 (0.000)
Al_2	P-UPS 1	108.6877 (0.000)	55.9814 (0.000)	108.6878 (0.000)	26.3532 (0.000)	26.3532 (0.000)	26.3532 (0.000)
	P-UPS 2	108.6877 (0.000)	56.6576 (0.000)	108.6877 (0.000)	26.2076 (0.000)	26.0092 (0.000)	26.0151 (0.000)
Al_2 Plastic Strain 1	P-UPS 1	108.6857 (0.005)	56.3431 (0.029)	108.7333 (0.063)	26.1832 (0.000)	26.1832 (0.000)	26.1832 (0.000)
	P-UPS 2	108.6838 (0.009)	56.3877 (0.120)	108.8246 (0.2481)	26.1832 (0.000)	26.1832 (0.000)	26.1832 (0.000)
Al_2 Plastic Strain 2	P-UPS 1	108.6878 (0.000)	56.3213 (0.000)	108.6877 (0.000)	26.1832 (0.000)	26.1832 (0.000)	26.1832 (0.000)
	P-UPS 2	108.6410 (0.002)	56.6085 (0.002)	108.6087 (0.004)	26.1481 (0.000)	25.9250 (0.000)	26.0990 (0.000)

The consistency between C_{11} and C_{22} on the one hand, and between C_{44}, C_{55} and C_{66} on the other hand clearly confirms the isotropic nature of both the aluminum samples Al_1 and Al_2. This was expected because both samples have been extruded, followed by a recrystallizing annealing process. To further ascertain the isotropic nature of the aluminum samples, one can evaluate the Zener anisotropy ratio $Z = \frac{2C_{44}}{C_{11} - C_{12}}$, in which $Z = 1$ corresponds to isotropy [35]. For Al_1, respectively Al_2, we obtain a Zener anisotropy ratio of $Z = 1.00065$, respectively $Z = 1.00368$, hence confirming the isotropic nature of the investigated aluminum samples. For isotropic symmetry, the inverted C_{ij} parameters can be easily converted in order to obtain the engineering constants E and ν. Table 7-3 lists the extracted engineering constants for the different aluminum samples. The relative error δ (in percent) with generally accepted engineering constants for aluminum, being $E = 70$ Gpa and $\nu = 0.34$, is added. It is clear that the P-UPS inversion results show excellent agreement with literature. Nevertheless, the statement that the slight differences in elastic properties are introduced by a different chemical composition could not be verified independently because of the limited sensitivity of a standard tensile test setup to measure the Young's modulus (in the order of ±2 GPa).

Table 7-3: Extracted engineering constants for the different aluminum samples. The error δ has been determined with respect to the literature values E = 70 GPa, ν = 0.34.

		E [GPa]	δ_E [%]	ν [-]	δ_ν [%]
LITERATURE		69 - 71	-	0.33 - 0.35	-
Al_1	P-UPS 1	68.41	-2.27%	0.3397	-0.09%
	P-UPS 2	68.37	-2.33%	0.3393	-0.21%
Al_2	P-UPS 1	70.62	+0.89%	0.3400	+0.00%
	P-UPS 2	69.86	-0.20%	0.3427	+0.79%
Al_2 Plastic Strain 1	P-UPS 1	70.24	+0.34%	0.3412	+0.35%
	P-UPS 2	70.25	+0.36%	0.3412	+0.35%
Al_2 Plastic Strain 2	P-UPS 1	70.24	+0.34%	0.3413	+0.38%
	P-UPS 2	69.85	-0.21%	0.3426	+0.76%

A further analysis is performed to the influence of a plastic deformation on the elastic material parameters of aluminum sample Al_2. Therefore, aluminum sample Al_2 has been loaded into its plastic regime by means of a displacement controlled hydraulic tensile machine at a load rate of 2 mm/min. After unloading and demounting the sample from the tensile machine, the sample has been scanned twice (near the region where plastic shear bands were observed visually) under similar circumstances as was done for the virgin sample. These steps were repeated for a second and higher tensile load level, inducing an even larger plastic deformation of the aluminum sample. The extracted material parameters for the plastically loaded aluminum samples have been added to Table 7-2 and Table 7-3. Compared to the results of the virgin aluminum sample, it can be stated that plastic straining does not affect the elastic material parameters. It is known from classical mechanics that a modest plastic deformation introduces strain hardening, but does not influence the elastic material properties.

Hence, the current results clearly demonstrate both the accuracy and reproducibility of the P-UPS technique for identifying the material parameters of isotropic media, even after a plastic loading cycle. The minor deviations between experiments and literature can be primarily attributed to five causes: (i) the presence of inevitable experimental errors and varying laboratory conditions, (ii) the fixed angular resolution ($\Delta\theta$ = 0.05°) of the P-UPS recording, (iii) errors induced by the inversion procedure, (iv) the

variation in chemical composition of different aluminum samples and (v) the variation of the elastic material properties within a single aluminum sample.

In order to demonstrate the influence of the different experimental pitfalls discussed in Chapter 5, several incorrectly recorded P-UPS experiments for aluminum have each been analyzed 10 times with the implemented system identification procedure. The inversion results are gathered in Table 7-4. The P-UPS experiments associated to rows "PITFALL 1", "PITFALL 2" and "PITFALL 2BIS" are each characterized by a corresponding misalignment of 1°, while the P-UPS experiment associated to row "PITFALL 5" corresponds to a gear clearance of 0.7°. Besides a deterioration of the accuracy of the inverted elastic parameters, also the standard deviation significantly increases, indicating that the inversion procedure get stuck in different suboptimal sets of data. This indicates the importance to counter the different experimental pitfalls according to the guidelines given in Chapter 5 in order to obtain good inversion results.

Table 7-4: Material parameters (mean value ± standard deviation) extracted from P-UPS recordings of an aluminum sample, exposing the influence of different experimental pitfalls discussed in Chapter 5.

	C_{11} [GPa]	C_{12} [GPa]	C_{22} [GPa]	C_{44} [GPa]	C_{55} [GPa]	C_{66} [GPa]
LITERATURE	107.74	55.50	107.74	26.12	26.12	26.12
NO PITFALLS	108.72 ± 0.13	56.92 ± 0.25	109.19 ± 0.58	26.20 ± 0.00	25.99 ± 0.00	26.02 ± 0.00
PITFALL 1	104.26 ± 11.04	58.64 ± 7.11	104.23 ± 11.02	23.43 ± 3.01	23.42 ± 3.04	22.80 ± 2.61
PITFALL 2	101.40 ± 11.22	54.23 ± 9.41	100.05 ± 13.26	27.04 ± 1.41	26.75 ± 1.17	24.08 ± 2.85
PITFALL 2 BIS	105.13 ± 22.28	56.08 ± 6.10	100.72 ± 12.19	27.79 ± 0.08	26.94 ± 1.89	24.54 ± 3.61
PITFALL 5	106.79 ± 6.14	52.53 ± 6.44	106.41 ± 6.68	27.05 ± 0.28	26.86 ± 0.18	26.78 ± 0.01

7. 4. 2. Cold-Rolled DC06 Steel

Cold-rolled DC06 steel, with a measured density of $\rho = 7704.7$ kg/m^3 (ASTM D792), is a very mild steel which is very popular in automobile industry because of its excellent formability. It is known for its pronounced anisotropic plastic behavior, which is best reflected in the famous cup drawing test [36]. Most materials form 4 cups, while the DC06 steel forms 6 cups because of its anisotropic plastic properties [37]. It is very tempting to

generalize this plastic anisotropy to the elastic regime. Though, such a generalization would definitely yield incorrect results. Here, the P-UPS technique is employed to check whether the cold-rolled DC06 steel possesses any anisotropy in its elastic region.

The recorded P-UPS for the DC06 steel is shown in Figure 7-8. At first sight it could be perceived that the characteristic patterns are circles, thus reflecting isotropic symmetry.

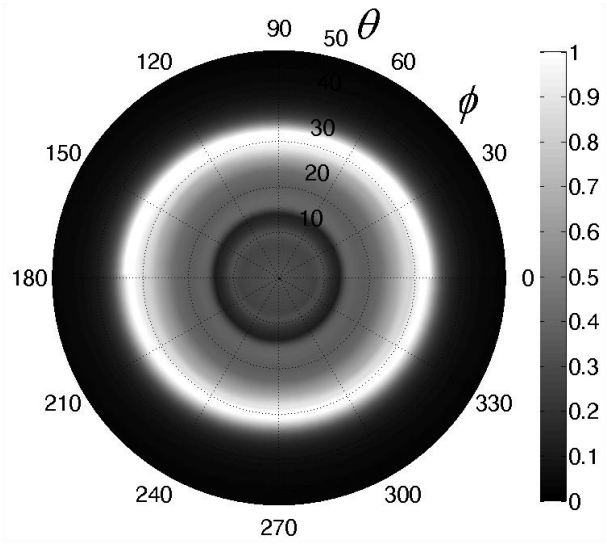

Figure 7-8: Recorded P-UPS at *fd* = 5 MHz x 0.8 mm for DC06 steel.

However, close observation reveals that the contours are slightly pressed inwards at $\varphi = 90° + n\pi$, thus having an elliptical shape. In the light of previous results, this implies that the DC06 steel has a certain elastic anisotropy. Similar to the aluminum samples, an inversion is performed to the C_{11}, C_{12}, C_{22}, C_{44}, C_{55} and C_{66} parameters. The results are listed in Table 7-5.

Table 7-5: Inversion results for the DC06 steel samples. Several DC06 samples have been scanned, from which the mean value and standard deviation is obtained.

C_{11} [GPa]	C_{12} [GPa]	C_{22} [GPa]	C_{44} [GPa]	C_{55} [GPa]	C_{66} [GPa]
301.7904 ±2.2681	157.0102 ±1.7143	294.2795 ±1.8371	71.6643 ±0.2084	69.8521 ±0.3714	71.5696 ±0.5127

Evaluation of the inverted results reveals some interesting particularities. The small deviation between C_{11} and C_{22} indicates that the DC06 samples cannot be considered strictly isotropic. This is further confirmed by the discrepancy between C_{44}, C_{55} and C_{66}. Unfortunately, no representative elastic data for the cold-rolled DC06 steel can be found in literature, which makes the validation of the inverted material parameters difficult. Anyway, our inversion results are qualitatively supported:

- Multiple P-UPS experiments at different DC06 samples have been performed to obtain a standard deviation of the inverted C_{ij} parameters. It can be readily verified that the inverted parameters systematically show a low standard deviation, which indicates the consistency of the inverted values.
- A finite element model, on the basis of the viscoplastic selfconsistent code (VPSC) [38], has been setup in a collaboration with Soroosh Naghdy, in order to estimate the elastic properties of a material after applying a rolling process in which only slip is considered. Since the chemical composition as well as the prehistory of the DC06 steel is unknown (trade secret), we assumed both pure body-centered cubic (bcc) iron alpha and pure face-centered cubic (fcc) austenitic stainless steel (see Figure 7-9).

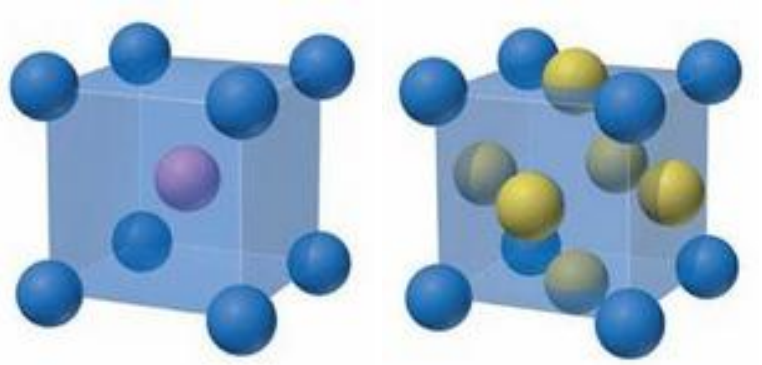

Figure 7-9: Schematic of bcc (left) and fcc (right) structure.

The stiffness matrix $\overset{=}{C}$ at the crystal level for the bcc, respectively fcc is given by (in GPa):

$$\underline{\underline{C}}_{bcc} = \begin{bmatrix} 233 & 135 & 135 & 0 & 0 & 0 \\ 135 & 233 & 135 & 0 & 0 & 0 \\ 135 & 135 & 233 & 0 & 0 & 0 \\ 0 & 0 & 0 & 117 & 0 & 0 \\ 0 & 0 & 0 & 0 & 117 & 0 \\ 0 & 0 & 0 & 0 & 0 & 117 \end{bmatrix} \tag{3}$$

and

$$\underline{\underline{C}}_{fcc} = \begin{bmatrix} 205 & 138 & 138 & 0 & 0 & 0 \\ 138 & 205 & 138 & 0 & 0 & 0 \\ 138 & 138 & 205 & 0 & 0 & 0 \\ 0 & 0 & 0 & 126 & 0 & 0 \\ 0 & 0 & 0 & 0 & 126 & 0 \\ 0 & 0 & 0 & 0 & 0 & 126 \end{bmatrix} \tag{4}$$

A poly-crystal has been composed, having 10,000 randomly oriented crystals. This is graphically shown in Figure 7-10 for three different crystal planes, having the Miller indices $\{100\}$, $\{110\}$ and $\{111\}$. Hence, the random distribution of the bcc and fcc crystals results in a structure having isotropic elasticity on the poly-crystal level.

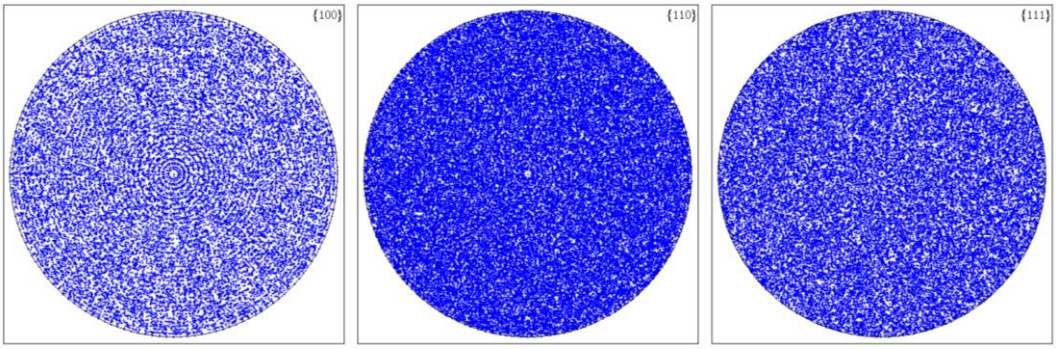

Figure 7-10: Crystal with 10000 random textured grains (before rolling). Visualization of the texture in the crystal plane having the Miller indices $\{100\}$ (a), $\{110\}$ (b) and $\{111\}$ (c).

Because of the applied rolling procedure, preferential axes are introduced, thus resulting in a poly-crystal which is textured. The introduced texture can be graphically verified in Figure 7-11 and Figure 7-12 for the bcc, respectively fcc crystal.

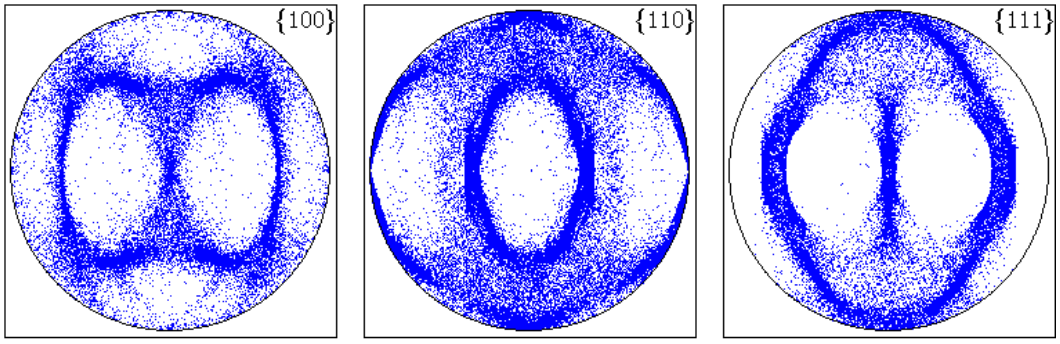

Figure 7-11: Body-centered cubic crystal with structured grains (after rolling). Visualization of the texture in the crystal plane having the Miller indices $\{100\}$ (a), $\{110\}$ (b) and $\{111\}$ (c).

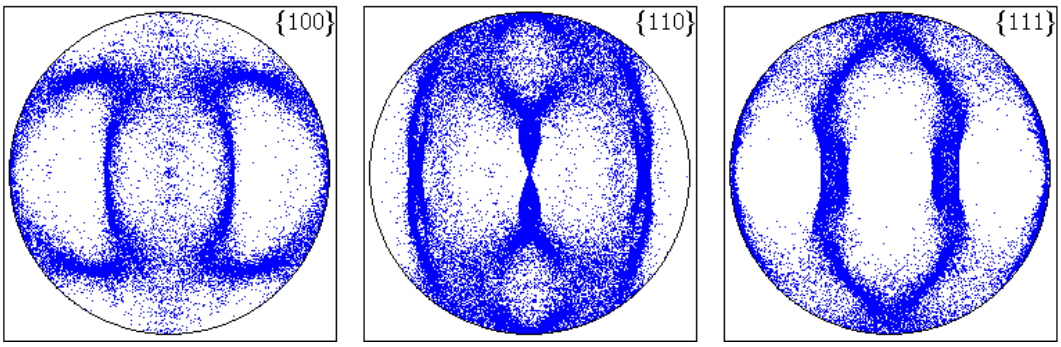

Figure 7-12: Face-centered cubic crystal with structured grains (after rolling). Visualization of the texture in the crystal plane having the Miller indices $\{100\}$ (a), $\{110\}$ (b) and $\{111\}$ (c).

Obviously, a single crystal does not transform its cubic symmetry, but on the poly-crystal level the elasticity properties do change because of the induced texture. This can be verified in the poly-crystal elasticity tensor C associated to the bcc and fcc textured grains of Figure 7-11 and Figure 7-12 (in GPa):

$$C_{bcc} = \begin{bmatrix} 283 & 108 & 112 & 0.030 & -0.056 & 0.009 \\ 108 & 296 & 99.5 & 0.072 & 0.066 & 0.026 \\ 112 & 99.5 & 291 & -0.101 & -0.010 & -0.036 \\ 0.030 & 0.072 & -0.101 & 117 & -0.035 & 0.057 \\ -0.056 & 0.066 & -0.010 & -0.035 & 117 & 0.024 \\ 0.009 & 0.026 & -0.036 & 0.057 & 0.024 & 117 \end{bmatrix} \quad (5)$$

and

$$C_{fcc} = \begin{bmatrix} 284 & 91.8 & 106 & 0.013 & 0.037 & 0.099 \\ 91.8 & 283 & 106 & -0.011 & 0.060 & -0.060 \\ 106 & 106 & 269 & -0.002 & -0.097 & -0.039 \\ 0.013 & -0.011 & -0.002 & 65.8 & -0.046 & 0.044 \\ 0.037 & 0.060 & -0.097 & -0.046 & 71.1 & 0.017 \\ 0.099 & -0.060 & -0.039 & 0.044 & 0.017 & 64.9 \end{bmatrix} \quad (6)$$

Hence, the elasticity changes from isotropy (before rolling), towards slight orthotropy (after rolling), which is in agreement with the P-UPS results. Note that the constants C_{ij}, with $i \neq j = 4,5,6$, slightly deviate from zero because of rounding errors. However, it may be clear that an exact quantitative comparison between the computed *C*-tensors and the P-UPS extracted *C*-tensor is useless because of the different unknown parameters as well as the assumed approximations in the simplified finite element model.

- Finally, few papers already demonstrated the orthotropic nature of rolled steel at the poly-crystal level [39]. They also found that the level of orthotropic symmetry on the poly-crystal level is very subtle.

On the other hand, computing the Zener anisotropy ratio when considering averaged C_{ij} parameters, a value of $Z^* = \frac{2(C_{44}+C_{55}+C_{66})/3}{(C_{11}+C_{22})/2-C_{12}} = 1.00732$ is obtained indicating that the material possesses a symmetry close to isotropy. Then, by simplifying the slightly orthotropic nature of the DC06 steel sample to isotropy, the following engineering constants are obtained: $E = 189.68 \pm 0.59$ GPa and $\nu = 0.345 \pm 0.001$. As the Poisson's ratio ν is higher than would be expected for steel, we performed additional tensile tests, provided with strain gages, on the DC06 steel in order to complement the ultrasonically determined values. A stiffness of $E = 192.36 \pm 1.64$ GPa and a Poisson's ratio of $\nu = 0.349 \pm 0.004$ have been determined, which are in excellent agreement with the P-UPS values. Though, it is clear that caution is required with these 'isotropic values' as the P-UPS revealed a small degree of elastic orthotropy for the DC06 steel. Nevertheless, for most engineering applications it can be considered as being effectively isotropic in the elastic regime.

7. 4. 3. $[0]_8$ Carbon/Epoxy Laminate

In this section, the experimental analysis is extended to the inversion of the local elasticity constants of a transversal isotropic carbon fiber reinforced plastic. The investigated $[0]_8$ carbon/epoxy laminates are composed of unidirectional prepreg layers, with thickness $d \approx 0.14$ mm and a measured fiber volume fraction $V_f \approx 55\%$, from the type Fibredux 920-CX (company Ciba-Geigy). The laminates have been autoclave manufactured according to the instructions of the supplier, i.e. a 60 minutes cycle at a temperature of $T = 125°C$ and a pressure of $p = 3.5$ bar. The density of the sample is measured according to ASTM D792, a value of $\rho = 1528.6$ kg/m^3 is determined. The elastic material properties of the material are listed in Table 7-6.

Table 7-6: Material properties for the carbon/epoxy laminate. Column 1 to 5 lists the data obtained from respectively the supplier (CIBA GEIGY), literature [40], conventional tests [41], micro-mechanical model Chamis [42] and micro-mechanical model Puck-Foye [43-44]. The last column lists the P-UPS inverted material parameters. Bold values have been obtained in our lab in a direct way, *italic* values are obtained indirectly, while *(italic)* values are estimations.

920 -CX	CIBA-GEIGY	SODEN [40]	DEGRIECK [41]	CHAMIS [42]	PUCK [43] FOYE [44]	P-UPS
V_f [%]	55	60	**55**	55	55	55
E_{11} [GPa]	*115.1*	*138*	**119.13**	*128.74*	*128.74*	**118.42**
E_{22} [GPa]	-	*11*	**8.85**	*10.50*	*12.23*	**10.18**
E_{33} [GPa]	-	*11*	*8.85*	*10.50*	*12.23*	*10.18*
ν_{12} [-]	-	*0.28*	**0.306**	*0.319*	*0.319*	**0.328**
ν_{13} [-]	-	*0.28*	*0.306*	*0.319*	*0.319*	*0.328*
ν_{23} [-]	-	*0.40*	*(0.475)*	*0.367*	*0.428*	*0.473*
G_{12} [GPa]	-	*5.5*	*(5.50)*	*4.51*	*4.89*	**6.25**
G_{13} [GPa]	-	*5.5*	*(5.50)*	*4.51*	*4.89*	**5.86**
G_{23} [GPa]	-	*3.93*	*(3.00)*	*3.84*	4.28	**3.398**

The values in **bold** are measured values, while the values in *italic* have been obtained indirectly. The mechanical properties provided by the supplier (CIBA GEIGY) are listed in the first column of Table 7-6. The second column lists the parameters for a similar unidirectional carbon/epoxy laminate though for a fiber volume fraction of $V_f = 60\%$ [40]. The third column contains values obtained within our research team by means of conventional testing procedures [41]. The fourth and fifth column represent

the results of the analytical micro-mechanical homogenization model of Chamis [42], respectively of Puck-Foye [43-44], in which the fiber properties [45] and epoxy properties (www.Hexcel.com: data sheet HexPly 920 125°C curing epoxy matrix) are used as input. It is clear that the different sets of parameters are not really consistent to each other, and therefore cannot be regarded as the actual material properties, but rather provide an order of magnitude.

The P-UPS has been recorded at fd = 5 MHz x 1.1 mm at an arbitrary material spot and is shown in Figure 7-13a. The sample has been placed randomly in the test setup, hence the fiber direction obviously deviates from the 0°-direction of the P-UPS setup. Hence, in addition to the inversion procedure described for isotropic solids, here we first extract the fiber direction of the laminate by searching for the orientation angle φ_{fiber} at which the inner characteristic contour in the P-UPS recording has a minimum incident angle θ. Indeed, a minimal incident angle θ of the inner contour corresponds to a maximal sound speed for the in-plane propagating QL polarized wave, which implies a high elasticity modulus in that particular direction. The latter obviously arises from the specific orientation of the designed carbon fiber reinforcement.

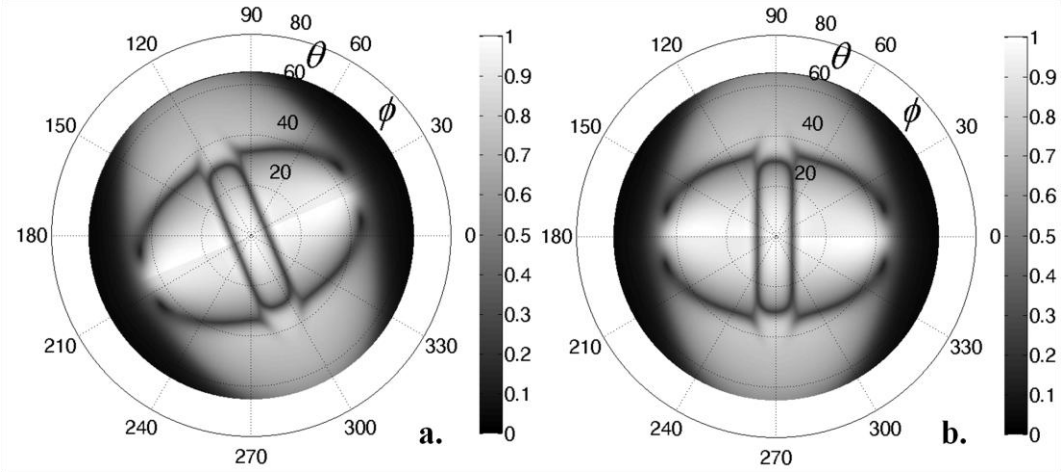

Figure 7-13: P-UPS recorded at fd = 5 MHz x 1.1 mm for an autoclave manufactured $[0]_8$ carbon/epoxy laminate (a) and after rotation over φ_{fiber} (b).

The P-UPS experiment is then rotated over the extracted fiber orientation angle φ_{fiber} (see Figure 7-13b). In this way, the optimization procedure is significantly accelerated since the principal axes of orthotropy are known

and consequently can be fixed at $\varphi = 0°$ and $\varphi = 90°$. Such a characterization of the local fiber direction *per se* is actually very interesting for the composite manufacturing industry where the stacking process of laminae is often done manually. The quality of the stacking procedure directly influences the stiffness properties, hence a spot-to-spot inspection of the local fiber direction is an easy way to assure the designed functionality of the composite structure. Even more, local wrinkling of reinforced fibers, which is an important failing mechanism for composite structures, can also be easily detected and evaluated.

In theory, the manufactured $[0]_8$ carbon/epoxy laminate belongs to the symmetry class of transversal isotropy, and thus is described by five independent elasticity parameters [46]. However, a real composite seldom exhibits pure symmetry because of (i) human error in the layer stacking procedure, (ii) small perturbations in the pressure and/or temperature distribution of the autoclave manufacturing cycle, (iii) production faults in the supplied prepreg material and (iv) unequal spatial distribution of the fibers in 2- and 3-direction due to the applied pressure level during manufacturing. Hence, it can be expected that the shear properties in the 12- and 13-direction are not equivalent. Therefore, we decoupled both and performed the system identification procedure to the optimization of C_{11}, C_{12}, C_{22}, C_{44}, C_{55} and C_{66}. The P-UPS obtained material properties are listed in the last column of Table 7-6. Compared to the information of the supplier as well as to the conventionally determined material constants, satisfying agreement is found. Comparison with the micro-mechanically predicted material properties reveals that the optimized set of material parameters are in the same range. Nevertheless, it is clear that a quantitative comparison cannot be made. The P-UPS extracted material parameters further reveal that G_{12} indeed differs by ~6% from G_{13}, indicating that the laminate does not possess perfect transversal isotropic symmetry, as was expected.

7. 5. Extension to Complex Material Parameters

Up to now, the analysis has been focused to the mechanical properties by evaluating the characteristic contours in a P-UPS image. First steps have also been taken to extract the attenuation tensor C'' from P-UPS data. Figure 7-14 displays the P-UPS sectors ($\varphi = 60°$) for two $[0]_8$ carbon/epoxy laminates having a C-tensor with the same real part C' (last column Table 7-6), but with a different imaginary part C''.

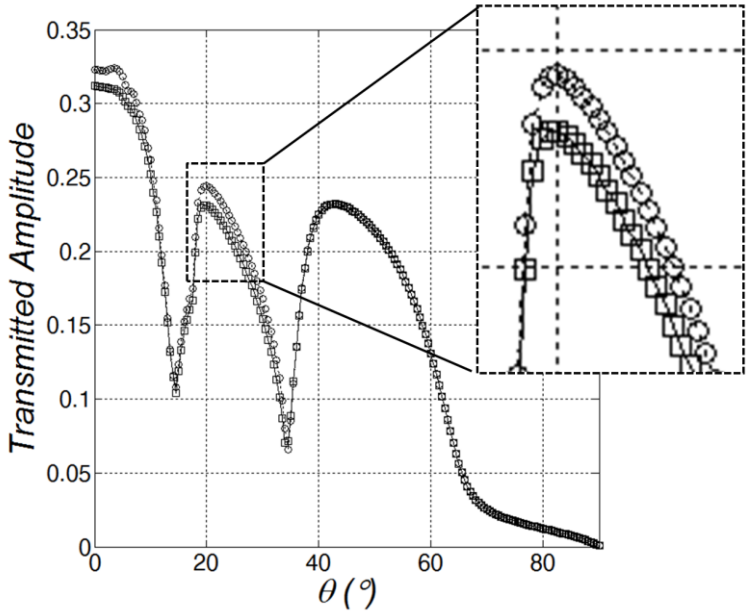

Figure 7-14: Effect of change in imaginary *C* constants for P-UPS sector at φ = 60° for an orthotropic plate with $C = C' - iC''$. *C′* is taken from Table 7-6, while *C″* equals -0.05 *C′* (squares). The circles represent a 15% reduction of C''_{33}.

The 15% reduction in the C''_{33} constant is well represented in the global amplitude level. Hence, extending the analysis to the global shape of the transmission characteristic provides a means to extract local damping properties of the insonified material spot. Ideally, the system identification procedure should comprise the total P-UPS image, however computationally this is not feasible as stated before. Therefore, a few P-UPS sectors are selected. In contrast with the previous inversion procedure which evaluated the position of characteristic contours, we are now interested in the global transmission amplitude. It is clear that the main features of the previous inversion procedure can be recycled. Preliminary results for the complex material properties $C = C' - iC''$, considering the experimentally recorded P-UPS of the $[0]_8$ carbon/epoxy laminate (Figure 7-13), are listed in Table 7-7.

Table 7-7: P-UPS inverted complex material parameters for the autoclave manufactured $[0]_8$ carbon/epoxy laminate.

$C = C' - iC''$	C' [GPa]	C'' [GPa]	$\kappa = C''/C'$ [%]
C_{11}	122.716	6.901	5.62
C_{12}	6.564	1.095	16.69
C_{22}	13.468	0.859	6.38
C_{44}	3.398	0.195	5.73
C_{55}	5.856	0.444	7.58
C_{66}	6.251	0.276	4.41

It is emphasized that the identification of viscoelastic parameters is ongoing research, and thus the inverted imaginary constants are preliminary results which cannot be seen as the true attenuation parameters. The reason why this is stressed out, is triggered by several approximations used in the present identification procedure. First of all, the viscoelastic parameters have been extracted from P-UPS data, in which the ultrasonic pulse is composed of a wide range of frequencies. As we put the imaginary moduli *C''* independent of frequency, we implicitly assumed in the Kelvin-Voigt model that the attenuation tensor varies linearly with frequency. However, in literature, several different relations can be found for the attenuation. Secondly, the inversion has been performed to C_{11}, C_{12}, C_{22}, C_{44}, C_{55} and C_{66}. For the real part, this is correct as the characteristic contours represent (more or less) in-plane bulk wave propagation, and thus are independent from C_{i3}, with i = 1,2,3. The global amplitude level on the other hand is a representation of wave propagation in all possible directions within the solid (see Figure 7-14 for C_{33}). Hence, the imaginary part of C_{i3}, with i = 1,2,3, should be decoupled from the other imaginary parameters during the inversion procedure. Thirdly, the investigation has been split to the separate analysis of the real and imaginary components for reasons of computability. For materials with large attenuation characteristics, it can be expected that this assumption yields erroneous results. For these reasons, it is expected that the additional analysis of H-UPS data offers valuable information for the accurate determination of the viscoelastic parameters because no assumptions have to be made about the frequency dependency of viscoelastic parameters.

7. 6. Conclusions

A two-step optimization procedure, on the basis of a genetic algorithm, has been described in order to inversely extract local material parameters from a P-UPS experiment. First, an analysis on the basis of the Christoffel equation is performed in order to match critical bulk wave angle profiles with the characteristic low-amplitude (or equivalently high curvature) P-UPS contours. It has been found that this is not sufficient to accurately extract the elasticity tensor C_{ij}. The next step of the inversion procedure uses the elasticity tensor C_{ij} obtained in the first step as a starting point to match the characteristic contours of P-UPS simulations with the contours of the P-UPS recording. To improve the computational performance, the second step has been limited to a few P-UPS sectors, shortening the whole processing time to less than 5 minutes.

The inversion procedure has been demonstrated for synthetic data with and without added noise as well as for P-UPS experiments of annealed aluminum (in different health conditions), cold-rolled DC06 steel and $[0]_8$ carbon fiber reinforced laminate. Comparison with material parameters obtained from literature on the one hand and from conventional testing on the other hand, yields satisfying agreement.

The optimization procedure has been extended to the identification of complex material parameters. Preliminary results have been presented for a $[0]_8$ C/E laminate.

7. 7. References

[1] Maynard, J., *Resonant ultrasound spectroscopy.* Physics Today, 1996. 49(1): p. 26-31.

[2] Muller, M., A. Sutin, R. Guyer, M. Talmant, P. Laugier, and P.A. Johnson, *Nonlinear resonant ultrasound spectroscopy (NRUS) applied to damage assessment in bone.* Journal of the Acoustical Society of America, 2005. 118(6): p. 3946-3952.

[3] Ohtani, T. and Y. Ishii, *Nonlinear Resonant Ultrasound Spectroscopy (NRUS) Applied to Fatigue Damage Evaluation in a Pure Copper*, in *Nonlinear Acoustics: State-of-the-Art and Perspectives,* T. Kamakura and N. Sugimoto, Editors. 2012. p. 204-207.

[4] Solodov, I., J.X. Bai, and G. Busse, *Resonant ultrasound spectroscopy of defects: Case study of flat-bottomed holes.* Journal of Applied Physics, 2013. 113(22).

[5] Baudouin, S. and B. Hosten, *Immersion ultrasonic method to measure elastic constants and anisotropic attenuation in polymer-matrix and fiber-reinforced composite materials.* Ultrasonics, 1996. 34(2-5): p. 379-382.

[6] Rokhlin, S.I. and W. Wang, *DOUBLE THROUGH-TRANSMISSION BULK WAVE METHOD FOR ULTRASONIC PHASE-VELOCITY MEASUREMENT AND DETERMINATION OF ELASTIC-CONSTANTS OF COMPOSITE-MATERIALS.* Journal of the Acoustical Society of America, 1992. 91(6): p. 3303-3312.

[7] Balasubramaniam, K. and N.S. Rao, *Inversion of composite material elastic constants from ultrasonic bulk wave phase velocity data using genetic algorithms.* Composites Part B-Engineering, 1998. 29(2): p. 171-180.

[8] Wu, T.T. and Y.H. Liu, *On the measurement of anisotropic elastic constants of fiber-reinforced composite plate using ultrasonic bulk wave and laser generated Lamb wave.* Ultrasonics, 1999. 37(6): p. 405-412.

[9] Vishnuvardhan, J., C.V. Krishnamurthy, and K. Balasubramaniam, *Genetic algorithm reconstruction of orthotropic composite plate elastic constants from a single non-symmetric plane ultrasonic velocity data*. Composites Part B-Engineering, 2007. 38(2): p. 216-227.

[10] Reddy, S.S.S., K. Balasubramaniam, C.V. Krishnamurthy, and M. Shankar, *Ultrasonic goniometry immersion techniques for the measurement of elastic moduli.* Composite Structures, 2005. 67(1): p. 3-17.

[11] Margueres, P. and F. Meraghni, *Damage induced anisotropy and stiffness reduction evaluation in composite materials using ultrasonic wave transmission.* Composites Part a-Applied Science and Manufacturing, 2013. 45: p. 134-144.

[12] Castaings, M., B. Hosten, and T. Kundu, *Inversion of ultrasonic, plane-wave transmission data in composite plates to infer viscoelastic material properties.* Ndt & E International, 2000. 33(6): p. 377-392.

[13] Karim, M.R., A.K. Mal, and Y. Barcohen, *INVERSION OF LEAKY LAMB WAVE DATA BY SIMPLEX ALGORITHM.* Journal of the Acoustical Society of America, 1990. 88(1): p. 482-491.

[14] Cawley, P. and B. Hosten, *The use of large ultrasonic transducers to improve transmission coefficient measurements on viscoelastic anisotropic plates.* Journal of the Acoustical Society of America, 1997. 101(3): p. 1373-1379.

[15] Wang, L. and F.G. Yuan, *Group velocity and characteristic wave curves of Lamb waves in composites: Modeling and experiments.* Composites Science and Technology, 2007. 67(7-8): p. 1370-1384.

[16] Vishnuvardhan, J., C.V. Krishnamurthy, and K. Balasubramaniam, *Genetic algorithm based reconstruction of the elastic moduli of orthotropic plates using an ultrasonic guided wave single-transmitter-multiple-receiver SHM array.* Smart Materials & Structures, 2007. 16(5): p. 1639-1650.

[17] Qu, J.M., Y. Berthelot, and Z.B. Li, *Dispersion of guided circumferential waves in a circular annulus*. Review of Progress in Quantitative Nondestructive Evaluation, Vols 15a and 15b, ed. D.O. Thompson and D.E. Chimenti. Vol. 15. 1996. 169-176.

[18] Wilcox, P.D., *Lamb Wave Inspection of Large Structures using Permanently Attached Transducers.* Imperial College of Science, Technology and Medicine (London); PhD Thesis, 1998: p. 223.

[19] Towfighi, S. and T. Kundu, *Elastic wave propagation in anisotropic spherical curved plates.* International Journal of Solids and Structures, 2003. 40(20): p. 5495-5510.

[20] Declercq, N.F., J. Degrieck, and O. Leroy, *Simulations of harmonic and pulsed ultrasonic polar scans.* Ndt & E International, 2006. 39(3): p. 205-216.

[21] Vandreumel, W.H.M. and J.L. Speijer, *Non-destructive composite laminate characterization by means of ultrasonic polar-scan.* Materials Evaluation, 1981. 39(10): p. 922-925.

[22] Degrieck, J. *Some possibilities of nondestructive characterisation of composite plates by means of ultrasonic polar scans*. in *Emerging technologies in nondestructive testing (ETNDT)*. 1996. Patras, Greece: A.A. Balkema.

[23] Degrieck, J., N.F. Declercq, and O. Leroy, *Ultrasonic polar scans as a possible means of non-destructive testing and characterisation of composite plates.* Insight, 2003. 45(3): p. 196-201.

[24] Declercq, N.F., J. Degrieck, and O. Leroy, *On the influence of fatigue on ultrasonic polar scans of fiber reinforced composites.* Ultrasonics, 2004. 42(1-9): p. 173-177.

[25] Declercq, N.F., J. Degrieck, and O. Leroy, *Ultrasonic polar scans: Numerical simulation on generally anisotropic media.* Ultrasonics, 2006. 45(1-4): p. 32-39.

[26] Satyanarayan, L., J.M. Vander Weide, and N.F. Declercq, *Ultrasonic Polar Scan Imaging of Damaged Fiber Reinforced Composites.* Materials Evaluation, 2010. 68(6): p. 733-739.

[27] Wang, L. and S.I. Rokhlin, *Ultrasonic wave interaction with multidirectional composites: Modeling and experiment.* Journal of the Acoustical Society of America, 2003. 114(5): p. 2582-2595.

[28] Wang, L. and S.I. Rokhlin, *Stable reformulation of transfer matrix method for wave propagation in layered anisotropic media.* Ultrasonics, 2001. 39(6): p. 413-424.

[29] Rokhlin, S.I. and L. Wang, *Ultrasonic waves in layered anisotropic media: characterization of multidirectional composites.* International Journal of Solids and Structures, 2002. 39(21-22): p. 5529-5545.

[30] Kersemans, M., A. Martens, K. Van Den Abeele, J. Degrieck, L. Pyl, F. Zastavnik, H. Sol, and W. Van Paepegem, *The Quasi-Harmonic Ultrasonic Polar Scan for Material Characterization: Experiment and Numerical Modeling.* Accepted for publication in Ultrasonics, 2014.

[31] Kersemans, M., W. Van Paepegem, K. Van Den Abeele, L. Pyl, F. Zastavnik, H. Sol, and J. Degrieck, *The Quasi-Harmonic ultrasonic Polar Scan for material Characterization: Experiment and Numerical Modeling*, in *Proceedings of the 12th International Conference for Non-Destructive Testing 2013 (ICNDT2013)*, J. Grum and T. Kek, Editors. 2013: Portoroz, Slovenia.

[32] Kersemans, M., W. Van Paepegem, K. Van Den Abeele, L. Pyl, F. Zastavnik, H. Sol, and J. Degrieck, *Pitfalls in the Experimental Recording of Ultrasonic (Backscatter) Polar Scans for Material Characterization.* Ultrasonics, 2014. In Press DOI: 10.1016/j.ultras.2014.04.013.

[33] Herakovich, C.T., *Mechanics of Fibrous Composites*. 1998, New York: John Wiley & Sons. 460.

[34] Kersemans, M., N. Lammens, J. Degrieck, K. Van Den Abeele, L. Pyl, F. Zastavnik, H. Sol, and W. Van Paepegem, *Extraction of bulk wave characteristics from a pulsed ultrasonic polar scan.* Wave Motion, 2014. In Press DOI: 10.1016/j.wavemoti.2014.05.001.

[35] Zener, C., *Elasticity and Anelasticity of Metals.* University Chicago Press, 1948.

[36] Padmanabhan, R., A.J. Baptista, M.C. Oliveira, and L.F. Menezes, *Effect of anisotropy on the deep-drawing of mild steel and dual-phase steel tailor-welded blanks.* Journal of Materials Processing Technology, 2007. 184(1-3): p. 288-293.

[37] Safaei, M., *Constitutive modelling of anisotropic sheet metals based on a non-associated flow rule.* Ghent University, Faculty of engineering sciences and architecture (Ghent), PhD thesis, 2013: p. 246.

[38] Lebensohn, R.A. and C.N. Tome, *A SELF-CONSISTENT ANISOTROPIC APPROACH FOR THE SIMULATION OF PLASTIC-DEFORMATION AND TEXTURE DEVELOPMENT OF POLYCRYSTALS - APPLICATION TO ZIRCONIUM ALLOYS.* Acta Metallurgica Et Materialia, 1993. 41(9): p. 2611-2624.

[39] Sayers, C.M., *ULTRASONIC VELOCITIES IN ANISOTROPIC POLYCRYSTALLINE AGGREGATES.* Journal of Physics D-Applied Physics, 1982. 15(11): p. 2157-2167.

[40] Soden, P.D., M.J. Hinton, and A.S. Kaddour, *Lamina properties, lay-up configurations and loading conditions for a range of fibre-reinforced composite laminates.* Composites Science and Technology, 1998. 58(7): p. 1011-1022.

[41] Degrieck, J., *Analyse van impact op een vezelversterkte kunststof (In Dutch).* Ghent University, Faculty of Applied Sciences, (Ghent), PhD Thesis, 1990.

[42] Chamis, C.C., *Mechanics of Composite Materials: Past, Present and Future*. 1984, NASA Technical Memorandum 100793.

[43] Puck, A., *Grundlagen der spannungs und veromungs to analyse.* Dopl. ing. Kunstoffe, C57, 1967.

[44] Foye, R.L., *An evaluation of various engineering estimates of the transverse properties of unidirectional composites*, in *Tenth national SAMPE symposium*. 1966: San Diego, California. p. 31.

[45] Daggumati, S., *Concurrent Modelling and Experimental Analysis of Meso-Scale Strain Fields and Damage in Woven Composites under Static and Fatigue Tensile Loading.* Ghent University, Faculty of engineering sciences and architecture (Ghent), PhD thesis, 2011.

[46] Auld, B.A., *Acoustic Fields and Waves in Solids, second edition*. 1990, Florida: Krieger publishing company. 856.

Chapter 8

The Harmonic Ultrasonic Polar Scan (H-UPS): Amplitude and Phase Analysis

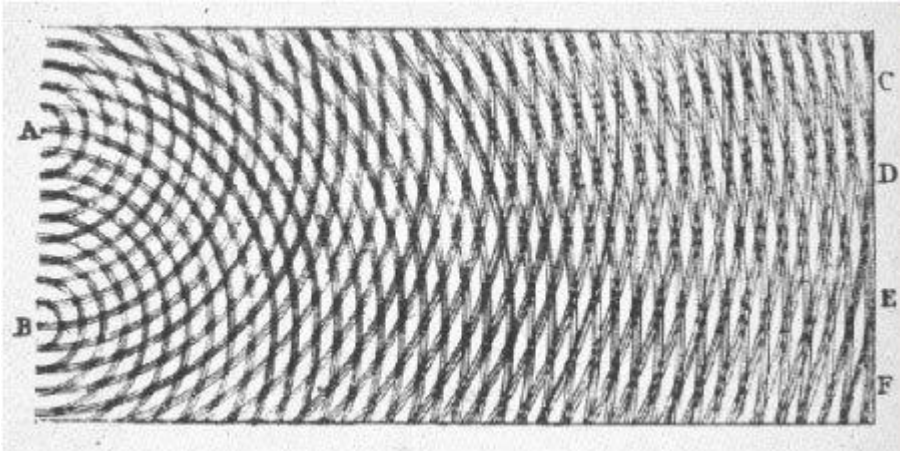

Thomas Young's double slit experiment in 1807, describing light waves in term of frequency, amplitude and phase. It was the first convincing evidence for the wave nature of light. (Figure reproduced from reference [1]).

Overview

For the first time, ultrasonic polar scan experiments have been obtained employing quasi-harmonic ultrasound, resulting in the harmonic ultrasonic polar scan (H-UPS). It is shown that plane wave simulation models show poor agreement to the experiments. Therefore, the spatial nature of a bounded beam is taken into account, yielding much better agreement with experiments. The results further show that the patterns in a H-UPS relate to the stimulation condition of Lamb waves, though not in a one-to-one relationship as previously stated in literature. As a harmonic signal with known frequency is defined by its amplitude and its phase, the data analysis is extended in order to obtain phase-based H-UPS results.

8. 1. Introduction

Till now, the UPS experiments have always been performed using short ultrasound pulses, resulting in images with characteristic contours that more or less relate to bulk wave phenomena. Since only three types of polarizations exist for traveling bulk waves, the ones corresponding to the three solutions prescribed by the Christoffel equation [2-3], only three critical contours may exist in a P-UPS experiment. Contrary to being linked to the critical bulk wave angles, the characteristic contours in plane wave H-UPS simulations were found to be related to the stimulation of Lamb waves [4-6]. So far, this premise has not been checked nor explored experimentally. In addition, the results of Chapter 4 indicated that the use of a bounded (in space) harmonic beam has an integrating effect on the transmission results. As such, the one-to-one relationship between the contours in a bounded beam simulation and the stimulation conditions of Lamb waves should not hold anymore.

In this chapter, we introduce and comment on several noteworthy extensions of the pulsed ultrasonic polar scan technique. To begin with, we report about the first ever experiments of ultrasonic polar scans using quasi-harmonic sound pulses (i.e. bursts of periodic cycles), resulting in the harmonic ultrasonic polar scan (H-UPS). The various H-UPS experiments have been

compared to both plane wave and bounded beam simulations. Further, since a quasi-harmonic wave with known frequency can be fully described by the combination of its amplitude and its phase, the conventional amplitude analysis has been extended towards the analysis of the phase of the transmitted wave. To the author's knowledge, such phase measurements are unprecedented in literature. Combination of the amplitude and the phase measurements yields knowledge of the complex transmission coefficient.

8. 2. Quasi-Harmonic Signal Generation

A pure harmonic signal cannot be generated experimentally because of obvious reasons, instead a quasi-harmonic wave train is excited by means of a programmable wave function generator (Tektronix). Basically a rectangular window has been put over a sinusoid, such that at least 10 periods are retained. The generated electrical signal, considering an input frequency $f = 5$ MHz, is shown in Figure 8-1a. One can readily verify the quasi-harmonic nature by evaluating the narrow peak in the spectrum of the electrical signal (Figure 8-1b). Side lobes are observed as a consequence of the applied rectangular window, i.e. due to the sudden beginning and ending of the electrical signal.

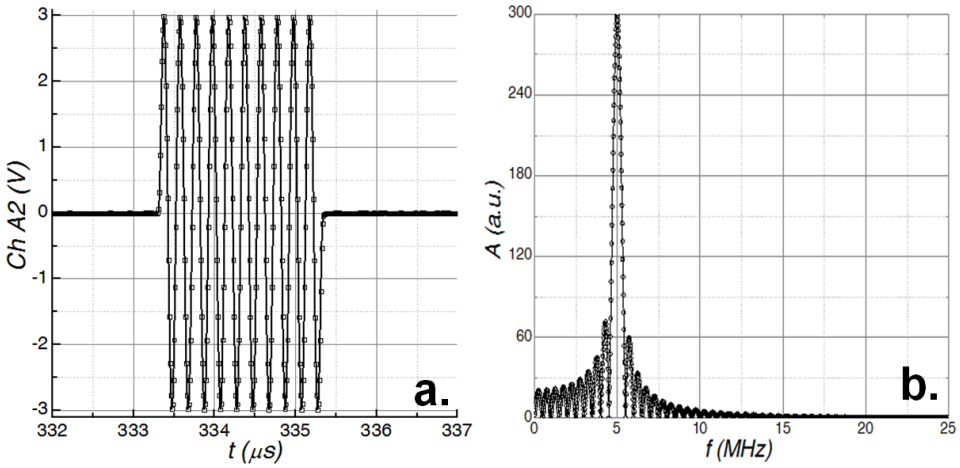

Figure 8-1: Input electrical signal in time domain (a) and in frequency domain (b), considering an input frequency of 5 MHz

The generated electrical signal is fed into the piezoelectric transducer, which itself has also a transmission characteristic. Therefore, the output pressure of

the transducer has been measured by means of a hydrophone, and is displayed in Figure 8-2. It may be observed that the time characteristic is more 'polluted' compared to the electrical input signal. Though, the frequency spectrum clearly reveals that the generated pressure can be considered quasi-harmonic.

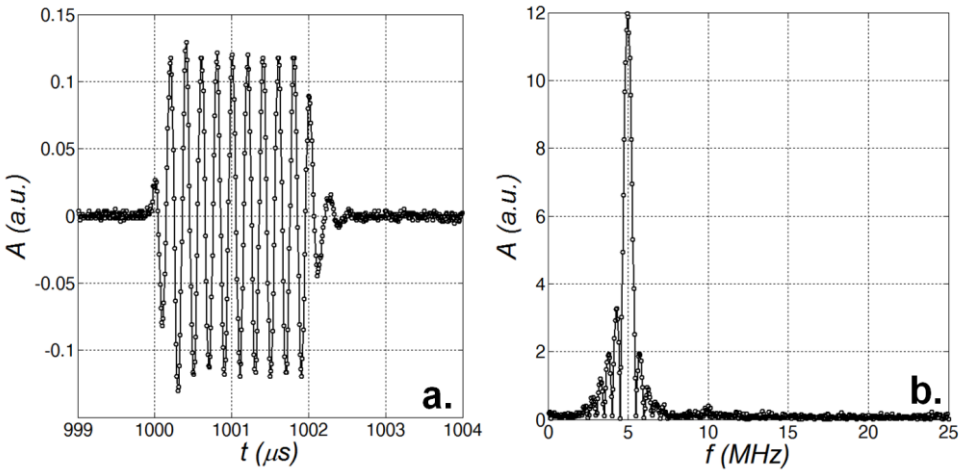

Figure 8-2: Output pressure of the piezo-electric transducer which has been excited by the electrical signal displayed in Figure 8-1a: time domain (a) and frequency domain (b).

To further ascertain the condition of harmonic stimulation, the outer cycles are ignored during the analysis and post-processing in order to avoid transient effects. In fact, the analysis has been performed to a single period in the middle of the wave train. To obtain an absolute measurement, the 'transmission' signal has been first recorded in the absence of a specimen (see Figure 8-3a), and secondly in the presence of a specimen (see Figure 8-3b). The data acquisition has been programmed such that both the maximum signal as well as the time value of the zero crossing at the negative flank is stored. This is explicitly indicated with the numbered arrows added to Figure 8-3: arrow 1 for the transmission amplitude and arrow 2 for the transmission phase. As such, the absolute amplitude and phase of the complex valued transmission coefficient can be determined. Doing so for many oblique incidence angles, a H-UPS image (amplitude or phase) is obtained.

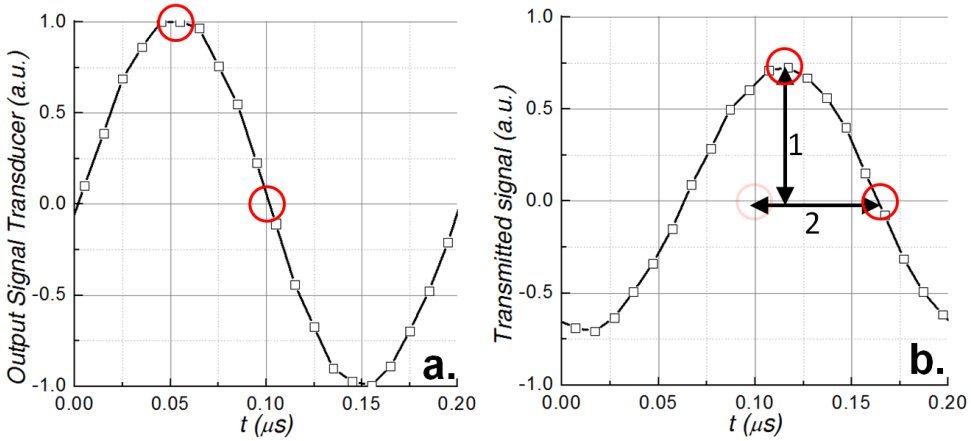

Figure 8-3: Recorded signal in the absence (a) and in the presence (b) of a specimen. The added indicators clarify how the amplitude and phase of the transmission signal are extracted.

8. 3. H-UPS: Amplitude Analysis

8. 3. 1. Fixed Polar Angle Investigation for Isotropic Media

For simplicity, we first concentrate on the comparison of experimental results and numerical simulations for an immersed homogeneous and isotropic aluminum plate. In this case it suffices to analyze the results at a single polar angle φ.

The dispersion curves for aluminum, which prescribe the condition for efficient Lamb wave stimulation under plane wave insonification, are shown in Figure 8-4. The dispersion curves are computed on the basis of a Legendre polynomial expansion for the displacement and stress vectors [7], assuming the material properties identified in Chapter 7, Section 7.4.1. Large parts of this numerically efficient and stable implementation code, which can handle up to layered magneto-electro-elastic media, has been kindly provided by Prof. Olivier Bou Matar from Université de Lille, France. The black vertical dashed lines represent the *fd*-values at which experiments have been performed. The open circles indicate the plane wave conditions for efficient Lamb wave stimulation. Contrary to the case of bulk waves, both the number and the existence condition of Lamb wave stimulation is dependent on the frequency-thickness *fd*.

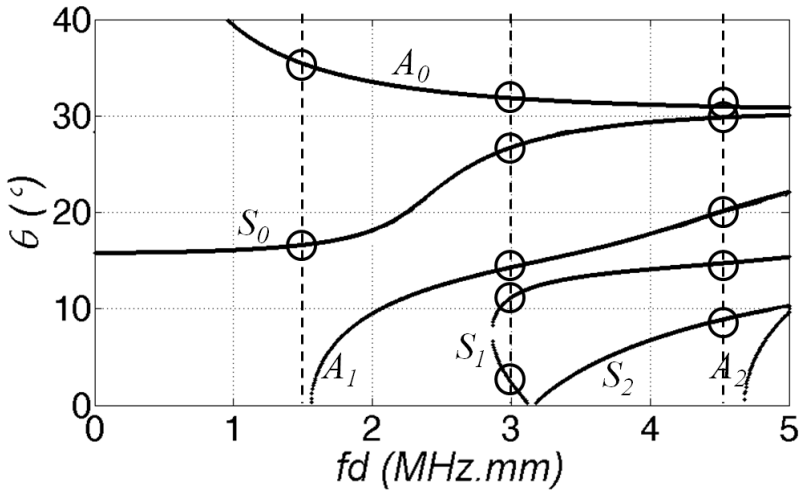

Figure 8-4: Dispersion curves *θ(fd)* for aluminum. The vertical dashed lines indicate the *fd*-values at which results have been obtained.

The experimental recordings of the transmission amplitude as a function of the incident angle θ are presented in Figure 8-5 at the various frequency-thickness values: fd = 1.5 MHz.mm, fd = 3 MHz.mm and fd = 4.5 MHz.mm. Plane wave and bounded beam computations have been superimposed, in order to evaluate their relation to the experiment. The modeling approach for both the plane wave and the bounded beam simulation can be found in Chapter 4.

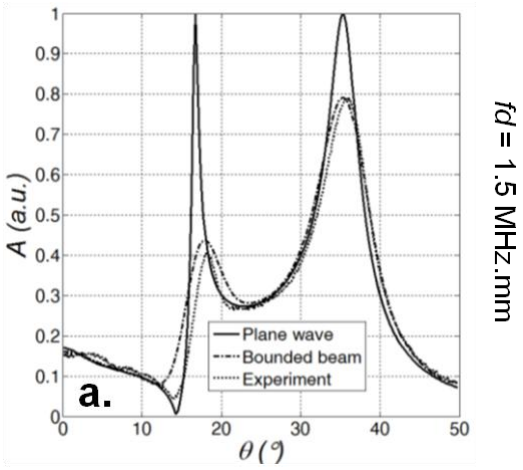

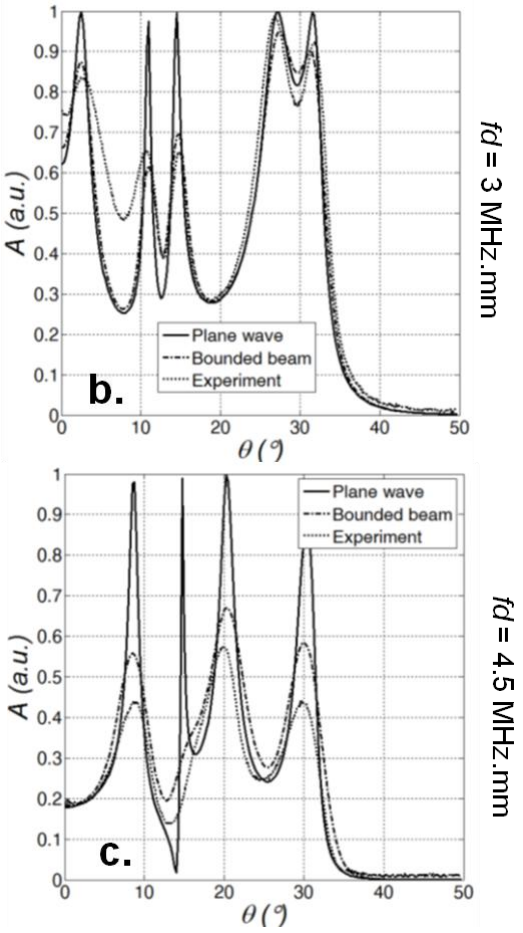

Figure 8-5: Transmission amplitude for an aluminum sample at *fd* = 1.5 MHz.mm (a), *fd* = 3 MHz.mm (b) and *fd* = 4.5 MHz.mm (c). Solid line = plane wave computation, dashed line = bounded beam computation and dotted line = experimental recording.

At *fd* = 1.5 MHz.mm (Figure 8-5a), we observe two peaks, namely at $\theta \approx 17°$ (the fundamental symmetrical S_0 Lamb mode) and $\theta \approx 35°$ (the fundamental anti-symmetrical A_0 Lamb mode), which is in good correspondence with the dispersion curves. Note that the location of the bounded beam transmission peaks (experiment and simulation) are slightly shifted compared to the numerical simulation results of the plane wave approach. Furthermore, the transmission amplitude profile resulting from the bounded beam simulation is significantly diminished compared to the plane wave approach, while the transmission peaks are widened. This could have been expected from a physics point of view. It is clear that the bounded beam simulation is

superior to the plane wave simulation as it resembles the experimental recording more closely.

According to the dispersion curves, surpassing the first cut-off frequency-thickness value ($fd \approx 1.6$ MHz.mm) should give rise to the excitation of higher order Lamb modes. Indeed, the results at $fd = 3$ MHz.mm (Figure 8-5b) show several additional transmission peaks belonging to the excitation of the S_1^b, S_1 and A_1 Lamb modes. Although the S_1^b mode is actually part of the S_1 mode, we label it differently because this mode transports its energy in the opposite direction with respect to its propagation direction [8-12]. Similar observations and conclusions hold as for the result at $fd = 1.5$ MHz.mm: the number of transmission peaks corresponds to the number of allowed leaky Lamb wave excitations, while the position of the transmission peaks coincides with the existence condition for efficient Lamb wave stimulation: $S_1^b \rightarrow \theta \approx 2°$, $S_1 \rightarrow \theta \approx 11°$, $A_1 \rightarrow \theta \approx 14°$, $S_0 \rightarrow \theta \approx 27°$and $A_0 \rightarrow \theta \approx 32°$). Although the plane wave simulation correctly models the number and location of the transmission peaks, it is clear that the overall transmission amplitude of the bounded beam simulation matches more closely with the experimental recording.

However, further increase of the frequency-thickness to $fd = 4.5$ MHz.mm reveals some particular concerns. First of all, we note that neither the simulations, nor the experimental result displayed in Figure 8-5c correspond to the number of possible Lamb wave excitations prescribed by the dispersion curves. This may be attributed to two reasons. First, the convergent nature of the fundamental A_0 and S_0 mode at higher *fd*-values implies that both modes are not resolved anymore. Hence, they merge into a single transmission amplitude peak. In addition to this, the transmission amplitude peak which should correspond to the stimulation of the S_1 mode is not at all represented in the bounded beam simulation, nor in the experimental recording. Considering the horizontal course of the S_1 mode in the dispersion curves at $fd = 4.5$ MHz.mm, the angle of Lamb mode stimulation for this mode is very critical. As such, it could have been expected that this mode was the first to be missed when applying a bounded beam. These results emphasize the need to account for the angular spectrum of the bounded beam when simulating a H-UPS experiment. As a further consequence, the present results also reveal that a H-UPS image cannot be simply conceived as a one-to-one match with the leaky Lamb wave angles (as previously stated in literature [4, 6]), exactly because of the integrating

effect of a realistic bounded beam. These observations are of utmost importance for the correct interpretation of a H-UPS experiment, and for its potential application as a NDT and characterization tool for materials.

8. 3. 2. Full H-UPS Investigation for (An)isotropic (Layered) Media

Up to now, results were obtained at a fixed polar angle φ. This was in fact sufficient since the investigated material possessed pure mechanical isotropy. In the following, the analysis is extended to all possible angles of incidence $\psi(\varphi,\theta)$ in order to include materials with different levels of mechanical anisotropy. Figure 8-6 displays a comparison between H-UPS experiments and the bounded beam simulations for: isotropic aluminum (a-b), orthotropic $[0_8]$ carbon/epoxy (c-d), orthotropic cross-ply $[0_2,90_2]_S$ carbon/epoxy (e-f) and a $[0_3,90_4]_S$ hybrid glass/epoxy-carbon/epoxy laminate (g-h). The latter is hybrid in the sense that the cross-ply stacking consists of both glass/epoxy laminae (along the 0° direction) and carbon/epoxy laminae (along the 90° direction). The material parameters for the aluminum and the carbon laminae have been obtained throug inversion of P-UPS data (see Chapter 7), while the properties of the glass fiber have been estimated to best knowledge.

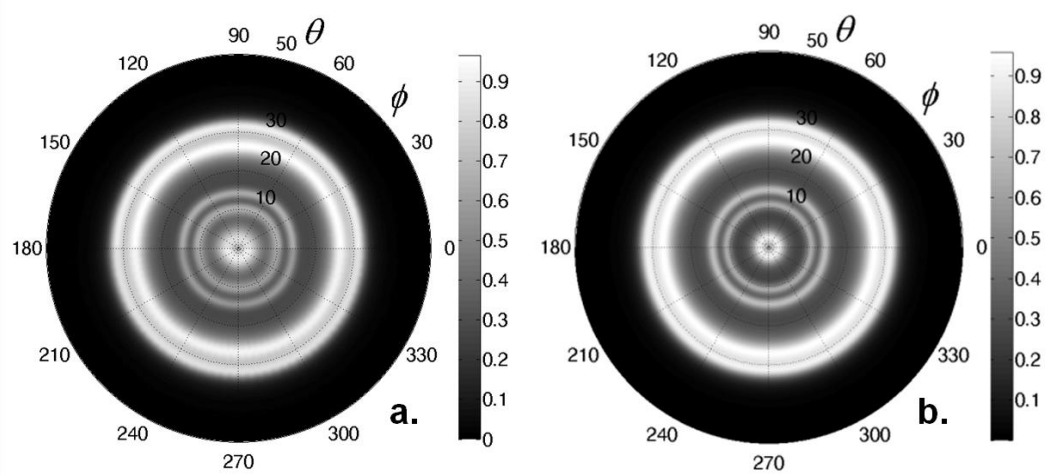

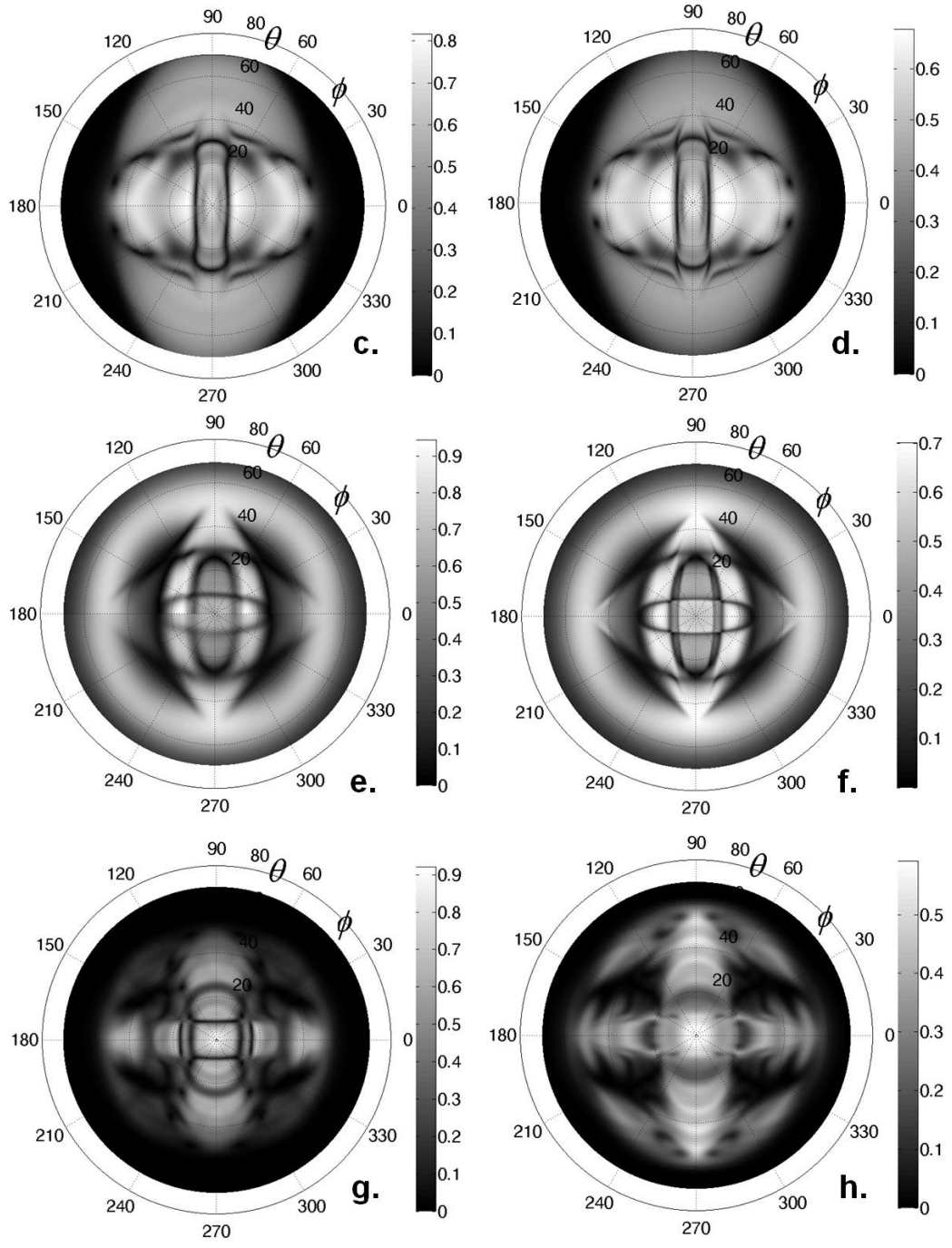

Figure 8-6: Amplitude-based H-UPS results: isotropic aluminum (a-b), orthotropic $[0_8]$ carbon/epoxy (c-d), orthotropic cross-ply $[0_2,90_2]_S$ carbon/epoxy (e-f) and hybrid glass/epoxy-carbon/epoxy $[0_3,90_4]_S$ laminate (g-h). Left colum corresponds to experiment, right column to simulation.

As mentioned before, the general view of the patterns clearly informs us about the (an)isotropy of the insonified material. In view of the above discussion, we know that these contours relate to the stimulation of leaky Lamb waves, though that they are not necessarily accounting for all allowed Lamb modes. The possibility to extract the complete complex C-tensor through inverse modeling from a single P-UPS experiment has been already investigated in previous chapter. The current H-UPS results suggest that the H-UPS too can be used for identification of the complex C-tensor, perhaps even in combination with P-UPS data. In addition, it seems that the inversion of H-UPS data obtained at different frequencies may lead to essential information on the frequency dependent attenuation tensor.

8. 4. H-UPS: Phase Analysis

Since a harmonic wave signal with known frequency can be fully described by the combination of an amplitude and a phase, the H-UPS concept is extended to incorporate phase features. The incorporation of the phase information of the transmitted signal can be viewed as a complement to the conventional amplitude measurement. Whereas it is relatively easy to include the computation of the phase of the transmitted wave in the numerical model from a delayed shift compared to a reference signal, experimentally capturing the phase of the transmitted wave with high accuracy becomes much more challenging. This is easily appreciated by bearing in mind that the phase is very sensitive to external influence as well as to experimental error. As a result, and for a long time, erroneous phase measurements have been obtained because of vibrations of heavy machinery in the neighboring laboratory. On the other hand, and precisely because of the sensitivity, phase-based H-UPS results could turn out to be very useful in the area of advanced material research.

The recorded and computed phase results at a fixed polar angle φ, for an (isotropic) aluminum sample insonified at $fd = 3$ MHz.mm, are shown in Figure 8-7. Overall, a good correspondence is obtained between experiment and simulation. However, for large incidence angles ($\theta > \theta_{A0} \approx 32°$) the experimentally recorded phase becomes unsteady and highly oscillatory, and a clear deviation from the numerical results can be observed. This unsteady behavior should be attributed to the small amplitude level of the transmitted wave for large incident angles θ (see Figure 8-5b), which obviously

complicates the accurate recording of the phase information of the transmitted sound field.

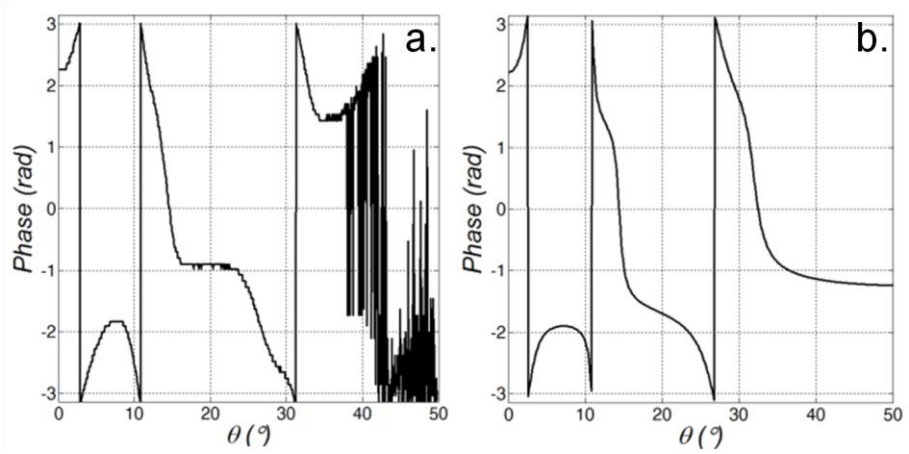

Figure 8-7: Phase of transmitted wave as a function of incident angle θ for an aluminum sample insonified at fd = 3 MHz.mm: experimental recording (a) and numerical simulation (b)

Comparison of the phase recording with the amplitude recording (Figure 8-5b) clearly reveals that the stimulation of a symmetrical Lamb mode is always associated to a sharp jump in phase because of phase wrapping. Similar results were obtained at different *fd*-values. For reasons of brevity, these are not shown.

Similar to the amplitude analysis given in the previous section, the recorded and computed phase-based H-UPS results for the materials with different level of anisotropy are presented in Figure 8-8. First of all, the overall shape of the phase polar scan again clearly reflects the anisotropic symmetry of the insonified material spot. In addition, the detail and sharpness of the characteristic phase patterns are much more outspoken and detailed in comparison with the amplitude results. Especially in view of the inverse characterization of the complex elasticity tensor of the insonified material spot, accurate amplitude and phase information may be essential to improve the precision of the inversion procedure. Satisfying agreement between experiment and numerical modeling is obtained, particularly for the aluminum sample. Despite the qualitative resemblance between the recorded and computed phase maps for the layered carbon and glass fiber composites, several differences can be observed. Most probably, this is partly attributed to inaccurate knowledge of the complex C-tensor for the layered materials.

A numerical study indeed confirms that the phase polar scan is sensitive to changes in the complex C-tensor. Even more, as the thickness of each lamina is difficult to control in an autoclave manufactured sample, it is easy to understand that small thickness variations may introduce a large shift in the phase of the transmitted wave.

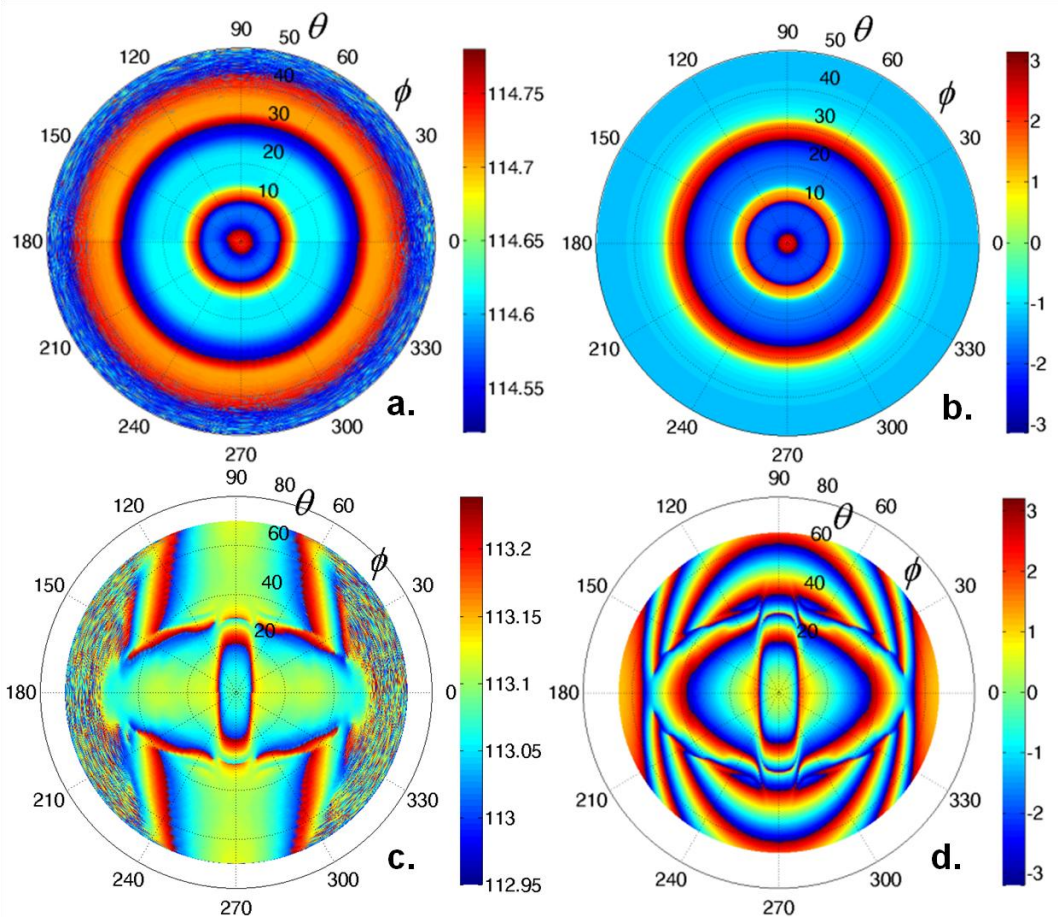

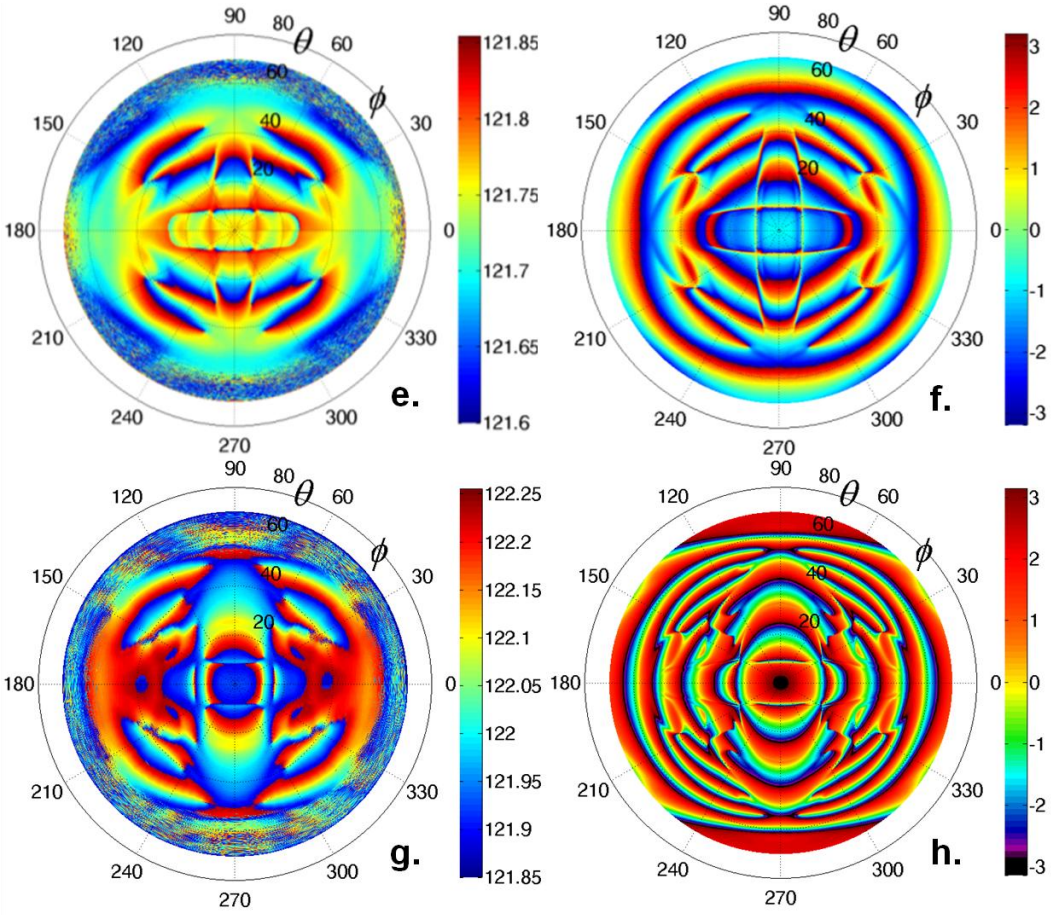

Figure 8-8: Phase-based H-UPS results: isotropic aluminum (a-b), orthotropic $[0_8]$ carbon/epoxy (c-d), orthotropic cross-ply $[0_2,90_2]_S$ carbon/epoxy (e-f) and hybrid glass/epoxy-carbon/epoxy $[0_3,90_4]_S$ laminate (g-h). Left colum corresponds to experiment, right column to simulation.

8. 5. Recording of the H-UPS in the Non-Specular Field

It has been shown that the integrating effect of a bounded beam could leave a Lamb wave stimulation condition undetected in the H-UPS results. This was explicitly shown for the aluminum sample at $fd = 4.5$ MHz.mm, in which the stimulation condition of the S_1 Lamb mode was not observed in the bounded beam simulation, nor in the experiment (see Figure 8-5c). However, it is clear that a S_1 Lamb wave should effectively be excited at $\theta \approx 14°$, even though it may be a weak excitation. Anyhow, the consequence of a Lamb stimulation should be observed in the associated energy leaking upon propagation. Hence, it is probable that a signature of the S_1 mode can

be found in the non-specular field. A schematic of the specular and non-specular fields is displayed in Figure 8-9. In general, the specular field corresponds to the geometrical reflection/transmission, while the non-specular field is associated to the forward displaced leaking field of a guided wave.

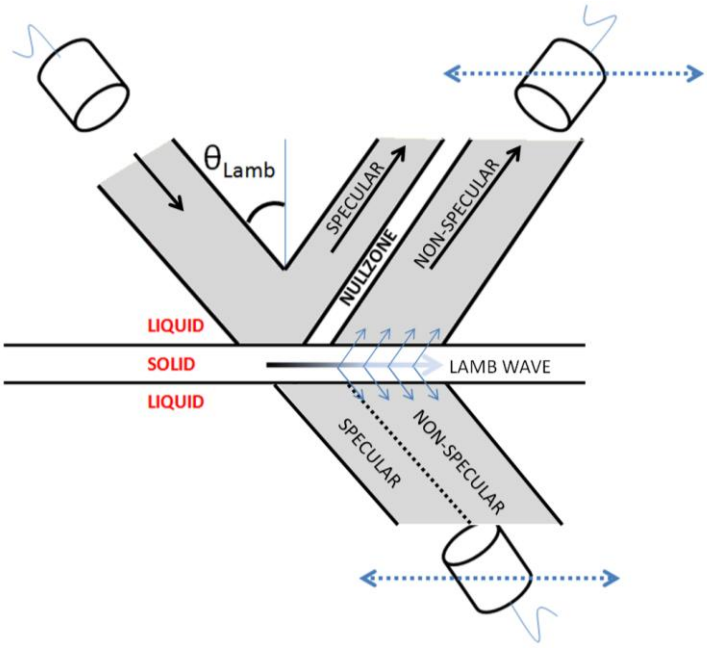

Figure 8-9: Schematic of the specular and the non-specular field.

A special fixture has been made in order to obtain H-UPS experiments in the non-specular transmission field. The H-UPS recordings for the aluminum sample at fd = 4.5 MHz.mm, obtained in the specular and the non-specular transmission field are shown in Figure 8-10. It can be observed that the recording in the specular field leaves the S_1 mode undetected (in agreement with Figure 8-5c), while the opposite is true for the recording in the non-specular field. Indeed, the non-specular recording reveals the presence of a high-intensity ring around $\theta = 14°$, which obviously corresponds to the leaking of the stimulated S_1 Lamb mode. Hence, this suggests that it may be advantageous to perform H-UPS experiments in the non-specular field. On the other hand, neither the specular recording, nor the non-specular recording can separate the A_0 and S_0 Lamb modes. It is further noted that the non-specular field has an arbitrary global amplitude level, which makes the extraction of attenuation characteristics impossible.

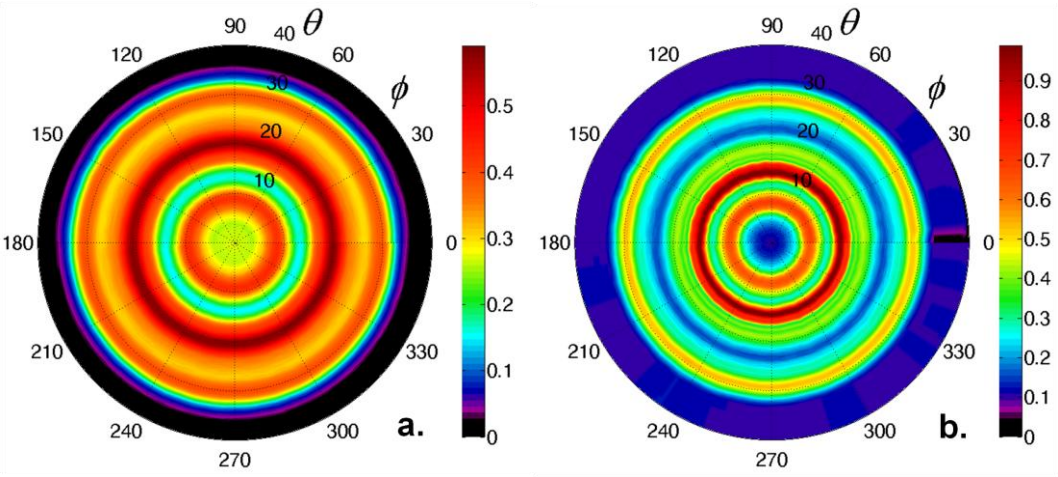

Figure 8-10: Amplitude-based H-UPS recording for aluminum at *fd* = 4.5 MHz.mm: specular transmission field (a) and non-specular transmission field (b).

8. 6. Conclusions

For the first time, ultrasonic polar scans have been recorded using quasi-harmonic pulses. Both numerical and experimental results have been presented for several materials with different levels of viscoelastic anisotropy. The numerical results confirm the link between the presence of a transmission amplitude peak and the stimulation of a leaky Lamb wave. Nonetheless, it is shown that the H-UPS cannot be regarded as a pure Lamb wave fingerprint, precisely because of the integrating effect of a realistic bounded beam. For future inverse modeling of the complex C-tensor, this observation is of great importance. It is further commented that the H-UPS measurements have potential for the inversion of the frequency-dependent complex elasticity tensor.

Besides conventional amplitude measurements, the methodology has been extended to the analysis of the phase of the transmitted signal. To the author's knowledge, this is unprecedented in literature. Good qualitative agreement is obtained between experiments and simulation. It is found that steep phase jumps are associated with the stimulation of symmetrical Lamb waves. Compared to the amplitude recording, the phase map provides even more intriguing and distinct patterns which may be useful to increase the accuracy of inversion procedures.

Finally, it was demonstrated that recording in the non-specular region can neutralize the integrating effect of a bounded beam. As such, Lamb wave excitations were imaged which were originally undetected in the H-UPS recording in the specular field.

8. 7. References

[1] Young, T., *Course of Lectures on Natural Philosophy and the Machanical Arts.* 1807.

[2] Rose, J.L., *Ultrasonic Waves in Solid Media*. 1999: Cambridge University Press. 454.

[3] Auld, B.A., *Acoustic Fields and Waves in Solids, second edition*. 1990, Florida: Krieger publishing company. 856.

[4] Declercq, N.F., J. Degrieck, and O. Leroy, *Ultrasonic polar scans: Numerical simulation on generally anisotropic media.* Ultrasonics, 2006. 45(1-4): p. 32-39.

[5] Degrieck, J. *Some possibilities of nondestructive characterisation of composite plates by means of ultrasonic polar scans*. in *Emerging technologies in nondestructive testing (ETNDT)*. 1996. Patras, Greece: A.A. Balkema.

[6] Declercq, N.F., J. Degrieck, and O. Leroy, *Simulations of harmonic and pulsed ultrasonic polar scans.* Ndt & E International, 2006. 39(3): p. 205-216.

[7] Matar, O.B., N. Gasmi, H. Zhou, M. Goueygou, and A. Talbi, *Legendre and Laguerre polynomial approach for modeling of wave propagation in layered magneto-electro-elastic media.* Journal of the Acoustical Society of America, 2013. 133(3): p. 1415-1424.

[8] Negishi, K., *Negative group velocities of lamb waves.* Journal of the Acoustical Society of America, 1978. 64: p. S63-S63.

[9] Wolf, J., T.D.K. Ngoc, R. Kille, and W.G. Mayer, *Investigation of lamb waves having a negative group-velocity*. Journal of the Acoustical Society of America, 1988. 83(1): p. 122-126.

[10] Negishi, K. and H.U. Li, *Strobo-photoelastic visualization of lamb waves with negative group velocity propagating on a glass plate.* Japanese Journal of Applied Physics Part 1-Regular Papers Short Notes & Review Papers, 1996. 35(5B): p. 3175-3176.

[11] Negishi, K., *Existence of negative group velocities in lamb waves.* Japanese Journal of Applied Physics Part 1-Regular Papers Short Notes & Review Papers, 1987. 26: p. 171-173.

[12] Marston, P.L., *Negative group velocity Lamb waves on plates and applications to the scattering of sound by shells.* Journal of the Acoustical Society of America, 2003. 113(5): p. 2659-2662.

PART II

This part extends the analysis of the traditional ultrasonic polar scan technique towards backscatter recording, and discusses several applications for NDT and material characterization.

Chapter 9

The Pulsed Ultrasonic Backscatter Polar Scan (P-UBPS) and Applications for NDT

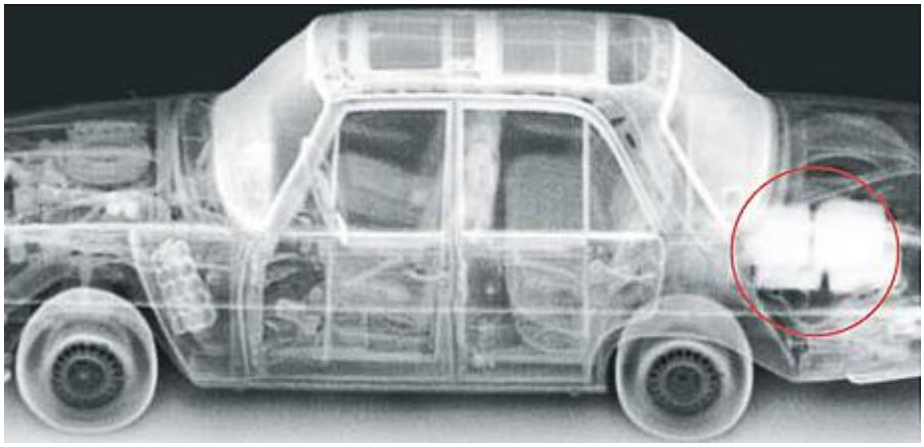

X-ray backscatter photography revealing the smuggling of drugs.

Summary

The data acquisition for the pulsed ultrasonic polar scan (P-UPS) has been changed to the recording of both the maximum amplitude and associated time-of-flight diffraction (TOFD) value for backscattered waves, hence resulting in the pulsed ultrasonic backscatter polar scan (P-UBPS). The P-UBPS technique is demonstrated for several applications, having particular interest in non-destructive testing of both metallic and composite structures. Examples include the characterization of the stacking sequence of layered composites, detection of sub-surface geometrical features, semi-quantification of hidden corrosion and the detection and localization of multiple surface breaking cracks. Whilst the P-UPS fingerprints elasticity related material properties, the P-UBPS provides a blueprint of (hidden) geometrical features.

9. 1. Introduction

In a conventional P-UPS experiment, the maximum amplitude or associated time-of-flight (TOF) value of the transmitted and/or reflected acoustic pulse are recorded for a wide range of incidence angles, in view of gaining knowledge about the elastic properties at the insonified material spot. Apart from the transmission and the reflection of sound waves, a small amount of acoustic energy can also be non-specularly back reflected to the emitting transducer. This backscattering phenomenon has been persistently observed during the recording of a P-UPS experiment, even at a large incident angle θ. Analysis of the corresponding time-of-flight-diffraction (TOFD) value indicate that the backscattered signal corresponds to a physical echo coming from the insonified material spot. (For backscatter geometry the term time-of-flight-diffraction, rather than time-of-flight, is used). This phenomenon is not new as Sasaki, already in the 1960's, discovered the occurrence of back reflected waves when insonifying a flat immersed metal at the Rayleigh angle [1]. From that date on, different physical mechanisms have been proposed to interpret these results, including the finite beam effect, backscatter due to material inhomogeneities, second order phenomena, etcetera [2-4]. Later on, several methods have been developed for a variety

of applications, precisely exploiting the detection of backscattered ultrasound. By proper time-gating, and subsequent analysis of the recorded backscattered signals in frequency domain, the backscattering technique has been applied successfully for a variety of applications in the research field of both metals and composites. Some of the major contributions of the backscattering technique include the evaluation of the fiber orientation [5-6], detection of notches [7], detection of corrosion [8], the ply-by-ply detection of matrix cracks [9-10], etcetera. However, these studies were always limited to a certain polar angle φ or a fixed incident angle θ, implying that a certain prior knowledge is required in order to obtain the envisioned results. Moreover, the selection of particular angles most likely entails that certain signatures are left unrecorded which could be important for the prediction of the life time and failure of the structure under investigation. Hence, until now the backscattering technique can only be applied successfully in a quantitative way for a limited number of applications.

In this chapter, we combine the P-UPS principle on a semi-spherical surface with the backscatter concept, resulting in the pulsed ultrasonic backscatter polar scan (P-UBPS). This combination, so far implemented on a laboratory scale and schematically represented in Figure 9-1, may pave the road to a more mature and quantitative non-destructive inspection technique based on the recording of ultrasonic backscatter.

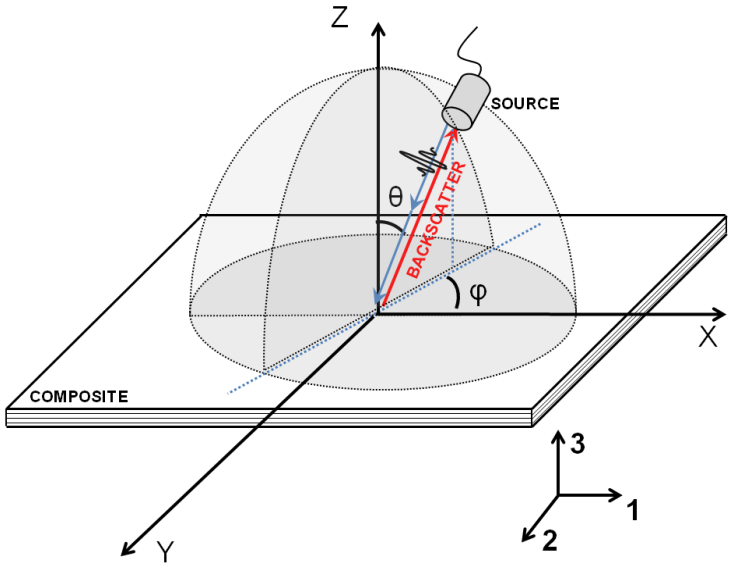

Figure 9-1: Schematic representation of the P-UBPS principle.

Very appealing with the P-UBPS method concerns the fact that only backscatter amplitudes (and/or their associated TOFD values) have to be recorded, for which no further analysis in frequency domain is required. Several cases, with particular importance for various industrial applications, are investigated and the experimentally obtained results are discussed. Examples include (i) determination of the stacking sequence in a cross-ply composite laminate, (ii) semi-quantification of a (possibly hidden) multi-directional surface corrugation, (iii) quantification of (possibly hidden) corrosion and (iv) detection and localization of a (possibly hidden) surface breaking crack in a laminated glass panel.

9. 2. Experimental Setup

The backscatter experiments have been obtained with the experimental setup discussed in Chapter 3, but now with the emitter employed in the pulse-echo mode. The acoustic signal is properly time-gated in order to record the backscattered signal with a sufficient sampling frequency. Basically, we put a wide time gate over the reflected signal when insonifying the sample of interest under normal incidence, to ensure that any backscattered signal is recorded. Within the gate, both the maximum amplitude and its associated TOFD value are stored on-the-fly. The physical width of the employed ultrasonic transducers in combination with the contribution of the specularly reflected acoustic energy, lead to intense signal amplitudes at near-normal incidence in a P-UBPS experiment. Therefore, a threshold was used for this region in the P-UBPS results to make the interpretation of the graphical data more straightforward.

9. 3. Results and Discussion

9. 3. 1. Determination of the Layer Stacking

In Figure 9-2, the results of both the P-UPS and the P-UBPS are shown for an autoclave manufactured orthotropic $[0]_8$ space grade carbon/epoxy laminate (thickness $d \approx 1.1$mm). It can be readily seen from the P-UPS recording that the local fiber direction is oriented at $\varphi \approx 32°$. The discrepancy with the manufactured orientation of 0°, is simply caused by the random cutting of a small sample from the $[0]_8$ laminate. The P-UBPS image on the other hand reveals an axis of enhanced backscatter at $\varphi \approx 121°$.

Although a single carbon fiber is too small to produce such intense backscatter patterns at f = 5MHz, fiber bundles are known to produce such patterns [6]. In a real composite material, the reinforcement fibers are often clustered into dense fiber bundles and therefore enhance the back-reflection of perpendicularly incident ultrasonic energy.

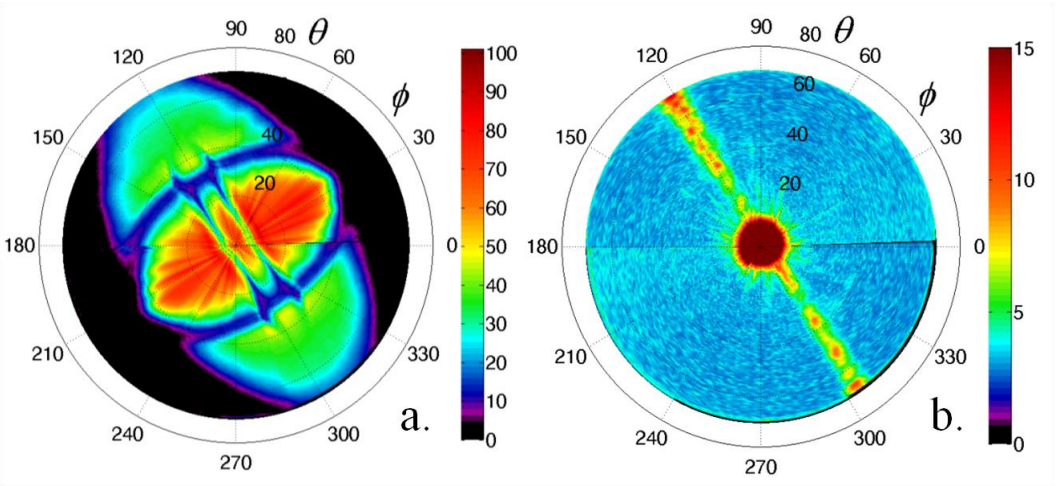

Figure 9-2: P-UPS (a) and P-UBPS (b) recording for an autoclave manufactured orthotropic $[0]_8$ space qualified carbon/epoxy laminate.

The results for a vacuum assisted resin transfer molded (VA-RTM) manufactured $[+45,-45]_s$ cross-ply glass/epoxy laminate, with thickness $d \approx 1.2$mm, are shown in Figure 9-3. The symmetry in the P-UPS clearly identifies the ±45° directions, though the discrimination as to which orientation is on top is far from straightforward. The P-UBPS recording of the $[+45,-45]_s$ glass/epoxy laminate on the other hand shows intense backscatter along φ = -45°, i.e. perpendicular to the fiber direction in the outer layer. A second axis of enhanced backscatter can be observed along φ = +45°, but with lower backscatter intensities. These results suggest that the P-UBPS is more sensitive to the fiber direction in the outer layers and thus provides valuable information about the layer stacking of the insonified material. This can be easily understood by considering the penetration depth which is function of the employed frequency of the acoustical wave.

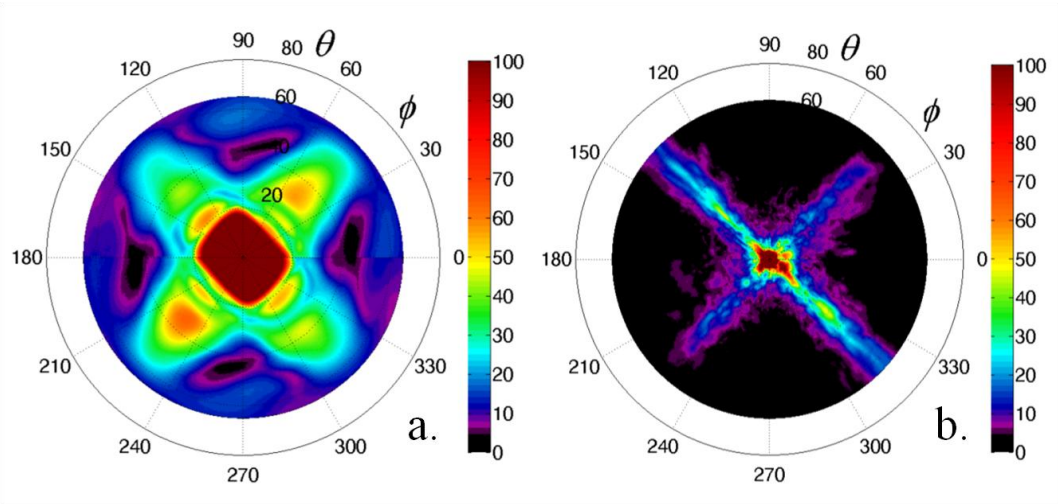

Figure 9-3: P-UPS (a) and P-UBPS (b) recording for a VA-RTM manufactured cross-ply $[+45°,-45°]_s$ glass/epoxy laminate.

It is mentioned that similar results were obtained in case of a $[0_2,90_2]_s$ cross-ply carbon/epoxy laminate, confirming the generality of the relation between the P-UBPS and the stacking sequence. Of course, for more complicated stacking sequences, e.g. $[0,90_2,0_2,90]_s$, the extraction of the stacking sequence becomes cumbersome without the use of extensive time-gating of the backscattered signal. Nevertheless, the P-UBPS offers an elegant and simple means to determine the stacking sequence of the most commonly used laminates.

9. 3. 2. Semi-quantitative Determination of a 2D (Sub)Surface Corrugation

During the manufacturing of composite samples, a so-called peel-ply is often employed in order to facilitate the release of the breather and bleeder from the sample. Since a peel-ply is a woven cloth, the surface of the composite sample may contain traces of the peel-ply imprint after fabrication. Figure 9-4 shows images of the surface texture of an autoclave manufactured peel-ply assisted $[0]_8$ carbon/epoxy laminate by means of both 2D optical microscopy and 3D confocal laser microscopy. Several symmetry directions, indicated by arrows to guide the eye, are clearly visible in the 2D map of the surface texture. The 3D surface map furthermore reveals the exact shape of the surface profile. The depth of the imprint is usually limited to $d \approx 85$ µm. Apart from manufacturing matters, such kind of surface structure is often

intentionally applied in order to improve the adhesion in case of adhesive bonding. In order to check whether the physical traces of these imprints can be detected by the P-U(B)PS, a thorough investigation was performed at different ultrasonic frequencies.

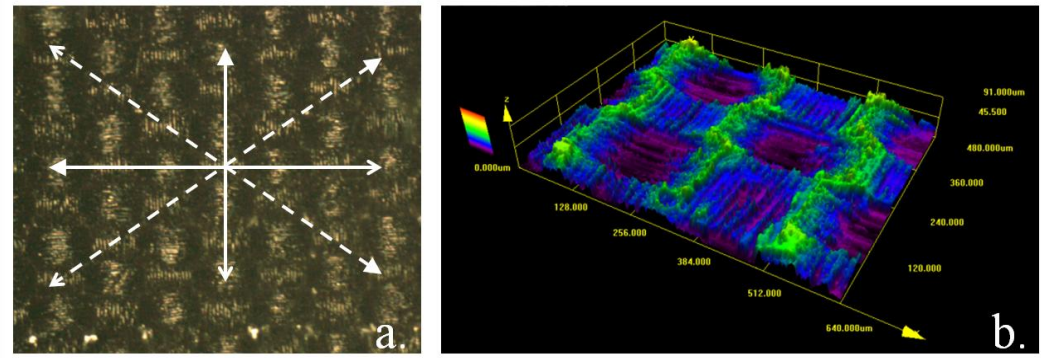

Figure 9-4: Surface map of an autoclave manufactured $[0]_8$ carbon/epoxy laminate: 2D optical microscopy (a) and 3D confocal laser microscopy (b). Full white arrows have been superposed to the 2D microscopy to highlight the angular direction of the lattice periodicities Λ which can be attributed to the surface profile. Dashed white arrows indicate the orientation of the diagonals of the rectangular surface cells.

The P-UPS as well as the P-UBPS image, both recorded at pulse frequency $f_c = 5$ MHz, are shown in Figure 9-5 for the $[0]_8$ C/E laminate. Both amplitude and TOF(D) recordings have been performed. Compared to the results for a flat $[0]_8$ carbon/epoxy laminate (see Figure 9-2a), no significant changes were observed in the obtained P-UPS image, indicating the lack of sensitivity of the P-UPS to detect such kind of microscopic surface features. The low sensitivity could have been expected since the backscatter amplitudes are at least an order of magnitude smaller than typical transmission amplitudes. In the P-UBPS recording on the other hand, several distinct traces emerge at which the backscatter intensity significantly increases. This can be seen at $\varphi \approx 0$, $\varphi \approx 57°$, $\varphi \approx 69°$, $\varphi \approx 90°$, $\varphi \approx 111°$ and $\varphi \approx 125°$, as well as at complementary angles.

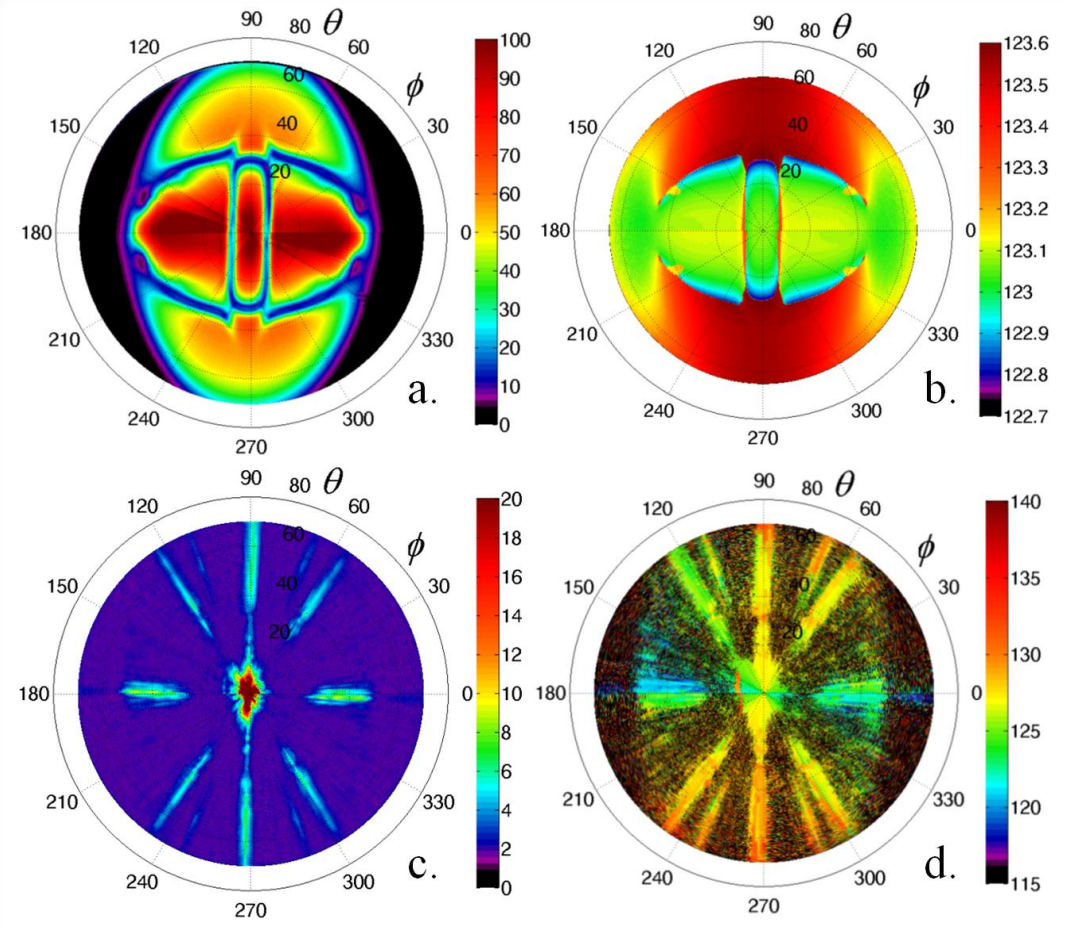

Figure 9-5: P-UPS (a-b) and P-UBPS (c-d) recordings at frequency f_c = 5MHz for the corrugated $[0]_8$ C/E laminate: amplitude (left) and TOF(D) (right).

Hence, the material symmetry of the insonified unidirectional carbon/epoxy laminate is not at all reflected in the P-UBPS image, indicating that the backscatter patterns are not solely related to the intrinsic material properties. Comparison with the optical microscopy of the surface profile on the other hand, immediately reveals the mutual relation between the observed backscatter and the surface texture. Indeed, the traces of enhanced backscatter can be straightforwardly identified as those perpendicular to the symmetry axes of the surface structure (full white arrows in Figure 9-4a). The backscatter patterns at $\varphi \approx 57°$ and $\varphi \approx 125°$ (and their complementary angle) can be understood by considering 1st order combinations between the reciprocal lattice constants (the angular directions of these have been added on Figure 9-4 by means of white dashed arrows). Obviously, the weak backscatter patterns at $\varphi \approx 69°$ and $\varphi \approx 111°$ then correspond to 2nd order

combinations. Further convincing evidence of the relation between the enhanced backscatter and the surface imprint can be found from the supplementary TOFD analysis. The TOFD-recorded P-UBPS image reveals a strong uniformity of the TOFD values at the axes of enhanced backscatter. Outside those regions of uniform TOFD values, highly oscillating TOFD measurements can be observed in the P-UBPS image. This rather chaotic behavior of the TOFD value arises when the level of the acoustic noise becomes too large, compared to the backscatter intensity, to perform a reliable TOFD measurement.

In view of these results, it is clear that the peel-ply imprint can be interpreted as an acoustic reflection grating. Different wave vectors, positioned in the 12-plane, can be assigned to the grating structure, explaining the dependency of the recorded backscatter patterns on the incident angle θ. To illustrate the grating concept in more detail, a P-UBPS experiment has been recorded at a different ultrasonic frequency f_c. Increase, respectively decrease, of the employed frequency would then result in an inward, respectively outward, shift in θ-direction of the recorded backscatter patterns. Figure 9-6 represents the P-UBPS recorded at f_c = 15MHz, confirming the expected inward shift.

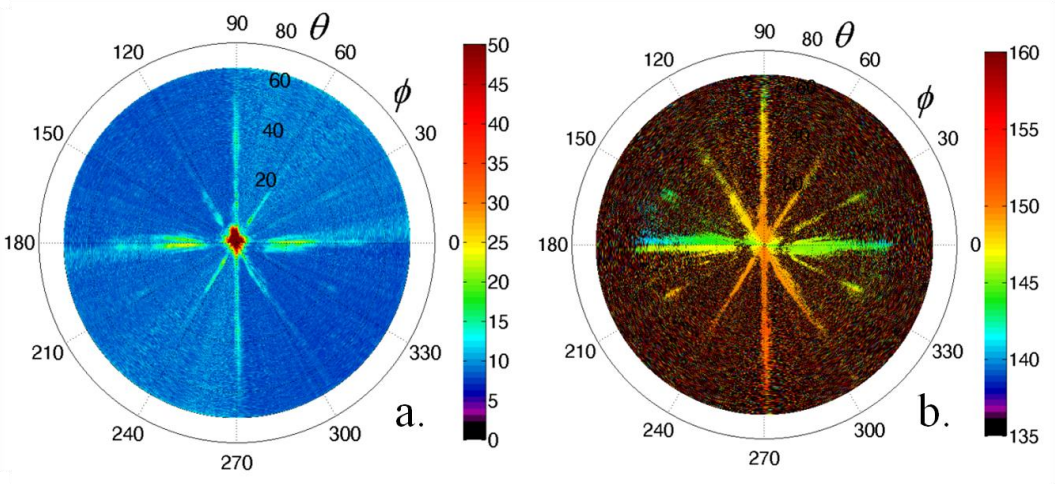

Figure 9-6: P-UBPS image of the corrugated $[0]_8$ C/E laminate recorded at a frequency f_c = 15MHz: amplitude (a) and TOFD (b).

This implies that the P-UBPS is not limited to the determination of the direction angle φ of a corrugation, but also provides valuable information about the periodicity of the corrugation. To support this, the recorded backscatter pattern in Figure 9-5c at the polar angle $\varphi \approx 0°$ is discussed.

Assuming the frequency of the acoustic pulse to be f_c = 5MHz, an acoustic wavelength λ_c = 0.295mm is obtained in water. Given the optically determined grating constant $\Lambda \approx$ 0.25mm of the peel-ply, the incident angle θ can be computed for which the -1st reflection order of diffraction coincides with the opposite direction of the incident ultrasonic beam, according to Bragg's law [11]:

$$\theta = \sin^{-1}\left(m\lambda / 2\Lambda\right) \tag{1}$$

with m the diffraction order and assuming that the backscattered signal has a measurable amplitude.

With the above mentioned parameters, the incident angle θ can be computed and corresponds to θ = 36°, at least when assuming an incident harmonic plane wave. This value is in qualitatively good agreement with the location of the maximum backscatter in the experiment ($\theta \approx$ 39°).

Because of Snell's law, the horizontal component of the wave vector $\boldsymbol{k}$ is conserved at a liquid-solid interface. This implies that similar, but not identical, diffraction phenomena should be present in case when the surface corrugation is located at the backside of the sample. In Figure 9-7, the P-UBPS recording of the $[0]_8$ C/E laminate, but now with the peel-ply imprint located at the backside, is shown. It can be observed that similar backscatter patterns are present as for the front-side insonification (Figure 9-5c). Though, we note that the backscatter related to the fiber bundles interferes strongly with the envisioned backscatter from the peel-ply imprint. This comes as no surprise since the ultrasonic signal associated with the hidden corrugation has to traverse the $[0]_8$ carbon/epoxy laminate twice. Supplementary experiments on a corrugated isotropic homogeneous plexi glass sample showed that this interfering effect was absent in this case. For brevity, these results are not included.

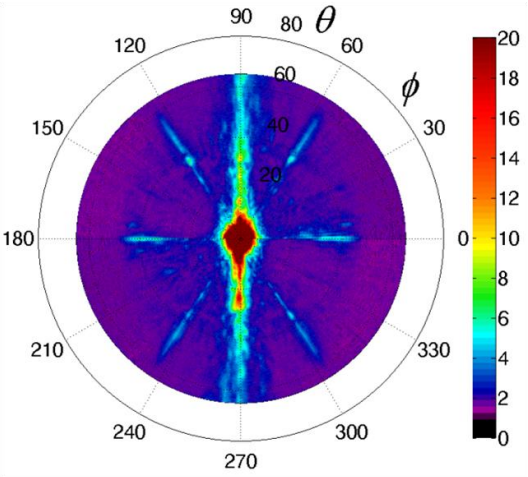

Figure 9-7: P-UBPS for the corrugated $[0]_8$ C/E laminate recorded at a frequency f_c = 5MHz. Compared to the situation of Figure 9-5c, the corrugation is now located at the backside of the sample.

The above results thus clearly demonstrate the capability of the P-UBPS to semi-quantify hidden multidirectional surface corrugations, which could be of great importance for the bonding industry. Indeed, as a multi-directional surface corrugation is often applied to a fiber reinforced composite to enhance its bonding capabilities, the P-UBPS could serve as a means to inspect the characteristics and quality of the applied surface corrugation.

In contrast to the bonding industry, several other engineering applications demand a smooth surface structure in order to increase the structural performance of the component. In view of previous results, we investigated the performance of the method for the inspection of the quality of polished surfaces. Generally, during the production process and depending on the polishing grade, a small residual roughness is left which is oriented in a specific direction due to the machining process. The sample under investigation is a VA-RTM manufactured epoxy plate. The molds used in the VA-RTM process have been micro-machined, resulting in a tolerance below 5 µm for the surface roughness. During manufacturing of the epoxy sample, this minimal surface profile of the molds may leave a negative imprint at the surface. The recorded P-UBPS of the epoxy sample is shown in Figure 9-8. A trace of enhanced backscatter can be clearly observed along the orientation φ = 90°, which is normal to the orientation of the machining process (φ = 0°) at which the molds have been fabricated. Note that the

recorded backscatter amplitudes are very small, owing to the small nominal depth of the surface imprint.

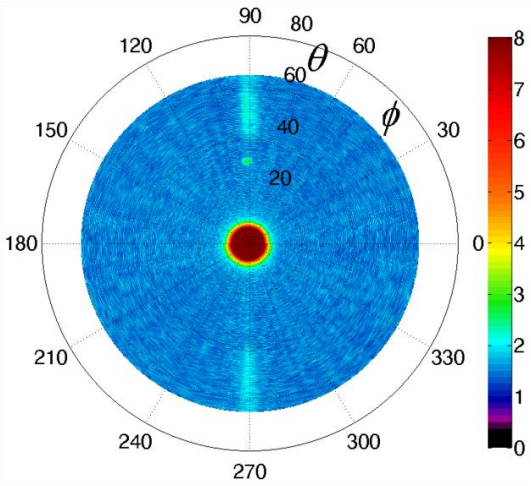

Figure 9-8: P-UBPS recorded at f_c = 5MHz of a VA-RTM manufactured epoxy sample, employing polished molds.

9. 3. 3. Corrosion Characterization

9. 3. 3. a. Front Side Corrosion

An additional commonly encountered problem in a variety of industrial applications concerns the presence of corrosion. In this subsection, the feasibility of the P-U(B)PS to detect corrosion in an early stage is investigated. To this end, several rolled steel samples (thickness d = 0.85mm) have been subjected to accelerated corrosion in a salt spray cabinet according to ASTM standards (ASTM B117-73: Standard Method of Salt Spray (Fog) Testing), i.e. permanent spray at 35°C, with a supply of the electrolytic (2.5kg NaCl/50l H_2O) at 1ml/hour. In order to introduce single-sided corrosion, which is often encountered in a realistic environment, one side has been covered with a layer of paint, which was afterwards removed, to prevent the initiation of corrosion. Several gradations of corrosion have been applied by varying the exposure time to the acid solution in the salt spray cabinet (see Table 9-1). All P-U(B)PS results reported in this section have been performed under exactly the same circumstances, hence the experimental results can be compared to each other without additional considerations.

Table 9-1: Characteristics of the different corroded steel samples.

	Thickness (mm)	Exposure time (days)	Level of corrosion	p_{Norm} (front)	p_{Norm} (back)
Sample 1	0.85	0	Virgin state	1.000	1.000
Sample 2	0.85	1	Mild	4.391	1.797
Sample 3	0.85	4	Moderate	7.846	2.254
Sample 4	0.85	25	Severe	13.329	8.865

In the left column of Figure 9-9, the different P-UPS images are shown for the case when the corrosion is located on the side of the sample facing the incident transducer (front side). The presence of moderate oxidation has a negligible influence on the results of the P-UPS. For the case of severe corrosion, an abrupt drop in transmitted amplitudes can be observed (note that the amplitude scale in Figure 9-9g was rescaled to [0;15]). This drop in transmitted amplitudes can be understood taking into account that the liquid-solid interface of the severely corroded sample cannot be seen anymore as a neat flat interface, but rather as a disorderly cluttered interface. In addition, the rust flakes cause the ultrasonic wave to traverse several liquid-solid interfaces, which obviously leads to larger damping of the transmitted ultrasonic wave.

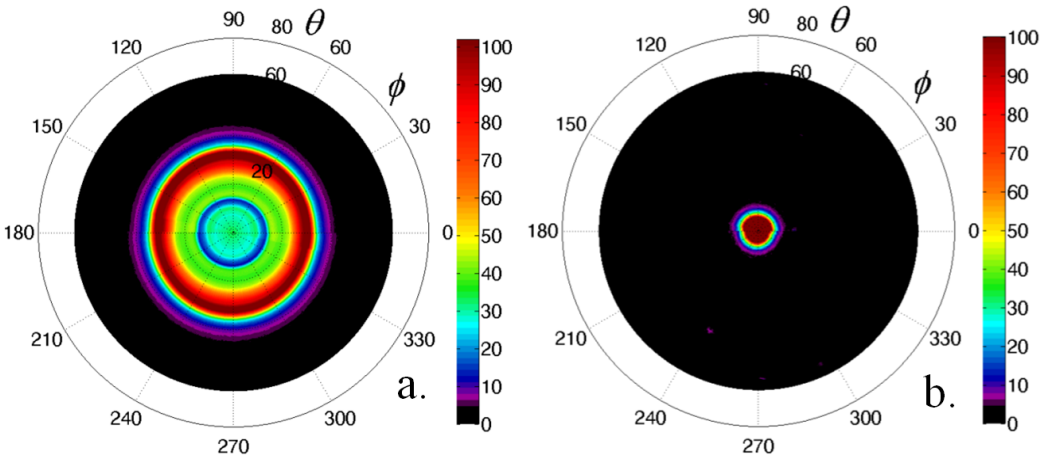

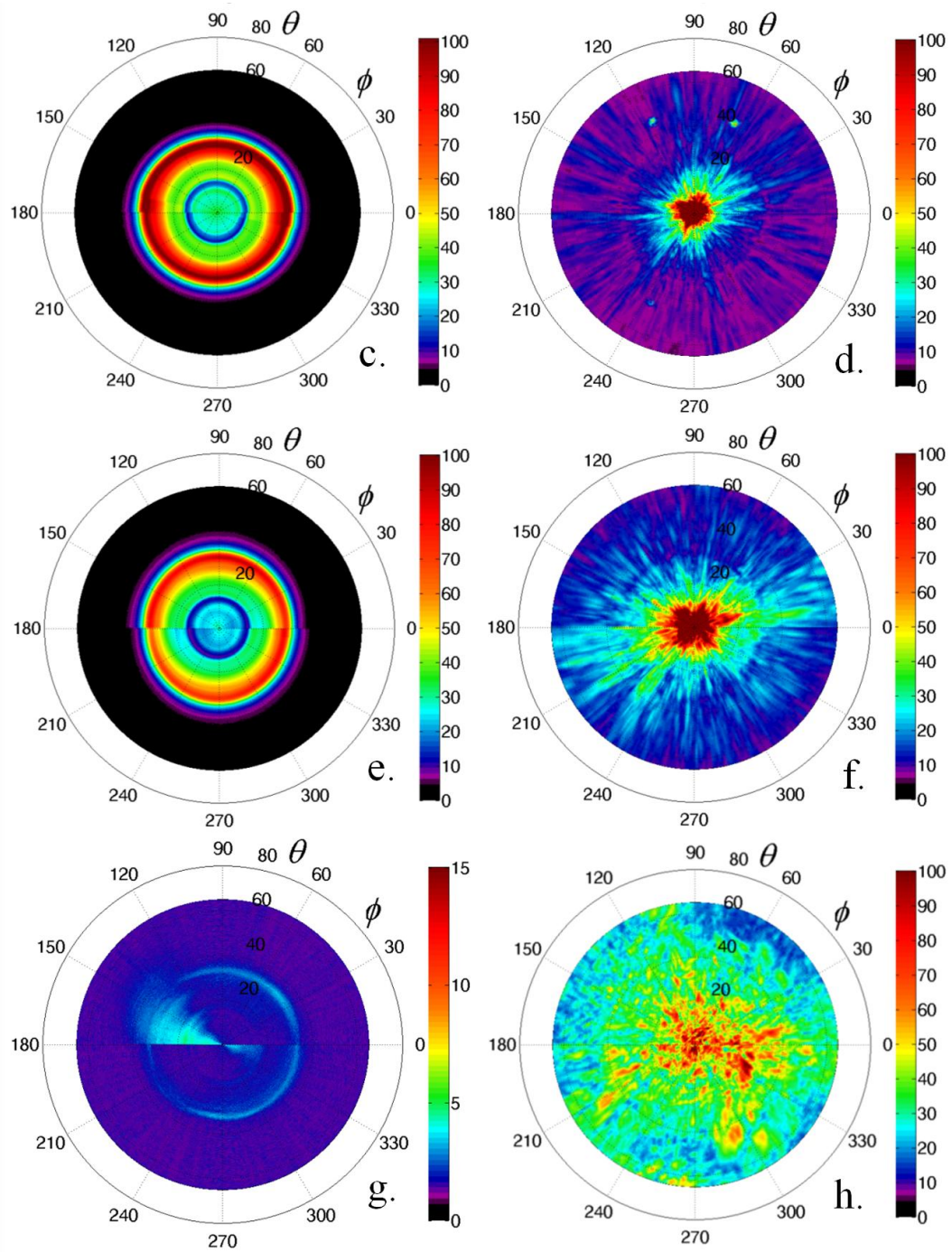

Figure 9-9: P-U(B)PS results for the steel samples: virgin state (a-b), mild corrosion (c-d), moderate corrosion (e-f) and severe corrosion (g-h). The left, right column corresponds to the results of the P-UPS, respectively P-UBPS. The

corrosion is located on the side of the sample facing the incident transducer (front side).

The results for the P-UBPS are shown in the right column of Figure 9-9, also considering the case of front side corrosion. For the steel sample in virgin state, a very limited amount of backscatter can be observed near normal incidence resulting from the finite size of the transducer. For sample 2 with mild corrosion, the backscatter fingerprint changed significantly compared to the virgin sample, illustrating the high sensitivity of the P-UBPS to detect the presence of corrosion in an early stage. The random backscatter pattern reflects the typical chaotic nature associated to corrosion. A supplementary TOFD analysis (not shown) revealed that the observed backscatter is highly incoherent, which could have been expected for the case of corrosion. For the more corroded steel samples (samples 3 and 4), similar chaotic patterns can be observed in which the recorded backscatter scales with the level of corrosion. To supply an objective means to compare the different P-UBPS recordings, a normalized scaling parameter p_{Norm} has been defined as follows:

$$p_{Norm} = \frac{\sum_{\theta=10}^{65} \sum_{\varphi=0}^{360} Backscatter\,Amplitude}{\sum_{\theta=10}^{65} \sum_{\varphi=0}^{360} Reference\,Backscatter\,Amplitude} \qquad (2)$$

Note that p_{Norm} has been computed for $\theta > 10°$, in order to exclude the large contribution of the specular reflection. The values of p_{Norm} for the different steel samples are listed in Table 9-1, and show an increasing trend as expected.

9. 3. 3. b. Backside Corrosion

The previous results applied to front side corrosion, and inevitably prompts the obvious question with particular interest for industry: "is the P-UBPS also capable to detect and semi-quantify corrosion at the backside of a structure?". In order to answer this question, the corroded samples have been scanned again, but now with the corrosion located at the backside of the sample. Since similar observations hold for the transmission P-UPS recordings when compared to the left column of Figure 9-9, these results have been omitted. The backscatter results for the samples with backside

corrosion are shown in Figure 9-10. First of all, we observe that the obtained backscatter pattern has changed in comparison with the front side results displayed in Figure 9-9. This change in fingerprint can be understood by realizing that the diffraction phenomenon at the bottom surface is similar but not equivalent to the diffraction mechanism at the top surface. Depending on the liquid and solid properties, it becomes impossible to efficiently couple acoustical energy into the solid when surpassing a certain incident angle θ. This can be easily observed in the P-UPS recordings shown in the left column of Figure 9-10. The absence of an acoustical wave inside the solid obviously implies that no diffraction can take place at the backside of the insonified sample, and consequently no backscatter can be recorded. Therefore, the backscatter related to the bottom-side corrosion is found to be enclosed within a certain incident angle θ, hence offering a means to verify that the corrosion is indeed located at the backside of the investigated sample. Similar as for the backscatter results obtained for the front side corrosion, the recorded backscatter intensity scales with the degree of corrosion. The result of p_{Norm} for the different backside corroded steel samples have been added to Table 9-1.

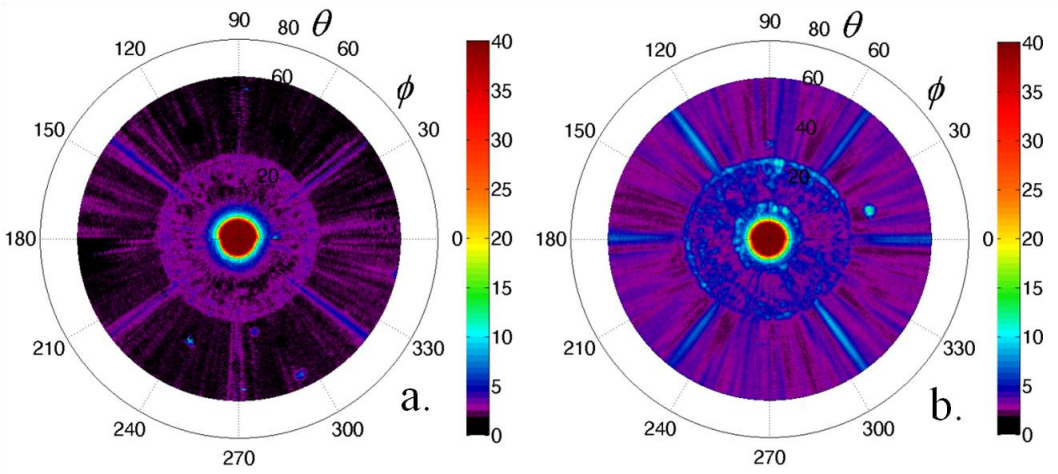

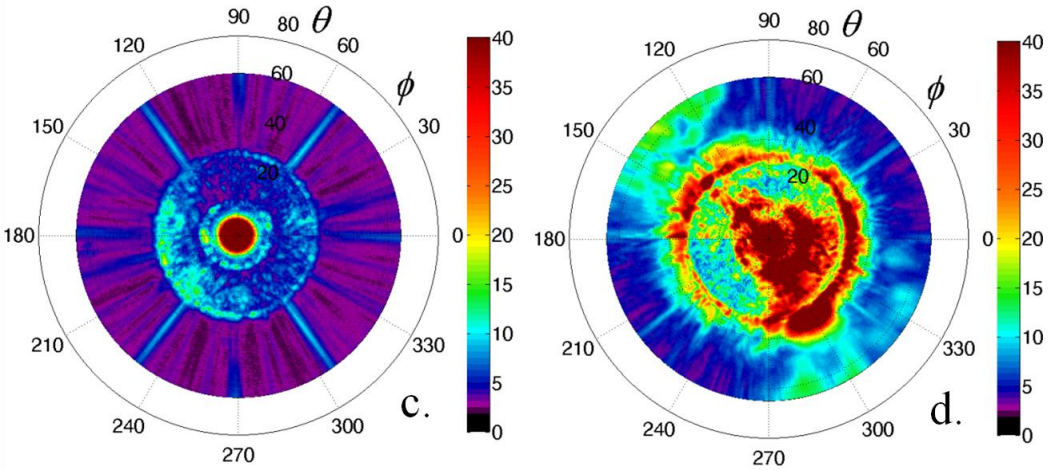

Figure 9-10: P-UBPS in case the corrosion is located at the back side of the steel sample: virgin state (a), mild corrosion (b), moderate corrosion (c) and severe corrosion (d). The superposed pattern of rays has to be attributed to the skin passing of the work rolls during manufacturing of the steel samples.

In addition to the backscatter information linked to the corrosion, a pattern of rays emerges in the P-UBPS recordings. As for the results discussed in the previous section, this pattern can be linked to the presence of a periodic surface structure. The fact that the octagonal pattern is not bounded in θ-direction reveals that the surface structure is located at the top side of the steel sample and has no relation with the corrosion at the back side. The origin of the surface structure is found in the skin passing of the rolls during manufacturing of the steel samples. This surface texture is investigated in Chapter 11 more into detail.

9. 3. 4. Detection and Localization of Closed Surface Breaking Cracks

Finally, we apply the P-U(B)PS technique to the inspection of a closed surface breaking crack (CSBC). Generally, this type of defect is very difficult to detect, if not impossible, with classical ultrasonic techniques such as the C-scan because of the specific orientation of the defect with respect to the direction of insonification. The polar scan method however, also uses oblique incidence and therefore stimulates lateral waves in the insonified sample. Hence, it is very tempting to check whether the P-U(B)PS technique adds to the detection and localization of a CSBC. The sample under investigation is a laminated annealed glass sample which is often used as a

structural glazing unit. Each glass ply has a nominal thickness of d = 4mm, the interlayer is polyvinylbutyral (PVB) with a nominal thickness d = 0.74 mm. The sample was provided by Solutia inc. In one of the glass plies, two cracks were initiated by means of a diamond wheel glass cutter. Application of a uniform pressure on the surface of the sample then resulted in the formation of two cracks, which both extend over a single glass layer. The induced cracks can be considered to be closed (see Figure 9-11). The zone of insonification is indicated on Figure 9-11, together with some physical dimensions.

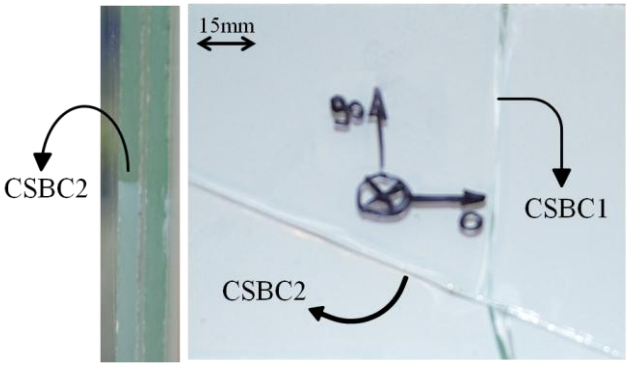

Figure 9-11: Laminated annealed glass sample in which 2 CSBC's have been introduced: side view (left) and top view (right). The insonification spot as well as some indicators have been added.

The P-UPS results for the cracked laminated glass sample is shown in Figure 9-12a-b and display a quite regular fingerprint containing circular patterns which are typical for undamaged isotropic and homogeneous materials. This indicates that the P-UPS is not sensitive at all to the presence of any of the CSBC's. Of course, this could have been expected, considering the fact that the zone of insonification is located relatively far from the induced damage, and thus the transmitted acoustic signal does not interact directly with the CSBC's.

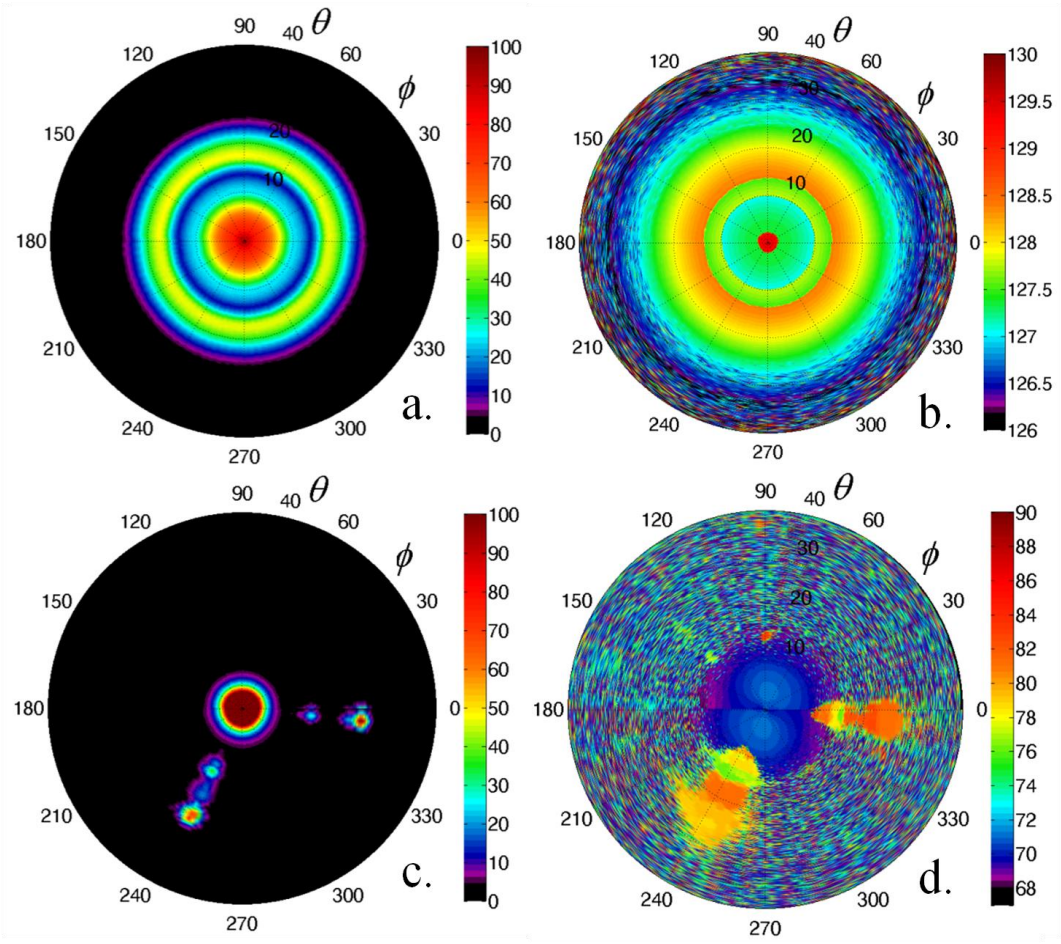

Figure 9-12: P-UPS (a-b) and P-UBPS (c-d) results for the laminated glass sample: amplitude (left) and TOF(D) (right).

The P-UBPS results on the other hand show intense backscatter signals at those polar angles φ, which are perpendicular to the physical orientations of both CSBC's (see Figure 9-12c). The origin of this backscatter is attributed to the interaction of stimulated lateral waves with the CSBC, resulting in a back reflection of the signals for certain angle combinations (similar to the analysis presented in Section 5.2.7). Since all possible orientation angles are involved in a P-UBPS experiment, one experiment should in principle suffice to detect the orientation φ of multiple CSBC's. Despite this fact, the exact location of the defects cannot be retrieved by means of the amplitude recorded P-UBPS. If however the TOFD values, associated to the registered backscatter amplitudes, are recorded in the P-UBPS experiment, additional information about the exact location of the CSBC can be revealed.

Considering Figure 9-12d, the TOFD value at $\psi(\varphi,\theta) = \psi(0,0)$ correspond to the echo of the surface and thus serves as a reference. The distance between the zone of impingement and the location of the CSBC's can now be easily computed by taking into account both the TOFD measurement and the relevant bulk wave speed of the insonified glass. Doing so, the following results have been obtained: $(d_1,\varphi_1) = (23.4\text{ mm}, 354°)$ and $(d_2,\varphi_2) = (19.7\text{ mm}, 244°)$, which agree very well with the actual situation.

Again, this investigation was repeated in the case where the CSBC's were located at the backside of the laminated glass structure. Although the involved amplitude values were lower, similar observations hold. For brevity however, these results have been omitted.

9. 4. Conclusions

In this chapter, the pulsed ultrasonic backscatter polar scan (P-UBPS) is introduced as a quantitative, single-sided, contactless, and non-destructive testing technique with a high potential for a variety of applications in material research and NDT in general. We have demonstrated the potential of the P-UBPS technique by presenting results for

(i) Quantitative determination of the local fiber direction for a $[0]_8$ carbon/epoxy laminate and for a cross-ply $[+45,-45]_s$ glass/epoxy laminate.

(ii) Semi-quantitative determination of a multidirectional surface structure, caused by the use of a peel-ply during manufacturing of a $[0]_8$ carbon/epoxy laminate. Even when located at the backside, the P-UBPS assessed and mapped the surface corrugation without additional difficulties.

(iii) Detection of corrosion on a rolled steel sample in an early stage. It is shown that the overall backscatter intensity scales with the grade of corrosion, which opens the possibility of quantification. Similar, but not equivalent, results have been obtained in case the corrosion was located at the backside of the sample. Even more, the effect of skin passing of the work rolls, used for the manufacturing of the steel samples, has been detected.

(iv) Detection of CSBC's in a laminated glass sample. Apart from the orientation of the cracks, the physical location of the CSBC was retrieved by an additional analysis of the TOFD recorded P-UBPS.

Further, it was found that no mutual influence exists between the P-UPS and the P-UBPS, at least for the here considered experiments. Hence, this implies that both techniques offer valuable and unique information and thus can be employed in a complementary way.

9. 5. References

[1] Sasaki, S., *Back reflection of ultrasonic wave obliquely incident to solid surface in water.* Japanese Journal of Applied Physics, 1963. 198.

[2] Nagy, P.B. and L. Adler, *Increased incoherent backscattering from a liquid-solid interface at the Rayleigh angle.* Journal of the Acoustical Society of America, 1994. 96(4): p. 2537-2545.

[3] Norris, A.N., *Back reflection of ultrasonic-waves from a liquid solid interface.* Journal of the Acoustical Society of America, 1983. 73(2): p. 427-434.

[4] Van Den Abeele, K.E.A., R. Briers, and O. Leroy, *Inhomogeneous plane-wave scattering and mode stimulation on periodic rough surfaces.* Journal of the Acoustical Society of America, 1996. 99(5): p. 2883-2897.

[5] Bechtold, G., K.M. Gaffney, J. Botsis, and K. Friedrich, *Fibre orientation in an injection moulded specimen by ultrasonic backscattering.* Composites Part a-Applied Science and Manufacturing, 1998. 29(7): p. 743-748.

[6] Nagy, P.B., A. Jungman, and L. Adler, *Measurements of backscattered leaky lamb waves in composite plates.* Materials Evaluation, 1988. 46(1): p. 97-100.

[7] Kwon, S.D., M.S. Choi, and S.H. Lee, *The applications of ultrasonic backward radiation from a layered substrate submerged in liquid.* Ndt & E International, 2000. 33(5): p. 275-281.

[8] Bar-cohen, Y. and R.L. Crane, *Acoustic-backscattering imaging of subcritical flaws in composites.* Materials Evaluation, 1982. 40(9): p. 970-975.

[9] Kinra, V.K., A.S. Ganpatye, and K. Maslov, *Ultrasonic ply-by-ply detection of matrix cracks in laminated composites.* Journal of Nondestructive Evaluation, 2006. 25(1): p. 39-51.

[10] Aymerich, F. and S. Meili, *Ultrasonic evaluation of matrix damage in impacted composite laminates.* Composites Part B-Engineering, 2000. 31(1): p. 1-6.

[11] Cowley, J.M., *Diffraction Physics*. 3th revised ed. 1995, Amsterdam (the Netherlands): Elsevier Science B.V. 481.

Chapter 10

Ultrasonic Characterization of a Multidirectional (Sub)surface Corrugation in the Bragg Regime

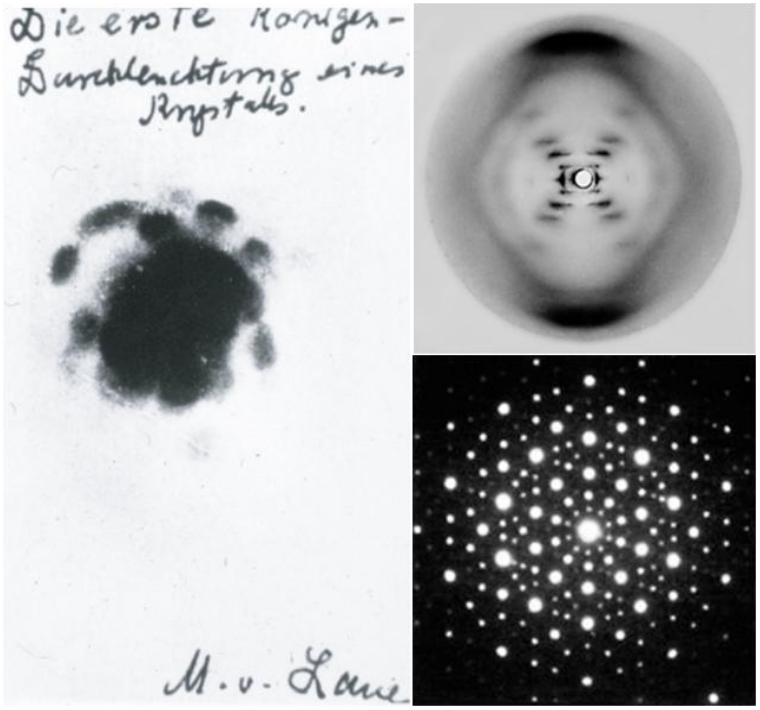

Left: Friedrich and Knipping's first successful X-ray diffraction photograph on copper. Upper right: X-ray diffractogram exposing the 3D helical structure of the DNA molecule (Figure reproduced from reference [1]). Lower right: X-ray diffractogram revealing the existence of aperiodic crystals (Figure reproduced from reference [2]).

Summary

This chapter handles the ultrasonic characterization of 1D and 2D periodic (sub)surface structures in the Bragg diffraction regime. First, the recently developed angular spectrogram methodology [3] is employed, from which the dominating surface periodicities are obtained through an optimization procedure. However, as the angular spectrogram method requires prior knowledge about the surface symmetry lines, it has limited use for real applications. To eliminate the necessity of prior knowledge, a harmonic version of the ultrasonic backscatter polar scan (H-UBPS) is considered. The H-UBPS extracted surface parameters, i.e. both the surface periodicities and the symmetry orientations, show excellent agreement with the true surface parameters. At last, the ultrasonic polar spectrogram scan (UPSS) is introduced to characterize periodicities and symmetry orientations. The UPSS combines the advantages of both the angular spectrogram method and the H-UBPS, while the complexity of the experimental implementation is significantly reduced.

Results are presented for 0D, 1D and 2D corrugated samples, with various grades of surface finishing quality. The presence of several ghost diffraction peaks within the experimental recordings are linked to periodic and aperiodic imperfections. In addition, the characterization of a hidden 2D surface structure has been successfully tackled.

10. 1. Introduction

In 1660, the Italian Grimaldi has been the first to observe the phenomenon of light diffraction. These observations have been posthumously described in 1665 [4]. Around 1900, different types of radiation were discovered such as X-rays, which had, at that time, the mind-boggling capability to traverse solid material. It was Von Laue in 1912 who realized that X-rays are ordinary electromagnetic waves, but on another scale, and that the short wave length makes them ideal for investigating the internal atomic structure of materials by exploiting the phenomenon of diffraction. A solid theoretical background of the involved phenomena was soon thereafter provided by Bragg [5], giving birth to X-ray diffraction crystallography which is still an

important and widely used research instrument in current material science research. It did not take long to realize that the underlying principles of the X-ray diffraction are valid for electrons and ultrasound waves. It is the work of Von Laue, Bragg as well as others which led to the decipherment of the 3D helical structure of DNA [1] and to the discovery of aperiodic crystals [2].

The deployment of periodic surface structures is indispensable for a variety of engineering applications, such as frequency filters, phononics, telecommunication, tailored sliding friction, etcetera [6-9]. Diffraction-based techniques obviously fit for the inspection of such periodically ordered features. However, the involved length scale of geometrical features are typically a few orders larger compared to length scales involved in crystallography, making optical waves, X-rays and electron beams useless. An alternative is the use of ultrasonic waves in the MHz range. Like X-rays and electron beams, ultrasound can penetrate inside solids, making them an ideal candidate for inspecting internal geometrical features.

Several studies have already investigated both experimentally and numerically the interaction of a normally incident broadband ultrasonic wave with a solid having surface structure. Subsequent analysis of the reflected or transmitted signal in frequency domain then yields features which are linked to geometrical and mechanical properties of the investigated specimen [10-14]. However, as the use of normal incidence limits the amount of obtainable data, several researchers have extended the experimental and theoretical investigation to the use of oblique incidence, and applied this to a variety of surface structures [3, 15-22]. Similar as periodic layers of atoms for X-rays and electron beams, a periodic surface acts as a diffraction grating for ultrasonic waves. Hence, analysis of the associated ultrasonic diffraction phenomena yields knowledge about the geometrical features of the insonified surface. Most often, experimental studies employ the ultrasonic transducer as both the emitter and the receiver (Bragg regime). Hence, a signal is only received at that angle, the Bragg angle, at which a diffracted component is scattered back to the emitter.

The different oblique incidence methods described in literature all assume *a priori* known symmetry lines of the surface grating under investigation. In references [19-20], a narrowband ultrasonic transducer, positioned along the symmetry lines, was used to investigate both 1D and 2D (im)perfect periodic

surface structures. Recording of the backscattered intensity versus the incident angle θ showed maxima, exposing the Bragg angles. The value of the Bragg angle was used to determine the periodicity, while the backscattering intensity was found to relate to the rms value of the surface roughness [19-20]. In addition, those researchers showed that defects in the surface periodicity give rise to "Rowland ghosts" and "satellites" in the ultrasonic diffraction process, as was already observed in optical spectroscopy [23-24]. With the same experimental methodology, an internal 1D grating was successfully inspected [20]. By using a broadband ultrasonic pulse and a spectroscopic analysis of the backscattered wave, the incident angle can be fixed to some discrete values to obtain equivalent results [19]. In the work of Herbison [3, 18], several experiments have been performed on plates superposed with an imperfect 1D or 2D surface corrugation. By combining the spectroscopic approach with the scanning of the incident angle θ, an angular spectrogram is obtained which exposes continuous Bragg scattering curves. Here again, the axis of rotation of the transducer is aligned with either the principal axes or the diagonal of a surface structure unit cell. When applied to a corrugated plate, the angular spectrograms further reveal amplitude variations [3], which have been explained by the appearance of backscattered leaky Lamb waves, as earlier observed in for example the work of Nagy [25]. Likewise, the method of angular spectroscopy has been further applied using air-coupled transducers to the inspection of 1D stacked cylindrical rods [26]. It has been commented that the recorded angular spectrogram can be used to determine the periodicity of the inspected surface structure. However, the application of an inversion procedure to actually determine the optimal periodicity from a recorded angular spectrogram has not yet been demonstrated.

In the present chapter, three different experimental methodologies have been investigated for characterization of 0D (flat sample), 1D and 2D corrugated samples in the ultrasonic Bragg regime. First, the recently developed angular spectrogram method is applied for the inspection of a 2D corrugated polycarbonate sample. An optimization procedure has been implemented in order to actually determine the surface periodicities. In order to extend the characterization to periodic surfaces with unknown symmetry orientations, a harmonic version of the ultrasonic backscatter polar scan, denoted as H-UBPS, is considered. This is in strong contrast with the above cited studies which were limited to a fixed vertical insonification plane, thus implying that certain prior knowledge about the symmetry orientations of the surface

structure is required to obtain the envisioned surface periodicities. Finally, a third methodology for the characterization of periodic surfaces is introduced, called the ultrasonic polar spectrogram scan (UPSS). The UPSS exploits the advantages of both the angular spectrogram and the H-UBPS, while reducing the complexity of the mechanical implementation significantly.

10. 2. Materials and Experimental Procedure

Both 1D and 2D surface corrugations have been applied to polycarbonate (PC) samples (thickness d = 1.1 mm). The PC substrate is characterized by a Young's modulus E = 3.3 GPa, Poisson coefficient ν = 0.37 and density ρ = 1200 kg/m^3. The sound speed in the immersion liquid water has been measured according to the analysis in Section 3.5, a value c = 1475.4 ± 1.27 m/s is obtained. High-precision, close-to-perfect, samples are manufactured by ablating a predefined structure with an excimer laser. The power of the excimer laser is adjusted such that the ablated surface structure matches a designed depth of $D \approx 17$ µm. The ablating process is performed in a controlled environment (temperature, pressure and humidity) in order to further improve the quality of the surface structure. The 1D grating consists of a set of traces with a periodicity of Λ = 250 µm and orientation Φ = 170° (see Table 10-1). The 2D grating can be conceived as two overlapping 1D gratings (further called grating A and grating B), characterized by the periodicities Λ_A = 250 µm and Λ_B = 375 µm and with traces oriented along the in-plane angles Φ_A = 100°, respectively Φ_B = 10° (see Table 10-1).

Table 10-1: Design parameters of the different surface corrugations.

	Λ_A [µm]	Φ_A [°]	Λ_B [µm]	Φ_B [°]
Sample 0D	-	-	-	-
Sample 1D	250	170	-	-
Sample 2D	250	100	375	10

A schematic of the here considered surface structures together with a designation of the characteristic physical parameters is shown in Figure 10-1.

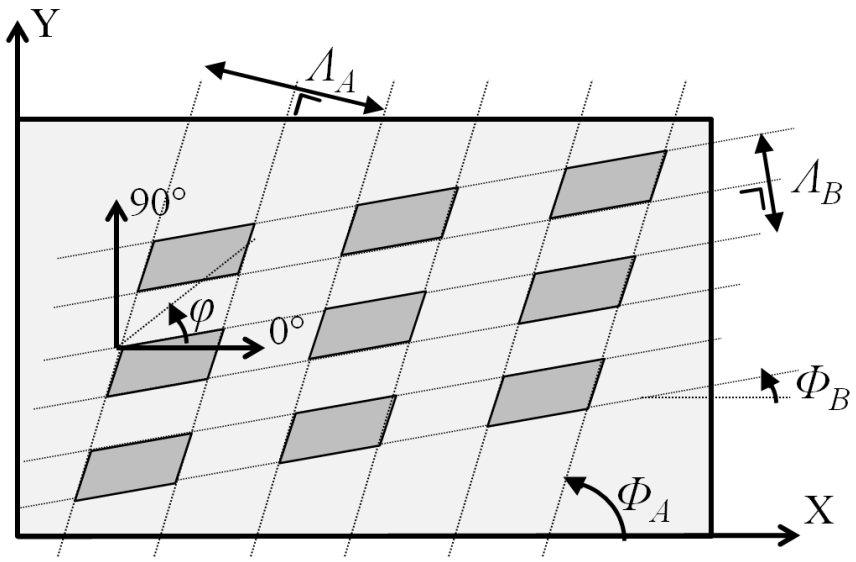

Figure 10-1: Schematic of 2D corrugation and definition of the characteristic parameters.

Besides the high-quality 2D corrugated sample manufactured by the excimer laser, other sets of 2D corrugated samples have been prepared by an ordinary laser burner which is commonly used by jewelry makers to inscribe a personal message in noble metals. Obviously, the quality of the burned corrugations is far less compared to the ablated surface structure, simply because traces are literally molten and burned in the surface. By adapting the laser power, the corrugation depth, and in extension the quality of the surface structure can be varied. Optical microscopic photographs demonstrate the surface quality for the differently manufactured 2D corrugated samples (see Figure 10-2). To discern between the differently manufactured 2D corrugated samples, a letter is assigned representing the finishing grade: high-, mid-, respectively low-quality 2D samples are denoted by 'sample 2Da', 'sample 2Db', respectively 'sample 2Dc'. Note that the 2D surface profile of sample 2Db-c is barely identifiable by optical investigation.

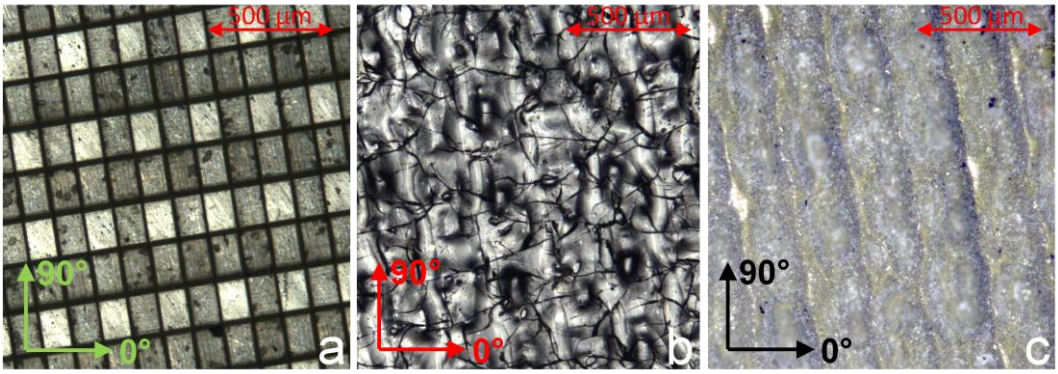

Figure 10-2: Optical microscopy of the surface finishing grade for the different 2D corrugated samples: high-quality sample 2Da (a), mid-quality sample 2Db (b) and low-quality sample 2Dc (c).

10. 3. Angular Spectrogram

In analogy with [3, 18], angular spectrograms are recorded employing a broadband pulse with center frequency f_c = 5 MHz. The distance between the transducer and the sample is kept constant at 65 mm during the experiment, as such the experiment takes place in the far-field regime (see Chapter 3). The incident angle θ ranges from 0° to 80° in steps of 0.05°, with the vertical insonification plane fixed to a certain polar angle φ. The pulse repetition frequency is chosen sufficiently low to avoid overlapping signals and multiple reflections. For each incident angle θ, 1024 points of the backscattered signal are acquired within a time frame of 50 µs, thus resulting in a sampling rate of ~20 MHz. The experimental time for the recording of an angular spectrogram is typically in the order of 5 seconds. Figure 10-3 displays the backscattered wave in time at different incident angles θ for sample 2Da, with the vertical insonification plane perpendicular to the orientation of grating B with periodicity Λ = 375 µm. The interacting section of the ultrasonic beam with the sample enlarges at large incident angles θ, with this the backscattered signal significantly broadens in time (see for example Figure 10-3e). This explains why such a large time window of 50 µs is set to record an angular spectrogram.

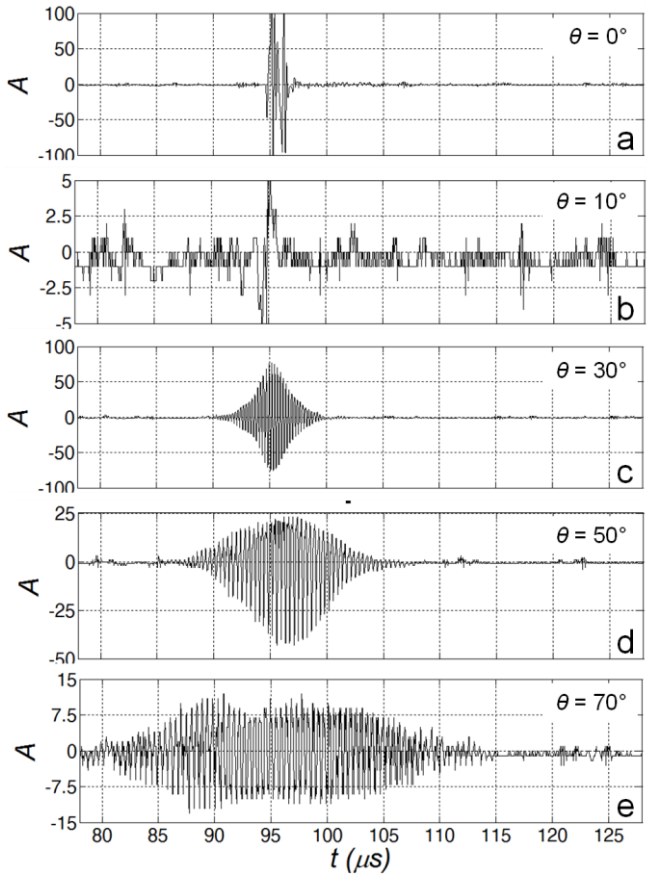

Figure 10-3: Time signal of backscattered wave for sample 2Da at φ = 100° at different incident angles: θ = 0°, θ = 10°, θ = 30°, θ = 50° and θ = 70°.

To minimize edge effects at the borders of the recorded time signal, which result in spectral leakage in the FFT spectrum, the time signals have been windowed by means of a Tukey (tapered cosine) function *w(x)* defined as [27-28]

$$w(x)=\begin{cases}\frac{1}{2}\left(1+\cos\left(\frac{2\pi}{r}\left(x-r/2\right)\right)\right) & 0\le x\le r/2\\ 1 & r/2\le x\le 1-r/2\\ \frac{1}{2}\left(1+\cos\left(\frac{2\pi}{r}\left(x-1+r/2\right)\right)\right) & 1-r/2\le x\le 1\end{cases} \quad (1)$$

with $r\in[0,1]$ the ratio of the cosine-tapered section length to the entire window length.

The window function, together with its spectral frequency density is shown in Figure 10-4. Note that the limits of the ratio r correspond to a rectangular window ($r = 0$) and a Von Hann window ($r = 1$). The experiments shown in this chapter have been windowed considering the parameter $r = 0.25$ in order to include as much as possible of the original time signal while keeping the influence of spectral side lobes reasonably low.

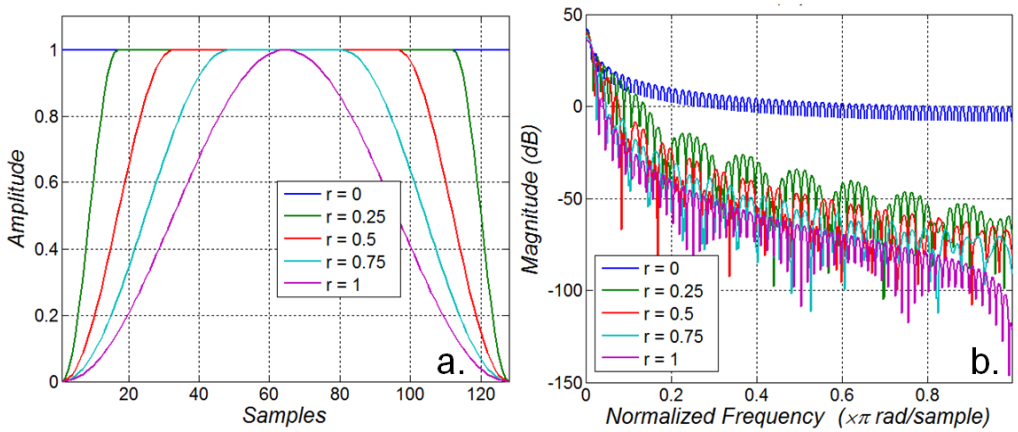

Figure 10-4: Tukey window for different values of the ratio *r*: time domain (a) and frequency domain (b).

Zero padding has been applied to the windowed signal, resulting in a FFT vector having an increased number of bins which are more closely spaced in frequency space. Obviously, zero padding does not add any information, but has the same effect as the application of a high-quality sinc-interpolation [29] to the original data. Zero padding is, compared to interpolation techniques, computationally more efficient to obtain a smoother spectrum in a graphical representation. The fast Fourier transform is then applied to the zero-padded data, which yields an angular spectrogram when plotted in function of incident angle θ.

Angular spectrograms have been recorded at different orientation planes (or at different fixed polar angles φ) of sample 2Da, and are displayed in Figure 10-5. The amplitudes around $\theta = 0°$ correspond to the specular reflection of the bounded beam, the periodic patterns are due to cut-off frequencies (thickness resonances) of the PC plate. Both Bragg backscatter curves (white squares) and Lamb wave dispersion curves (green dots) have been superimposed to the angular spectrograms. The Bragg curves are computed considering the design parameters of the 2D corrugation of sample 2Da

(Table 10-1), and match well with the high-amplitude curves within the experiment (Figure 10-5a and Figure 10-5d). It can be observed that several other low-intensity curves emerge in the angular spectrograms, which are found to be an artifact of aliasing. As the number of stored data points is fixed to 1024 for each recording, one should reduce the time window to avoid aliasing. However, the recorded signal displayed in Figure 10-3e shows that it is impossible to narrow down the time frame without losing a portion of the backscattered wave at large incident angles θ. Anyway, the portion of aliasing can be readily identified in the angular spectrograms, and is further neglected from the analysis. The dispersion curves are computed on the basis of a Legendre polynomial expansion for the displacement and stress vectors [30], assuming the material properties of the PC substrate.

The angular spectrogram at $\varphi = 40°$ shows a faint Bragg curve (note the reduced amplitude scale), while the recording at $\varphi = 70°$ does not provide any sign of backscatter. The former most probably consists of backscatter associated to the diagonal ($\varphi = 43.7°$) of the surface structure [3, 19-20].

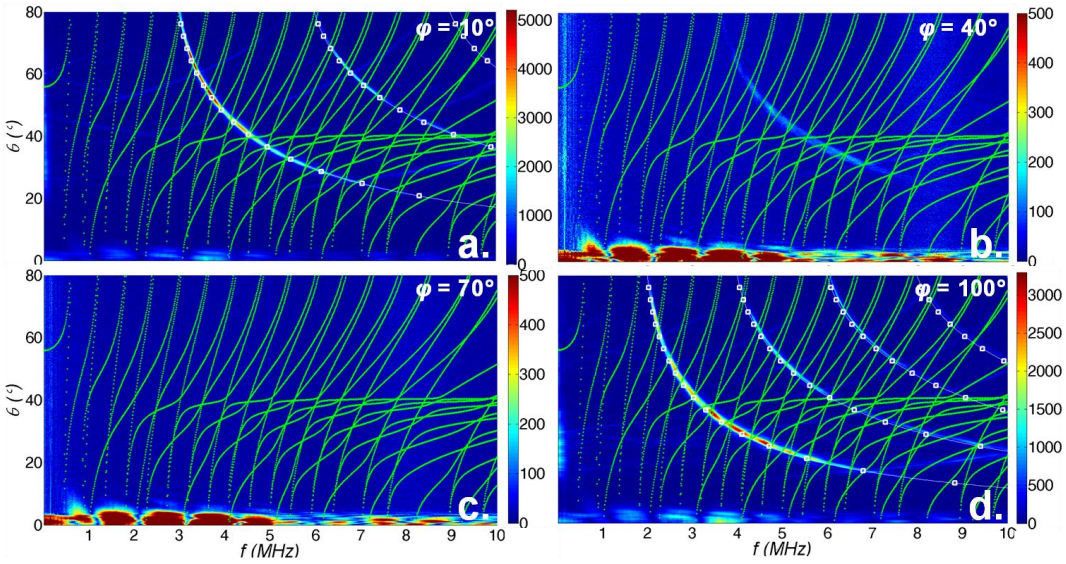

Figure 10-5: Angular spectrograms recorded at different orientation planes for sample 2Da: $\varphi = 10°$ (a), $\varphi = 40°$ (b), $\varphi = 70°$ (c) and $\varphi = 100°$ (d). The Bragg conditions (white squares) and the Lamb wave dispersion curves (green dots) are superimposed.

Close observation of Figure 10-5 reveals some small discrepancies between the position of the superimposed Bragg curves and the experimentally

recorded Bragg scattering curves. This is explicitly shown in Figure 10-6, and indicates that the true periodicity slightly deviates from the designed periodicity.

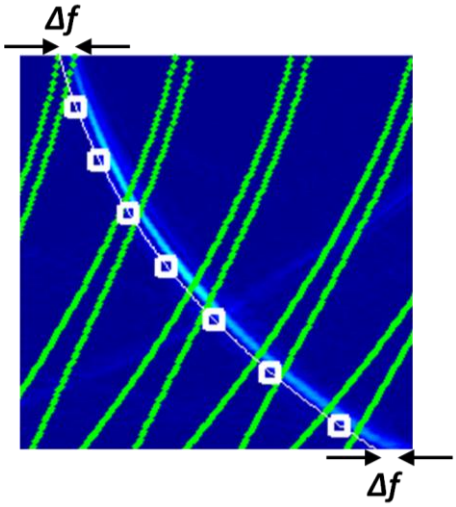

Figure 10-6: Magnification of a small portion of Figure 10-5d revealing a small discrepancy between the angular spectrogram and the superimposed Bragg curves.

For this reason, an optimization procedure has been implemented in order to extract the periodicities which match the experimental recordings best. The Bragg conditions, i.e. the incident angles θ, have been computed for a wide range of frequencies f and periodicities Λ according to the well-known Bragg law [5]:

$$\theta(m, f, \Lambda) = \sin^{-1}\left(m\frac{c}{2f\Lambda}\right) \tag{2}$$

with m the diffraction order and c the wave speed in the liquid.

As such, a grid of Bragg curves with $\Delta f = 2$ kHz and $\Delta\Lambda = 0.2$ µm is computed. Each set of computed Bragg curves has been superimposed to the experimental recording. The experimental backscatter amplitudes are then interpolated to the (f,Λ)-grid, and consequently summed

$$\sum_m \sum_f A(f, \theta(m, f, \Lambda)) \tag{3}$$

Then by maximizing Equation (3), the optimal Bragg curves for the different angular spectrograms are identified, and thus the periodicities of the inspected surface are determined. A graphical representation of the summed amplitudes for different superimposed Bragg lines, assuming a varying periodicity, is presented in Figure 10-7 for the different angular spectrograms of Figure 10-5 (φ = 10°,40°,70°,100°). The results show a steadily increasing trend, with multiple sharp and well-defined peaks. The increasing trend relates to the presence of acoustic noise combined with the increasing number of possible diffraction orders m for increasing periodicity Λ. The sharp peaks identify those Bragg curves which have a superior match with the high-amplitude curves in the angular spectrograms. In Figure 10-7a (φ = 10°) for example, the maximum peak corresponds to the set of Bragg curves computed with a periodicity Λ = 248.4 μm, which agrees well to the design parameter of Λ = 250 μm. Other suboptimal peaks are observed, which have been explicitly identified and labeled in Figure 10-7a. These maxima have an associated periodicity which is a fraction p/q, with p and q integer, of the optimum periodicity. Obviously, the analysis can be done in exactly the same way for the other angular spectrograms. The various (sub)optimal periodicities are added to Figure 10-7, and are in good agreement with the design parameters of sample 2Da (see Table 10-1). The optimization procedure reveals that Bragg lines with a periodicity of Λ = 205.6 μm match the angular spectrogram recorded at φ = 40°. Probably, this has to be linked to a diagonal of the surface structure.

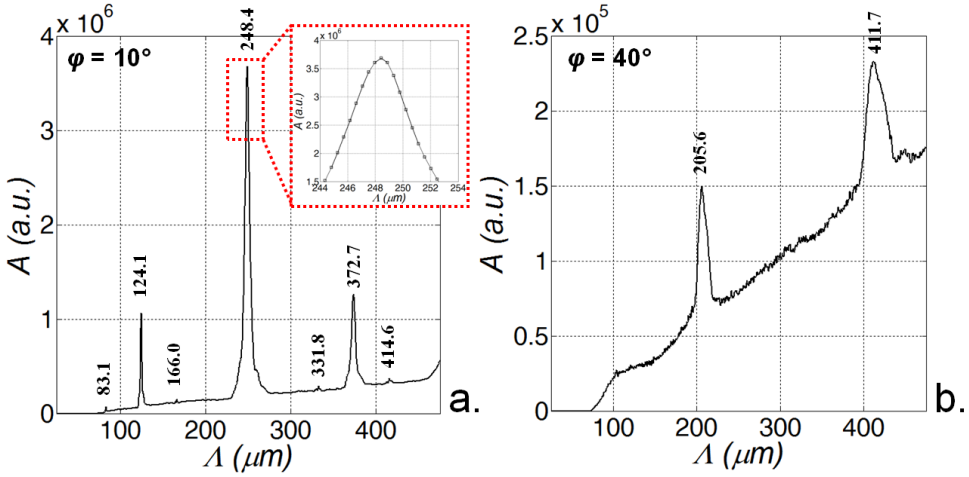

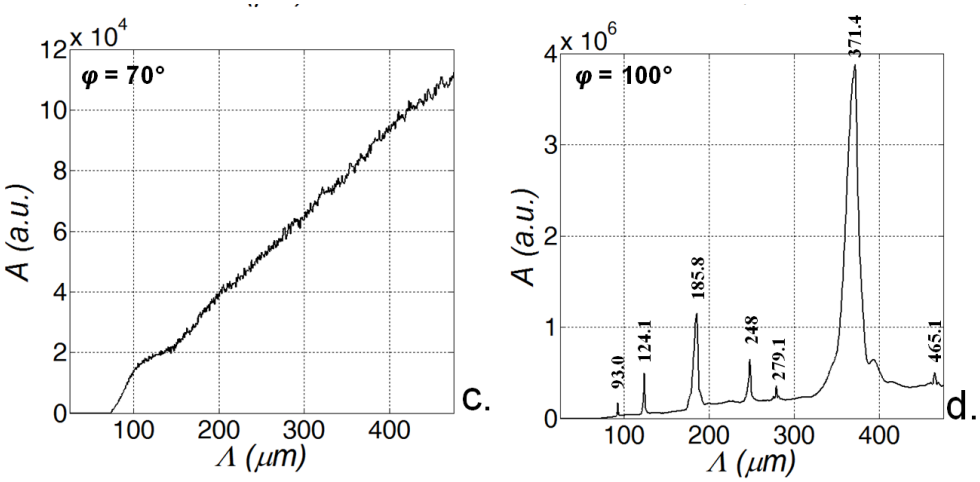

Figure 10-7: Summed amplitude of computed Bragg curves in function of the periodicity for the angular spectrograms shown in Figure 10-5: φ = 10° (a), φ = 40° (b), φ = 70° (c) and φ = 100° (d).

Small discrepancies between the optimized values and the design parameters can be understood by accounting for experimental factors which are difficult to control or to compensate for:

- The most obvious factor concerns the inaccurate knowledge of the ultrasonic wave length λ, which is dependent on both water temperature T as well as water purity (see Section 3.5). This is graphically represented in Figure 10-8 for different uncertainties on the wave speed c. The measured uncertainty on the sound speed $\Delta c = \pm 1.27$ m/s matches an uncertainty for the periodicity of $\Delta\Lambda \approx 0.2$ µm at $\Lambda = 250$ µm.

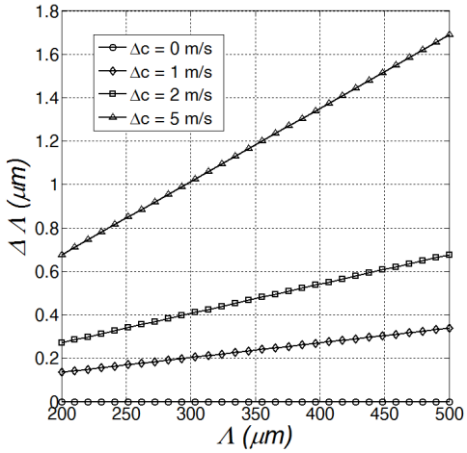

Figure 10-8: Effect of the wave speed c on the uncertainty $\Delta\Lambda$ of the periodicity Λ (f = 5 MHz).

- The resolution in frequency domain sets a limit to the accuracy by which the periodicity can be optimized. This is demonstrated in Figure 10-9. The angular spectrograms in this thesis have been obtained with a resolution of 4 kHz, thus resulting in an uncertainty in the order of $\Delta\Lambda$ = 0.25 µm. Further reduction of the resolution leads to a rather large post-processing time. Note that Figure 10-9 reveals that the error associated to frequency resolution increases for small incident angles θ, thus suggesting that the optimization procedure is ideally performed by adding a weighting procedure as a function of the incident angle θ. This however is not considered in the present thesis.

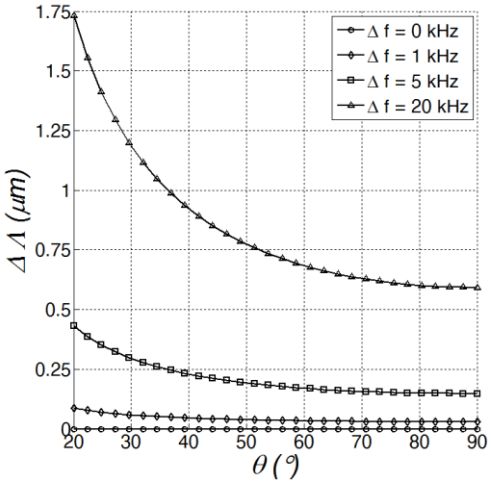

Figure 10-9: Effect of the resolution in frequency domain for the periodicity determination of sample 1 (Λ = 250 µm) in function of the incident angle θ (f = 5 MHz).

- Errors could be introduced during the fabrication process of the corrugation as the resolution of the ablating laser source is finite. Furthermore, the excimer laser ablates traces in a specific controlled environment at ambient temperature T = 20°C. Though, local heating can be induced during the chemical ablation of the surface corrugation. In addition, the ultrasonic experiments have been performed at a water temperature of T = 15.3°C. Hence, temperature effects could play a significant role for the actual periodicity of the corrugation during investigation (see Figure 10-10).

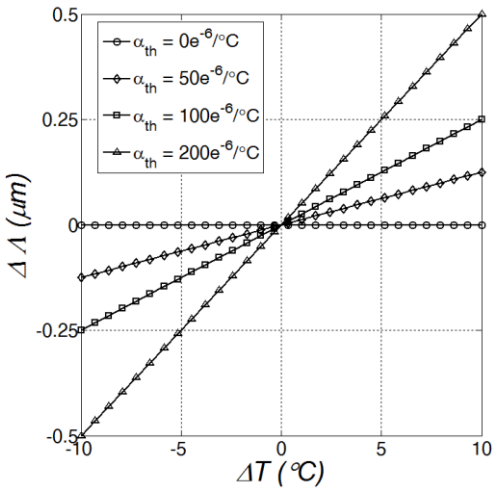

Figure 10-10: Effect of the thermal properties of the substrate for the periodicity determination of sample 1D (Λ = 250 µm).

For example, assuming a linear thermal expansion coefficient of $\alpha_T = 65 \cdot 10^{-6}$ /C for the PC sample, a temperature difference of $\Delta T = 5$°C already introduces a rescaling of $\Delta\Lambda \approx 0.08$ µm for the 250 µm surface periodicity. Therefore, a reexamination of the surface corrugation of sample 2Da has been performed by means of optical microscopy at ambient temperature $T = 20$°. From this investigation a periodicity of $\Lambda_A = 250.11 \pm 0.09$ µm, respectively $\Lambda_B = 374.84 \pm 0.50$ µm, along the orientation $\Phi_A = 99.2$°, respectively $\Phi_B = 9.1$°, was obtained. Hence, the angular spectrograms were obtained at polar angles φ which slightly deviate from the surface symmetry orientations. Obviously, this mismatch influences the accuracy of the periodicity characterization, indicating the main shortcoming of the angular spectrogram method for periodicity characterization: how can one know the surface symmetry orientations in advance?

It can be further observed in Figure 10-5 that the recorded Bragg curves reveal a non-uniform amplitude course indicating that the diffraction efficiency is not constant along a single Bragg curve. A magnified view of the results shown in Figure 10-5a and Figure 10-5d is displayed in Figure 10-11a, respectively Figure 10-11b. The amplitude variations in the different Bragg scattering curves have been extracted and are plotted as a function of the incident angle (see Figure 10-11c-d). Oscillatory variations can be observed, having a small period for $\theta < 40$°, and a large period for $\theta > 40$°.

These amplitude variations have been previously [3] interpreted in terms of phase-matching Lamb waves which are backscattered. Within that same study however, amplitude variations can be observed at frequency-angle combinations (see figure 3.11 in [3]) which should not stimulate or excite a Lamb wave. This suggests that Lamb waves solely do not explain this behavior. In addition, the present results (Figure 10-11) indicate that the interpretation of the backscatter amplitude variations in terms of the stimulation of phase-matching Lamb modes is, at first sight, not supported by the superimposed dispersion curves (green dots). It is however remarked that caution is required with the last statement as the superimposed Lamb dispersion curves are computed for a smooth and flat PC plate. It is shown in literature that the nature of Lamb waves changes in case of a periodic structure, and becomes function of the exact periodicity parameters [31-38].

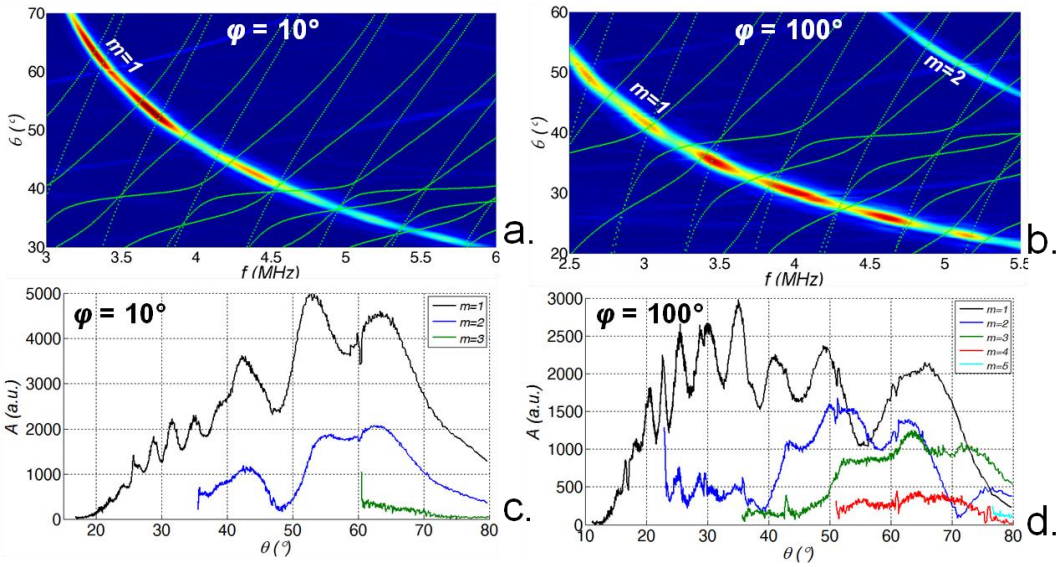

Figure 10-11: Magnified view of Figure 10-5a: φ = 10° (a) and of Figure 10-5d: φ = 100° (b). Backscatter amplitude at the optimal Bragg curves as a function of incident angle θ for Figure 10-5a: φ = 10° (c) and for Figure 10-5d: φ = 100° (d).

In order to further investigate these amplitude oscillations, the incident angle θ is extended in order to cover every possible angle of incidence. As such, the surface corrugation is also insonified from the backside. The incident angle θ is defined as indicated in the schematic shown in Figure 10-12.

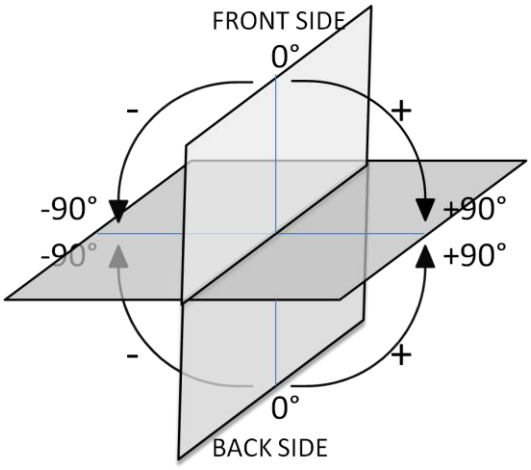

Figure 10-12: Definition of incident angle θ.

Considering Snell-Descartes' law [39-40], which entails the conservation of the horizontal component of the wave vector at a liquid-solid interface, the diffraction conditions should remain the same for front side and backside insonification. Similarly, classical Lamb waves are guided plate waves and the excitation conditions should not be dependent on which side the insonification takes place [39-40]. Hence apart from a global amplitude drop, the backside insonification should reveal similar amplitude variations in the Bragg scattering curves as observed for the front side insonification, at least when interpreting the amplitude variations in the Bragg scattering curves in terms of backscattered phase matching Lamb waves. The recorded angular spectrogram along $\varphi = 100°$ is presented in Figure 10-13.

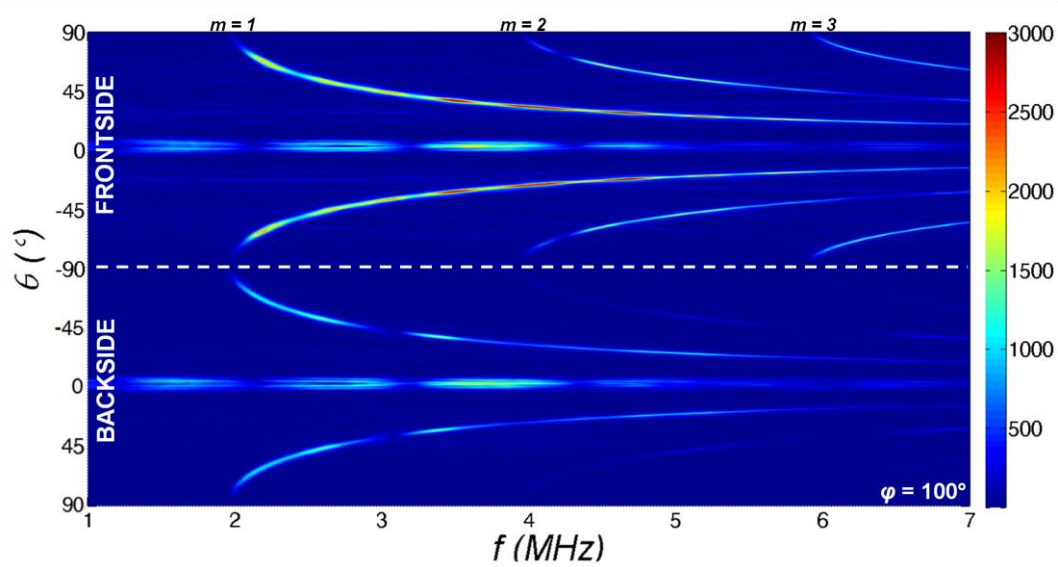

Figure 10-13: Angular spectrogram for sample 2Da along φ = 100°, covering the full circular range of incident angles θ.

It can be observed that the diffraction conditions do not change, i.e. the Bragg scattering curves are not shifted, while the global amplitude of the Bragg scattering curves decreases in case of backside insonification which is in accordance with expectance. The amplitude variations within a Bragg curve however are completely different for front side and backside insonification. This is explicitly shown by extracting the amplitude distribution of the 1st order Bragg scattering curve as a function of incident angle θ (see Figure 10-14) for both front side and backside insonification. The only feature which seems to be identical is the sharp minimum around θ = 40°, which agrees well with the longitudinal critical bulk wave angle for the PC substrate ($\theta_{crit} = \sin^{-1}(1475.4/2270) \approx 40.5^{\circ}$ [41]).

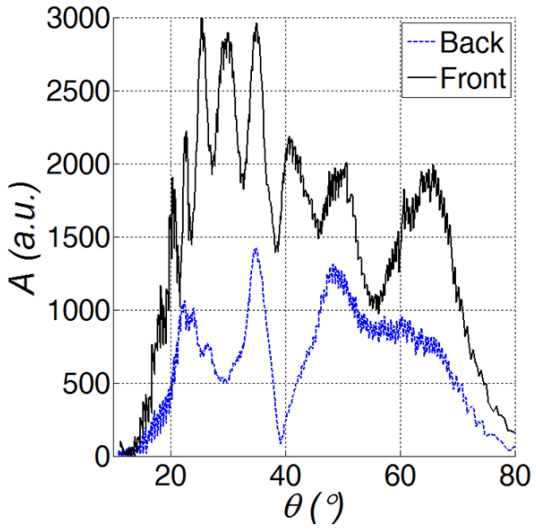

Figure 10-14: Extracted 1st order (*m* = 1) Bragg scattering curve from the angular spectrogram shown in Figure 10-13.

The difference between the front side and backside insonification results thus suggests that backscattered Lamb waves are not the sole cause for the observed amplitude oscillations. Again, it is remarked that caution is required since it is imaginable that the presence of a single-sided surface corrugation could introduce asymmetry, i.e. dependency on the insonification side, in the guided wave excitation conditions making it impossible to speak of classical Lamb waves. As a matter of fact, the presence of interface modes along a one-dimensional solid-fluid phononic crystal has already been demonstrated in reference [42].

Comparison of the front side (or backside) Bragg scattering curves at complementary angles with respect to the vertical, i.e. positive and negative incident angles θ, reveals some additional peculiarity. Figure 10-15 displays an angular spectrogram for the front side of sample 2Da along $\varphi = 100°$. It is observed that a shift in backscatter amplitude is present, while theoretically the same Bragg diffraction amplitudes should be observed. This shift in amplitude was also noted in [3], and has been linked to imperfections in the periodicity of the surface. The here investigated sample 2Da however has a superimposed high-quality, almost perfect, 2D corrugation, and thus this shift in amplitude should not be present, or at least be limited. To complicate the case, the experiment displayed in Figure 10-13 does not reveal any sign of an amplitude shift for positive and negative angles.

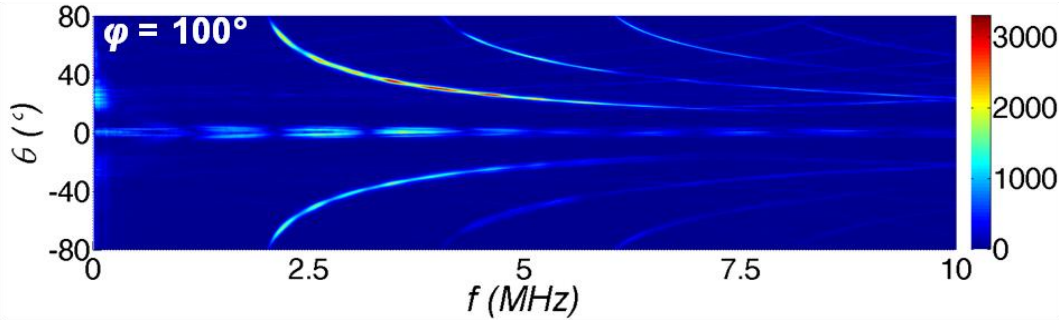

Figure 10-15: Angular spectrograms showing a discrepancy in amplitude at complementary angles.

Similar inconsistent features have already been observed for the P-UPS twin effect (see Section 5.2.1), which has been linked to the slightly asymmetric radiation profile of typical ultrasound transducers. Hence, it seems plausible that the amplitude shift encountered here is inflicted by small deviations in the shape of the employed sound beam, rather than imperfections in the corrugation periodicity. To verify this statement, two angular spectrograms for sample 2Da are recorded along $\varphi = 100°$. The first experiment is obtained by orienting the transducer such that its radiation field is slightly asymmetric in the vertical insonification plane. The second experiment is recorded by rotating the transducer around the transducer axis over 90°. As such, the beam section in the vertical insonification plane has a nearly symmetric amplitude profile. The extracted 1st order Bragg scattering curves of these two angular spectrograms are displayed in Figure 10-16. The effect of the 90° rotation of the transducer can be clearly observed in the global amplitude level of the Bragg scattering curves for positive and negative incident angles θ. Hence, the Bragg diffraction efficiency seems to be highly sensitive to the amplitude profile of the bounded beam, more specific to the tail of the bounded beam. In fact, this is not surprising as a bounded beam can be conceived as a collection of inhomogeneous waves [43]. The tail of the bounded beam is dominated by an inhomogeneous wave, whose inhomogeneity parameter has a major influence for a variety of wave phenomena including Lamb wave stimulation, diffraction efficiency and others [44-47].

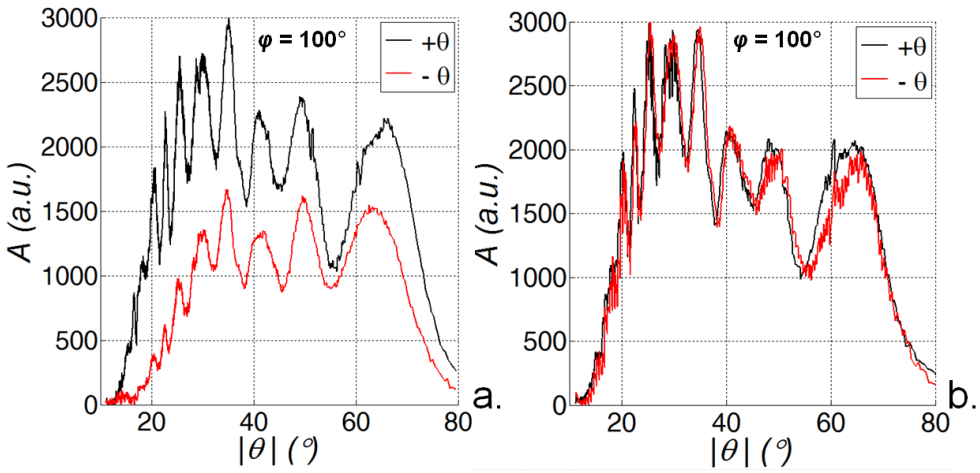

Figure 10-16: Amplitude at the 1st order Bragg scattering curves for both positive (black) and negative (red) incident angles, extracted from the angular spectrogram of sample 2Da along φ = 100°: asymmetric radiation field (a) and symmetric radiation field (b).

In conclusion, the surface periodicities of sample 2Da have been obtained on the basis of angular spectrograms showing acceptable agreement with the design periodicities. The above results indicate that the Bragg scattering curves have a non-uniform amplitude distribution, which is different for front side and backside insonification. Hence, the present results indicate that the interpretation solely in terms of backscattered Lamb waves is not satisfying. In addition, it is shown that the backscatter amplitude for complementary angles, i.e. positive and negative incident angles θ, differ. This was shown to be related to the spatial shape of the sound field, rather than to imperfections in the corrugation periodicity as stated in previous studies.

10. 4. Harmonic Ultrasonic Backscatter Polar Scan (H-UBPS)

The angular spectrogram requires prior knowledge about the symmetries of the surface structure to extract surface periodicities, which obviously limits its applicability in a real industrial environment where such knowledge is not available. This section investigates whether it is feasible to characterize a periodic surface structure without any prior knowledge. For this, both the H-UPS and the H-UBPS methodology is considered and have been applied to

the various PC samples. Hence the upper hemisphere is scanned, while the analysis is limited to the evaluation of the maximum amplitude of the transmitted and backscattered signal. Compared to the angular spectrograms, the experimental implementation becomes more involved and the experimental time increases to 15 minutes. On the other hand, the complexity of the post-processing is reduced significantly.

10. 4. 1. Sample 0D: Flat Surface

As a reference, the H-UPS and H-UBPS image, both recorded at f = 5 MHz, are shown in Figure 10-17 for sample 0D. The circular symmetry in the H-UPS image clearly exposes the isotropic nature of the sample. The H-UPS result indicates that with the present parameters, i.e. frequency f and plate thickness d, the wave phenomena in the PC sample are bulk wave dominated. Indeed, the amplitude dip at $\theta = 42.4°$ is identified as the critical angle for longitudinal waves, which is in good agreement with literature [41]. This observation supports the conclusion that the amplitude variations in the angular spectrograms shown in previous section are probably not invoked by backscattered Lamb waves.

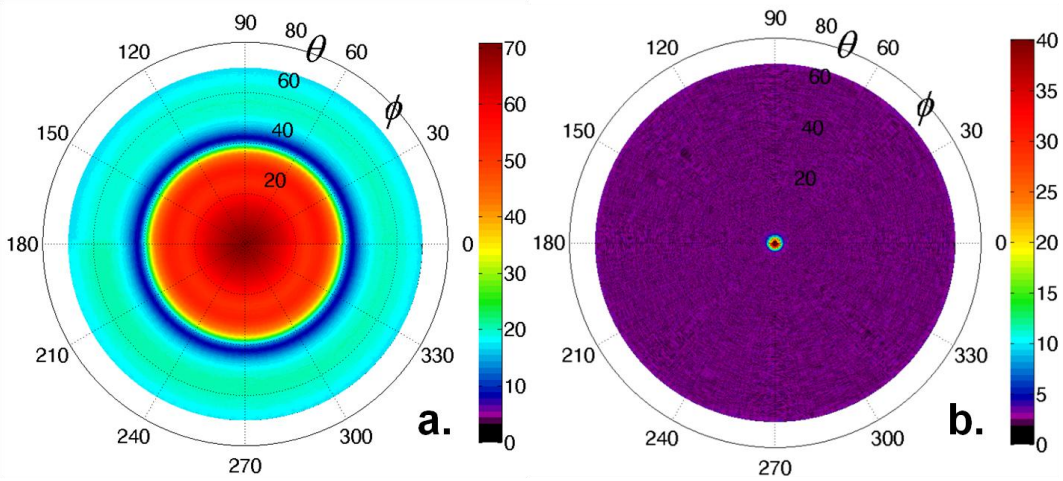

Figure 10-17: H-UPS (a) and H-UBPS (b) of sample 0, recorded at f = 5 MHz.

The H-UBPS image on the other hand reveals strong 'backscatter' around $\psi(\varphi,\theta) = \psi(0,0)$, corresponding to the specular reflection as expected for a flat and homogeneous plate. It is noted that change of acoustical frequency f does not invoke any peculiarities for the H-UBPS image, at least when disregarding thickness resonances of the solid sample. Although the position

of the specular reflection $\psi(\varphi,\theta)$ does not contain information about the surface structure, it does provide a handy means to obtain the normal of the investigated sample and to neutralize any positional misalignments during the recording of the H-UBPS experiment.

10. 4. 2. Sample 1D: 1D Surface Corrugation

The H-UPS and H-UBPS image, both recorded at f = 5 MHz, are shown in Figure 10-18.

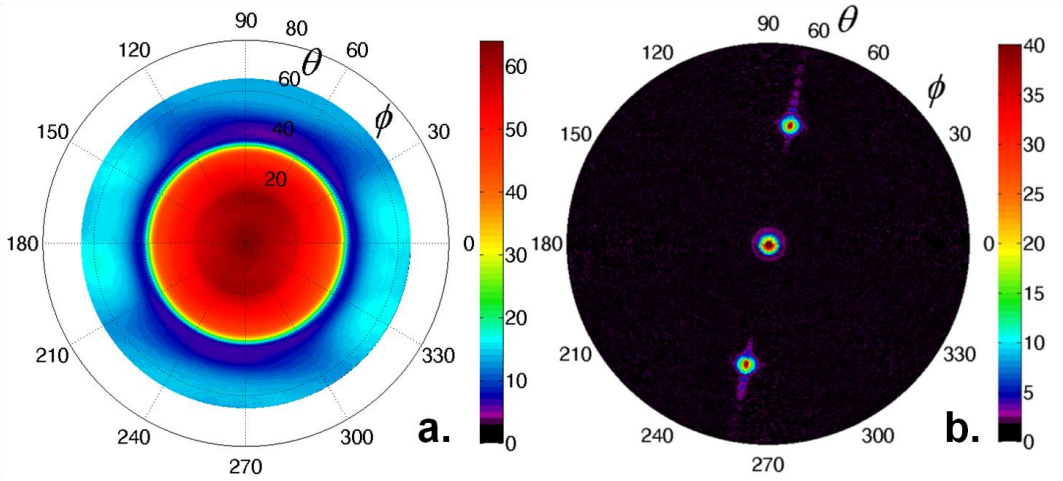

Figure 10-18: H-UPS (a) and H-UBPS (b) of sample 1, recorded at f = 5 MHz.

With respect to the H-UPS image of sample 0D, some peculiarities can be observed in Figure 10-18a. The global amplitude scale of the transmission field decreased by 9.2%. Obviously, this deficit in transmission amplitude is coupled into several diffracted fields. The amplitude map further shows variations along the polar angle φ (best seen for large incident angles θ), having a symmetry line aligned with the orientation of the superimposed corrugation. Hence the orientation of the surface structure is well reflected in the H-UPS image. However, the extraction of the grating periodicity is impossible solely from a H-UPS experiment.

The H-UBPS image (Figure 10-18b) on the other hand reveals two extra narrow spikes with respect to the reference H-UBPS, which can be clearly associated to the 1D structure by means of Bragg diffraction. The polar angle φ of the backscatter spikes yields the symmetry orientation Φ of the corrugation according to

$$\Phi = \varphi - 90^{\circ} \tag{4}$$

The periodicity Λ is encrypted in the incident angle θ of the backscatter spikes according to the Bragg relationship for backscatter geometry [5]

$$\Lambda = \frac{m\lambda}{2\sin\theta} \tag{5}$$

with m the diffraction order (integer) and λ the ultrasonic wave length in water.

The location $\psi(\varphi,\theta)$ of the increased backscatter spike thus coincides with the 1st Bragg order, by which the periodicity and the orientation of the insonified corrugation can be characterized. The two recorded diffraction peaks in Figure 10-18b are complementary to each other, hence a single H-UBPS experiment offers 2 independent measurements. The accuracy and reproducibility of the extracted surface parameters depends on the precision with which the spike locations can be determined in the experimental recording. In fact, the two main complicating factors are: the smearing of the experimentally recorded peaks due to the angular frequency content of the employed transducer, and the presence of experimental noise. To tackle both in order to obtain a robust analysis, the experimental recording has been first convolved by a Gaussian kernel (400 adjacent points in a 20x20 grid) being representative for the amplitude distribution of the employed ultrasonic wave (see Section 3.4.2). A background noise level has been defined as

$$A_{noise} = \alpha \frac{\sum_{\varphi,\theta} A(\varphi,\theta)}{N} \tag{6}$$

with α a parameter usually chosen between 1 and 3, and N the total number of experimental data points.

Only peaks above the background level can be identified as true diffraction peaks. A periodicity of $\Lambda = 249.75$ µm and orientation angle $\Phi = 169.55°$ have been determined from Figure 10-18b, which is in excellent agreement with the optically determined parameters (see Table 10-2). Small discrepancies can be understood by accounting for the different experimental factors already discussed in Section 10.3. Though, for the H-UBPS the angular resolution $\Delta\theta$, instead of the frequency resolution Δf, is the limiting factor to the accuracy of the inversion procedure. This is graphically represented in Figure 10-19 for different scan resolutions. It is clear that the error on the periodicity can be lowered significantly by reducing both the angular resolution and scan frequency. The here employed angular resolution of $\Delta\theta = 0.05°$ corresponds to an uncertainty of $\Delta\Lambda \approx 0.3$ µm at $f = 5$ MHz for sample 1D.

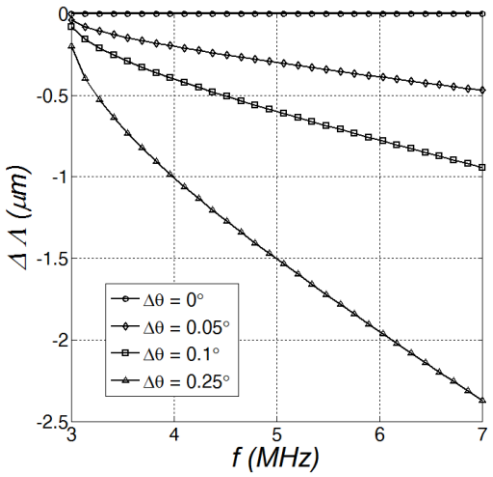

Figure 10-19: Effect of the resolution of the incident angle θ for the periodicity determination of sample 1D in function of the ultrasonic frequency.

In order to investigate the influence of the employed frequency for the H-UPS and H-UBPS images, additional experiments have been obtained at $f = 4$ MHz and $f = 6$ MHz. The results are shown in Figure 10-20 and Figure 10-21.

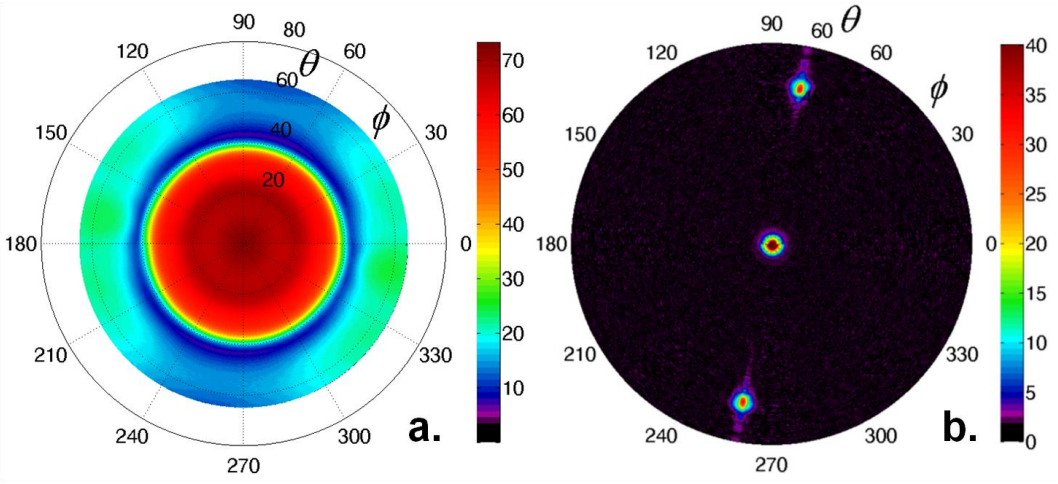

Figure 10-20: H-UPS (a) and H-UBPS (b) of sample 1D, recorded at *f* = 4 MHz.

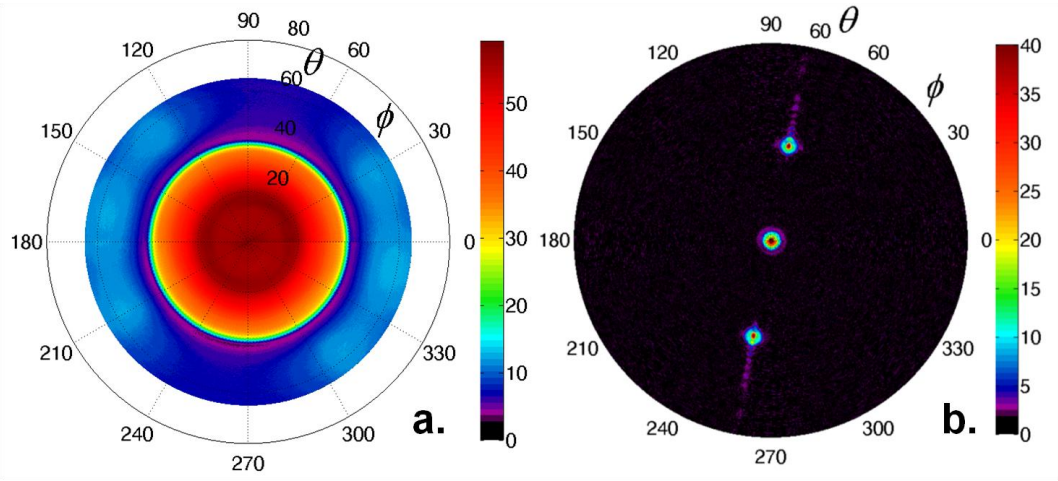

Figure 10-21: H-UPS (a) and H-UBPS (b) of sample 1D, recorded at *f* = 6 MHz.

The H-UPS results at $f = 4$ MHz and $f = 6$ MHz show more or less the same features as observed for $f = 5$ MHz: the surface structure introduces a distortion of the circular symmetry, exposing the orientation of the corrugation. Note that the changes in the global amplitude level, with respect to the recording at $f = 5$ MHz, are very likely related to the viscoelastic nature of the PC substrate. The H-UBPS images on the other hand reveal a positional shifting in θ-direction of the backscatter spikes, in accordance with Bragg's law. Hence, Bragg's law indicates a lower limit for the ultrasonic frequency in order to generate a backscatter spike and in extension

to characterize a surface profile: $\lambda < \Lambda$. For sample 1D, this condition is equivalent to $f > 2.96$ MHz.

The extracted lateral dimensions for sample 1D, at the different applied frequencies, have been gathered in Table 10-2. As a check for the robustness of the inverted corrugation parameters, two independent H-UBPS experiments have been performed at the various frequencies. It can be stated that the ultrasonically determined parameters are very consistent (i) to each other, (ii) to the investigation with optical microscopy as well as (iii) to the design parameters.

Table 10-2: Comparison of the results for sample 1D. The "Design" row represents the design parameters, the "Optical" and "H-UBPS" rows correspond to the optically, respectively ultrasonically determined parameters. The error ε, with respect to the design parameters, is added.

	Λ [µm]	ε_Λ [%]	Φ [°]	ε_Φ [°]
Design	250	-	170	-
Optical	249.89	0.04	169.5	0.5
H-UBPS 4MHz	250.2	0.08	169.6	0.4
	249.8	0.08	169.6	0.4
H-UBPS 5MHz	249.8	0.08	169.55	0.45
	249.7	0.12	169.55	0.45
H-UBPS 6MHz	251	0.4	169.45	0.55
	250.5	0.2	169.45	0.55

It is further noted that each diffraction peak is accompanied by several other low amplitude spikes which are periodically ordered along the θ-direction, hence resulting into a tail along both sides. This can be explicitly observed in Figure 10-22, which represents the amplitude results at $\varphi = 80°$ for the H-UBPS experiment recorded at $f = 5$ MHz. The origin of this tail probably has to be sought in an internal diffraction process in the substrate material on the one hand, and the occurrence of diffracted side-lobes of the employed acoustic beam (see Section 3.4.2) on the other hand. The latter qualitatively supports the observed change in periodicity with applied frequency, as well as the narrow profile in φ-direction of the tail. The presumable effect of side-lobes can also be seen in the shape of the specular reflection field (see Figure 10-22 at small incident angles θ).

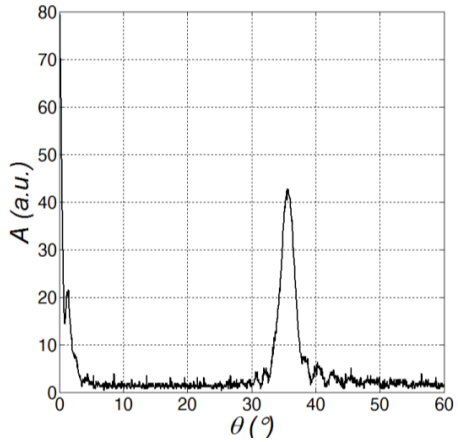

Figure 10-22: Backscatter results at fixed polar angle φ = 80° for the insonification of sample 1D at f = 5 MHz.

10. 4. 3. Sample 2Da: 2D Surface Corrugation

The previous results show the capabilities of the H-UBPS methodology for characterizing the in-plane dimensions, i.e. periodicity and symmetry, of a 1D surface corrugation. In this section, the analysis is extended to 2D surface structures [48]. For this, the high-quality sample 2Da, with surface parameters listed in Table 10-1, is investigated. The H-UPS and H-UBPS images, both recorded at f = 5 MHz, are shown in Figure 10-23.

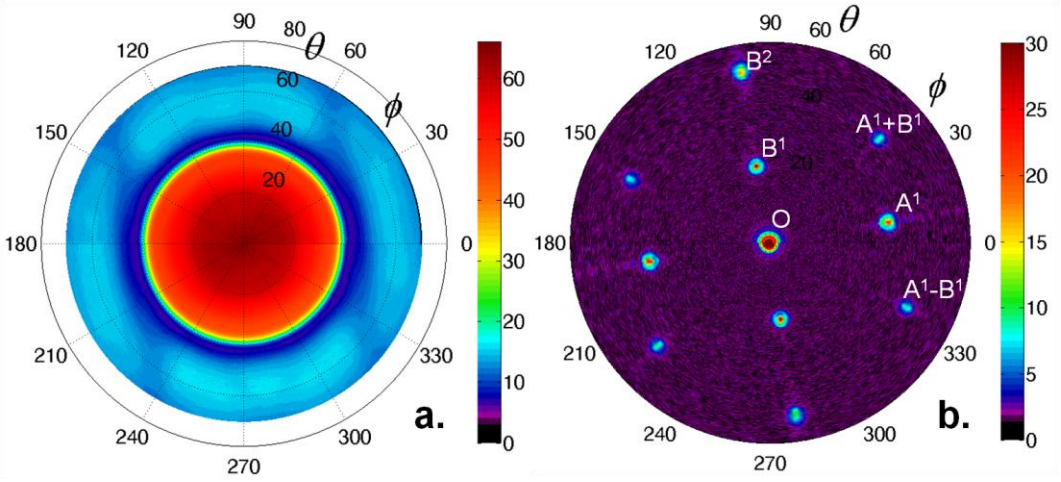

Figure 10-23: H-UPS (a) and H-UBPS (b) of sample 2Da, recorded at f = 5 MHz.

The H-UPS recording of sample 2Da shows similar features as was observed for sample 1, i.e. the distorted circular symmetry exposes the symmetry orientation. However quantification of surface periodicities is not possible with the H-UPS methodology. More interesting results are obtained with the H-UBPS recording. As previous, spike O corresponds to the specular reflection and is taken as the reference direction for normal incidence. Spikes A^1, respectively B^1, correspond to 1st order diffraction peaks associated with grating A, respectively grating B. Spikes B^2 obviously correspond to 2th order diffraction peaks ($m = 2$ in Bragg's law) associated to grating B. These spikes can be analyzed by means of Equation (4) and (5), the obtained results are listed in Table 10-3.

Table 10-3: Analysis results of the diffraction peaks according to Equation (4) and (5). The first row "Design" corresponds to the design parameters of the 2D grating. The "Optical" and "H-UBPS" rows correspond to the optically, respectively ultrasonically extracted parameters. The error, with respect to the design parameters, is added.

	Λ_{A^1} [µm]	Φ_{A^1} [°]	Λ_{B^1} [µm]	Φ_{B^1} [°]	Λ_{B^2} [µm]	Φ_{B^2} [°]
Design	250	100	375	10	375	10
Optical	250.11 + 0.04%	99.2 -0.8	374.84 -0.04%	9.1 -0.9	/	/
H-UBPS 4MHz	249.6 -0.16%	99.3 -0.7	374.5 -0.13%	9.0 -1	/	/
H-UBPS 5MHz	249.8 -0.08%	99.3 -0.7	375.3 +0.08%	9.0 -1	374.7 -0.08%	9.1 -0.9
H-UBPS 6MHz	250.3 +0.12%	99.3 -0.7	372.5 -0.67%	8.9 -1.1	371.7 -0.88%	9.2 -0.8

In addition to these peaks, several other spikes can be observed. Spikes (A^1+B^1) and (A^1-B^1) are diffraction spikes associated to both grating A and grating B. They are understood by considering the addition, respectively subtraction of the reciprocal parameters of grating A and grating B. The orientation $\Phi_{A\pm B}$ of a joint diffraction spike thus corresponds to

$$\Phi_{A\pm B} = \tan^{-1}\left(\frac{\left(\frac{1}{\Lambda_A}\sin(\Phi_A) \mp \frac{1}{\Lambda_B}\sin(\Phi_B)\right)}{\left(\frac{1}{\Lambda_A}\cos(\Phi_A) \mp \frac{1}{\Lambda_B}\cos(\Phi_B)\right)}\right) \pm 90 \qquad (7)$$

while its associated periodicity $\Lambda_{A\pm B}$ can be written as

$$\Lambda_{A\pm B} = \left(\sqrt{\frac{1}{{\Lambda_A}^2} + \frac{1}{{\Lambda_B}^2} - 2\frac{\cos(\Phi_B - \Phi_A)}{\Lambda_A \Lambda_B}} \right)^{-1} \tag{8}$$

It is clear that these spikes cannot be observed when limiting the investigation to the principal symmetry axes of the surface structure. The extracted values for the joint diffraction peaks are listed in Table 10-4.

Table 10-4: Analysis results of the joint diffraction peaks according to Equation (7) and (8). The first row "Design" corresponds to the design parameters of the 2D grating. The rows "H-UBPS" correspond to the ultrasonically extracted parameters. The error, with respect to the design parameters, is added

	$\Lambda_{A^1+B^1}$ [µm]	$\Phi_{A^1+B^1}$ [°]	$\Lambda_{A^1-B^1}$ [µm]	$\Phi_{A^1-B^1}$ [°]	$\Lambda_{A^1+B^2}$ [µm]	$\Phi_{A^1+B^2}$ [°]	$\Lambda_{A^1-B^2}$ [µm]	$\Phi_{A^1-B^2}$ [°]
Design	208.0	43.7	208.0	-23.7	150	63.1	150	-43.1
H-UBPS 4MHz	208.8 +0.38%	43.1 -0.6	208.8 +0.38%	-24.8 -1.1	/	/	/	/
H-UBPS 5MHz	208.3 +0.14%	42.9 -0.8	209.3 +0.63%	-24.9 -1.2	/	/	/	/
H-UBPS 6MHz	208.0 0.00%	43 -0.7	207.0 -0.48%	-24.8 -1.1	150.3 +0.20%	62.9 -0.2	149.9 -0.07%	-44.4 -1.3

In analogy with the previous investigation of sample 1D, sample 2Da has been insonified at the various frequencies. The H-UPS and H-UBPS results, recorded at f = 4 MHz, respectively f = 6 MHz, are shown in Figure 10-24 and Figure 10-25. Note that the H-UBPS image at f = 6 MHz shows joint diffraction peaks of the 3th order. The extracted parameters for the experiments at the various frequencies on the basis of Equation (4) and (5) are added to Table 10-3. The periodicities are in excellent agreement with the design parameters. The extracted symmetry orientations on the other hand deviate by ~1° from the design orientations. The deviation of the orientations has also been optically verified, affirming the precision of the H-UBPS results. As such, the angular spectrograms in previous section were obtained at slightly incorrect orientation angles which probably explains the larger error in the determined periodicities. The results of the analysis of the joint diffraction peaks on the basis of Equation (7) and (8) are listed in Table

10-4 for the different frequencies. Also here, excellent agreement with the design parameters is obtained.

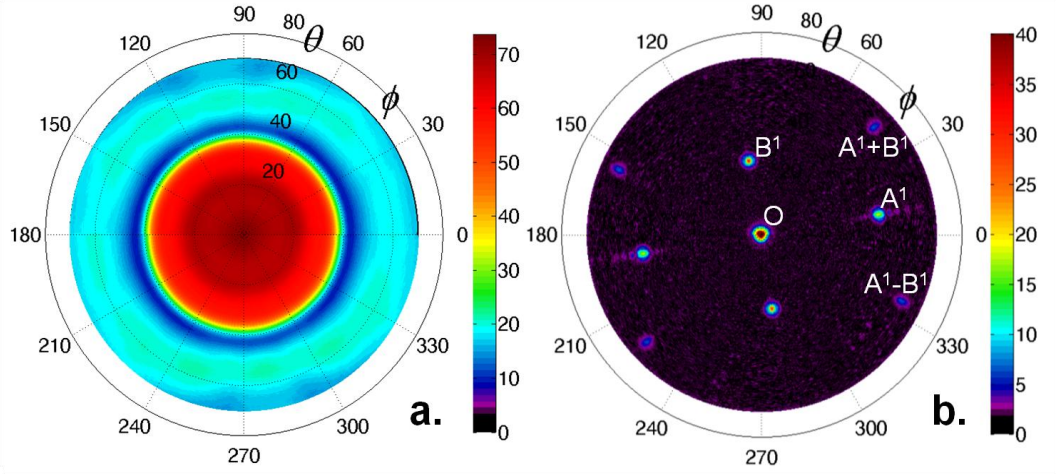

Figure 10-24: H-UPS (a) and H-UBPS (b) of sample 2Da, recorded at *f* = 4 MHz.

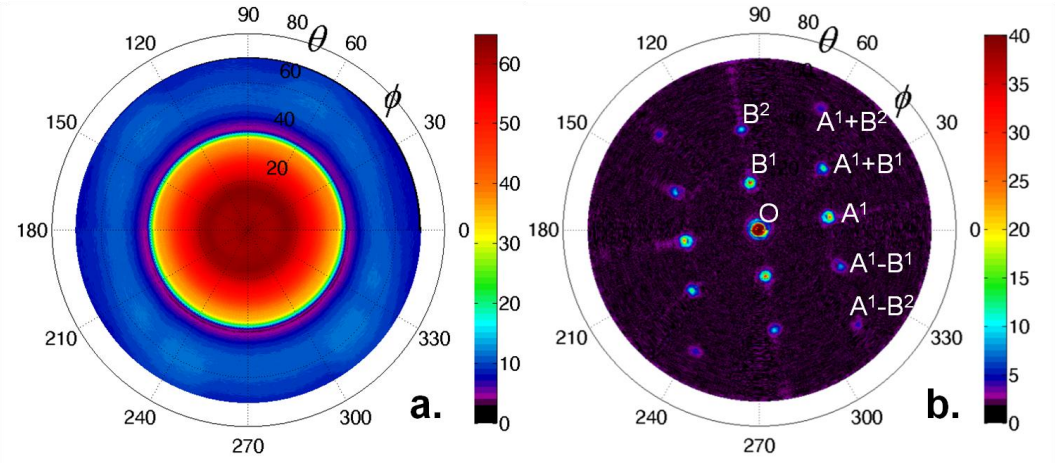

Figure 10-25: H-UPS (a) and H-UBPS (b) of sample 2Da, recorded at *f* = 6 MHz.

10. 4. 4. Sample 2Db-c: 2D Surface Corrugation with Imperfections

This section extends the H-UBPS analysis to the characterization of 2D corrugated samples having different grades of surface finishing quality (see Figure 10-2). This is important for industrial applications as the quality of a

surface structure is dependent on the environmental conditions as well as on the level of wear during operation. The H-UBPS recordings (f = 5 MHz) for sample 2Db and sample 2Dc are shown in Figure 10-26.

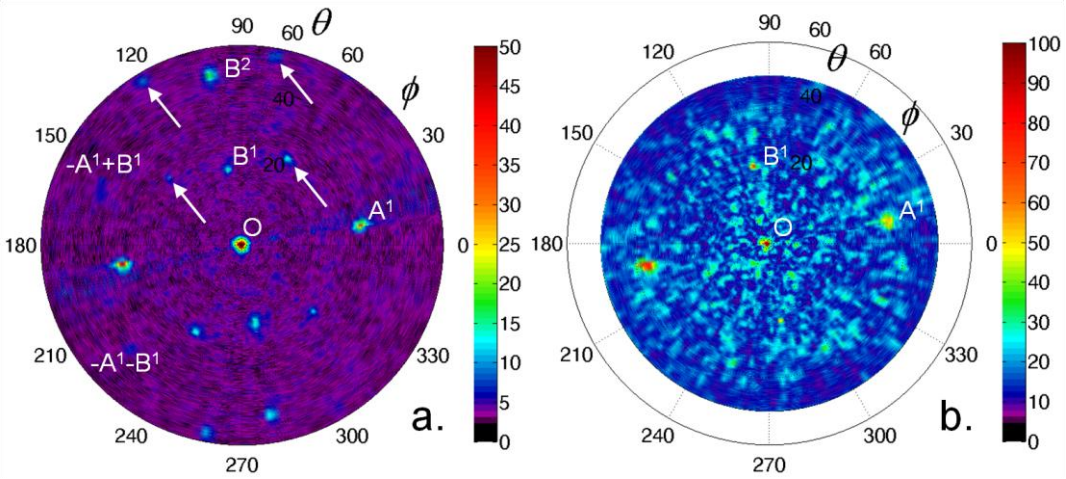

Figure 10-26: H-UBPS recorded at f = 5 MHz: sample 2Db (left) and sample 2Dc (right). The white arrows identify ghost peaks.

Compared to the H-UBPS image of sample 2Da (see Figure 10-23b), the results of sample 2Db show an increased level of background noise, while several additional diffraction peaks, with well-defined position (see white arrows in Figure 10-26a), are present. Similar to electromagnetic waves diffracted by imperfect gratings, these additional peaks are linked to imperfections in the periodicity giving rise to Lyman ghosts, Rowland ghosts as well as other phenomena [23-24, 49-51]. The H-UBPS image of sample 2Dc on the other hand becomes highly chaotic, showing a high level of background noise (note the amplitude scale) obscuring all but the 1st order diffraction peaks of grating A and grating B. In optics, a similar obscuring effect has already been observed for low-quality gratings with randomly distributed imperfections and the effect is commonly referred to as 'grass' [52-53]. These results thus demonstrate that the presence of these additional scattering features can be exploited to 'measure' the purity, or the impurity, of the insonified 2D grating. The H-UBPS results of the different 2D corrugated samples have been analyzed in order to extract the surface parameters, the results are listed in Table 10-5. It is noted that the implemented peak identification procedure found many diffraction peaks for sample 2Dc, indicating that it is not well-suited for the characterization of low-quality surface corrugations. Therefore, the sought peaks have been

manually selected in the list of identified diffraction peaks. The determined surface parameters are in good correspondence with the design parameters, even for the low-quality sample 2Dc. Optical extraction of surface parameters however was impossible due to the low quality of sample 2Db and sample 2Dc.

Table 10-5: Analysis results of the diffraction peaks according to Equation (4) and (5). The first row "Design" corresponds to the design parameters. The other rows to the H-UBPS results for sample 2Da, sample 2Db and sample 2Dc.

	Λ_{A^1} [µm]	Φ_{A^1} [°]	Λ_{B^1} [µm]	Φ_{B^1} [°]	Λ_{B^2} [µm]	Φ_{B^2} [°]
Design	250	100	375	10	375	10
Sample 2Da	249.8 -0.08%	99.3 -0.7	375.3 +0.08%	9.0 -1	374.7 -0.08%	9.1 -0.9
Sample 2Db	250.8 +0.32%	99.8 -0.2	372.0 -0.80%	9.8 -0.2	376.4 +0.37%	9.8 -0.2
Sample 2Dc	249.6 -0.16%	100.3 +0.3	371.7 -0.88%	10.5 +0.5	/	/

It is clear that the above results reveal the excellent capability of the H-UBPS methodology to characterize both periodicities and symmetry orientations of 2D surface structures with various degrees of surface finishing quality. The H-UBPS images reveal several ghost diffraction peaks which relate to both periodic and aperiodic imperfections of the insonified surface structure. As such, the H-UBPS methodology provides also a 'measure' for the quality level of the inspected surface structure.

10. 4. 5. Sample 2Da-back: 2D Subsurface Corrugation

This section extends the H-UBPS analysis to subsurface 2D corrugations. Up to now, the inspection and characterization of subsurface 2D gratings has not yet been performed in literature despite its importance for several NDE applications in industry. Sample 2Da is investigated at a frequency f = 5MHz, but now with the 2D corrugation located at the back side. The front side and backside H-UBPS images are shown in Figure 10-27.

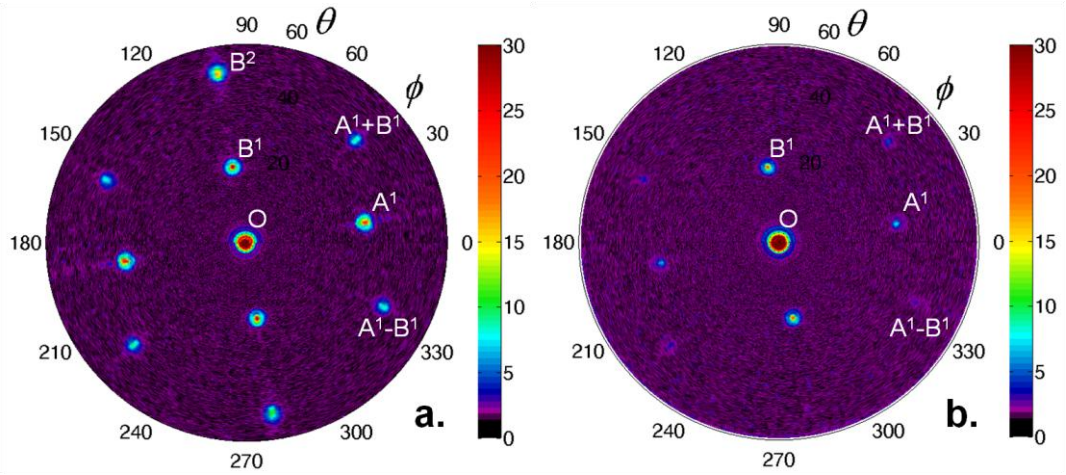

Figure 10-27: H-UBPS recorded at *f* = 5MHz for sample 2Da with the 2D corrugation located at the front side (a) and at the backside (b).

The similarity between both images is evident. This comes as no surprise by recalling Snell-Descartes' law which states that the horizontal component of the incident wave vector is conserved [39-40]. As such, the diffraction conditions remain unchanged, even though mode conversion may occur, resulting to diffraction peaks having a fixed position in *(φ,θ)*-space. The only remarkable change between the H-UBPS experiments is the amplitude of the backscatter peaks. The amplitudes of the H-UBPS experiment for the subsurface 2D corrugation is significantly lower (with the exception of the spike at normal incidence). This is not surprising as the involved ultrasonic waves, incident at oblique angles, have to traverse the PC sample before being backscattered to the emitter/receiver. The same was already observed for the angular spectrograms (Figure 10-13). Additionally, we remark for the backside results that the 1st order spikes A^1 along $\varphi \approx 10°$ show a more drastic drop in amplitude level compared to the 1st order spikes B^1 along $\varphi \approx 100°$. Even more, the 2th order spikes B^2 along $\varphi \approx 100°$ cannot be discerned anymore. As the 2th order diffraction peaks B^2 could not be cut off by any critical angle phenomena (the PC sample only has a critical angle for the longitudinally polarized bulk wave, $\theta_{crit} = \sin^{-1}(1475.4/2270) \approx 40.5°$ [41]), the cause has to be found elsewhere. The H-UPS images of the corrugated PC sample at *f* = 5MHz (see for example Figure 10-23a) reveals a transmission transparent window (longitudinal dominated coupling) for $\theta < 41.6°$, while at larger incident angle θ (shear dominated coupling) the transmission coefficient tends to zero. This implies that, although the diffraction conditions prescribed by Bragg's law remain unchanged, a proper

characterization of the in-plane parameters of the subsurface corrugation demands a lower limit for the ultrasonic frequency f such that the 1st order diffraction peaks are located within the transparent transmission window. For the PC sample considered here, this leads to the condition that $f > 4.45$MHz. Obviously, for other substrates this frequency condition is function of the elastic properties. Based on the visible diffraction peaks, the extracted corrugation parameters for the subsurface 2D corrugation are listed in Table 10-6. For clarity, the design parameters as well as the H-UBPS extracted parameters for the visible 2D corrugation have also been added to Table 10-6. Good agreement is obtained with the different sets of parameters.

It is noted that the angular spectrogram of the backside corrugation (Figure 10-13) does reveal faint 2th order backscatter signals for $\theta > 41.6°$, which is in sharp contrast with the current H-UBPS results giving not a single indication of backscatter. Several additional experiments have been performed, affirming this discrepancy.

Table 10-6: Analysis results of the diffraction peaks. The first row "Design" corresponds to the design parameters. Row "FRONT", respectively "BACK", corresponds to the H-UBPS results when insonifying sample 2Da from the front side, respectively from the backside.

	Λ_{A^1} [μm]	Φ_{A^1} [°]	Λ_{B^1} [μm]	Φ_{B^1} [°]	Λ_{B^2} [μm]	Φ_{B^2} [°]	$\Lambda_{A^1+B^1}$ [μm]	$\Phi_{A^1+B^1}$ [°]	$\Lambda_{A^1-B^1}$ [μm]	$\Phi_{A^1-B^1}$ [°]
Design	250	100	375	10	375	10	208.0	43.7	208.0	-23.7
FRONT	249.8 -0.08%	99.3 -0.7°	375.3 +0.08%	9.0 -1°	374.7 -0.08%	9.1 -0.9°	208.3 +0.14%	42.9 -0.8°	209.3 +0.63%	-24.9 -1.2°
BACK	251.4 +0.56%	99.6 -0.4°	374.7 -0.08%	9.3 -0.7°	/	/	208.9 +0.43%	44.5 +0.8°	208.4 +0.19%	-24.7 -1°

In contrast to the elasticity independent diffraction conditions, expressed by means of the Bragg angles, the amplitudes of the diffraction peaks are clearly dependent on the substrate material characteristics. Hence, the extraction of the height parameters of a subsurface structure cannot be simply done by solely evaluating the recorded backscatter intensities. Furthermore, we note that the mode conversion process in refraction at the upper liquid-solid interface inhibits the inspection of a local spot at the back surface, limiting the usability of the H-UBPS technique to the characterizing of subsurface structures with spatially uniform dimensions. The above

observations become even more important in case of inspecting a subsurface grating superimposed on anisotropic elastic substrates as the transmission characteristics of anisotropic media display a more complex shape (see for example Figure 3-22) in which multiple (non-)transparent transmission windows are observed. In addition, wave propagation in an anisotropic solid does not necessarily take place within the insonification plane (see the analysis in Chapter 6) making the interpretation of backscattered sound, originating at the bottom surface, impossible without profound knowledge of the substrate characteristics.

10. 5. Ultrasonic Polar Spectrogram Scan (UPSS)

On the one hand, the angular spectrogram requires prior knowledge about the symmetries of the surface profile to successfully determine periodicities. The H-UBPS on the other hand does capture all relevant surface parameters, but on the expense of a more complex experimental setup and an increased experimental time. In this section, the ultrasonic polar spectrogram scan (UPSS) is introduced which combines the advantages of the angular spectrogram (short experimental time) with the advantages of the H-UBPS (characterization of both periodicities and orientations), while reducing the complexity of the experimental implementation significantly. Basically, a broadband emitter/receiver with central frequency f_c = 5 MHz is fixed at a certain incident angle θ, after which it is rotated along the polar angle φ in steps of $\Delta\varphi = 0.05°$. Here, a fixed incident angle of $\theta = 45°$ is considered. Compared to the scanning of the incident angle θ, varying the polar angle φ (rotation around vertical axis) is far more straightforward to implement mechanically. The typical time to record a UPSS experiment is around 10 seconds. The backscatter signals are recorded in a 25 μs time window, which is sufficient to record the complete backscattered wave at $\theta = 45°$ (see Figure 10-3d) and to reduce the previously encountered aliasing. The recordings are subsequently analyzed in frequency domain in a similar fashion as done for the angular spectrograms (see Section 10.3). The processed UPSS recording for the flat sample 0D is displayed in Figure 10-28, with the frequency (in MHz) on the radial axis, the polar angle φ on the angular axis and the color pigment representing the backscattered amplitude. Theoretically, the UPSS image for sample 0D should be identical to zero. Instead, the UPSS shows a circular pattern of increased backscatter around f = 8.5 MHz. It is found by extensive experimenting that the circular pattern has no physical origin, but corresponds to a systematic self-interfering signal produced by the

experimental setup. In addition, some other randomly distributed backscatter signals can be observed which are attributed to redundant reflections within the water tank.

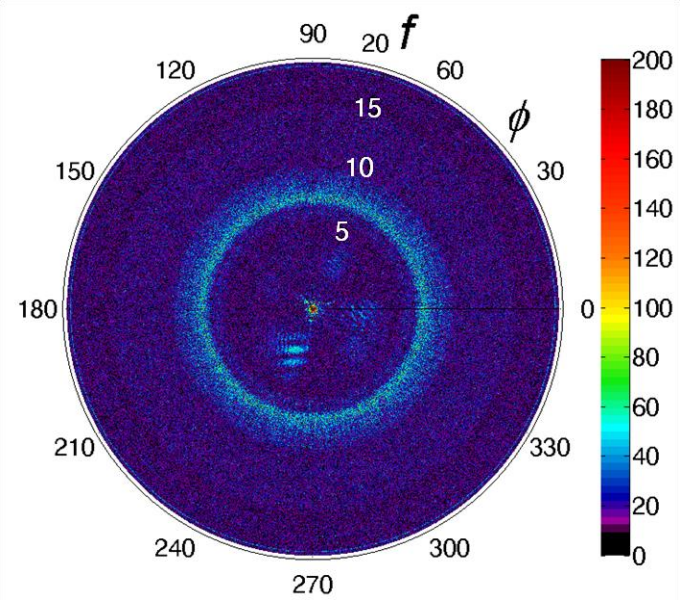

Figure 10-28: UPSS recorded at θ = 45° for sample 0. The radial axis spans the frequency f (in MHz), the angular axis the polar angle φ (in degrees).

The UPSS experiments for sample 1D and sample 2Da are displayed in Figure 10-29. The left column correspond to front side insonification, the right column to back side insonification. For matters of visualization, the frequency axis has been cut off at 10 MHz. The circular blueprint of the systematic interfering signal as well as random background noise can be observed in all the UPSS images. Though, their associated amplitude is low compared to the amplitude of the envisioned backscatter signals, making it easy to filter them out in the post-processing analysis. The interpretation of the multiple well-defined high-intensity peaks can be done in a similar manner as done for the H-UBPS images, i.e. in terms of pure diffraction peaks and joint diffraction peaks. The peaks have been explicitly labeled in Figure 10-29 according to their physical origin.

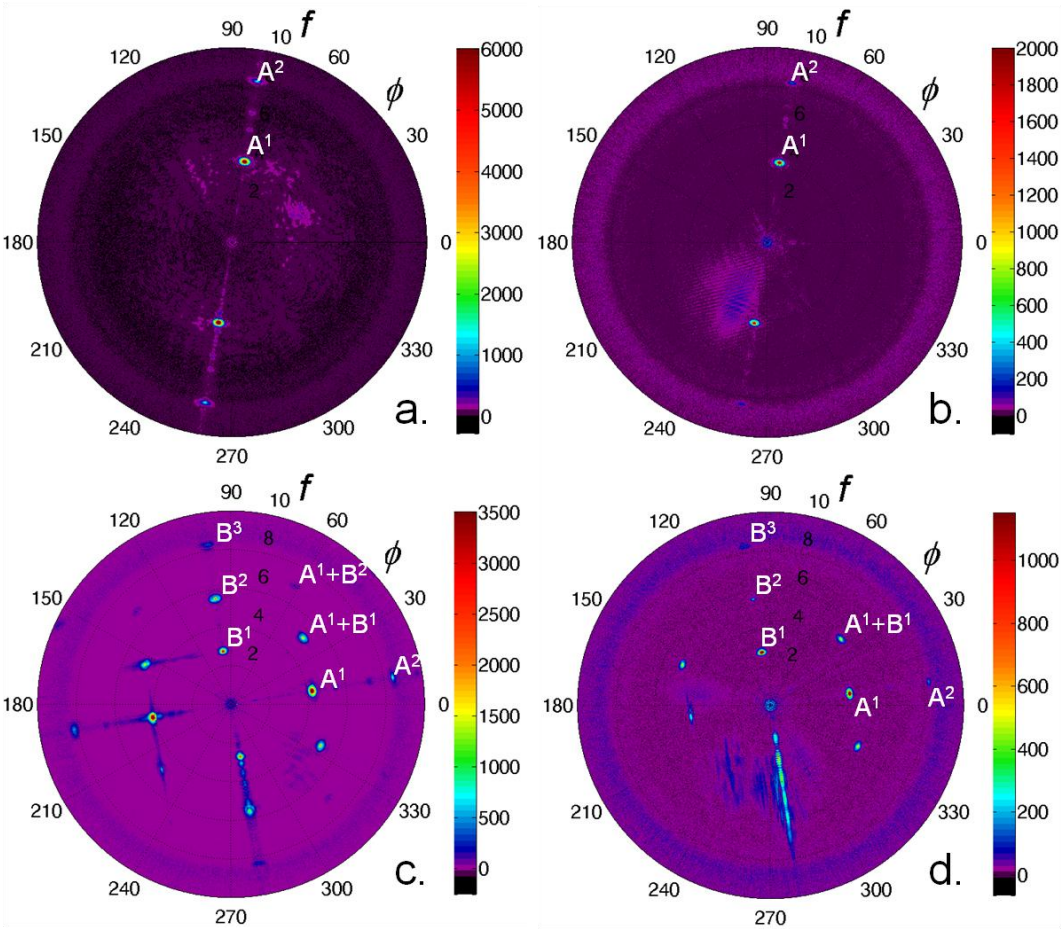

Figure 10-29: UPSS experiments recorded at θ = 45° for sample 1D (a-b) and sample 2Da (c-d). Left column corresponds to front side insonification, right column to backside insonification.

To extract surface parameters, the UPSS images have been convolved with a 2D Gaussian profile, while the background noise has been removed in a similar way as done for the H-UBPS experiments. The extraction procedure has been performed up to 4th order Bragg diffraction peaks. The UPSS extracted surface parameters are listed in Table 10-7 for sample 1D and in Table 10-8 for sample 2Da. It can be verified that excellent agreement is obtained with the design parameters. The joint-diffraction peaks in Figure 10-29 can also be analyzed to extract surface parameters, though this is not done here because of the obvious similarity with the analysis given for the H-UBPS.

Note that the backside insonification produces several Bragg diffraction peaks in the UPSS image, although the angle of incidence does not lie within the transmission transparent window ($\theta < 41.6°$). This is in sharp contrast with the results of the H-UBPS experiments. The origin of this different behavior is unknown at this moment.

Table 10-7: UPSS extracted surface parameters for sample 1D.

Order	TOP		BOTTOM	
	Λ_A [µm]	Φ_A [°]	Λ_A [µm]	Φ_A [°]
m = 1	249.35	169.45	250.10	169.45
m = 2	249.60	169.45	250.5	169.4
m = 3	249.30	169.45	250.5	169.4
m = 4	249.40	169.50	252.8	169.4

Table 10-8: UPSS extracted surface parameters for sample 2Da.

Order	TOP				BOTTOM			
	Λ_A [µm]	Φ_A [°]	Λ_B [µm]	Φ_B [°]	Λ_A [µm]	Φ_A [°]	Λ_B [µm]	Φ_B [°]
m = 1	250.15	99.40	376.7	9.15	251.25	98.15	375.2	9.30
m = 2	250.30	99.30	374.8	9.10	252.05	98.30	375.15	9.30
m = 3	250.20	99.40	375.6	8.95	--	--	376.8	9.7
m = 4	250.40	99.45	--	--	--	--	--	--

The UPSS images show a higher degree of 'pollution' when compared to the corresponding H-UBPS images (Figure 10-18b, Figure 10-23b and Figure 10-27). This can be clearly seen in the UPSS image representing the backside insonification of sample 2Da. To check whether this increased level of noise is inherent to the UPSS methodology, scans have been recorded for the front side of the mid-quality sample 2Db and the low-quality sample 2Dc (Figure 10-30).

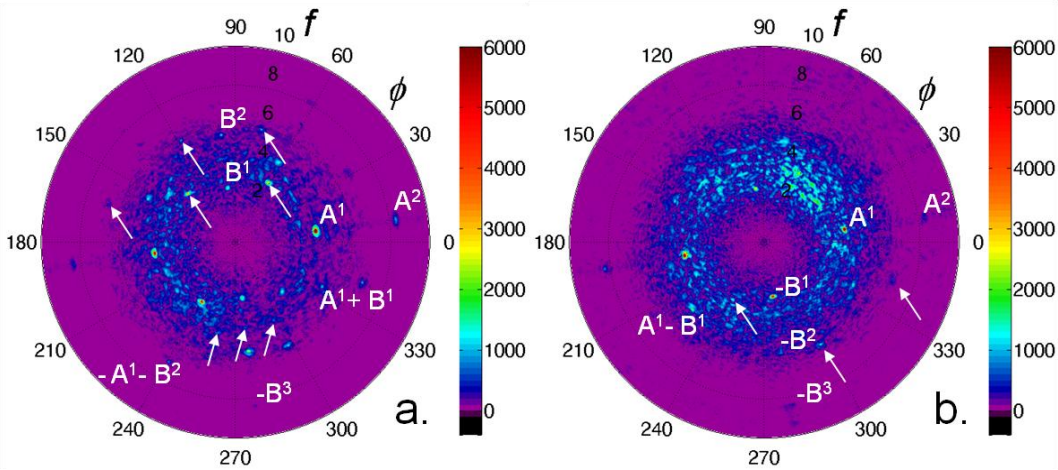

Figure 10-30: UPSS experiments recorded at θ = 45° for sample 2Db (a) and sample 2Dc (b). The white arrows identify ghost diffraction peaks.

The UPSS image of sample 2Db shows that besides the expected peaks several well-defined diffraction peaks can be observed at fractional positions (indicated with white arrows), thus enlightening imperfections in the periodicity of the corrugation. In addition, the multiple randomly located diffraction peaks within the frequency band 2-6 MHz expose the crumble nature of the inspected surface. The UPSS image of sample 2Dc shows that the latter becomes dominant, exposing its low-quality surface finishing. When compared to the H-UBPS results, the ghost diffraction peaks have a more pronounced presence, indicating that the UPSS setup is more sensitive to imperfections in the periodic surface structure.

Finally, a remark has to be given concerning the feasibility of the here presented UPSS method for industrial applications. Contrary to the H-UBPS, no reference direction can be identified in the UPSS results. As such, the UPSS can only provide accurate results for surfaces of which the direction of the normal is known exactly. Hence, the UPSS requires, just like the angular spectrogram, prior knowledge about the surface under investigation. However, if one could employ a second emitter/receiver positioned at a known angle $\Delta\theta$ with respect to the first emitter/receiver, this additional information can be used to extract the normal direction of the inspected surface. As such, the UPSS becomes, just like the H-UBPS, a method to characterize in-plane parameters of periodic surface structures without the necessity of any prior knowledge. Unfortunately, no occasion was found during the research term to experimentally implement this extension.

10. 6. Conclusions

Both 1D and 2D periodic surface structures have been ultrasonically inspected in the Bragg imaging regime using three different experimental methodologies and dedicated post-processing procedures.

First, the recently introduced angular spectrogram method has been employed. An optimization procedure is implemented in order to determine the optimal Bragg parameters, i.e. the surface periodicity. Reasonable agreement with the true surface parameters is obtained (~1% deviation). The experimental Bragg scattering curves have been extracted, revealing a non-uniform amplitude which shows characteristic oscillations. Interpretation of these oscillations in terms of backscattered phase-matching Lamb waves is, at first sight, not supported by the Lamb wave dispersion curves (computed for a flat and smooth PC sample). Further evidence of this statement is found in the asymmetry between the amplitude oscillations for front side and backside insonification. In addition, H-UPS results indicate that the investigated samples are rather subject to bulk wave dominated features. Angular spectrograms recorded at both positive and negative incident angles sometimes reveal a shift in the global backscatter amplitude level. It is shown that this shift in amplitude has to be linked to the asymmetric beam profile of the bounded beam, rather than to imperfections in the surface structure.

Secondly, a harmonic version of the UBPS principle has been applied for characterization of a periodic surface structure. Contrary to the angular spectrogram methodology, the H-UBPS method does not require any prior knowledge about the symmetry lines of the surface. Besides the specular reflection field from which a reference direction is obtained, a H-UBPS image displays multiple diffraction spikes which can be classified according to the origin of diffraction, i.e. pure diffraction peaks and joint diffraction peaks. Both classes of peaks expose surface periodicities as well as symmetry orientations of the insonified structure. As such, the H-UBPS provides a complete characterization of the in-plane parameters of a periodic surface structure without the need of prior knowledge. The H-UBPS extracted parameters are in excellent agreement with the true surface parameters (~0.1% deviation).

Thirdly, the ultrasonic polar spectrogram scan (UPSS) is introduced. The UPSS method combines the advantages of both the angular spectrogram

method and the H-UBPS, resulting in a highly simplified methodology yielding diffraction peaks which expose both the surface periodicities and the symmetry orientations in the polar angle-frequency space. The obtained surface parameters are very competitive to the H-UBPS extracted parameters.

The analysis has been further extended to the inspection of 2D corrugated samples having different levels of surface finishing quality. It is shown that periodic imperfections lead to structured ghost diffraction peaks, while aperiodic imperfections give rise to randomly distributed diffraction peaks. The results suggest that these additional peaks provide a measure of the purity, or the impurity, of the inspected surface structure. In addition, the characterization of a subsurface 2D corrugation has also been tackled. It is shown that the Bragg diffraction conditions remain unchanged due to Snell-Descartes law. However a proper characterization of the in-plane parameters of the subsurface corrugation by means of the H-UBPS method demands a lower limit for the ultrasonic frequency f such that the 1st order diffraction peaks are located within the transparent transmission window. It is further commented that characterization of subsurface features is only applicable to surface structures having uniform spatial dimensions due to the mode conversion process in refraction at the upper liquid-solid interface.

10. 7. References

[1] Franklin, R.E. and R.G. Gosling, *Molecular configuration in sodium thymonucleate.* Nature, 1953. 171: p. 740-741.

[2] Shechtman, D., I. Blech, D. Gratias, and J.W. Cahn, *METALLIC PHASE WITH LONG-RANGE ORIENTATIONAL ORDER AND NO TRANSLATIONAL SYMMETRY.* Physical Review Letters, 1984. 53(20): p. 1951-1953.

[3] Herbison, S.W., *Ultrasonic diffraction effects on periodic surfaces.* PhD thesis; Georgia Institute of Technology, 2011: p. 214.

[4] Grimaldi, F.M., *Physico mathesis de lumine, coloribus, et iride, aliisque annexis libri duo.* Vittorio Bonati, 1665.

[5] Bragg, W.L., *The diffraction of short electromagnetic waves by a crystal.* Proc. Cambridge Phil. Soc., 1913. 17: p. 43-57.

[6] Yang, S.X., J.H. Page, Z.Y. Liu, M.L. Cowan, C.T. Chan, and P. Sheng, *Focusing of sound in a 3D phononic crystal.* Physical Review Letters, 2004. 93(2).

[7] Kapasi, H., J. Blackburn, and C. Mias, *The use of corrugated surfaces to improve wireless signal strength in the shadow region of buildings.* Microwave and Optical Technology Letters, 2005. 46(5): p. 467-469.

[8] Torres, E.S., S. Goncalves, C. Scherer, and M. Kiwi, *Nanoscale sliding friction versus commensuration ratio: Molecular dynamics simulations.* Physical Review B, 2006. 73(3).

[9] Khelif, A., B. Aoubiza, S. Mohammadi, A. Adibi, and V. Laude, *Complete band gaps in two-dimensional phononic crystal slabs.* Physical Review E, 2006. 74(4).

[10] Jungman, A., L. Adler, and G. Quentin, *ULTRASONIC ANOMALIES IN THE SPECTRUM OF ACOUSTIC-WAVES DIFFRACTED BY PERIODIC INTERFACES.* Journal of Applied Physics, 1982. 53(7): p. 4673-4680.

[11] Claeys, J.M., O. Leroy, A. Jungman, and L. Adler, *DIFFRACTION OF ULTRASONIC-WAVES FROM PERIODICALLY ROUGH LIQUID SOLID-SURFACE.* Journal of Applied Physics, 1983. 54(10): p. 5657-5662.

[12] Roberts, R., J.D. Achenbach, R. Ko, L. Adler, A. Jungman, and G. Quentin, *REFLECTION OF A BEAM OF ELASTIC-WAVES BY A PERIODIC SURFACE PROFILE.* Wave Motion, 1985. 7(1): p. 67-77.

[13] Nagy, P.B. and L. Adler, *SURFACE-ROUGHNESS INDUCED ATTENUATION OF REFLECTED AND TRANSMITTED ULTRASONIC-WAVES.* Journal of the Acoustical Society of America, 1987. 82(1): p. 193-197.

[14] Mampaert, K., P.B. Nagy, O. Leroy, L. Adler, A. Jungman, and G. Quentin, *ON THE ORIGIN OF THE ANOMALIES IN THE REFLECTED ULTRASONIC SPECTRA FROM PERIODIC SURFACES.* Journal of the Acoustical Society of America, 1989. 86(1): p. 429-431.

[15] Declercq, N.F., J. Degrieck, R. Briers, and O. Leroy, *Theoretical verification of the backward displacement of waves reflected from an interface having superimposed periodicity.* Applied Physics Letters, 2003. 82(15): p. 2533-2534.

[16] Declercq, N.F., J. Degrieck, R. Briers, and O. Leroy, *Theory of the backward beam displacement on periodically corrugated surfaces and its relation to leaky Scholte-Stoneley waves.* Journal of Applied Physics, 2004. 96(11): p. 6869-6877.

[17] Declercq, N., *The interaction of complex harmonic elastic waves with periodically corrugated surfaces and with anisotropic viscoelastic or piezoelectric layered media.* Phd, 2005: p. 636.

[18] Herbison, S.W., J.M. Vander Weide, and N.F. Declercq, *Observation of ultrasonic backward beam displacement in transmission through a solid having superimposed periodicity.* Applied Physics Letters, 2010. 97(4).

[19] De Billy, M., F. Cohentenoudji, A. Jungman, and G.J. Quentin, *POSSIBILITY OF ASSIGNING A SIGNATURE TO ROUGH SURFACES USING ULTRASONIC BACKSCATTERING DIAGRAMS.* Ieee Transactions on Sonics and Ultrasonics, 1976. 23(5): p. 356-363.

[20] De Billy, M. and G. Quentin, *MEASUREMENT OF THE PERIODICITY OF INTERNAL SURFACES BY ULTRASONIC TESTING.* Journal of Physics D-Applied Physics, 1982. 15(10): p. 1835-1841.

[21] Shin, Y.C., S.J. Oh, and S.A. Coker, *SURFACE-ROUGHNESS MEASUREMENT BY ULTRASONIC SENSING FOR IN-PROCESS MONITORING.* Journal of Engineering for Industry-Transactions of the Asme, 1995. 117(3): p. 439-447.

[22] Sukmana, D.D. and I. Ihara, *Surface roughness characterization through the use of diffuse component of scattered air-coupled ultrasound.* Japanese Journal of Applied Physics Part 1-Regular Papers Brief Communications & Review Papers, 2006. 45(5B): p. 4534-4540.

[23] Rowland, H.A., *XXXIX. Gratings in theory and practice.* Philosophical Magazine Series 5, 1893. 35(216): p. 397-419.

[24] Gale, H.G., *Rowland Ghosts.* Astrophysical journal, 1937. 85(2): p. 49-61.

[25] Nagy, P.B., A. Jungman, and L. Adler, *Measurements of backscattered leaky lamb waves in composite plates.* Materials Evaluation, 1988. 46(1): p. 97-100.

[26] Liu, J.F. and N.F. Declercq, *Air-coupled ultrasonic investigation of stacked cylindrical rods.* Journal of the Acoustical Society of America, 2012. 131(6): p. 4500-4507.

[27] Tukey, J.W., *An introduction to the calculations of numerical spectrum analysis*. Spectral Analysis of Time Series, ed. B. Harris. 1968, New York: Wiley. 25-46.

[28] Harris, F.J., *On the use of windows for harmonic analysis with the discrete Fourier transform.* Proceedings of the IEEE, 1978. 66(1): p. 51-83.

[29] Unser, M., *Sampling - 50 years after Shannon.* Proceedings of the Ieee, 2000. 88(4): p. 569-587.

[30] Matar, O.B., N. Gasmi, H. Zhou, M. Goueygou, and A. Talbi, *Legendre and Laguerre polynomial approach for modeling of wave propagation in layered magneto-electro-elastic media.* Journal of the Acoustical Society of America, 2013. 133(3): p. 1415-1424.

[31] El-Bahrawy, A., *Stopbands and passbands for symmetric Rayleigh-Lamb modes in a plate with corrugated surfaces.* Journal of Sound and Vibration, 1994. 170(2): p. 145-160.

[32] Morvan, B., A.C. Hladky-Hennion, D. Leduc, and J.L. Izbicki, *Phonon phenomenon in the interaction of guided ultrasonic waves with a surface grating*, in *12th International Conference on Phonon Scattering in Condensed Matter*, B. Perrin, et al., Editors. 2007.

[33] Kundu, T., S. Banerjee, and K.V. Jata, *An experimental investigation of guided wave propagation in corrugated plates showing stop bands and pass bands.* Journal of the Acoustical Society of America, 2006. 120(3): p. 1217-1226.

[34] Potel, C., D. Leduc, B. Morvan, C. Depollier, A.C. Hladky-Hennion, J.L. Izbicki, P. Pareige, and M. Bruneau, *Lamb wave attenuation in a rough plate. I. Analytical and experimental results in an anisotropic plate.* Journal of Applied Physics, 2008. 104(7).

[35] Potel, C., D. Leduc, B. Morvan, C. Depollier, A.C. Hladky-Hennion, J.L. Izbicki, P. Pareige, and M. Bruneau, *Lamb wave attenuation in a rough plate. II. Analytical and numerical results in a fluid plate.* Journal of Applied Physics, 2008. 104(7).

[36] Valier-Brasier, T., C. Potel, M. Bruneau, and P. Gatignol, *Analytical approach of Lamb waves coupling in rough isotropic plates.* Journal of Applied Physics, 2011. 109(6).

[37] Laude, V., R.P. Moiseyenko, S. Benchabane, and N.F. Declercq, *Bloch wave deafness and modal conversion at a phononic crystal boundary.* Aip Advances, 2011. 1(4).

[38] Laude, V., Y. Achaoui, S. Benchabane, and A. Khelif, *Evanescent Bloch waves and the complex band structure of phononic crystals.* Physical Review B, 2009. 80(9).

[39] Rose, J.L., *Ultrasonic Waves in Solid Media*. 1999: Cambridge University Press. 454.

[40] Auld, B.A., *Acoustic Fields and Waves in Solids, second edition*. 1990, Florida: Krieger publishing company. 856.

[41] Selfridge, A.R., *APPROXIMATE MATERIAL PROPERTIES IN ISOTROPIC MATERIALS.* Ieee Transactions on Sonics and Ultrasonics, 1985. 32(3): p. 381-394.

[42] Moiseyenko, R.P., N.F. Declercq, and V. Laude, *Guided wave propagation along the surface of a one-dimensional solid-fluid phononic crystal.* Journal of Physics D-Applied Physics, 2013. 46(36).

[43] Claeys, J.M. and O. Leroy, *REFLECTION AND TRANSMISSION OF BOUNDED SOUND BEAMS ON HALF-SPACES AND THROUGH PLATES.* Journal of the Acoustical Society of America, 1982. 72(2): p. 585-590.

[44] Declercq, N.F., J. Degrieck, R. Briers, and O. Leroy, *Diffraction of homogeneous and inhomogeneous plane waves on a doubly corrugated liquid/solid interface.* Ultrasonics, 2005. 43(8): p. 605-618.

[45] Vandenabeele, K. and O. Leroy, *BOUNDED BEAM REFLECTION AND TRANSMISSION EFFECTS IN TERMS OF COMPLEX HARMONIC-WAVES.* Journal De Physique Iv, 1992. 2(C1): p. 675-678.

[46] Van Den Abeele, K.E.A., R. Briers, and O. Leroy, *Inhomogeneous plane-wave scattering and mode stimulation on periodic rough surfaces.* Journal of the Acoustical Society of America, 1996. 99(5): p. 2883-2897.

[47] Declercq, N.F., R. Briers, J. Degrieck, and O. Leroy, *The history and properties of ultrasonic inhomogeneous waves.* Ieee Transactions on Ultrasonics Ferroelectrics and Frequency Control, 2005. 52(5): p. 776-791.

[48] Kersemans, M., W. Van Paepegem, K. Van Den Abeele, L. Pyl, F. Zastavnik, H. Sol, and J. Degrieck, *Ultrasonic Characterization of Subsurface 2D Corrugation.* Journal of Nondestructive Evaluation, 2014. In Press DOI: 10.1007/s10921-014-0239-7.

[49] Lyman, T., *An explanation of the false spectra from diffraction gratings.* Proceedings of the American Academy of Arts and Sciences, 1903. 39(3): p. 39 - 47.

[50] Palenius, H.P., Zetterbe.Po, and Magnusso.Ce, *GRATING GHOSTS OF AN UNUSUAL KIND.* Journal of the Optical Society of America, 1972. 62(12): p. 1525-&.

[51] Damany, N. and J.M. Esteva, *OBSERVATION OF GHOSTS PRODUCED BY GRATINGS IN FAR ULTRAVIOLET.* Optics Communications, 1975. 13(3): p. 333-334.

[52] Dusseaux, R., C. Faure, J. Chandezon, and F. Molinet, *NEW PERTURBATION-THEORY OF DIFFRACTION GRATINGS AND ITS APPLICATION TO THE STUDY OF GHOSTS.* Journal of the Optical Society of America a-Optics Image Science and Vision, 1995. 12(6): p. 1271-1282.

[53] Breidne, M. and D. Maystre, *VARIATIONAL THEORY OF DIFFRACTION GRATINGS AND ITS APPLICATION TO THE STUDY OF GHOSTS.* Journal of the Optical Society of America, 1982. 72(4): p. 499-506.

Chapter 11

A Novel Ultrasonic Method for the Measurement of a 3D Strain Field

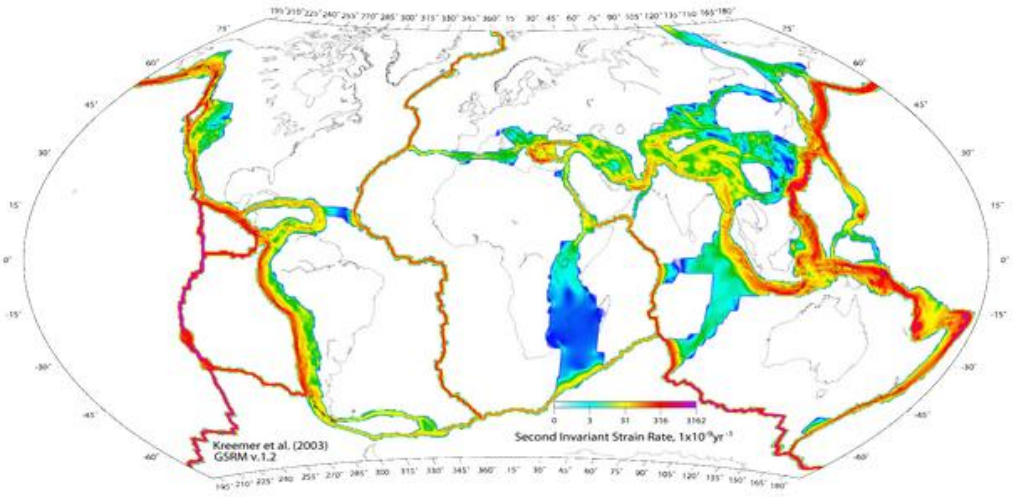

Contour plot of the second invariant of the model strain rate tensor field for the earth's plate tectonics (Figure reproduced from reference [1]).

Overview

A novel method is introduced for the measurement of a 3D strain field by exploiting the interaction between ultrasound waves and geometrical characteristics of the insonified specimen. First, the response of obliquely incident harmonic waves to a deterministic surface roughness is utilized according to the H-UBPS methodology. Analysis of backscattered amplitudes in Bragg diffraction geometry then yields a measure for the in-plane strain field by mapping any shift in angular dependency. Secondly, the analysis of the reflection characteristics of normal incident pulsed waves in frequency domain provides a measure for the out-of-plane normal strain field component, simply by tracking any change in the stimulation condition for a thickness resonance. As such, the developed ultrasonic strain gauge yields an absolute, contactless and single-sided mapping of a local 3D strain field, in which both sample preparation and alignment procedure are needless. Results are presented for cold-rolled DC06 steel samples onto which skin passing of the work rolls is applied. The samples have been mechanically loaded, introducing plastic strain levels ranging from 2% up to 35%. The ultrasonically measured strains have been validated with various other strain measurement techniques, including manual micrometer, longitudinal and transverse mechanical extensometer and optical mono- and stereovision digital image correlation. As the ultrasonic strain gauge provides all three normal strain field components, it has been employed for the extraction of Lankford ratios at different applied longitudinal plastic strain levels, revealing a strain dependent plastic anisotropy of the investigated DC06 steel sheet.

11. 1. Introduction

Measurement of strain (evolution) is indispensible to understand the response of materials under external loads, as well as to ensure the safety and integrity of a structure during its life time. The strain phenomenon can be subdivided in two main regimes: the elastic and the plastic region. While

the reversible elastic region is typically characterized by small strain levels, the irreversible plastic region involves large strains up to tens of percent. On a laboratory scale, the elastic region is of great importance for materials characterization. Most (metallic) industrial structures on the other hand can be subject to extreme or accidental loading conditions during their life time, inducing plastic deformation. Long-distance (off-shore) pipelines for example are exposed to high internal pressure in combination with bending and tension, resulting in large plastic strains [2-3]. Apart from operationally induced plastic strains, offshore pipelines are already plastically deformed during their installation with a layship, because of reeling strains (before the pipe is released), strains during the release (overbend in S-lay) and strains at the area of laying (sagbend in S-lay) [4]. Buried pipelines on the other hand are exposed to both temporary (earthquake) and permanent (soil liquefaction) geological settings. For pipelines with, respectively without a girth weld, global plastic strain values up to 5%, respectively 7.5% are acceptable. Exceeding the safety limit for plastic deformation could result in failure and rupture of the pipeline.

At present, several different gauging techniques have been developed, including electrical, optical and mechanical methods, for inspecting and monitoring the strain of an engineering structure in order to assure its mechanical health [5-11]. However, most of the existing strain measurement techniques have several drawbacks for use in an industrial environment, including (i) the need for a reference measurement, (ii) the inability to provide strain history, (iii) the necessity to physically attach the gauge, (iv) the limited range of measurable strain fields, (v) the inapplicability for offshore applications and (vi) the large sensitivity to small misalignments and external vibration. Because of the above mentioned factors, pipelines are inspected by inserting a robot provided with a GPS tracking system. Comparison of the original position of the pipeline to its current position, then provides a coarse measure for the global plastic strain. However, it is clear that on the local level, much higher strains are involved which could jeopardize the designed functionality of the pipeline. Hence, there is a need for an innovative means to locally measure a strain field in difficult environmental circumstances.

The previous chapter revealed that the in-plane parameters of a periodic (sub)surface structure, i.e. periodicities and symmetry orientations, can be ultrasonically characterized in the Bragg scattering regime [12], simply by

evaluating the backscattered wave amplitude for a wide range of oblique incidence angles $\psi(\varphi,\theta)$ (H-UPBS methodology) [13]. In this chapter, we propose an ultrasonic strain gauge (USG) which is partly based on the detection of shifting diffraction peaks in a H-UBPS image and partly on the detection of changes in the stimulation condition for a thickness resonance. The former is linked to a transformation of the surface parameters of the inspected material spot, and thus provides a measure for the in-plane strain field. The latter puts on view thickness variations, and thus is linked to the out-of-plane strain component. Instead of manufacturing a specific surface corrugation which introduces residual stress concentrations and thus effectively weakens the material, we directly employ the surface roughness left during the manufacturing process. As such, the here presented technique provides a non-contact and single-sided measurement of the local strain field (the in-plane components as well as the out-of-plane normal component) without the necessity of sample preparation. As the direction of the sample's normal is directly captured in the H-UBPS image, alignment is of minor concern. The USG technique is demonstrated for the widespread cold-rolled DC06 deep drawing steel, at different levels of plastic strain. The USG measurements are supported and verified by conventional strain measurement techniques, including (i) manual micrometer (MM), (ii) longitudinal and transverse mechanical extensometers (ME), and (iii) both mono- and stereovision digital image correlation (2D-DIC and 3D-DIC). As a matter of fact, we also employed electrical strain gauges and optical fibers to measure the strain field. However, as both have only a measurement range of maximum 5%, many of the obtained results were useless. In addition, the adhesive used to bond the electrical strain gauge and optical fibers to the surface of the DC06 steel was found to be inappropriate as debonding was frequently observed during the tests. Therefore, the electrical strain gauge and optical fiber data has been excluded from the results presented in the remainder of the Chapter.

11. 2. Materials and Experimental Procedure

Cold-rolled DC06 steel is considered in this study, having a thickness of $d = 0.7819 \pm 0.0026$ mm, a Young's modulus $E = 189.86 \pm 0.59$ GPa, a Poisson's ratio $\nu = 0.345 \pm 0.001$ and a density $\rho = 7704.7 \text{kg/m}^3$ (see Chapter 7). Its chemical composition can be summarized as: Carbon C = 0.02% (max), Manganese Mn = 0.25% (max), Phosporus P = 0.02% (max), Sulfur S = 0.02% (max), Silicium Si = 0.02% (max) and Aluminum Al = 0.01%

(min) [14]. Like many materials, the DC06 steel is provided with a deterministic surface roughness which has been applied through skin passing of the work rolls in order to meet a designed functionality. In this case (i) to improve the paint bonding capability, (ii) to reduce the waviness after coating and (iii) to lower the friction in a forming process [15]. A microscopic image of the DC06 steel surface texture is shown in Figure 11-1a.

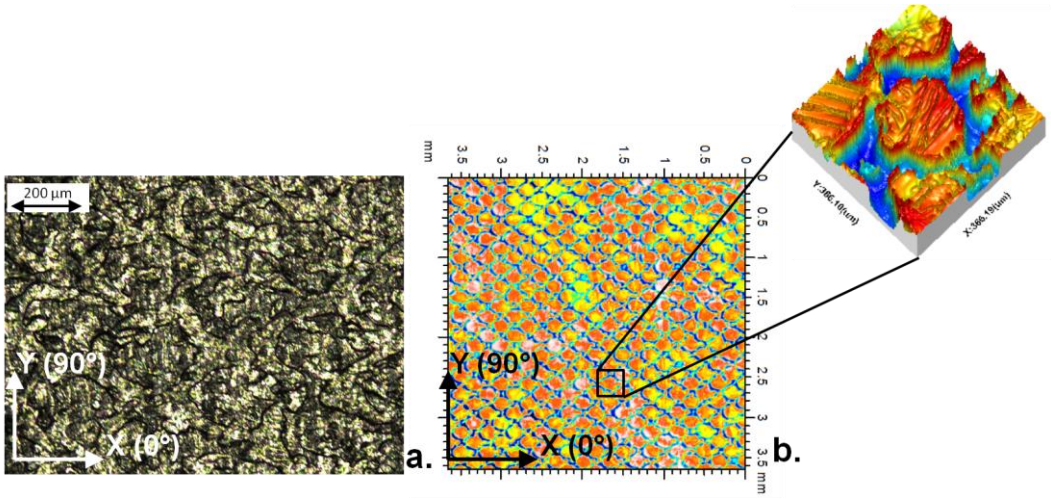

Figure 11-1: Optical visualization of the surface structure of DC06 steel: standard 2D microscopy (a) and 3D coherence correlation interferometry (after processing) (b).

Due to the low surface finishing quality (skin passing), the surface structure is difficult to identify by standard optical microscopy. Therefore, an investigation is performed by means of 3D optical interferometry. An area of 3.6 x 3.6 mm^2, with spatial sampling of ~3.6 µm in both directions, has been investigated by coherence correlation interferometry (CCI) [16]. The vertical range is 100 µm with a depth resolution of 0.01 nm. The processed and filtered image is shown in Figure 11-1b. Following the EN10049 standard (with 0.8 mm Gauss filter cut-off), an average roughness R_a = 1.1 µm with standard deviation σ_{Ra} = 0.0502 µm has been determined. From the average power spectrum density, several dominating wave lengths in the surface texture have been extracted: Λ_1 = 243 ± 20.2 µm, Λ_{1+2} = 191 ± 16.0 µm and Λ_2 = 243±23.6 µm with orientation Φ_1 = 53°, Φ_{1+2} = 90° and Φ_2 = 125° respectively. With the present CCI setup, we were not able to

further increase the resolution in spatial frequency domain in order to narrow the error bars.

Tensile tests on DC06 sheet material coupons are conducted in accordance to the ASTM E8-08 standard [17]. All experimental tests are performed at room temperature on a 50 kN servo-hydraulic INSTRON 8801 testing machine with FastTrack controller 8800, and are displacement-controlled with a crosshead speed of 2 mm/min. Plastic strains ranging from 2% up to 35% are considered (the manufacturer guarantees a minimum elongation of 38% in the skin passed condition [14]). The induced strains are measured by different strain gauge techniques: (i) manual micrometer (MM), (ii) longitudinal and transverse mechanical extensometers (ME), (iii) mono- and stereovision Digital Image Correlation (2D and 3D DIC) and (iv) the newly developed ultrasonic method (USG). Figure 11-2a shows the tensile test setup with the extensometers mounted.

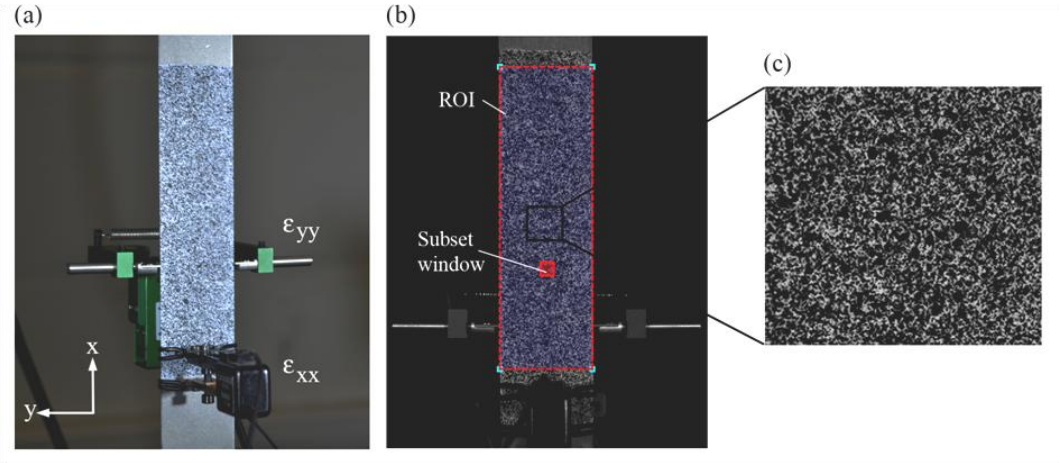

Figure 11-2: Experimental setup: longitudinal and transverse mechanical extensometers (a), image correlation window with subset size (b) and detail of the spray-paint speckle-pattern (c).

Alternatively to the use of extensometers, full field strain maps can be obtained by DIC [18]. This method is based on tracking the geometrical changes in the grey-scale distribution of a speckle pattern which is attached to the specimen surface (see Figure 11-2b-c). A deformed image is taken at incremental loading steps and compared to the undeformed reference image taken prior to loading. This reference image is mapped by a square correlation subset window which is defined by the subset size and step size,

being the pixel dimension of one single subset, and the centre distance between two adjacent subset windows, respectively. A correlation algorithm computes the displacement of each subset centre on the deformed image, estimating the displacement field across the region of interest (ROI). Determination of the specimen's surface displacement field and subsequent calculation of the strain contours was done using the MatchID software [19]. By calibrating the camera system, intrinsic and extrinsic parameters are taken into account during the image correlation process, ensuring accurate strain results. A random speckle pattern was applied on the specimen's surface by aerosol spray-paint and is monitored with 2 mega-pixel 8-bit CCD AVT Stingray F-201 B 1/1.8" cameras throughout the loading event. During quasi-static loading, images with a 1624 x 1232 pixel resolution are acquired at a sampling rate of 1 Hz and are synchronized with the load-displacement signals from the tensile machine. Both mono- and stereovision DIC is used to measure the surface displacement fields. In a monovision setup the specimen has to be positioned parallel to the camera sensor plane, and must undergo ideal planar deformation without any out-of-plane displacement. However in practice, out-of-plane motion is likely to occur, introducing an apparent strain [20]. The latter is of no importance when a stereovision setup is used as 2 cameras are setup which can compensate for out-of-plane motion.

The ultrasonic measurements have been obtained with the in-house developed automated 5-axes scanner (see Chapter 3) [21] which is provided with a standard piezoelectric transducer (diameter D = 13 mm and frequency f = 5 MHz) operating as both emitter and receiver. Both the H-UBPS methodology and pulse-echo at normal incidence is considered. As the current ultrasonic setup is immobile, the samples are first demounted from the tensile machine before scanning in the H-UBPS setup. This is the main reason why only plastic strain fields are considered.

11. 3. Ultrasonic Strain Gauge: Physical Background

11. 3. 1. In-plane Strain Field

It was demonstrated in the previous chapter that the H-UBPS methodology provides a blueprint of the characteristic surface parameters $\left\{\Lambda_1^V, \Phi_1^V, \Lambda_2^V, \Phi_2^V\right\}$ of a 2D periodic structure. The superscript 'V' denotes the virgin (or

unstrained) state of the insonified specimen, the subscript refers to the corresponding 1D grating.

When subjected to an external load, the structure gets strained and in extension the parameters of the deterministic surface roughness transform. As such, the peaks in the H-UBPS image of the strained sample shift position with respect to the results of the unstrained sample. Hence, when analyzing the H-UBPS image for a strained sample, an updated set of surface parameters $\left\{\Lambda_1^S, \Phi_1^S, \Lambda_2^S, \Phi_2^S\right\}$ can be extracted (the superscript '*S*' denotes the strained state). Knowledge of the in-plane surface parameters $\left\{\Lambda_1, \Phi_1, \Lambda_2, \Phi_2\right\}$ of both the virgin and the strained sample is in principle sufficient to extract the induced in-plane strain field. A schematic of the geometry of a typical surface unit cell is displayed in Figure 11-3 for a sample in the virgin state and in the strained state. The coordinate system can be chosen in an arbitrary way. Then, by fixing the extracted surface parameters $\left\{\Lambda_1, \Phi_1, \Lambda_2, \Phi_2\right\}$ and constructing their normals, a quadrangle with vertices $\{A, B, C, D\}$ and $\{A', B', C', D'\}$ for the virgin, respectively strained case is obtained.

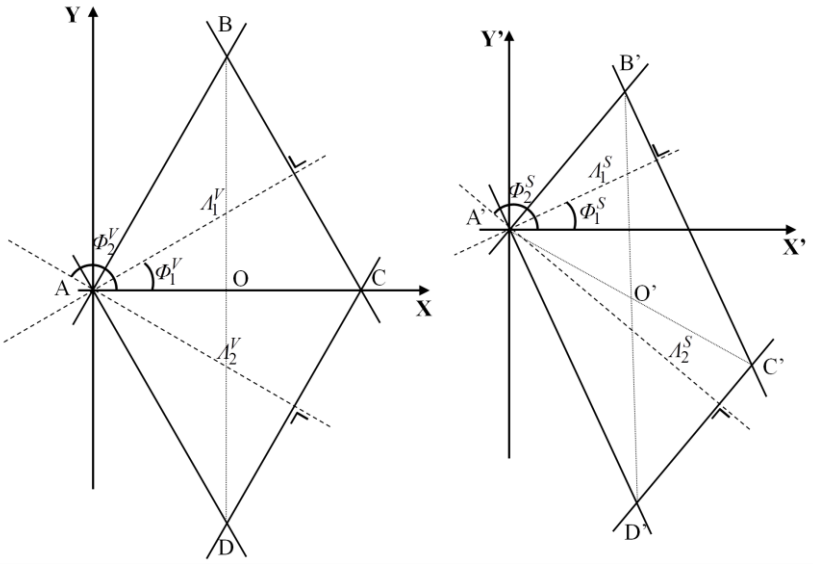

Figure 11-3: Schematic of the surface parameters of a virgin (superscript V) (a) and a strained (superscript S) (b) sample.

The coordinates of the vertices can be written in terms of the ultrasonically extracted surface parameters for the virgin and strained sample

$$\begin{cases} A(x,y)=(0,0) \\ B(x,y)=\left(\dfrac{\Lambda_1^V}{\cos\left(\Phi_2^V-90-\Phi_1^V\right)}\cos\left(\Phi_2^V-90\right),\dfrac{\Lambda_1^V}{\cos\left(\Phi_2^V-90-\Phi_1^V\right)}\sin\left(\Phi_2^V-90\right)\right) \\ C(x,y)=\left(\dfrac{\Lambda_1^V}{\cos\left(\Phi_1^V\right)},0\right)=\left(\dfrac{\Lambda_2^V}{\cos\left(\Phi_2^V\right)},0\right) \\ D(x,y)=\left(\dfrac{\Lambda_2^V}{\cos\left(\Phi_1^V-90-\Phi_2^V\right)}\cos\left(\Phi_1^V-90\right),\dfrac{\Lambda_2^V}{\cos\left(\Phi_1^V-90-\Phi_2^V\right)}\sin\left(\Phi_1^V-90\right)\right) \\ O(x,y)=\left(\dfrac{\Lambda_1^V}{2\cos\left(\Phi_1^V\right)},0\right) \end{cases} \tag{1}$$

respectively

$$\begin{cases} A'(x',y')=(0,0) \\ B'(x',y')=\left(\dfrac{\Lambda_1^S}{\cos\left(\Phi_2^S-90-\Phi_1^S\right)}\cos\left(\Phi_2^S-90\right),\dfrac{\Lambda_1^S}{\cos\left(\Phi_2^S-90-\Phi_1^S\right)}\sin\left(\Phi_2^S-90\right)\right) \\ C'(x',y')=\left(\begin{array}{l}\dfrac{\Lambda_1^S}{\cos\left(\Phi_2^S-90-\Phi_1^S\right)}\cos\left(\Phi_2^S-90\right)+\dfrac{\Lambda_2^S}{\cos\left(\Phi_1^S-90-\Phi_2^S\right)}\cos\left(\Phi_1^S-90\right), \\ \dfrac{\Lambda_1^S}{\cos\left(\Phi_2^S-90-\Phi_1^S\right)}\sin\left(\Phi_2^S-90\right)+\dfrac{\Lambda_2^S}{\cos\left(\Phi_1^S-90-\Phi_2^S\right)}\sin\left(\Phi_1^S-90\right)\end{array}\right) \\ D'(x',y')=\left(\dfrac{\Lambda_2^S}{\cos\left(\Phi_1^S-90-\Phi_2^S\right)}\cos\left(\Phi_1^S-90\right),\dfrac{\Lambda_2^S}{\cos\left(\Phi_1^S-90-\Phi_2^S\right)}\sin\left(\Phi_1^S-90\right)\right) \\ O'(x',y')=\left(\begin{array}{l}\dfrac{\Lambda_1^S}{2\cos\left(\Phi_2^S-90-\Phi_1^S\right)}\cos\left(\Phi_2^S-90\right)+\dfrac{\Lambda_2^S}{2\cos\left(\Phi_1^S-90-\Phi_2^S\right)}\cos\left(\Phi_1^S-90\right), \\ \dfrac{\Lambda_1^S}{2\cos\left(\Phi_2^S-90-\Phi_1^S\right)}\sin\left(\Phi_2^S-90\right)+\dfrac{\Lambda_2^S}{2\cos\left(\Phi_1^S-90-\Phi_2^S\right)}\sin\left(\Phi_1^S-90\right)\end{array}\right) \end{cases} \tag{2}$$

Evaluation of the translation and rotation of the vertices then provides a measure for the local strain field. Assuming a linear approximation, the engineering strain field components are obtained

$$\begin{cases} \varepsilon_{xx} = \dfrac{\left\|\overrightarrow{A_xC_x}\right\| - \left\|\overrightarrow{A_x'C_x'}\right\|}{\left\|\overrightarrow{A_xC_x}\right\|} \\ \varepsilon_{yy} = \dfrac{\left\|\overrightarrow{B_yD_y}\right\| - \left\|\overrightarrow{B_y'D_y'}\right\|}{\left\|\overrightarrow{B_yD_y}\right\|} \\ \gamma_{xy} = \cos^{-1}\left(\dfrac{\overrightarrow{AO}\cdot\overrightarrow{OB}}{\left\|\overrightarrow{AO}\right\|\left\|\overrightarrow{OB}\right\|}\right) - \cos^{-1}\left(\dfrac{\overrightarrow{AO}\cdot\overrightarrow{OB}}{\left\|\overrightarrow{AO}\right\|\left\|\overrightarrow{OB}\right\|}\right) \end{cases} \tag{3}$$

By means of Equation (1)-(3), the three in-plane engineering strain components can be explicitly written as a function of the ultrasonically determined surface parameters. As the obtained strain components are determined in the coordinate system of the scanner with basis $\left(\overrightarrow{e_x},\overrightarrow{e_y}\right)$, a transformation is applied in order to obtain the engineering strain components in the material coordinate system $\left(\overrightarrow{e_{x^*}},\overrightarrow{e_{y^*}}\right)$:

$$\begin{bmatrix} \varepsilon_{xx}^{*} & \varepsilon_{xy}^{*} \\ \varepsilon_{xy}^{*} & \varepsilon_{yy}^{*} \end{bmatrix} = \overline{\overline{R}} \begin{bmatrix} \varepsilon_{xx} & \varepsilon_{xy} \\ \varepsilon_{xy} & \varepsilon_{yy} \end{bmatrix} \overline{\overline{R}}^{\mathrm{T}} \tag{4}$$

with $\overline{\overline{R}}^{(T)}$ the (transposed) rotation tensor defined as

$$\overline{\overline{R}}^{(T)} = \begin{bmatrix} e_{x^*}\cdot e_x & e_{x^*}\cdot e_y \\ e_{y^*}\cdot e_x & e_{y^*}\cdot e_y \end{bmatrix}^{(T)} \tag{5}$$

The principal directions are then easily found by setting $\varepsilon_{xy}^{*} = 0$, for which the following equation is obtained in case of plane strain:

$$\tan(2\alpha) = \frac{2\varepsilon_{xy}}{\varepsilon_{xx} - \varepsilon_{yy}} \tag{6}$$

Solving for α and substituting in Equation (4) then yields the principal in-plane strain components at the surface.

It is clear that the imposed strain field could transform the surface parameters such that the inequality $\lambda < \Lambda$ (Bragg condition) is not satisfied anymore. Therefore, the bounds for the operational frequency of the ultrasonic wave should be chosen more narrow. Considering a maximum strain of ε, the inequality becomes $\lambda < (1-\varepsilon)\Lambda$ and thus imposes no real limitation to the here described technique.

11. 3. 2. Out-of-plane Strain Field

As we investigate in-plane plastic strain fields up to 35%, it is clear that also the out-of-plane deformation will play an important role. However, with the above described procedure it is not possible to extract the out-of-plane normal strain component ε_{zz}. By insonifying the sample at normal incidence and simply evaluating changes in the difference of the time-of-flight (TOF) values between the ultrasonic echoes from top and bottom interface, one could get a measure for the thickness. Such a thickness measurement technique is already well adopted in industry, despite its lack of accuracy when small thickness variations have to be measured. More importantly, often thin sections have to be inspected (as in the present case), which causes overlapping of the top and bottom echo making the unambiguous determination of the TOF values difficult, if not impossible. For these reasons, we exploit the phenomenon of thickness resonances for the extraction of thickness information, and in extension the out-of-plane normal strain component. Figure 11-4a displays the dispersion curves *θ(fd)*, prescribing the conditions for efficient stimulation of Lamb waves under plane-wave insonification, for an immersed DC06 steel plate. The dispersion curves have been computed on the basis of a Legendre polynomial expansion [22], while the DC06 steel is modeled as a Kelvin-Voigt solid. The real valued elastic parameters were already given above, the imaginary valued attenuation parameters are taken a fraction 0.5% of the real valued elastic parameters.

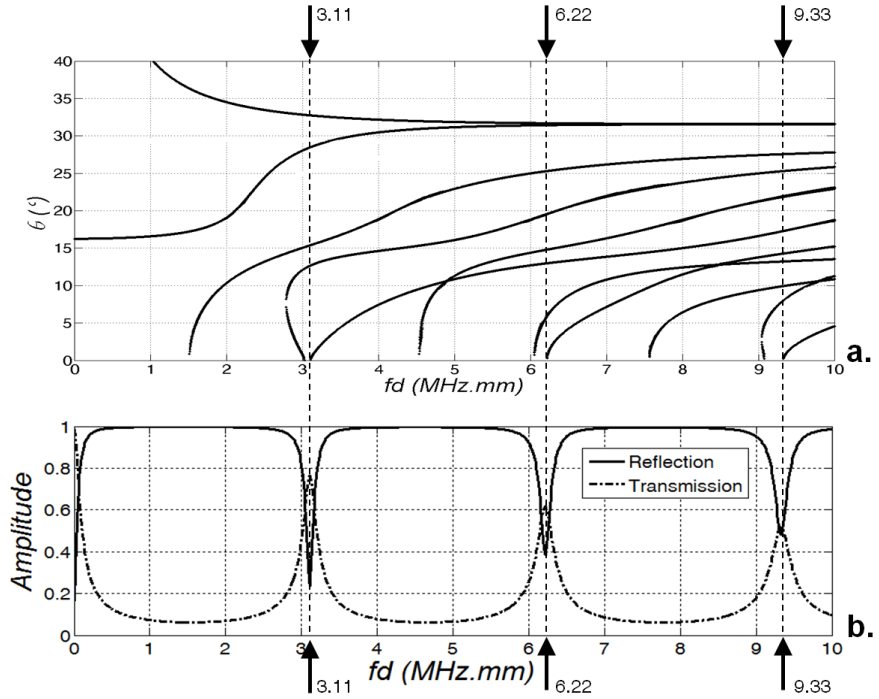

Figure 11-4: Dispersion curves *θ(fd)* (a) and reflection/transmission characteristics at $\theta = 0°$ (b) for water-immersed DC06 steel. The thickness resonances are indicated by the arrows.

At normal incidence, i.e. $\theta = 0°$, several frequency-thickness values *fd* (indicated with arrows in Figure 11-4) give rise to the stimulation of a thickness resonance, causing a dip in the reflection and a peak in the transmission characteristic (see Figure 11-4b). This resonance phenomenon can be roughly considered as the ultrasonic analogue of the well-known Fabry-Perot optical interferometer. Hence, by evaluating the spectral frequency response of a specularly reflected (or transmitted) broadband pulse at normal incidence, one can track down these dips (or peaks). Since neither the viscoelastic properties of the investigated sample, nor the frequency of the emitting transducer change upon straining, any positional shift of the dip (or peak) in *fd*-space is thus linearly related to a variation in thickness *d* and in extension to the normal out-of-plane engineering strain component ε_{zz}:

$$\varepsilon_{zz} = \frac{d^S - d^V}{d^V} \tag{7}$$

11. 4. Results and Discussion: Sample DC06-10 (30%)

As an example, we present and discuss the results obtained for the DC06-10 sample which has been subjected to a plastic strain field of more or less 30% in the longitudinal direction (Figure 11-5a).

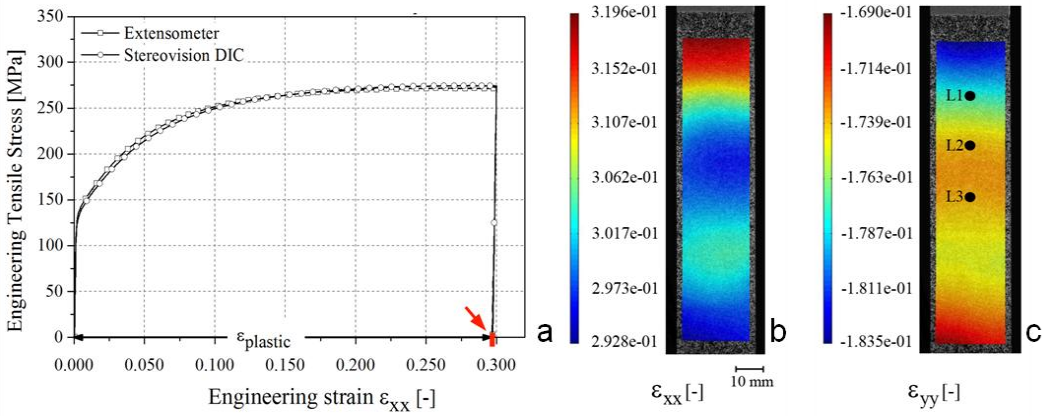

Figure 11-5: Tensile stress-strain response of sample DC06-010 (a), stereovision DIC extracted contours of the longitudinal (b) and transverse (c) strain component.

11. 4. 1. Manual Micrometer

The most rudimentary strain measurement comprises the use of a micrometer (MM). By measuring the width and thickness of both the virgin and the strained sample, the engineering strain in both *y*- and *z*-direction can be extracted. Because of obvious reasons, the measurement of the strain component in *x*-direction cannot be done. The MM measurements have been obtained at three different physical locations L_1, L_2 and L_3 (see Figure 11-5c) in order to track down lateral non-uniformity of the induced plastic strain field. To lower the error on the MM measurements, each time ten sets of measurements have been performed from which an average value and a measure for the standard deviation is obtained. The MM results for the three locations of DC06-10 are listed in Table 11-1. It can be observed that the obtained results suggest a small degree of non-uniformity for the strain field of the DC06-10 sample.

Table 11-1: Micrometer strain field measurements (average values ± standard deviation) for the three different locations on the sample DC06-10.

Location L_1			Location L_2			Location L_3		
ε_{xx} (%)	ε_{yy} (%)	ε_{zz} (%)	ε_{xx} (%)	ε_{yy} (%)	ε_{zz} (%)	ε_{xx} (%)	ε_{yy} (%)	ε_{zz} (%)
--	-17.022	-6.501	--	-16.575	-6.272	--	-16.711	-6.120
--	± 0.094	± 0.220	--	± 0.057	± 0.135	--	± 0.082	± 0.094

11. 4. 2. Mechanical Extensometer

Secondly, the strain during loading of the specimen was also measured with mechanical extensometers (ME), both in longitudinal and in transverse direction. Transverse strain measurements could only be captured at lower strain amplitudes, because the travel of the transverse extensometer is limited to ± 2.5 mm. The results of the ME measurements are added to Table 11-2. Note that the ME results have been obtained at one fixed location which differs from L_1, L_2 and L_3 in order to avoid overlap with the DIC speckle pattern (see Figure 11-2a). As such, comparison with results obtained at locations L_1, L_2 and L_3 should be done with caution considering the slight non-uniformity of the strain field. Furthermore, the ME signal in the transverse direction saturated for the DC06-10 sample, making the measurement in *y*-direction useless.

Table 11-2: Strain field measurement for sample DC06-10 by means of the EM. Note that only a single measurement has been obtained at a fixed and different location, while the signal in the *y*-direction saturated.

ε_{xx} (%)	ε_{yy} (%)	ε_{zz} (%)
29.672	-8.33 (saturated)	--

11. 4. 3. Optical Digital Image Correlation

To support previous results, we performed both mono- and stereovision digital image correlation (2D DIC and 3D DIC). For both methods a correlation subset window of 31 pixels was used, with a step size of 5 pixels. The reference subset is mapped to the deformed subset using an affine transformation function relating the coordinates of the undeformed image and the deformed image. Cross-correlation between reference and subsequent subsets is based on the zero-normalized sum of squared

differences (ZNSSD) criterion. This algorithm compensates for illumination differences by taking into account the offset and linear scale of light intensity, thus providing a robust noise-proof performance. Sub-pixel correlation is performed by using bicubic polynomial gray level interpolation. The surface strain field is computed using the sub-pixel measured displacement field. A strain window containing 25 x 25 discrete displacement data points is approximated using a bilinear polynomial. The Biot strain tensor is then computed using these estimated displacement terms. In the absence of material rotations, which may be assumed to be valid for the here presented results, the Biot tensor simply corresponds to the engineering strain [23].

The size of the subset window depends on the quality and granularity of the speckle pattern and characterizes the displacement spatial resolution. Strain spatial resolution can be controlled by the size of the strain window and the step size. Lowering the step size, and therefore overlapping adjacent subsets increases the strain spatial resolution. A larger strain window yields higher precision and accuracy, however this is less advantageous for describing heterogeneous deformations. Therefore, a compromise must be found between these different parameters. The correlation criteria and calculation parameters for the experimental DIC setups used in this study are listed in Table 11-3.

Table 11-3: Optical system and correlation parameters.

	Monovision 2D DIC	Stereovision 3D DIC
Noise Camera 0	0.68 %	0.73 %
Noise Camera 1	-	0.97 %
Pre-Filtering	Gaussian 5	Gaussian 5
Subset	31	31
Step	5	5
Correlation criterion	ZNSSD[a]	ZNSSD[a]
Shape function	Affine	Affine
Interpolation function	Bicubic polynomial	Bicubic Polynomial
Displacement		
Spatial resolution	31 pixels	31 pixels
In-plane resolution	0.00947 mm	0.00242mm
Out-of-plane resolution	-	0.01433 mm
Strain		
Strain window	25	25

Smoothing method	Polynomial Bilinear	Polynomial Bilinear
Virtual strain gauge	121 pixels	121 pixels
Spatial resolution	151 pixels	151 pixels
Resolution	153 µs	167 µs

[a] Zero-normalized sum of squared differences

A visualization of the longitudinal and transverse strain field (3D DIC) for the DC06-10 sample is displayed in Figure 11-5b-c. The results clearly reveal the non-uniformity of the strain field, which was already indicated by the MM extracted results. Both the 2D and 3D DIC extracted longitudinal and transverse strains are listed in Table 11-4 for the three aforementioned locations L_1, L_2 and L_3. Differences between mono- and stereovision data can be attributed to both out-of-plane displacements due to Poisson's contractions and to deviations from the ideal planarity [20]. Comparison of the DIC data with the MM and ME data yields good correspondence, indicating the consistency of the determined strain values.

Table 11-4: Strain field measurements for the three different spots of sample DC06-10 by means of digital image correlation: 2D DIC = monovision, 3D DIC = stereovision.

	Location L_1			Location L_2			Location L_3		
	ε_{xx} (%)	ε_{yy} (%)	ε_{zz} (%)	ε_{xx} (%)	ε_{yy} (%)	ε_{zz} (%)	ε_{xx} (%)	ε_{yy} (%)	ε_{zz} (%)
2D DIC	31.125	-17.491	--	29.981	-17.274	--	29.595	-17.101	--
3D DIC	31.538	-17.523	--	29.740	-17.212	--	29.352	-17.012	--

11. 4. 4. Ultrasonic Strain Gauge

Finally, the results obtained with the proposed ultrasonic strain gauge are discussed. Instead of externally applying a specific surface corrugation to the DC06 steel, which would obviously weaken the steel sheet, we simply exploit the deterministic surface roughness (see Figure 11-1) left by the work rolls during manufacturing. This surface roughness is an imperfect but periodic structure which can be conceived as two overlapping 1D gratings (see Figure 11-1). The H-UBPS of a virgin DC06 sample is shown in Figure 11-6.

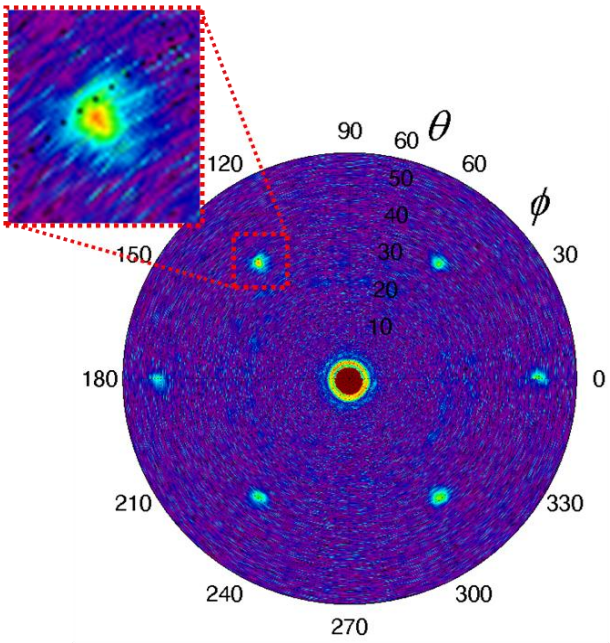

Figure 11-6: H-UBPS recording at f = 5 MHz for cold-rolled DC06 steel in virgin state.

Despite the low surface finishing quality, the presence of many defects in the surface periodicities as well as the limited corrugation depth, distinct diffraction peaks can be observed. In analogy with the previous chapter, the experimental recording has been convolved by a Gaussian kernel to improve the accuracy and reproducibility of the spike extraction procedure. The surface parameters, extracted from the H-UBPS experiments of 7 different virgin DC06 samples, are listed in Table 11-5. It can be verified that the H-UBPS extracted parameters are within the range of the optically determined values (see also Figure 11-1b).

Table 11-5: Obtained results for the surface texture of cold-rolled DC06 steel sheet: CCI corresponds to the optically measured parameters (see Figure 11-1b), H-UBPS are the ultrasonically (at f = 5 MHz) determined parameters.

	Λ_1^V [µm]	Φ_1^V [°]	Λ_2^V [µm]	Φ_2^V [°]	Λ_{1+2}^V [µm]	Φ_{1+2}^V [°]
CCI	243 ±20.2	53 -	243 ±23.6	125 -	191 ±16	0 -
H-UBPS	233.9033 ± 0.8533	53.0167 ± 0.0816	233.8183 ± 0.7765	127.9250 ± 0.1369	193.7360 ± 1.4119	0.96 ± 0.1782

More important, the robustness of both the H-UBPS methodology and the subsequent extraction procedure is well reflected in the small standard deviation. It is noted that the spatially bounded nature of the employed ultrasonic beam insonifies a local circular area with radius ~4 mm, and as such images a set of ~900 surface unit cells. This immediately explains the insensitivity of the H-UBPS methodology to random defects in the surface structure. As a matter of fact, some samples were slightly corroded when measured. Since every sheet of steel manufactured with the same set of work rolls has an identical surface texture, the extracted surface parameters listed in Table 11-5 are used as the reference parameters for the deterministic surface structure of the here considered cold-rolled DC06 steel.

The H-UBPS image of the strained DC06-10 sample (location L_1) is shown in Figure 11-7a. One can clearly discern the positional shift of the diffraction peaks with respect to the H-UBPS results for the virgin sample (Figure 11-6). This is explicitly demonstrated in Figure 11-7b, which shows the extracted diffraction spots for both the virgin and the strained DC06-10 sample. Evaluation of the coordinate transformation of the diffraction peaks $\left(\varphi^V,\theta^V\right)\rightarrow\left(\varphi^S,\theta^S\right)$ according to the analysis presented in Section 11.3.1, then yields the local in-plane strain field components.

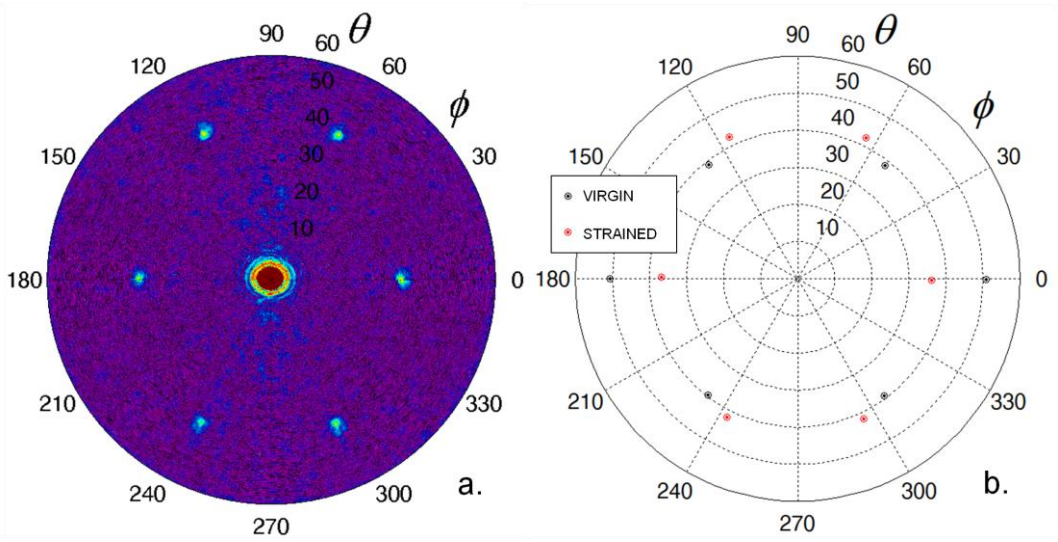

Figure 11-7: H-UBPS recording at *f* = 5 MHz for the strained DC06-10 sample (a) and extracted diffraction peaks for the virgin DC06 sample (black) and the strained (red) DC06-10 sample (b).

Four H-UBPS experiments have been performed to each of the three locations L_1, L_2 and L_3 from which the average value and the standard deviation is obtained. The results are tabulated in Table 11-6. Good agreement is obtained with the in-plane normal strain field components obtained with the other techniques. The low standard deviation further indicates the reproducibility of the H-UBPS results for measuring in-plane strain components by exploiting changes in the residual surface roughness.

Table 11-6: Strain field measurements (average values ± standard deviation) for the three different spots of sample DC06-10 obtained by means of the developed ultrasonic strain gauge.

Location L_1			Location L_2			Location L_3		
ε_{xx} (%)	ε_{yy} (%)	ε_{zz} (%)	ε_{xx} (%)	ε_{yy} (%)	ε_{zz} (%)	ε_{xx} (%)	ε_{yy} (%)	ε_{zz} (%)
32.350 ± 0.160	-17.808 ± 0.136	-6.609 ± 0.274	30.320 ± 0.131	-16.800 ± 0.183	-6.221 ± 0.112	30.443 ± 0.137	-17.158 ± 0.234	-6.338 ± 0.194

The determination of the out-of-plane strain field is done according to the scheme given in Section 11.3.2. An ultrasonic pulse is emitted to the zone of interest at normal incidence (identifiable in the H-UBPS image), after which the reflected signal is recorded in a time window of 50 μs at 10-bit resolution (time grid of 1024 points). Similar as in Section 10.3, the data has been first windowed by means of a Tukey window, after which zero padding is applied. The fast Fourier transform is then applied to the zero-padded data. It was found that the true thickness resonance occurred at fd = 3.19 MHz.mm, which is in close agreement with the numerically computed thickness resonance (fd = 3.11 MHz.mm), thus indicating the precision of the considered material parameters. Note that the presence of a surface corrugation induces additional phenomena for normal incident waves [24-27], though it is found that these effects do not interfere with the envisioned phenomenon, probably because of the very limited depth (~1.1 μm) of the here considered surface structure. The dip in reflected amplitude has been tracked as a function of frequency. Ten measurements have been performed at the different spots from which an average value and a standard deviation is obtained. The results are added to Table 11-6. Unfortunately, neither the ME, nor the DIC technique can measure the out-of plane strain field component. Therefore, only comparison with the MM measurements can be done, yielding good agreement.

11. 4. 5. Overview of Results

The obtained strain field measurements for sample DC06-10 have been collected and listed in Table 11-7 in order to have a clear overview. It can be observed that the ultrasonically determined strain field values show good agreement with the partial data sets obtained by the conventional strain measurement techniques.

Table 11-7: Strain field measurements (average values ± standard deviation) for the three different locations of sample DC06-10. MM = micrometer, EM = extensometer, 2D/3D DIC = mono-/stereovision digital image correlation and USG = ultrasonic strain gauge. The EM row is put in gray because only 1 measurement was obtained at a fixed and different location, while the signal in the *y*-direction saturated.

	Location L_1			Location L_2			Location L_3		
	ε_{xx} (%)	ε_{yy} (%)	ε_{zz} (%)	ε_{xx} (%)	ε_{yy} (%)	ε_{zz} (%)	ε_{xx} (%)	ε_{yy} (%)	ε_{zz} (%)
MM	-- --	-17.022 ± 0.094	-6.501 ± 0.220	-- --	-16.575 ± 0.057	-6.272 ± 0.135	-- --	-16.711 ± 0.082	-6.120 ± 0.094
ME	29.672 --	-8.33 saturated	-- --	29.672 --	-8.33 saturated	-- --	29.672 --	-8.33 saturated	-- --
2D DIC	31.125 --	-17.491 --	-- --	29.981 --	-17.274 --	-- --	29.595 --	-17.101 --	-- --
3D DIC	31.538 --	-17.523 --	-- --	29.740 --	-17.212 --	-- --	29.352 --	-17.012 --	-- --
USG	32.350 ± 0.160	-17.808 ± 0.136	-6.609 ± 0.274	30.320 ± 0.131	-16.800 ± 0.183	-6.221 ± 0.112	30.443 ± 0.137	-17.158 ± 0.234	-6.338 ± 0.194

11. 5. Generalization to other Strain Levels

Several other plastically strained DC06 samples (all loaded transverse to the rolling direction) have been processed and analyzed in a similar way as done for the DC06-10 sample. For brevity, we only graphically display the strain values extracted by the different measurement techniques (see Figure 11-8a-c). It has been found that several strain values were corrupted/missing because of (i) the insensitivity of a method for a certain strain field component, (ii) the limited range for strain amplitude in case of the transverse ME and (iii) occasional debonding of the speckle pattern for the mono- and stereovision DIC. For clarity, these corrupted/missing values are set at fictitious values of -1% for the longitudinal strain component, and at +1% for the transverse and the thickness strain component. In fact, the USG

is the only method which successfully determined both the in-plane and the out-of-plane strain components for all the tested samples without any difficulty encountered. It can be verified in Figure 11-8a-c that the USG extracted strain values show good correspondence with the other sets of partial strain data, and this over the full range of considered plastic strains.

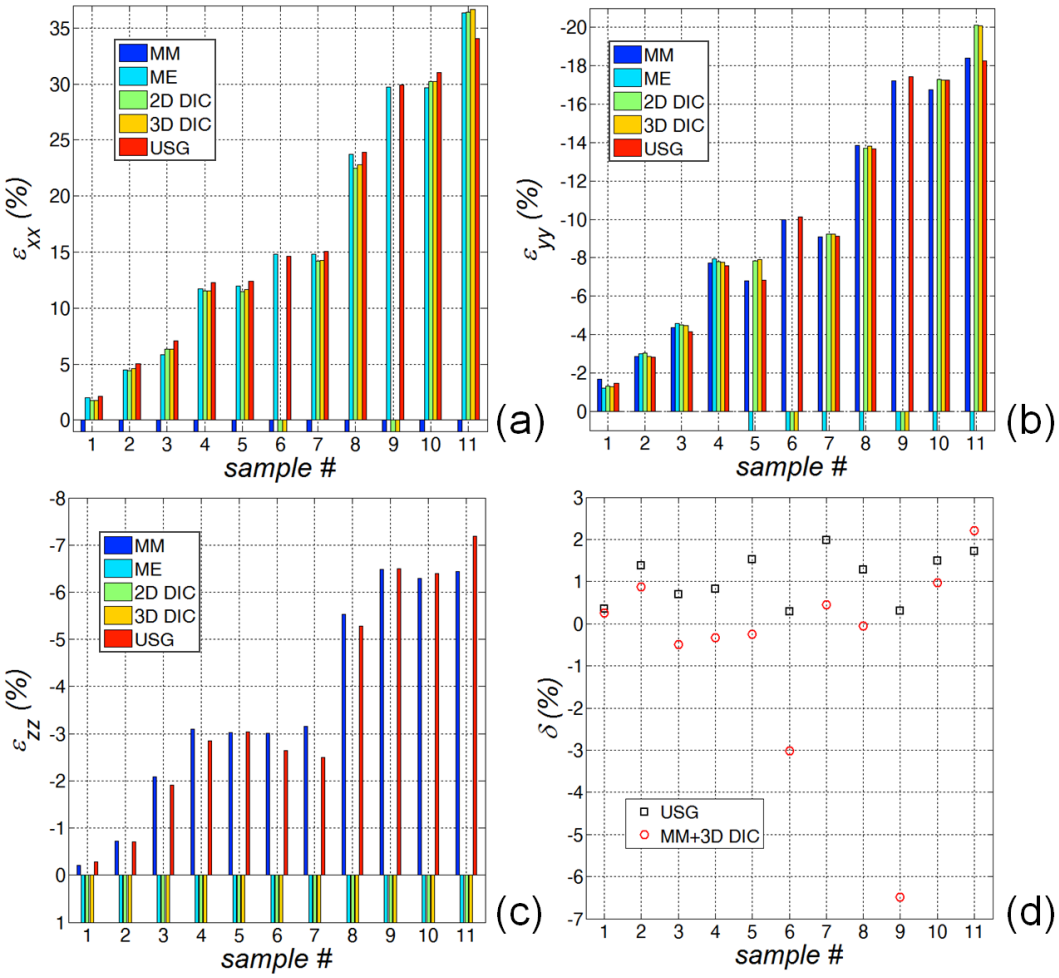

Figure 11-8: Extracted strain values: longitudinal (a), transverse (b) and thickness (c) component. Error δ on the incompressibility hypothesis (d).

The incompressibility hypothesis, which states that volume remains constant upon plastically straining a sample, provides another check for the accuracy and validity of the extracted strain field components. This is graphically presented for the USG data set in Figure 11-8d (black squares). It can be readily verified that the error δ (in %) on the incompressibility hypothesis is

within narrow bounds. Unfortunately, this hypothesis cannot be checked for the strain values obtained by the other strain gauge techniques as none of them provide the three needed normal strain field components ε_{xx}, ε_{yy} and ε_{zz}. However, if one would consider the combination of the 3D DIC in-plane components ε_{xx} and ε_{yy} and the MM out-of-plane component ε_{zz}, a hybrid measure of the incompressibility hypothesis (see red circles in Figure 11-8d) is obtained. Except for the two outliers (corrupted DIC data), it can be observed that the error δ has the same order of magnitude as was found for the USG data set.

11. 6. Lankford Coefficient

Knowledge of the three normal plastic strain components further allows the determination of the Lankford coefficient R_{ij} which is a measure of strain-anisotropy in the plastic regime. For a uniaxial test on a rectangular sheet specimen the Lankford coefficient R_{ij} is defined by [28]

$$R_{ij} = -\frac{\varepsilon_{jj}^{PL}}{\varepsilon_{ii}^{PL}} \tag{8}$$

with ε_{ii}^{PL} and ε_{jj}^{PL} the plastic strain in the width, respectively the thickness direction of the sample.

As tensile tests have been performed at various strain levels, the Lankford coefficient can be evaluated as a function of applied longitudinal strain. In order to backup the USG extracted Lankford coefficients, we have also determined the Lankford ratios on the basis of the MM measurements. Strictly speaking, the latter is impossible as the MM does not provide a measure for the longitudinal strain component. However, as there is no alternative we set the longitudinal strain component equal to the USG extracted value. The obtained results are graphically displayed in Figure 11-9. Except for the Lankford parameter at $\varepsilon_{xx} \approx 2\%$ (division of small numbers), good agreement is obtained between both sets of data. The results indicate a dependency of the Lankford parameter on the applied longitudinal strain level, similar observations have recently been done in literature [28]. However, contrary to literature we extracted the Lankford ratios by direct ultrasonic measurement of all the required normal strain field components without further assumptions or restrictions.

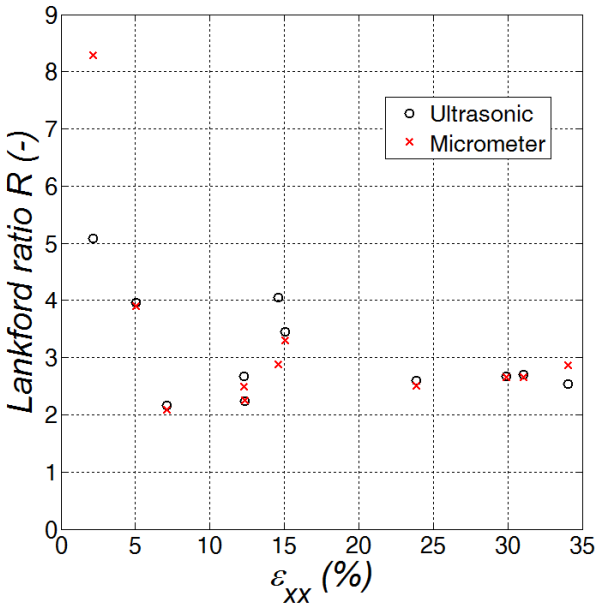

Figure 11-9: Lankford ratio transverse to the rolling direction as a function of applied longitudinal strain ε_{xx}: USG (black +) and MM (red x).

According to [28], a Lankford ratio of $R \sim 2.5$ (loading transverse to the rolling direction) should be obtained at large longitudinal strain levels, which agrees well with the presented data in Figure 11-9. Due to the rolling process, the plastic anisotropy is dependent on the in-plane orientation. Therefore other Lankford ratios will be obtained for DC06 specimens cut at a different direction [28]. As such a yield surface can be constructed in order to capture the anisotropic plastic behavior of steel sheet. Though, the latter is beyond the scope of this thesis.

11. 7. Conclusions

A novel ultrasonic strain gauge method has been introduced for the local measurement of a 3D strain field. The in-plane strain field is measured by exploiting the interaction of oblique incident ultrasonic waves with a deterministic surface roughness, while the out-of-plane component is extracted by tracing changes in the stimulation condition of a thickness resonance. The method has been applied to cold-rolled DC06 steel samples for which skin passing of the work rolls was applied during rolling. Several DC06 samples have been loaded by means of a tensile machine to induce various plastic strain fields ranging from ~2% up to ~35%. The ultrasonic

strain measurements have been validated with several conventional strain gauge techniques: good correspondence with the other sets of (partial) strain data is obtained, and this for all considered strain levels. In addition, the capability of the ultrasonic strain gauge has been demonstrated by extracting the Lankford ratios transverse to the rolling direction for the DC06 steel as a function of applied longitudinal strain.

The here presented ultrasonic strain gauge locally measures all normal strain field components in an absolute way using a single-sided non-contact approach without the need of sample preparation, and for which alignment is of minor concern. As such, it has great appeal for industrial applications, especially when the occasional assessment of a strain field over long periods is required because the method provides an absolute strain measure at every moment in time, when a measurement is performed.

11. 8. References

[1] Kreemer, C., W.E. Holt, and A.J. Haines, *An integrated global model of present-day plate motions and plate boundary deformation.* Geophysical Journal International, 2003. 154(1): p. 8-34.

[2] Ostby, E., K.R. Jayadevan, and C. Thaulow, *Fracture response of pipelines subject to large plastic deformation under bending.* International Journal of Pressure Vessels and Piping, 2005. 82(3): p. 201-215.

[3] Jayadevan, K.R., E. Ostby, and C. Thaulow, *Fracture response of pipelines subjected to large plastic deformation under tension.* International Journal of Pressure Vessels and Piping, 2004. 81(9): p. 771-783.

[4] Mohr, W., *Strain-Based design of Pipelines.* Report Project No. 45892GTH, U.S. Department of Interior, Minerals Management Service and U.S. Department of Transportation Research and Special Programs Administration, 2003.

[5] Arshak, A., K. Arshak, D. Morris, O. Korostynska, and E. Jafer, *Investigation of TiO2 thick film capacitors for use as strain gauge sensors.* Sensors and Actuators a-Physical, 2005. 122(2): p. 242-249.

[6] Herrmann, J., K.H. Muller, T. Reda, G.R. Baxter, B. Raguse, G. de Groot, R. Chai, M. Roberts, and L. Wieczorek, *Nanoparticle films as sensitive strain gauges.* Applied Physics Letters, 2007. 91(18).

[7] Betz, D.C., G. Thursby, B. Culshaw, and W.J. Staszewski, *Advanced layout of a fiber Bragg grating strain gauge rosette.* Journal of Lightwave Technology, 2006. 24(2): p. 1019-1026.

[8] Viotti, M.R., A.G. Albertazzi, and W. Kapp, *Experimental comparison between a portable DSPI device with diffractive optical element and a hole drilling strain gage combined system.* Optics and Lasers in Engineering, 2008. 46(11): p. 835-841.

[9] Zhao, B., H.M. Xie, and A. Asundi, *Optical strain sensor using median density grating foil: Rivaling the electric strain gauge.* Review of Scientific Instruments, 2001. 72(2): p. 1554-1558.

[10] Cofaru, C., W. Philips, and W. Van Paepegem, *A three-frame digital image correlation (DIC) method for the measurement of small displacements and strains.* Measurement Science & Technology, 2012. 23(10).

[11] Pinto, J.M.T., F. Touchard, S. Castagnet, C. Nadot-Martin, and D. Mellier, *DIC Strain Measurements at the Micro-Scale in a Semi-Crystalline Polymer.* Experimental Mechanics, 2013. 53(8): p. 1311-1321.

[12] Bragg, W.L., *The diffraction of short electromagnetic waves by a crystal.* Proc. Cambridge Phil. Soc., 1913. 17: p. 43-57.

[13] Kersemans, M., W. Van Paepegem, K. Van Den Abeele, L. Pyl, F. Zastavnik, H. Sol, and J. Degrieck, *Ultrasonic Characterization of Subsurface 2D Corrugation.* Journal of Nondestructive Evaluation, 2014. In Press DOI: 10.1007/s10921-014-0239-7.

[14] ArcelorMittal(SouthAfrica), *Data sheet: B3.1 Cold Rolled Steel Sheet for Drawing and Forming EN 10130 DC01-DC06*. 2010.

[15] Scheers, J., C. De Mare, Iron, and S.O.C. Steel, *The use of 'fine-deterministic' steel sheet textures to improve the drawability and paint quality of high strength body panels*, in *40th Mechanical Working and Steel Processing Conference Proceedings, Vol Xxxvi*. 1998. p. 93-99.

[16] Lee-Bennett, I. *Advances in non-contacting surface metrology*. in *Frontiers in Optics 2004/Laser Science XXII/Diffractive Optics and Micro-Optics/Optical Fabrication and Testing*. 2004. Rochester, New York: Optical Society of America.

[17] ASTM, *E8/E8M-08. Standard Test Methods for Tension Testing of Metallic Materials.*

[18] Sutton, M.A., J.-J. Orteu, and H.W. Schreier, *Image correlation for shape, motion and deformation measurements*. 2009, New York: Springer.

[19] MatchID_software. <http://www.macthid.org/>.

[20] Sutton, M.A., J.H. Yan, V. Tiwari, H.W. Schreier, and J.J. Orteu, *The effect of out-of-plane motion on 2D and 3D digital image correlation measurements.* Optics and Lasers in Engineering, 2008. 46(10): p. 746-757.

[21] Kersemans, M., W. Van Paepegem, K. Van Den Abeele, L. Pyl, F. Zastavnik, H. Sol, and J. Degrieck, *Pitfalls in the Experimental Recording of Ultrasonic (Backscatter) Polar Scans for Material Characterization.* Ultrasonics, 2014. In Press DOI: 10.1016/j.ultras.2014.04.013.

[22] Matar, O.B., N. Gasmi, H. Zhou, M. Goueygou, and A. Talbi, *Legendre and Laguerre polynomial approach for modeling of wave propagation in layered magneto-electro-elastic media.* Journal of the Acoustical Society of America, 2013. 133(3): p. 1415-1424.

[23] Bazant, Z.P.A., M.D. and Y. Xiang, *Finite Strain Analysis of Deformations of Quasibrittle Material during Missile Impact and Penetration*, in *Advances in Failure Mechanics in Brittle Materials*, R.J. Clifton and H.D. Espinosa, Editors. 1996, The American Society of Mechanical Engineers: Atlanta, Georgia.

[24] Mampaert, K., P.B. Nagy, O. Leroy, L. Adler, A. Jungman, and G. Quentin, *ON THE ORIGIN OF THE ANOMALIES IN THE REFLECTED*

ULTRASONIC SPECTRA FROM PERIODIC SURFACES. Journal of the Acoustical Society of America, 1989. 86(1): p. 429-431.

[25] Claeys, J.M., O. Leroy, A. Jungman, and L. Adler, *DIFFRACTION OF ULTRASONIC-WAVES FROM PERIODICALLY ROUGH LIQUID SOLID-SURFACE.* Journal of Applied Physics, 1983. 54(10): p. 5657-5662.

[26] Roberts, R., J.D. Achenbach, R. Ko, L. Adler, A. Jungman, and G. Quentin, *REFLECTION OF A BEAM OF ELASTIC-WAVES BY A PERIODIC SURFACE PROFILE.* Wave Motion, 1985. 7(1): p. 67-77.

[27] Jungman, A., L. Adler, and G. Quentin, *ULTRASONIC ANOMALIES IN THE SPECTRUM OF ACOUSTIC-WAVES DIFFRACTED BY PERIODIC INTERFACES.* Journal of Applied Physics, 1982. 53(7): p. 4673-4680.

[28] Safaei, M., *Constitutive modelling of anisotropic sheet metals based on a non-associated flow rule.* Ghent University, Faculty of engineering sciences and architecture (Ghent), PhD thesis, 2013: p. 246.

PART III

This part combines the developed methodologies in Part I and Part II to inspect and characterize various damage features in fiber reinforced plastics.

Chapter 12

Characterization of Delaminations in Thin Composites with the Ultrasonic Polar Scan

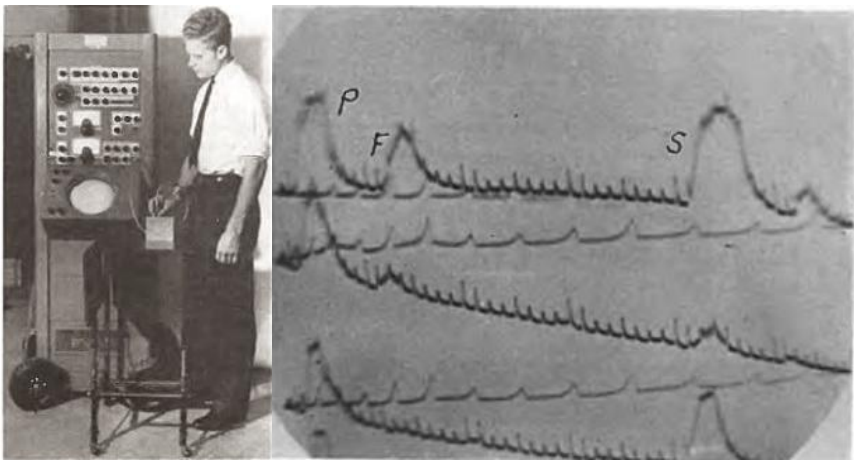

Floyd Firestone with the original Supersonic Reflectoscope Type A in 1945 (left), introducing the concept of a C-scan for flaw detection in materials (right). (Figures taken from reference [1]).

Summary

Delamination is one of the most important and critical failure mechanisms for composite structures. Therefore, it is investigated both numerically and experimentally by means of the UPS method. Since the UPS method puts on view guided wave stimulation conditions, rather than recording discrete interface echoes, it has great appeal for the inspection of thin plate-like materials having a thickness comparable to the ultrasonic wave length. The obtained results reveal that the H-UPS method cannot only detect, but also exposes the depth location of a delamination in the laminate. The potential of the H-UPS technique has been further demonstrated for the situation of multiple overlapping delaminations. The obtained H-UPS results suggest that a mixed numerical-experimental inversion technique could lead to a system identification procedure for delamination characteristics.

Contrary to the H-UPS, it is demonstrated that the P-UPS methodology shows limited sensitivity to the presence of a delamination.

12. 1. Introduction

Up to now, the UPS analysis has been limited to the inspection and characterization of virgin fiber reinforced laminates. Considering that in-service components are subjected to a variety of loading conditions, which include tensile, shear, fatigue and impact, a lot of composite structures have degraded mechanical properties. This chapter focuses on one of the most common and critical failure mechanisms for fiber reinforced plastics, namely the presence of a delamination. Basically, two adjacent laminae physically delaminate from each other, obviously leading to a different mechanical setting. While the delaminated interface can pass on pressure, both its tensile and its shear characteristics significantly reduce. As such, the mechanical integrity of the structural component is affected, which eventually could lead to failure of the component.

Several research teams have already proposed various methods for detecting a delamination, in which ultrasonics is the most popular approach. Examples include the classical C-scan [2-4], normal incident ultrasound transmission [5], nonlinear elastic wave spectroscopy (NEWS) [6-11], guided wave inspection [12-16], tomography [17-18], as well as others. However, till now, only the ultrasonic C-scan has found a widespread implementation in industry, most likely because of its simplicity of the analysis (amplitude measurement). In spite of this, a recognized disadvantage of C-scan reflection techniques is its inability to inspect samples with a small thickness-to-wave-length ratio in a reliable way. Indeed, the method suffers from overlapping echoes coming from (i) the top side, (ii) the interfaces of the potential damage and (iii) the bottom side, even though considerable progress has been made in recent years for inspecting thin sections [19-21]. Given the plate-like aspect of many structural composite components, combined with the frequent occurrence of delaminations, more suitable and more advanced non-destructive testing techniques are needed.

One such a technique could be the UPS methodology as it combines multiple advantages of the above listed techniques. It is a simple amplitude measurement which does not rely on the recording of discrete interface echoes, but rather put on view guided wave stimulation conditions.

Since a delamination basically divides a laminate in different sub-laminates, each having a thickness which is dependent on the depth position of the delamination, a guided wave is subject to different boundary conditions, resulting in different stimulation conditions. This is demonstrated for an immersed aluminum sample (see Figure 12-1). By doubling the frequency-thickness parameter fd from 1.5 MHz.mm to 3 MHz.mm, the stimulation conditions (incident angle θ) shift while the number of potential Lamb wave excitation increases from two to five (see the circles in Figure 12-1). These features are well reflected in the characteristic amplitude contours of the corresponding H-UPS simulations at the different frequency-thicknesses (see Figure 12-2).

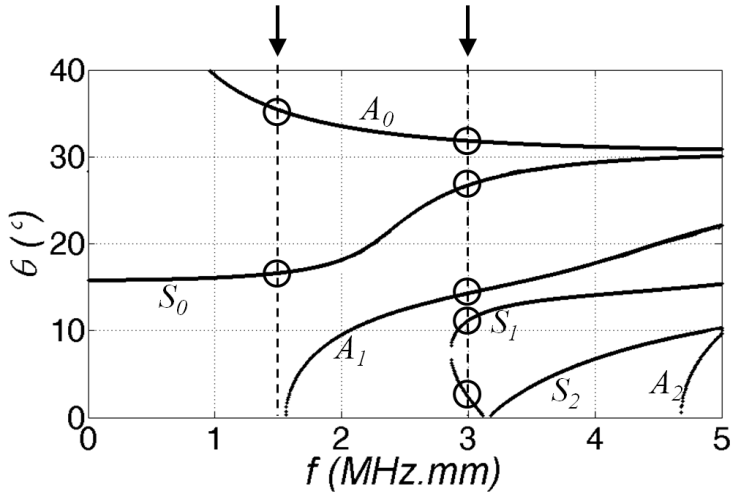

Figure 12-1: Computed dispersion curves *θ(fd)* for an immersed aluminum plate. A_j and S_j stand for the j^{th} anti-symmetrical, respectively j^{th} symmetrical Lamb mode.

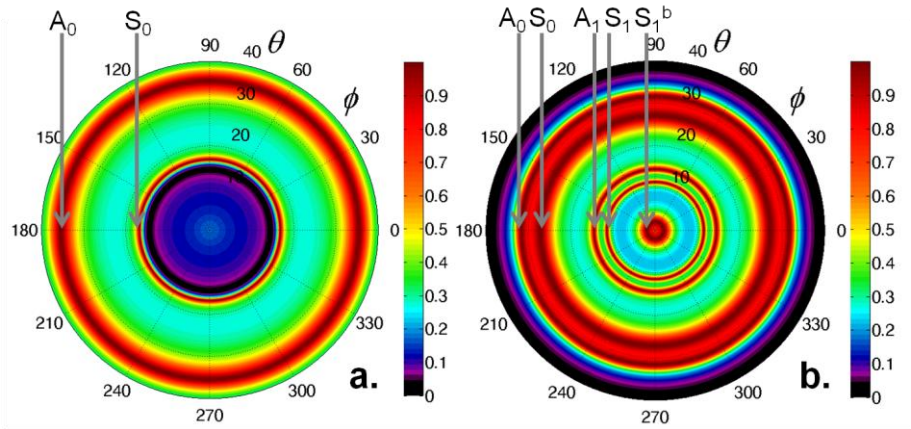

Figure 12-2: Numerically computed amplitude-based H-UPS in transmission for aluminum: *fd* = 1.5 MHz.mm (a) and *fd* = 3 MHz.mm (b). The different Lamb mode stimulations have been explicitly indicated.

12. 2. Hybrid Compliance-Stiffness Matrix Method

The hybrid compliance-stiffness matrix method [22-23] has been implemented in MATLAB, in order to perform simulations of the ultrasonic polar scan setup and analysis procedure, i.e. oblique insonification at all possible incidence angles $\psi(\varphi,\theta)$. The hybrid matrix method is closely related to both the transfer matrix method and the stiffness matrix method

(see Chapter 4) for calculating wave propagation in multi-layered anisotropic viscoelastic media. It is well-known that the transfer matrix method is ill-conditioned for large layer thicknesses (or equivalently high frequencies), while the recursive stiffness matrix approach is unstable for small layer thicknesses (or equivalently small frequencies). The hybrid compliance-stiffness matrix method patches both setbacks by clever reformulation of the governing equations, anticipating the different numerical instabilities. As such, the hybrid matrix formulation comprises an unconditionally stable method for the analysis of wave propagation in multi-layered anisotropic viscoelastic media, while preserving the convenience for incorporating imperfect interfaces (like a thin delamination layer). In addition, the hybrid matrix method is found to be computationally more efficient compared to both the transfer matrix method and stiffness matrix method [23]. This advantage can be quite significant for both the H-UPS simulation and P-UPS simulation as they correspond to 1 million, respectively 400 million computational operations. More details about the hybrid compliance-stiffness matrix method can be found in references [22-23].As an example, Figure 12-3 displays the numerical results for the amplitude and phase of the transmission and reflection coefficient as a function of delamination thickness d for a cross-ply carbon/epoxy laminate with thickness D = 1.1 mm, insonified under an arbitrarily chosen oblique incidence angle $\psi(\varphi,\theta)$ = ψ(7°,20°) at a harmonic frequency of f = 3 MHz.

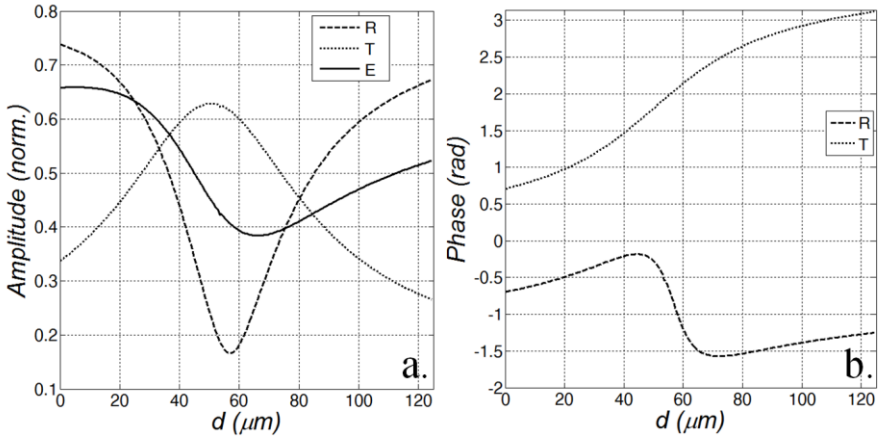

Figure 12-3: Reflection (*R*) and transmission (*T*) characteristics as a function of delamination thickness *d*, for a cross-ply carbon/epoxy laminate insonified under the oblique incidence angle *ψ(φ,θ) = ψ(7°,20°)* at a frequency *f* = 3 MHz: amplitude (normalized to input) (a) and phase (b).

The delamination has been modeled by means of a water layer, in order to represent a realistic fluid-filled edge delamination. The complex material properties of the carbon/epoxy laminate, used in the numerical computation, have been obtained by inversion of P-UPS data [24-26] (see Chapter 7).

Figure 12-3 clearly shows that both the reflection and the transmission characteristics are modified by the presence of a delamination, as they become a non-constant function of the thickness *d* of the delamination. It can be observed that for a certain range of delamination thicknesses *d*, the transmission amplitudes are higher than without a delamination, at least for the here considered incidence angle $\psi(\varphi,\theta)$. The solid line in Figure 12-3a represents the summed energy *E* of the transmitted and reflected signal. Note that for a lossless medium, i.e. a real-valued elasticity tensor, *E* equals 1. Figure 12-3 demonstrates that, even for a small thickness value of the delamination, there is a notable change of the reflection and transmission characteristics. This opens perspectives to use the H-UPS as a robust technique for inverse thickness characterization of delaminations.

To concretize, Figure 12-4 displays the results when subtracting the transmitted amplitude of two H-UPS images from each other, considering different thicknesses of delamination in the carbon/epoxy laminate. The obtained "difference H-UPS plots" clearly show characteristics which put on view delamination characteristics.

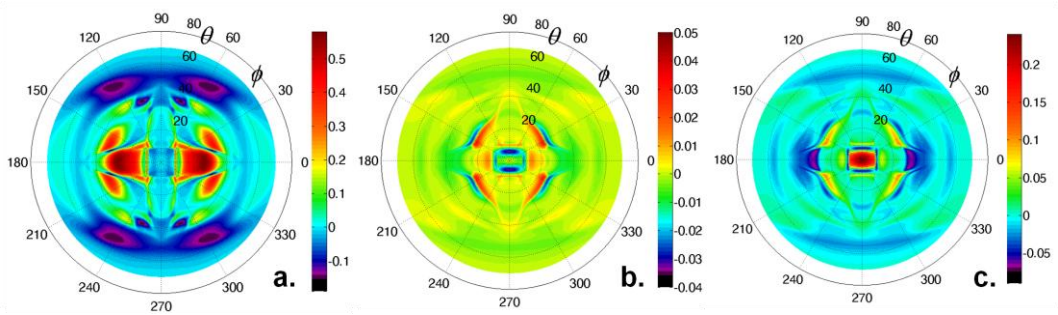

Figure 12-4: H-UPS subtraction in transmission for cross-ply carbon/epoxy laminates: [0,90,90,0] - [0,90,U_1,90,0] with d_{U1} = 1 µm (a), [0,90,U_1,90,0] - [0,90,U_2,90,0] with d_{U1} = 1 µm and d_{U2} = 5 µm (b) and [0,90,U_1,90,0] - [0,90,U_2,90,0] with d_{U1} = 5 µm and d_{U2} = 25 µm (c).

12. 3. Materials

Several sets of carbon fiber reinforced plastics have been autoclave manufactured by stacking multiple prepreg layers in a specific orientation, in which each lamina has a thickness of ~0.28 mm. Both unidirectional $[0]_4$ and cross-ply $[0,90]_s$ composites have been manufactured, having a total thickness of ~ 1.1 mm. To mimic a representative edge delamination, strips of Upilex foil with a thickness of 50 µm have been inserted. After the manufacturing cycle, the foil has been carefully removed by pulling it out from the edge (see schematic in Figure 12-5). The use of Upilex foil is mainly motivated by (i) its wide availability in different sizes, (ii) its high consistency in thickness profile, (iii) its excellent resistance against thermal exposure and (iv) its easy removability after applying the autoclave manufacturing cycle.

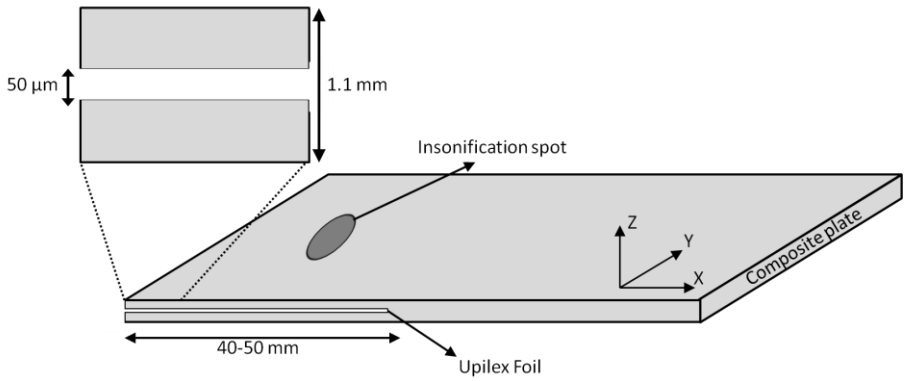

Figure 12-5: Schematic of manufactured composites provided with an artificial edge delamination.

The following set of samples have been manufactured (U represents the location of the removed Upilex insert):

- Unidirectional $[0]_4$ carbon/epoxy (C/E) laminate
  - [0,0,0,0]
  - [0,0,U,0,0]
- Cross-ply $[0,90]_s$ carbon/epoxy (C/E) laminate
  - [0,90,90,0]
  - [0,U,90,90,0]
  - [0,90,U,90,0]

- [0,90,90,U,0]
- [0,U,90,U,90,0]
- [0,U,90,90,U,0]

As the stacking procedure has been manually performed, small deviations in the envisioned stacking sequence could occur. Nevertheless, as will be shown, these small errors have only minor influence on the here investigated phenomena.

12. 4. H-UPS Results and Discussion

12. 4. 1. Delaminated Unidirectional Carbon/Epoxy Laminate

Figure 12-6 displays the H-UPS results for the intact unidirectional C/E laminate at multiple frequencies, ranging from f = 3 MHz to f = 6 MHz. The left and right column represent the numerical computation using the basic layer parameters for the elasticity tensor, and the experimental recording respectively.

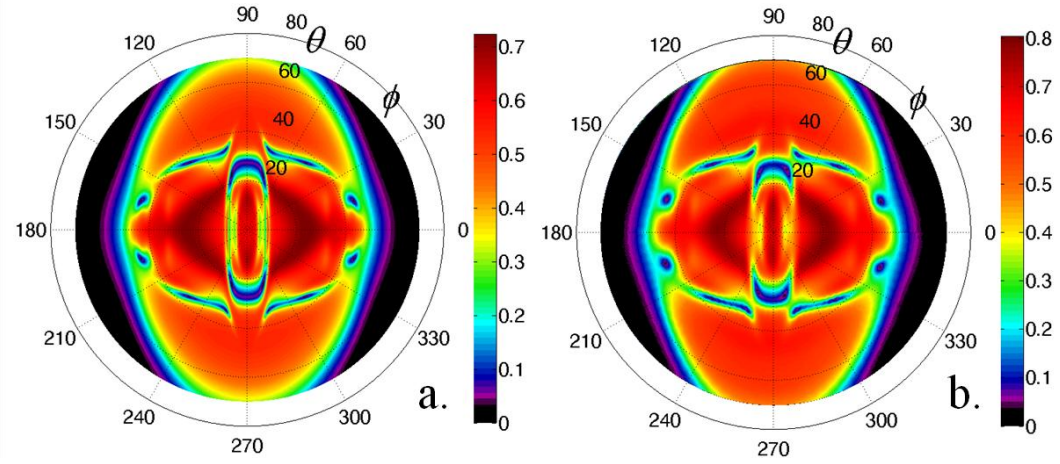

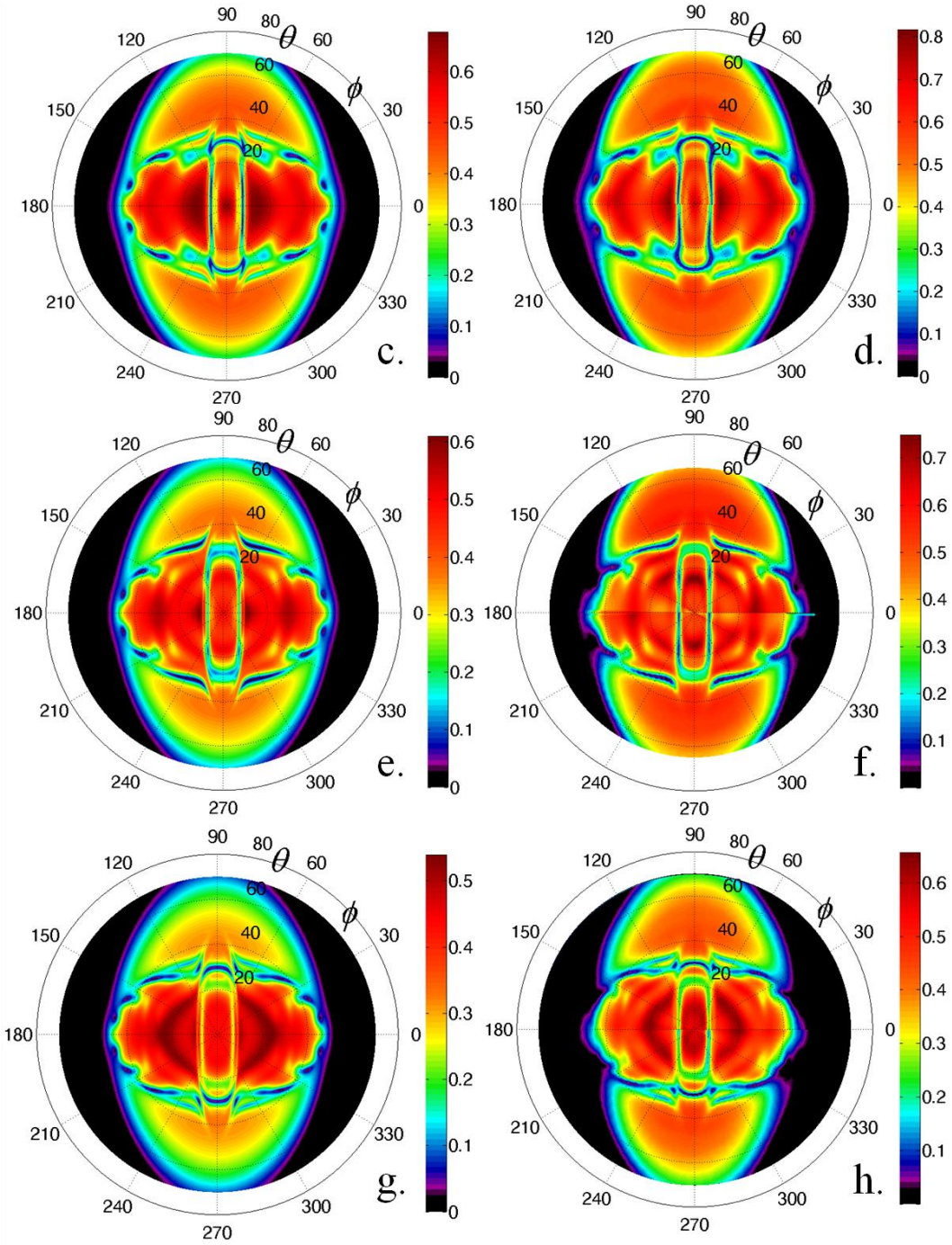

Figure 12-6: Amplitude-based H-UPS results in transmission for a $[0]_4$ C/E laminate at various excitation frequencies: *f* = 3 MHz (a-b), *f* = 4 MHz (c-d), *f* = 5 MHz (e-f) and *f* = 6 MHz (g-h). Left column corresponds to the numerical simulation, right column to the experimental recording.

In general, very good agreement is obtained between the simulation and the experimental recording for the unidirectional C/E laminate for all possible incidence angles $\psi(\varphi,\theta)$ at the different selected frequencies *f*. As mentioned before, the resulting H-UPS images are highly dependent on the applied frequency because they put on view the dispersive characteristics of Lamb waves. A close comparison of the numerical data with the experimental data at a fixed frequency reveals that the location of the characteristics amplitude contours are very well reproduced, while the global amplitude level only reveals a small discrepancy (in the order of ~10%). Most probably, this discrepancy is caused by an inaccurate knowledge of the frequency dependent imaginary elasticity constants which were used for the numerical computation. Indeed, the currently used set of imaginary constants has been obtained through inversion of P-UPS data of a $[0]_8$ carbon/epoxy laminate, assuming constant imaginary parameters (See Chapter 7). A second source of mismatch can be due to the fact that the stacking of the laminates has been performed manually, and thus could deviate from the envisioned unidirectional sequence. It can be verified in the experimentally obtained H-UPS images that they all have a symmetry line along -1°, which thus slightly deviates from the envisioned fiber reinforcement orientation of 0°. Finally, it is well known for autoclave manufactured reinforced plastics that the pressure and temperature cycle during manufacturing could introduce local matrix pockets as well as fiber clusters, which obviously influence the local material characteristics. In spite of this, it can be stated that globally a very good agreement is obtained between the H-UPS simulation and the H-UPS experiment for the intact $[0_4]$ C/E laminate.

Figure 12-7 displays the results for the delaminated $[0_2,U,0_2]$ C/E laminate at the different frequencies *f*. The delamination has been numerically modeled as a thin water layer of 50 μm, which is in accordance with the thickness of the removed Upilex foil. The presence of the delamination changes the characteristics of the H-UPS results with reference to the results of the intact C/E laminate. The position shift of features in the H-UPS image is easily understood bearing in mind the dispersive nature of Lamb waves (see Figure 12-1 and Figure 12-2) in combination with the geometrical discontinuity in thickness induced by the delamination. Indeed, the delamination basically divides the C/E laminate into two C/E sub-laminates, each having half the thickness of the original laminate. As such, the ultrasonic wave is subject to different boundary conditions, resulting in different Lamb mode stimulation conditions and as a consequence in a different H-UPS image. In accordance

with Figure 12-3a, the presented H-UPS results in Figure 12-7 show that the presence of a water-filled delamination enhances the transmission amplitude at certain incidence angles $\psi(\varphi,\theta)$. In addition, it can be verified that the amplitude value at normal incidence $\psi(0,0)$, which corresponds to the setup of a C-scan in transmission employing harmonic sound, only shows limited sensitivity to the presence of the water-filled delamination for most of the H-UPS images. Hence, the current results suggest that it is highly advantageous to employ oblique incidence angles $\psi(\varphi,\theta)$ for the detection of edge delaminations.

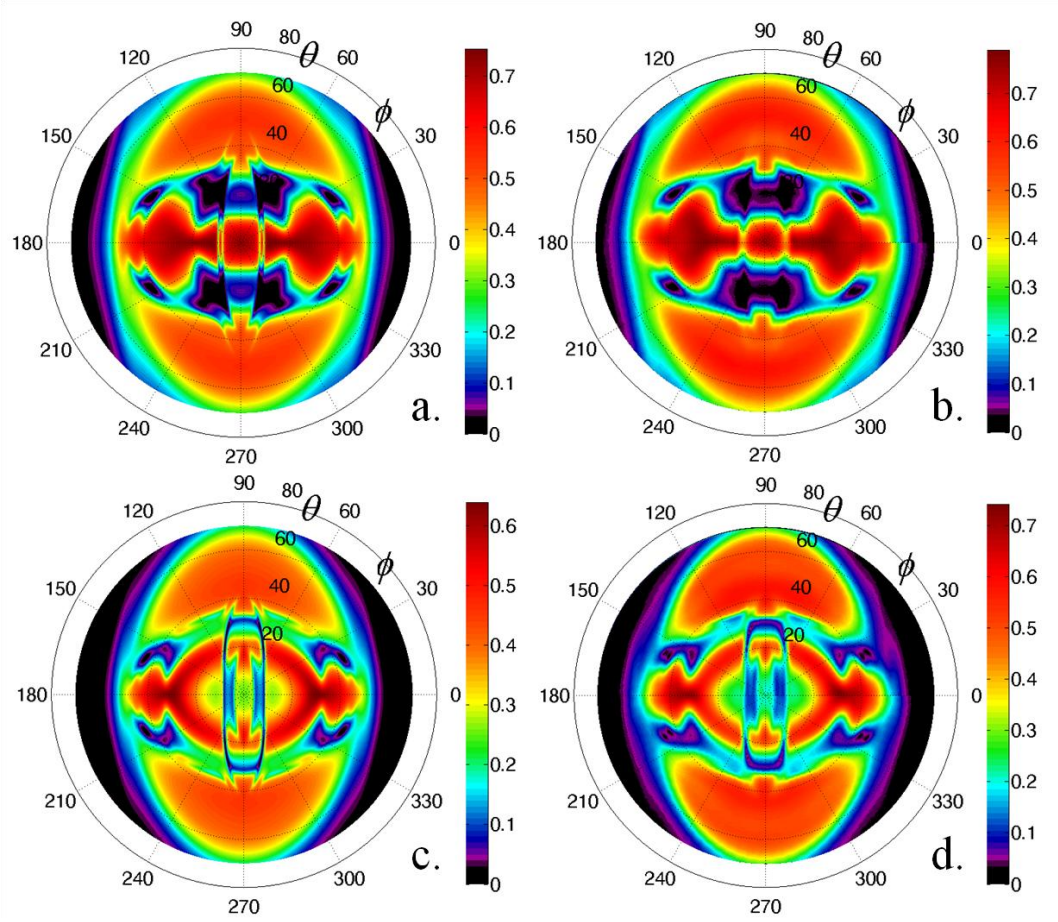

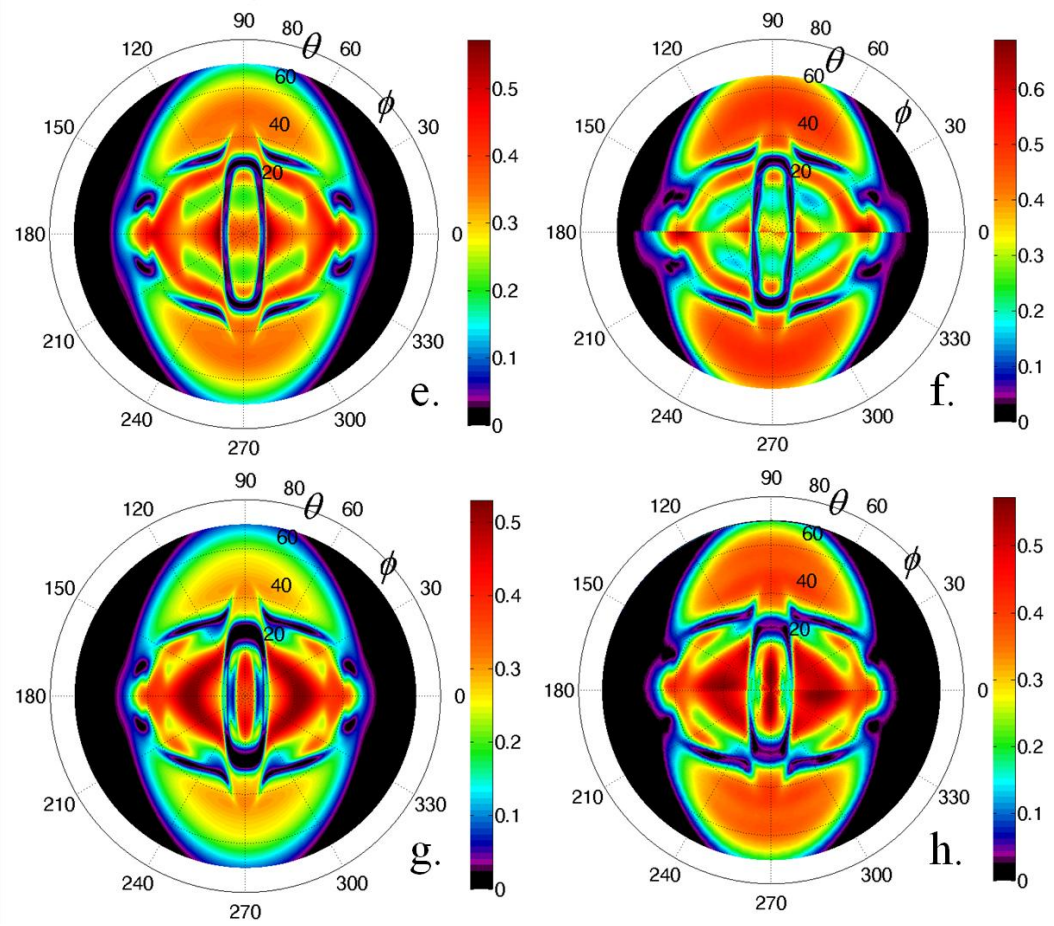

Figure 12-7: Amplitude-based H-UPS results in transmission for a delaminated [0,0,U,0,0] C/E laminate at various excitation frequencies: f = 3 MHz (a-b), f = 4 MHz (c-d), f = 5 MHz (e-f) and f = 6 MHz (g-h). Left column corresponds to the numerical simulation, right column to the experimental recording.

Because of the equivalence of frequency and thickness for the stimulation conditions of Lamb waves (see dispersion curves of Figure 12-1), the H-UPS at f = 6 MHz for the [0_2,U,0_2] C/E sample can be understood as the equivalent of two H-UPS's at f = 3 MHz of a virgin [0_4] C/E sample having half thickness, at least when ignoring attenuation effects as well as multiple reflections inside the delamination. According to this interpretation, the global amplitude level may shift as the attenuation is function of the frequency, however the characteristic amplitude contours should remain fixed. Comparison of Figure 12-6a-b with Figure 12-7g-h fully supports this interpretation.

In general, for all frequencies considered, satisfying agreement is obtained between simulation and experiment, which indicates the appropriateness of the hybrid compliance-stiffness matrix method for simulating wave phenomena associated to the oblique incidence insonification of an immersed delaminated multilayered medium with viscoelastic anisotropy.

12. 4. 2. Delaminated Cross-ply Carbon/Epoxy Laminate

In the previous section, the discussion was focused on a laminate with unidirectional carbon fiber reinforcement. Here, the analysis is extended to cross-ply C/E laminates with "man-made" edge delaminations at different locations throughout the thickness. The location of the different delaminations has been chosen in accordance with common failure modes known in engineering applications. For example, when transverse cracks are introduced in the 90° laminae during an impact loading, these cracks will propagate through the laminate until they encounter a 0° layer. Due to the increased strength of the 0° layer, such a transverse crack will not be able to progress further through the sample's thickness. As a result, it is either put on hold or it is deflected over 90° and thus delaminates the 90° lamina from the 0° lamina. As a second example of failure mode, one can consider a sample that is loaded in bending. Under these circumstances, large shear stresses are encountered in the middle of the laminate. Once the shear stress exceeds the interlaminar shear strength of the sample, a delamination will be introduced between two equally oriented laminae.

The H-UPS results for the cross-ply laminate have all been recorded at a fixed frequency of $f = 5$ MHz. In analogy with the results for the unidirectional C/E laminate, one could also repeat the study for a number of frequency values of f. However, even though the resulting H-UPS images will be different, the underlying interpretation will obviously remain the same.

Figure 12-8 displays the amplitude results for the (delaminated) cross-ply C/E laminate, with the left column corresponding to the simulation results and the right column to the experimental recordings. In comparison with the results obtained for the unidirectional $[0]_4$ C/E laminate, one can readily observe that the global H-UPS images have changed their symmetry characteristics, reflecting in this case the more complex anisotropy of the cross-ply C/E laminates. Similar as in previous section, very good agreement

is obtained between the simulation and the experimental recording for the intact and the various delaminated cross-ply C/E laminates. The presence of an edge delamination in the cross-ply laminate can be clearly recognized in the amplitude-based H-UPS results, for all possible locations. Furthermore, the results indicate that not only the presence, but also the location of the edge delamination through the thickness of the laminate influences the details that can be observed in the H-UPS images. This is easily understood based on the interpretation that a delaminated sample can be conceived as a system composed of two separate 'sub-laminates'. Depending on the location of the delamination, different sub-laminates are created, and thus different Lamb wave stimulation conditions apply. This interpretation also clarifies why the H-UPS results for the [0,U,90,90,0] sample and [0,90,90,U,0] sample, besides some minor deviations in the experimental recording, are identical to each other. Indeed, the inserted Upilex foil divides each of the two laminates into a system of two sub-stackings, and each such system is a mirrored twin of the other. Hence, the boundary conditions for Lamb wave stimulation are in both cases identical, thus (theoretically) resulting in the same H-UPS image. In addition, we remark that the sample having a delamination in the middle, shows a marked non-transparent angular window for transmitting ultrasonic waves at a frequency $f = 5$ MHz. Such ultrasonic pass and stop bands for the transmission characteristic have already been observed by various researchers, and have been interpreted in terms of Floquet waves [27-28].

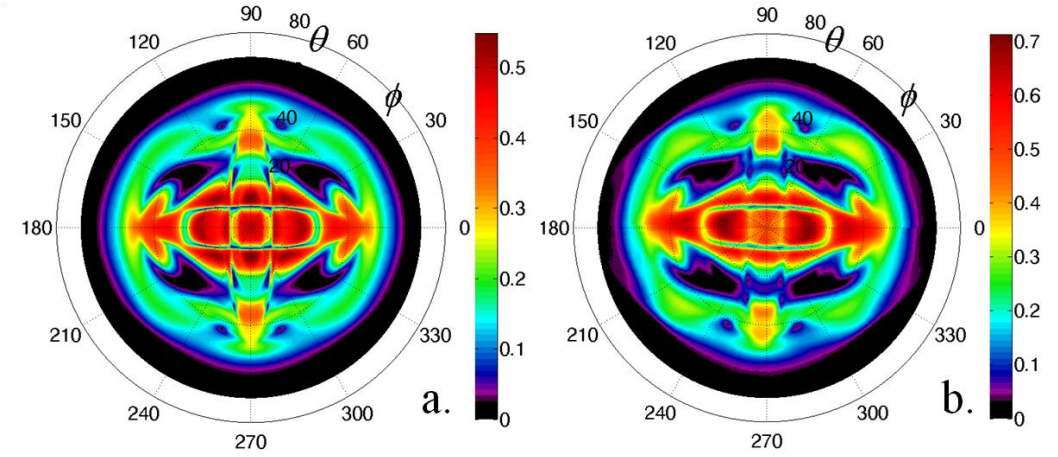

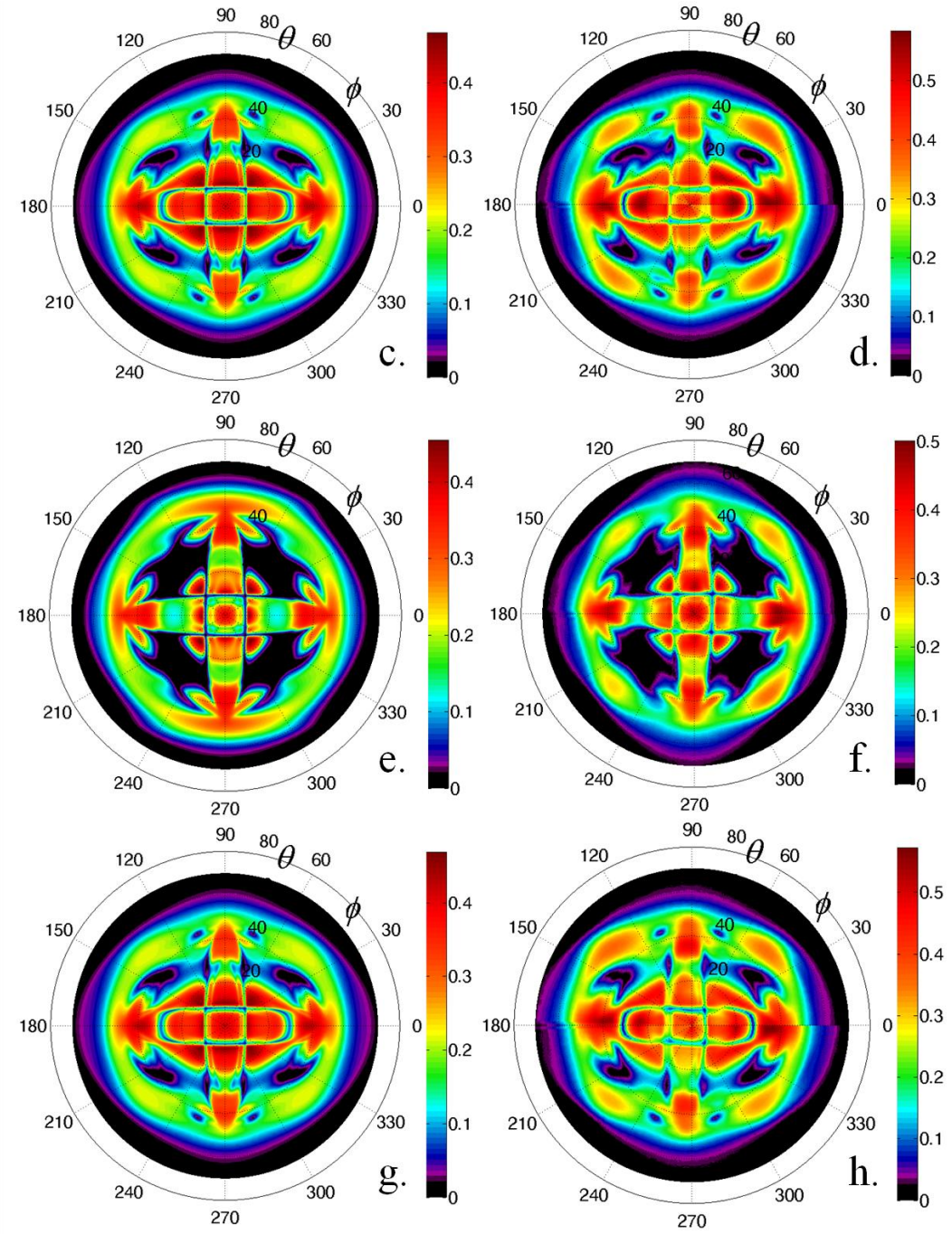

Figure 12-8: Amplitude-based H-UPS results in transmission, left column corresponds to the simulation, right column to the experimental recording: [0,90,90,0] (a-b), [0,U,90,90,0] (c-d), [0,90,U,90,0] (e-f) and [0,90,90,U,0] (g-h).

Since a harmonic signal (with known frequency) can be described by both its amplitude and phase (see Chapter 8), we have extended the study with an investigation concerning the phase information of the transmitted wave. As can be verified in Figure 12-3b, the phase characteristic of an ultrasonic wave also shows a significant responsiveness to the presence of an edge delamination. The experimentally obtained phase results, displayed in Figure 12-9, have been shifted such that in absence of a sample a phase equal to zero is obtained (see Figure 8.3). Comparison of the numerically predicted and the experimentally observed phase based H-UPS results for the intact cross-ply C/E laminate (Figure 12-9a-b), reveals that the global patterns in the phase map are well captured. However, several discrepancies in the details between simulation and experiment are obvious. The discrepancy may be attributed to a variety of causes, among which the most important certainly includes the high sensitivity of the phase characteristics to small perturbations in the thickness as well as to variations in the viscoelastic tensor. As the samples have been provided with a peel-ply to ease the removal of the breather/bleeder after the autoclave manufacturing cycle, an imperfect periodic surface imprint is left behind on the outer surfaces of the samples. The depth of the imprint has been measured optically and is in the order of ~85 μm (see Section 9.3.2). It is clear that this periodic surface roughness has consequences for the reliability of the phase recording. In addition, since the experimental recording of a phase is much more challenging than a simple amplitude recording, a phase measurement is acutely prone to small deviations and inaccuracies in the recording (e.g. vibration noise due to machinery operating in neighboring laboratories). Nevertheless, the global phase results for the delaminated samples basically show similar distortion features (with respect to the patterns of the virgin sample) as was observed in the amplitude based H-UPS results. Hence, we may safely state that, in addition to the amplitude characteristics, the phase of the transmission of an obliquely incident wave is also a sensitive parameter for detecting and evaluating a delamination. Yet again, like in the case of the amplitude recording, due to symmetry of the Lamb wave stimulation conditions, the phase results are not able to discern between a [0,U,90,90,0] laminate and a [0,90,90,U,0] laminate.

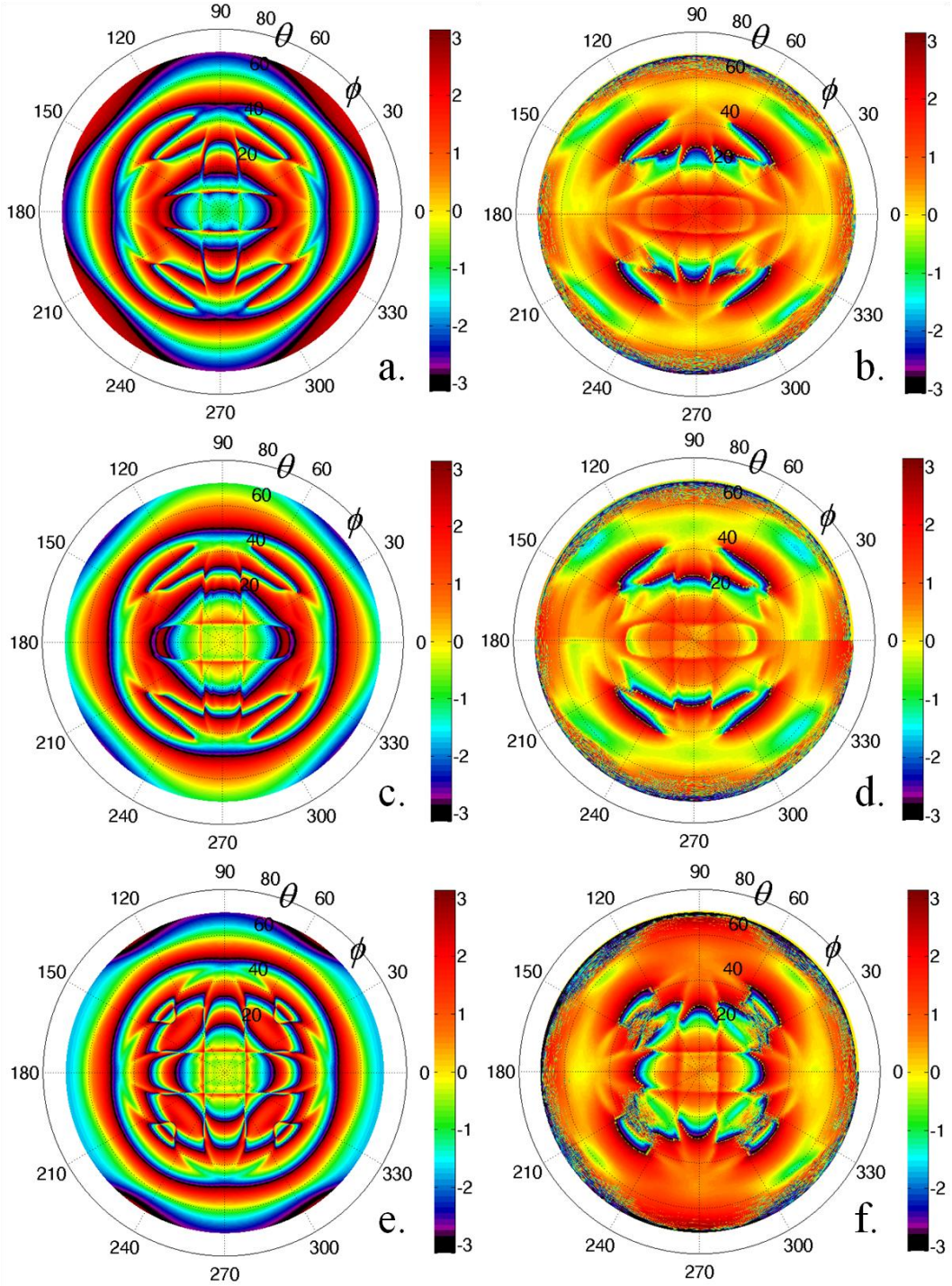
a.
b.
c.
d.
e.
f.
θ
ϕ

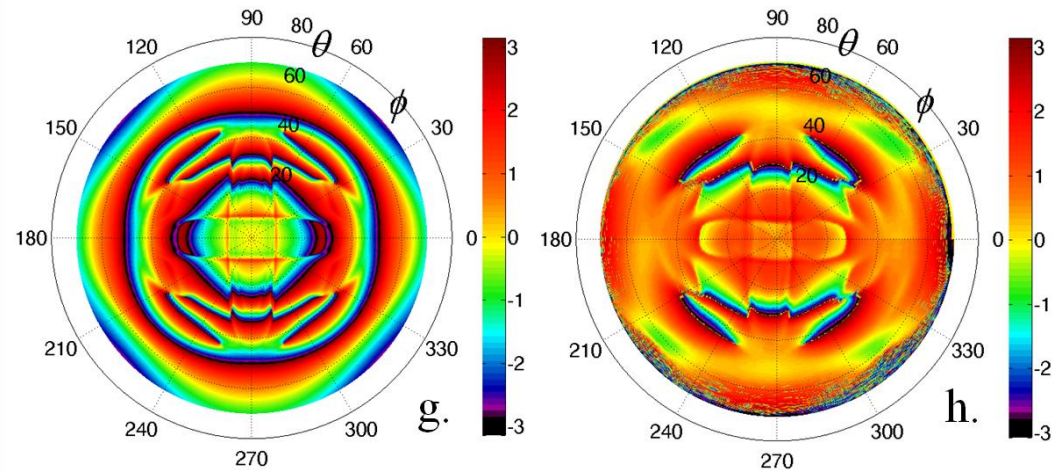

Figure 12-9: Phase-based H-UPS results in transmission, left column corresponds to the simulation, right column to the experimental recording: [0,90,90,0] (a-b), [0,U,90,90,0] (c-d), [0,90,U,90,0] (e-f) and [0,90,90,U,0] (g-h).

In some cases, e.g. when a structure is subject to extreme loading conditions, the damage process can lead to the initiation and formation of multiple overlapping delaminations, which are extremely difficult to detect and localize with traditional normal incidence techniques such as the classical C-scan. In Figure 12-10 and Figure 12-11, we show the amplitude-based, respectively phase-based H-UPS results for cross-ply C/E laminates having multiple overlapping delaminations.

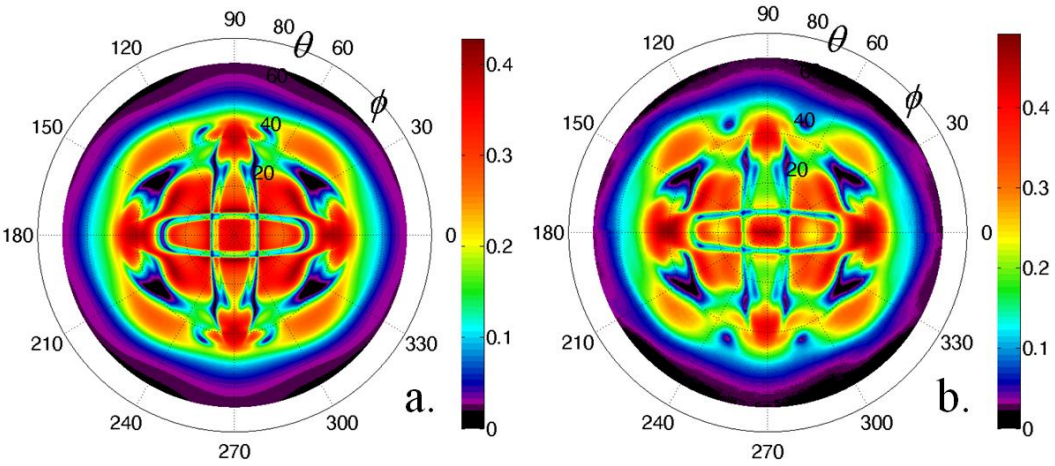

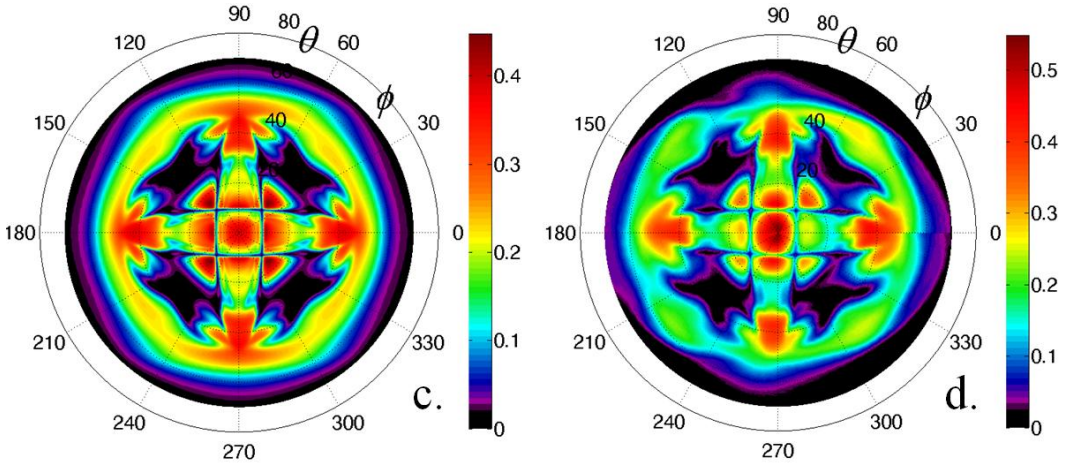

Figure 12-10: Amplitude-based H-UPS results in transmission, left column corresponds to the simulation, right column to the experimental recording: [0,U,90,90,U,0] (a-b) and [0,U,90,U,90,0] (c-d).

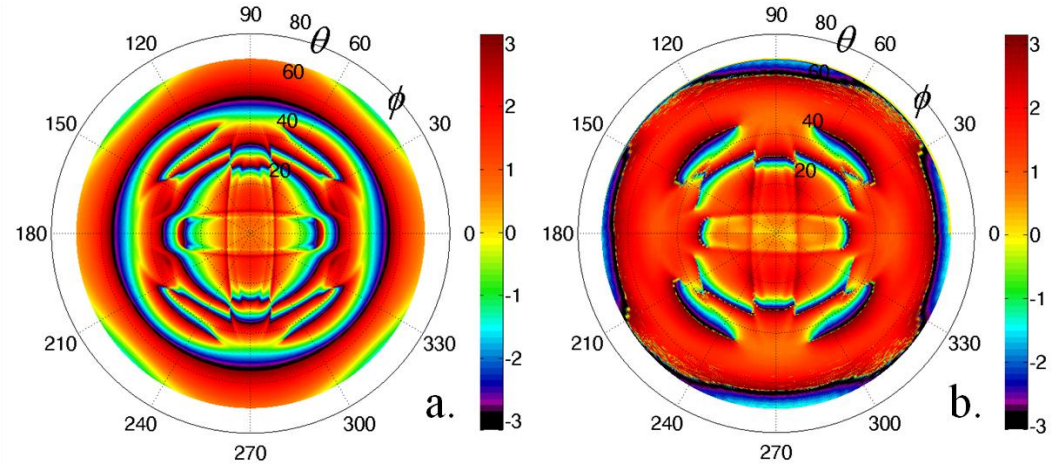

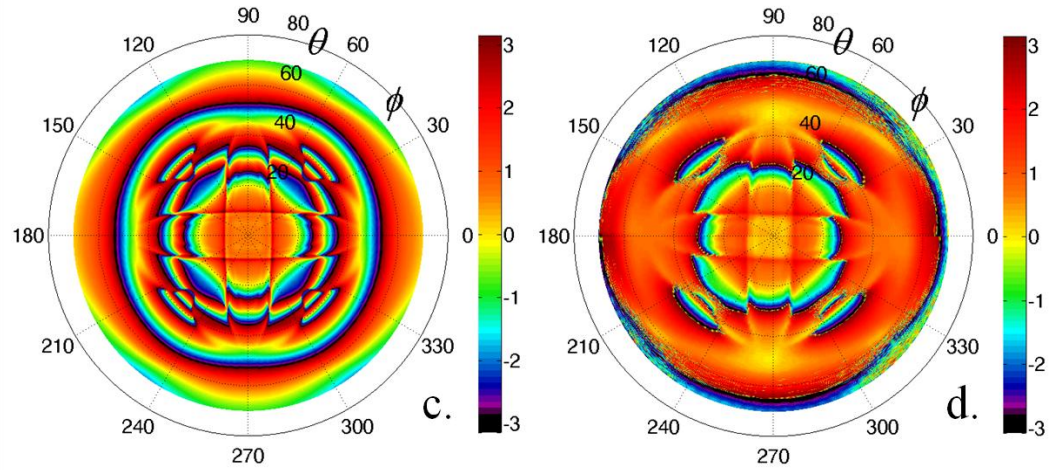

Figure 12-11: Phase-based H-UPS results in transmission, left column corresponds to the simulation, right column to the experimental recording: [0,U,90,90,U,0] (a-b) and [0,U,90,U,90,0] (c-d).

Compared to the H-UPS results for the intact sample (see Figure 12-8a-b and Figure 12-9a-b), one can clearly observe the alterations in the H-UPS images for the sample with multiple delaminations. More importantly, the H-UPS images also show significant changes with respect to the results for the C/E laminates that only have a single delamination. Hence, the H-UPS technique is able to detect overlapping delaminations. As previously observed, excellent agreement is obtained between the simulation and the experimental recording for the amplitude-based results, while the phase-based results again show some discrepancies in the details. Likewise, it was also verified in our lab (however not shown for brevity), both experimentally and numerically, that the H-UPS results for a [0,U,90,U,90,0] laminate is equivalent to the results for a [0,90,U,90,U,0] laminate, again indicating a shortcoming of the H-UPS technique in a transmission setup to absolutely locate delaminations.

The above discussed results clearly reveal the potential of both the amplitude-based and the phase-based H-UPS method in transmission to detect, localize and characterize multiple edge delaminations in a carbon fiber reinforced plastic. Though, the transmission results also bear a shortcoming as they cannot differentiate between a $[0_m,U,0_n]$ and a $[0_n,U,0_m]$ laminate because the composing sub-systems are, from a Lamb wave stimulation point of view, identical to each other. Indeed, as the ultrasonic signal propagates through the sample, crossing both sub-laminates, it picks

up the characteristics of both sub-systems. However, if one would operate in reflection mode, the ultrasonic wave is forced to traverse an additional solid-fluid interface if it wants to interact with the lower sub-laminate. Hence, one can expect that the reflection characteristic will be more sensitive to the upper sub-laminate, and thus should be able to effectively discern between a $[0_m,U,0_n]$ and a $[0_n,U,0_m]$ laminate. Unfortunately, our mechanical setup was not able to perform high-level UPS experiments in reflection at the time of performing the research described in this Chapter. In the meanwhile, the scanner has been successfully extended towards the reflection regime. Unfortunately, time was too short to actually perform experiments in reflection and add them to this dissertation. Therefore, the author only performed a numerical study, employing the hybrid compliance-stiffness matrix technique, to check whether the reflection characteristics discriminate between a $[0_m,U,0_n]$ and a $[0_n,U,0_m]$ laminate. Based on the excellent agreement obtained for the transmission results, it may be expected that the hybrid compliance-stiffness matrix method is also fully valid for computing reflection characteristics. As an example, Figure 12-12 shows the computed H-UPS results in reflection (amplitude and phase) for the [0,U,90,90,0] laminate and the [0,90,90,U,0] laminate (the corresponding H-UPS results in transmission are displayed in Figure 12-8c-d and Figure 12-8g-h for the amplitude, and in Figure 12-9c-d and Figure 12-9g-h for the phase).

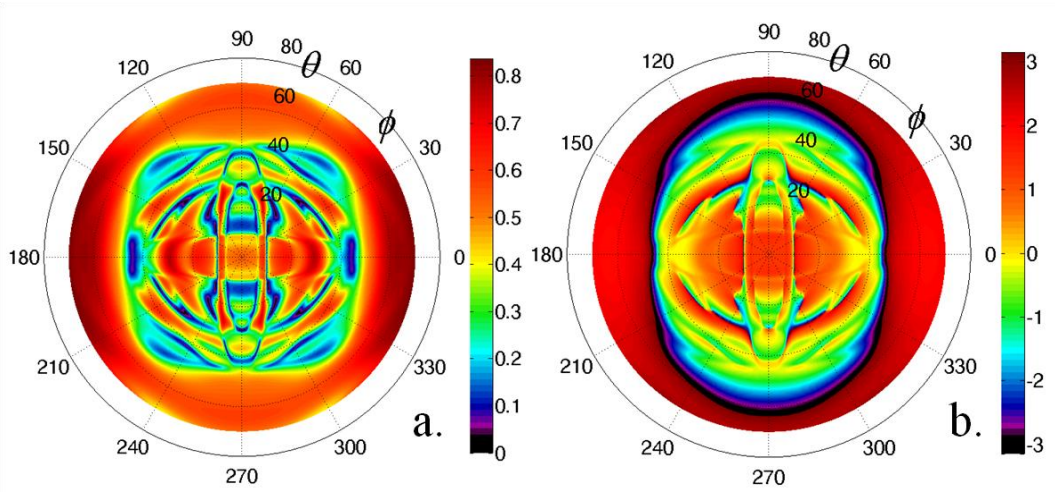

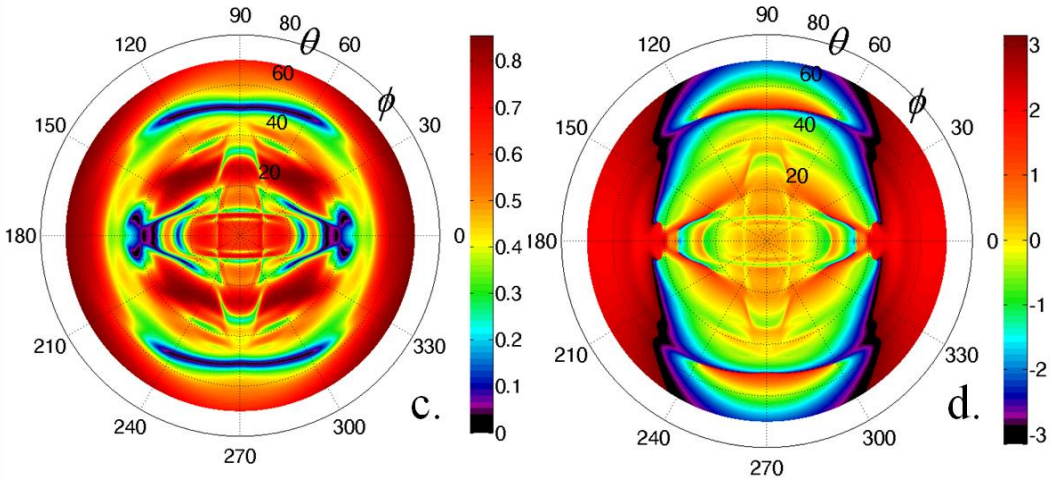

Figure 12-12: Numerically computed H-UPS results in reflection, left column corresponds to the amplitude, right column to the phase: [0,U,90,90,0] (a-b) and [0,90,90,U,0] (c-d).

Contrary to the H-UPS results in transmission, both the amplitude based and phase based H-UPS results in reflection clearly show a radical difference between the different delaminated laminates. The reflection results for the [0,U,90,90,0] laminate display a stretched appearance (most clearly observable in the phase map), similar as can be observed for the unidirectional laminate (see Figure 12-6). Hence, it proves that the reflected signal is mainly influenced by the upper sub-laminate above the delamination, being a single 0° lamina in case of the [0,U,90,90,0] laminate. The results for the [0,90,90,U,0] laminate on the other hand clearly show features which are characteristic for a cross-ply laminate, confirming the present interpretation concerning the dominant influence of the upper sub-layer for reflection measurements. Similar results have been obtained for the other C/E laminates having delaminations at symmetric locations. For brevity, these results are not shown.

The above analysis has been limited to water-filled edge delaminations. In practice however, a delamination is not always infiltrated by water. Here, the numerical analysis is focused to air-filled delaminations. In Figure 12-13, the H-UPS simulation in transmission is shown for a [0,U,90,90,0] carbon/epoxy laminate, with U representing an air-filled delamination. It can be readily seen that only a small amount of wave energy is transmitted through the sample, which is due to the increased mismatch between the acoustic impedances at the solid-air and air-solid interface. It has been verified that

the reduced transmission amplitude is more or less independent from the location, nor the thickness of the air-filled delamination. Hence, the delamination is easily detected, however the characterization of the delamination properties (location and thickness) becomes impossible. The phase results show better performance with respect to the amplitude results, though it is clear that the vital condition for successfully performing a phase measurement is the presence of a sufficient transmission amplitude.

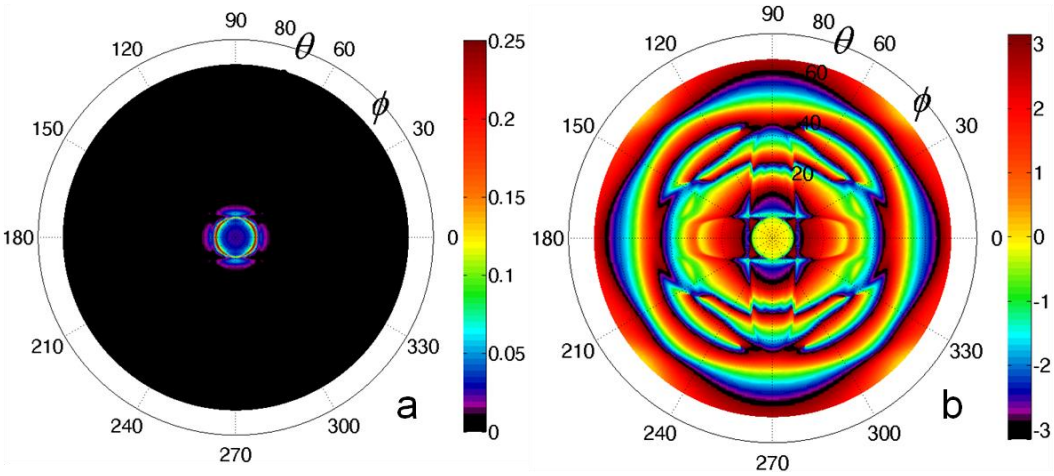

Figure 12-13: Numerically computed H-UPS results in transmission for a [0,U,90,90,0] carbon/epoxy laminate with U representing an air-filled delamination: amplitude (a) and phase (b).

The analysis in reflection provides more interesting results (see Figure 12-14). The location of the delamination is well-represented in both the amplitude and phase H-UPS simulations. The air layer basically transforms the original laminate to the top sub-laminate for ultrasonic reflection measurements.

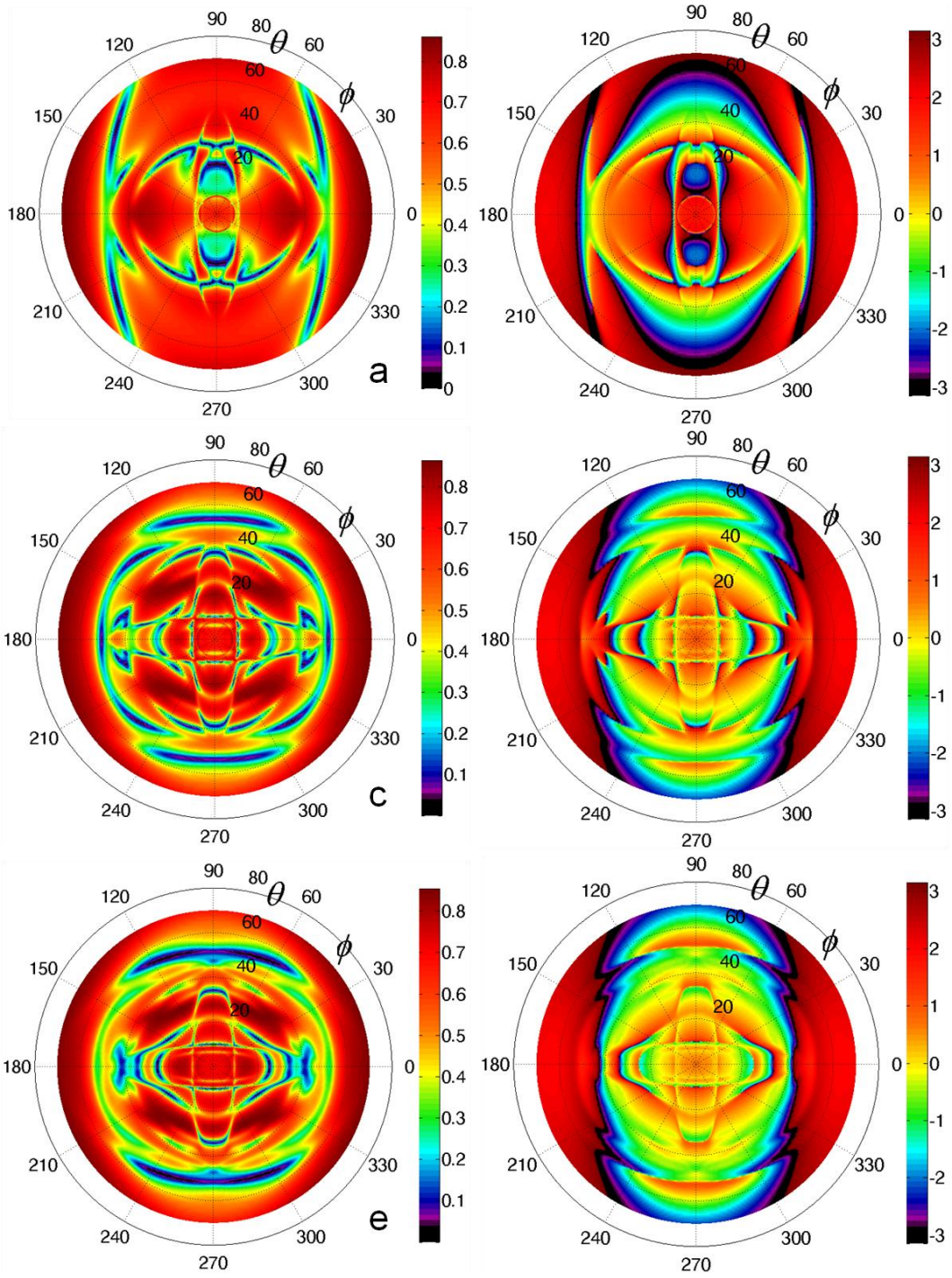

Figure 12-14: Numerically computed H-UPS results in reflection, left column corresponds to the amplitude, right column to the phase: [0,U,90,90,0] (a-b), [0,90,U,90,0] (c-d) and [0,90,90,U,0] (e-f).

To summarize the results of this section, it can be stated that the H-UPS technique, combining transmission and reflection, is fully capable to detect and quantify the presence of multiple, and possibly overlapping, edge delaminations in thin fiber reinforced plastics. Given the quality of the experimental data and the excellent agreement with numerical simulations, the inversion of relevant delamination parameters, such as depth and physical thickness (see Figure 12-3) becomes feasible based on a mixed numerical/experimental methodology (e.g. using genetic algorithms [26]). It is further shown numerically that the methodology is also applicable to air-filled delaminations in thin fiber reinforced plastics.

12. 5. P-UPS Results and Discussion

Till now the above discussion was concerned to the opportunities and limitations of the harmonic version of the ultrasonic polar scan for detecting and characterizing edge delaminations in thin fiber reinforced plastics. In this section, we go back to the traditional UPS implementation using broadband ultrasonic pulses. Numerically, the ultrasonic pulse can be decomposed in a plane wave spectrum by means of a Fourier integral. However, for computational efficiency, we employ the fast Fourier transform (FFT) and select 400 discrete frequency values in the spectrum of the ultrasonic pulse. For each frequency, the reflection and transmission characteristic is calculated and used in an inverse FFT to attain the received or transmitted pulse signal (see Section 4.7.2). Figure 12-15 displays the numerical and experimental P-UPS results (amplitude analysis) for an intact $[0]_4$ laminate and a delaminated $[0_2,U,0_2]$ laminate.

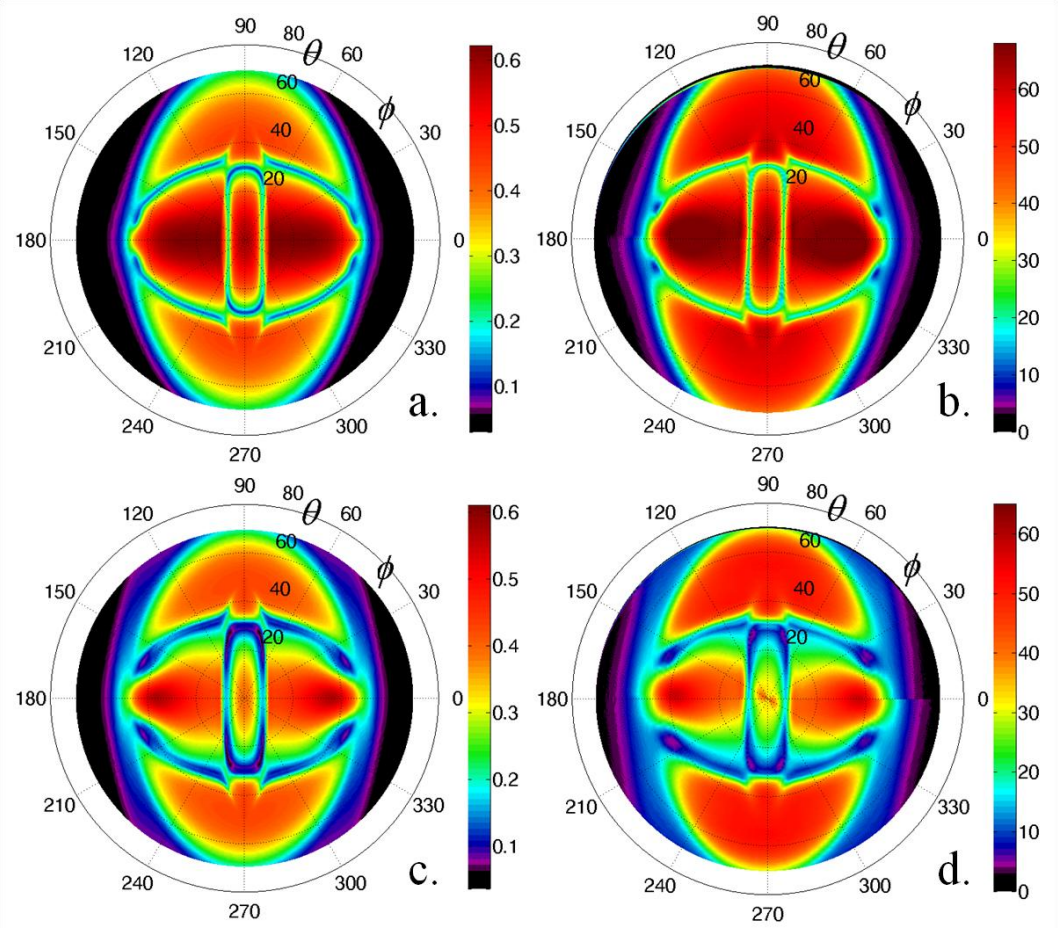

Figure 12-15: Amplitude-based P-UPS results in transmission, left column corresponds to the simulation, right column to the experimental recording: $[0]_4$ (a-b) and [0,0,U,0,0] (c-d).

First of all, as for the case of H-UPS, the numerical results are in excellent agreement with the experimental recordings, indicating that the hybrid matrix method is also appropriate for analyzing oblique incidence interaction of a broadband ultrasound pulse, consisting of a spectrum ranging from very small frequencies to very large frequencies, with an immersed (delaminated) multilayered anisotropic viscoelastic medium.

Comparing the intact and the delaminated case, the P-UPS results do not reveal the radical positional shifting of the characteristic contours in the presence of a delamination that we have observed for H-UPS (see Figure 12-6 and Figure 12-7), thus indicating the limited sensitivity of P-UPS for detecting delaminations. As the P-UPS image is mainly governed by bulk

wave characteristics [29-32], this insensitivity comes as no surprise given the non-dispersive nature of these waves. The sole indication of a change in material configuration may be the global amplitude level decrease of the P-UPS in the presence of a delamination. However, such a drop in global amplitude can also be attributed to other phenomena such as the presence of matrix cracks which serve as secondary scatterers for the ultrasonic waves [33]. Therefore, we can conclude that the P-UPS method has only limited potential and significance for detecting, and -by extension- for inferring the characteristics of (multiple) delaminations in thin fiber reinforced plastics.

12. 6. Conclusions

The hybrid compliance-stiffness matrix method for simulating wave propagation in (delaminated) multilayered media with viscoelastic anisotropy has been confronted for the first time with high-level ultrasonic polar scan experiments. The method was fully validated on intact and edge delaminated viscoelastic carbon/epoxy laminates for both quasi-harmonic and pulsed ultrasonic waves, insonifying the samples at a wide range of oblique incidence angles. An investigation, including both the amplitude and the phase of the transmitted signal, has been performed and good agreement was found.

We have further demonstrated, both experimentally and numerically, the excellent capability of the harmonic version of the ultrasonic polar scan technique for detecting and localizing the depth of multiple, and possibly overlapping, edge delaminations in thin fiber reinforced plastics. The H-UPS investigation has been successfully extended to the presence of air-filled delaminations. For the latter it was found that particularly the reflection regime provides interesting results. It was further found that the pulsed version of the ultrasonic polar scan technique shows limited sensitivity to the presence of a delamination. These features can be understood by considering that the H-UPS image puts on view the conditions for efficient stimulation of dispersive Lamb waves, whereas the P-UPS image provides a representative map of non-dispersive bulk wave characteristics.

12. 7. References

[1] Firestone, F.A., *The Supersonic Reflectoscope, an Instrument for Inspecting the Interior of Solid Parts by Means of Sound Waves.* The Journal of the Acoustical Society of America, 1946. 17(3): p. 288 - 299.

[2] di Scalea, F.L. and R.E. Green, *High-sensitivity laser-based ultrasonic C-scan system for materials inspection.* Experimental Mechanics, 1999. 39(4): p. 329-334.

[3] Iyer, S.R., S.K. Sinha, and A.J. Schokker, *Ultrasonic C-scan imaging of post-tensioned concrete bridge structures for detection of corrosion and voids.* Computer-Aided Civil and Infrastructure Engineering, 2005. 20(2): p. 79-94.

[4] Pandey, J.C., M. Raj, T.K. Roy, and T. Venugopalan, *A novel method to measure cleanliness in steel using ultrasonic c-scan image analysis.* Metallurgical and Materials Transactions B-Process Metallurgy and Materials Processing Science, 2008. 39(3): p. 439-446.

[5] Fahim, A.A., R. Gallego, N. Bochud, and G. Rus, *Model-based damage reconstruction in composites from ultrasound transmission.* Composites Part B-Engineering, 2013. 45(1): p. 50-62.

[6] Van den Abeele, K.E.A., P.A. Johnson, and A. Sutin, *Nonlinear elastic wave spectroscopy (NEWS) techniques to discern material damage, part I: Nonlinear wave modulation spectroscopy (NWMS).* Research in Nondestructive Evaluation, 2000. 12(1): p. 17-30.

[7] Van den Abeele, K.E.A., J. Carmeliet, J.A. Ten Cate, and P.A. Johnson, *Nonlinear elastic wave spectroscopy (NEWS) techniques to discern material damage, Part II: Single-mode nonlinear resonance acoustic spectroscopy.* Research in Nondestructive Evaluation, 2000. 12(1): p. 31-42.

[8] Maynard, J., *Resonant ultrasound spectroscopy.* Physics Today, 1996. 49(1): p. 26-31.

[9] Solodov, I., J.X. Bai, and G. Busse, *Resonant ultrasound spectroscopy of defects: Case study of flat-bottomed holes.* Journal of Applied Physics, 2013. 113(22).

[10] Meo, M., U. Polimeno, and G. Zumpano, *Detecting Damage in Composite Material Using Nonlinear Elastic Wave Spectroscopy Methods.* Applied Composite Materials, 2008. 15(3): p. 115-126.

[11] Aymerich, F. and W.J. Staszewski, *Impact damage detection in composite laminates using nonlinear acoustics.* Composites Part a-Applied Science and Manufacturing, 2010. 41(9): p. 1084-1092.

[12] Lammering, R., A. Eremin, M.N. Neumann, U. Gabbert, and S.M.H. Hosseini, *Structural health monitoring of lightweight structures by use of Lamb waves.* 2nd International Symposium on NDT in Aerospace, 2010: p. 8.

[13] Toyama, N. and J. Takatsubo, *Lamb wave method for quick inspection of impact-induced delamination in composite laminates.* Composites Science and Technology, 2004. 64(9): p. 1293-1300.

[14] Yashiro, S., J. Takatsubo, and N. Toyama, *An NDT technique for composite structures using visualized Lamb-wave propagation.* Composites Science and Technology, 2007. 67(15-16): p. 3202-3208.

[15] Chimenti, D.E. and R.W. Martin, *Nondestructive evaluation of composite laminates by leaky lamb waves.* Ultrasonics, 1991. 29(1): p. 13-21.

[16] Tan, K.S., N. Guo, B.S. Wong, and C.G. Tui, *EXPERIMENTAL EVALUATION OF DELAMINATIONS IN COMPOSITE PLATES BY THE USE OF LAMB WAVES.* Composites Science and Technology, 1995. 53(1): p. 77-84.

[17] Sekhar, B.V.S., K. Balasubramaniam, and C.V. Krishnamurthy, *Structural health monitoring of fiber-reinforced composite plates for low-velocity impact damage using ultrasonic lamb wave tomography.* Structural Health Monitoring-an International Journal, 2006. 5(3): p. 243-253.

[18] Barth, M., F. Schubert, B. Koehler, and Ieee, *Where X-Ray Imaging Fails - Delamination, Crack, and Micro-Pore Detection Using Ultrasonic Reflection Tomography in a Scanning Acoustic Microscope*, in *2008 Ieee Nuclear Science Symposium and Medical Imaging Conference*. 2009. p. 5479-5483.

[19] Kazys, R. and L. Svilainis, *Ultrasonic detection and characterization of delaminations in thin composite plates using signal processing techniques.* Ultrasonics, 1997. 35(5): p. 367-383.

[20] Baskaran, G., K. Balasubramaniam, C.V. Krishnamurthy, and C.L. Rao, *Ray based model for the ultrasonic time-of-flight diffraction simulation of thin walled structure inspection.* Journal of Pressure Vessel Technology-Transactions of the Asme, 2005. 127(3): p. 262-268.

[21] Satyanarayan, L., K.B. Kumaran, C. Krishnamurthy, and K. Balasubramaniam, *Inverse method for detection and sizing of cracks in thin sections using a hybrid genetic algorithm based signal parametrisation.* Theoretical and Applied Fracture Mechanics, 2008. 49(2): p. 185-198.

[22] Tan, E.L., *Stiffness matrix method with improved efficiency for elastic wave propagation in layered anisotropic media.* Journal of the Acoustical Society of America, 2005. 118(6): p. 3400-3403.

[23] Tan, E.L., *Hybrid compliance-stiffness matrix method for stable analysis of elastic wave propagation in multilayered anisotropic media.* Journal of the Acoustical Society of America, 2006. 119(1): p. 45-53.

[24] Kersemans, M., N. Lammens, G. Luyckx, J. Degrieck, and W. Van Paepegem, *Quantitative Measurement of the Elastic Properties of Orthotropic Composites by means of the Ultrasonic Polar Scan Method.* JEC Composites, 2012. 75(75): p. 48 - 52.

[25] Kersemans, M., K. Van Den Abeele, N. Lammens, J. Degrieck, F. Zastavnik, J. Gu, L. Pyl, H. Sol, and W. Van Paepegem. *Determination of the Fiber Direction and the C-Tensor of a UD Carbon/Epoxy Composite by means of the Ultrasonic Polar Scan*. in *Proceedings of the 2013 International Congress on Ultrasonics (ICU 2013)*. 2013. Singapore.

[26] Kersemans, M., A. Martens, N. Lammens, K. Van Den Abeele, J. Degrieck, F. Zastavnik, L. Pyl, H. Sol, and W. Van Paepegem, *Identification of the elastic properties of isotropic and orthotropic thin-plate materials with the pulsed ultrasonic polar scan.* Experimental Mechanics, 2014. In Press DOI: 10.1007/s11340-014-9861-7.

[27] Rokhlin, S.I. and L. Wang, *Ultrasonic waves in layered anisotropic media: characterization of multidirectional composites.* International Journal of Solids and Structures, 2002. 39(21-22): p. 5529-5545.

[28] Wang, L. and S.I. Rokhlin, *Ultrasonic wave interaction with multidirectional composites: Modeling and experiment.* Journal of the Acoustical Society of America, 2003. 114(5): p. 2582-2595.

[29] Degrieck, J. *Some possibilities of nondestructive characterisation of composite plates by means of ultrasonic polar scans*. in *Emerging technologies in nondestructive testing (ETNDT)*. 1996. Patras, Greece: A.A. Balkema.

[30] Declercq, N.F., J. Degrieck, and O. Leroy, *Simulations of harmonic and pulsed ultrasonic polar scans.* Ndt & E International, 2006. 39(3): p. 205-216.

[31] Kersemans, M., N. Lammens, J. Degrieck, K. Van Den Abeele, L. Pyl, F. Zastavnik, H. Sol, and W. Van Paepegem, *Extraction of bulk wave characteristics from a pulsed ultrasonic polar scan.* Wave Motion, 2014. In Press DOI: 10.1016/j.wavemoti.2014.05.001.

[32] Kersemans, M., A. Martens, K. Van Den Abeele, J. Degrieck, L. Pyl, F. Zastavnik, H. Sol, and W. Van Paepegem, *The Quasi-Harmonic Ultrasonic Polar Scan for Material Characterization: Experiment and Numerical Modeling.* Accepted for publication in Ultrasonics, 2014.

[33] Kersemans, M., I. De Baere, J. Degrieck, K. Van Den Abeele, L. Pyl, F. Zastavnik, H. Sol, and W. Van Paepegem, *Nondestructive damage assessment in fiber reinforced composites with the pulsed ultrasonic polar scan.* Polymer Testing, 2014. 34(0): p. 85-96.

Chapter 13

P-U(B)PS Signature of Quasi-Statically Damaged Fiber Reinforced Plastics

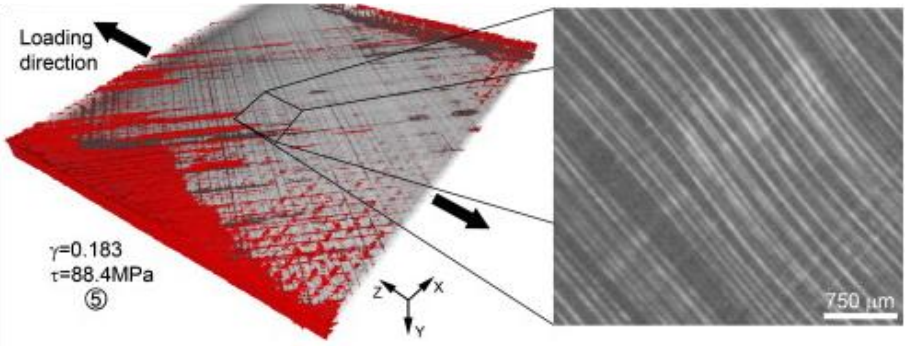

Tomographic reconstruction of a shear loaded composite. The magnification clearly shows the presence of fiber distortion. (Figure reproduced from reference [1]).

Summary

The response of fiber reinforced plastics to a quasi-static hysteretic shear-dominated loading cycle is investigated. Typically, such loading cycle leads to the initiation, accumulation and progression of micro damage features, which on the macro level is manifested by a directional degradation of elastic properties. Obviously, this perfectly matches the design of the UPS technique. The P-U(B)PS methodology has been applied for the nondestructive inspection of various damaged glass/epoxy and carbon/epoxy laminates. Several indicators have been identified in the P-UPS map, which expose the type, the location, the directionality as well as the extent of material damage. The P-UPS extracted characteristics are fully supported by literature, simulations, visual inspection as well as conventional destructive test procedures .

13. 1. Introduction

Considering that in-service fiber reinforced components are subject to a variety of loading conditions, a reliable inspection method to ascertain the integrity of the component during its lifetime is of crucial importance. Although several non-destructive testing techniques are already present in literature [2-15], in which ultrasonics can be considered to be the largest class, none of them are fully capable of detecting, identifying and following up different types of damage, especially when bearing in mind that microscopic damage features in fiber reinforced plastics often manifests itself in a directional reduction of the macroscopic mechanical properties [16-17]. Indeed, damage in composite materials is often not detectable by visual inspection from the outside, but rather manifests itself by a reduction of the local elastic properties through fiber/matrix interface debonding, matrix cracks, fiber bridging/pull-out/failure on the micro-scale [18-21]. Furthermore, considering that disassembling a component is often difficult, if not impossible, most of the existing inspection methods already fail on this point. In short, an in-situ non-destructive inspection technique, capable of quantifying various types of directional composite degradation, is needed.

Until now, the application of the P-U(B)PS technique to non-destructive detection and evaluation of elasticity related damage phenomena has hardly been investigated. In this chapter, we extend the applicability of the P-U(B)PS technique for the inspection and evaluation of damaged fiber reinforced plastics. Both the opportunities as well as the limitations of the P-U(B)PS method (amplitude and TOF(D)) as a damage sensor for fiber reinforced plastics are investigated and discussed. We mainly focus on damage features induced by quasi-static loading and which affecting the elastic properties of a laminate.

13. 2. Physical interpretation of P-UPS

PART I of this dissertation already provided an adequate background of the features observed in the P-UPS image. In short: a P-UPS image contains characteristic contours, which relate to the stimulation of the different polarized lateral bulk waves [22-26]. As these waves are vigorously connected with the stiffness parameters [27-28], the P-UPS contours put on view the mechanical properties of the insonified material spot. This has been explicitly demonstrated in Chapter 7 by inverting the local stiffness tensor of a $[0]_8$ carbon fiber reinforced laminate [29-31]. Any change in the elasticity tensor alters the directional wave speed and thus yields a positional shift of the P-UPS contours. Inward, respectively outward shifting of the contours corresponds to an increase, respectively reduction of elasticity parameters. As it is known that various types of damage in fiber reinforced plastics can be characterized through an estimation of stiffness reduction [32-33], it is clear that such types of material degradation perfectly match the nature and design of the P-UPS method. In order to visually demonstrate this, P-UPS simulations are performed for both a virgin and a degraded angle-ply $[-45,+45]_s$ glass/epoxy laminate (see Figure 13-1). The material properties for the virgin material are listed in Table 13-1, in which the complex elasticity tensor C is split in a real part C' and an imaginary part C''. The first describes the mechanical stiffness, while the latter accounts for damping in the material (Chapter 4) [27]. These material constants can be considered to be realistic for a typical UD glass/epoxy lamina.

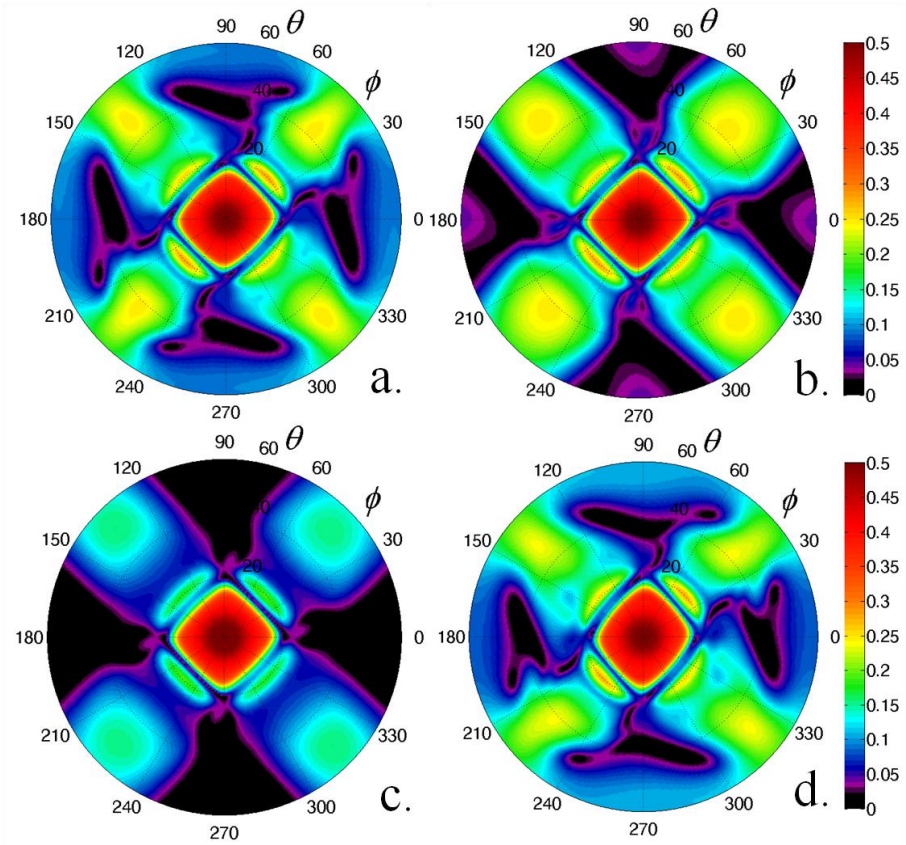

Figure 13-1: P-UPS simulation of [-45,+45]$_s$ UD glass/epoxy at *f* = 5MHz: virgin material (a), 50% reduction of real G'_{12} modulus (b), in addition to (b) a 80% increase of imaginary E''_{ii}, with *i* = 1,2,3 (c) and effect of 5° fiber distortion (d).

Table 13-1: Material properties used for the P-UPS simulation shown in Figure 13-1a.

LIQUID		**Glass/Epoxy**	
K [GPa]	2.2	E_{11} [GPa]	$38.9\cdot(1-0.11i)$
		E_{22} [GPa]	$13.3\cdot(1-0.11i)$
		E_{33} [GPa]	$13.3\cdot(1-0.05i)$
		$v_{12} = v_{13}$ [-]	$0.258\cdot(1-0.03i)$
		v_{23} [-]	$0.47\cdot(1-0.005i)$
		G_{12} [GPa]	$5.13\cdot(1-0.19i)$
		G_{13} [GPa]	$3.2\cdot(1-0.19i)$
		G_{23} [GPa]	$3.2\cdot(1-0.05i)$
ρ [kg/m^3]	1000	ρ [kg/m^3]	1615

The effect of 50% reduction of the shear modulus $G_{12}^{'}$ is clearly represented and identified in the positional shifting of the star-shaped P-UPS contours. Typically, such a large reduction in shear properties is triggered by intensive shear loading, causing the initiation, accumulation and progression of multiple cracks in the epoxy matrix. Obviously, these cracks serve as a secondary source of wave attenuation (through scattering of the propagating ultrasonic waves), and thus effectively increase the damping characteristics of the sample. Figure 13-1c shows the P-UPS simulation considering additionally increased imaginary stiffness moduli $E_{ii}^{''}$, with i = 1,2,3. It can be observed that this additional change corresponds to a drop in the global amplitude level of the transmitted wave, especially for large incident angles θ. Finally, shear loading also introduces a distortion in the fiber orientations, which obviously influences the global stiffness of the laminate. Figure 13-1d shows a simulation of the effect of a 5° fiber rotation, which is equivalent to a $[+40,-40]_s$ UD G/E laminate, on the P-UPS image. In comparison with the P-UPS result for the virgin sample (Figure 13-1a), the inner square transformed to a rhombus, while the global P-UPS image has a skewed look.

13. 3. Materials and Procedure

Two types of stiffness degrading mechanisms for composites have been considered. First, we investigate the influence of faults in the stacking sequence of layered composites. Secondly, we apply consecutive quasi-static loading and unloading with increasing maximum load level (a small number of sequential loading-unloading cycles) to fiber reinforced plastics. The quasi-static tests have been performed on an electromechanical Instron 5800R machine with 100 kN load cell. The specimens have been tested according to the ASTM D3519/D3518M-94 (2001) "Standard test method for in-plane shear response of polymer matrix composite materials by tensile test of a ±45º laminate". They were instrumented with a clip-on extensometer and strain gauges to calculate the in-plane shear strain. A testing speed of 2 mm/min was applied.

Two different sets of materials have been tested:

- A brittle epoxy matrix, reinforced with unidirectional carbon fibers, in different stacking sequences. The laminates are made from prepreg and have been autoclave manufactured according to the instruction of the supplier, i.e. a 60 minutes cycle at a temperature of

T = 125°C and a pressure p = 3.5 bar. The different samples have a length of 250 mm, a width of 25 mm and a thickness of 1.1 mm.

- A tough and visco-elastic cold-curing epoxy matrix, reinforced with a unidirectional glass fabric, in the stacking sequence $[-45°,+45°]_s$. The laminate was made by vacuum-assisted resin transfer molding (VA-RTM), and has a thickness of 2 mm. Samples have been cut at a length of 285 mm and a width of 35 mm.

13. 4. Results and Discussion

13. 4. 1. Stacking Sequence

At present, stacking of fiber reinforced plastics is most of the time done in a manual way, which is obviously prone to faults due to human error. The detection of an erroneous stacking sequence is of crucial importance to guarantee the designed functionality of the component. For example, a $[0]_8$ carbon/epoxy (C/E) laminate loses 11.42% of its stiffness E'_{00} if one lamina is placed under 90°. On the other hand, if the unidirectional fiber reinforcement direction deviates 5°, respectively 10°, from the intended direction i, the stiffness E'_{ii} reduces by 10.99%, respectively 32.71% [34]. The strong dependence of the in-plane stiffness components as a function of the fiber reinforcement angle is displayed in Figure 13-2 for a typical UD C/E laminate.

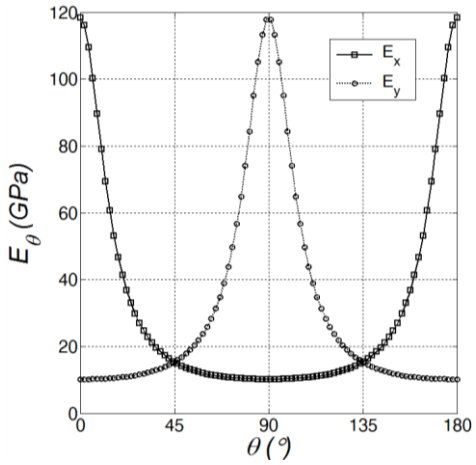

Figure 13-2: Variation of in-plane stiffness moduli with respect to the orientation θ of the UD fiber reinforcement.

We scanned several composites with the P-UPS technique in order to detect nondestructively an erroneous stacking sequence (which has been applied intentionally). Figure 13-3a-b displays both the amplitude-based and TOF-based P-UPS image for the reference $[0]_8$ C/E laminate. The unidirectional nature of the C/E laminate is clearly reflected in the P-UPS images. The insets show a small part of the P-UPS image, which is found to be more sensitive to slight deviations in the stacking sequence.

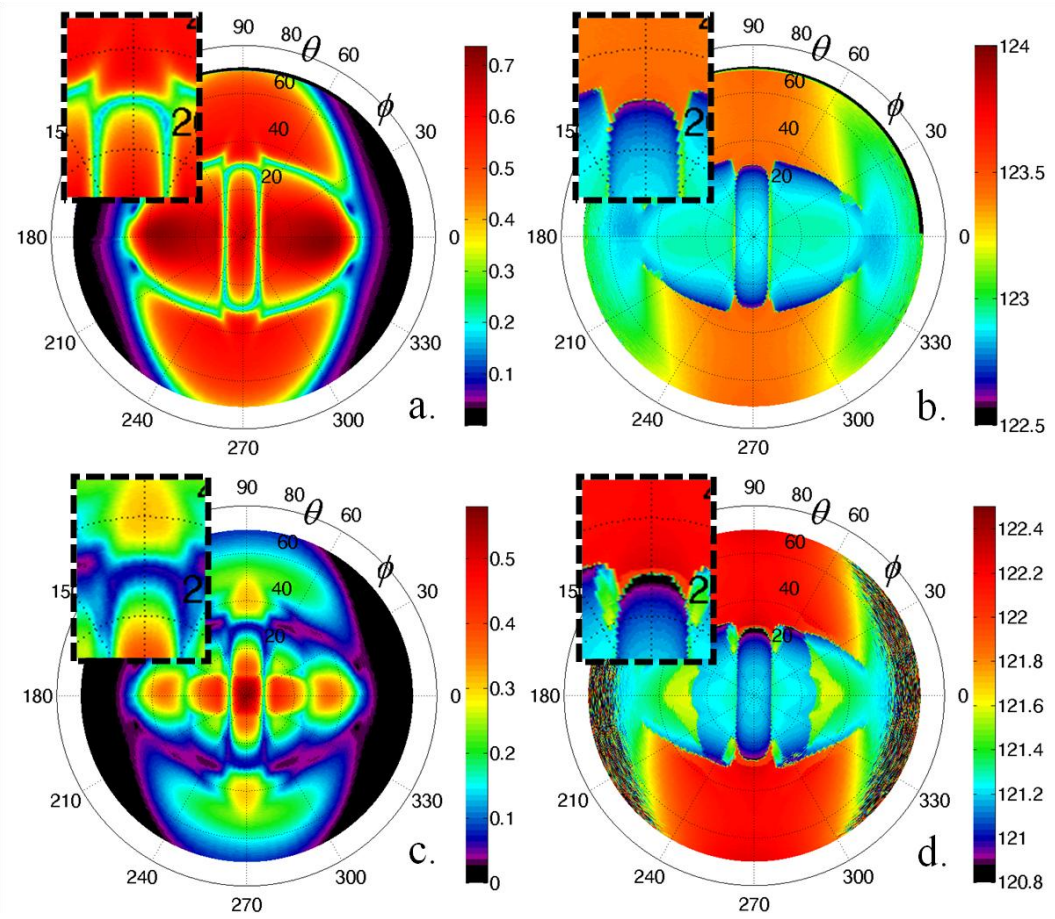

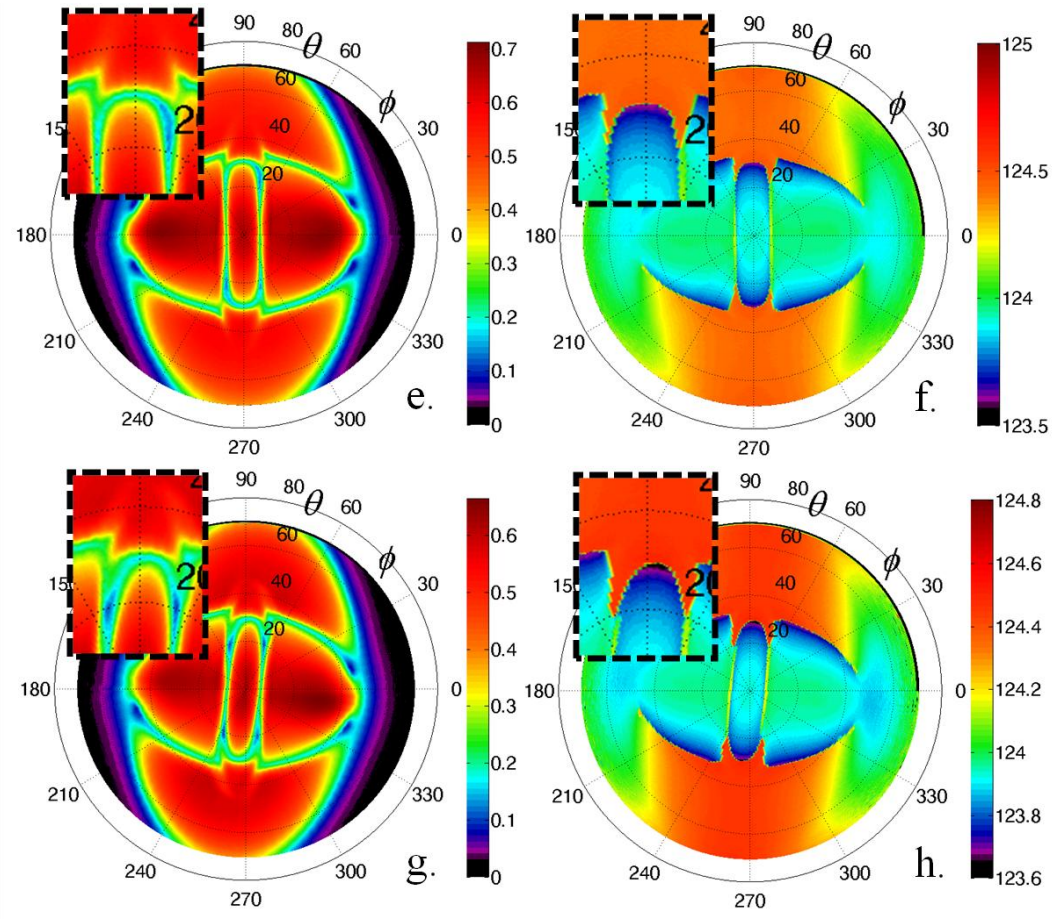

Figure 13-3: Stacking sequence C/E: $[0]_8$ (a-b), $[0_6,90,0]$ (c-d), $[0_2,5,0]$ (e-f) and [0,-10,0,5] (g-f). Left column corresponds to amplitude recording, right column to TOF recording.

By replacing the 7th 0° lamina by a 90° lamina, we obtain the P-UPS results shown in Figure 13-3c-d. A clear shift can be observed for both the amplitude and the TOF recording with respect to the results of the virgin C/E laminate, and thus a 90° rotated lamina is easily detected. In addition, numerical simulations indicate that the depth position of the 90° layer can be easily detected. However, it is clear that such large stacking errors rarely occur. More realistic fiber orientation errors are in the range of 5°-10°. Figure 13-3e-f shows the P-UPS results for a four-layer unidirectional C/E laminate in which one layer has been rotated over 5°. At first sight, these results are very similar to Figure 13-3a-b. However, close inspection (see the inset) reveals an indicator which is most clear in the amplitude recorded P-UPS results. Indeed, the inner low-amplitude contour has no longer any

mirror symmetry with respect to the radial axis at $\varphi = 90°$, although, it has to be mentioned that the effect of a single lamina distorted by 5° is rather small for the P-UPS image. Finally, we manufactured a C/E laminate with a stacking sequence of [0,-10,+5,0]. The P-UPS results are presented in Figure 13-3g-h. One can immediately observe that the global P-UPS image is rotated. The global rotation angle has been determined as $\varphi_{rot} = -4°$, which corresponds to a global stiffness reduction of 7.33% in the direction of $\varphi = 0°$. Similar to Figure 13-3e-f, the inset reveals a slight distortion of the inner low-amplitude P-UPS contour.

13. 4. 2. Shear Loading, Glass/epoxy $[-45,+45]_s$

The applied loading sequence is displayed in Table 13-2, the stress-strain curve is shown in Figure 13-4a. Note that the curve could only be constructed up to $\tau_4 = 42.5$ MPa because the strain gauges saturated and eventually detached from the laminate.

Table 13-2: Applied loading levels to the $[-45,+45]_s$ G/E laminate.

Applied Shear Stress Level	τ_1 = 27.5 MPa	τ_2 = 32.5 MPa	τ_3 = 37.5 MPa	τ_4 = 42.5 MPa	τ_5 = 47.5 MPa	τ_F = 49.8 MPa

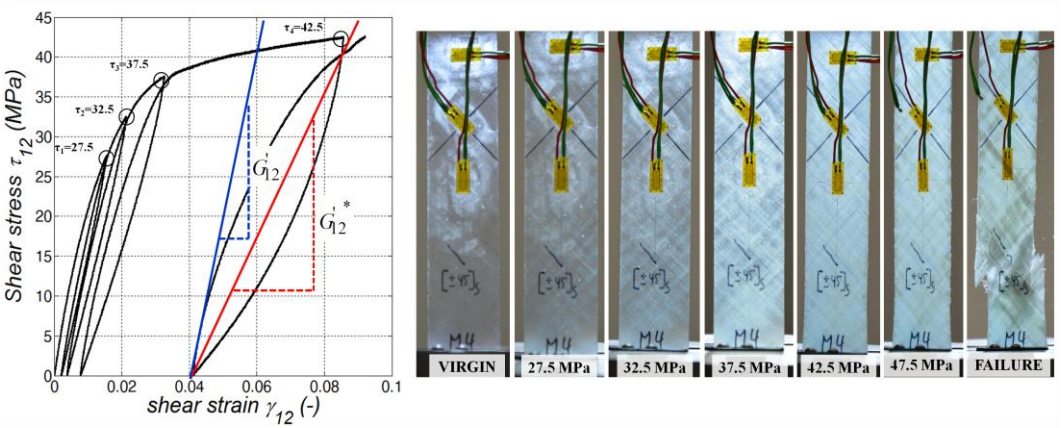

Figure 13-4: Stress-strain curve for the $[-45,+45]_s$ UD G/E laminate (a) and photographs of the specimen at the different load levels (b).

From the stress-strain curves, the shear modulus G'_{12} as well as the apparent shear modulus G'^{*}_{12} can be obtained by evaluating the initial slope of the loading curve, respectively the secant for one loading-unloading cycle (see

Figure 13-4a) [19-20]. Both slopes decline with each new loading and unloading, indicating a reduction of shear properties. The stress-strain curves indicate that $G_{12}^{'}$ decreases from 2.357 GPa to 1.679 GPa, corresponding to a reduction of 28.7%. The apparent shear modulus $G_{12}^{'\,*}$ on the other hand decreases to 0.912 GPa, corresponding to a reduction of 61.3% which is consistent with previous results [19-20]. The envelope shows a non-linear course which is related to the initiation and progression of matrix cracks. In addition, the glass/epoxy laminate shows hysteretic behavior, which is mainly triggered by sliding of matrix crack surfaces relative to each other upon loading and subsequent unloading, in combination with the viscoelastic nature of the matrix. After each load cycle, the sample has been demounted from the tensile machine and scanned with the P-UPS setup. Since the same material spot has been insonified with exactly the same acoustic parameters, the different P-UPS results can be compared to each other without any restrictions in order to explore the influence of the loading to the P-UPS image.

The amplitude recorded P-UPS result of the virgin material is shown in Figure 13-5a. The orthotropic nature of the scanned sample is clearly reflected by the geometrical symmetry in the P-UPS image. However, small amplitude variations between orthogonal in-plane directions indicate that both directions (φ = +45° and φ = -45°) are not completely equivalent. This of course is easily understood by considering the specific positioning of the different layers through the thickness. It was verified numerically that the P-UPS image of a $[+45°,-45°]_s$ laminate slightly differs from a $[-45°,+45°]_s$ laminate, which implies that the process of homogenization through the thickness is not fully legitimate. Nevertheless, for the phenomena investigated here, this is of minor importance and, therefore, we assume the laminate to be effectively homogeneous through thickness for the ultrasonic waves. It is furthermore noted that, compared to the amplitude recordings, the TOF based P-UPS images show little detail for this material and these results are therefore omitted.

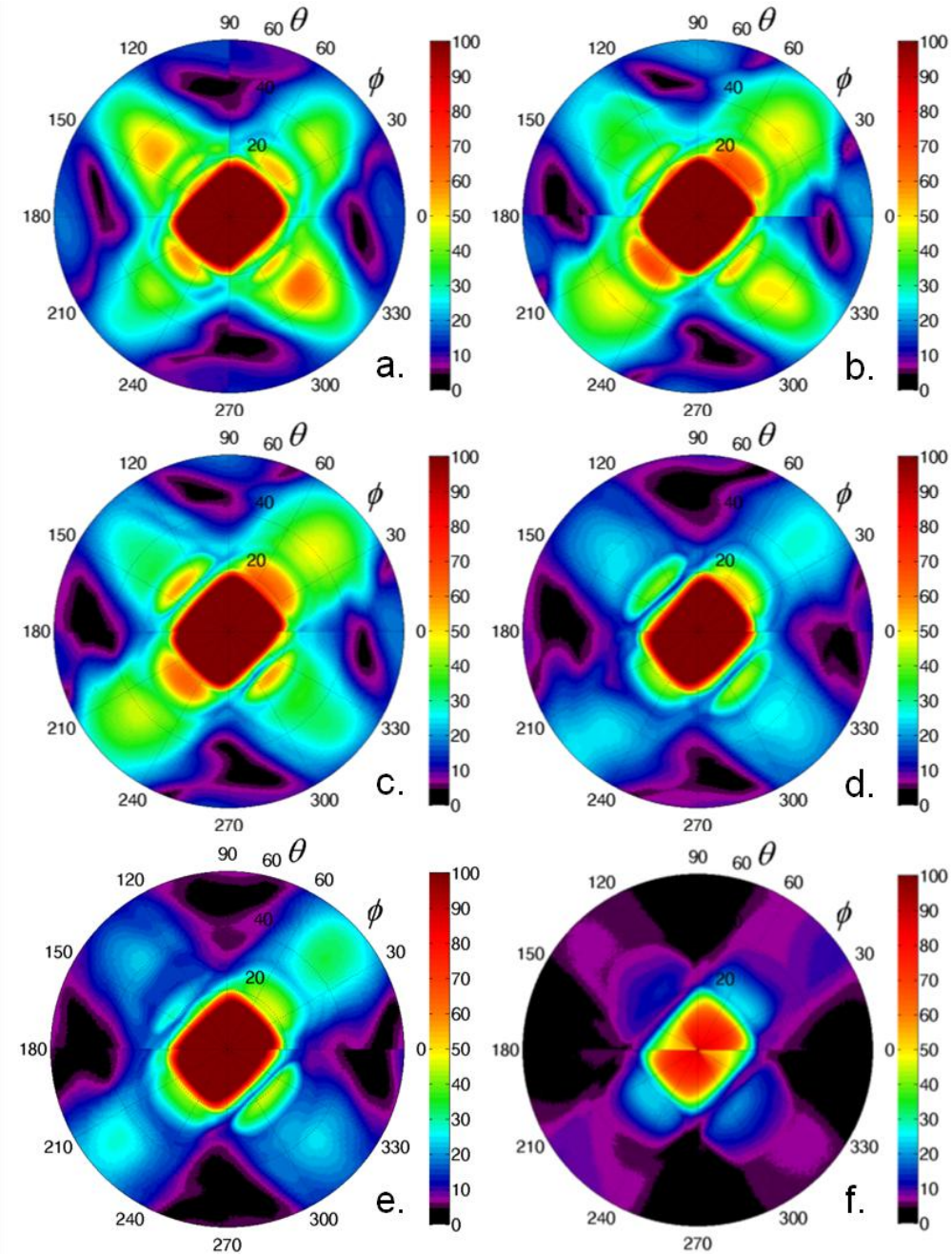

Figure 13-5: Amplitude recorded P-UPS results for the [-45,+45]$_s$ UD G/E laminate: τ_0 = 0 MPa (virgin specimen) (a), τ_2 = 32.5 MPa (b), τ_3 = 37.5 MPa (c), τ_4 = 42.5 MPa (d), τ_5 = 47.5 MPa (e) and τ_F = 49.8 MPa (failed specimen) (f).

After applying the second load cycle (τ_2 = 32.5 MPa) and scanning with the P-UPS technique, one already observes that the outer star-shaped contours

have slightly expanded with respect to the virgin results. With the physical interpretation of the P-UPS image given in previous section (see Figure 13-1b), this shifting of the contours can be immediately linked to a small reduction of the shear properties $G_{12}^{'}$ (the strains induced by the ultrasonic wave are typically small) of the insonified region. This is further affirmed on the basis of the stress-strain curve, in which the average slope of subsequent loops steadily declines (see Figure 13-5a). The decrease in shear properties is understood by realizing that the glass/epoxy has a fiber reinforcement which contains binding yarns. Upon loading, these binding yarns try to straighten and thus 'cut' through the matrix of a single lamina. As an obvious consequence, the shear properties of the glass/epoxy degrade. In contrast with the star-shaped contour, the inner square, which relates to the QL wave, and by extension to $E_{ii}^{'}$ (with i = 1,2), remains largely unaffected, as could have been expected for the here considered loading type.

Increase of the loading level reveals a further shifting of the characteristic star-shaped P-UPS contours, and eventually leads to parallelization of its outskirts, indicating a further reduction of the local shear properties. It can also be observed that additional features appear in the P-UPS image (see Figure 13-5d) once the maximum load level reaches τ_4 = 42.5 MPa. Besides a shifting of the outer polar contours, a drop in the overall transmitted amplitude is observed. This is due to the initiation and progression of multiple micro cracks upon which the incoming wave scatters, thus leading to additional attenuation of the transmitted wave. This behavior can also be verified in the numerical computation shown in Figure 13-1c.

It can be expected that the formation of multiple matrix cracks enhances the amount of ultrasound which is backscattered. The amplitude-based P-UBPS for both the virgin sample and the sample loaded at τ_4 = 42.5 MPa are displayed in Figure 13-6. The result for the virgin sample shows an axis of enhanced backscatter along φ = +45°. Also, at polar axis φ = -45° a small amount of backscattered energy is recorded, reflecting the scattering at the fiber bundles of the internal laminae (see Chapter 9). The P-UBPS image for the loaded sample shows similar features, but has a much higher amplitude scale. The ultrasonic parameters are identical in both recordings, hence the increased backscatter has a secondary physical origin. It is well known that shear loading introduces matrix cracks which are mainly aligned with the fiber orientations. Hence, the increased backscatter amplitude is probably a consequence of the dense field of accumulated micro cracks. This statement

is further supported by the recorded stress-strain curve in which the advanced non-linear course of the envelope at the third load level reflects the increased formation of micro cracks, resulting in a high micro crack density. Also optical inspection on a similar sample, which was loaded at a shear stress of τ = 42.5 MPa, indeed reveals accelerated formation and progression of micro cracks, eventually leading to a dense field of micro cracks which literally bleaches the specimen (see photograph taken at loading level of τ = 42.5 MPa in Figure 13-4b).

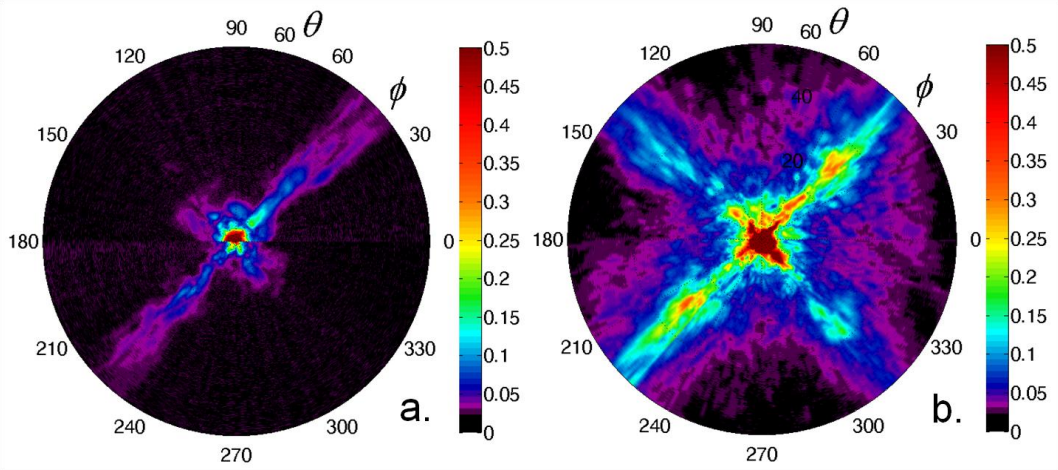

Figure 13-6: Backscattered signal for the [-45,+45]$_S$ UD G/E laminate: virgin state (a) and loaded at τ_4 = 42.5 MPa (b).

Finally, the sample failed at a stress level of τ_F = 49.8 MPa, at a distance of more or less 60 mm from the insonification spot. Since material degradation is clearly discerned by the P-UPS method, this strongly indicates that the induced material damage cannot be considered to be localized, but rather progresses through the complete sample. In addition to previous observations, the P-UPS result of the failed specimen shows a drastic drop in global amplitude. In the light of Chapter 12, this drop in transmission efficiency is attributed to the presence of an air-filled delamination in the failed specimen [35]. The fiber angular distortion is measured to be 2.5° for the fractured glass/epoxy specimen, which can be considered to be rather low.

13. 4. 3. Shear Loading, Carbon/epoxy [-45,+45]s

To complement the results discussed in previous Section, a similar investigation was performed on the carbon fiber reinforced composite with loading sequence given in Table 13-3. The $[-45,+45]_S$ C/E laminate has been loaded in multiple steps in which each loading level increases up to the point where failure occurred at a stress level of $\tau_F = 90.5$ MPa, which is in agreement with earlier studies [36].

Table 13-3: Applied loading levels to the $[-45°,+45°]_s$ C/E laminate and P-UPS extracted opening angles η.

Applied Stress Level [MPa]	$\tau_0 = 0$	$\tau_1 = 43$	$\tau_2 = 55$	$\tau_3 = 62$	$\tau_4 = 65$	$\tau_F = 90.5$
Opening Angle η	91.5°	88°	87°	85.5°	84°	81.5°

The stress-strain curve is shown in Figure 13-7. The strain gauges saturated at a shear stress of $\tau = 72.5$ MPa. It is observed that the C/E laminate can withstand a higher shear load, compared to the G/E sample. In addition, the stress-strain curve shows some extraordinary features: $G_{12}^{'}$ slightly increases from 5046.7MPa (virgin state) to 5176.9MPa, corresponding to a stiffening of 2.6%. The apparent shear modulus $G_{12}^{'*}$ on the other hand steadily decreases with loading; a reduction of 46.3% has been determined. To further investigate this response, P-UPS experiments have been obtained.

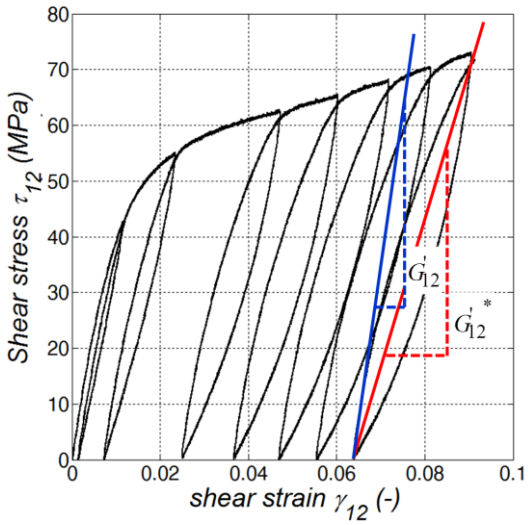

Figure 13-7: Stress-strain curve for the $[-45,+45]_s$ C/E laminate.

In Figure 13-8, the amplitude recorded P-UPS of both the virgin and failed C/E laminate is shown. The insonification spot is located at a distance of ~40 mm from the zone where failure occurred. Except for a small skewing of the amplitude recorded P-UPS fingerprint, similar as was observed in the simulation displayed in Figure 13-1d, no clear indicators are visible which expose the presence of potential material damage.

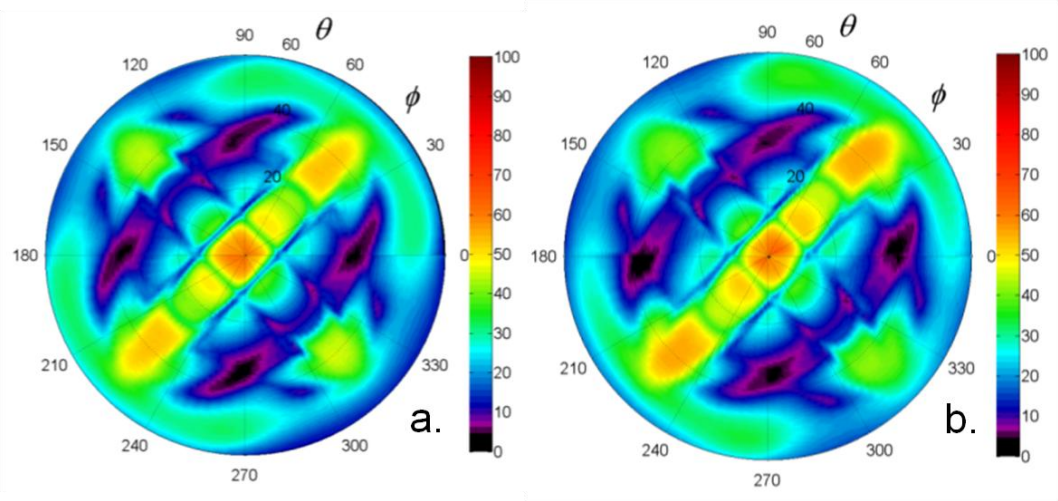

Figure 13-8: Amplitude recorded P-UPS results for a [-45,+45]$_s$ UD C/E laminate: virgin (a) and failed (b) specimen.

Since the C/E laminate is built of prepreg laminae which, contrary to the G/E laminate, do not contain binding yarns, a different response could have been expected. It was verified that the backscattered energy did increase with loading, although it was found to be significantly lower compared with the G/E sample. This is in accordance with the brittle failure of the specimen, as damage could not propagate in a progressive manner through the sample, as well as with the absence of reduction of $G_{12}^{'}$ obtained from the stress-strain curves. The permanent shear strain cannot be extracted because of the insensitivity of the P-UPS for this quantity. On the other hand, the nonlinear envelope in combination with the hysteretic loops and the reduction of the apparent shear modulus $G_{12}^{'*}$ indicate that the sample is effectively degraded. Visual inspection of the failed specimen indeed revealed that the orientation of the fibers were changed significantly, supporting the hypothesis that damage did occur. Contrary to the amplitude recordings, the TOF recordings give more distinct and detailed characteristic patterns and are therefore used to extract additional information about the distorted fiber orientation.

An overview of the TOF recordings is given in Figure 13-9. Originally, the geometry of the inner contour should form a perfect square, reflecting the orthotropic nature of the $[-45,+45]_s$ C/E sample. However, because of human error during the stacking of the carbon prepreg layers, this is not exactly valid. Indeed, the TOF recorded P-UPS of the virgin sample reveals that the different fiber directions have an overlap angle of $\eta = 91.5°$. Hence, the manufactured material cannot be considered perfectly orthotropic, i.e. the principal axes do not coincide with the orientation of the fiber reinforcement and therefore, the inner contour is not a perfect square. However, for the remainder, let us assume that the stacking was done correctly, and that the virgin material possesses perfect orthotropic symmetry, thus having a squared inner contour.

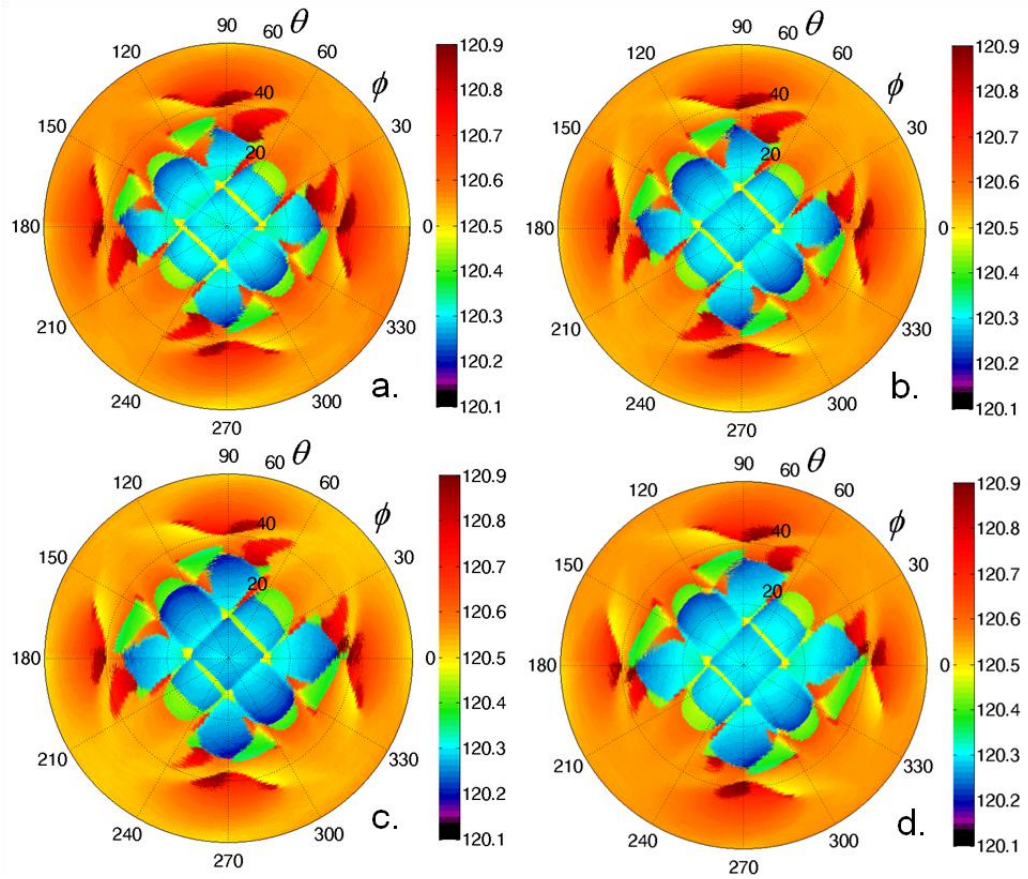

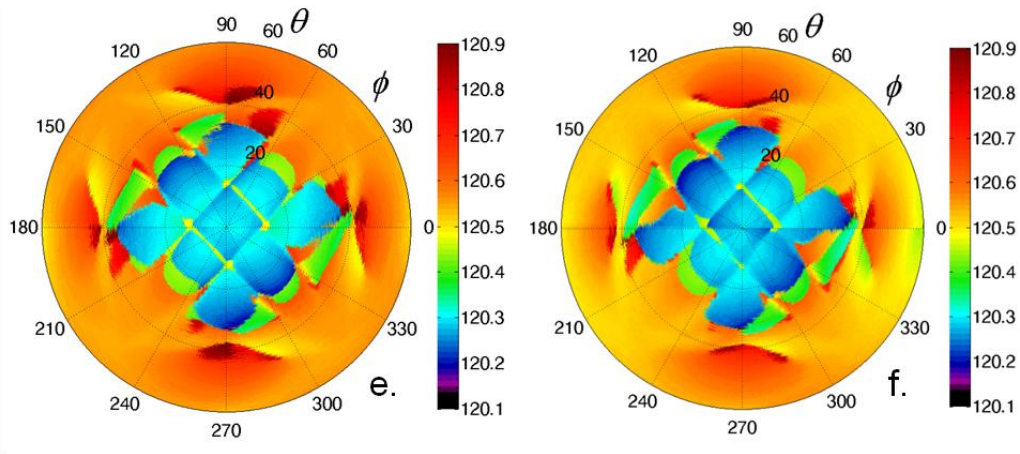

Figure 13-9: TOF recorded P-UPS results for a $[-45,+45]_S$ UD C/E laminate: τ_0 = 0 MPa (virgin specimen) (a), τ_1 = 43 MPa (b), τ_2 = 55 MPa (c), τ_3 = 62 MPa (d), τ_4 = 65 MPa (e) and τ_F = 90.5 MPa (failed specimen) (f).

After applying the first load level, the inner square of the TOF recorded P-UPS already shows a change in topology with respect to the reference. The inner contour is not a square anymore, but is rhomboid. As a consequence, the degraded material cannot be considered anymore to be globally orthotropic of nature, but effectively acquired a lower anisotropic symmetry as a consequence of the applied loading. The importance of this observation cannot be overrated since at present most modeling and simulation tools hold onto a predefined symmetry class and, consequently, do not cope with a possible symmetry transformation of the structure upon loading. Further increase of the load level leads to further distortion of the fiber orientation until finally the specimen failed. The results clearly indicate the relation between the observed fiber distortion and the applied shear load level. A close up of the TOF recorded P-UPS result for both the virgin and the failed specimen is given in Figure 13-10, together with a measure of the overlap angle η. A global fiber distortion of η = 10°, with respect to the original fiber orientations has been extracted.

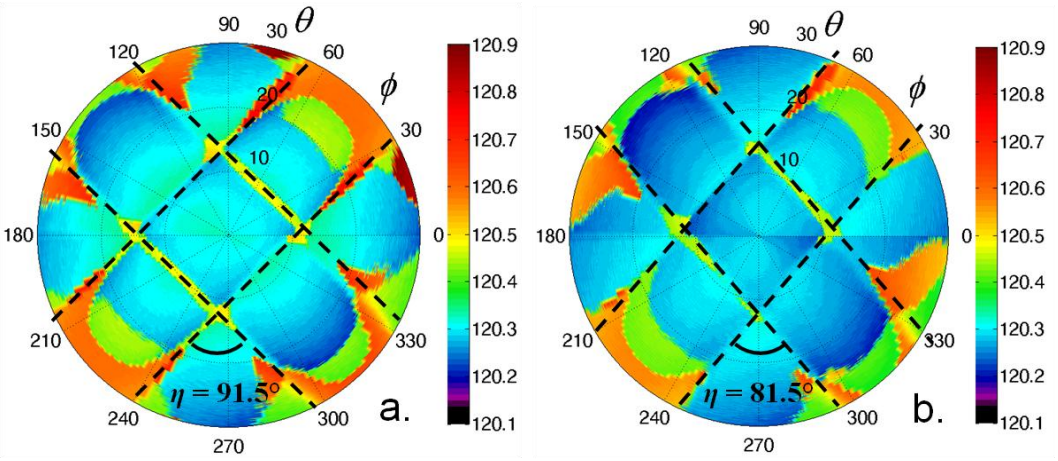

Figure 13-10: Close up of the TOF recorded P-UPS results shown in: Figure 13-9a (a) and Figure 13-9f (b). Dashed lines are superimposed to accentuate the distortion of the fibers after loading, the extracted overlap angle η is added.

This value is consistent with recent X-ray computed tomography results [1, 37], and is also fully supported by optical investigation. A microscopic photograph of the failed region of the C/E laminate is presented in Figure 13-11, showing a total angular distortion of $\eta = 13.5°$. Since the P-UPS measurements were obtained at a distance of ~40 mm from this failure location, it is clear that the final P-UPS extracted fiber distortion has to be lower. The much lower fiber distortion in case of the previously discussed glass/epoxy laminate is most probably invoked by the binding yarns which resist angular distortion.

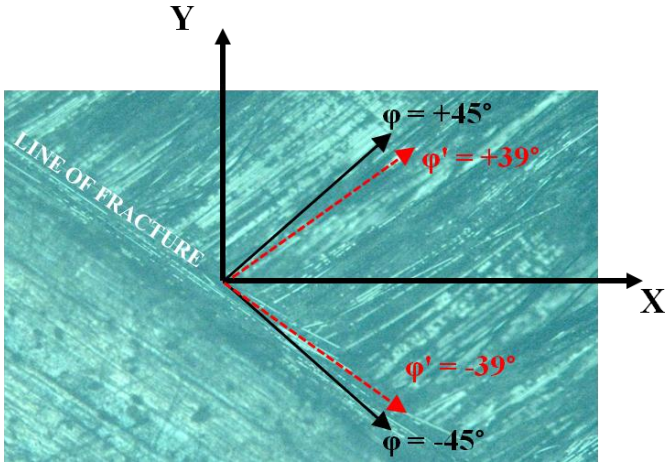

Figure 13-11: Microscopy of the failed region. The black arrows denote the virgin fiber orientations, the red arrows denote the distorted fiber orientations.

The P-UPS extracted opening angles η for all applied stress levels are listed in Table 13-3. The large fiber distortion, which takes place towards the loading direction, obviously explains the slight increase in 'shear properties' with loading. In fact, the present analysis of the stress-strain curve is not valid whenever an angular distortion is present. These results also indicate that the interpretation of P-UPS data for damaged composites has to be done with caution. Indeed, an ultrasonic wave generates typically small strains and, as a consequence, the P-UPS gives a measure of the stiffness properties at the onset of loading. On the other hand, the apparent shear modulus $G_{12}^{'*}$ is typically used to cope with the non-linear behavior of shear damaged composites. Nevertheless, it is clear that the P-UPS technique comprises a nondestructive measure of both $G_{12}^{'}$ and the angular distortion, and thus is a useful tool for quantifying damaged composites.

13. 5. Conclusions

Several fiber reinforced composites, subjected to various static damage mechanisms, have been investigated with the P-U(B)PS method in order to (semi-)quantify material degradation. Focus is put on stiffness-related material degradation phenomena. Results have been presented and discussed for stiffness reduction related to errors in stacking sequence as well as material degradation induced by shear-dominated quasi-static hysteresis loading (a small number of sequential loading-unloading cycles).

It is shown that P-UPS can detect and quantify local deviations in the prescribed stacking sequence. The P-UPS results for the shear loaded specimens on the other hand show different features, depending on the type of fiber reinforced plastic. For the viscoelastic glass/epoxy sample, a clear reduction in global shear properties is obtained by means of the P-UPS technique. The results for the brittle C/E laminate, on the other hand, do not show a significant reduction of the shear properties upon loading. However, the P-UPS results clearly indicate the relation between the observed fiber distortion and the applied shear load level. The P-UPS extracted characteristics are fully supported by literature, simulations, conventional tests as well as visual inspection.

The present results show the great potential of the P-UPS method to monitor stiffness-related damage phenomena in fiber reinforced composites. The fact

that the P-UPS method puts on view local damage characteristics from which the extent and directionality of the material degradation can be directly obtained in a (semi-)quantitative way has great appeal. The next chapter extends the analysis to fiber reinforced plastics, subject to high cycle fatigue loading.

13. 6. References

[1] Sket, F., A. Enfedaque, C. Alton, C. González, J.M. Molina-Aldareguia, and J. Llorca, *Automatic quantification of matrix cracking and fiber rotation by X-ray computed tomography in shear-deformed carbon fiber-reinforced laminates.* Composites Science and Technology, 2014. 90(0): p. 129-138.

[2] Zastavnik, F., L. Pyl, J. Gu, H. Sol, M. Kersemans, and W. Van Paepegem, *Comparison of Shearography to Scanning Laser Vibrometry as Methods for Local Stiffness Identification of Beams.* Strain, 2013.

[3] Van den Abeele, K.E.A., P.A. Johnson, and A. Sutin, *Nonlinear elastic wave spectroscopy (NEWS) techniques to discern material damage, part I: Nonlinear wave modulation spectroscopy (NWMS).* Research in Nondestructive Evaluation, 2000. 12(1): p. 17-30.

[4] Armitage, P.R. and C.D. Wright, *Design, development and testing of multi-functional non-linear ultrasonic instrumentation for the detection of defects and damage in CFRP materials and structures.* Composites Science and Technology, 2013. 87: p. 149-156.

[5] Solodov, I.Y., N. Krohn, and G. Busse, *CAN: an example of nonclassical acoustic nonlinearity in solids.* Ultrasonics, 2002. 40(1-8): p. 621-625.

[6] Wooh, S.C. and C. Wei, *A high-fidelity ultrasonic pulse-echo scheme for detecting delaminations in composite laminates.* Composites Part B-Engineering, 1999. 30(5): p. 433-441.

[7] Auld, B.A. and J.C. Moulder, *Review of advances in quantitative eddy current nondestructive evaluation.* Journal of Nondestructive Evaluation, 1999. 18(1): p. 3-36.

[8] Liao, T.W. and J.W. Ni, *An automated radiographic NDT system for weld inspection .1. Weld extraction.* Ndt & E International, 1996. 29(3): p. 157-162.

[9] Liao, T.W. and Y.M. Li, *An automated radiographic NDT system for weld inspection: Part II - Flaw detection.* Ndt & E International, 1998. 31(3): p. 183-192.

[10] Busse, G., D. Wu, and W. Karpen, *Thermal wave imaging with phase sensitive modulated thermography.* Journal of Applied Physics, 1992. 71(8): p. 3962-3965.

[11] Manohar, A. and F.L. di Scalea, *Determination of Defect Depth and Size Using Virtual Heat Sources in Pulsed Infrared Thermography.* Experimental Mechanics, 2013. 53(4): p. 661-671.

[12] Kim, J.T. and N. Stubbs, *Improved damage identification method based on modal information.* Journal of Sound and Vibration, 2002. 252(2): p. 223-238.

[13] Kim, J.T., Y.S. Ryu, H.M. Cho, and N. Stubbs, *Damage identification in beam-type structures: frequency-based method vs mode-shape-based method.* Engineering Structures, 2003. 25(1): p. 57-67.

[14] Carden, E.P. and P. Fanning, *Vibration based condition monitoring: A review.* Structural Health Monitoring, 2004. 3(4): p. 355-377.

[15] Rippert, L., M. Weavers, and S. Van Huffel, *Optical and acoustic damage detection in laminated CFRP composite materials.* Composites Science and Technology, 2000. 60(14): p. 2713-2724.

[16] Whitworth, H.A., *A stiffness degradation model for composite laminates under fatigue loading.* Composite Structures, 1997. 40(2): p. 95-101.

[17] Whitworth, H.A., *Evaluation of the residual strength degradation in composite laminates under fatigue loading.* Composite Structures, 2000. 48(4): p. 261-264.

[18] Wisnom, M.R., *THE EFFECT OF FIBER ROTATION IN +/-45-DEGREES TENSION TESTS ON MEASURED SHEAR PROPERTIES.* Composites, 1995. 26(1): p. 25-32.

[19] Van Paepegem, W., I. De Baere, and J. Degrieck, *Modelling the nonlinear shear stress-strain response of glass fibre-reinforced composites. Part I: Experimental results.* Composites Science and Technology, 2006. 66(10): p. 1455-1464.

[20] Van Paepegem, W., I. De Baere, and J. Degrieck, *Modelling the nonlinear shear stress-strain response of glass fibre-reinforced composites. Part II: Model development and finite element simulations.* Composites Science and Technology, 2006. 66(10): p. 1465-1478.

[21] De Baere, I., W. Van Paepegem, and J. Degrieck, *Modelling the Nonlinear Shear Stress-Strain Behavior of a Carbon Fabric Reinforced Polyphenylene Sulphide From Rail Shear and (45 degrees,-45 degrees) (4s) Tensile Test.* Polymer Composites, 2009. 30(7): p. 1016-1026.

[22] Vandreumel, W.H.M. and J.L. Speijer, *Non-destructive composite laminate characterization by means of ultrasonic polar-scan.* Materials Evaluation, 1981. 39(10): p. 922-925.

[23] Degrieck, J., N.F. Declercq, and O. Leroy, *Ultrasonic polar scans as a possible means of non-destructive testing and characterisation of composite plates.* Insight, 2003. 45(3): p. 196-201.

[24] Declercq, N.F., J. Degrieck, and O. Leroy, *Ultrasonic polar scans: Numerical simulation on generally anisotropic media.* Ultrasonics, 2006. 45(1-4): p. 32-39.

[25] Declercq, N.F., J. Degrieck, and O. Leroy, *Simulations of harmonic and pulsed ultrasonic polar scans.* Ndt & E International, 2006. 39(3): p. 205-216.

[26] Kersemans, M., A. Martens, K. Van Den Abeele, J. Degrieck, L. Pyl, F. Zastavnik, H. Sol, and W. Van Paepegem, *The Quasi-Harmonic Ultrasonic Polar Scan for Material Characterization: Experiment and Numerical Modeling.* Accepted for publication in Ultrasonics, 2014.

[27] Rose, J.L., *Ultrasonic Waves in Solid Media*. 1999: Cambridge University Press. 454.

[28] Auld, B.A., *Acoustic Fields and Waves in Solids, second edition*. 1990, Florida: Krieger publishing company. 856.

[29] Kersemans, M., N. Lammens, G. Luyckx, J. Degrieck, and W. Van Paepegem, *Quantitative Measurement of the Elastic Properties of Orthotropic Composites by means of the Ultrasonic Polar Scan Method.* JEC Composites, 2012. 75(75): p. 48 - 52.

[30] Kersemans, M., K. Van Den Abeele, N. Lammens, J. Degrieck, F. Zastavnik, J. Gu, L. Pyl, H. Sol, and W. Van Paepegem. *Determination of the Fiber Direction and the C-Tensor of a UD Carbon/Epoxy Composite by means of the Ultrasonic Polar Scan*. in *Proceedings of the 2013 International Congress on Ultrasonics (ICU 2013)*. 2013. Singapore.

[31] Kersemans, M., A. Martens, N. Lammens, K. Van Den Abeele, J. Degrieck, F. Zastavnik, L. Pyl, H. Sol, and W. Van Paepegem, *Identification of the elastic properties of isotropic and orthotropic thin-plate materials with the pulsed ultrasonic polar scan.* Experimental Mechanics, 2014. In Press DOI: 10.1007/s11340-014-9861-7.

[32] Daggumati, S., I. De Baere, W. Van Paepegem, J. Degrieck, J. Xu, S.V. Lomov, and I. Verpoest, *Fatigue and post-fatigue stress-strain analysis of a 5-harness satin weave carbon fibre reinforced composite.* Composites Science and Technology, 2013. 74: p. 20-27.

[33] Hwang, W. and K.S. Han, *CUMULATIVE DAMAGE MODELS AND MULTI-STRESS FATIGUE LIFE PREDICTION.* Journal of Composite Materials, 1986. 20(2): p. 125-153.

[34] Herakovich, C.T., *Mechanics of Fibrous Composites*. 1998, New York: John Wiley & Sons. 460.

[35] Kersemans, M., A. Martens, K. Van Den Abeele, J. Degrieck, L. Pyl, F. Zastavnik, H. Sol, and W. Van Paepegem, *Detection and localization of delaminations in thin carbon fiber reinforced composites with the ultrasonic polar scan.* Journal of Nondestructive Evaluation, 2014. In Press DOI: 10.1007/s10921-014-0249-5.

[36] Zitoune, R., L. Crouzeix, F. Collombet, T. Tamine, and Y.H. Grunevald, *Behaviour of composite plates with drilled and moulded hole under tensile load.* Composite Structures, 2011. 93(9): p. 2384-2391.

[37] Sket, F., A. Enfedaque, C. Alton, C. Gonzalez, J.M. Molina-Aldareguia, and J. Llorca, *X-Ray Tomography Assessment of Shear Damage in Carbon Fiber Laminates*, in *6th International Conference on Composites Testing and Model Identification – CompTest 2013*. 2013: Aalborg, Denmark.

Chapter 14

P-UPS Signature of Fatigue Damage in Textile Composites

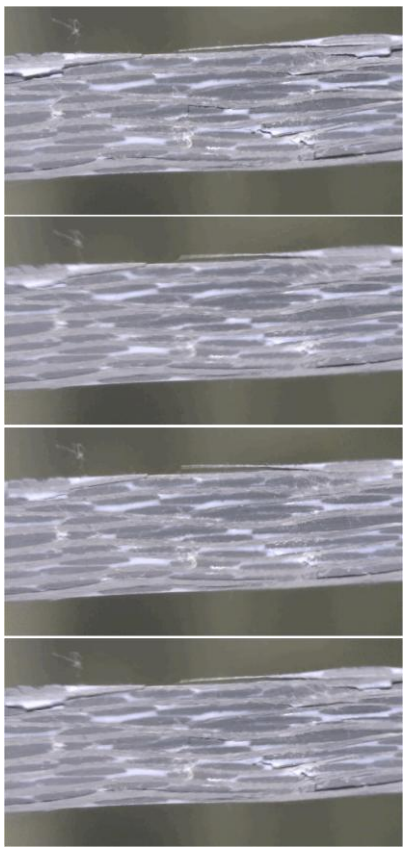

Subsequent microscopic pictures of damage features in a textile composite, induced during tension-tension fatigue loading.

Overview

In analogy with the previous chapter, the response of fabric reinforced plastics to different types of fatigue loading is investigated with the P-UPS technique. Several thermoplastic carbon fabric reinforced plastics (CETEX) loaded under various fatigue conditions have been scanned at multiple material spots according to the P-UPS technique. Several indicators have been identified in the P-UPS map which expose the type, the location, the directionality as well as the extent of material degradation. The P-UPS extracted characteristics are fully supported by literature, simulations, visual inspection as well as conventional destructive test procedures .

14. 1. Introduction

It is well known for fiber reinforced plastics that loading, and in particular fatigue loading, has an elasticity related damage signature. Indeed, fatigue loading leads to the initiation, progression and accumulation of micro defects, which manifest themselves in a directional reduction of the stiffness properties at the macro level [1-7]. However, the application of the UPS technique for nondestructive detection and evaluation of fatigue damage in fiber-reinforced plastics has hardly been investigated. There is some account on this subject [8], though that study showed a single amplitude-based P-UPS experiment for a tension-tension fatigued glass fabric reinforced plastic which only underwent 39,060 load cycles at 60% of its ultimate tensile strength (UTS). In general, it can be stated that these settings correspond to a very mild fatigue loading. The presented P-UPS experiment showed poor distinctness and clarity of characteristic contours, and was furthermore only partially captured making the interpretation difficult when considering the many pitfalls which could occur during the experimental recording of a P-U(B)PS (see Chapter 5). In fact, the observed features in that study indicate a global stiffness reduction, which contradicts common sense. To concretize, for a composite one would expect a softening of the stiffness along the loading direction due to transverse matrix cracks when subjected to unidirectional tension-tension fatigue loading [9-12]. In addition, the

obtained results have only been discussed in a limited qualitative matter, with no attempt to map or estimate the induced material damage.

Hence, it is clear that additional and more thorough experimental data is required to make trustworthy observations. For these reasons, multiple fabric reinforced plastics have been fatigued under various loading conditions (both in tension and in shear). The material under investigation is a carbon fabric reinforced plastic, which is already in use as a structural component in the Airbus A380. It is clear that those components are subject to fatigue loading during their lifetime, emphasizing the necessity to understand, and even monitor, their material response. It can be expected that the here considered material shows an equivalent, but less pronounced, response to fatigue loading when compared to a glass fabric reinforced plastic such as the one considered in reference [8]. The various samples have been scanned before and after the fatigue loading, considering both the amplitude and the TOF value. The P-UPS experiments have been performed at multiple locations in order to spatially map fatigue related damage features.

14. 2. Materials and Methods

Several carbon fabric reinforced polyphenylene sulphide (PPS) samples, called CETEX (Ten Cate, The Netherlands), have been subjected to fatigue loading, both in tensile and shear. The fiber type is the carbon T300J 3K and the weaving pattern is a 5-harness satin weave with a mass per surface unit of 286 g/m^2. The material thickness corresponds to d = 2.5 mm. The amplitude-based P-UPS experiment for the virgin CETEX material is shown in Figure 14-1 considering a broadband pulse with frequency f_c = 2 MHz and f_c = 5 MHz.

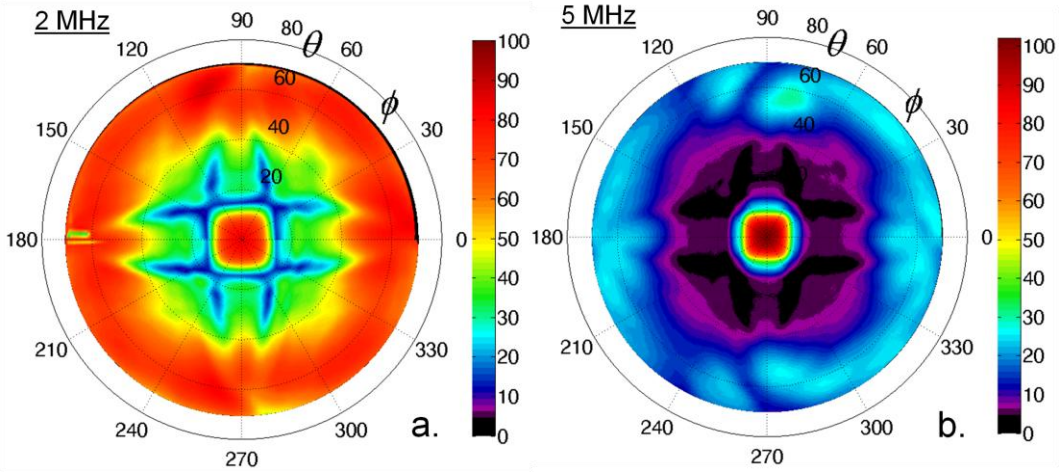

Figure 14-1: P-UPS result (amplitude) for virgin $[0°,90°]_{4s}$ CETEX fabric: f = 2 MHz (a) and f = 5 MHz (b).

It is clear that the 5 MHz recording leads to a largely reduced transmission characteristic due to the damping properties of the CETEX material. Similar as in reference [8], poorly detailed results are obtained which obviously complicate the extraction of features, and in extension the assessment of fatigue damage. Therefore, a pulse with central frequency f_c = 2 MHz has been employed for the results shown in this chapter. The other settings are analogous to previous investigations in this dissertation. P-UPS experiments have been performed before and after applying the fatigue cycles, in order to identify any damage signature associated to fatigue loading.

Tension-tension fatigue loading has been applied on two stacking sequences, $[+45°,-45°]_{4s}$ and $[0°,90°]_{4s}$, while a $[0°,90°]_{4s}$ has also been loaded in a rail shear setup. All the fatigue tests have been performed on a servo-hydraulic INSTRON 8801 testing machine with FastTrack controller 8800.

- The $[+45°,-45°]_{4s}$ sample is cut at a length of 250 mm and a width of 30 mm, and has been subjected to tension-tension fatigue loading at a frequency of 2 Hz, which thus corresponds to shear-dominated fatigue. The fatigue loading, with shear stress range [0-50 MPa], has been manually stopped after ±135,000 load cycles without fracture of the sample.

  A square $[0°,90°]_{4s}$ CETEX sample was placed in a rail shear setup inducing a loading with shear stress range [0-50 MPa] at a frequency of 2 Hz. A photograph of the rail shear setup, together with a schematic of

the induced deformation, is shown in Figure 14-2. The fatigue cycle has been manually stopped after ±63,000 load cycles without fracture of the sample.

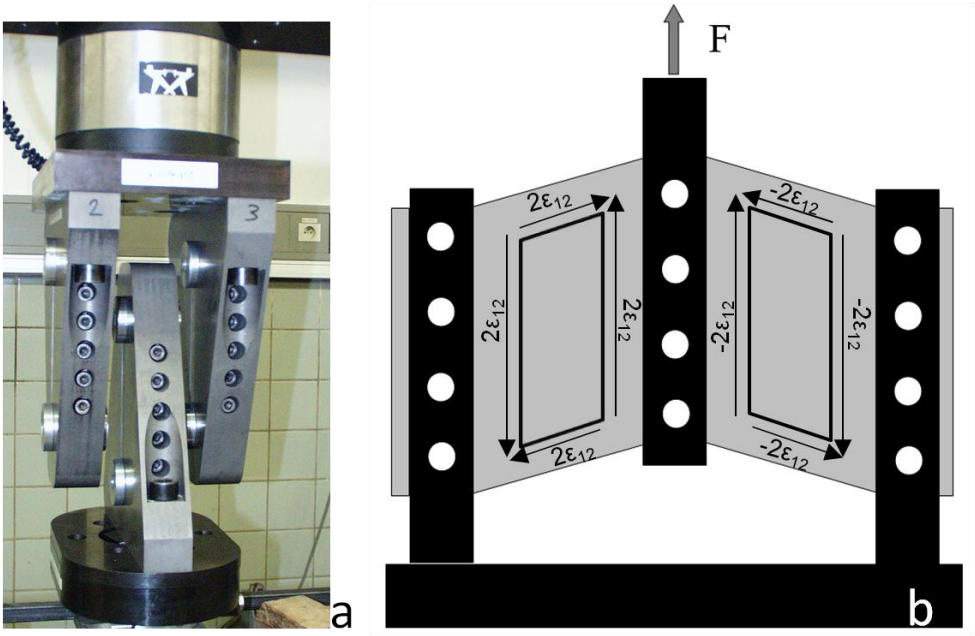

Figure 14-2: Rail shear setup mounted on the tensile machine (a) and schematic of the rail shear setup with the induced deformation (b).

- Several $[0°,90°]_{4s}$ CETEX samples with a dumbbell shape have been prepared. Recently, it has been shown that this specific geometry shows an excellent performance during tension-tension fatigue for this specific material [13]. The UTS of the CETEX material is determined at 760MPa. The specimens have been subjected to different tension-tension fatigue cycles at various load levels, until sudden failure of the specimens occurred:
  - Sample 1: 55 load cycles with stress range [0-700 MPa] (92% UTS) at a frequency of 2 Hz.
  - Sample 2: 99,123 load cycles with stress range [0-650 MPa] (86% UTS) at a frequency of 5 Hz.
  - Sample 3: 314,111 load cycles with stress range [0-625 MPa] (82% UTS) at a frequency of 5 Hz.

Where possible, the specimens have been equipped with a clip-on extensometer and thermocouple. As such, the axial strain, load, actuator displacement and temperature have been measured simultaneously.

In analogy with previous chapter, P-UPS simulations [14-16] have been performed for a virgin and degraded CETEX fabric when considering pulsed ultrasound with center frequency f_c = 2 MHz (see Figure 14-3). Here, we model the fabric as if it consists of 16 unidirectional laminae stacked in a [0°,90°] sequence. The complex-valued symmetrical stiffness tensor $C = C' + iC''$ for each lamina is listed in Table 14-1.

Table 14-1: Material properties used for the P-UPS simulation shown in Figure 14-3a. The parameters *k* and *m* are set to 1 or to 0.7, in order to explore the influence of changed material parameters on the P-UPS image.

LIQUID		**SOLID**	
K [GPa]	2.2	E_{11} [GPa]	$103 \cdot (\boldsymbol{k} - 0.06i)$
		E_{22} [GPa]	$13.7 \cdot (1 - 0.4i)$
		E_{33} [GPa]	$13.7 \cdot (1 - 0.04i)$
		$\nu_{12} = \nu_{13}$ [-]	$0.29 \cdot (1 - 0.02i)$
		ν_{23} [-]	$0.35 \cdot (1 - 0.04i)$
		G_{12} [GPa]	$4.28 \cdot (\boldsymbol{m} - 0.05i)$
		G_{13} [GPa]	$3.1 \cdot (1 - 0.02i)$
		G_{23} [GPa]	$3.1 \cdot (1 - 0.02i)$
ρ [kg/m^3]	1000	ρ [kg/m^3]	1600

It has been verified that the P-UPS simulation for a CETEX fabric with homogenized elasticity constants (see table 4 in reference [17]) basically shows equivalent features as our current modeling approach. This can be easily understood considering the large number of thin laminae which have a homogenization effect for ultrasonic waves. For simulating fiber distortions, the current modeling approach is found to be advantageous. Considering the results of previous chapter, it may be expected that shear-dominated fatigue loading results in large fiber distortions.

The simulation for the virgin CETEX material is shown in Figure 14-3a. Note that the contour associated with the shear vertically polarized bulk wave is not visible because of the rather low G'_{13} and G'_{23} values. Since the immersion liquid acts as a 'lens' for the P-UPS [18], one could employ a different liquid in order to get a zoomed out P-UPS image (see Section 6.4).

Though, this is not considered here. The effect of a 30% reduction of stiffness $E_{11}^{'}$ in the 0°-laminae is shown in Figure 14-3b. One observes a stretching of the inner polar contour, in correspondence with the physical interpretation given in Section 2.3.2. Reduction of the shear modulus $G_{12}^{'}$ by 30% is displayed in Figure 14-3c, leading to a stretching of the cross-shaped contour. Figure 14-3d displays the P-UPS image when, in addition to the reduction of $G_{12}^{'}$, a fiber distortion of 8° is considered. It is clear that these features are well represented in the P-UPS image and can be easily identified by the positional shifting of the P-UPS contours.

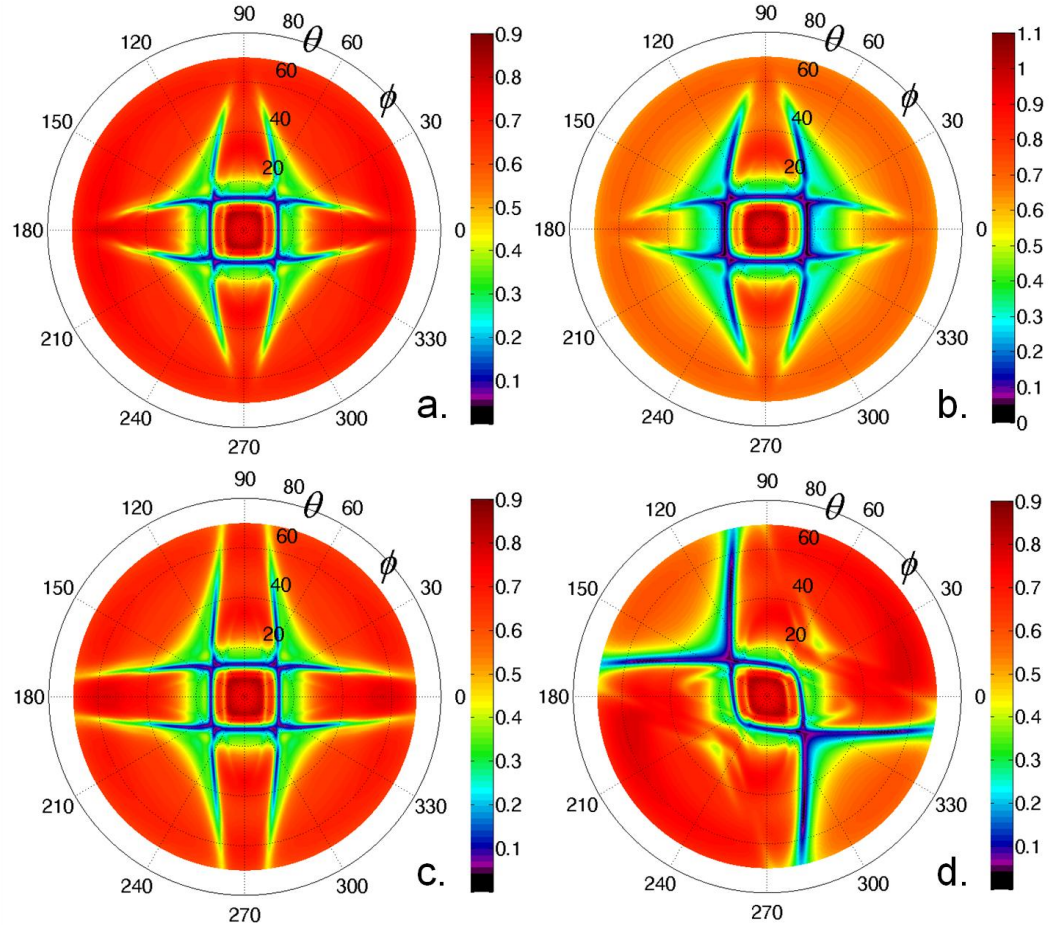

Figure 14-3: P-UPS simulation of CETEX fabric (material parameters are listed in Table 14-1) with thickness 2.5 mm at central frequency f_c = 2 MHz: $[0°,90°]_{4s}$ with $k = m = 1$ (virgin material) (a), $[0°,90°]_{4s}$ with $k = 0.7$ and $m = 1$ (b), $[0°,90°]_{4s}$ with $k = 1$ and $m = 0.7$ (c) and $[8°,82°]_{4s}$ with k = 1 and m = 0.7 (d).

14. 3. Results and Discussion

14. 3. 1. Shear-dominated Fatigue Loading

The P-UPS results for the virgin $[+45°,-45°]_{4s}$ CETEX sample are presented in Figure 14-4. The geometrical shape of the P-UPS image reflects the perfect orthotropic nature of the investigated CETEX sample, i.e. the principal axes of orthotropy coincide with the fiber reinforcement structure.

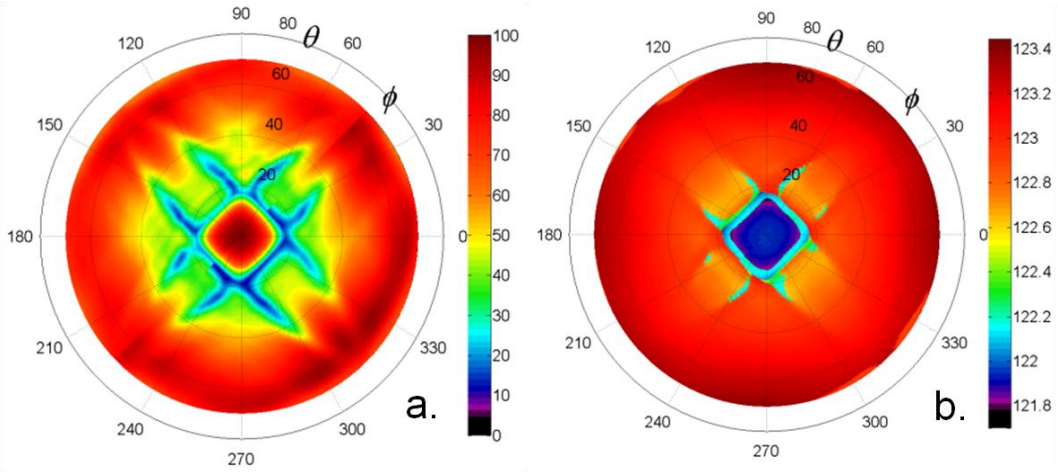

Figure 14-4: P-UPS result for virgin $[+45°,-45°]_{4s}$ CETEX fabric: amplitude (a) and TOF (b) recording.

The $[+45°,-45°]_{4s}$ fabric has first been subjected to a running-in load cycle: the desired shear stress level of 50 MPa is achieved by cyclic loading and unloading at the frequency $f = 2$ Hz, while gradually increasing the tensile force (see Figure 14-5a). After this initiation process, the fatigue loading itself takes place until the test has been manually stopped after ±135,000 load cycles without failure of the specimen. The variation in longitudinal strain ε_{xx} as well as the temperature evolution during fatigue is shown in Figure 14-5b. The sudden temperature rise near the end of the fatigue loading originates from the internal friction of both multiple matrix cracks and overlapping fibers. Together with the temperature T, the longitudinal strain evolves in a similar way, which is a strong indicator that the material effectively underwent severe damage.

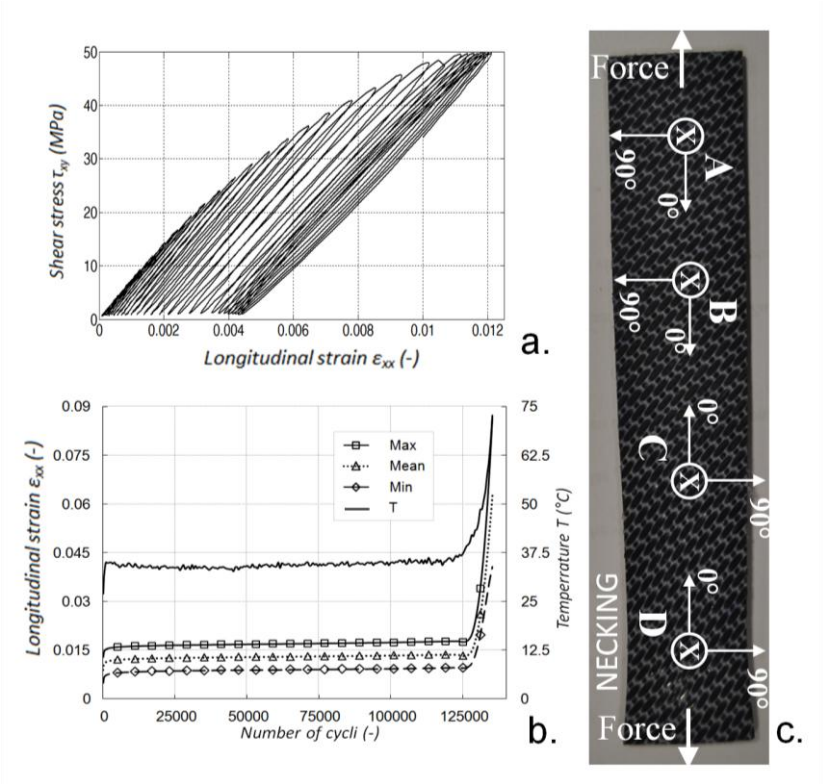

Figure 14-5: Running-in load cycles (a), evolution of longitudinal strain ε_{xx} and temperature *T* during fatigue loading (b) and photograph of shear dominated fatigued CETEX fabric (c). The labels denote the P-UPS scan locations, while the added coordinate systems coincide with the polar directions in the corresponding P-UPS images.

A photograph of the specimen after fatigue loading is shown in Figure 14-5c, here necking of the specimen can be clearly observed. Both TOF and amplitude P-UPS have been obtained at four different locations, which basically can be categorized from little visual damage (A and B) over reasonable visual damage (C) to severe visual damage (D).

With respect to the P-UPS results of the virgin material, the results at scan location A (see Figure 14-6a-b) do not reveal any significant changes, implying that the material can be considered to be locally intact, in accordance with visual inspection.

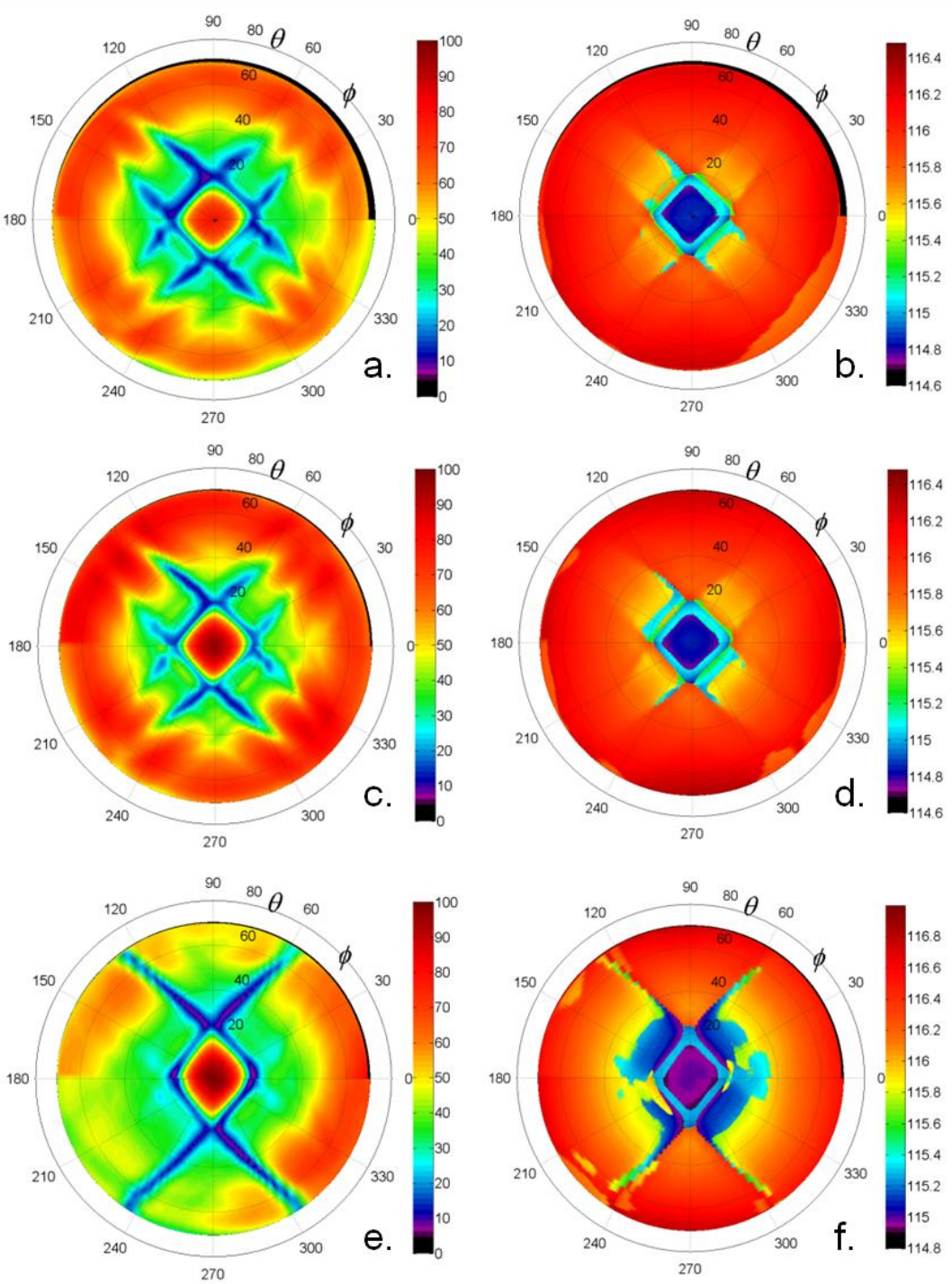
a.
b.
c.
d.
e.
f.
θ
ϕ

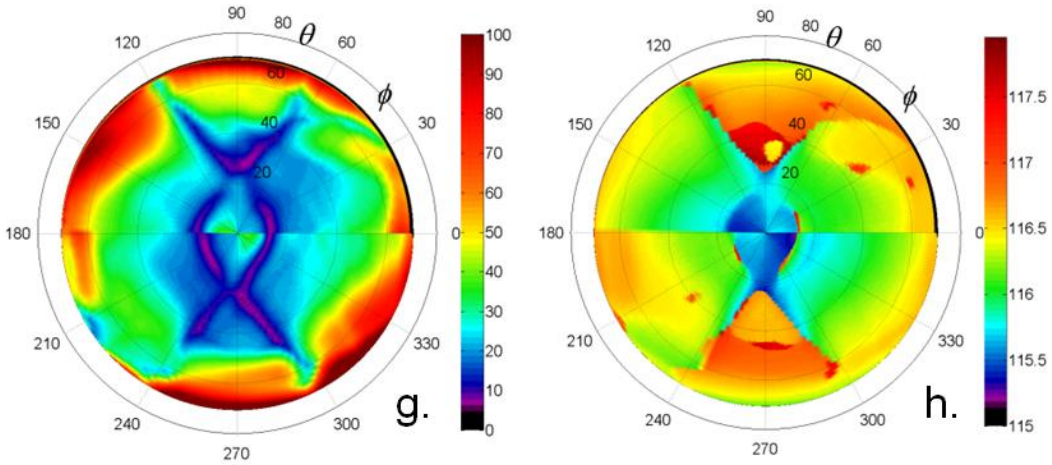

Figure 14-6: P-UPS results for a shear-dominated fatigued $[+45°,-45°]_{4s}$ CETEX fabric: amplitude (left column) and TOF (right column) recording. Material spot A (a-b), material spot B (c-d), material spot C (e-f) and material spot D (g-h).

This is clearly not valid anymore for scan location B (Figure 14-6c-d). The inner QL-contour does not resemble a square anymore, but is rhomboid. In addition, the amplitude recorded P-UPS reveals that the cross-like contour, which is connected to the shear properties, is subjected to both a shortening and lengthening of its branches. These features indicate that the initially perfect orthotropic material locally transformed to a lower symmetry class.

These indicators become even more outspoken at scan location C, both in the amplitude and the TOF recording (Figure 14-6e-f). First of all, one could actually question whether the principal axes of orthotropy, which are here defined as that direction with highest stiffness and its normal, have rotated over 45° with respect to the virgin sample. Indeed, along $\varphi = 0°$, the inner contour has shrunk from 18.1° to 17.25°. Assuming that the physical interpretation of Section 2.3.2 is still valid for damaged materials, this implies that the global stiffness of the sample in that particular direction increases. On the contrary, along $\varphi = 90°$ the opposite takes place as the inner contour widens, i.e. the loading induces a directional weakening of the sample. This directional strengthening and weakening of the material is easily understood when considering the angular distortion of the fibers upon shear loading. Secondly, the observed phenomena in the shear-related contour become very prominent. Although some minor artifacts are left from the 8 branches of the original cross-like contour, the contour basically

transformed its topology into 4 symmetric long branches, further indicating the directional nature of the damage. Note the good agreement with the numerical result (rotated over 45°) displayed in Figure 14-3d. It is also interesting to note that incidence angles which were initially equivalent ($\psi(\varphi,\theta)$ and $\psi(\varphi+\pi,\theta)$) in the amplitude map, are not equivalent anymore. Indeed, the recorded amplitude map does not possess any point symmetry anymore. This can be understood by considering that the scanned material spot has a slightly asymmetric corrugated surface due to damage accumulation, which makes the coupling efficiency of the ultrasonic waves dependent upon the exact entrance angle. It is further noted that the time scale of the TOF recorded P-UPS spans a larger range. In other words, in some material directions, the ultrasonic signal needs more time to traverse the sample, and thus propagates at a lower rate. Obviously, this is an additional indicator of the presence of material damage.

Finally, the most heavily damaged spot (D) is investigated. The distortion of the local fiber orientation becomes even worse, and reaches a maximum rotation of more or less 13°. With X-ray, fiber distortions in the same order of magnitude have already been measured for composites loaded in a quasi-static shear state [19]. Note that the extracted distortion is on average since each layer has its own distortion level. In fact, the broadening (in θ-direction) of the inner contour in the amplitude recorded P-UPS suggests that this is exactly what is happening. The appearance of such large fiber distortions can be understood by realizing that the CETEX material belongs to the class of thermoplastics. Hence, the temperature rise during cyclic loading (see Figure 14-5b) brings the PPS matrix close to its softening temperature ($T_g \approx 85$°C), making it relatively easy for the fibers to realign upon loading. For similar composites, we have even measured temperatures up to 110°C at the necking area. The extracted values for the distorted local fiber distribution are listed in Table 14-2 for all scan positions. Since the surface of the sample is marked with a characteristic pattern (see Figure 14-5c), we also determined optically the local fiber distortion of the outer layers. However, note that the optically determined values could deviate from the actual internal fiber distribution.

Table 14-2: Ultrasonically and optically extracted local fiber orientation for the $[+45°,-45°]_{4s}$ CETEX fabric subjected to shear dominated fatigue loading.

Scan Location	Virgin	A	B	C	D
P-UPS	-45° +45°	-46° (-1°) +44° (-1°)	-40 (+5) +42 (-3)	-37° (+8°) +37° (-8°)	-31° (+14°) +34° (-11°)
Optical	-45° +45°	-45° (0°) +44° (-1°)	-41° (+4°) +42° (-3°)	-38° (+7°) +38° (-7°)	-33° (+12°) +36° (-9°)

The amplitude recorded P-UPS further shows that that part of the transmission field dominated by QL polarized waves ($\theta < 20°$) drops in amplitude level, thus making the sample QL opaque. This is most probably related to scattering of QL polarized waves on damage related geometrical discontinuities [20]. However, the opposite is observed for large incident angles ($\theta > 60°$). The transmission field, which is now dominated by QSV polarized waves, reveals a significant increase in transmitted amplitude. In fact, saturation is observed. Hence, the induced damage effectively works as a catalyst for QSV polarized waves, making the sample close to QSV transparent. This could be due to the high temperature level attained during loading, which weakens the PPS matrix and thus could influence its crystalline structure. The TOF recorded P-UPS at spot D reveals a further increase of the range of the time scale. For the virgin material, the range amounts $\Delta t = 1.85$ µs, while material spot D shows a range of $\Delta t = 2.85$ µs. Note that the increased travel time mainly manifests itself in certain material orientations, which again accentuates the directional nature of the induced fatigue damage.

The present results clearly show that the induced damage has a very local characteristic, i.e. the damage level gradually increases towards the necking zone, while the damage possesses a directional dependency. This implies that a mapping of damage induced by shear-dominated fatigue has to be done in a local and multidirectional way. Both the amplitude and TOF recorded P-UPS results offer several indicators which can be used to assess shear-dominated fatigue damage. It is found that the local fiber distortion is an important and straightforward indicator to monitor fatigue in shear loading for the CETEX laminate. The present results even suggest that the principal axes of orthotropy for the fatigued sample are effectively rotated over 45°. Indeed, the induced fiber distortion leads to a stiffening of the sample along the loading direction. The position θ_{QL} of the inner contour, which is inversely proportional to the stiffness, has been extracted along

φ = 0° for all scan positions: [$\theta_{QL}^{REF}, \theta_{QL}^{A}, \theta_{QL}^{B}, \theta_{QL}^{C}, \theta_{QL}^{D}$] = [18.1°,18.05°, 17.6°,17.25°, 14.2°].

It has been found that equivalent results are obtained for the $[0,90]_{4s}$ CETEX sample fatigued in a rail shear setup. For brevity however, only few results are given here. The CETEX sample tested in the rail shear setup is shown in Figure 14-7: one can clearly identify the geometrical distortion of the sample. The recorded P-UPS images at the shear-damaged zone are presented in Figure 14-8. The correspondence with Figure 14-6g-h is evident. The discussion of the above shear loaded $[+45°,-45°]_{4s}$ CETEX sample is equally valid for the $[0°,90°]_{4s}$ CETEX fabric loaded in a rail shear setup. Though, it is noted that the $[0°,90°]_{4s}$ CETEX sample is characterized by large fiber distortions of mainly the 0° layers, while the 90° layers are less affected.

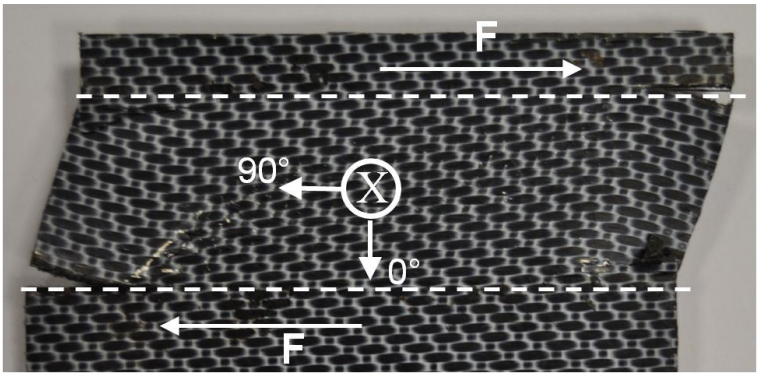

Figure 14-7: Photograph of the $[0°,90°]_{4s}$ CETEX specimen fatigued in a rail shear setup.

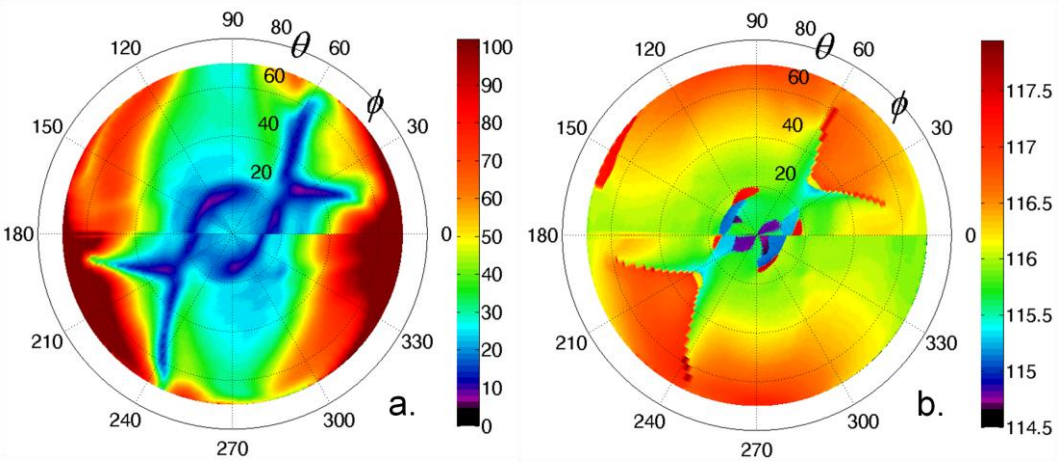

Figure 14-8: P-UPS results for a $[0°,90°]_{4s}$ CETEX fabric fatigued in a rail shear setup: amplitude (a) and TOF (b) recording

14. 3. 2. Tensile fatigue loading

In analogy with previous paragraph, the influence of fatigue on the P-UPS image is investigated but now for the CETEX sample with the $[0°,90°]_{4s}$ stacking sequence subjected to cyclic tensile loading. First, the P-UPS results for a virgin $[0,90]_{4s}$ CETEX sample are given as a reference (see Figure 14-9). Obviously, these results correspond to the P-UPS results of the virgin $[+45°,-45°]_{4s}$ CETEX sample, but rotated over an angle $\varphi = 45°$. In the 0°-direction, respectively 90°-direction, the inner contour is positioned at $\theta = 13.88°$, respectively $\theta = 13.57°$. This correspond to a homogenized stiffness of $E_{xx} = 54$ GPa and $E_{yy} = 57$ GPa, which is in close agreement with literature [17, 21]. The deviation between both stiffness values is a result of the difference in pre-stress between warp and weft yarns during the weaving.

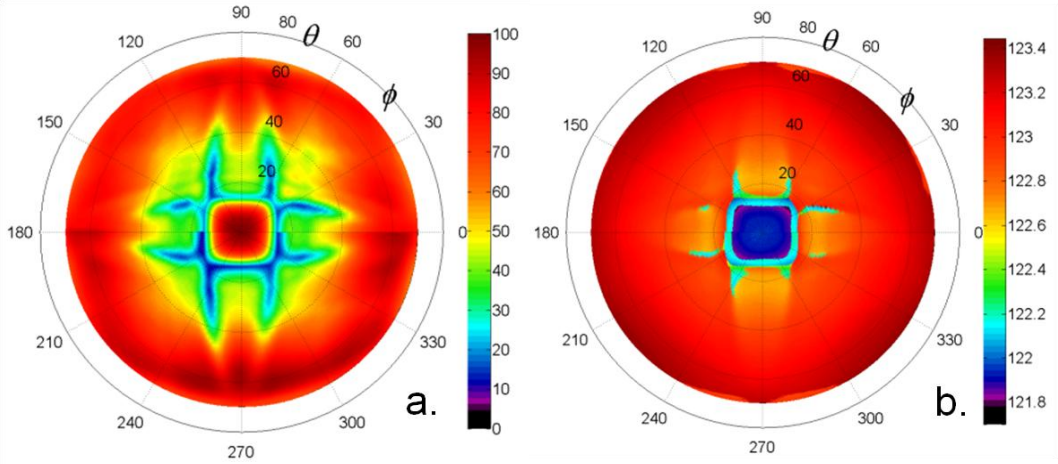

Figure 14-9: P-UPS result for virgin $[0°,90°]_{4s}$ CETEX fabric: amplitude (a) and TOF (b) recording.

Sample 1 was loaded at a frequency of 2 Hz, with the longitudinal stress level varying between 0 MPa and 700 MPa. The maximum applied stress corresponds to 92% of the ultimate tensile strength (UTS). The specimen withstood only 55 load cycles before failing and thus underwent low-cycle fatigue. The P-UPS results of the shear-dominated specimen revealed the spatial distribution of fatigue damage (see Figure 14-6), thus P-UPS scans are ideally performed at that spot where maximum material degradation occurred, obviously being the fractured region. However, this is not recommended because geometrical discontinuities near the failed zone would obviously influence the P-UPS image, making a straightforward interpretation in terms of a reduction of material stiffness difficult. Therefore, the insonification spot is chosen at a distance of $D \approx 15$ mm from the failed zone in order to avoid any 'edge' effects in the P-UPS image. Both the amplitude and TOF based P-UPS scans for the 'fatigued' sample 1 are shown in Figure 14-10a-b. The amplitude map shows more detailed features in comparison with the TOF recording, therefore we focus the further discussion on the amplitude result. In addition, the TOF results of the fatigued samples do not reveal any significant change in its range, indicating the insensitivity of the TOF parameter for the material damage associated to tension-tension fatigue loading.

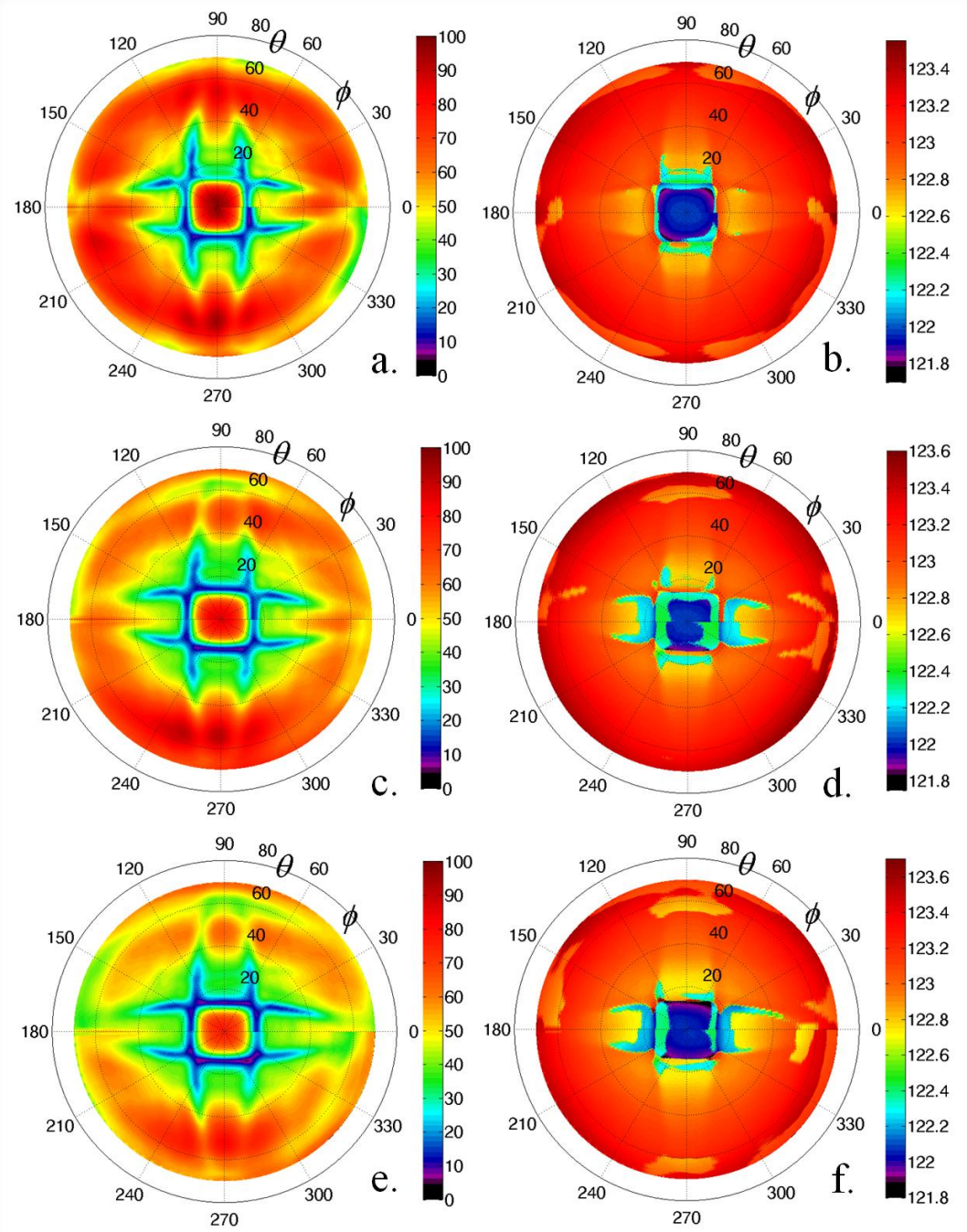

Figure 14-10: Amplitude (left column) and TOF (right column) based P-UPS results for tension-tension fatigued CETEX fabric: sample 1 [0-700 MPa] (a-b), sample 2 [0-650 MPa] (c-d) and sample 3 [0-625 MPa] (e-f).

Apart from a slight drop in transmitted amplitude, which can be attributed to the scattering of the ultrasonic waves on multiple matrix cracks and material clusters, a slight directional stretching of the polar contours can be observed. According to the physical background provided in Section 2.3.2, this positional shifting indicates a change in stiffness properties. After fatigue, the inner contour is positioned at $\theta = 14.38°$ along $\varphi = 0°$, and $\theta = 13.64°$ along $\varphi = 90°$. Based on P-UPS simulations, we extracted a 3.7% reduction of E_{xx}, while the stiffness modulus transverse to the loading direction remains more or less constant. Notwithstanding the very limited number of load cycles, a small stiffness reduction along the loading direction is obtained, in agreement with literature [2, 13].

The P-UPS results of sample 2 (loading frequency $f = 5$Hz and longitudinal stress [0-650 MPa]) show a larger drop in the global amplitude level, while the stretching of the inner contour becomes more outspoken (see Figure 14-10c-d). The inner contour is now positioned at $\theta = 15.23°$ and $\theta = 13.79°$, along 0°-direction, respectively 90°-direction, affirming the directional nature of stiffness degradation associated to tension-tension fatigue loading. A reduction of 10.5% is extracted for the stiffness along the loading direction. With respect to sample 1, the reduction in stiffness along the loading direction is larger, as could have been expected considering the higher number of load cycles. The extracted stiffness reduction along the loading direction is in full agreement with earlier observations reported in [2], where it was shown that the stress-strain response of the $[0°,90°]_{4s}$ laminate after high-cycle fatigue is nonlinear, showing a considerably lower stiffness for small strains, and a much higher stiffness for high strains. This is due to the geometrical stiffening of the laminate: because of the fatigue damage, the warp yarns are delaminated from the surrounding matrix and weft yarns, and can straighten up when tensile loading is applied. In case of ultrasonic inspection, the applied mechanical strains are negligible, so the stiffness is measured in the small-strain regime. In addition, the fatigue damage also influences the shear-related contour, causing the branches to split apart along the 90°-direction. As seen in the P-UPS simulation in which a reduced stiffness is considered (see Figure 14-3b), this splitting is also observed. Considering that the particle displacement of the shear horizontally polarized bulk wave, guided by the structure along $\varphi = 90°$, is aligned with the tensile loading direction during fatigue, such a splitting could have been expected.

Finally, sample 3 is fatigued at a loading frequency of 5 Hz, with the tensile stress level varying between 0 MPa and 625 MPa. After 314,111 load cycles, the specimen suddenly failed. The P-UPS results show very similar features as observed for sample 2. The inner contour is now positioned at $\theta = 15.41°$, respectively $\theta = 13.56°$, along 0°-direction, respectively 90°-direction. A stiffness reduction of 12.8% is extracted along the loading direction. As this sample was provided with an extensometer (positioned at a different spot where P-UPS experiments have been obtained), we performed an additional analysis of the stress-strain data at small strains. A stiffness reduction of ~11% has been extracted which is in good agreement with the P-UPS data.

The P-UPS results for the tensile fatigued CETEX samples clearly reveal the directional nature of the stiffness reduction. This is in sharp contrast with the results, though for a glass fabric reinforced plastic, presented in a previous study [8]. As the reference [8] only discussed a single P-UPS experiment, which was furthermore only partially recorded at the inappropriately high frequency of $f = 5$ MHz, it is difficult to check the validity of their conclusions. Anyway, the material degradation extracted from the P-UPS experiments shown in this chapter corresponds well to simulation, analysis of tensile data in the small strain area (sample 3) as well as to literature (except for reference [8]).

14. 4. Conclusions

In this chapter, the P-UPS technique has been applied to fatigued carbon fabric reinforced plastics. Several CETEX samples, subjected to either shear-dominated or tension-tension fatigue at various load levels, are investigated at multiple material spots with the P-UPS technique in order to assess fatigue damage.

For the CETEX samples fatigued in the shear-dominated condition, the P-UPS results reveal the spatial and directional nature of the induced damage, and indicate a reduction of shear properties. In addition, the P-UPS results reveal large fiber distortions (up to 13°) at the place where necking was observed, suggesting that the principal axes of orthotropy could be rotated over 45°. On the basis of these results, one could actually question whether damage simulation models should be extended to account for fiber distortion and in extension to transformations in material symmetry class.

The P-UPS results for the tension-tension fatigued CETEX samples show a reduction of stiffness up to 12.8% along the loading direction. Even the sample which was barely subjected to fatigue loading (55 cycles) did reveal a stiffness reduction of 3.7% along the loading direction. The P-UPS results for the tension-tension fatigued CETEX samples do not reveal any significant change in stiffness transverse to the loading direction, revealing the directional nature of damage features associated to tension-tension fatigue.

Overall, good correspondence is obtained with simulations, conventional destructive tests, visual inspection as well as literature, indicating the excellent feasibility of the P-UPS technique to monitor and evaluate fatigue damage in fabric reinforced composites.

14. 5. References

[1] Van Paepegem, W., I. De Baere, E. Lamkanfi, and J. Degrieck, *Monitoring quasi-static and cyclic fatigue damage in fibre-reinforced plastics by Poisson's ratio evolution.* International Journal of Fatigue, 2010. 32(1): p. 184-196.

[2] Daggumati, S., I. De Baere, W. Van Paepegem, J. Degrieck, J. Xu, S.V. Lomov, and I. Verpoest, *Fatigue and post-fatigue stress-strain analysis of a 5-harness satin weave carbon fibre reinforced composite.* Composites Science and Technology, 2013. 74: p. 20-27.

[3] Taheri-Behrooz, F., M.M. Shokrieh, and L.B. Lessard, *Residual stiffness in cross-ply laminates subjected to cyclic loading.* Composite Structures, 2008. 85(3): p. 205-212.

[4] Whitworth, H.A., *A stiffness degradation model for composite laminates under fatigue loading.* Composite Structures, 1997. 40(2): p. 95-101.

[5] Hwang, W. and K.S. Han, *CUMULATIVE DAMAGE MODELS AND MULTI-STRESS FATIGUE LIFE PREDICTION.* Journal of Composite Materials, 1986. 20(2): p. 125-153.

[6] Payan, J. and C. Hochard, *Damage modelling of laminated carbon/epoxy composites under static and fatigue loadings.* International Journal of Fatigue, 2002. 24(2-4): p. 299-306.

[7] Giancane, S., F.W. Panella, and V. Dattoma, *Characterization of fatigue damage in long fiber epoxy composite laminates.* International Journal of Fatigue, 2010. 32(1): p. 46-53.

[8] Declercq, N.F., J. Degrieck, and O. Leroy, *On the influence of fatigue on ultrasonic polar scans of fiber reinforced composites.* Ultrasonics, 2004. 42(1-9): p. 173-177.

[9] Joffe, R. and J. Varna, *Analytical modeling of stiffness reduction in symmetric and balanced laminates due to cracks in 90 degrees layers.* Composites Science and Technology, 1999. 59(11): p. 1641-1652.

[10] Varna, J., R. Joffe, N.V. Akshantala, and R. Talreja, *Damage in composite laminates with off-axis plies.* Composites Science and Technology, 1999. 59(14): p. 2139-2147.

[11] Barbero, E.J., F.A. Cosso, and F.A. Campo, *Benchmark solution for degradation of elastic properties due to transverse matrix cracking in laminated composites.* Composite Structures, 2013. 98: p. 242-252.

[12] Barbero, E.J., F.A. Cosso, R. Roman, and T.L. Weadon, *Determination of material parameters for Abaqus progressive damage analysis of E-glass epoxy laminates.* Composites Part B-Engineering, 2013. 46: p. 211-220.

[13] De Baere, I., W. Van Paepegem, C. Hochard, and J. Degrieck, *On the tension-tension fatigue behaviour of a carbon reinforced thermoplastic part II: Evaluation of a dumbbell-shaped specimen.* Polymer Testing, 2011. 30(6): p. 663-672.

[14] Declercq, N.F., J. Degrieck, and O. Leroy, *Ultrasonic polar scans: Numerical simulation on generally anisotropic media.* Ultrasonics, 2006. 45(1-4): p. 32-39.

[15] Declercq, N.F., J. Degrieck, and O. Leroy, *Simulations of harmonic and pulsed ultrasonic polar scans.* Ndt & E International, 2006. 39(3): p. 205-216.

[16] Kersemans, M., A. Martens, K. Van Den Abeele, J. Degrieck, L. Pyl, F. Zastavnik, H. Sol, and W. Van Paepegem, *The Quasi-Harmonic Ultrasonic Polar Scan for Material Characterization: Experiment and Numerical Modeling.* Accepted for publication in Ultrasonics, 2014.

[17] Daggumati, S., W. Van Paepegem, J. Degrieck, J. Xu, S.V. Lomov, and I. Verpoest, *Local damage in a 5-harness satin weave composite under static tension: Part II - Meso-FE modelling.* Composites Science and Technology, 2010. 70(13): p. 1934-1941.

[18] Kersemans, M., N. Lammens, J. Degrieck, K. Van Den Abeele, L. Pyl, F. Zastavnik, H. Sol, and W. Van Paepegem, *Extraction of bulk wave characteristics from a pulsed ultrasonic polar scan.* Wave Motion, 2014. In Press DOI: 10.1016/j.wavemoti.2014.05.001.

[19] Sket, F., A. Enfedaque, C. Alton, C. González, J.M. Molina-Aldareguia, and J. Llorca, *Automatic quantification of matrix cracking and fiber rotation by X-ray computed tomography in shear-deformed carbon fiber-reinforced laminates.* Composites Science and Technology, 2014. 90(0): p. 129-138.

[20] Kersemans, M., I. De Baere, J. Degrieck, K. Van Den Abeele, L. Pyl, F. Zastavnik, H. Sol, and W. Van Paepegem, *Nondestructive damage assessment in fiber reinforced composites with the pulsed ultrasonic polar scan.* Polymer Testing, 2014. 34(0): p. 85-96.

[21] Jacques, S., I. De Baere, and W. Van Paepegem, *Application of periodic boundary conditions on multiple part finite element meshes for the meso-scale homogenization of textile fabric composites.* Composites Science and Technology, 2014. 92C: p. 41-54.

PART IV

The last part contributes to several full field techniques in order to visualize and to interpret complex ultrasonic wave phenomena.

Chapter 15

Visualization of Ultrasound: Acousto-Optics and Finite Element Modeling

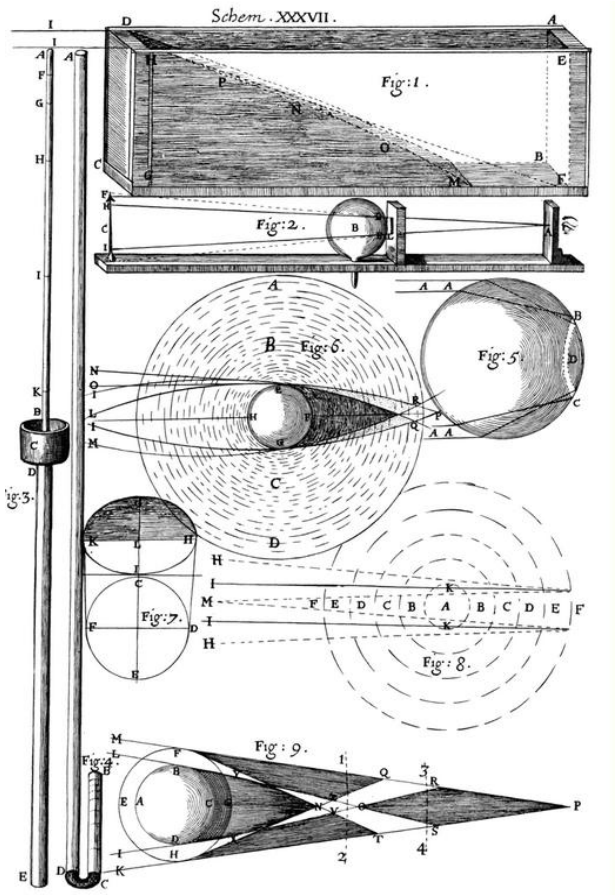

Drawing of a visualization system by Robert Hooke, which is now known under the name of schlieren/shadowgraph photography (Figure reproduced from reference [1]).

Summary

This chapter gives an account on the implemented acousto-optic schlieren setup. The built setup allows to visualize ultrasonic phenomena in real space as well as in spatial frequency domain. In addition, a numerical analogue of the acousto-optic schlieren technique has been implemented on the basis of a coupled fluid-structure interaction finite element method (FEM). As a way of demonstrating the capabilities of these techniques, the famous ultrasonic Schoch effect has been successfully generated.

This chapter forms the basis for the next chapter on the leakage and scattering phenomena of Lamb waves interacting with the plate end.

15. 1. Introduction

The interpretation and understanding of complex ultrasonic phenomena becomes easier and more straightforward when a full-field image is available, in which the different ultrasonic components can be readily identified and viewed. Unfortunately, ultrasound is not detectable by the human senses, thereby indirect methods have to be employed. Several methods have been developed and exploited in the last hundred years for this task. Though, only one method became really popular due to its simplicity for imaging ultrasound waves: the acousto-optic schlieren technique.

The invention of the schlieren (and shadowgraph) method probably needs to be dated back to the 17th century on the account of the great Robert Hooke who described in his famous book 'Microscopia (Observation LIII)' the direct observation of a thermal plume: *"... you shall find such a tremulation and wavering of the remote object, as will very much offend your eye"* [1]. The schlieren technique has been reinvented in the centuries thereafter by multiple researchers, including Huygens, Marat, Foucault and Toepler. It was August Toepler around 1860 who named the schlieren technique after the German word 'schlieren' which was used to describe 'optical inhomogeneities in glass'. Since then, the schlieren technique has been widely recognized and gained tremendous popularity for the study of physical phenomena involving variations in the refractive index [2-10].

Refinements in the experimental methodology as well as the use of high-quality optical components led to a quantitative imaging system applicable to the study of air flow, shock waves, thermal waves, ultrasonic waves, and others. Applied to ultrasound, the imaging technique is often referred to as 'acousto-optic schlieren technique'.

15. 2. Acousto-optic Schlieren Technique

15. 2. 1. Real Space

Figure 15-1 shows a schematic of the implemented acousto-optical Schlieren setup for the visualization of the sound waves in water, in which *L* stands for lens and *M* for mirror. A laser beam is focused by L_1 onto a pinhole with diameter $d \approx 15\mu m$ to simulate a point source, thus spatially filtering the laser light. The pinhole is placed in the focal point of L_2 in order to generate a collimated beam, which then passes through the water tank where the acoustical phenomenon takes place. The ultrasonic transducer, which can rotate around the Z-axis in order to vary the incident angle θ, generates a bounded beam in the water tank which impinges onto the elastic solid plate under investigation. An ultrasonic beam propagating along the X-axis acts as a refractive index grating $\mu(x,t)$ (phase grating) for normal incident light, hence causing a diffraction of the collimated laser beam (Raman-Nath diffraction regime [11-15])

$$\mu(x,t) = \mu_0 - \mu_1 \sin\left(2\pi x/\lambda - \omega t\right) \tag{1}$$

with μ_1 the maximum variation of the refractive index from μ_0, λ the ultrasonic wave length and ω the angular frequency.

The parabolic mirror M_4 focuses the light in the so-called Fourier plane, where a black spot blocks the non-diffracted light. The light which is able to pass the black spot is then projected onto a screen. This light contains a 2D visualization in real space of the intensity of the acoustical phenomenon in the water tank, and is captured with a digital camera.

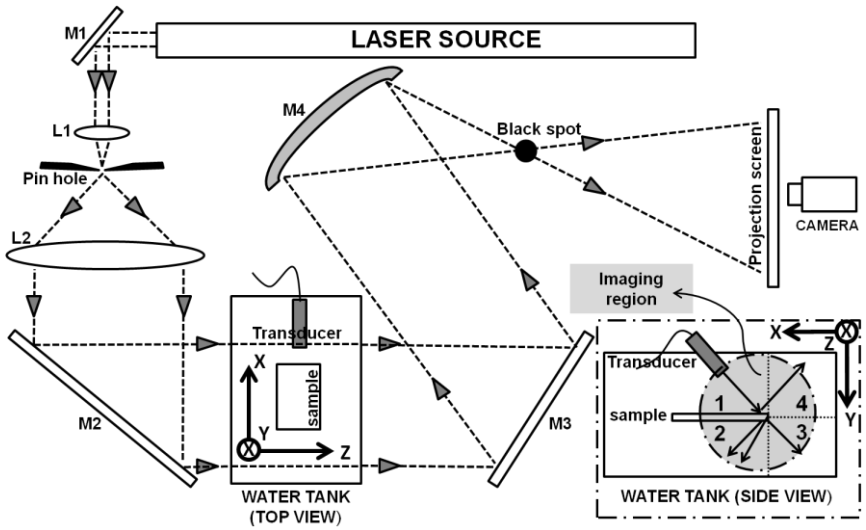

Figure 15-1: Schematic of the implemented acousto-optical schlieren setup to visualize an ultrasonic phenomenon in real space. Replacement of the black spot by a CCD chip leads to a visualization in spatial frequency domain. In the inset, the imaging region is divided in 4 quadrants.

A real photograph of the implemented setup is shown in Figure 15-2. Several components are explicitly labeled, while the laser light path is superimposed. A laser (λ_{light} = 633 nm) with nominal power of 20 mW is used.

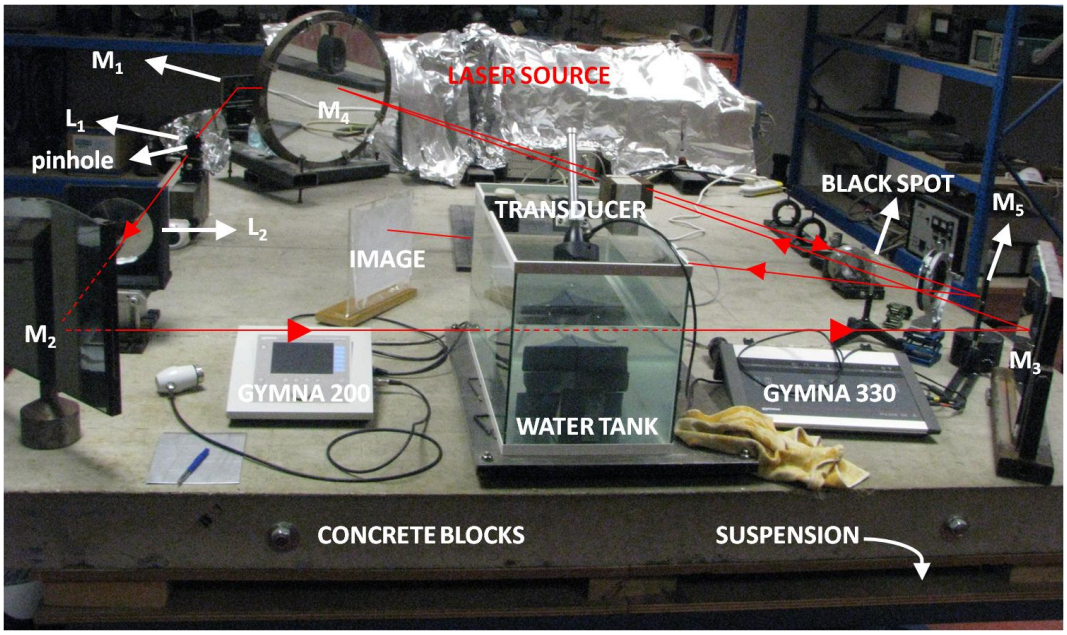

Figure 15-2: Photograph of the constructed acousto-optic schlieren setup.

The amplitude generated by standard transducers (see Chapter 3) is not sufficient to obtain a clear visualization with the acousto-optical setup. Therefore, a physiotherapeutic apparatus (type GYMNA) has been employed to generate harmonic ultrasound waves having high intensity. The generated beam has a more or less Gaussian amplitude with a circular area equal to 0.8 cm^2, 1.4 cm^2 or to 4.7 cm^2, while the frequency can be set at 1.1MHz, 3 MHz or 3.2 MHz. The time-domain signal and the spectral frequency content is shown in Figure 15-3 for a 1.1 MHz finite amplitude wave generated by the GYMNA 200 apparatus at different electrical input power. The wave signal has been measured by means of a calibrated pressure sensor, which is specifically designed for measuring dynamic shock wave pressures during water slamming applications [16-17]. It can be readily seen that a low electrical power generates a more or less sine profile. However, increase of the electrical power induces a distortion of the generated ultrasonic signal. This is understood in terms of nonlinear wave propagation: the high intensity wave locally alters the characteristics of the medium, and thus changes its own conditions of existence. Further confirmation of the nonlinear wave propagation can be found in the FFT spectrum of the time signals, indicating that wave energy is transferred to higher harmonics (see Figure 15-3b). Obviously, for higher ultrasound amplitude, a better imaging with the acousto-optic schlieren setup can be obtained, but on the expense of increased nonlinearity. The high amplitude has another consequence, namely heating of the insonified sample. This was observed several times in the form of a plume-like object in the schlieren image, as if the insonified spot was 'on fire'. Further schlieren results in this thesis have been obtained using an electrical power input between P = 1.5 W/cm^2 and P = 2 W/cm^2, i.e. in the nonlinear regime.

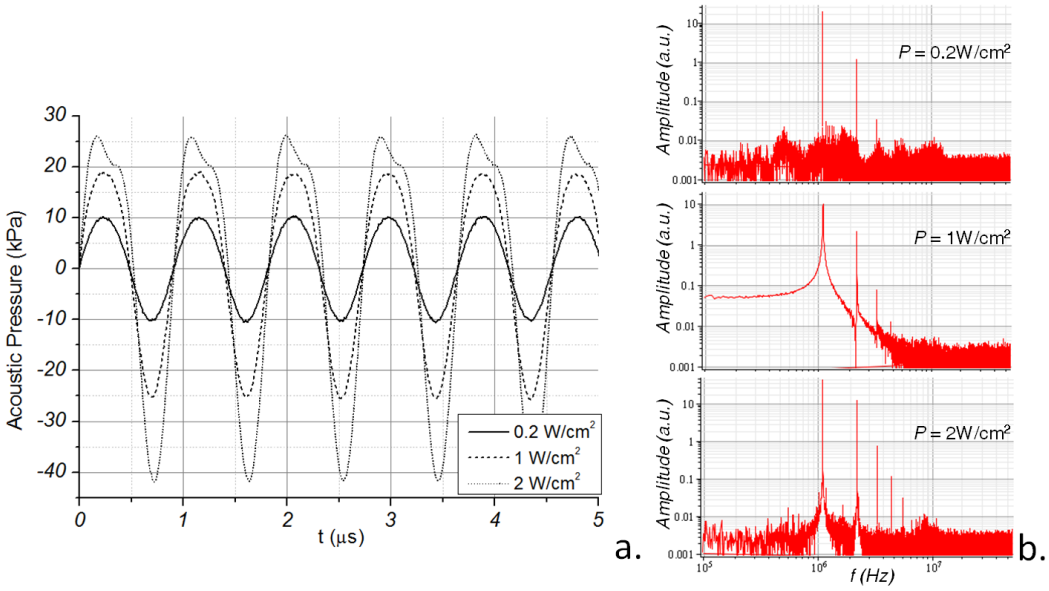

Figure 15-3: Time domain signal (a) and frequency spectrum (b) generated by the GYMNA apparatus for different electrical input power.

The devised black spot has a diameter of ~3 mm. Further reduction of the dimensions of the black spot is not recommended as the generated laser beam has a diameter of ~2 mm. The complete setup is put on heavy concrete blocks which are suspended by several inner tubes of a vehicle's tire in order to exclude external vibrations as much as possible. The constructed acousto-optical schlieren setup has a total laser path length of ~10 m, and a circular imaging range with diameter ~200 mm. However, it is noted that the outer part of the imaging region suffers from all kinds of optical distortions, such as comatic aberration, spherical aberration, astigmatism, etcetera.

To demonstrate the operation of the acousto-optic schlieren arrangement, the well-known Schoch effect [18] is demonstrated. The Schoch effect occurs during the bounded beam insonification of an immersed plate at specific angles (Lamb angle or Rayleigh angle), and is identified by the formation of two reflected beams split by a nullzone. The Schoch effect can be considered the ultrasonic analogue of the electromagnetic Goos-Hanchen effect [19]. The physical origin of the Schoch effect is found in the leaky behavior of stimulated surface waves, such as leaky Lamb waves and leaky Rayleigh waves. These waves are guided by the plate-like structure [20], and leak energy in the immersion liquid upon their propagation in the solid, which thus results in a laterally displaced non-specular reflection (and

transmission) field in the liquid [21]. The specular and non-specular reflection fields are 180° out-of-phase [22]. Hence, interference of the specular reflection and the leaking field leads to phase-cancelling, producing the famous Schoch effect [23]. The Schoch effect is commonly used to identify the stimulation condition of a leaky Lamb wave, i.e. the Lamb angle [6].

Here we consider the insonification of an aluminum plate with thickness 1.45 mm using the 10 mm wide bounded beam at $f = 3$ MHz. Figure 15-4 displays the computed dispersion curves for aluminum (Legendre polynomial expansion [24]), considering the material parameters found by the system identification procedure (see Chapter 7). At $fd = 4.35$ MHz.mm, the dispersion curves indicate the existence of 5 Lamb angles: $\theta_{A0} = 31.03°$, $\theta_{S0} = 29.72°$, $\theta_{A1} = 19.36°$, $\theta_{S1} = 14.52°$ and $\theta_{S2} = 8.27°$.

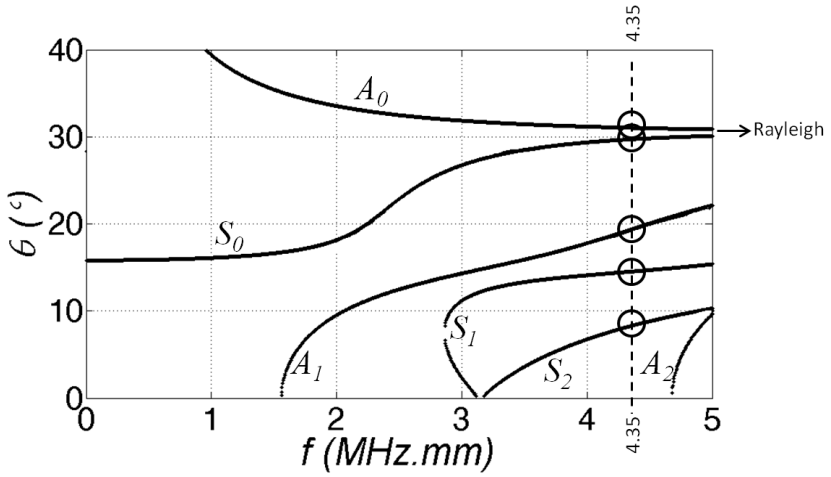

Figure 15-4: Dispersion curves *fd(θ)* for aluminum.

Acousto-optical experiments have been obtained by insonifying the aluminum sample at $fd = 4.35$ MHz.mm under several oblique incident angles θ (see Figure 15-5a-e). One can readily observe in Figure 15-5a that the experiment obtained at the arbitrary incident angle $\theta = 33°$ does not produce any beam shift. The other experiments (Figure 15-5b-e) have been obtained at the Lamb wave stimulation conditions (see the dashed vertical line in Figure 15-4), and clearly display the presence of the Schoch effect. Though, separation of the Schoch effect associated to the A_0 mode and the S_0 mode was not possible due to their convergent nature towards the Rayleigh wave. Further note that the leaking field associated to the S_1 Lamb mode

extends over a considerable region. This is understood considering that the stimulated S_1 Lamb mode has a longitudinal character [21], i.e. the S_1 mode has a limited vertical displacement field at the liquid-solid boundaries, hence only limited energy leakage into the immersion liquid takes place. Figure 15-5f shows the bounded beam insonification of an aluminum sample at the Rayleigh angle (fd = 45 MHz.mm). Again, the Schoch effect can be clearly discerned, which is now induced by the leaking of a stimulated Rayleigh wave. No transmission field is present as a Rayleigh wave is confined near the liquid-solid interface at which the stimulation takes place [21].

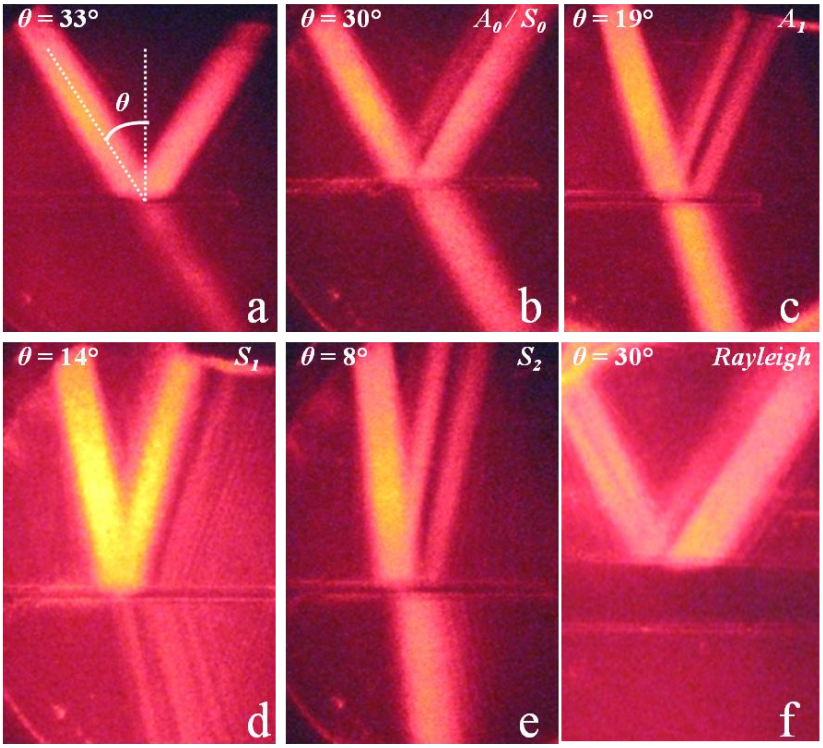

Figure 15-5: Acousto-optical experiments of the bounded beam insonification of aluminum at different incident angles θ: arbitrary angle (a), Lamb angles (b-e) and Rayleigh angle (f).

15. 2. 2. Spatial Frequency Domain

Besides the traditional acousto-optic schlieren experiments in real space, the setup was extended to visualize ultrasound phenomena in spatial frequency domain, simply by adding a CCD chip in the focal point of parabolic mirror M_4. That spot lies in the so-called Fourier plane which provides a

representation of the diffractive behavior of the acoustical phenomenon in the spatial frequency domain. Figure 15-6 displays the bounded beam insonification of a thick solid at an arbitrary incident angle θ, visualized both in real space and in spatial frequency domain. In real space (Figure 15-6a), the incident field I and the reflected field R can be readily identified. The visualization of the ultrasonic phenomenon in spatial frequency domain is shown in Figure 15-6b, a (k_x,k_y) coordinate system has been added for the ease of interpretation. The incident and reflected ultrasonic beam can be identified in the high-intense diffraction spots, oriented along both the ultrasonic wave propagation directions (roughly speaking along the two diagonals of Figure 15-6b). The position of these basis spikes in the (k_x,k_y)-plane is imposed by the wave vector $\boldsymbol{k}$ of the incident ultrasonic wave. For a sinusoidal variation in the refraction index, one should expect only first order diffraction peaks. However, it was already shown above that the GYMNA apparatus produces an ultrasonic wave having nonlinear propagation characteristics. In addition, the photon-phonon interaction itself is also nonlinear for even a modest ultrasound amplitude. The theory for the position and the intensity of the multiple light diffraction orders produced by a single ultrasound wave has already been developed in the 1930's by Nobel prize winner C.V. Raman, together with his student N. Nath [11-15]. They showed that the relative intensity of the m^{th} diffraction component to the n^{th} diffraction component is given by the ratio of the respective m^{th} and n^{th} order Bessel functions

$$\frac{I_m}{I_n} = \frac{J_m^2\left(\frac{2\pi\mu L}{\lambda}\right)}{J_n^2\left(\frac{2\pi\mu L}{\lambda}\right)} \tag{2}$$

with L the acousto-optic interaction length.

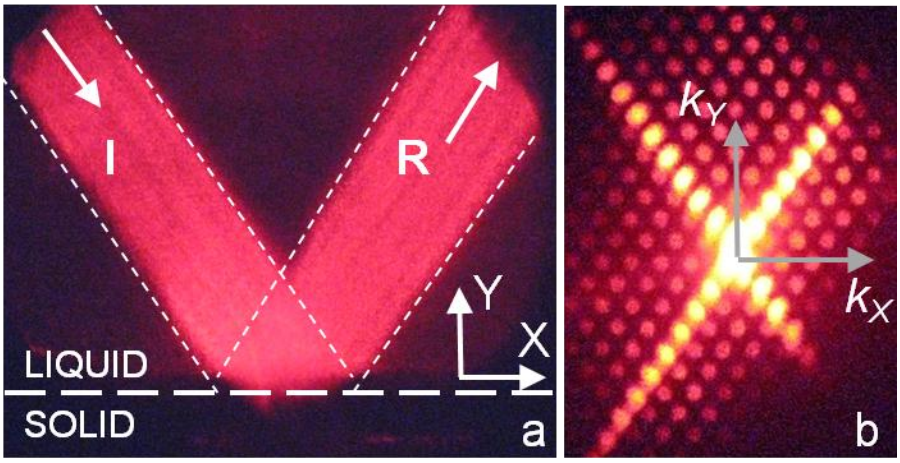

Figure 15-6: Bounded beam insonification of a thick solid at an arbitrary incident angle θ: acousto-optic visualization in real space (a) and in spatial frequency domain (b).

Both the phonon-phonon and photon-phonon nonlinearity have the same effect for the results in spatial frequency domain, and are reflected in the appearance of multiple higher-order diffraction peaks.

In addition to the spots related to the incident and reflected beam, several other spots can be observed in Figure 15-6b. On the one hand, these spots originate from the diffraction of multiple ultrasonic beams traveling along different directions. On the other hand, a light beam diffracted by one ultrasonic wave in a certain direction is diffracted again by an ultrasonic wave propagating in a different direction. As such, inter-modulation spots are formed which are a nonlinear combination of the incident and the reflected ultrasonic beam. Their position in (k_x,k_z)-space is thus found by addition and/or subtraction of the wave vectors $\boldsymbol{k}$ associated to the incident and reflected beam. In order to demonstrate this, we have applied spatial filtering in the Fourier plane. By retaining certain spikes, one can selectively determine their contribution to the total visualization in real space. When the set of spikes shown in Figure 15-7a is selected, the retained spatial frequency domain information only consists of spikes corresponding to the shared presence of the incident and the reflected acoustic field. The corresponding image in real space is shown in Figure 15-7b, only the triangular zone where the incident and reflected acoustic field overlap is illuminated. The regions which consist solely of the incident or reflected acoustic beam do not light up in real space by selecting the current set of spikes in spatial frequency

domain. Similar results are obtained when selecting the set of spikes shown in Figure 15-7c, for which the corresponding result in real space is shown in Figure 15-7d.

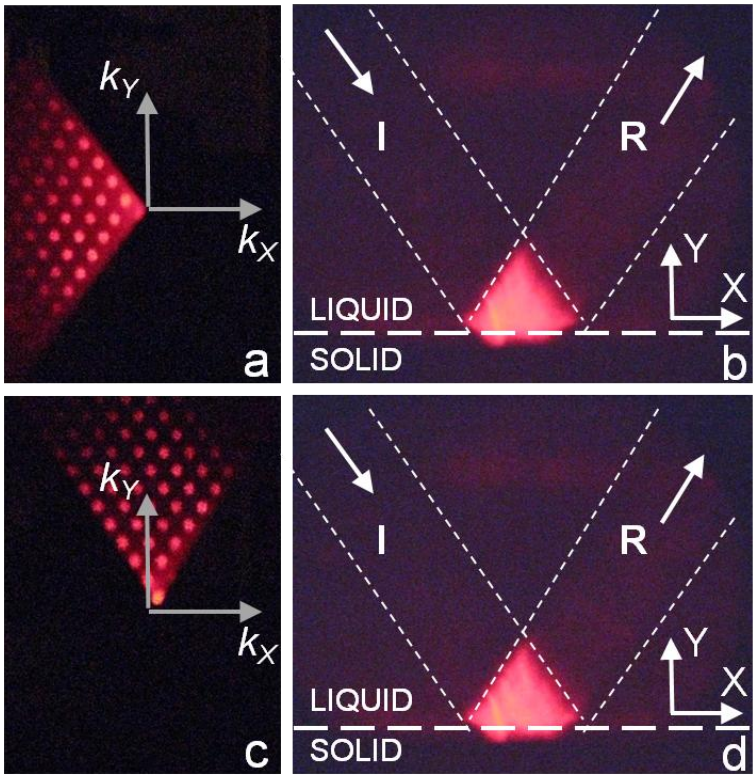

Figure 15-7: Bounded beam insonification of a thick solid at an arbitrary incident angle θ. Selection of spikes in the Fourier plane (left) and corresponding visualization in real space (right).

The above shows that the employed ultrasonic wave amplitudes are sufficient to generate nonlinear effects, which are partly generated by nonlinear ultrasound wave propagation, and partly by the nonlinear acousto-optic interaction. The nonlinearity can be readily identified in the visualization in spatial frequency space in the form of harmonics, cross-modulation and inter-modulation.

15. 3. Coupled Fluid-Structure Interaction Finite Element Method

15. 3. 1. Real Space

In order to simulate the acousto-optic schlieren experiments true-to-nature, a 2D finite element method (FEM) model, with plane strain assumption, is setup in the commercial software ABAQUS. For isotropic materials, the 2D assumption holds no restrictions as the wave propagation is bounded to the insonification plane (see Chapter 6). The computations have been performed with a direct integration scheme in the time domain. Both the fluid and solid domain are incorporated in the model. The discretized finite element equations for the coupled fluid-structure system are expressed as

$$M^F \frac{\partial^2 P}{\partial t^2} + K^F P = -R^F - \rho_F I^T \frac{\partial^2 U}{\partial t^2} \tag{3}$$

and

$$M^S \frac{\partial^2 U}{\partial t^2} + R^{\text{int}} = R^{ext} + IP\,, \tag{4}$$

with M^F and M^S the fluid resp. structural mass matrix, P the pressure in the fluid, K^F the fluid stiffness matrix, R^F the external force vector on the fluid, I the interaction matrix, U the position of the nodes, R^{int} the internal force vector of the solid and R^{ext} the external force vector on the solid.

A schematic of the computational environment is shown in Figure 15-8. Interaction conditions BC1 are invoked at the fluid-solid interface in order to have a fully coupled fluid-structure system, i.e. energy can be transferred and converted from fluid to solid domain as well as from solid to fluid domain. Discretizing the interaction surface $S^{S\text{-}F}$ into r elements, the expression for the global interaction matrix I is written as

$$I = \sum_1^r \iint_{S^{S_e - F_e}} \rho_F H^T \vec{n}^F H dS^e\,, \tag{5}$$

with H the matrix containing the interpolation functions for an element.

To avoid wave reflections at the boundary of the fluid domain, absorbing conditions BC2 have been used. Similarly, infinite solid elements BC3 are

used to efficiently absorb the elastic energy at the left and the right boundary of the solid domain. Like the experimental approach, Lamb modes are stimulated by means of an externally applied harmonic beam, with f = 3MHz, which insonifies an aluminum layer at the corresponding Lamb angle. The use of point sources together with a FFT decomposition, generates the acoustic beam (BC4) which is modeled as a Gaussian amplitude profile having a physical width of 10 mm. Note that the FEM simulation does not model the nonlinear beam characteristics, simply because such a modeling approach becomes too involved for the present investigation.

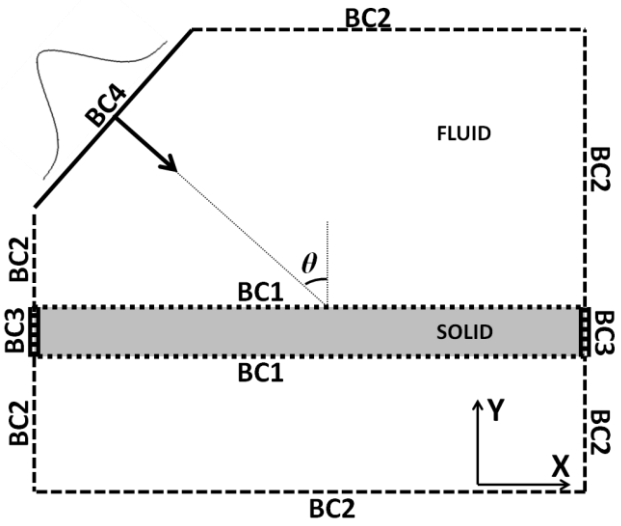

Figure 15-8: Representation of the numerical environment. The coupling between liquid and solid domain is invoked by continuity conditions (BC1). The liquid domain is surrounded by absorbing edges (BC2), while the left and the right end of the solid domain are modeled with infinite solid elements (BC3). The Gaussian-like acoustic beam is generated by application of the spatial Fourier transform (BC4).

To overcome spurious reflections [25-26], a uniform mesh with element size $1/10^{th}$ of the smallest possible wavelength is used. Typically, the number of finite elements is around 1,000,000. The fluid is characterized by dedicated fluid elements which cannot transfer shear, while the solid is built with general plane strain elements.

To demonstrate the validity of the used FEM procedure, several of the acousto-optic schlieren experiments displayed in Figure 15-5 have been simulated. Because the acousto-optic schlieren images are captured using a continuous laser source the results put on view a measure for the sound intensity. Similarly, the FEM acoustic pressures have been averaged over time to obtain an equivalent for the acoustic intensity. The simulation results are presented in Figure 15-9. The contour in the solid region represents the instantaneous magnitude of the displacement field.

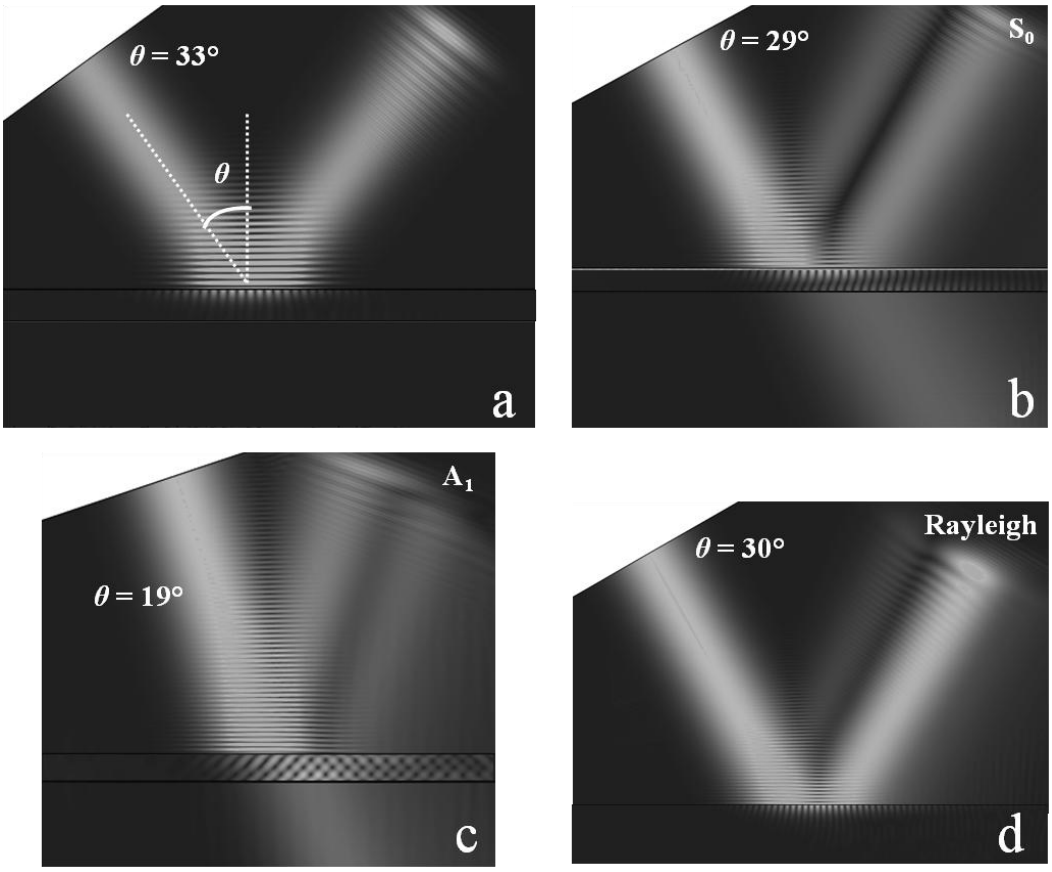

Figure 15-9: FEM simulation of the bounded beam insonification of aluminum at different incident angles: arbitrary angle θ (a), Lamb angle θ_{S0} (b), Lamb angle θ_{A1} (c) and Rayleigh angle $\theta_{Rayleigh}$ (d).

It can be readily seen that good agreement is obtained with the acousto-optic schlieren experiments: the Schoch effect is well reproduced whenever insonification takes place at a Lamb or Rayleigh angle. The FEM simulations give further the opportunity to analyze the displacement field

components in the solid domain. Figure 15-10 provides a comparison between the displacement components obtained by theory and by FEM simulation for the A_0 Lamb mode in brass at fd = 1.5 MHz.mm. The 90° phase shift between U_X and U_Y has been implicitly taken into account. It is clear from the figure that excellent agreements is obtained.

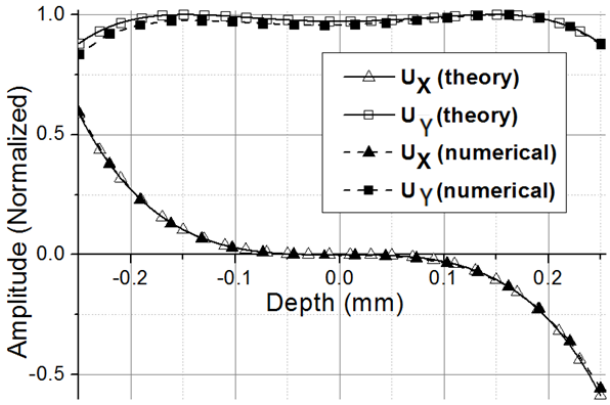

Figure 15-10: Comparison of the displacement components of the A_0 mode in brass at fd = 1.5 MHz.mm according to theory and FEM.

15. 3. 2. Spatial Frequency Domain

Roughly speaking, the numerical equivalent of the experiments obtained in spatial frequency domain involves the application of the spatial 2DFFT to the instantaneous pressures computed by the FEM model. The reason why instantaneous pressures are considered here is found in the fact that experimentally the ultrasound wave propagates at a different pace compared to the crossing light wave. Hence for the light wave, it is as if the ultrasound wave is frozen in time. Similar to the experiment, the FFT analysis can be performed in quadrants (see inset of Figure 15-1) to ease the interpretation. Though, because the developed FEM model does not take into account nonlinear wave propagation in the liquid, while application of the FFT neglects the nonlinearity of the photon-phonon interaction, the observed nonlinearity in the experiments cannot be reproduced. Therefore, we introduce nonlinearity in an artificial manner. Basically, the instantaneous pressures are plotted in a RGB color scheme, after which discontinuous phase jumps are introduced by converting the image to gray scale. It is clear that the introduced phase jumps are not representative for the experiments obtained in real space. But in spatial frequency domain, the introduced phase jumps produce equivalent features as observed in the experiments, leading to

the introduction of harmonics, cross-modulation and inter-modulation. Figure 15-11 displays the results in the upper liquid part of Figure 15-9a in spatial frequency domain.

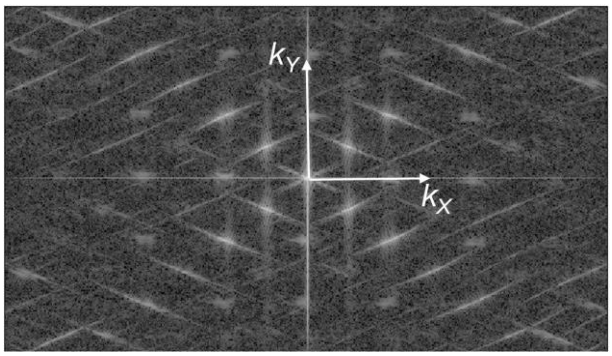

Figure 15-11: Representation of Figure 15-9a (upper liquid domain) in spatial frequency domain.

15. 4. Conclusions

A short discussion of the implemented acousto-optic schlieren setup for the visualization of ultrasonic phenomena is given. With the implemented setup, ultrasonic phenomena can be visualized both in real space and in spatial frequency domain. Results have been shown for the famous Schoch effect which is characterized by a nullzone in the reflection field. To support the schlieren images, a numerical analogue is implemented on the basis of a coupled structure-fluid interaction finite element method. The various experiments have been successfully simulated. The next chapter will use the here discussed techniques to investigate the complex leakage and scattering phenomena of Lamb waves interacting with a structural discontinuity.

15. 5. References

[1] Hooke, R., *Micrographia: or, Some physiological descriptions of minute bodies made by magnifying glasses*. 1665, London: Martyn, J., Allestry, J.

[2] Pitts, T.A., J.F. Greenleaf, J.Y. Lu, and R.R. Kinnick, *TOMOGRAPHIC SCHLIEREN IMAGING FOR MEASUREMENT OF BEAM PRESSURE AND INTENSITY*, in *1994 Ieee Ultrasonics Symposium Proceedings, Vols 1-3*, M. Levy, S.C. Schneider, and B.R. McAvoy, Editors. 1994. p. 1665-1668.

[3] Breazeale, M.A., *From monochromatic light diffraction to colour Schlieren photography*. Journal of Optics a-Pure and Applied Optics, 2001. 3(4): p. S1-S7.

[4] Breazeale, M.A., *Schlieren photography in physics*, in *Acousto-Optics and Applications Iii*, A. Sliwinski, B.B.J. Linde, and P. Kwiek, Editors. 1998. p. 41-47.

[5] Declercq, N.F., J. Degrieck, and O. Leroy, *Schlieren photography to study sound interaction with highly absorbing materials.* Ultrasonics, 2005. 43(7): p. 505-507.

[6] Declercq, N.F. and E. Lamkanfi, *Study by means of liquid side acoustic barrier of the influence of leaky Rayleigh waves on bounded beam reflection.* Applied Physics Letters, 2008. 93(5).

[7] Don-Liyanage, D.K.L. and D.C. Emmony, *Schlieren imaging of laser-generated ultrasound.* Applied Physics Letters, 2001. 79(20): p. 3356-3357.

[8] Neumann, T. and H. Ermert, *Schlieren visualization of ultrasonic wave fields with high spatial resolution.* Ultrasonics, 2006. 44: p. E1561-E1566.

[9] Settles, G.S., *Schlieren and Shadowgraph Techniques: visualizing phenomena in transparant media*. 1st edition ed. 2006, Berlin: Springer-Verlag. 376.

[10] Teklu, A., M.A. Breazeale, N.F. Declercq, R.D. Hasse, and M.S. McPherson, *Backward displacement of ultrasonic waves reflected from a periodically corrugated interface.* Journal of Applied Physics, 2005. 97(8).

[11] Raman, C.V. and N.S. Nath, *The diffraction of light by high frequency sound waves: part I.* Proceedings of the Indian academy of sciences, 1935. 2: p. 406 - 412.

[12] Raman, C.V. and N.S. Nath, *The diffraction of light by high frequency sound waves: part II.* Proceedings of the Indian academy of sciences, 1936. 2: p. 413 - 420.

[13] Raman, C.V. and N.S. Nath, *The diffraction of light by high frequency sound waves: part III.* Proceedings of the Indian academy of sciences, 1936. 3: p. 75 - 84.

[14] Raman, C.V. and N.S. Nath, *The diffraction of light by high frequency sound waves: part IV.* Proceedings of the Indian academy of sciences, 1936. 3: p. 119 - 125.

[15] Raman, C.V. and N.S. Nath, *The diffraction of light by high frequency sound waves: part V.* Proceedings of the Indian academy of sciences, 1936. 3: p. 459 - 465.

[16] Van Nuffel, D., *Experimental study of the slamming induced pressures, forces and deformations experienced by quasi-rigid and deformable bodies during vertical water entry, PhD Thesis*, in *Materials Science and Engineering*. 2014, Ghent University: Gent. p. 289.

[17] Van Nuffel, D., K.S. Vepa, I. De Baere, P. Lava, M. Kersemans, J. Degrieck, J. De Rouck, and W. Van Paepegem, *A comparison between the experimental and theoretical impact pressures acting on a horizontal quasi-rigid cylinder during vertical water entry.* Ocean Engineering, 2014. 77(0): p. 42-54.

[18] Schoch, A., *Der Schalldurchgang durch plate.* acustica, 1952. 2.

[19] Goos, F. and H. Hänchen, *Ein neuer und fundamentaler Versuch zur Totalreflexion.* Annalen der Physik, 1947. 436: p. 333–346.

[20] Lamb, H., *On Waves in an Elastic Plate.* Proceedings of the Royal Society A-Mathematical Physical and Engineering Sciences, 1917(93): p. 114-128.

[21] I.A.Viktorov, *Rayleigh and Lamb waves*. 1967, New York: Plenum. 154.

[22] Bertoni, H.L. and T. Tamir, *Unified theory of Rayleigh-angle phenomena for acoustic beams at liquid-solid interfaces.* Applied physics, 1973. 2(4): p. 157-172.

[23] Tamir, T. and H.L. Bertoni, *Lateral displacement of optical beams at multilayered and periodic structures.* Journal of the Optical Society of America, 1971. 61(10): p. 1397-1413.

[24] Matar, O.B., N. Gasmi, H. Zhou, M. Goueygou, and A. Talbi, *Legendre and Laguerre polynomial approach for modeling of wave propagation in layered magneto-electro-elastic media.* Journal of the Acoustical Society of America, 2013. 133(3): p. 1415-1424.

[25] Bazant, Z.P. and Z. Celep, *Spurious reflection of elastic-waves in nonuniform meshes of constant and linear strain finite-elements.* Computers & Structures, 1982. 15(4): p. 451-459.

[26] Celep, Z. and Z.P. Bazant, *Spurious reflection of elastic-waves due to gradually changing finite-element size.* International Journal for Numerical Methods in Engineering, 1983. 19(5): p. 631-646.

Chapter 16

Leakage and Scattering of Lamb Waves Interacting with a Vertical Plate Edge

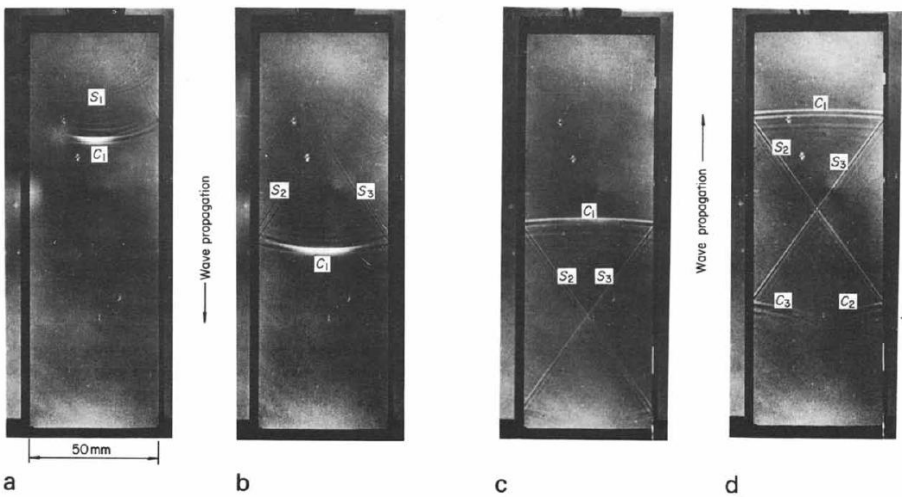

One of the first demonstrations of bulk wave conversion at the sidewalls of a glass block (Figure reproduced from reference [1]). Incident waves (a), conversion of compression wave C_1 to shear waves S_2 and S_3 at the sidewalls (b), back-reflection at bottom edge (c) and conversion of shear waves S_2 and S_3 to compression wave C_2 and C_3 at the sidewalls (d).

Overview

The bounded beam insonification at characteristic Lamb angles near the extremity of an immersed plate gives rise to considerable leakage and scattering phenomena in the surrounding liquid. For water-coupled NDT, this scattering should not be underrated as it 'pollutes' large parts of the immersion liquid, and thus could become a potential source of misinterpretation (see for example pitfall 7: 'Distortion by Edge Effects of the Sample' in chapter 5). Therefore, acousto-optic schlieren experiments as well as FEM simulations have been performed, both in real space and in spatial frequency domain.

The backward radiation field is interpreted in terms of the leaking fields of backward propagating mode-converted Lamb waves. The forward leaking field on the other hand is successfully modeled by assuming the vertical edge to be an oscillating acoustic line source, with an amplitude distribution corresponding to the horizontal component U_x of the incident Lamb mode.

Excellent agreement has been found between theory, acousto-optics and FEM, giving confidence in the obtained results. Though, the obtained results seem to contradict with the findings in a few papers in literature.

16. 1. Introduction

The inspection of finite size structures with oblique incidence techniques could yield erroneous results due to edge effects. Already in Section 5.2.7, it has been discussed and demonstrated for the P-UBPS that the plate ending introduces parasitic backscatter spots at certain oblique incidence angles. Obviously, it is crucial to interpret the data correctly and to rule out possible artifacts in the recordings to assure the designed functionality of the inspected structure. As such, it is important to acknowledge the leakage and scattering of guided wave interaction with a plate ending.

Ample research has been performed and reported on the interaction of guided waves, and more specifically Lamb waves, with a vertical plate extremity. By generating a (leaky) Lamb mode in the neighborhood of the edge of a(n) (immersed) solid plate, the incident forward propagating (leaky) Lamb mode is converted into several backward propagating (leaky) Lamb modes due to mode conversions at the plate edge [2-6]. In order to maintain continuity at the (free) edge, non-propagating modes come into play as well, though they are confined to the close neighborhood of the scatterer [7-8]. During the last decades, several high-quality studies investigated and reported on the interaction of a Lamb mode with a vertical plate end in great detail [9-13], however most of these studies are limited to highlight and explain those phenomena which are confined to the solid domain. Yet, for practical water-coupled NDT and SHM measurements, emission and reception of ultrasonic waves is most commonly performed within a surrounding liquid or gas medium. Therefore, it is certainly equally, if not more interesting to focus the investigation on the leakage and scattering phenomena that can be observed within the liquid domain as a consequence of insonification at a Lamb angle near a vertical plate ending. To our knowledge, only a few papers deal with the associated leaky Lamb wave scattering phenomena in the liquid domain as a result of the interaction with the plate end [14-18]. In reference [14-17], several experimental studies have been performed by means of hydrophone measurements. The studies reveal the existence of a critical path length, which has been interpreted via the description of Lamb waves in terms of a Debye series, necessary to complete the leaking process. The results in reference [18] however, seem to contradict this and suggest that the conversion process is completed near the plate edge.

This chapter revisits the involved leakage phenomena of Lamb waves scattered by a vertical plate edge using a combined experimental-numerical approach. Acousto-optical experiments have been obtained, both in real space and in spatial frequency domain, which are assisted by finite element method simulations. The FEM simulations further extend the imaging range to the phenomena occurring in the solid domain.

16. 2. Material and Method

A brass plate with thickness 0.5 mm is taken as subject of investigation. The brass plate is assumed to have a Young's modulus $E = 113.5$ GPa, a

Poisson's coefficient $\nu = 0.359$ and a mass density $\rho = 8100$ kg/m^3. The dispersion curves, represented both in *(k,fd)*-space and in *(θ,fd)*-space, are displayed in Figure 16-1.

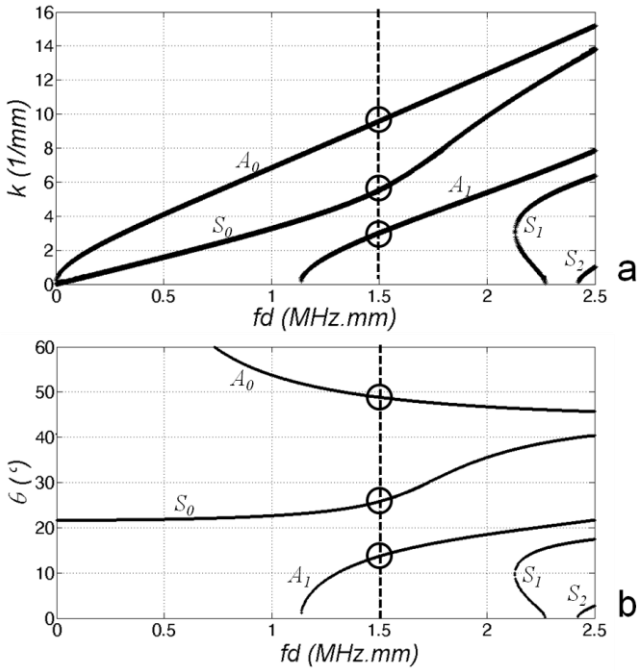

Figure 16-1: Dispersion curves for brass: (*k*,*fd*)-space (a) and (*θ*,*fd*)-space (b).

The brass plate has been insonified by a harmonic bounded beam (f = 3MHz and circular area of 0.8 cm^2) at oblique incidence angle. With the present parameters, the dispersion curves indicate the presence of 3 incident angles at which a Lamb wave is stimulated in the brass plate: $\theta_{A0} = 48.8°$, $\theta_{S0} = 25.8°$ and $\theta_{A1} = 13.7°$ (see vertical dashed line in Figure 16-1b). As we are interested in the leakage and scattering of guided waves interacting with the plate edge, we have performed acousto-optic schlieren experiments whereby insonification at the various Lamb angles takes place near the plate ending.

Besides schlieren experiments, simulations have been performed using FEM. The numerical setup is similar as discussed in Chapter 15, but now for a semi-infinite plate. A schematic is displayed in Figure 16-2, the different abbreviations are identical as introduced in Figure 15-8. The incident angle θ corresponds to one of the three Lamb wave angles (see dispersion curves in Figure 16-1).

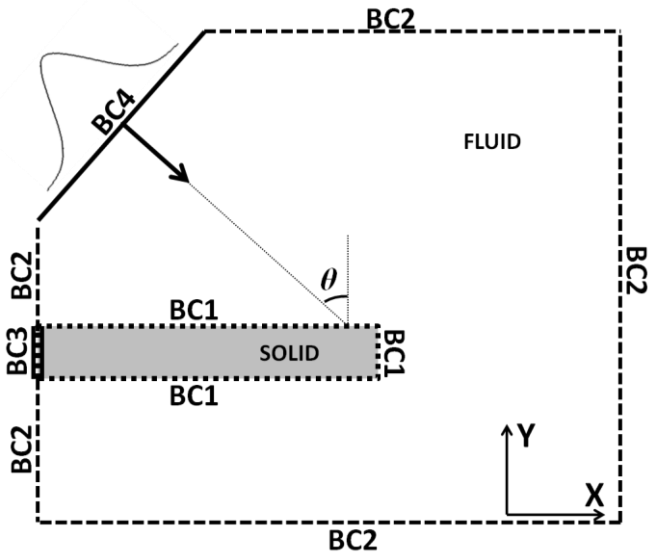

Figure 16-2: Schematic of the FEM implementation. BC1: coupling between liquid and solid domain, BC2: absorbing edges, BC3, infinite solid elements and BC4: generation of ultrasonic beam.

In the remainder of the chapter, we use the subscript '+', respectively '-' to denote a Lamb wave propagating in positive, respectively negative *x*-direction. Hence, A_{0+} denotes a forward propagating A_0 mode, i.e. traveling towards the plate extremity. In addition, the propagation direction of a leaking field associated to a forward, respectively backward propagating Lamb mode is assigned a positive, respectively negative angle θ. Hence, if a leaking field is identified to propagate along $\theta = -13.7°$ in the immersion liquid, it should be associated to the backward propagating A_{1-} Lamb wave. For clarity, the sign convention is schematically represented in Figure 16-3. Obviously, the incident and reflected beam transport energy in the positive *x*-direction, and are therefore assigned a positive angle.

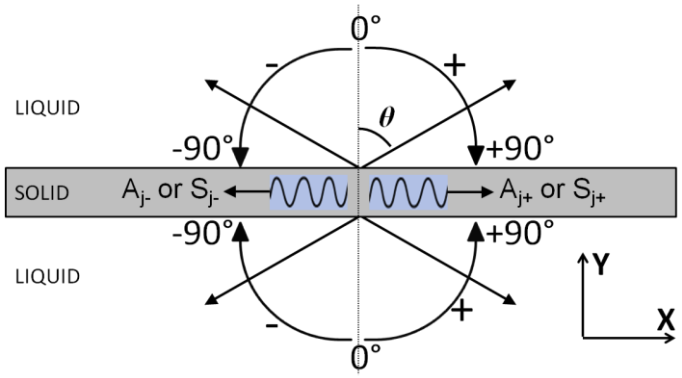

Figure 16-3: Schematic of sign convention. Leaking field of a forward, respectively a backward propagating Lamb wave is assigned a positive, respectively a negative angle θ. The incident and reflected field are assigned a positive angle θ.

16. 3. Backward Leakage and Scattering

First, the backward leakage and scattering phenomena of Lamb wave interaction with the vertical plate end are investigated in real space and spatial frequency domain. Correct understanding of the backward leakage is of great importance for water-coupled NDT and material characterization as it could be a source of parasitic signals.

16. 3. 1. Interaction of A_{0+} Lamb mode

16. 3. 1. a. Real Space

Figure 16-4a-b displays the bounded beam insonification of the infinite brass plate at the A_{0+} Lamb angle according to the schlieren experiment and the FEM simulation. For clarity, the incident beam (I) and reflected beam (R) have been explicitly indicated with yellow arrows. For the simulation, a measure for the acoustic intensity is plotted in the liquid domain, while the solid domain comprises a visualization of the displacement field. The presence of the Schoch effect (splitting and forward translation of the reflected field [19-21]) in the images ensures the stimulation of the forward propagating A_{0+} Lamb wave in the brass plate. To further ascertain the latter statement, the FEM computed displacement components U_x and U_y within the solid domain are analyzed. Figure 16-4c-d represents the displacement components in the solid, evaluated along the x-coordinate at a given time frame. The center of the bounded beam impinges at $x \approx 16$ mm (in the

figure). Since the solid is immersed, energy is leaking back into the immersion liquid, resulting into the typical exponentially decaying tail. Application of the spatial FFT onto the U_y component yields the associated spatial frequency content (see Figure 16-4e). A clear peak is observed at the value of k_x = 9.715 /mm which is in excellent agreement with the dispersion curves (see Figure 16-1a), and thus affirms the stimulation of the A_{0+} Lamb wave in the brass plate.

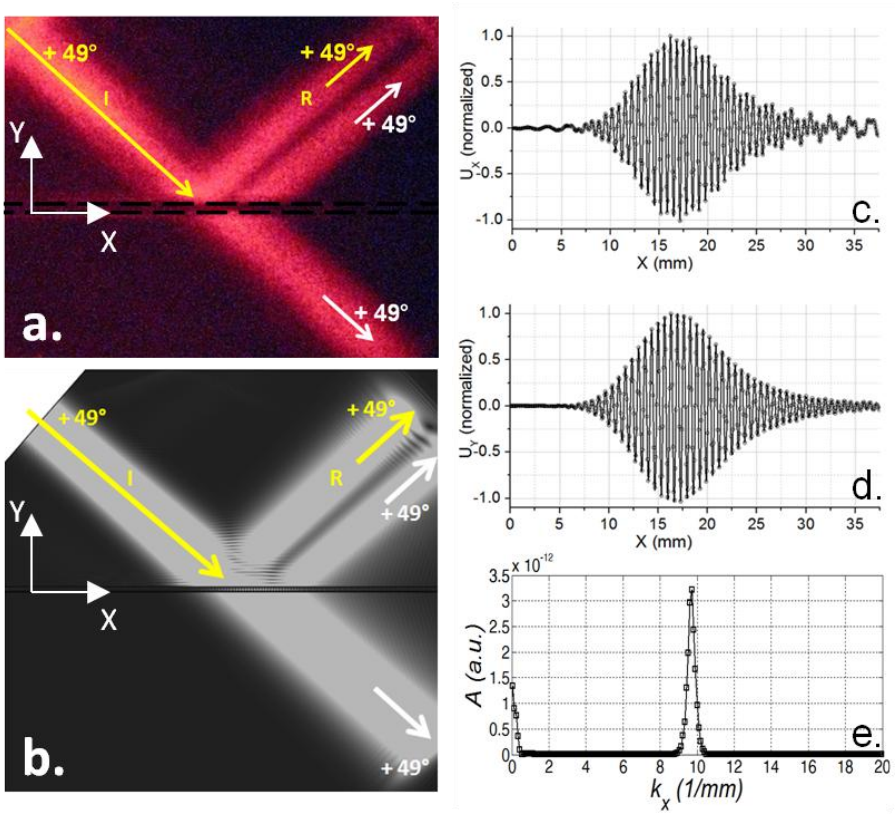

Figure 16-4: Insonification of an immersed infinite brass plate at the A_{0+} Lamb angle, showing the Schoch effect: acousto-optics (a) and FEM (b). Evaluation of the displacement components in the solid: U_x (c) and U_y (d). Spatial frequency content of the U_y signal (e).

Translation of the bounded beam towards the end of the plate leads to a complex diffraction pattern in which several additional acoustic beams are discernible (Figure 16-5a-b). The different propagation angles of those beams can be readily identified with the leaking angles of converted Lamb modes which are propagating in backward direction, i.e. away from the

vertical edge. This confirms that the incoming A_{0+} mode is converted to several backward propagating Lamb modes.

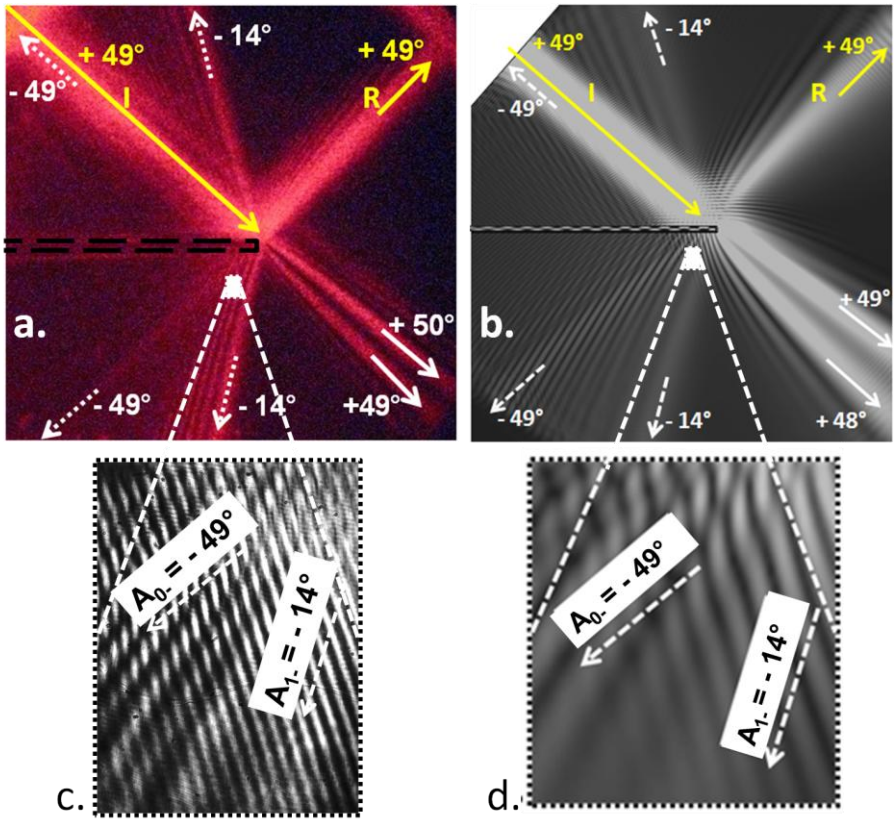

Figure 16-5: Similar as in Figure 16-4, but now the incident bounded beam impinges near the end of the brass plate: acousto-optics (a) and FEM (b). A magnification of the results is shown in (c-d), in which several rays of acoustic energy show up. For clarity, arrows indicating the propagation direction have been added.

Since the vertical end of a plate is a scatterer with a symmetric shape, it may be expected that the symmetry of the incident Lamb mode is conserved during the interaction. This can be validated by an analysis of the FEM results through the depth of the solid plate. In Figure 16-6, a comparison is presented between FEM and theory [22-24] for both the forward and the backward propagating energy inside the solid domain. The subfigures on the left-hand side represent the displacement components U_x and U_y through the depth of the solid plate (90° phase shift taken implicitly into account), the right-hand side subfigures display the spatial frequency content of the

signals along the *x*-direction. Note that the displacement components of the backward propagating A_{0-} mode are omitted in Figure 16-6b because of the similarity with the components for the forward propagating A_{0+} mode. Excellent agreement is obtained between theory and FEM, which again confirms the driving mechanism behind the observed complex leakage phenomenon: the leaking nature of several backward propagating mode-converted Lamb waves. The results in the spatial frequency domain further reveal that the A_{1-} Lamb wave becomes more efficiently stimulated upon reflection at the plate end, relative to the A_{0-} Lamb wave. It is further found that localized non-propagating vibrations [7-8] do not noticeably contribute to the leakage phenomenon.

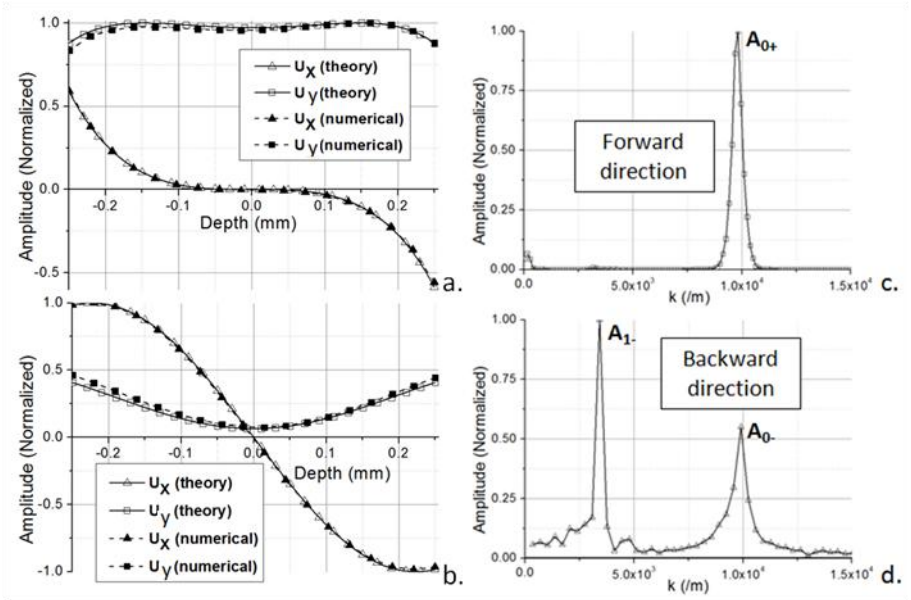

Figure 16-6: Comparison between theoretically and numerically computed displacement components within the brass plate (normalized): forward (a) and backward direction (b). Because of the similarity of the displacement components for the A_{0-} mode and the A_{0+} mode, they have been omitted in (b). The spatial frequency content inside the brass plate: forward (c) and backward (d) direction.

It can be observed that the leakage starts from the immediate neighborhood of the vertical edge, indicating that the mode conversion is already completed near the edge. The numerical results fully support this observation. However, these findings are in clear contrast with the scanning hydrophone measurements obtained in reference [14-15], in which it was

found that a critical path length of several centimeters is required to complete the mode-conversion and consequently to initiate the associated leakage phenomenon.

Close observation of the results in real space reveals the presence of a faintly visible standing wave pattern where multiple acoustic beams overlap. To have a more clear view, Figure 16-5c-d displays a magnification of these patterns. Experimentally this zoom has been obtained by placing a bare CCD chip (pixelink-6.6 Megapixel CMOS sensor) directly in the object plane, while numerically the same was achieved by zooming in on the FEM results. Similar patterns have been experimentally, though without the zooming, observed in reference [18] which were interpreted as rays of energy emanating from a linear interference of multiple overlapping acoustic fields. Considering that our transducers induce nonlinear wave propagation (see Chapter 15), it is likely that caution is required with the sole interpretation in terms of linear interference. It was suggested in reference [18] to use the angular orientation of these rays for the purpose of extracting the leaking angles of the different overlapping fields, and in extension for determining the mode-converted Lamb waves. However, it is clear that this is not straightforward at all for the experimental data, especially when more than two leaking fields interfere with each other (for example when the *fd*-value is higher). The here presented FEM results partly mediate this difficulty, though it would be more wise to perform an analysis in spatial frequency domain. Indeed, it is well known that the visibility in spatial frequency domain does not suffer from overlapping beams.

16. 3. 1. b. Spatial Frequency Domain

The scattering of the A_{0+} Lamb mode with the vertical plate edge is further analyzed in spatial frequency domain for the different quadrants (see inset Figure 15-1).

Quadrant 1

The result for quadrant 1 (above the brass plate in Figure 16-5a) is shown in Figure 16-7. The spatial frequency domain photographs consist of a set of intensity spikes, where each spike corresponds to a certain wave vector $\boldsymbol{k}$. For this purpose, a coordinate system (k_x, k_y) is defined at the spike which corresponds to the undiffracted spike (0^{th} order of diffraction). It is clear that the results show point-symmetry with respect to the origin of the coordinate system. The wave vector magnitude $|\boldsymbol{k}|$ of a spike then corresponds to the

Euclidean distance between the origin and the considered spike, while its direction is prescribed by the angular position. The angles are defined according to the schematic of Figure 16-3. To aid the interpretation, a circle with a radius equal to the magnitude of the wave vector ***k*** of the incoming beam I is superimposed on the figure. The spikes on the superimposed circle correspond to the expected repartition of the energy in forward and backward scattered plane waves with the same wave vector (linear process), and are identified as the incident beam (I), the reflected beam (R) and the leaking fields (A_{0-} and A_{1-}). Note that the spike associated to A_{0-} coincides with the spike associated to -I. Sommerfeld's criterion is taken into account to disregard non-physical spikes [22]. In other words: it is taken care of that no energy can emerge from infinity. For the results shown in Figure 16-7 this results into two non-physical spikes located at the circle (see the red crosses).

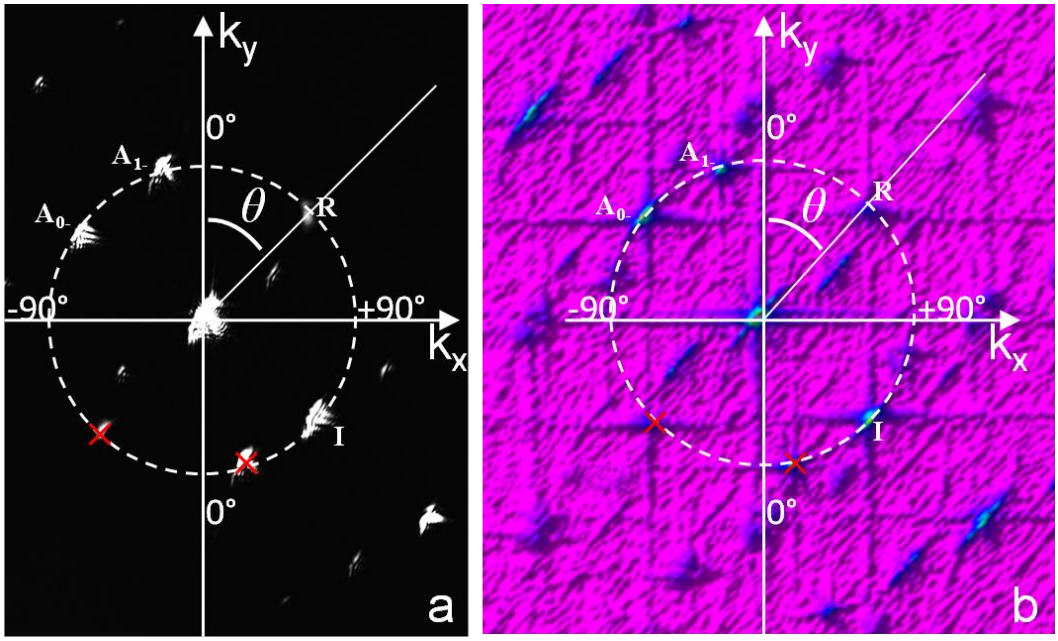

Figure 16-7: Results in spatial frequency domain for quadrant 1 (above the brass plate): experiment (a) and simulation (b). Several indicators have been added to ease the interpretation.

In addition to the "on-circle" spikes, several supplementary spikes can be observed to which wave vectors ***k*** of different magnitude and direction can be attributed. The results indicate that the "off-circle" spikes can be constructed by a combination (addition or subtraction) of multiple "on-

circle" spikes, i.e. spikes associated to I, R and leaking fields. This suggests that the origin of these spikes has to be sought in a nonlinear interaction, which is found in the phonon-phonon interaction and the photon-phonon interaction (see Chapter 15). Certain wave vectors ***k*** originating from such a nonlinear interaction are explicitly labeled and drawn with their vectorial representation in Figure 16-8a-b. As both the phonon-phonon and photon-phonon interaction produce the same characteristic features in spatial frequency domain, we only discuss the phonon-phonon interaction here.

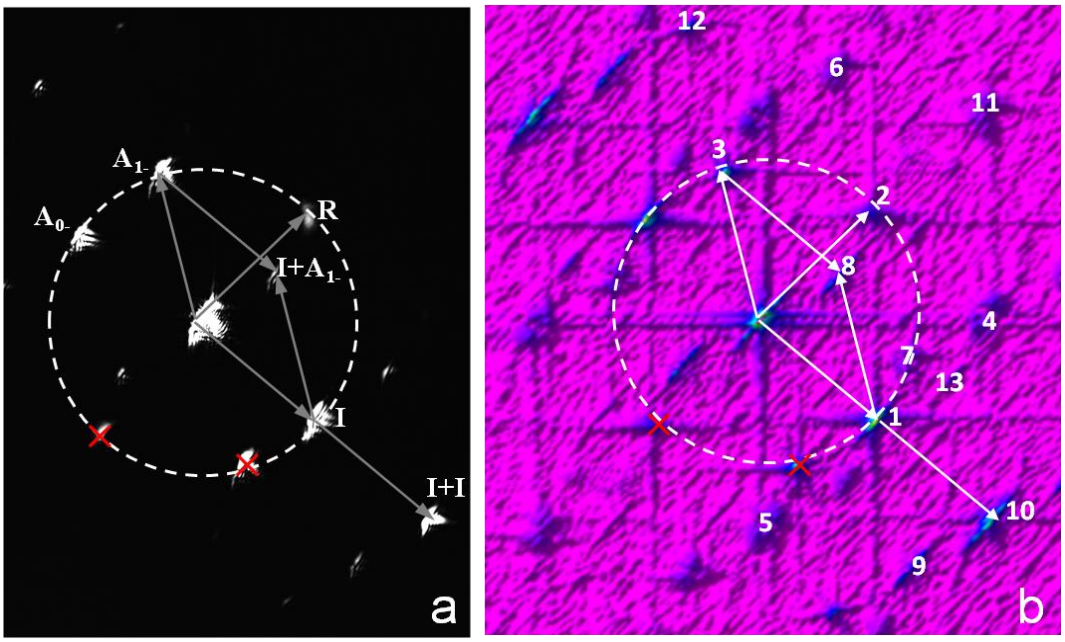

Figure 16-8: Interpretation of the "off-circle" spikes: experiment (a) and simulation (b). The numbers in (b) identify several spikes which will be further analyzed (see Table 16-1).

Generally speaking, in a first-order nonlinear wave approximation involving multiple waves, the total acoustic potential ψ, omitting the $\exp(i\omega t)$-factor, contains product terms of the elementary plane waves ψ_j (including self-interactions). If we simply consider the mutual interaction between ψ_1 and ψ_2, the nonlinear contribution can be expressed as follows:

$$\psi_{NL(12)} = ... + \beta\,\psi_1 \cdot \psi_2 + ... \quad with \quad \beta\,\psi_1 \cdot \psi_2 \sim \beta A_1 A_2 \prod_{j=1}^{2} \exp\left(\pm i\vec{k}_j \cdot \vec{r}\right) \quad (1)$$

where $\overrightarrow{k_j}$ denotes the wave vector of the j^{th} plane wave, A_j its (complex) amplitude, and β is the nonlinear efficiency parameter of the immersion liquid.

Rewriting the nonlinear interaction term of the sound field by means of the leaking angles θ_j, associated with the j^{th} elementary plane wave component, we obtain contributions of the form

$$\psi_{NL(12)} \sim \beta A_1 A_2 \exp\left(\pm i(k_1 \sin\theta_1 \pm k_2 \sin\theta_2)x + (k_1 \cos\theta_1 \pm k_2 \cos\theta_2)\, z\right) \quad (2)$$

As a result of the nonlinear interaction, a set of new wave vectors has been formed corresponding to

$$\left|\overrightarrow{k_{NL(12)-}}\right| = \sqrt{\left(k_1 \sin\theta_1 - k_2 \sin\theta_2\right)^2 + \left(k_1 \cos\theta_1 - k_2 \cos\theta_2\right)^2} \quad (3)$$

and

$$\left|\overrightarrow{k_{NL(12)+}}\right| = \sqrt{\left(k_1 \sin\theta_1 + k_2 \sin\theta_2\right)^2 + \left(k_1 \cos\theta_1 + k_2 \cos\theta_2\right)^2} \quad (4)$$

while the angular direction θ_{NL} of the wave vector $\boldsymbol{k}_{NL(12)-}$, resp. $\boldsymbol{k}_{NL(12)+}$, is given by

$$\theta_{NL(12)-} = \tan^{-1}\left(\frac{k_1 \sin\theta_1 - k_2 \sin\theta_2}{k_1 \cos\theta_1 - k_2 \cos\theta_2}\right) \quad (5)$$

and

$$\theta_{NL(12)+} = \tan^{-1}\left(\frac{k_1 \sin\theta_1 + k_2 \sin\theta_2}{k_1 \cos\theta_1 + k_2 \cos\theta_2}\right) \quad (6)$$

With this set of equations, the magnitude and orientation of the various off-circle spots can be verified up to first order. Obviously, higher order approximations explain the existence of multiple wave vector combinations. Table 16-1 encloses the magnitudes and angular orientation for all the observed diffraction spikes according to theory, experiment and simulation. Apart from the fact that some spikes were not observed experimentally, good agreement is found. The main cause why several spikes are missing in the experimental case is found in the specifications of the used CCD chip. An attenuator was used to decrease the light intensity of the 0^{th} order of diffraction in order to prevent overexposure and damaging of the sensitivity

of the pixels. As a consequence, spikes which already had a low intensity may have dropped below the detection threshold of the CCD chip.

Table 16-1: Spatial frequency domain analysis of quadrant 1 (above brass plate) for the A_{0+} Lamb wave interaction with plate end. The number of the different combinations are also put in Figure 16-8b.

MODE	Theory		Schlieren		FEM	
	$\|\boldsymbol{k}\|$ [1/mm]	θ [°]	$\|\boldsymbol{k}\|$ [1/mm]	θ [°]	$\|\boldsymbol{k}\|$ [1/mm]	θ [°]
1: I	12.7	+48.8	12.8	+48.4	12.9	+48.7
2: R	12.7	+48.8	12.8	+48.1	12.9	+46.2
3: A_{1-}	12.7	-13.7	12.7	-12.6	12.7	-14.0
4: I+R	19.2	90	18.9	+88.8	19.3	+86.6
5: I-R	16.8	0	17.4	0	17.8	+1.2
6: R+A_{1-}	21.8	+17.6	--	--	21.6	+15.5
7: R-A_{1-}	13.2	+72.4	12.6	+74.1	13.0	+78
8: I+A_{1-}	7.7	+58.7	7.7	+61.5	8.0	+59.0
9: I-A_{1-}	24.3	+31.2	24.6	+29.6	24.8	+31
10: 2I	25.4	+48.8	25.5	+45.8	25.7	+47.4
11: 2R	25.4	+48.8	--	--	25.9	+46.8
12: 2A_{1-}	25.4	-13.7	25.7	-12.2	25.4	-13.6
13: 2I+ A_{1-}	16.7	+74.8	16.9	+76.1	16.6	+74.5

Quadrant 2

The results for quadrant 2 (below the brass plate in Figure 16-5a) are shown in Figure 16-9. For clarity, the non-physical spikes have been indicated with a red cross. Now only three physical "on-circle" spikes are present which correspond to the leaking field of the A_{0+}, the A_{0-} and the A_{1-} Lamb modes. The analysis can be done in a similar way as was done for quadrant 1. The obtained results are collected in Table 16-2. Again good agreement is found between theory, experiment and simulation.

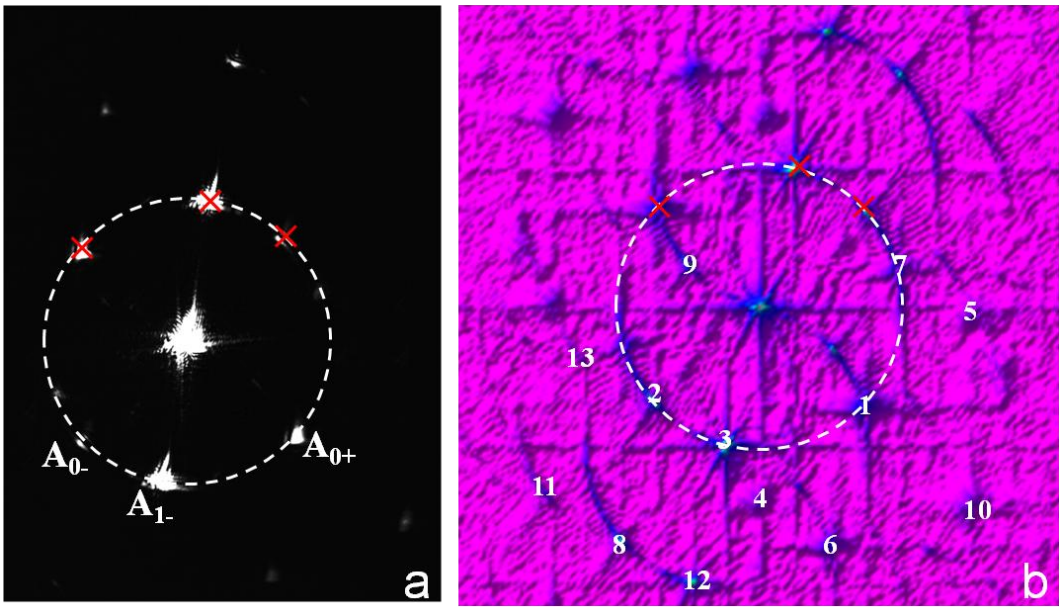

Figure 16-9: Results in spatial frequency domain for quadrant 2 (below the brass plate): experiment (a) and simulation (b). The numbers in (b) identify several spikes which will be further analyzed (see Table 16-2)

Table 16-2: Spatial frequency domain analysis of quadrant 2 (below brass plate) for the A_{0+} Lamb wave interaction with plate end.

MODE	Theory		Schlieren		FEM	
	$\|\boldsymbol{k}\|$ [1/mm]	θ [°]	$\|\boldsymbol{k}\|$ [1/mm]	θ [°]	$\|\boldsymbol{k}\|$ [1/mm]	θ [°]
1: A_{0+}	12.7	+ 48.8	13.0	+46.8	13.0	+46.8
2: A_{0-}	12.7	- 48.8	12.8	-46.2	12.8	-47.4
3: A_{1-}	12.7	- 13.7	12.9	-13	12.8	-13.9
4: $A_{0+}+A_{0-}$	16.8	0	17.0	0	17.8	-1.2
5: $A_{0+}-A_{0-}$	19.2	+ 90	--	--	19.1	+88.3
6: $A_{0+}+A_{1-}$	21.8	+ 17.6	22.5	+17.5	22.5	+15.9
7: $A_{0+}-A_{1-}$	13.2	+72.4	12.7	+70.3	12.9	+73.5
8: $A_{0-}+A_{1-}$	24.3	- 31.2	24.8	-29.4	24.5	-30.8
9: $A_{0-}-A_{1-}$	7.7	- 58.3	7.8	-60.3	7.6	-59.5
10: $2A_{0+}$	25.4	+ 48.8	25.2	+48.7	25.7	+46.2

11: $2A_{0-}$	25.4	- 48.8	23.8	-47.0	26.0	-48.0
12: $2A_{1-}$	25.4	- 13.7	25.6	-11.7	25.6	-13.7
13: $2A_{0-}$-A_{1-}	16.7	-74.7	15.8	-68.5	16.8	-75.3

Compared to the conventional real space images, the visualization in spatial frequency domain offers additional information which is more transparent and straightforward to interpret. This is especially beneficial in case multiple Lamb waves are involved where the various leaking fields overlap. Moreover, by selecting a specific set of spikes, it is possible to highlight solely that part of the acoustical phenomenon which is of interest (this was explicitly demonstrated in Figure 15-7). In this way, the geometrical position of the different involved leaking fields can be checked separately. In particular, for the immersed brass plate, it was confirmed that the energy leakage of each converted mode originated in the immediate neighborhood of the scatterer (plate end), which is in contradiction with the references [14-17] where a critical path length was observed.

16. 3. 2. Interaction of S_{0+} Lamb mode

In analogy with previous section, the brass plate has been insonified at the S_{0+} Lamb angle.

16. 3. 2. a. Real space

The results in real space are shown in Figure 16-10. Figure 16-10a-b shows the insonification far away from the plate end, resulting in the Schoch effect. Translation of the bounded beam towards the plate end induces the leakage and scattering displayed in Figure 16-10c-d. It can be readily observed that the complexity of the scattering process is largely reduced, simply because only one symmetrical mode can be stimulated at the considered frequency-thickness of fd = 1.5 MHz.mm. Both the experimental and numerical results confirm the previous statement that the leakage initiates at the close neighborhood of the plate end.

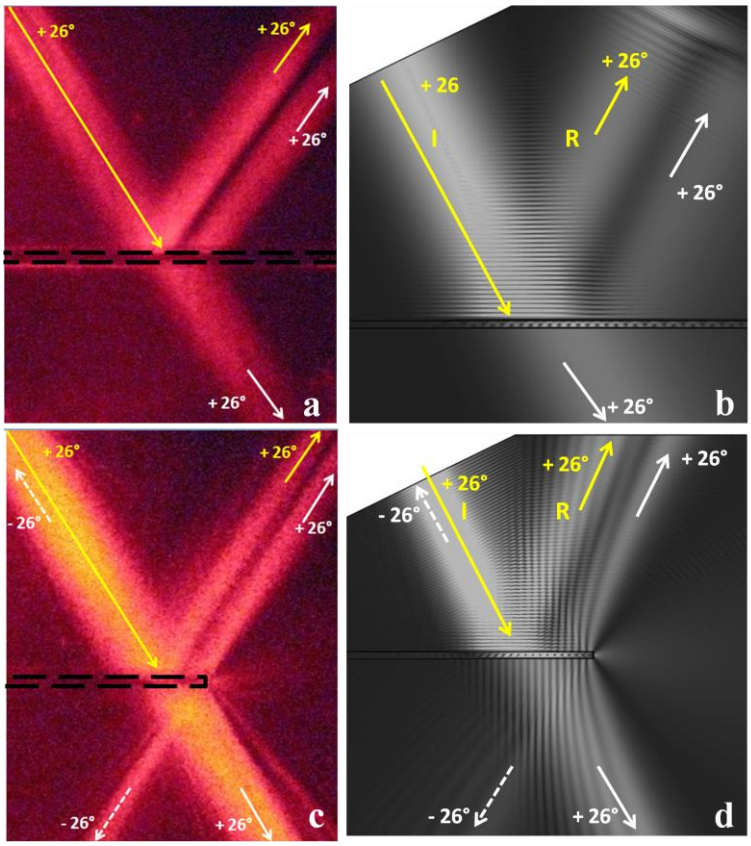

Figure 16-10: Experimental (left) and numerical (right) results for the bounded beam insonification of the brass plate at the S_{0+} Lamb angle: infinite plate (a-b) and semi-infinite plate (c-d).

It can be further observed that a modest forward scattering field is present, as if the plate end acts as an acoustic source. The forward scattering field is later on investigated and discussed more into detail.

16. 3. 2. b. Spatial Frequency Domain

The results in spatial frequency domain for the scattering of the S_{0+} Lamb mode at the plate end (see Figure 16-10c-d in real space) are shown in Figure 16-11. The analysis has been performed again in quadrants. Quadrant 1 is shown in Figure 16-11a-b, quadrant 2 in Figure 16-11c-d. Because only a single symmetrical Lamb mode can be stimulated at fd = 1.5 MHz.mm, it is clear that the distribution of the diffraction spikes for quadrant 1 and quadrant 2 should be symmetric to the vertical axis. This can be readily verified in Figure 16-11. Similar as for the A_{0+} interaction with the plate

edge, the spatial frequency domain results can be analyzed to extract the various (nonlinear) wave vectors. Excellent agreement has been obtained between theory, experiment and simulation. For brevity, the obtained results are not tabulated.

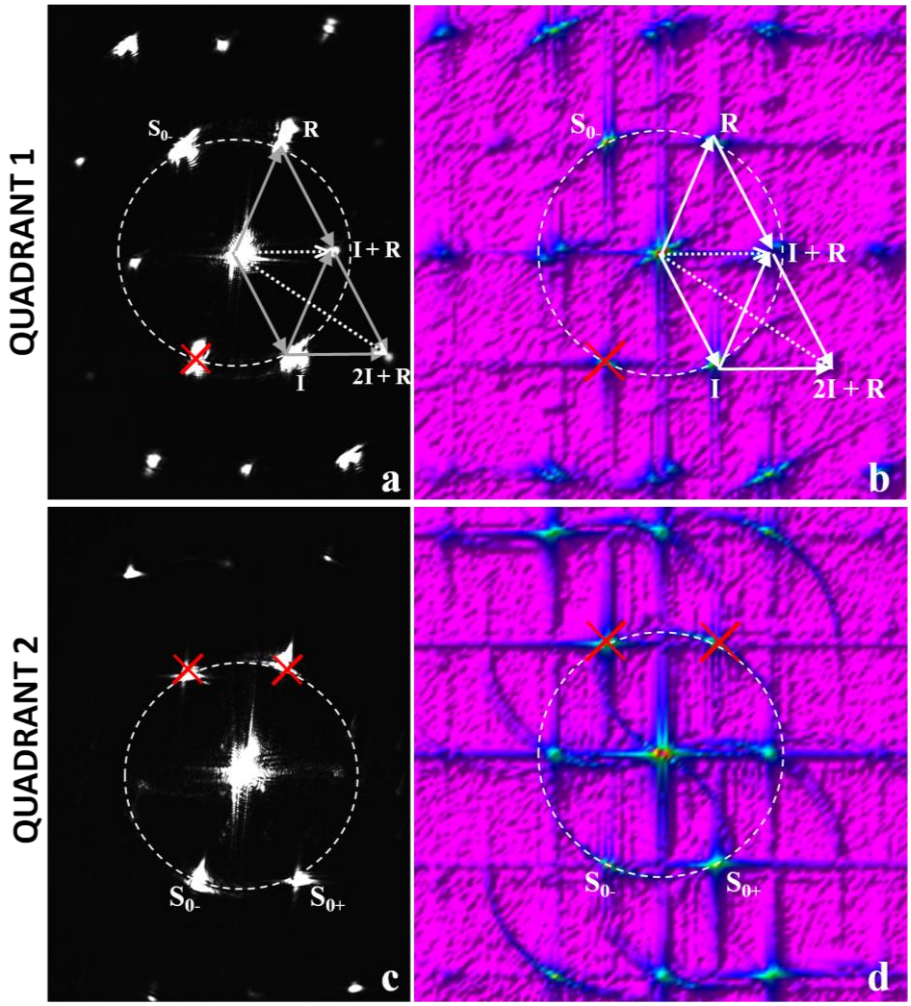

Figure 16-11: Experimental (left) and numerical (right) results in spatial frequency domain for the scattering of S_{0+} mode at the plate end: quadrant 1 (a-b) and quadrant 2 (c-d).

16. 3. 3. Interaction of A_{1+} Lamb mode

Finally, the brass plate is insonified at the third Lamb angle, thus stimulating the A_{1+} Lamb wave.

16. 3. 3. a. Real Space

The obtained results in real space are displayed in Figure 16-12. Figure 16-12a-b shows the insonification far away from the plate end, resulting in the Schoch effect. In comparison with the previous results it can be seen that the leaking field is more widespread. This can be understood considering that the stimulated A_{1+} Lamb mode has a longitudinal character [24]. Or in other words: the vertical displacement component of the Lamb mode is rather small, causing the leakage of energy to be more gently. In addition, a small but non-negligible backward leakage phenomenon can be identified in Figure 16-12a (indicated with green arrows), even though the zone of incidence is located relatively far from the vertical plate end. This observation reveals that relatively large areas in the liquid domain are 'polluted' with scattered ultrasound when quasi-longitudinal modes are in play. Obviously, notion of this observation is of great importance for water-coupled ultrasonic NDT to avoid possible misinterpretation of measurement data.

Translation of the bounded beam towards the plate end results in the leakage and scattering shown in Figure 16-12c-d. It seems that the incident A_{1+} mode is only converted to the A_{0-} mode, and not to the A_{1-} mode. This is in violation with the energy-flux reciprocity principle, which states that the conversion of elastic energy at the plate end is reversible [25]. Possibly, this violation is rather induced by the low intensity associated to the A_{1-} mode, causing it to be masked by the other leaking fields.

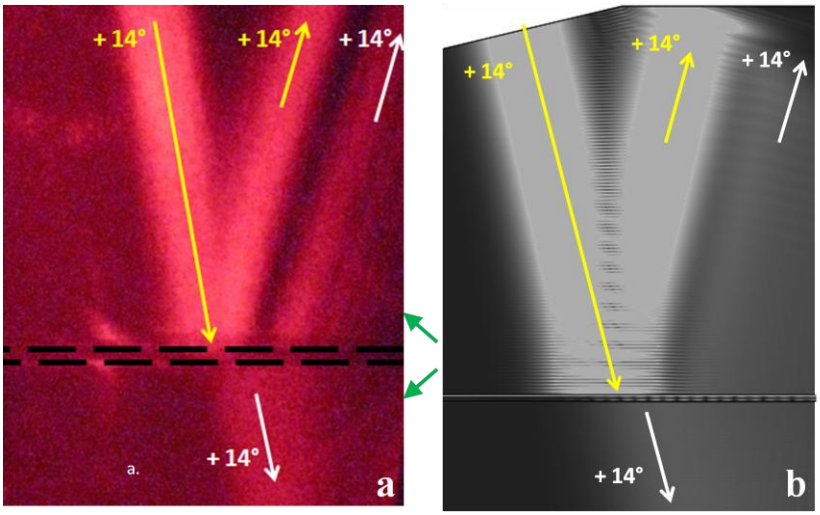

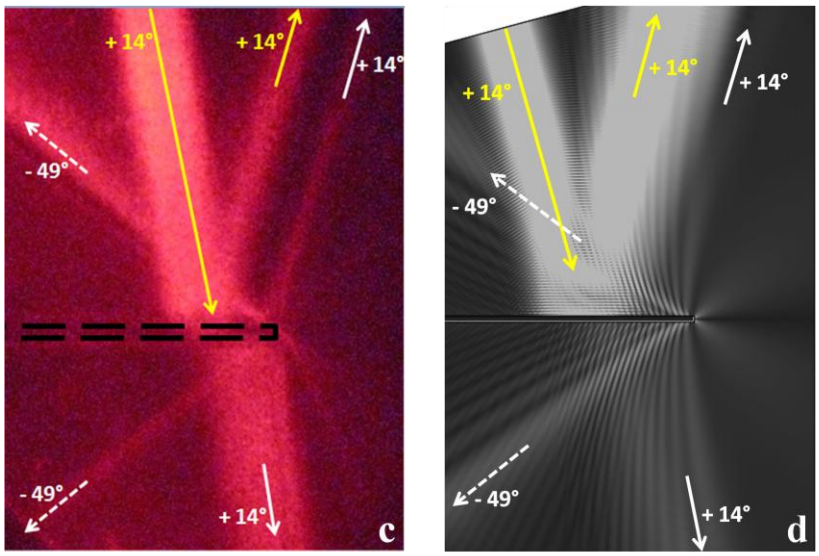

Figure 16-12: Experimental (left) and numerical (right) results for the bounded beam insonification of the brass plate at the A_{1+} Lamb angle: infinite plate (a-b) and semi-infinite plate (c-d).

16. 3. 3. b. Spatial Frequency Domain

The results in spatial frequency domain for the scattering of the A_{1+} Lamb mode at the plate end (see Figure 16-12c-d in real space) are shown in Figure 16-13. Figure 16-13a-b and Figure 16-13c-d display the results for quadrant 1, respectively quadrant 2. The interpretation can be done in a similar way as previously. The numerical result (Figure 16-13d) reveals the presence of a faint spike associated to the A_{1-} Lamb mode, confirming the validity of the energy flux reciprocity principle [25]. This is not seen in the experimental recording, probably due to the limited sensitivity of the CCD chip.

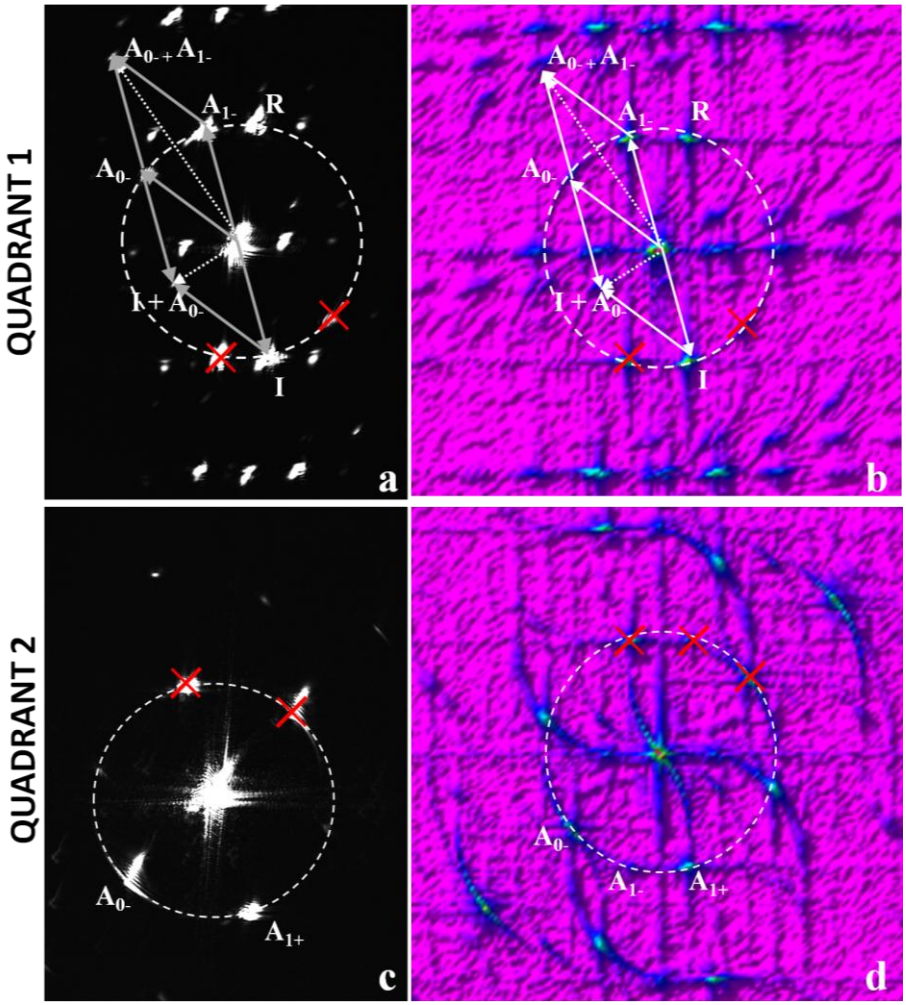

Figure 16-13: Experimental (left) and numerical (right) results in spatial frequency domain for the scattering of A_{1+} mode at the plate end: quadrant 1 (a-b) and quadrant 2 (c-d).

Note that the above results for the brass plate equally hold when considering different Lamb modes. In fact, we also investigated an aluminum sample at fd = 4.35 MHz.mm for which higher order Lamb waves can be stimulated (see Figure 16-14). Of course, when the number of possible Lamb waves increases, the overlapping of the multiple leaking fields makes the identification of the different involved Lamb waves in real space even more difficult, if not impossible. Though, the masking effect of the overlapping acoustic fields is largely sorted out by performing and analyzing the experiment in the spatial frequency domain. For brevity however, these experiments are not shown in this thesis.

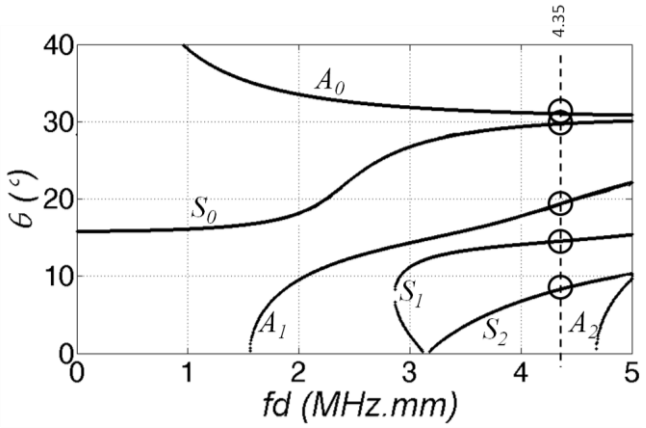

Figure 16-14: Dispersion curves $\theta(fd)$ for aluminum.

16. 4. Forward Leakage and Scattering

In this section we examine both experimentally and numerically the forward radiation pattern emerging from a vertical plate ending (see Figure 16-10c-d and Figure 16-12c-d). Though, we now consider an aluminum sample at fd = 4.35 MHz.mm because more clear and distinct forward radiation patterns appear with respect to the brass plate. The second reason why the aluminum sample is discussed, is found in the fact that our experimental results are not consistent with neither the experimental results, nor the numerical results presented in reference [18]. With the aluminum plate, we are in the same situation as in reference [18], and thus straightforward comparison should be possible. A schematic of the problem is shown in Figure 16-15, together with the definition of the directivity angle β.

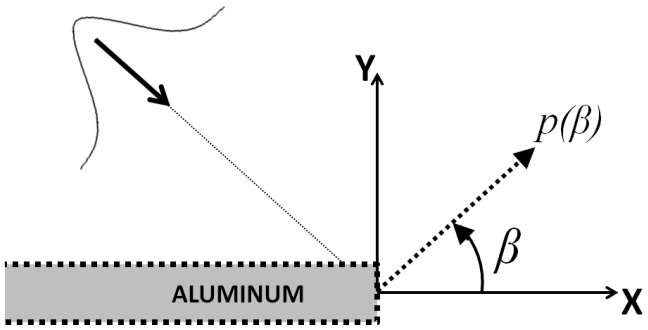

Figure 16-15: Definition of the directivity angle β.

At fd = 4.35 MHz.mm, five Lamb waves can be stimulated (see Figure 16-14). Real space schlieren images have been obtained for the insonification near the plate end at the different Lamb angles, and are displayed in Figure 16-16. However, no clear visualization of the distinct forward radiation patterns for the A_{0+} and the S_{0+} mode (Figure 16-16a) could be made due to the competition between the convergent nature of these waves (see dispersion curves in Figure 16-14) and the slightly divergent acoustic beam.

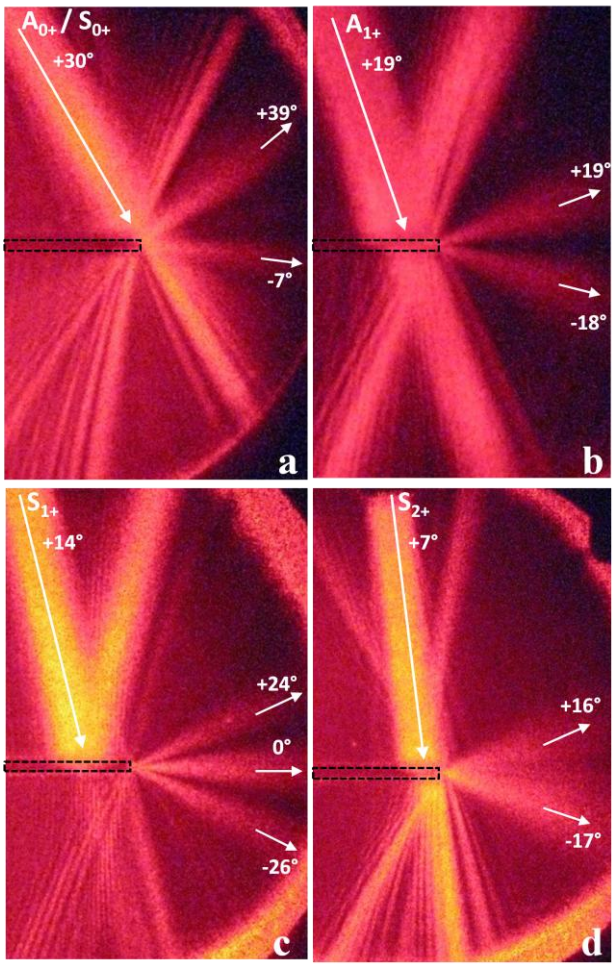

Figure 16-16: Forward radiation patterns for the insonification near the aluminum edge at the various Lamb angles: A_{0+}/S_{0+} angle (a), A_{1+} angle (b), S_{1+} angle (c) and S_{2+} angle (d).

The insonification at the other three Lamb angles (A_{1+}, S_{1+} and S_{2+}) shows intriguing forward radiation patterns with characteristic lobes. Recently, the forward scattering has been interpreted in terms of acoustic multipoles [18]. Basically, the horizontal displacement (*x*-direction) of the stimulated Lamb mode is evaluated at the plate edge. The maxima are then replaced by oscillating point sources having the same amplitude and phase. As such, it was found that the U_x component of the A_{1+} mode can be described by a quadrupole, resulting in two symmetrical forward radiation lobes, in agreement with experiment (Figure 16-16b). The U_x component of the S_{1+} mode was found to be equivalent to a disturbed quadrupole, resulting in a diffuse forward scattering. This however does not agree with the corresponding experiment in which three distinct lobes are seen (Figure 16-16c). This probably indicates that the multipole approach is too simple for accurate describing the forward radiation patterns.

In order to improve the above modeling, the plate edge is assumed to be an oscillating discretized acoustic line source. The amplitude distribution $g(0,y)$, with $y \in \left[-d/2, d/2\right]$, of the line source corresponds to the horizontal displacement field U_x of the incident Lamb mode along the depth direction. For reasons of implementation in FEM, the amplitude distribution is approximated by a shape function according to:

$$\tilde{g}(0,y) = \sum_{i=0}^{n} A_i \cos(\zeta_i y) + B_i \sin(\zeta_i y) \qquad \text{with } y \in \left[-d/2, d/2\right] \tag{7}$$

Note that when the source function $g(0,y)$ is taken a constant *C*, the radiation pattern reduces to the classical case of single-slit diffraction of a plane wave. The left part of Figure 16-17 compares the *x*-component of the displacement field associated with the different Lamb modes A_{1+}, S_{1+} and S_{2+} to the approximated shape function used for the numerical computation. More importantly, the middle column of Figure 16-17 shows contour plots of the numerically computed radiation patterns. Here, we do not show the time-averaged intensity, but explicitly incorporate the phase information. As such, it is clear that several phase reversals appear, which give rise to the formation of the high intensity lobes as a consequence of interference. It is interesting to point out the drastic change of the radiation pattern corresponding to the S_{1+} and S_{2+} mode, even though the associated shape functions are very similar, except for a vertical shift. In contrast to the

multipole approximation [18], the here computed forward radiation fields agree well with the experimentally recorded radiation fields for the different incident Lamb modes. The here given model for the forward radiation pattern has also been considered in a more or less similar way by various other research teams [26-28].

Finally, the numerically computed acoustic pressure *p(β)* is presented in the right column of Figure 16-17 as a function of the directivity angle *β*. Based on these patterns and supported by additional simulations, we conclude that in case of anti-symmetric, respectively symmetric Lamb modes, the number of phase reversals, rather than the number of radiation lobes as stated in [26-27], is odd, respectively even.

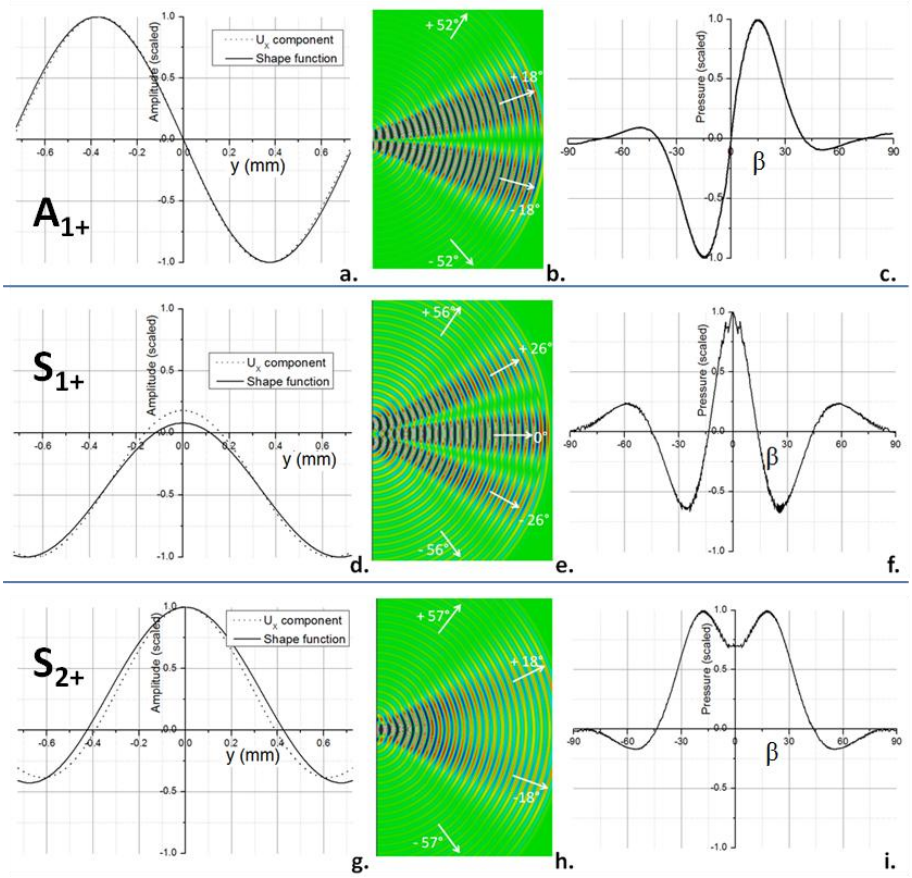

Figure 16-17: Comparison between U_x component of A_{1+} Lamb mode and proposed shape function (a), contour plots of computed radiation field (b) and pressure field p as a function of directivity angle β (c). Part (d-f) and part (g-i) correspond to the analysis of the S_{1+}, respectively the S_{2+} Lamb mode.

16. 5. Conclusions

The leakage and scattering associated with the plate end insonification at the Lamb angle is investigated by the combined use of acousto-optics and FEM. Besides the traditional acousto-optic schlieren experiments in real space, we further performed experiments in spatial frequency domain by inserting a CCD-chip directly in the so-called Fourier plane. The numerical analogue for this concerns the application of the spatial 2D Fast Fourier transform.

The results in real space reveal a complex backward radiation pattern in real space, which is composed of several leaking fields belonging to backward propagating mode-converted Lamb modes. The geometrical position of the scattered beams firmly indicates that the conversion process is completed in the near neighborhood of the vertical plate edge. These experimental findings have been fully validated by means of the FEM simulations. The results also call attention to the likelihood that extended zones inside the immersion liquid get polluted by the leakage, especially when quasi-longitudinal Lamb modes are involved. For practical NDT application based on the stimulation of Lamb modes, these observations have important consequences since the discussed leakage and scattering potentially 'pollutes' the measurement zone, which may lead to misinterpretation of the mechanical health of the insonified structure. As a matter of fact, the here discussed effects were already identified as a potential pitfall during the experimental recording of ultrasonic backscatter polar scans (see Chapter 5).

The results obtained in spatial frequency domain reveal a set of intense diffraction spikes, whose position reveal the magnitude and orientation of the associated wave vectors. These spikes clearly reveal the linearity of the conversion process, i.e. the scattered beams have their spikes located at a circle with its radius equal to the magnitude of the wave vector of the incident beam. Besides the on-circle diffraction spikes, many off-circle spikes are observed, which thus have to be attributed to a nonlinear interaction process, in our case the phonon-phonon and the photon-phonon interaction. The results in spatial frequency domain have been analyzed in quadrants to ease the interpretation. Excellent agreement is obtained between theory, experiment and FEM. It is however pointed out that the nonlinearity of the FEM results in spatial frequency domain has been obtained artificially by introducing non-physical phase shifts. Finally, it is worth noting that the results in spatial frequency domain do not suffer from overlapping beams, which is advantageous when investigating a sample at a higher *fd*-value.

Apart from backward radiation patterns, it was also found that the plate edge causes energy to be radiated in the forward direction. The forward radiation has been successfully modeled by assuming the vertical edge to be an oscillating acoustic line source, with an amplitude distribution corresponding to the horizontal component U_x of the incident Lamb mode. It was found that the number of phase reversals in the forward radiation pattern is linked to the symmetry of the incident Lamb mode: an incident symmetric, respectively antisymmetric Lamb wave corresponds to an even, respectively uneven number of phase reversals.

16. 6. References

[1] Hall, G., *ULTRASONIC WAVE VISUALIZATION AS A TEACHING AID IN NONDESTRUCTIVE TESTING.* Ultrasonics, 1977. 15(2): p. 57-69.

[2] Cho, Y.H. and J.L. Rose, *A boundary element solution for a mode conversion study oil the edge reflection of Lamb waves.* Journal of the Acoustical Society of America, 1996. 99(4): p. 2097-2109.

[3] Torvik, P.J., *Reflection of Wave Trains in Semi-infinte Plates.* Journal of the Acoustical Society of America, 1967. 41(2): p. 346-353.

[4] Galan, J.M. and R. Abascal, *Lamb mode conversion at edges. A hybrid boundary element-finite-element solution.* Journal of the Acoustical Society of America, 2005. 117(4): p. 1777-1784.

[5] Le Clezio, E., M.V. Predoi, M. Castaings, B. Hosten, and M. Rousseau, *Numerical predictions and experiments on the free-plate edge mode.* Ultrasonics, 2003. 41(1): p. 25-40.

[6] Lowe, M.J.S. and O. Diligent, *Reflection of the fundamental Lamb modes from the ends of plates*, in *Review of Progress in Quantitative Nondestructive Evaluation, Vols 20a and 20b*, D.O. Thompson and D.E. Chimenti, Editors. 2001. p. 89-96.

[7] Pagneux, V., *Revisiting the edge resonance for Lamb waves in a semi-infinite plate.* Journal of the Acoustical Society of America, 2006. 120(2): p. 649-656.

[8] Diligent, O., M.J.S. Lowe, E. Le Clezio, M. Castaings, and B. Hosten, *Prediction and measurement of nonpropagating Lamb modes at the free end of a plate when the fundamental antisymmetric mode A(0) is incident.* Journal of the Acoustical Society of America, 2003. 113(6): p. 3032-3042.

[9] Zhang, S.Y., J.Z. Shen, and C.F. Ying, *The reflection of the Lamb wave by a free plate edge - visualization and theory.* Materials Evaluation, 1988. 46(5): p. 638-641.

[10] Morvan, B., N. Wilkie-Chancellier, H. Duflo, A. Tinel, and J. Duclos, *Lamb wave reflection at the free edge of a plate.* Journal of the Acoustical Society of America, 2003. 113(3): p. 1417-1425.

[11] Predoi, M.V. and M. Rousseau, *Recent results about Lamb waves reflection at the free edge of an elastic layer.* Acta Acustica United with Acustica, 2003. 89(4): p. 632-639.

[12] Diodati, P., G. Tassi, and A. Alippi, *Lamb wave reflection at plate edges.* Applied Physics Letters, 1985. 47(6): p. 573-575.
[13] Morse, S.F. and P.L. Marston, *Meridional ray backscattering enhancements for empty truncated tilted cylindrical shells: Measurements, ray model, and effects of a mode threshold.* The Journal of the Acoustical Society of America, 2002. 112(4): p. 1318-1326.
[14] Elkettani, M.E., P. Pareige, and F. Luppe, *Conversion of Lamb waves at the edge of a submerged plate.* Journal De Physique Iv, 1994. 4(C5): p. 873-876.
[15] Elkettani, M.E., P. Pareige, F. Luppe, and J. Ripoche, *Experimental study of the conversion of lamb waves at the end of an immersed plate.* Acustica, 1996. 82(2): p. 251-259.
[16] Pareige, P., F. Luppe, M.E.C. Elkettani, and J. Ripoche, *LAMB WAVE SCATTERING ALONG THE EDGE OF AN IMMERSED BEVELED PLATE.* Journal De Physique Iv, 1992. 2(C1): p. 1079-1082.
[17] Elkettani, M.E.C., P. Pareige, and F. Luppe, *Scattering by a semi-infinite elastic plate immersed in water.* Journal De Physique Iv, 1992. 2(C1): p. 1015-1018.
[18] Declercq, N.F., J. Degrieck, and O. Leroy, *Bounded beam interaction with plate-edge at lamb angle.* Acta Acustica United with Acustica, 2005. 91(2): p. 326-332.
[19] Schoch, A., *Der Schalldurchgang durch plate.* acustica, 1952. 2.
[20] Tamir, T. and H.L. Bertoni, *Lateral displacement of optical beams at multilayered and periodic structures.* Journal of the Optical Society of America, 1971. 61(10): p. 1397-1413.
[21] Bertoni, H.L. and T. Tamir, *Unified theory of Rayleigh-angle phenomena for acoustic beams at liquid-solid interfaces.* Applied physics, 1973. 2(4): p. 157-172.
[22] Auld, B.A., *Acoustic Fields and Waves in Solids, second edition*. 1990, Florida: Krieger publishing company. 856.
[23] Rose, J.L., *Ultrasonic Waves in Solid Media*. 1999: Cambridge University Press. 454.
[24] I.A.Viktorov, *Rayleigh and Lamb waves*. 1967, New York: Plenum. 154.
[25] Rokhlin, S.I., *Interaction of Lamb Waves with elongated delaminations in thin sheets.* International Advances in Nondestructive Testing, 1979. 6: p. 263-285.
[26] Zhu, Q.G., H.J. Ruf, and W.G. Mayer, *Lamb wave radiation from plate termination in a liquid.* Ultrasonics, 1991. 29(6): p. 459-463.
[27] Piet, J.F., G. Quentin, M. Debilly, Q.G. Zhu, and W.G. Mayer, *Phase of Lamb wave radiation from a plate immersed in a liquid.* Ultrasonics, 1992. 30(5): p. 297-300.
[28] Pareige, P., F. Luppe, and J. Ripoche, *Scattering of Lamb waves at the edge of a semi-infinite plate embedded in water.* Journal of the Acoustical Society of America, 1992. 92(2): p. 1056-1060.

Chapter 17

The Ultrasonic Talbot Effect

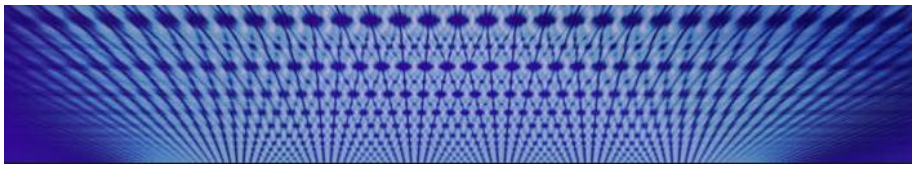

Header of the Nature Physics' website containing a simulation of the Talbot effect.

Summary

The Talbot effect is named after Henry Fox Talbot, who observed in 1836 "a curious pattern of alternating lines" when illuminating a grating [1]. In 1881, the self-imaging or lensless imaging has been rediscovered by Lord Rayleigh [2], who explained it as a natural consequence of Fresnel diffraction. As such, the Talbot effect can be observed for any feature having a wave-like nature, and has already been demonstrated for light, electrons, atoms, molecules, plasmons, etcetera. In this chapter, we demonstrate for the first time that also an ultrasonic Talbot effect can be observed. Though, it is shown that the ultrasonic Talbot effect is a mixture of an amplitude-based and a phase-based Talbot effect. This is in sharp contrast with the classical optical Talbot effect. The experiments are compared with numerical results, yielding excellent agreement. An acoustic surface wave device is proposed on the basis of the ultrasonic Talbot effect.

17. 1. Introduction

The Talbot effect is named after Henry Fox Talbot, who observed in 1836 'a curious pattern of alternating lines' when illuminating a Ronchi grating (black/white ratio of 50%) [1]. In 1881, the self-imaging or lensless imaging has been rediscovered by Lord Rayleigh [2], who explained it as a natural consequence of Fresnel diffraction. The region of Fresnel diffraction is limited by the relation $z \leq \rho^2/\lambda$ with ρ the illuminated portion of the grating and λ the wave length. Just like far-field phenomena, the Talbot effect is the summation of different diffracted waves which interfere with each other, though with the exception that the curvature of the wave fronts, which have a strong influence on the resulting intensity distribution, cannot be ignored. According to Huygens' wavelet principle, each point on a wave acts as a secondary source having the same frequency and phase as the primary wave. Assuming a 2D situation, the Huygens radiator can be taken as a cylindrical wave:

$$\psi(r,t) = \frac{e^{i(kr-\omega t)}}{\sqrt{r}} \tag{1}$$

with $k = 2\pi/\lambda$ the wave number and ω the angular frequency.

Hence, the slits of a grating can be described as a collection of Huygens radiators, oscillating in phase with each other (see schematic in Figure 17-1) [3].

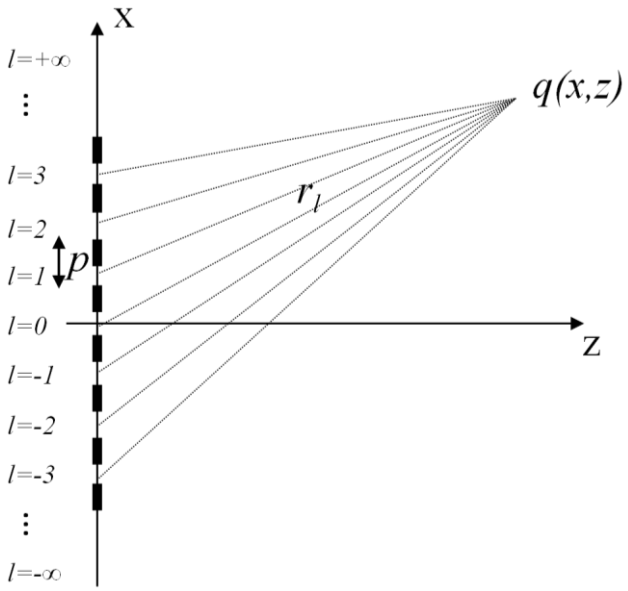

Figure 17-1 A grating with an infinite number of slits, each slit is modeled by a cylindrical radiator.

Considering a grating with an infinite number of slits, each populated with a single radiator (which is equivalent to neglecting the slit width), the wave function in an arbitrary point *q* can be written as

$$\Psi(x,z,t) = \sum_{l=-\infty}^{+\infty} \frac{e^{i\left(k\sqrt{x^2+z^2-2xlp+l^2p^2}-\omega t\right)}}{\sqrt{x^2+z^2-2xlp+l^2p^2}} \qquad (2)$$

with *p* the period of the grating.

Averaging over time yields the wave intensity at point *q*

$$I(x,z)=\left\langle \left| \sum_{l=-\infty}^{+\infty} \frac{\cos\left(k\sqrt{x^2+z^2-2xlp+l^2p^2}\right)}{\sqrt{x^2+z^2-2xlp+l^2p^2}} \right|^2 + \left| \sum_{l=-\infty}^{+\infty} i\frac{\sin\left(k\sqrt{x^2+z^2-2xlp+l^2p^2}\right)}{\sqrt{x^2+z^2-2xlp+l^2p^2}} \right|^2 \right\rangle \tag{3}$$

Hence, self-images of the grating can be observed at distance z when satisfying the condition (for $x = 0$)

$$\frac{2\pi}{\lambda}\sqrt{z^2+lp^2} = 2s\pi \tag{4}$$

for any integer l, with s an arbitrary integer.

In the paraxial approximation, $lp < z$, this condition can be expanded to $(lp/z)^2$ using a Taylor expansion

$$\frac{2\pi}{\lambda} z\left(1+\frac{1}{2}\left(\frac{lp}{z}\right)^2 - O\left(\frac{lp}{z}\right)^4 + \ldots\right) = 2s\pi \tag{5}$$

This expansion may be cut at the first order term whenever $\lambda << p$, requiring that z does not overweight $(lp)^2/\lambda$ as the Talbot effect is a near-field phenomenon in the Fresnel region. Subtraction of the linear term $z/\lambda = s_0$ then yields the condition for a self-image

$$z = \frac{1}{2}\frac{l^2p^2}{s\lambda} \tag{6}$$

For $l = 1$ and $n = 1$, the Talbot distance z_T then becomes

$$z_T = \frac{p^2}{2\lambda} \tag{7}$$

The Talbot distance z_T is fully defined in terms of the grating periodicity p and the wave length λ. At every integer of the Talbot distance z_T a self-image

is produced. Rayleigh proposed to use this effect to copy gratings by placing a photographic film at an integer Talbot distance [2]. For a black/white ratio different from 50%, a reproduction of the original image is formed at fractional Talbot distances, having different spatial dimensions compared to the original image. Hence, the Talbot effect produces ever smaller fractional revivals, resulting in a so-called Talbot carpet [4].

In reality, a grating has a finite number of slits. The accuracy of simulations on the other hand increases by discretizing each slit by multiple radiators (see schematic in Figure 17-2). Considering (2*L*+1) slits, with each slit populated by (2*M*+1) Huygens radiators, the resulting field at the physical point *q* can be calculated by summing all contributing sources

$$\Psi(x,z,t)=\sum_{l=-L}^{L}\left(\sum_{m=-M}^{M}\frac{e^{i\left(k\sqrt{l^2p^2+\frac{2lmpa}{2M+1}+\frac{m^2a^2}{(2M+1)^2}-2xlp-\frac{2xma}{2M+1}+x^2+z^2}-\omega t\right)}}{\sqrt{l^2p^2+\frac{2lmpa}{2M+1}+\frac{m^2a^2}{(2M+1)^2}-2xlp-\frac{2xma}{2M+1}+x^2+z^2}}\right) \quad (8)$$

with *p* the periodicity of the grating and *a* the slit region of a period.

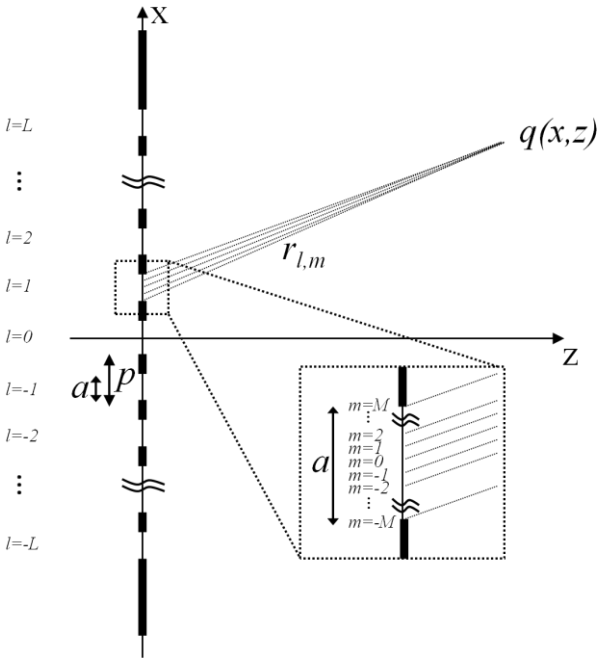

Figure 17-2: Model of a finite grating having (2*L*+1) slits, with each slit populated by (2*M*+1) radiators.

The intensity *I* is found again by the relation

$$I(x,z) = \Psi\left(x,z,\overline{t}\right) \cdot \Psi^{*}\left(x,z,\overline{t}\right) \tag{9}$$

with the * denoting the complex conjugate.

A numerical example of a Talbot carpet is shown in Figure 17-3 for a grating with 21 slits and a black/white ratio of 97%. Each slit is populated by 11 radiators. One can clearly identify the different rescaled revivals of the original image at the fractional Talbot distances in the diffracted field (explicitly indicated with arrows).

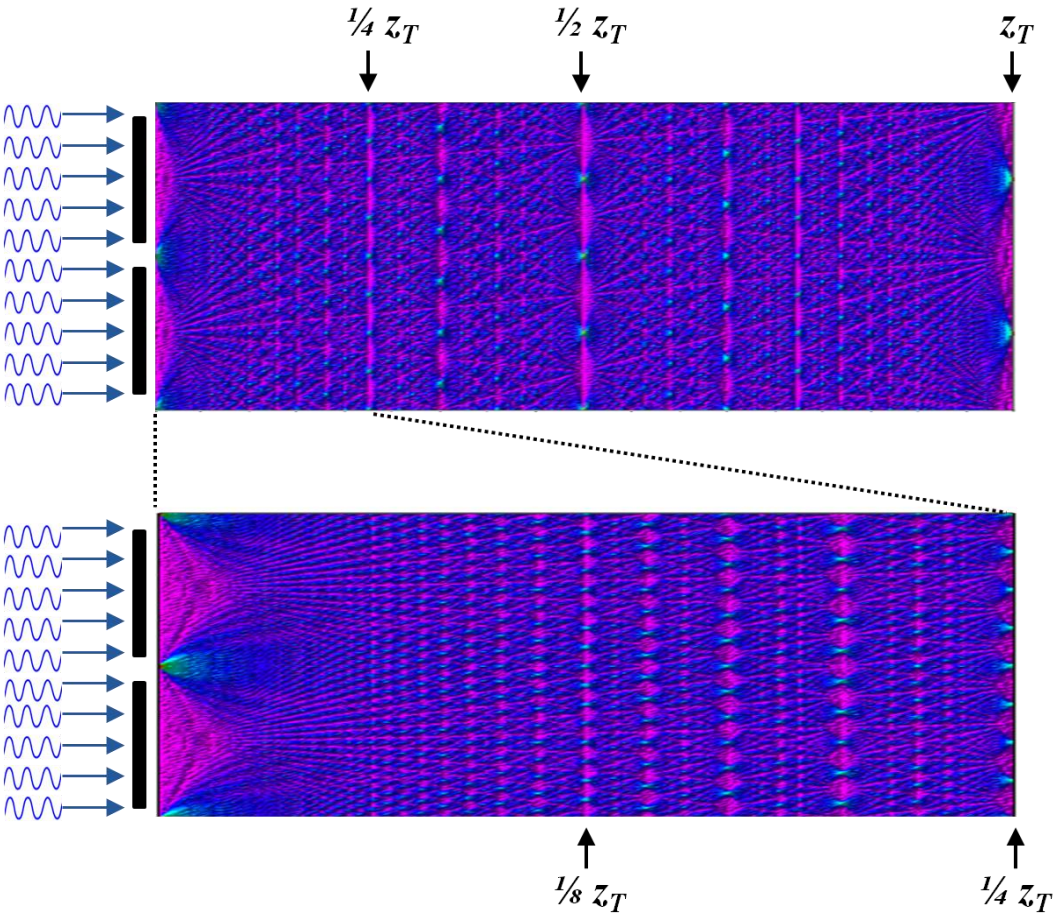

Figure 17-3: Numerical simulation of the illumination of a grating with 21 slits, each populated by 11 radiators. The period is 10, the slit width is 0.3 and the wave length is 0.01. Only 2 periods of the grating are shown.

Note that the above numerical example describes the interaction of a plane wave with an amplitude-based grating. The above analysis can also be performed for a phase-based grating, yielding similar though not equivalent results. For brevity however, this is not shown here.

As the Talbot effect is the result of a diffraction and interference phenomenon, it should be observed for any object having a wave-like nature. So far, the effect has been investigated for light [1-2, 5], electrons [6], atoms [7-8], molecules [9] and plasmons [10-11], and has been exploited for different applications, among which include interferometry, atom lithography, grating reproduction, spectrometry and others [2, 12-15].

In this chapter, the ultrasonic analogue of the Talbot effect is demonstrated by means of acousto-optic schlieren experiments. The experiments are assisted and validated with theory and numerical results.

17. 2. Experimental Results

A Ronchi grating, with periodicity 2.9 mm, has been produced by wire cutting an aluminum plate with thickness $d = 0.5$ mm. The grating is immersed in water and has been insonified under normal incidence by a 37 mm wide ultrasonic beam operating at a harmonic frequency of $f = 3.2$ MHz. With these parameters, the self imaging should take place at $z_T \approx 18.18$ mm. The acousto-optical image is shown in Figure 17-4.

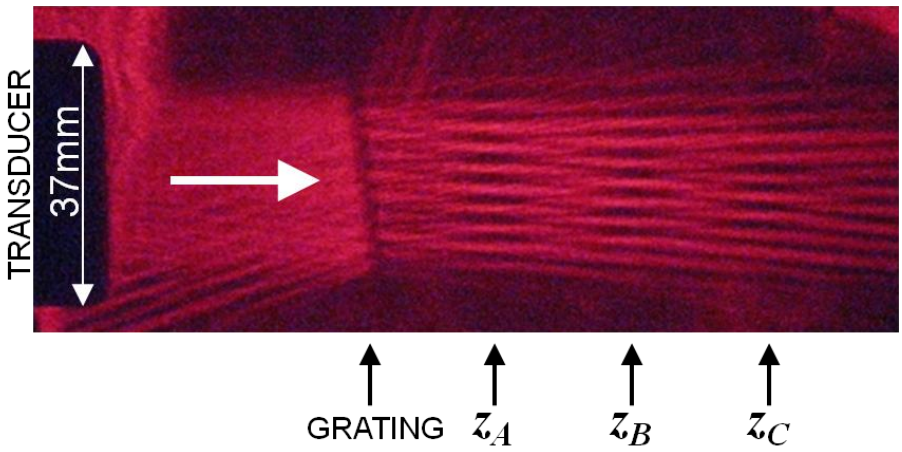

Figure 17-4: Acousto-optical visualization of the ultrasonic Talbot effect using a Ronchi grating. Several indicators have been added for the ease of interpretation.

One can clearly identify a Talbot pattern with its half-period phase jumps and its self-images. With the physical dimension of the transducer given in the photograph, the locations of self-images are experimentally determined: $z_A = 18.07$ mm, $z_B = 37.86$ mm and $z_C = 56.79$ mm. These values are in good agreement with multiples of the theoretical Talbot distance z_T. Since the above experiment is obtained with a Ronchi grating, no minified self-reproductions are observed at fractional Talbot distances. For these to observe, a second aluminum grating (thickness $d = 0.5$ mm) was manufactured having a black/white ratio of 80% with a periodicity of 5 mm. For the 3.2 MHz ultrasonic beam, this should theoretically result in a self-

image at Talbot distance z_T = 54.1 mm, while at fractional Talbot distances minified self-images should be observed. The acousto-optical experiment is shown in Figure 17-5.

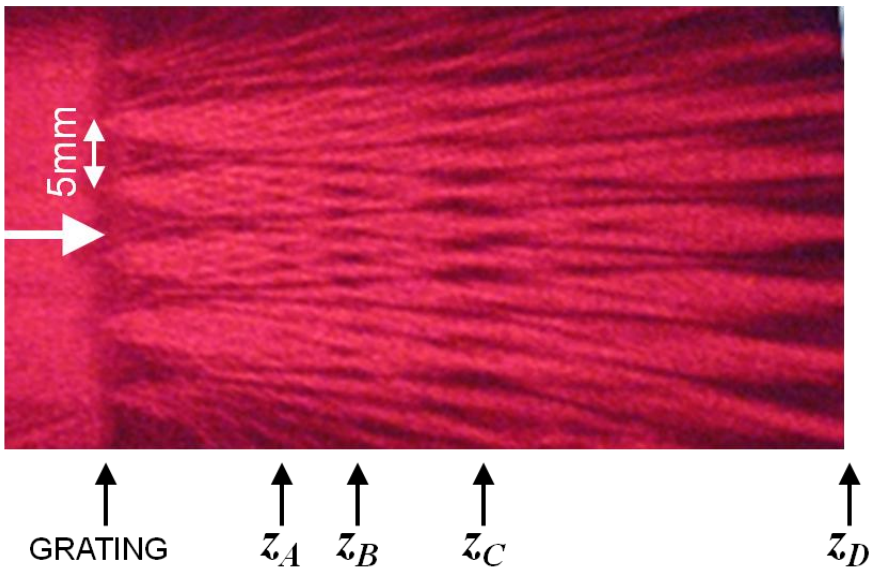

Figure 17-5: Acousto-optical visualization of the ultrasonic Talbot effect using a grating with 80% black/white ratio. Several indicators have been added for the ease of interpretation.

One can clearly observe that the complexity of the diffracted field increases in comparison with the results of Figure 17-4. Instead of producing only self-images, also minified images can be observed at fractional Talbot distances (see indicators in Figure 17-5). The periodicity of the grating corresponds to 5 mm, and is used as a reference measure for determining the distances where image formation occurs. The following distances have been extracted: z_D = 56 mm, z_C = 27.6 mm, z_B = 18.4 mm and z_A = 13.2 mm; which compare well to the theoretical fractional Talbot distances z_T = 54.1 mm, $\frac{1}{2}z_T$ = 27.1 mm, $\frac{1}{3}z_T$ = 18.0 mm and $\frac{1}{4}z_T$ = 13.5 mm.

However, some discrepancies can be observed in the experimental images. First of all, it is noted that the position of the grating deviates from the vertical position (best seen for the experiment shown in Figure 17-4). Secondly, the various approximations in the theoretical analysis are barely valid for the shown ultrasonic experiments. Thirdly, a bounded beam, rather than a plane wave, is used in the experiment which is subject to non-

negligible diffraction effects upon propagation in the liquid, resulting into self-imaging planes which are slightly curved. The limited sensitivity of both the acousto-optical setup and the employed CCD camera further leads to a blurring of the visualization. As such, fractional self-images can only be observed up to a fraction of 4. Note that according to the classical grating equation, fractions up to 10 should form. Fourthly, the grating has a physical thickness of 0.5 mm, while theoretically this should be zero. Combined with the applied ultrasonic wave having a wave length $\lambda \approx 0.46$ mm, it is clear that additional scattering effects could take place within the slits of the grating. Finally, part of the incident ultrasonic field is coupled in the aluminum bars of the grating. Hence, in the experiment the total transmitted field of the grating is a superposition of the ultrasonic fields transmitted separately through the slits and through the bars. Obviously, both transmission fields have different amplitude and phase profiles just behind the grating structure, making the experimental recordings in Figure 17-4 and Figure 17-5 a result of both an amplitude-based and a phase-based Talbot effect. In order to investigate these different factors, a numerical model is implemented in a FEM architecture, in which the experimental conditions can be easily adopted and mimicked.

17. 3. Numerical Results

A 2D FEM model is set up, assuming plane strain conditions. The ultrasonic beam is modeled as a beam with Gaussian amplitude profile having a width of 35 mm and frequency $f = 3.2$ MHz by application of the spatial Fourier transform. The beam is generated in a liquid computation domain (no shear stress allowed) having water properties, and propagates towards the immersed grating structure. To study the effect of the grating structure for the scattering phenomenon, simulations have been performed in different ways.

- In a first approximation, the grating has slits and bars which are open, respectively closed. In the context of FEM, a closed feature corresponds to an ideal acoustic absorber, i.e. no sound is reflected nor transmitted at that particular region. This situation actually compares to the optical situation where the grating exists of alternating transparent and opaque lines, at least when ignoring the thickness of the current grating. In analogy with the acousto-optical experiments, the time-averaged intensity

has been computed in the FEM simulation. The result is shown in Figure 17-6.

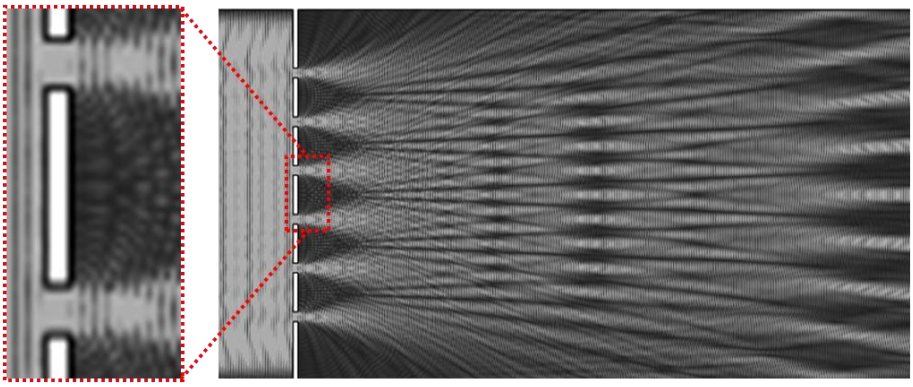

Figure 17-6: FEM simulation of the diffraction pattern by approximating the aluminum grating having open slits and closed bars.

Globally, a similar diffraction pattern is observed as in the experiment. The magnification shows the distribution of the sound field exactly behind the grating, showing a uniform intensity at the location of the slits and a (near) zero intensity at the location of the bars. The diffraction pattern shows a slight curvature, comparable to the curvature in the previously displayed experiments. However, as ultrasonic waves do penetrate in solids, this open/close approximation for the slits/bars is not realistic.

- The second approximation reverses the open/close characteristics of the slits/bars, i.e. the aluminum bars are open and the slits are closed. This situation is very similar to the first case as the aluminum bars now take up the role of slits. However, in contrast with the previous approximation, the incident longitudinal sound is subject to mode conversion (longitudinal ↔ shear) as well as internal reflections in the aluminum slits, leading to the formation of a complex field at the backside of the grating (see Figure 17-7). In fact, each aluminum bar radiates as if it were composed of 3 smaller slits. With this, the diffracted field behind the grating drastically changes, and does not correspond with the experiment. Self-images are now observed at different positions, resembling the apparent grating parameters rather than the real grating parameters. It is noted that the acoustic intensity behind the grating is function of the solid material properties of the bars. For the aluminum bars, the intensity is a factor 4 smaller compared to previous simulation.

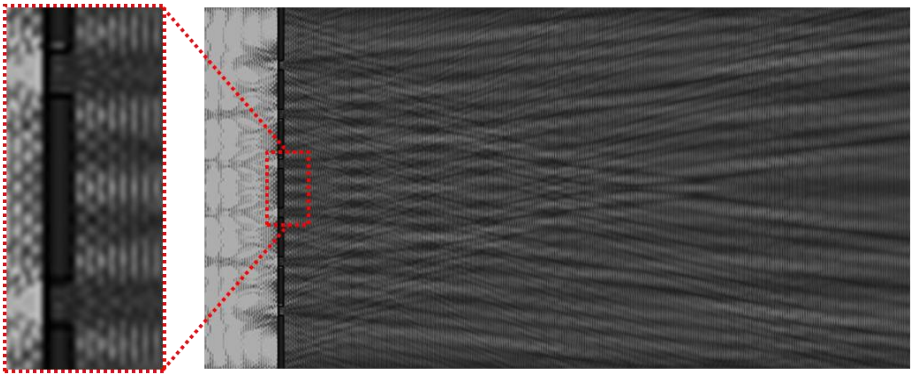

Figure 17-7: FEM simulation of the diffraction pattern by approximating the aluminum grating having closed slits and open bars.

- At last, both the water slits and aluminum bars are modeled corresponding to the physical reality, i.e. ultrasonic waves can penetrate through both water slits and aluminum bars. The combination of the thickness of the grating with the different wave speed in the aluminum bars and water slits, leads to a phase distribution behind the grating which is dependent on the *x*-coordinate. Hence, the third modeling approach cannot simply be conceived as the superposition of the two above amplitude-based diffraction phenomenon. The result for a grating with both slits and bars open is shown in Figure 17-8. It is clear that the observed patterns agree well with the experiment (Figure 17-5).

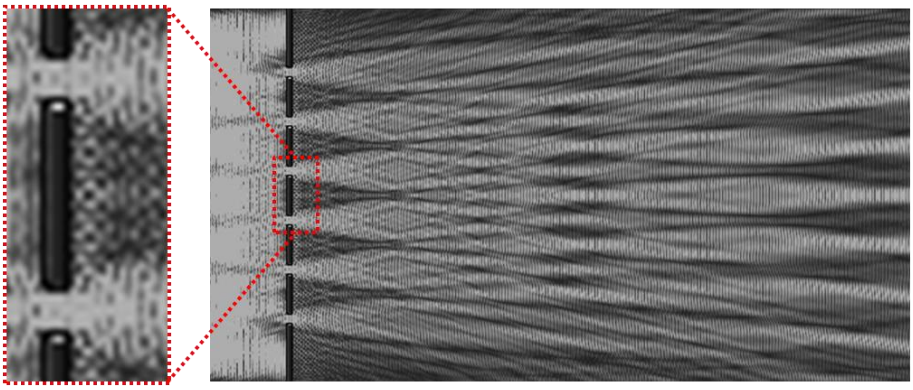

Figure 17-8: FEM simulation of the diffraction pattern by approximating the grating having open slits and open bars.

The experiment and the numerical results are collected in Figure 17-9. The dimensions of the different results have been put on the same scale for the ease of interpretation.

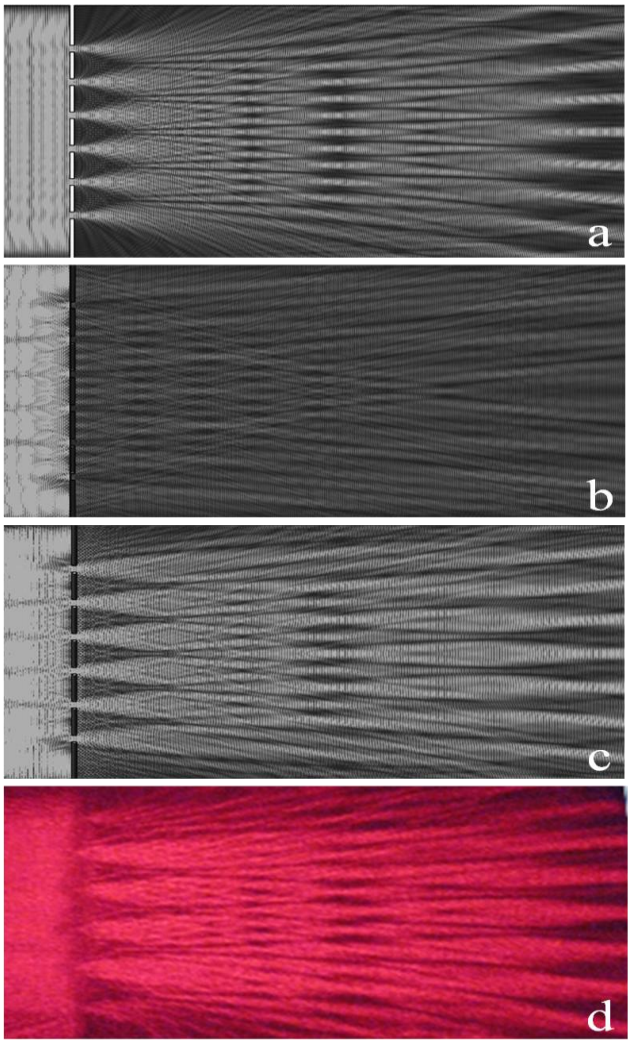

Figure 17-9: Overview of different FEM simulations (a-c) and acousto-optic schlieren experiment (d).

The simulation with both the slits and bars open (Figure 17-9c) clearly matches the experiment best. This indicates that the ultrasonic Talbot effect realized with a solid grating cannot be conceived as the equivalent of the optical Talbot effect. Indeed, the above results reveal that the demonstrated ultrasonic Talbot effect consists of both amplitude-based and phase-based diffraction phenomena, which furthermore are not only dependent on physical dimensions of the grating but also on the material properties of the employed grating.

17. 4. Surface Acoustic Wave Stimulation

The stimulation of surface acoustic waves by insonifying a corrugated solid under normal incidence has already been investigated intensively [16-20]. However, as the application of a surface structure is often detrimental to the functionality of the specimen, one could also consider the insonification of a separate grating positioned at some distance from the specimen. Tuning of the grating parameters, or equivalently the ultrasonic frequency, then allows the excitation of a diffracted wave, matching the stimulation conditions for a surface wave in the specimen. The orientation of the insonified 1D grating in the horizontal plane yields the propagation direction for stimulated surface waves. Hence, simple rotation of the grating around its vertical axis then allows to inspect a structure in an omnidirectional way. However, a grating induces a considerable loss of ultrasonic energy because of reflection losses, therefore it may be better to construct an ultrasonic transducer composed by multiple linear piezo-electric elements. Obviously, such a array transducer is equivalent to the use of a Ronchi grating. A simulation has been performed considering the insonification of an aluminum plate with thickness d = 1 mm. An ultrasonic transducer is modeled as a periodic array of 1D acoustic sources with its normal oriented perpendicular to the aluminum plate. A periodicity Λ = 1.82 mm is considered, which corresponds to a horizontal wave vector with magnitude $2\pi/\Lambda$ = 3.45 mm^{-1}. Hence, excitation of the transducer invokes a radiation field having a wave vector with both a vertical (wave vector associated to the excitation frequency) and a horizontal (wave vector associated to the excitation structure) component. According to Snell-Descartes' law, a guided wave is excited in the solid whenever phase matching conditions are fulfilled. Or in the present context, whenever the horizontal wave vector component of the incident field equals the wave vector of a guided mode. To concretize, the dispersion curves are shown for the aluminum plate in Figure 17-10.

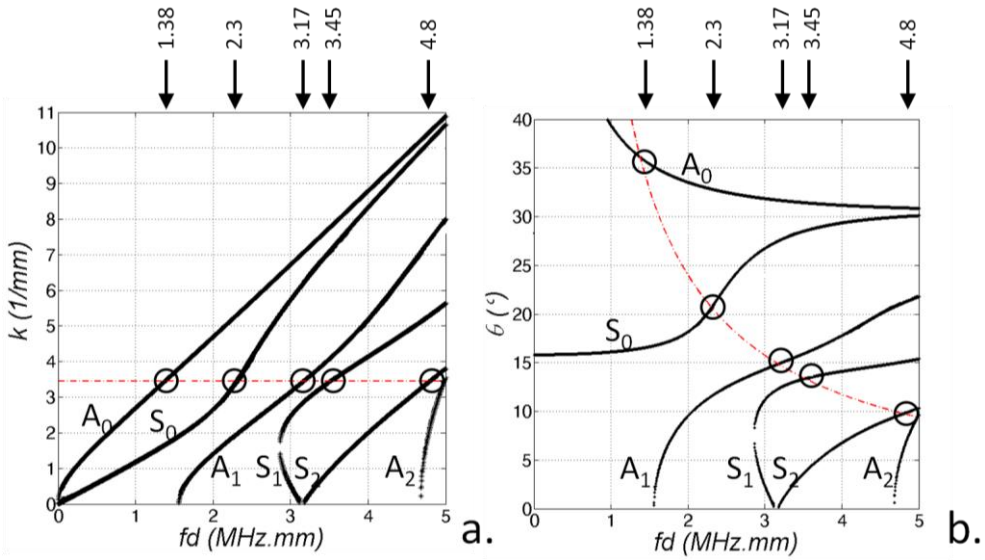

Figure 17-10: Dispersion curves for aluminum: (*k*,*fd*)-space (a) and (*θ*,*fd*)-space (b). The periodic character of the transducer is enclosed by the red dashed line.

In Figure 17-10a, the curves are put in (*k*,*fd*)-space. As such, the periodic character of the transducer can be easily identified by the constant red line at $k = 3.45$ mm^{-1}. It can be observed that five intersections with the dispersion curves are present, thus five guided waves can be stimulated in the aluminum plate at the different indicated frequencies. As the physical interpretation of the dispersion curves may be unclear in (*k*,*fd*)-space, the results have been transformed to (*θ*,*fd*)-space (see Figure 17-10b). Obviously, the periodic character of the transducer is not represented anymore by a constant line. The intersections at which guided mode stimulations occur on the other hand can now be interpreted in terms of the stimulation conditions, i.e. incident angle *θ*, as if a standard transducer would have been used. To ascertain the action and performance of the proposed surface wave device, the periodic array has been excited by harmonic bursts at the different frequencies indicated in Figure 17-10. The radiated field propagates to the aluminum plate. The horizontal displacement component U_X of the induced signal in the aluminum plate is then transformed using a FFT scheme in order to retrieve the dominating wave vector(s). The results are shown in Figure 17-11. It can be observed that the different results show a narrow peak around $k = 3450$ m^{-1}, which is in good correspondence with the magnitude of the wave vector of the different envisioned Lamb modes (see Figure 17-10a). However, it can be observed that the spectrum of the displacement field shows several other sharp peaks,

indicating that the induced guided wave is not pure. This could have been expected considering that a harmonic burst is excited without cutting off the transient parts. As such, the onset of the harmonic burst, including a range of frequencies, has not been removed from the analysis. In addition, the bounded nature of the modeled transducer yields an angular frequency spectrum. This was already commented for Figure 17-4 and Figure 17-5, in which a slight curvature of the wave front was observed. Obviously, the radiation field of the array transducer is not limited to 1st order diffraction features. Hence, these factors make that different modes could be excited. In Figure 17-11a for example, three peaks can be discerned at $k = 246$ m^{-1}, $k = 1692$ m^{-1} and $k = 3376$ m^{-1}. Except for the first peak (whose origin is not clear), the two other peaks can be clearly identified with the S_0 and the A_0 Lamb mode (see Figure 17-10a).

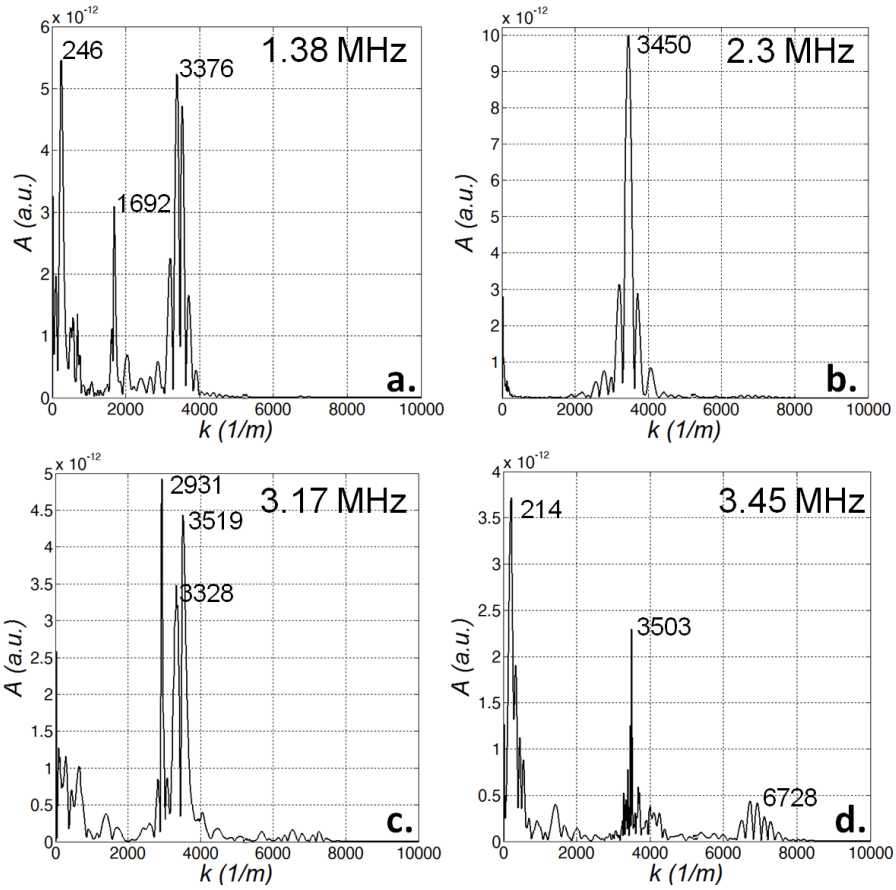

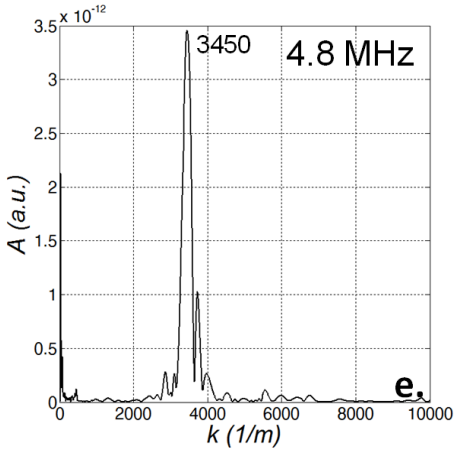

Figure 17-11: FFT (magnitude in arbitrary units) of the horizontal displacement field U_X in the aluminum plate at different excitation frequencies: f = 1.38 MHz (a), f = 2.3 MHz (b), f = 3.17 MHz (c), f = 3.45 MHz (d) and f = 4.8 MHz (e).

17. 5. Conclusions

The ultrasonic analogue of the Talbot effect has been, to the author's knowledge, for the first time experimentally demonstrated by means of acousto-optic schlieren imaging. The insonification of a Ronchi grating formed self-images at multiples of the Talbot distance, while the insonification of a non-balanced grating induced minified image reproductions at fractional Talbot distances. FEM simulations showed that the ultrasonic Talbot effect is not strictly equivalent to the well-known optical Talbot effect. It has been demonstrated that ultrasonic waves traverse through both the slits and the bars of the grating. As such, the ultrasonic diffraction field behind the grating is composed of two superimposed amplitude-based Talbot effects. In addition, as a real grating has a physical thickness, the phase profile cannot be considered uniform for the two amplitude fields behind the grating. Hence, the ultrasonic analogue of the optical Talbot effect should be partly interpreted as a phase-based Talbot effect.

The employment of a grating structure has been demonstrated for the construction of a device which stimulates surface waves considering normal incidence. Numerical results have demonstrated the feasibility of such an acoustic surface wave device.

17. 6. References

[1] Talbot, H.F., *Facts relating to optical science.* The London and Edinburgh philosophical magazine and journal of science, Third series, 1836. 9(56).

[2] Lord Rayleigh, F.R.S., *On copying diffraction-gratings, and on some phenomena connected therewith.* Philosophical Magazine Series 5, 1881. 11(67): p. 196-205.

[3] Li, H., Z.P. Chen, J. Xiong, and G.H. Zeng, *Periodic diffraction correlation imaging without a beam-splitter.* Optics Express, 2012. 20(3): p. 2956-2966.

[4] Berry, M., I. Marzoli, and W. Schleich, *Quantum carpets, carpets of light.* Physics World, 2001. 14(6): p. 39-44.

[5] Case, W.B., M. Tomandl, S. Deachapunya, and M. Arndt, *Realization of optical carpets in the Talbot and Talbot-Lau configurations.* Optics Express, 2009. 17(23): p. 20966-20974.

[6] McMorran, B.J. and A.D. Cronin, *An electron Talbot interferometer.* New Journal of Physics, 2009. 11.

[7] Nowak, S., C. Kurtsiefer, T. Pfau, and C. David, *High-order Talbot fringes for atomic matter waves.* Optics Letters, 1997. 22(18): p. 1430-1432.

[8] Chapman, M.S., C.R. Ekstrom, T.D. Hammond, J. Schmiedmayer, B.E. Tannian, S. Wehinger, and D.E. Pritchard, *NEAR-FIELD IMAGING OF ATOM DIFFRACTION GRATINGS - THE ATOMIC TALBOT EFFECT.* Physical Review A, 1995. 51(1): p. R14-R17.

[9] Gerlich, S., L. Hackermuller, K. Hornberger, A. Stibor, H. Ulbricht, M. Gring, F. Goldfarb, T. Savas, M. Mueri, M. Mayor, and M. Arndt, *A Kapitza-Dirac-Talbot-Lau interferometer for highly polarizable molecules.* Nature Physics, 2007. 3(10): p. 711-715.

[10] Dennis, M.R., N.I. Zheludev, and F.J. de Abajo, *The plasmon Talbot effect.* Optics Express, 2007. 15(15): p. 9692-9700.

[11] Maradudin, A.A. and T.A. Leskova, *The Talbot effect for a surface plasmon polariton.* New Journal of Physics, 2009. 11.

[12] Lohmann, A., *TALBOT INTERFEROMETER.* Journal of the Optical Society of America, 1971. 61(5): p. 687-&.

[13] Yeh, W.H., M. Mansuripur, M. Fallahi, and R.S. Penner, *Talbot imaging with increased spatial frequency: a technique for replicating truncated self-imaging objects.* Optics Communications, 1999. 170(4-6): p. 207-212.

[14] Spagnolo, G.S., D. Ambrosini, and D. Paoletti, *Displacement measurement using the Talbot effect with a Ronchi grating.* Journal of Optics a-Pure and Applied Optics, 2002. 4(6): p. S376-S380.

[15] Martinez-Leon, L., M. Araiza, B. Javidi, P. Andres, V. Climent, J. Lancis, and E. Tajahuerce, *Single-shot digital holography by use of the fractional Talbot effect.* Optics Express, 2009. 17(15): p. 12900-12909.

[16] Claeys, J.M., O. Leroy, A. Jungman, and L. Adler, *DIFFRACTION OF ULTRASONIC-WAVES FROM PERIODICALLY ROUGH LIQUID SOLID-SURFACE.* Journal of Applied Physics, 1983. 54(10): p. 5657-5662.

[17] Jungman, A., L. Adler, and G. Quentin, *ULTRASONIC ANOMALIES IN THE SPECTRUM OF ACOUSTIC-WAVES DIFFRACTED BY PERIODIC INTERFACES.* Journal of Applied Physics, 1982. 53(7): p. 4673-4680.

[18] Mampaert, K., P.B. Nagy, O. Leroy, L. Adler, A. Jungman, and G. Quentin, *ON THE ORIGIN OF THE ANOMALIES IN THE REFLECTED*

ULTRASONIC SPECTRA FROM PERIODIC SURFACES. Journal of the Acoustical Society of America, 1989. 86(1): p. 429-431.

[19] Nagy, P.B. and L. Adler, *SURFACE-ROUGHNESS INDUCED ATTENUATION OF REFLECTED AND TRANSMITTED ULTRASONIC-WAVES.* Journal of the Acoustical Society of America, 1987. 82(1): p. 193-197.

[20] Roberts, R., J.D. Achenbach, R. Ko, L. Adler, A. Jungman, and G. Quentin, *REFLECTION OF A BEAM OF ELASTIC-WAVES BY A PERIODIC SURFACE PROFILE.* Wave Motion, 1985. 7(1): p. 67-77.

Chapter 18

Elastico-Mechanoluminescent Visualization of Ultrasound Waves

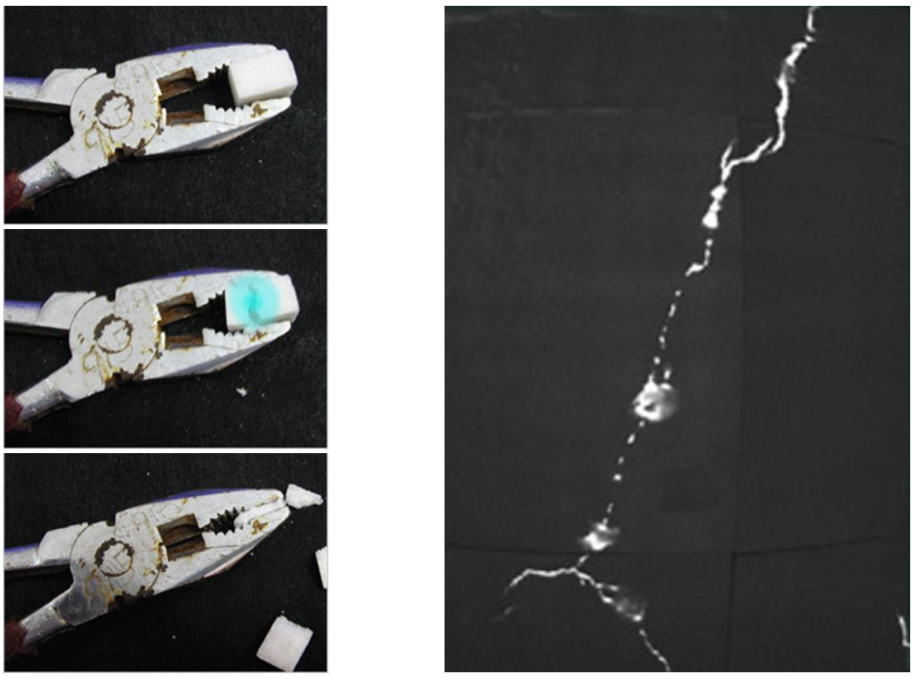

Mechanoluminescence generated when fracturing sucrose (left) and mechanoluminescent visualization of crack initiation and propagation in a structure (right).

Overview

Elastico-mechanoluminescence is already well established in a number of engineering fields for stress visualization. Very recently, it has been shown that the effect can also be excited by ultrasound waves, showing a clear linear trend between the power of the ultrasound wave and the intensity of the light emission. In the present chapter, we go one step further and demonstrate the use of the mechanoluminescent effect for spatially mapping the radiation field of an ultrasonic transducer (f = 3.2 MHz). Basically, an epoxy sample has been injected with mechanoluminescent $BaSi2O_2N_2$:Eu powder, which is then insonified under normal incidence at some distance (water immersed). As such, the insonified region is activated and thus emits light. The enlightened region has a specific geometrical shape, representing the local spatial distribution of the incident pressure field. By varying the insonification distance, multiple 2D slices are obtained which are then combined to reconstruct the 3D sound field. Qualitative correspondence has been obtained between the elastico-mechanoluminescent experiments and numerical computations.

18. 1. Introduction and Background

Humans have the natural ability to sense an internal or external pressure applied to the skin. As such, people can react whenever touched, and are alerted in case of danger. Few materials have a similar ability of alerting pressure, though in a different way: they emit light under the presence of an applied stress. This phenomenon was discovered by Sir Francis Bacon who first observed it in 1605 when scraping sugar [1]. In literature, different names are used depending on the stimulating mechanical action, including fractoluminescence, triboluminescence, thermoluminescence and piezoluminescence. The latter refers to light emission caused by pressure which results only in elastic deformation, and is therefore also known as elastico-mechanoluminescence (EML) [2-3].

Last decades, several research teams have developed different materials exhibiting increased light emission at various wave lengths when mechanically loaded. As such, the EML effect is already successfully employed as a non-destructive dynamic pressure sensing technique, simply by covering the structure of interest with an active ZnS:Mn film [4]. Visualization of quasi-dynamic crack propagation (up to 15 m/s) has been performed by use of the fractoluminescent $SrAL_2O_4$:Eu,Dy phosphor [5-6]. More recently, the EML effect has also been used in combination with ultrasound waves. As such, it has been found that the intensity of the light emission is proportional to the applied ultrasonic power [7-11]. Coating the surface of an ultrasonic transducer with an EML film provided a rough image of the power distribution at the surface, simply by measuring the EML distribution [7]. Although the recent interest in ultrasonically induced EML, only preliminary research results are available during writing this dissertation. In the present chapter, we take the ultrasonically induced EML one step further and demonstrate the feasibility of the EML effect for 3D sound field reconstruction.

18. 2. Material

The recently designed $BaSi2O_2N_2$:Eu powder [3] is embedded as an active EML component in a standard RIM epoxy matrix using a 1 to 10 mixture rule. The choice for the $BaSi2O_2N_2$:Eu material is mainly motivated by its strong light emission when stimulated in the elastic regime. The wave length of the emitted green light corresponds to 498 nm with a full-width-half-maximum of 32 nm. The experiments in this chapter have all been obtained for a circular sample. The sample has been optically charged by means of a 15 W black light with an emission maximum around 450 nm. Basically, the EML sample has been put in front of the black light source at a distance of more or less 50 mm. Typical irradiation time is set in the order of 10 seconds. After optically charging, a sufficient time is respected in order to reduce the persistent luminescence.

18. 3. 3D Spatial Visualization of Ultrasonic Beam

18. 3. 1. Positive Imaging

The charged EML sample is placed under water parallel to the transducer's face (XY plane). As such, insonification takes place at normal incidence. The employed ultrasonic beam operates at 3.2 MHz (GYMNA 200) using an electrical power input of 2 W/cm^2. The area of the transducer equals 4.7 cm^2. A photograph of the experimental setup is displayed in Figure 18-1. It has been verified qualitatively that the light emission is proportional to the power of the ultrasonic beam, as stated in literature [7-11]. A translation stage has been provided in order to insonify the EML sample at different distances *z*.

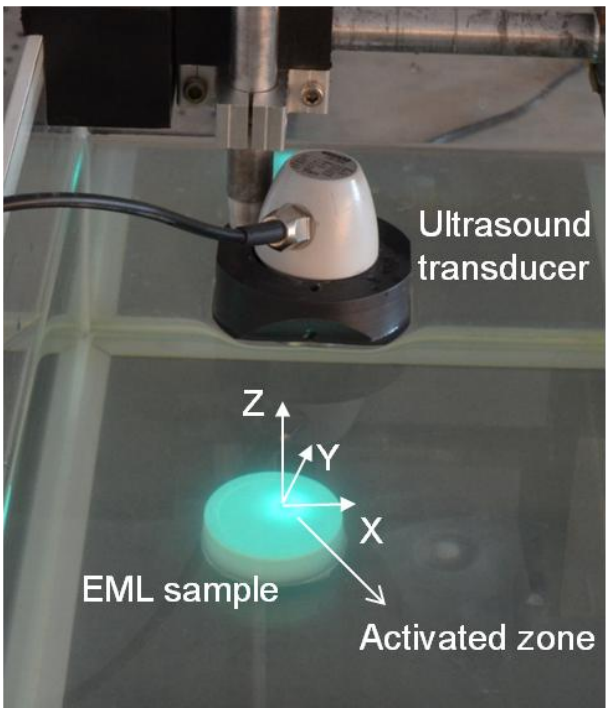

Figure 18-1: Setup for ultrasonically induced elastico-mechanoluminescence experiments.

An insonification time of ~2 s is considered after which a photograph has been taken with a digital camera to obtain a cross-sectional visualization of the spatial pressure distribution produced by the transducer. The experiments have been performed in a darkened room to enhance the contrast. Figure 18-2 displays the obtained results at different distances *z*.

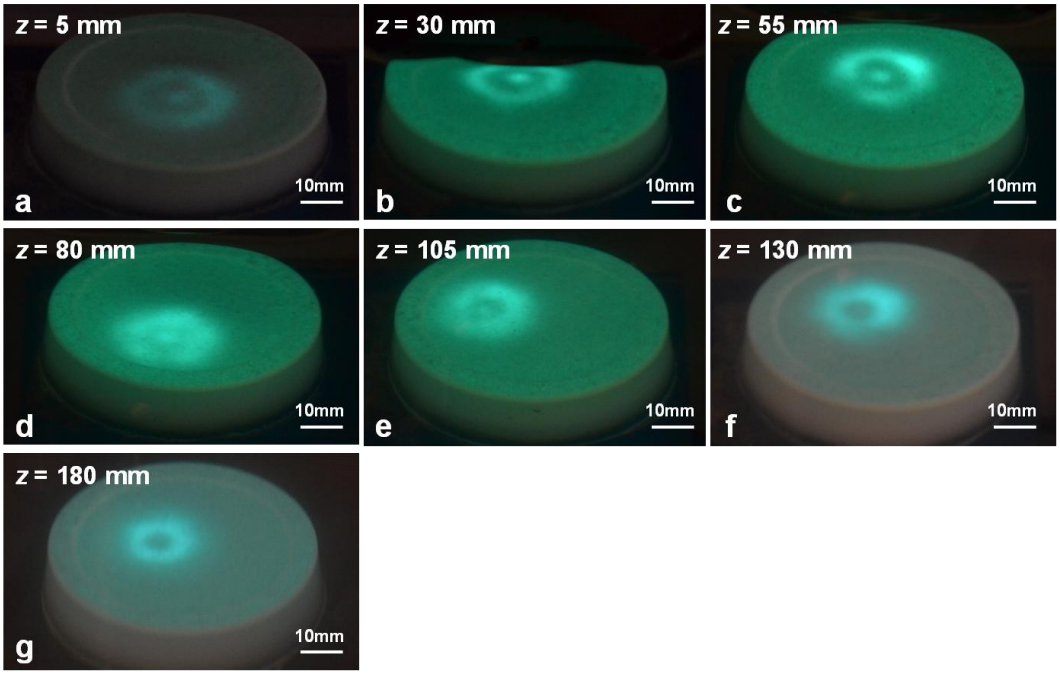

Figure 18-2: Insonification of EML sample at different distances *z*.

First of all, it can be noted that the background intensity differs for several experiments due to the persistent luminescence. Hence, the time period after optically charging the EML sample is most probably not respected to the same extent for the different experiments. Anyway, as we only perform a qualitative study about the effect of ultrasound waves on EML materials, the presence of persistent luminescence has limited negative impact.

The photograph obtained at $z = 5$ mm reveals an activated zone having global dimensions corresponding to the dimension of the employed transducer (diameter ~22 mm). The activated zone has an annular shape with a disc inside. Hence the light intensity, and in extension the ultrasonic power, varies in radial direction. The same can also be observed for the light intensity in angular direction, though more irregular and on a much lesser scale. As the experiment has been performed at a distance $z = 5$ mm, it is clear that the radial variations have to be attributed to near field features of the transducer. The angular variations however cannot be linked to near field features, nor to the geometry of the circular transducer. It has been further verified that the origin of the angular emission variations should not be found in the inhomogeneous distribution of the dispersed powder (experiments have been obtained at different regions on the EML sample).

This leaves us with one source for the angular variation: small deviations in the manufacturing of the transducer. In this regard, the most probable manufacturing error concerns the inappropriate fixation of the piezoelectric crystal, causing a spatially non-uniform vibration amplitude. Similar observations have already been obtained during the investigation and discussion in Chapter 3. Comparison of the results obtained at different insonification distances z yields a change in geometry of the activated zone. One would expect that at a sufficient distance the near-field region gradually evolves towards the far-field region. The results obtained at an insonification distance z = 130 mm and z = 180 mm however, reveal an annular shape for the pressure distribution indicating that we are still operating in the near field region. The intensity at a linear section (centered to the activated zone in Figure 18-2) has been extracted for various insonification distances (see Figure 18-3). The horizontal axis represents the pixel number (200 pixels physically correspond to more or less 32 mm), the vertical axis is a measure for the normalized gray scale value. It can be readily identified that the intensity profile gradually transforms from three to two lobes.

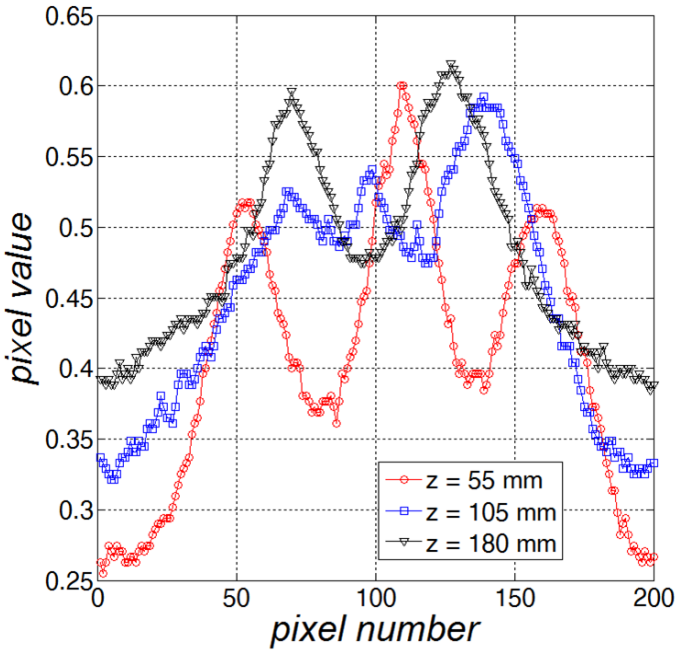

Figure 18-3: Intensity profile extracted at a line section for different insonification distances *z*.

In order to assist these observations, numerical computations on the basis of a fast Fourier transform beam propagation model (FFT-BPM) have been

performed (see Chapter 3). The transducer is modeled as a circular radiator with area 4.7 cm^2 having a uniform pressure distribution oscillating at frequency $f = 3.2$ MHz. Obviously, the assigned uniform pressure distribution most likely deviates from the true pressure distribution considering that the edge of the circular radiator is somehow fixed to the housing. Anyway, this is of minor importance as we perform a qualitative investigation in the current chapter. The computed beam pattern in the YZ-plane is shown in Figure 18-4, several sections in the XY-plane have been added.

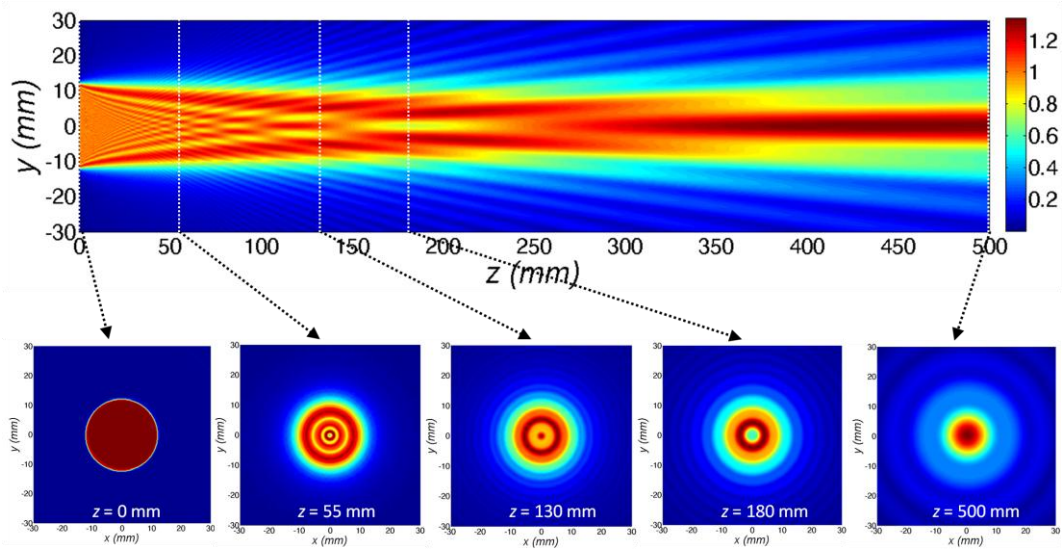

Figure 18-4: FFT-BPM simulation of the pressure field of a circular radiator with area 4.7 cm^2 and uniform pressure distribution oscillating at a frequency of $f = 3.2$ MHz: YZ-section (top) and XY-section (bottom).

The region between 0 mm < z < 130 mm reveals a set of lobes in the YZ-plane, resulting in a collection of intensity rings in the XY-plane. Such a characteristic pressure distribution can also be discerned in the light distribution of the EML experiments displayed in Figure 18-2a-f. The region between 130 mm < z < 250 mm reveals the presence of two high-intensity lobes, which represents an annular distribution in 3D. Such a distribution can be clearly identified in the EML experiments shown in Figure 18-2g-h.

The far-field of the modeled transducer starts more or less at $z = 300$ mm. Unfortunately, it was not possible to further increase the insonification

distance *z* with the current experimental setup. As such, we were not able to capture an EML view of the far-field of the transducer. However, based on the above results, it may be expected that a larger insonification distance *z* results to the presence of a single pressure lobe.

In analogy with the experimental results, Figure 18-5 displays the intensity distribution at a line section for the different insonification distances. It can be seen that the intensity profile evolve from six lobes, over three lobes, to two lobes. The discrepancy with the experimental result (three to two lobes) is probably invoked by inaccurate modeling of the pressure distribution at the transducer's surface and by the inaccurate optical recording (simple digital photograph) during the experiments. It is however clear that globally a good qualitative agreement is obtained between experiment and simulation.

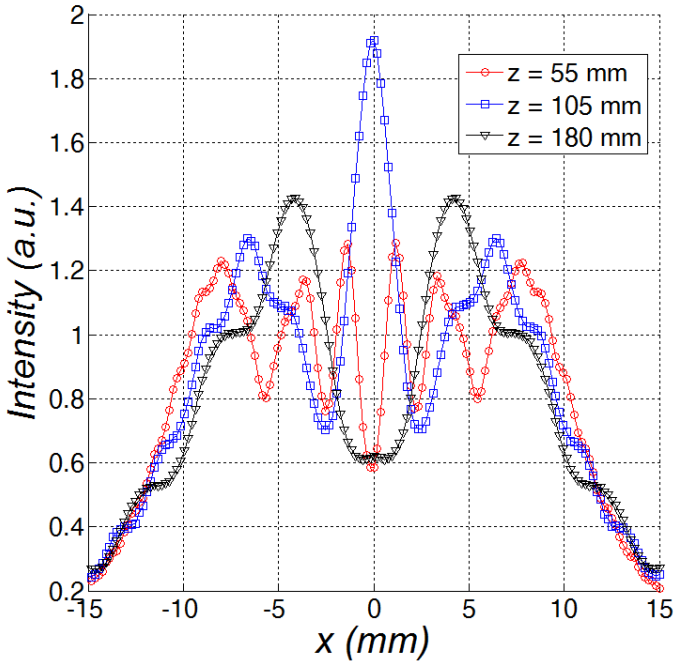

Figure 18-5: Computed intensity profile at a line section for different insonification distances *z*.

A large collection of XY sections then enables to reconstruct the 3D pressure distribution of an ultrasonic transducer, simply by photographing EML images. Compared to conventional techniques (hydrophone scanning of several XY sections), the EML approach provides a more simple and much

faster way. Though, it has to be mentioned that the spatial resolution in the present results is rather low. Concerning the latter, it is expected that the use of an array of optical fibers together with calibrated photometers will improve the accuracy and detail of the recording significantly.

18. 3. 2. Negative Imaging

After performing the various EML experiments, it has been noted that the ultrasound waves leave a negative image in the EML samples. This is shown in Figure 18-6 for two different insonification distances. Figure 18-6a-b displays the EML effect during insonification of the sample. After turning off the ultrasound source, it can be observed that the originally lighted region is dimmed. This is easily understood considering that the EML effect is generated by electrons trapped in an excited state, which jump to a state with lower energy level while clearing its excess of energy in the form of photon emission. Due to the applied ultrasound waves, the depletion of excited electrons is accelerated. Turning off the ultrasound waves then leaves a region where few excited electrons are present. As such, limited permanent luminescence can take place, causing that particular region to be less active. Interestingly, the resolution of the negative image seems to outperform the positive image. However, it is stressed out that caution is required with the last statement as only a limited set of experiments have been performed. It is furthermore worth noting that the negative images are easier to photograph as the exact time of capturing is of minor importance. This is understood by considering that the permanent luminescence emits light at a much more steady state compared to the EML.

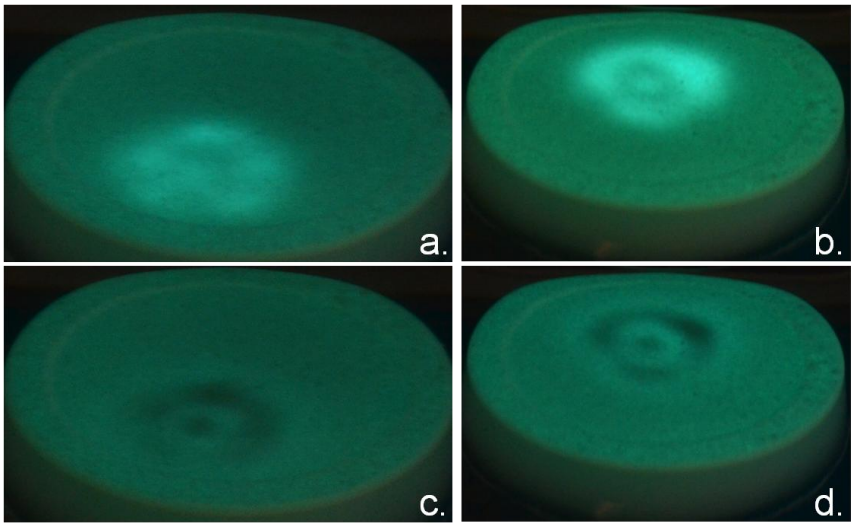

Figure 18-6: EML visualization of ultrasonic beam section at different insonification distances (a-b) and negative image after turning off the ultrasound source (c-d).

18. 4. Conclusions

Epoxy samples have been injected with the recently developed mechanoluminescent $BaSi2O_2N_2$:Eu powder for the purpose of optically visualizing ultrasonic pressure waves by exploiting the elastico-mechanoluminescent effect. The obtained results indicate that the insonified region displays strong light emission, and that the activated region has a clear spatial character which is dependent on the insonification distance. Numerical computations show that the observed features are in accordance with the typical radiation patterns of an oscillating circular aperture. As such, the obtained EML images put on view local cross-sections of the pressure distribution generated by the employed transducer. Reconstruction of a 3D sound field is then simply done by photographing a collection of EML images at different insonification distances.

18. 5. References

[1] Bacon, F., *The advancement of learning*. book IV, chapter 3. 1605, Oxford.

[2] Xu, C.N., X.G. Zheng, M. Akiyama, K. Nonaka, and T. Watanabe, *Dynamic visualization of stress distribution by mechanoluminescence image.* Applied Physics Letters, 2000. 76(2): p. 179-181.

[3] Botterman, J., K. Van den Eeckhout, I. De Baere, D. Poelman, and P.F. Smet, *Mechanoluminescence in BaSi2O2N2:Eu.* Acta Materialia, 2012. 60(15): p. 5494-5500.

[4] Xu, C.N., H. Matsui, Y. Liu, X.G. Zheng, and L.Y. Li, *Novel approach to dynamic imaging of stress distribution with piezoluminescence.* Ferroelectrics, 2001. 263(1-4): p. 1303-+.

[5] Kim, J.S., Y.N. Kwon, N. Shin, and K.S. Sohn, *Mechanoluminescent SrAl2O4 : Eu, Dy phosphor for use in visualization of quasidynamic crack propagation.* Applied Physics Letters, 2007. 90(24).

[6] Timilsina, S., K.H. Lee, I.Y. Jang, and J.S. Kim, *Mechanoluminescent determination of the mode I stress intensity factor in SrAl2O4:Eu2+,Dy3+.* Acta Materialia, 2013. 61(19): p. 7197-7206.

[7] Zhan, T.Z., C.N. Xu, O. Fukuda, H. Yamada, and C.S. Li, *Direct visualization of ultrasonic power distribution using mechanoluminescent film.* Ultrasonics Sonochemistry, 2011. 18(1): p. 436-439.

[8] Terasaki, N., H. Yamada, and C.N. Xu, *Ultrasonic wave induced mechanoluminescence and its application for photocatalysis as ubiquitous light source.* Catalysis Today, 2013. 201: p. 203-208.

[9] Zhan, T.Z., C.N. Xu, O. Fukuda, H. Yamada, and C.S. Li. *Mechanoluminescent Film Sensor for Visualizing Ultrasonic Power Distribution*. in *IOP Conference Series: Materials Science and Engineering*. 2011.

[10] Zhang, J.-C., C.-N. Xu, S. Kamimura, Y. Terasawa, H. Yamada, and X. Wang, *An intense elastico-mechanoluminescence material CaZnOS:Mn2+ for sensing and imaging multiple mechanical stresses.* Optics Express, 2013. 21(11): p. 12976-12986.

[11] Sonwane, V.D., A.S. Gaur, B.K. Haldar, S. Pandey, and B.P. Chandra, *Ultrasonic pulse induced mechanoluminescence of europium doped strontium aluminate micro-crystals.* Recent Research in Science & Technology, 2012. 4(8).

Chapter 19

Conclusions and Prospects

Artwork of M.C. Escher

Overview

The conclusions for the four parts of this dissertation are shortly summarized in this chapter. In addition, a few directions are presented for further research lines which, in the author's opinion, have a lot of potential.

19. 1. General Overview and Conclusions

The increasing use of high performance composite materials in primary components of several engineering applications, demands qualified and reliable non-destructive testing and characterization tools. In recent years, many techniques with high potential have been developed by scientists and engineers. Up to now, the complexity and limitations of those techniques have prevented them to be widely implemented in industry. Since the discovery of the ultrasonic polar scan technique in 1981, several research groups have praised the method for its promising capabilities. However, the progress in the ultrasonic polar scan method has hardly evolved during the last thirty years, leaving it behind as an ever promising and immature technique.

In this dissertation, the ultrasonic polar scan has been experimentally and numerically investigated in-depth in order to bring it into a new era. An era in which it hopefully gets the respect it deserves: to be explored in research and to be employed in industry. The presented research consists of four major parts, the main conclusions of each part are collected here.

Part I: Ultrasonic Polar Scan

An in-depth investigation has been performed on the ultrasonic polar scan methodology in its traditional implementation (transmission). A versatile 5 axis scanner has been constructed in order to automate the experimental procedure, and to obtain superior-quality experiments. In addition, a high-level numerical modeling technique has been implemented to simulate the experiments true-to-nature. The coupling of these two research approaches resulted in several noteworthy observations:

- Several pitfalls in the experimental recording, whereof some have been overlooked for more than fifteen years, have been identified. A feasible solution, whether experimental, numerical or a combination of both, has been proposed for each pitfall.

- It was numerically demonstrated that the P-UPS fingerprint contains 'hidden' information which has particular interest for NDT and material characterization: the slowness curves, the phase velocity curves, the critical angle profiles, the walk-off angle profile and the group velocity curves. By extensive post-processing, these curves have been successfully extracted for several materials. In addition, the role of the immersion liquid as an acoustical lens for the UPS has been demonstrated both numerically and experimentally.

- The long standing conjecture that the ultrasonic polar scan 'fingerprints' material properties has been successfully tackled by coupling experiment to simulation, employing an inverse optimization procedure on the basis of a genetic algorithm.

- Originally, the technique was introduced using pulsed ultrasound. In this dissertation, the use of quasi-harmonic waves has also been investigated. It has been shown that the nature of the fingerprint drastically changed with respect to the pulsed version. The fingerprint of a H-UPS experiment should be attributed to Lamb wave characteristics, though not in a one-to-one relationship as previously commented in literature.

- The conceptual introduction of the phase-based H-UPS has been done, displaying even more intriguing and distinct patterns compared to the amplitude-based results.

Part II: Ultrasonic Backscatter Polar Scan

The original implementation of the ultrasonic polar scan was done in transmission (or reflection) recording. Part II extends the ultrasonic polar scan methodology to the analysis of backscattered waves, resulting into the ultrasonic backscatter polar scan.

- A pulsed version of the ultrasonic backscatter polar scan has been introduced (P-UBPS), and was demonstrated to be useful for several NDT applications, including (hidden) corrosion characterization, detection of fiber orientation as well as detection and localization of surface breaking cracks.

- The ultrasonic backscatter polar scan implementation has been further extended with the use of harmonic signals (H-UBPS). It has been demonstrated to be well suited for the characterization of multidirectional subsurface corrugations in the Bragg regime. The effect of random roughness, superimposed to the structured roughness, has also been explicitly investigated. Basically, the random roughness leads to additional diffraction phenomena, which can be compared to the Rowland and the Lyman ghosts in optics.

- A novel ultrasonic strain gauge has been proposed to measure a local 3D strain field in a single-sided and absolute way. The obtained results show excellent agreement with conventional strain measurement techniques.

Part III: Ultrasonic (Backscatter) Polar Scan and Damage

The developed methodologies in Part I and Part II have been applied to discern both geometrical and elasticity-related damage features in various types of composite materials.

- It is demonstrated that the H-UPS, in contrast to the P-UPS, shows excellent sensitivity to the presence of delaminations in thin carbon/epoxy composites. Even more, the H-UPS methodology provides a means for characterizing a delamination, i.e. its position through depth and its thickness. Numerical and experimental results have also been presented for the case of multiple overlapping delaminations.

- Damage induced by quasi-static shear loading in various composites has been investigated with the P-U(B)PS. The results indicate mainly a reduction of shear properties in the case of glass fiber composites and a large distortion of fiber orientation in case

of carbon fiber composites. The latter suggests that damage models in literature should actually be extended to account for possible transformation of the anisotropic symmetry upon loading.

- At last, the damage signature of fatigue has been investigated for carbon fabric reinforced plastics using the ultrasonic polar scan methodology. Shear-dominated fatigue is shown to manifest itself mainly in the form of fiber distortion. An extraordinary distortion up to 13° has been extracted from the ultrasonic polar scan measurements. The results for tension fatigued samples showed a directional stretching of the polar contours, which indicates a directional reduction of stiffness properties. A maximal stiffness reduction of 12.8% has been measured in the direction of the applied loading, while the stiffness transverse to the loading direction remained more or less unaltered.

Part IV: Ultrasound Visualization

The last part handles the visualization of ultrasonic wave fields in view of making the interpretation of complex ultrasonic phenomena more straightforward. For this, an acousto-optic schlieren setup has been built. In addition, a numerical analogue for the schlieren imaging has been implemented on the basis of finite element method.

- The leakage and scattering of leaky Lamb waves interacting with the vertical plate edge has been investigated and discussed both experimentally and numerically. The obtained results indicate that the incident Lamb mode redistributes its energy into several backward propagating mode-converted Lamb modes upon interaction with the plate edge. The associated leakage field of the backward propagating Lamb waves immediately emerge in the neighborhood of the plate end. Besides the traditional schlieren experiments in real space, experimental results have also been obtained in spatial frequency domain. In this way, the complex leaking field has been decomposed in individual wave fields, facilitating the interpretation. It was shown that large areas of the immersion liquid get 'polluted' by the investigated leakage and scattering phenomenon.

- An experimental and numerical demonstration of the ultrasonic analogue of the Talbot effect (self-imaging or lensless imaging) is given. It is shown that the ultrasonic Talbot effect is actually a mixture of amplitude and phase features. This is in contrast with the Talbot effect originally discovered in optics, which has been interpreted as a pure amplitude phenomenon.

- Finally, an account is given on elastico-mechanoluminescence in combination with ultrasound. Preliminary results have been presented, showing the potential of elastico-mechanoluminescent visualization of ultrasonic wave fields.

19. 2. Recommendations

A short overview is given about potential future work which, in the author's opinion, may be considered promising for those who want to further explore the capabilities of the various discussed techniques. Only recommendations for future work are given which have already been partially tackled by the present author, and as a consequence for which it should be possible to execute them in a relatively short time frame.

Hand-held scanner device

Most difficulties encountered during this research were related to the obsolete mechanical robot. Although high-level experiments were obtained, the scanning time is too high (~15 minutes), while the scanner is not transferable to perform *in situ* inspection. Therefore, it would be a major breakthrough if the current scanner system could be miniaturized to a hand-held apparatus which meets in-field requirements. Ideally, such a device should exploit phase matrix technology to electronically mimic the complex mechanical movement involved in an ultrasonic polar scan. However, as such technology is currently in development (and very expensive), it may be better, for the time being, to use more conventional methods. At present, efforts are going in that way and a first design of a next generation UPS scanner has already been produced during the research (see Section 3.7).

Ultrasonic polar scan experiments recorded in reflection modus

It has been stated in literature that the ultrasonic polar scan yields the same results in transmission as in reflection. However, this has not yet been

investigated in-depth. In addition, the implemented simulation model reveals that the equivalence between reflection and transmission is not completely true for the case of layered media. More specifically, the simulation results indicate that the characteristics of the reflected signal is more sensitive to the upper layers, in which the applied frequency is more or less the controlling factor for the penetration depth. Hence, this implies that it would be possible to inspect a specimen layer-by-layer, simply by using different frequencies in a reflection UPS setup. Several experiments in reflection modus have already been obtained by the present author. Because of time constraints, they have not been included in this dissertation.

Ultrasonic polar scan experiments recorded in the non-specular field

The recording of H-UPS scan experiments in the non-specular transmission or reflection field may be useful to neutralize the integrating effect of a bounded beam which causes some Lamb waves to be undetected. Few experiments in the non-specular field have already been obtained for aluminum by the author, showing great appeal (see chapter 8). Unfortunately, no results have been obtained for composite materials due to time restrictions.

Identification of layered composites

It would be worthy to investigate the obvious extension of the present inversion procedure: the characterization of viscoelastic layered media. Some first preliminary steps have already been taken in this regard.

Closed-container inspection

The implemented numerical model indicates that the ultrasonic polar scan methodology is able to distinguish between liquids in closed containers. As such, it could become an important inspection technique for the harbor, to discourage smuggling of hazardous liquids. Unfortunately, time was too short to verify the numerical results with experiments. Therefore, this research part has not been included in the dissertation.

Nonlinear version of the ultrasonic polar scan

The ultrasonic polar scan results of this dissertation have been obtained in the linear regime. This can be considered the standard way of working in ultrasonic NDT, especially when involving transmission and reflection coefficients. Few researchers however use nonlinear ultrasonics (at a fixed incident angle) because of the superior sensitivity to damage features.

Hence, it seems promising to implement a nonlinear version of the ultrasonic polar scan. The experimental implementation and post-processing of such a nonlinear ultrasonic polar scan has already been performed by the present author, though it has not yet been applied to damaged composite samples because of time constraints. Concerning the numerical approach, completely new simulation methods should be developed for which no attempt has been undertaken by the present author.

Measurement of shear strain field

The introduced ultrasonic strain gauge (Chapter 11) has been applied for the measurement of a 3D normal strain field, with no shear strain component involved. However, the developed method should also be able to measure in-plane shear strain. Hence, it would be useful to actually measure such a shear strain field by the developed ultrasonic strain gauge, and to confront the obtained results with other conventional strain gauge techniques.

Elastico-mechanoluminescence and ultrasound

The elastico-mechanoluminescent visualization of ultrasonic waves has the potential to become a first-class NDT technique. At present, the technique has only been used for ultrasonic power measurements in literature and for spatial characterization of an ultrasonic field in the present dissertation. As the technique is still in its infancy, many potential research lines may be considered.

Scientific Output

Publications in international scientific journals of the Science Citation Index (SCI Web of Science - Thomson Reuters)

A1 papers

[1] **Mathias Kersemans**, Wim Van Paepegem, Babs Lemmens, Koen Van Den Abeele, Lincy Pyl, Filip Zastavnik, Hugo Sol and Joris Degrieck. (2014). *The Pulsed Ultrasonic Backscatter Polar Scan and its Applications for NDT and Material Characterization.* Experimental Mechanics**,** vol. 54(6): pp 1059-1071.

Impact Factor 1.567, quartile 1 (4/33 Materials science, characterization and testing)

[2] **Mathias Kersemans**, Ives De Baere, Joris Degrieck, Koen Van Den Abeele, Lincy Pyl, Filip Zastavnik, Hugo Sol and Wim Van Paepegem. (2014). *Nondestructive damage assessment in fiber reinforced composites with the pulsed ultrasonic polar scan*. Polymer Testing, vol. 34: pp. 85-96.

Impact Factor 1.816, quartile 1 (2/33 Materials science, characterization and testing)

[3] **Mathias Kersemans**, Wim Van Paepegem, Koen Van Den Abeele, Lincy Pyl, Filip Zastavnik, Hugo Sol and Joris Degrieck. (2014). *Pitfalls in the Experimental Recording of Ultrasonic (Backscatter) Polar Scans for Material Characterization.* Ultrasonics, vol. 54(6): pp. 1509-1521.

Impact Factor 2.028, quartile 1 (5/31 Acoustics)

[4] Filip Zastavnik, Lincy Pyl, Jun Gu, Hugo Sol, **Mathias Kersemans**, Wim Van Paepegem. (2014). *Comparison of Shearography to Scanning Laser Vibrometry as Methods for Local Stiffness Identification of Beams.* Strain, vol. 50(1): pp. 82–94.

Impact Factor 0.619, quartile 3 (18/32 Materials science, characterization and testing)

[5] **Mathias Kersemans**, Arvid Martens, Nicolas Lammens, Koen Van Den Abeele, Joris Degrieck, Filip Zastavnik, Lincy Pyl, Hugo Sol and Wim Van Paepegem. (2014). *Identification of the elastic properties of isotropic and orthotropic thin-plate materials with the pulsed ultrasonic polar scan*. Experimental Mechanics, vol. 54(6): pp. 1121-1132.

Impact Factor 1.567, quartile 1 (4/33 Materials science, characterization and testing)

[6] Nicolas Lammens, **Mathias Kersemans**, Geert Luyckx, Wim Van Paepegem, Joris Degrieck. (2014). *Improved accuracy in the determination of flexural rigidity of textile fabrics by the Peirce cantilever test (ASTM D1388).* Textile research journal, vol. 84(12): pp. 1307-1314.

Impact Factor 1.135, quartile 1 (4/22 Materials science, textiles)

[7] **Mathias Kersemans**, Wim Van Paepegem, Koen Van Den Abeele, Lincy Pyl, Filip Zastavnik, Hugo Sol and Joris Degrieck. (2014). *Ultrasonic Characterization of subsurface 2D corrugation.* Journal of Nondestructive Evaluation, vol. 33(3): pp. 438-442.

Impact Factor 1.091, quartile 1 (7/32 Materials science, characterization and testing)

[8] **Mathias Kersemans**, Nicolas Lammens, Joris Degrieck, Koen Van Den Abeele, Lincy Pyl, Filip Zastavnik, Hugo Sol and Wim Van Paepegem. (2014). *Extraction of bulk wave characteristics from a pulsed ultrasonic polar scan.* Wave Motion, vol. 51(7): pp. 1071-1081.

Impact Factor 1.467, quartile 2 (47/138 Mechanics)

[9] Diederik Van Nuffel, Kameswara Sridhar Vepa; Ives De Baere, Pascal Lava, **Mathias Kersemans**; Joris Degrieck, Julien De Rouck. (2014). *A comparison between the experimental and theoretical impact pressures acting on a horizontal quasi-rigid cylinder during vertical water impact.* Ocean Engineering, vol. 77: pp. 42-54.

Impact Factor 1.161, quartile 1, (2/14 Engineering, Marine)

[10] **Mathias Kersemans**, Arvid Martens, Koen Van Den Abeele, Joris Degrieck, Lincy Pyl, Filip Zastavnik, Hugo Sol and Wim Van Paepegem. (2014). *The quasi-harmonic ultrasonic polar scan for material characterization: experiment and numerical modeling.* Accepted for publication in Ultrasonics.

Impact Factor 2.028, quartile 1 (5/31 Acoustics)

[11] **Mathias Kersemans**, Arvid Martens, Koen Van Den Abeele, Joris Degrieck, Filip Zastavnik, Lincy Pyl, Hugo Sol and Wim Van Paepegem. (2014). *Detection and localization of multiple delaminations in thin carbon fiber reinforced composites with the ultrasonic polar scan.* Journal of nondestructive evaluation, vol. 33(4): pp. 522-534.

Impact Factor 1.091, quartile 1 (7/32 Materials science, characterization and testing)

[12] Filip Zastavnik, Lincy Pyl, Jun Gu, Hugo Sol, **Mathias Kersemans**, Wim Van Paepegem (2014). *Errors in shearography measurements due to the creep of the PZT shearing actuator.* Measurement Science and Technology, vol. 25(8).

Impact Factor 1.435, quartile 1 (21/90 Engineering, multidisciplinary)

[13] **Mathias Kersemans**, Ives De Baere, Joris Degrieck, Koen Van Den Abeele, Lincy Pyl, Filip Zastavnik, Hugo Sol and Wim Van Paepegem. (2014). *Damage Signature of Fatigued Fiber Reinforced Composites in the Pulsed Ultrasonic Polar Scan*. Experimental Mechanics, vol. 54(8): pp 1467-1477.

Impact Factor 1.567, quartile 1, (4/33 Materials science, characterization and testing)

[14] **Mathias Kersemans**, Ives De Baere, Philippe Smet, Joris Degrieck and Wim Van Paepegem. *Elastico-mechanoluminescent Reconstruction of 3D Ultrasonic Beam.* Under review at Measurement Science and Technology.

Impact Factor 1.435, quartile 1 (21/90 Engineering, multidisciplinary)

[15] **Mathias Kersemans**, Klaas Allaer, Wim Van Paepegem, Koen Van Den Abeele, Lincy Pyl, Filip Zastavnik, Hugo Sol and Joris Degrieck. (2014). *A Novel Ultrasonic Strain Gauge for Single-Sided Measurement of a Local 3D Strain Field*. Experimental mechanics, vol. 54(9): pp. 1673-1685.

Impact Factor 1.567, quartile 1 (4/33 Materials science, characterization and testing)

[16] Filip Zastavnik, Lincy Pyl, Jun Gu, Hugo Sol, **Mathias Kersemans**, Wim Van Paepegem (2014). *Calibration and Correction Procedure for Quantitative Out-of-Plane Shearography*. Under review at Measurement Science and Technology.

Impact Factor 1.435, quartile 1 (21/90 Engineering, multidisciplinary)

[17] Ramiro Daniel Verastegui Flores, Gemmina Di Emidio, Adam Bezuijen, Joachim Vanwalleghem, **Mathias Kersemans** (2014). *Non-destructive Evaluation of Stiffness Moduli of Cemented Soils out of Resonant Frequency*. Under review at Soils and Foundations.

Impact Factor 0.413, quartile 4 (26/32 Engineering, Geological)

A1 papers in preparation

[18] **Mathias Kersemans**, Wim Van Paepegem, Koen Van Den Abeele, Lincy Pyl, Filip Zastavnik, Hugo Sol and Joris Degrieck. *Leakage and Scattering of Leaky Lamb Wave Interaction with the Plate End: Acousto-optics and FEM*. In preparation.

[19] **Mathias Kersemans**, Wim Van Paepegem, Koen Van Den Abeele, Lincy Pyl, Filip Zastavnik, Hugo Sol and Joris Degrieck. *2D Corrugation Characterization by Means of Ultrasonic Polar Spectroscopy Scan*. In preparation.

[20] **Mathias Kersemans**, Wim Van Paepegem, Koen Van Den Abeele, Lincy Pyl, Filip Zastavnik, Hugo Sol and Joris Degrieck. *The Ultrasonic Talbot effect: Experiment and Modeling*. In preparation.

Publications in international scientific journals not included in the Science Citation Index

A4 paper

[21] **Mathias Kersemans**, Nicolas Lammens, Geert Luyckx, Joris Degrieck and Wim Van Paepegem. (2012) *Quantitative Measurement of the Elastic Properties of Orthotropic Composites by means of the Ultrasonic Polar Scan Method.* JEC Composites, vol. 75: pp. 48-52.

Conference papers available in ISI Proceedings (SCI Web of Science - Thomson Reuters)

P1 papers

[1] **Mathias Kersemans**, Wim Van Paepegem, Diederik Van Nuffel, Geert Luyckx, Ives De Baere, Filip Zastavnik, Jun Gu, Hugo Sol, Koen Van den Abeele and Joris Degrieck. *Polar scan technique for material characterization and identification of new operating regimes*. International Conference on Experimental Mechanics (ICEM15), Porto, Portugal, 22-27 July 2012.

[2] **Mathias Kersemans**, Wim Van Paepegem, Koen Van Den Abeele and Joris Degrieck. *Leakage and Scattering of a Leaky Lamb Wave by a Structural Discontinuity: Acousto-Optics and FEM*. IEEE International Ultrasonics Symposium, Dresden, Germany, 7-10 October 2012.

[3] **Mathias Kersemans**, Wim Van Paepegem, Nicolas Lammens, Koen Van den Abeele, Filip Zastavnik, Jun Gu, Hugo Sol and Joris Degrieck. *'Gradient' Polar Scan Technique for Material Characterization*. IEEE International Ultrasonics Symposium, Dresden, Germany, 7-10 October 2012..

[4] **Mathias Kersemans**, Koen Van Den Abeele, Wim Van Paepegem and Joris Degrieck. *Implications of structural discontinuities for water*

coupled NDT and SHM: experiment and modeling. International Conference on Experimental Mechanics (ICEM15), Porto, Portugal, 22-27 July 2012.

[5] Ives De Baere, Stefan Jacques, **Mathias Kersemans**, Wim Van Paepegem and Joris Degrieck. *Experimental study of the crack growth of a carbon fabric reinforced PPS under mode I and mode II loading conditions*. International Conference on Experimental Mechanics (ICEM15), Porto, Portugal, 22-27 July 2012.

[6] **Mathias Kersemans**, Ives De Baere, Wim Van Paepegem, Joris Degrieck, Filip Zastavnik, Jun Gu and Hugo Sol. *Experimental and numerical polar scans of several anisotropic materials using pulsed and harmonic ultrasonic beams*. Emerging Technologies in Non-Destructive Testing (ETNDT5), Ioannina, Greece, 19-21 September 2011.

Publications in international conference proceedings not included in ISI Proceedings

C1 papers

[7] **Mathias Kersemans**, Wim Van Paepegem, Filip Zastavnik, Jun Gu, Hugo Sol and Joris Degrieck, *Nondestructive Characterization of the Elastic Properties of Orthotropic Composites with Ultrasound*. SAMPE Europe Technical Conference - SETEC 11, Leiden, the Netherlands, 14-16 September 2011.

[8] Lincy Pyl, Filip Zastavnik, Hugo Sol, Wim Van Paepegem and **Mathias Kersemans**. *Damage identification of prepreg composites subject ot accelerated fatigue tests*. 10th international conference on durability of composites systems (Duracosys), Brussels, Belgium, 17-19 September 2012.

[9] **Mathias Kersemans**, Wim Van Paepegem, Koen Van Den Abeele, Lincy Pyl, Filip Zastavnik, Hugo Sol and Joris Degrieck. *Efficient Extraction of the Directional Wave Curves from a Pulsed Ultrasonic Polar Scan Experiment*. 12th International Conference for Non-Destructive Testing 2013 (ICNDT2013), Portoroz, Slovenia, 4-6 September 2013.

[10] **Mathias Kersemans**, Wim Van Paepegem, Koen Van Den Abeele, Lincy Pyl, Filip Zastavnik, Hugo Sol and Joris Degrieck, *The Quasi-Harmonic ultrasonic Polar Scan for material Characterization: Experiment and Numerical Modeling*, 12th International Conference for Non-Destructive Testing 2013 (ICNDT2013), Portoroz, Slovenia, 4-6 September 2013.

[11] Filip Zastavnik, Lincy Pyl, Hugo Sol, **Mathias Kersemans** and Wim Van Paepegem. *Local Stiffness Identification of Beams Using Shearography and Inverse Methods*. Annual Conference on Experimental and Applied Mechanics. Chicago, USA, 3-6 June, 2013.

[12] **Mathias Kersemans**, Koen Van Den Abeele, Nicolas Lammens, Joris Degrieck, Filip Zastavnik, Jun Gu, Lincy Pyl, Hugo Sol and Wim Van Paepegem. *Determination of the Fiber Direction and the C-Tensor of a UD Carbon/Epoxy Composite by means of the Ultrasonic Polar Scan*. International Congress on Ultrasonics (ICU 2013), Singapore, 2-5 May 2013.

[13] **Mathias Kersemans**, Wim Van Paepegem, Koen Van Den Abeele, Lincy Pyl, Filip Zastavnik, Hugo Sol and Joris Degrieck. *Pitfalls in Experimental Recording of Ultrasonic Polar Scans for Composite Material Characterization*. International Congress on Ultrasonics (ICU 2013), Singapore, 2-5 May 2013.

[14] **Mathias Kersemans**, Ives De Baere, Joris Degrieck, Koen Van Den Abeele, Lincy Pyl, Filip Zastavnik, Hugo Sol and Wim Van Paepegem. *Ultrasonic polar scan imaging of fatigued fiber reinforced composites*. 16th European conference on composite materials (ECCM16), Seville, Spain, 22-26 June 2014.

[15] **Mathias Kersemans**, Wim Van Paepegem, Koen Van Den Abeele, Babs Lemmens, Lincy Pyl, Filip Zastavnik, Hugo Sol and Joris Degrieck. *The pulsed ultrasonic backscatter polar scan for NDT and material evaluation*. 16th international conference on experimental mechanics (ICEM16), Cambridge, United Kingdom, 7-11 July 2014

[16] **Mathias Kersemans**, Koen Van Den Abeele, Klaas Allaer, Wim Van Paepegem, Lincy Pyl, Filip Zastavnik, Hugo Sol and Joris Degrieck. *An Ultrasonic Strain Gauge*. 7th European workshop on structural health monitoring (EWSHM7), Nantes, France, 8-11 July, 2014.

[17] Filip Zastavnik, Lincy Pyl, Jun Gu, Hugo Sol, **Mathias Kersemans** and Wim Van Paepegem. *Calibration of Quatitative Shearography for Use in Local Stiffness Identification*. 16th international conference on experimental mechanics (ICEM16), Cambridge, United Kingdom, 7-11 July 2014

Short publications in international conference proceedings not included in ISI Proceedings

C3 papers

[18] **Mathias Kersemans**, Ebrahim Lamkanfi, Wim Van Paepegem and Joris Degrieck. *Ultrasound as Non-Destructive Evaluation Tool*. 13th FEA PhD symposium, Ghent, Belgium, 2010.

[19] Jun Gu, Hugo Sol, Filip Zastavnik, Wim Van Paepegem and **Mathias Kersemans**. *An inverse method for local stiffness identification based on scanning laser measurements.* 12th Pan-American Congress of Applied Mechanics (PACAM XII), Port of Spain, Trinidad, 2-6 January, 2012.

[20] **Mathias Kersemans**, Wim Van Paepegem, Diederik Van Nuffel, Geert Luyckx, Ives De Baere, Filip Zastavnik, Jun Gu, Hugo Sol, Koen Van den Abeele and Joris Degrieck. *Polar scan technique for material characterization and identification of new operating regimes*. International Conference on Experimental Mechanics (ICEM15), Porto, Portugal, 22-27 July 2012.

[21] **Mathias Kersemans**, Koen Van Den Abeele, Wim Van Paepegem and Joris Degrieck. *Implications of structural discontinuities for water coupled NDT and SHM: experiment and modeling*. International Conference on Experimental Mechanics (ICEM15), Porto, Portugal, 22-27 July 2012.

[22] Ives De Baere, Stefan Jacques, **Mathias Kersemans**, Wim Van Paepegem and Joris Degrieck. *Experimental study of the crack growth of a carbon fabric reinforced PPS under mode I and mode II loading conditions*. International Conference on Experimental Mechanics (ICEM15), Porto, Portugal, 22-27 July 2012.

About the Author

Mathias Kersemans was born on December 2, 1982 in Lommel, Belgium. After his secondary school, he obtained an engineering degree both in Electromechanics (2005) and in Applied Physics (2008) from Ghent University. After his education, he worked as a lecturer at different locations. In April 2010, he returned to Ghent University to start his research work on ultrasonic NDT and material characterization in the department Materials Science and Engineering.

His research work entitled "Combined Experimental-Numerical Study to the Ultrasonic Polar Scan for Inspection and characterization of (Damaged) Anisotropic Materials" has been financially supported by the FWO-Flanders (Fonds voor Wetenschappelijk Onderzoek in Vlaanderen) through grant number G012010N. The work presented in this dissertation has been performed under the guidance of Prof. Wim Van Paepegem and Prof. Joris Degrieck.

Mathias Kersemans has assisted four years in the 1st bachelor course 'Ingenieursproject I', and successfully guided several bachelor and master thesis students in the field of NDT and Ultrasonics.

Mathias Kersemans is author of 17 scientific publications in international journals with peer-review (Science Citation Index SCI, Web of Science - Thomson Reuters), from which 11 publications as the first author. In addition, Mathias Kersemans has 1 publication in a popularizing scientific journal and 22 publications in international conference proceedings. He is a member of the 'Society for the Advancement of Materials and Process Engineering (SAMPE)'.